

# Flow around Oscillating Circular Cylinders

by

**Mehdi Nazarinia**

---

---

A Thesis submitted to Monash University  
for the degree of  
Doctor of Philosophy

---

---

March 2010

Department of Mechanical and Aerospace Engineering  
Monash University



*For Elham my dear wife,  
and  
For my parents, sister and brother.*



# Statement of Originality

I, Mehdi Nazarinia declare that this thesis is my own work and contains no material that has been accepted for the award of a degree or diploma in this, or any other, university. To the best of my knowledge and belief, information derived from the published and unpublished work of others has been acknowledged in the text of the thesis and a list of references is provided in the bibliography.

---

Candidate: Mehdi Nazarinia

Submitted: 31 March 2010



*If we knew what it was  
we were doing,  
it would not be called research,  
would it?*

Albert Einstein.





# Abstract

This thesis investigates the flow behind an oscillating circular cylinder, it consists of three main parts. The first part, using particle image velocimetry and flow visualisations, experimentally examines the near-wake of a circular cylinder oscillating translationally in a quiescent fluid, or, alternatively, oscillating flow past a stationary cylinder, at low amplitude and frequency. All but one of the two- and three-dimensional regimes of the Tatsuno & Bearman (1990) map were investigated. Cylinders in simple harmonic translational oscillations in a quiescent fluid exhibit a wide range of flow regimes over a range of amplitudes and frequencies. The identification and location of the different regimes has previously been done qualitatively using experimental visualisation of dye and particle shedding patterns. Here flow fields are presented that are successfully compared with previous experimental observations and numerical simulations. Each of the wake regimes are analysed and elucidated individually. Detailed quantitative results are compared with the previous studies.

The second part explores the effect of forced *combined* rotational and translational oscillatory motions in a quiescent fluid on the wake structures and three-dimensionality of flow. Previous two-dimensional numerical studies have shown that a circular cylinder undergoing combined oscillatory motion can generate thrust so that it will actually self-propel through a stationary fluid (Blackburn *et al.* 1999). Although, cylinders undergoing a single oscillation have been thoroughly studied, the combination of the two oscillations has received little attention until now. The research reported here extends the numerical study of Blackburn *et al.* (1999) experimentally and numerically. It records the vorticity fields of the wake and uses these to elucidate the underlying physics, examining the three-dimensional wake development experimentally, and determining the three-dimensional stability of the wake through a Floquet stability analysis. Experiments were performed for parameters that were shown previously to result in a net thrust *i.e.* the swimming cylinder case. The velocity fields were measured in multiple planes using particle image velocimetry. In particular, we confirm the thrust generation in a circular cylinder undergoing combined oscillatory motions. Importantly, we also find that the wake undergoes three-dimensional transition at low Reynolds numbers to a instability mode with a wavelength of about two cylinder diameters. The stability analysis indicates that the base flow is also unstable to another mode at slightly higher Reynolds numbers, broadly analogous to the three-dimensional wake transition

mode for a stationary circular cylinder, despite the distinct differences in wake/mode topology. The stability of these flows was confirmed by experimental measurements.

The third part of the research investigates the addition of cross flow to the *combined* oscillatory motion of the second part. The motivation of this part lies in its application to vortex-induced vibration and its suppression, and to bio-mimetic motion. Focus is on the effect of the phase difference between the two motions, which was found to be an important independent variable. The results show that there is an unexpected loss of synchronisation of the wake with the motion of the cylinder for a finite range of phase differences. The effect of velocity ratio between the two oscillatory motions on the synchronisation effect was also examined. It was found that at lower velocity ratios no evidence of synchronisation can be observed. Increasing the velocity ratio not only introduces synchronisation in the wake but also changes the shedding wake mode as well. Previous studies have extensively investigated the effect of these motions individually on cylinder wakes; however, the investigation of their combined effect is new.

# Acknowledgements

Firstly, I would like to express my gratitude to my supervisors, Prof. John Sheridan, Prof. Mark Thompson, Dr. David Lo Jacono and Dr. Josie Carberry for their guidance throughout my candidature. Since I began, both John and Mark have provided continual enthusiasm, direction and support without which this work would not have been possible. They all have had a critical influence on the work presented in this thesis. Prof. John Sheridan's sharp sense of logic and scientific method, and Prof. Mark Thompson's ability to explain complicated concepts in a simple way, have been integral in my development as a researcher and allowing me to write this thesis. In particular I would like to extend my heartfelt thanks to David who has both provided the numerical simulations employed in this thesis and for all the countless hours of guidance and technical assistance. David, I am truly thankful for the injection of energy.

Mention must be made also of the contribution of other FLAIR academic staff. Associate Professor Hugh Blackburn and Dr. John Elston are thanked for their continual support and guidance during the course of this research. Dr. Andreas Fouras is thanked for his assistance in providing some of the experimental equipments, and in particular his work on the PIV software. To Professor Kerry Hourigan and Drs. Kris Ryan and Greg Sheard, I extend my thanks for providing critical feedbacks on my work and your help during my candidature. Also my thanks go to Dr. Justin Leontini for his valuable time and discussions throughout this work and also for proof-reading parts of this thesis.

For making my candidature such an enjoyable experience, I would like to thank all of my fellow postgraduate students in the Department of Mechanical and Aerospace Engineering with whom I shared an office, laboratory or corridor, but especially my lab cohorts, who all contributed to the thesis in their own particular way. In no particular order, my thanks go to Mr. Michael Sherry, Mr. Jisheng Zhao, Dr. Karlis Atvars, Dr. Hyeok Lee, Dr. Patryk Burka, Dr. Joe Berry and Dr. Martin Griffith. Your company, good times and many critical discussions on topics that even occasionally related to fluid dynamics are greatly appreciated. Thank you for providing good company and a stimulating environment for research over the course of our degrees. These guys have made my work a joy, and have left me with many fond memories of postgraduate life.

PhD research requires resources, and I am grateful to the Department of Mechanical and Aerospace Engineering, Monash University, for providing the office space and

resources necessary for the completion of this study and also financially supporting at various stages of my candidature in the form of a Monash Departmental Scholarship. Furthermore, I wish to acknowledge the support of a Monash Graduate Scholarship (MGS) and Monash International Postgraduate Research Scholarship (MIPRS). Thank you also to Jane Moodie for suggesting structural and language improvements throughout the preparation process of my thesis. Support at various stages of candidature was also given to me by Stelios Konstantinidis, Helen Frost, Hugh Venables and Ken Sheridan which I am grateful for all their support. Most importantly I extend my thanks to the Mechanical and Aerospace Engineering Department's staff who made things happen.

For the support of my family and friends I am indebted. Mum, dad, Honey and Ali, without your constant support and belief in me over many years, I just would not have been capable of completing this thesis.

Lastly, but most importantly, I must extend my gratitude to my wife, Elham. Your love, support and understanding continue to astound me, and inspire me. Thank you.

# List of Publications

## Arising from the work reported in this Thesis

### Journal papers

NAZARINIA, M., LO JACONO, D., THOMPSON, M. C. & SHERIDAN, J. 2010 An experimental study of the near-wake structure of a cylinder undergoing combined translational and rotational oscillatory motions. *in preparation for submission to Physics of Fluids*.

NAZARINIA, M., LO JACONO, D., THOMPSON, M. C., SHERIDAN, J. & CARBERRY, J. 2010 An experimental study of flow structures generated by a circular cylinder oscillating in a quiescent fluid. *in preparation for submission to J. Fluid Mech.*

NAZARINIA, M., LO JACONO, D., THOMPSON, M. C. & SHERIDAN, J. 2009 The three-dimensional wake of a cylinder undergoing a combination of translational and rotational oscillation in a quiescent fluid. *Physics of Fluids* **21** (6), 064101.

NAZARINIA, M., LO JACONO, D., THOMPSON, M. C. & SHERIDAN, J. 2009 Flow behind a cylinder forced by a combination of oscillatory translational and rotational motions. *Physics of Fluids* **21**, (5), 051701.

### Conference papers

NAZARINIA, M., LO JACONO, D., THOMPSON, M. C. & SHERIDAN, J. 2010 An experimental study of the near-wake structure of a cylinder undergoing combined translational and rotational oscillatory motions. *In the proceedings of the 7th International Symposium on Fluid-Structure Interactions, Flow-Sound Interactions, and Flow-Induced Vibration & Noise*, Montreal, Canada, 1–4 August 2010.

NAZARINIA, M., LO JACONO, D., THOMPSON, M. C. & SHERIDAN, J. 2009 Flow around a cylinder swimming in a quiescent fluid. *In proceedings of the 7th World Conference on Experimental Heat Transfer, Fluid Mechanics and Thermodynamics*, Krakow, Poland, 28 June – 03 July 2009.

NAZARINIA, M., LO JACONO, D., CARBERRY, J., THOMPSON, M. C. & SHERIDAN, J. 2008 The three-dimensional wake of a swimming cylinder. *In proceedings of the 61st APS DFD meeting*, San Antonio, Texas, USA, 23–25 November 2008.

LO JACONO, D., NAZARINIA, M., THOMPSON, M. C. & SHERIDAN, J. 2008 Flow behind a cylinder forced by a combination of oscillatory translational and rotational motions. *In proceedings of the XXII International Congress of Theoretical and Applied Mechanics (ICTAM)*, Adelaide, South Australia, Australia, 25–28 August 2008.

WADE, S., NAZARINIA, M., WONG, S. B. & LO JACONO, D. 2008 Fibre Bragg Grating use in Fluid Dynamic Studies. *In proceedings of The 19th International Conference on Optical Fibre Sensors (OFS-19)*, Perth, Western Australia, Australia, 14–18 April 2008.

NAZARINIA, M., SHERIDAN, J., THOMPSON, M. C. & CARBERRY, J. 2007 PIV Study of the Vortex Wake behind a Translationally Oscillating Cylinder in a Quiescent Fluid. *In proceedings of The 16th Australasian Fluid Mechanics Conference (16AFMC)*, Crown Plaza, Gold Coast, Australia, 2–7 December 2007.

## **Arising from other work conducted during candidature**

### **Journal papers**

LO JACONO, D., NAZARINIA, M. & BRØNS, M. 2009 Experimental vortex breakdown topology in a cylinder with a free surface. *Physics of Fluids* **21**, (11), 111704.

# Nomenclature

## Abbreviations

Symbol	Description
2D	two-dimensional
2D-PIV	planar particle image velocimetry
3D	three-dimensional
CCD	charge coupled device
DNS	Direct Numerical Simulation
FLAIR	Fluids Laboratory for Aeronautical and Industrial Research
Hz	Hertz
LDV	laser Doppler velocimetry
PIV	particle image velocimetry
TTL	transistor-transistor logic
VIV	Vortex-induced vibration

## English Symbols

Symbol	Description
$A_\theta$	Amplitude of rotational oscillation in radians
$A_t$	Amplitude of translational oscillation
$D$	Cylinder diameter
$f$	frequency of oscillation (Hz)
$f_N$	Natural frequency of vortex shedding (Hz)
$f_v$	Frequency of vortex shedding (Hz)
$F_R$	Frequency ratio between translational and rotational oscillation = $f_t/f_\theta$
$F_{RN}$	Frequency ratio between oscillatory motion and natural frequency = $f/f_N$

*Continued on next page...*

*Continued from previous page...*

<b>Symbol</b>	<b>Description</b>
$F_{Rt}$	Frequency ratio between translational oscillation and natural frequency = $f_t/f_N$
$F_{R\theta}$	Frequency ratio between rotational oscillation and natural frequency = $f_\theta/f_N$
$k$	Spanwise wavenumber
$KC$	Keulegan-Carpenter number
$L/D$	cylinder length/diameter ratio
$M$	camera magnification factor (px/mm)
px	pixels
$Re$	Reynolds number based on free-stream velocity and cylinder diameter
$St$	Strouhal number
$t$	Time
$\mathcal{T}$	Temperature ( $^{\circ}\text{C}$ )
$T$	Oscillation period
$U, V, W$	Velocity components in the x (streamwise), y (transverse) and z (spanwise) directions, respectively
$U_{\max}$	Peak velocity of an oscillating cylinder
$U_\infty$	Free-stream velocity
$V_R$	Velocity ratio between translational and rotational oscillation = $U_{\max_t}/U_{\max_\theta}$
$x, y, z$	rectangular Cartesian coordinates in physical space (mm)
$X, Y, Z$	rectangular Cartesian coordinates in image space (px)

## Greek Symbols

<b>Symbol</b>	<b>Description</b>
$\S$	Thesis section
$\int$	Integration
$\beta$	Stokes number
$\delta$	standard deviation
$\Delta x, \Delta y, \Delta z$	change in $x, y, z$ location in physical space (mm)
$\Delta X, \Delta Y$	change in $X, Y$ location in image space (px)
$\Delta t$	PIV time interval separating each image pair (ms)

*Continued on next page...*



Continued from previous page...

Symbol	Description
$\Gamma$	circulation
$\eta$	The angle between the transverse oscillation motion and the free-stream
$\lambda$	Spanwise wavelength
$\lambda_c$	Critical spanwise wavelength
$\mu$	Dynamic viscosity ( $\text{kg}\cdot\text{m}^{-1}\cdot\text{s}^{-1}$ ), Floquet multiplier
$\nu$	Kinematic viscosity, $\mu/\rho$ ( $\text{m}^2\cdot\text{s}$ )
$\omega_x, \omega_y, \omega_z$	Vorticity components along the x, y and z axis respectively ( $\text{s}^{-1}$ )
$\psi$	Angle between translational oscillation and free-stream flow
$\rho$	Density ( $\text{kg}\cdot\text{m}^{-3}$ )
$\sigma$	Floquet exponent = $\log(\mu/T)$
$\theta$	Angular displacement
$\Phi$	Phase angle between rotational and translational motions

## Subscripts & Superscript

Symbol	Description
$\theta$	rotational oscillation component
<i>avg</i>	average
<i>cyl</i>	cylinder
f	fluid
<i>i, j, k</i>	spatial coordinate indices
<i>max</i>	maximum addition value
p	particle
rand	random component
rms	root-mean-square value
<i>t</i>	translational oscillation component
$\infty$	free-stream value
<i>'</i>	fluctuating value



# Contents

<b>1</b>	<b>Introduction</b>	<b>1</b>
	Structure of the Thesis . . . . .	4
<b>2</b>	<b>Literature Review</b>	<b>5</b>
2.1	Introduction . . . . .	5
2.2	Flow past a fixed cylinder . . . . .	6
2.2.1	Wake regimes: Variation with Reynolds number . . . . .	8
2.2.1.1	Laminar Steady Regime ( $0 < Re < 49$ ) . . . . .	8
2.2.1.2	Primary Wake Instability ( $Re \simeq 49$ ) . . . . .	10
2.2.1.3	Laminar Vortex Shedding Regime ( $49 < Re < 140 - 190$ ) . . . . .	11
2.2.1.4	Secondary Instability ( $Re \simeq 190$ ) . . . . .	11
2.2.1.5	3-D Wake Transition Regime ( $190 < Re < 260$ ) . . . . .	12
2.2.1.6	Fine Scale 3-D Wake Regime ( $260 < Re < 1000 - 2000$ ) . . . . .	14
2.3	Flow past a translationally oscillating cylinder . . . . .	15
2.3.1	Transverse Oscillations . . . . .	16
2.3.1.1	Lock-on . . . . .	17
2.3.1.2	Vortex Shedding Structures and Wake modes . . . . .	21
2.3.2	In-line and Oblique Oscillations . . . . .	24
2.4	Flow Past a Rotationally Oscillating Cylinder . . . . .	26
2.5	Translational Oscillation in Quiescent Fluid . . . . .	32
2.6	Combined Rotational and Translational Oscillation Motion . . . . .	48
2.6.1	Carangiform Motion . . . . .	58
2.7	Summary . . . . .	59

<b>3</b>	<b>Experimental Methodology</b>	<b>61</b>
3.1	Introduction . . . . .	61
3.2	Problem definition and Parameter Space . . . . .	61
3.3	Experimental Set-up . . . . .	63
3.3.1	Flow System . . . . .	63
3.3.1.1	Quiescent Fluid . . . . .	63
3.3.1.2	Streaming Flow . . . . .	63
3.3.2	Experimental Apparatus . . . . .	64
3.3.2.1	Cylinder Model and Coordinates . . . . .	65
3.3.2.2	Motion Controller and Stepper Motors . . . . .	68
3.3.2.3	Means of obtaining Quiescent Flow . . . . .	70
3.3.3	Experimental measurement systems . . . . .	72
3.3.3.1	Flow Visualisation . . . . .	73
3.3.3.2	PIV - Particle Image Velocimetry imaging system . . . . .	74
3.3.4	Experimental procedures . . . . .	79
3.3.4.1	PIV measurement procedure . . . . .	79
<b>4</b>	<b>Translationally oscillating cylinder in quiescent fluid</b>	<b>85</b>
4.1	Introduction . . . . .	85
4.2	Experimental Arrangement and Parameters . . . . .	87
4.3	Flow Visualisation . . . . .	88
4.3.1	Validation . . . . .	88
4.3.2	Results . . . . .	88
4.3.2.1	Case I: Regime A*, Two-dimensional patterns without vortex shedding and flow separation . . . . .	89
4.3.2.2	Case II: Regime A, Symmetrical patterns with vortex shedding; two-dimensional . . . . .	92
4.3.2.3	Case III: Regime B, Onset of three-dimensional insta- bility; longitudinal vortices . . . . .	95

4.3.2.4	Case IV: Regime C, Rearrangement of large vortices; three-dimensional . . . . .	95
4.3.2.5	Case V: Regime D, Flow convected obliquely to one side of the axis of oscillation; three-dimensional . . . . .	95
4.3.2.6	Case VI: Regime E, Irregular switching of flow convection direction; three-dimensional . . . . .	100
4.3.2.7	Case VII: Regime F Flow convected diagonally; three-dimensional . . . . .	100
4.3.2.8	Case VIII: Regime G, Transverse vortex street; three-dimensional . . . . .	104
4.4	PIV results . . . . .	106
4.4.1	Validation . . . . .	106
4.4.2	Generation and decay of vorticity . . . . .	107
4.4.3	Regime A* . . . . .	110
4.4.4	Regime A . . . . .	122
4.4.5	Regime B . . . . .	124
4.4.6	Regimes D . . . . .	139
4.4.7	Regime E . . . . .	141
4.4.8	Regimes F . . . . .	143
4.5	Chapter Summary . . . . .	149
<b>5</b>	<b>The ‘Swimming’ Cylinder</b>	<b>151</b>
5.1	Introduction . . . . .	151
5.2	Experimental Arrangement and Parameters . . . . .	153
5.3	Validation . . . . .	156
5.4	Numerical formulation . . . . .	157
5.5	Experimental technique: Spanwise wavelength measurement . . . . .	159
5.5.1	Autocorrelation . . . . .	159
5.5.2	Wavelength Extraction . . . . .	160
5.6	Results and discussions . . . . .	162

5.6.1	Wake profile in the streamwise direction . . . . .	163
5.6.1.1	Comparison between experimental and numerical re- sults: Effect of varying $\Phi$ . . . . .	167
5.6.2	Wake profile in the spanwise direction . . . . .	169
5.6.2.1	Spanwise PIV set-up . . . . .	169
5.6.2.2	Effect of varying Reynolds number . . . . .	170
5.7	Chapter Summary . . . . .	177
<b>6</b>	<b>Combined translational and rotational oscillatory motion in free-stream</b>	<b>181</b>
6.1	Introduction . . . . .	181
6.2	Experimental Arrangement and Parameters . . . . .	182
6.3	Results . . . . .	187
6.3.1	Effect of varying $V_R$ . . . . .	187
6.3.2	Comparison with numerical simulations . . . . .	197
6.3.3	Effect of varying $F_{RN}$ . . . . .	205
6.3.4	Effect of varying $F_R$ . . . . .	207
6.4	Chapter Summary . . . . .	209
<b>7</b>	<b>Conclusions and recommended future work</b>	<b>223</b>
7.1	Translational Oscillations of a Circular Cylinder . . . . .	223
7.2	The “Swimming” Cylinder . . . . .	224
7.3	Combined translational and rotational oscillatory motion in free-stream	225
7.4	Recommendations for Future Work . . . . .	227
<b>A</b>	<b>Symmetry Definitions</b>	<b>229</b>
<b>B</b>	<b>Journal publications arising from research reported in this thesis</b>	<b>231</b>
<b>C</b>	<b>Other publications during candidature</b>	<b>243</b>
	<b>Bibliography</b>	<b>248</b>

# List of Tables

2.1	Flow patterns observed in previous investigations, TB=Tatsuno & Bearman (1990). . . . .	49
4.1	Flow Visualisation test cases conducted in this chapter. One value of $KC_t$ and $\beta_t$ was chosen as a representative of each regime. . . . .	86
4.2	Experimental (PIV) test cases conducted in this chapter. One value of $KC_t$ and $\beta_t$ was chosen as a representative of each regime. . . . .	89
6.1	Summary of the values of $A_t$ and $A_\theta$ used when $F_R=1.0$ . . . . .	184
6.2	Summary of the synchronisation around the unlocked regime. L (light green), QP (orange) and C (dark red) stands for locked-on, quasi-periodic and chaotic respectively. The unlocked regime (UL, dark red) for the experimental results are likely to be chaotic. $f_t$ and $f_N$ stands for forced frequency and natural frequency for a fixed cylinder. . . . .	202





# List of Figures

2.1	Kármán vortex street behind a circular cylinder at $Re = 105$ . The image shows streaklines produced by electrolytic precipitation in water. <i>Photograph by Sadatoshi Taneda and is then reproduced from Van Dyke (1982)</i> . . . . .	8
2.2	Regimes of flow around a smooth circular cylinder in steady current. <i>Reproduced from Sumer &amp; Fredsøe (1997)</i> . . . . .	9
2.3	The shear layer. The shear layer on both sides roll up to form the lee-wake vortices, vortices A and B. <i>Reproduced from Sumer &amp; Fredsøe (1997)</i> . . . . .	9
2.4	Variation of Strouhal number with Reynolds number for the cylinder wake. Shown are experimental results: $\circ$ , Williamson (1989); $\bullet$ , Ham-mache & Gharib (1991) and numerical results: $+$ , Barkley & Henderson (1996). Wake instabilities up to $Re = 300$ are labelled: $Re_1$ (the primary instability), $Re_2$ (the secondary instability) and $Re'_2$ (a point of further three-dimensional instability; the trinary instability (Elston 2005)). <i>Re-produced from Barkley &amp; Henderson (1996)</i> . . . . .	10
2.5	The saturated mode structure for mode B (left), and mode A (right). The bottom images were obtained through dye visualisation during ex-periments such as those by Williamson (1996c). The top images were obtained through particle tracking three-dimensional simulations such as those by Thompson <i>et al.</i> (1996). Both show the development of span-wise vortices. The waviness of the vortex cores in mode A is clear, as is the finer-scale structure of mode B. Flow is from left to right. <i>Reproduced from Thompson et al. (2006b)</i> . . . . .	15

2.6	Primary lock-on regime. Shown are the boundaries of the lock-on regime as a function of the frequency ratio between the excitation and natural shedding frequency and the non-dimensionalised amplitude of oscillation. Low Reynolds number results from Koopmann (1967) are at: $\Delta$ , $Re = 100$ ; $\square$ , $Re = 200$ and $\circ$ , $Re = 300$ . The experimental results of Cheng & Moretti (1991) were obtained at Reynolds numbers of 1500, $\blacksquare$ , and 1650, $\blacktriangle$ ; <i>The graph appeared in Elston (2005) and is reproduced by permission.</i> . . . . .	20
2.7	Map of vortex synchronisation patterns near the fundamental lock-on region. The critical curve marks the transition from one mode of vortex formation to another. <i>Reproduced from Williamson &amp; Roshko (1988).</i> . . . . .	22
2.8	The major wake modes during synchronised VIV and driven oscillation. Left: the $2P$ mode (Williamson & Roshko 1988). Top right: the $2S$ mode (Koopmann 1967). Bottom right: the $P + S$ mode (Williamson & Govardhan 2004). Flow is from left to right in all images. <i>The graph appeared in Leontini (2007) and is reproduced by permission.</i> . . . . .	23
2.9	Representation of basic modes of vortex formation from cylinder oscillating translationally at angle $\eta$ with respect to the free-stream. <i>The graph originally appeared in Ongoren &amp; Rockwell (1988b) and then is reproduced from Al-Mdallal (2004) by permission.</i> . . . . .	23
2.10	Spanwise correlation of vortex shedding for a rigid cylinder during lock-on. <i>The graph originally appeared in Blevins (1977) and then is reproduced from Elston (2005) by permission.</i> . . . . .	24
2.11	Streamline and streak-line patterns at $Re = 33.7$ , $D = 1.0\text{cm}$ , $\theta = 45^\circ$ . (a) $St_f = 0$ , (b) $St_f = 3.4$ . At a critical frequency of oscillation the wake region behind the cylinder is much reduced. <i>Reproduced from Taneda (1978a).</i> . . . . .	27

2.12	Cylinder wake mean velocity profiles, measured at midspan ( $\Omega_1 = 2$ ): □, unforced; ○, $St_f \approx 0.2$ ; △, $St_f \approx 1$ (Tokumaru & Dimotakis 1991). <i>The graph appeared in Elston (2005) and is reproduced by permission.</i> . . . . .	28
2.13	Effect of forcing amplitude on the wake. The forcing frequency is $F_\theta = 5$ (low drag situation), the forcing amplitude is (a) $\Omega = 1$ , (b) $\Omega = 2$ , (c) $\Omega = 4$ , (d) $\Omega = 5$ , (e) $\Omega = 7$ and (f) $\Omega = 9$ . <i>Reproduced from Thiria et al. (2006).</i> . . . . .	31
2.14	Contours of vorticity of the two-dimensional base flow past a cylinder undergoing several amplitudes of rotation at $Re = 300$ . The flow is from left to right. The amplitudes of the imposed rotation are expressed in radians. Amplitude of rotation ( $A_\theta$ ) increases as: $A_\theta = 0, 0.20, 0.40, 0.60, 0.80, 1.00$ from (a) to (f), respectively. All the images are taken at $\theta = 0$ . White (black) represents positive (negative) vorticity. For all the cases considered the near-wake was synchronized to the forcing frequency. <i>Reproduced from Lo Jacono et al. (2010).</i> . . . . .	32
2.15	Secondary streaming induced by an oscillating cylinder. This image was produced by illuminating glass beads with a stroboscope. The image was taken at an oscillation amplitude of $A_t/D = 0.085$ and at $Re = 70$ (based on frequency). <i>Reproduced from Van Dyke (1982). Photograph by Masakazu Tatsuno.</i> . . . . .	35
2.16	An approximate guide to the flow patterns from an oscillating cylinder as a function of the $KC$ number. Annotations describe the number of vortices shed per oscillation half-cycle. Regimes are based on observations conducted for $\beta$ values of 255 and 730. <i>Reproduced from Williamson (1985).</i> . . . . .	36
2.17	Transverse street wake for $KC = 12.0$ . The cylinder is approaching its lowest point of its oscillation. This regime is delineated by the distinctive trail of vortices which convects away at around $90^\circ$ to the oscillation axis. <i>Reproduced from Williamson (1985).</i> . . . . .	37

2.18	Parameter-space map created by Tatsuno & Bearman (1990) identifying eight different flow regimes in the $(KC_t-\beta_t)$ plane indicated. A: symmetric with vortex shedding, two-dimensional; A: symmetric and attached, two-dimensional; B: longitudinal vortices, three-dimensional streaked flow; C: rearrangement of large vortices, three-dimensional; D: transverse street, three-dimensional; E: transverse street with irregular switching, three-dimensional; F: diagonal double-pair, three-dimensional; G: transverse vortex street, three-dimensional. The triangles indicate the cases investigated here. <i>Reproduced from Tatsuno &amp; Bearman (1990) by permission.</i> . . . . .	39
2.19	Two-dimensional visualisations of the vortex shedding patterns found for Regimes A*–G. The cylinder is shown oscillating along the horizontal axis of the page. The image for regime F appeared in Tatsuno & Bearman (1988), while the others are from Tatsuno & Bearman (1990); <i>All images are reproduced with their permission.</i> . . . . .	40
2.20	Visualisations of the three-dimensional structures observed in Regimes B to F. The images were produced using an electrostatic precipitation method and show the variation in the flow along the cylinder span. The span of the cylinder ( $z$ -axis) is orientated horizontally in all these images with the cylinder oscillating along the $y$ -axis. Images (a), (d), (f), (g) and (h) are taken in the $y-z$ plane while images (b), (c) and (e) are taken in the $x-z$ plane. Presented are Regime B [(a), (b) & (c)], Regime C [(d) & (e)], Regime D [(f)], Regime E [(g)] and Regime F [(h)]. <i>All the images appeared in Tatsuno &amp; Bearman (1990) and are reproduced with their permission.</i> . . . . .	42
2.21	Locations and characteristics of the primary and secondary symmetry-breaking bifurcations. <i>Reproduced from Elston et al. (2006).</i> . . . . .	46

2.22	Interrelation of vortex pattern with secondary flow stream. (a) Mode I, lateral vortex street; (b) mode I, inclined vortex street; (c) mode II; (d) mode III. Bold arrows: secondary flow stream; dotted arrows: ambient water flow; dot-dashed lines: typical length of cylinder stroke. <i>Reproduced from Lam et al. (2010).</i> . . . . .	47
2.23	Instantaneous vorticity contours for a cylinder with both translational and rotational oscillation, shown at $t/T = 45.75$ for a range of phase angles: (a), $\Phi = 0^\circ$ ; (b), $\Phi = 22.5^\circ$ ; (c), $\Phi = 45^\circ$ ; (d), $\Phi = 67.5^\circ$ ; (e), $\Phi = 90^\circ$ ; (f), $\Phi = 112.5^\circ$ ; (g), $\Phi = 135^\circ$ ; (h), $\Phi = 157.5^\circ$ . <i>The graph originally appeared in Blackburn et al. (1998) and then is reproduced from Elston (2005) by permission.</i> . . . . .	52
2.24	Flows produced by a cylinder with oscillatory translation and rotation: (a) instantaneous vorticity contours; (b) fluid particle transport. The cylinder is at its maximum vertical position and most negative angular displacement at the instant shown. The rest position of the cylinder is indicated by cross-hairs, and the radial line shows the radial displacement of the cylinder from the horizontal. <i>The graph originally appeared in Blackburn et al. (1999) and then is reproduced from Elston (2005) by permission.</i> . . . . .	53
2.25	Flows produced by a cylinder with oscillatory translation and rotation with no restraints applied in the horizontal direction: (a) instantaneous vorticity contours; (b) fluid particle transport. The cylinder is moving at terminal speed in the $-x$ direction. <i>The graph originally appeared in Blackburn et al. (1999) and then is reproduced from Elston (2005) by permission.</i> . . . . .	53
2.26	Representation of basic modes of vortex formation from cylinder undergoing combined translational and rotational oscillation. <i>Reproduced from Al-Mdallal (2004) by permission.</i> . . . . .	55

2.27	Equivorticity lines over one period of oscillation, $T$ , for the combined transverse and rotational oscillation case ( $\eta = 90^\circ$ , $15^\circ \leq A_\theta \leq 75^\circ$ ) when $Re = 855$ , $A_t/D = 0.26$ : $f/f_N = 1$ ( $T = 9.09, 81.82 \leq t \leq 90.91$ ). <i>Reproduced from Al-Mdallal (2004) by permission.</i> . . . . .	57
2.28	Equivorticity lines over one period of oscillation, $T$ , for the combined in-line and rotational oscillation case ( $\eta = 0^\circ$ , $15^\circ \leq A_\theta \leq 75^\circ$ ) when $Re = 855$ , $A_t/D = 0.26$ : $f/f_N = 1$ ( $T = 9.09, 81.82 \leq t \leq 90.91$ ). <i>Reproduced from Al-Mdallal (2004) by permission.</i> . . . . .	58
2.29	Carangiform motion involves a twist at each extreme of the oscillation. Successive positions a, b, c, d and e, assumed by a lunate tail's airfoil cross-section at equal time-intervals, are sketched for half of the cycle of oscillation. The other half of the cycle is a mirror image of that shown. <i>Reproduced from Lighthill (1989).</i> . . . . .	59
3.1	A photograph showing cylinder and oscillation system in the tank working section. . . . .	64
3.2	Water tank assembly. . . . .	65
3.3	Schematic showing dimensions of the circular cylinder model. . . . .	66
3.4	Schematic of the problem geometry and important parameters relevant to the oscillatory forcing motions. (a): the two-dimensional overview ( $xy$ -plane) of the cylinder and the sinusoidal motions parameters, (b): spanwise view of the cylinder ( $yz$ -plane) with end plate and field of view (PIV), (c): the two-dimensional overview of the cylinder and the sinusoidal motion parameters in a free-stream. . . . .	67
3.5	A photograph showing the rotational stepper motor housed in a bracket, where the circular cylinder is vertically mounted to. . . . .	69
3.6	Schematic of the 2-axis controller, drivers, digital scale and PC used. . .	70
3.7	A photograph showing the controller and the oscilloscope inside the box!. . .	70
3.8	Schematic of the digital scale. . . . .	71

3.9	Room and water temperature variation during the course of experiment for different days throughout the year. The horizontal axis shows time in hour and the vertical axis shows the temperature. The solid line denotes the room temperature, whereas the dashed line denotes water temperature.	71
3.10	A photograph showing the honeycomb used to settle the flow for the quiescency experiments.	72
3.11	This figure shows a sample quiescency case, $KC=5$ , $\beta=20$ and $U_{\max}=5.56$ mm s <sup>-1</sup> . The vertical axis shows the norms of either standard deviation of the velocity fields (red color) or the velocity fields (black color). The horizontal axis is showing the time in hours. The average room temperature during the quiescency experiments is 18.1°C.	73
3.12	Comparison of quiescency with (black color) and without (red color) honeycomb, $KC=5$ , $\beta=20$ and $U_{\max}=5.56$ mm s <sup>-1</sup> . The vertical axis shows the velocity norms of the measurement field. The horizontal axis is showing the time in hours. The average room temperature for the cases with and without honeycomb are 21.4°C and 22.0°C, respectively	74
3.13	A sample of (a) instantaneous and (b) phase-averaged PIV results. (c) shows a typical harmonic motion of the cylinder and the circles on the curve show the pre-selected phase in the cycle at which the PIV images were taken. The measurement has been taken over a translationally oscillating cylinder at $KC_t=6.25$ , $\beta_t=18$ corresponding to regime D of Tatsuno & Bearman (1990), refer to §2.3 and §4.4.6 for further information. The arrows represent the direction of the oscillation.	77
3.14	Schematic of PIV imaging system.	82
3.15	A photograph showing the experimental PIV set-up and the laser sheet.	83
4.1	Comparison of the flow visualisation of the present study with Tatsuno & Bearman (1990), Regime D: (a) Present study: $KC=8.17$ , $\beta=11.11$ , exposure time=1.6 sec; (b) Tatsuno & Bearman (1990): $KC_t=8.16$ , $\beta_t=11.0$ , exposure time=2 sec.	90

4.2	Plane views of flows at various stages of motion in regime A* (case 1 in table 4.1) showing flow patterns and structures for over half a cycle: Flow visualisation method, $A_t = 10$ mm, $f_t = 0.132$ Hz (equivalent to $KC_t = \pi$ , $\beta_t = 53$ , respectively), exposure time=0.6 sec. (a) is showing the cylinder at its left most position and starting its motion from left to right and (h) is showing the cylinder at the most right end of its motion, the end of first half cycle. The arrow in image (a) shows the direction of oscillation. . . . .	91
4.3	Numerically generated particle shedding image. Over 15 periods of motion conducted at $KC_t=2$ , $\beta_t=80$ , with two-dimensional DNS, ten equally spaced points on the cylinder surface released massless particles into the surrounding fluid; <i>the image appeared in Elston (2005) and reproduced by permission.</i> . . . . .	93
4.4	Plane views of flows at various stages of motion in regime A (case 2 in table 4.1) showing flow patterns and structures for over half a cycle: Flow visualisation method, $A_t = 26$ mm, $f_t = 0.02$ Hz (equivalent to $KC_t = 8.17$ , $\beta_t = 8.11$ , respectively), exposure time=1.1 sec. (a) is showing the cylinder at its left most position and starting its motion from left to right and (h) is showing the cylinder at the most right end of its motion, the end of the first half of the cycle. The arrow in image (a) shows the direction of oscillation. . . . .	94
4.5	Plane views of flows at various stages of motion in regime C (case 4 in table 4.1) showing flow patterns and structures for over half a cycle: Flow visualisation method, $A_t = 14$ mm, $f_t = 0.11$ Hz (equivalent to $KC_t = 4.40$ , $\beta_t = 44.44$ , respectively), exposure time=1.0 sec. (a) is showing the cylinder at its left most position and starting its motion from left to right and (e) is showing the cylinder at the most right end of its motion, the end of first half cycle. The arrow in image (a) shows the direction of oscillation. . . . .	96



4.6	Plane views of flows at various stages of motion in regime D (case 5 in table 4.1) showing flow patterns and structures for over half a cycle: Flow visualisation method, $A_t = 26$ mm, $f_t = 0.0275$ Hz (equivalent to $KC_t = 8.17$ , $\beta_t = 11$ , respectively), exposure time=1.6 sec. (a) is showing the cylinder at its left most position and starting its motion from left to right and (h) is showing the cylinder at the most right end of its motion, the end of first half cycle. The arrow in image (a) shows the direction of oscillation. . . . .	97
4.7	Plane views of flows at various stages of motion in regime E (case 6 in table 4.1) showing flow patterns and structures for over half a cycle: Flow visualisation method, $A_t = 20$ mm, $f_t = 0.0655$ Hz (equivalent to $KC_t = 2\pi$ , $\beta_t = 26.23$ , respectively), exposure time=1.0 sec. (a) is showing the cylinder at its left most position and starting its motion from left to right and (h) is showing the cylinder at the most right end of its motion, the end of first half cycle. The arrow in image (a) shows the direction of oscillation. . . . .	101
4.8	Plane views of flows at various stages of motion in regime F (case 7 in table 4.1) showing flow patterns and structures for over half a cycle: Flow visualisation method, $A_t = 40$ mm, $f_t = 0.454$ Hz (equivalent to $KC_t = 12.57$ , $\beta_t = 18.16$ , respectively), exposure time=1.0 sec. (a) shows the cylinder at its left most position and starting its motion from left to right and (h) is showing the cylinder at the most right end of its motion, the end of first half cycle. The arrow in image (a) shows the direction of oscillation. . . . .	102
4.9	Instantaneous vorticity contours for two-dimensional flow in regime F shown at $y = y_{max}$ . The flows were computed at: <b>(a)</b> $KC_t = 8$ , $\beta_t = 25.0$ ; and <b>(b)</b> $KC_t = 10$ , $\beta_t = 20.0$ . The arrows in the figure shows the single vortex shed per cycle. <i>The image appeared in Elston (2005) and reproduced by permission.</i> . . . . .	104

4.10	Plane views of flows at various stages of motion in regime G (case 8 in table 4.1) showing flow patterns and structures for over half a cycle: Flow visualisation method, $A_t = 26.25$ mm, $f_t = 0.967$ Hz (equivalent to $KC_t = 8.25$ , $\beta_t = 38.68$ , respectively), exposure time=0.5 sec. (a) is showing the cylinder at its left most position and starting its motion from left to right and (h) is showing the cylinder at the most right end of its motion, the end of first half cycle. The arrow in image (a) shows the direction of oscillation. . . . .	105
4.11	Comparison of the present PIV results with numerical results of Iliadis & Anagnostopoulos (1998) in regime A*. The full lines represent positive (counter-clockwise) and the broken lines negative (clockwise) values of vorticity. (a) Present study, $KC_t = 3$ & $\beta_t = 30$ ; (b) Iliadis & Anagnostopoulos (1998)'s study, $KC_t = 2$ & $\beta_t = 100$ . . . . .	108
4.12	Comparison of the velocity components at three cross-sections of the translationally oscillating cylinder in a quiescent fluid at constant $y/D$ values. The $y/D$ values from the top to bottom rows are $-0.6$ , $0.0$ , $0.6$ and $1.2$ , respectively. The measurements are taken at $KC_t = 5$ and $\beta_t = 20$ , similar to previous numerical and experimental results (Dütsch <i>et al.</i> 1998). This places the flow generated from the cylinder in two-dimensional regime A (see figure 2.18). The left column depicts the $V/U_{\max_t}$ and the right column $U/U_{\max_t}$ . The solid lines (red) show the present experiment, the dashed lines (black) the present numerical simulation and the filled circle points (blue) the experimental results of Dütsch <i>et al.</i> (1998). . . . .	109
4.13	Distance between the two streaked flows on one side of a cylinder in regime B (wavelength, $\lambda/D$ ). $\bullet$ , $KC_t=3.77$ ; $\ominus$ , $KC_t=3.35$ ; $\circ$ , $KC_t=3.14$ ; $\oplus$ , $KC_t=2.51$ ; $\oplus$ , $KC_t=2.09$ ; the image appeared in Tatsuno & Bearman (1990) and is reproduced by permission. . . . .	110

4.14	A sequence of phase-averaged non-dimensionalised out-of-plane vorticity contours, $\omega_z^*$ , extracted over one motion period, $T$ , at $KC_t = 3$ , $\beta_t = 30$ in regime A*. Positive (counter-clockwise) and negative vorticity contours are denoted by red and blue colours, respectively. Vorticity contours are evenly spaced over the range [-6.0:6.0]; with $\Delta[\omega_z^*] = 0.6$ . . . . .	112
4.15	A sequence of phase-averaged non-dimensionalised $V$ velocity contours, extracted over one motion period, $T$ , at $KC_t = 3$ , $\beta_t = 30$ in regime A*. Positive and negative velocity contours are denoted by red and blue colours respectively. $V$ velocity contours are evenly spaced over the range [-0.8:0.8]; with $\Delta[V/U_{\max}] = 0.08$ . . . . .	113
4.16	A sequence of phase-averaged non-dimensionalised $U$ velocity contours, extracted over one motion period, $T$ , at $KC_t = 3$ , $\beta_t = 30$ in regime A*. Positive and negative velocity contours are denoted by red and blue colours respectively. $U$ velocity contours are evenly spaced over the range [-0.6:0.6]; with $\Delta[U/U_{\max}] = 0.06$ . . . . .	114
4.17	A sequence of phase-averaged velocity vector fields, extracted over one motion period, $T$ , at $KC_t = 3$ , $\beta_t = 30$ in regime A*. . . . .	118
4.18	Phase-averaged streamline patterns extracted over one motion period, $T$ , at $KC_t = 3$ , $\beta_t = 30$ in regime A*. Images are in a frame moving with instantaneous velocity of the cylinder. . . . .	119
4.19	Two-dimensionality of flow along the cylinder axis in regime A* ( $KC_t = 3$ & $\beta_t = 30$ ); Instantaneous dimensionless velocity vectors after 50 cycles. The solid rectangle lines denote the position of the cylinder in this phase. . . . .	120
4.20	Comparison of time history of dimensionless peak vorticity of vortices C (narrow solid lines) and D (dotted lines), labelled in figure 4.29, adjacent to the cylinder body surface for regimes A*(squares), A (diamonds) and B(circles) at different phase locations. Thick solid lines/symbols indicate the average peak vorticity value for both vortices C and D. . . . .	120

4.21	Time history of dimensionless circulation of vortices C and D, adjacent to the cylinder body surface for regimes A*(black color) and A (blue color) at different phase positions. The vortices C and D are symmetric with respect to the axis of oscillation. This results the absolute value of dimensionless circulation of vortices C and D coincides in this figure. . .	121
4.22	$V/U_{\max}$ velocity component and $\omega_z^*$ distribution of flow at the cross-section $y/D=0.0$ for four different phases of flow in the cycle in regime A*, $KC_t=3$ and $\beta_t=30$ . The phases are selected to locate at the middle and the end of the cycle where the velocity of the cylinder is maximum and zero, respectively. The square symbols show the $t = 0$ (figure 4.14a and 4.15a) phase, the circle $t = 4T/8$ (figure 4.14e and 4.15e) phase, the triangle $t = 2T/8$ (figures 4.15c and 4.15c) and the diamond shape $t = 6T/8$ (figures 4.15g and 4.15g). . . . .	121
4.23	A sequence of phase-averaged non-dimensionalised out-of-plane vorticity contours, $\omega_z^*$ , extracted over one motion period, $T$ , at $KC_t=5$ , $\beta_t=20$ in regime A. Positive (counter-clockwise) and negative vorticity contours are denoted by red and blue colours respectively. Vorticity contours are evenly spaced over the range $[-6.0:6.0]$ ; with $\Delta[\omega_z^*] = 0.15$ . . . . .	125
4.24	A sequence of phase-averaged non-dimensionalised $V$ velocity contours, extracted over one motion period, $T$ , at $KC_t=5$ , $\beta_t=20$ in regime A. Positive and negative velocity contours are denoted by red and blue colours respectively. $V$ velocity contours are evenly spaced over the range $[-0.3:1.0]$ ; with $\Delta[V/U_{\max}] = 0.1$ . . . . .	126
4.25	A sequence of phase-averaged non-dimensionalised $U$ velocity contours, extracted over one motion period, $T$ , at $KC_t=5$ , $\beta_t=20$ in regime A. Positive and negative velocity contours are denoted by red and blue colours respectively. $U$ velocity contours are evenly spaced over the range $[-0.6:0.6]$ ; with $\Delta[U/U_{\max}] = 0.06$ . . . . .	127

- 4.26 A sequence of phase-averaged velocity vector fields extracted over one motion period,  $T$ , at  $KC_t=5$ ,  $\beta_t=20$  in regime A. Positive and negative velocity contours are denoted by red and blue colours respectively. . . . 128
- 4.27 Two-dimensionality of flow along the cylinder axis in regime A ( $KC_t=5$  &  $\beta_t=20$ ); Instantaneous dimensionless velocity vectors after 50 cycles. The solid rectangle lines denote the position of the cylinder in this phase. 129
- 4.28 Three-dimensionality of flow along the cylinder axis in regime B ( $KC_t = 3$  &  $\beta_t = 80$ ); Instantaneous spanwise dimensionless velocity vector at the 36<sup>th</sup> cycle and phase angle of 270°. The solid rectangle lines denote the position of the cylinder in this phase which moves from right to left. 129
- 4.29 A sequence of phase-averaged non-dimensionalised out-of-plane vorticity contours,  $\omega_z^*$ , extracted over one motion period,  $T$ , at  $KC_t=3$ ,  $\beta_t=80$  in regime B. Positive (counter-clockwise) and negative vorticity contours are denoted by red and blue colours respectively. Vorticity contours are evenly spaced over the range [-5.0:5.0]; with  $\Delta[\omega_z^*] = 0.5$ . . . . . 130
- 4.30 A sequence of phase-averaged non-dimensionalised  $V$  velocity contours, extracted over one motion period,  $T$ , at  $KC_t=3$ ,  $\beta_t=80$  in regime B. Positive and negative velocity contours are denoted by red and blue colours respectively.  $V$  velocity contours are evenly spaced over the range [-0.5:0.7]; with  $\Delta[V/U_{\max}] = 0.04$ . . . . . 131
- 4.31 A sequence of phase-averaged non-dimensionalised  $U$  velocity contours, extracted over one motion period,  $T$ , at  $KC_t=3$ ,  $\beta_t=80$  in regime B. Positive and negative velocity contours are denoted by red and blue colours respectively.  $U$  velocity contours are evenly spaced over the range [-0.6:0.6]; with  $\Delta[U/U_{\max}] = 0.06$ . . . . . 132
- 4.32 A sequence of phase-averaged velocity vector fields extracted over one motion period,  $T$ , at  $KC_t=3$ ,  $\beta_t=80$  in regime B. Positive and negative velocity contours are denoted by red and blue colours respectively. . . . 133

- 4.33 A sequence of phase-averaged non-dimensionalised out-of-plane vorticity contours,  $\omega_z^*$ , extracted over one motion period,  $T$ , at  $KC_t=6.28$ ,  $\beta_t=18$  in regime D. Positive (counter-clockwise) and negative vorticity contours are denoted by red and blue colours respectively. Vorticity contours are evenly spaced over the range  $[-1.5:1.5]$ ; with  $\Delta[\omega_z^*] = 0.1$ . . . . . 135
- 4.34 A sequence of phase-averaged non-dimensionalised  $V$  velocity contours, extracted over one motion period,  $T$ , at  $KC_t=6.28$ ,  $\beta_t=18$  in regime D. Positive and negative velocity contours are denoted by red and blue colours respectively.  $V$  velocity contours are evenly spaced over the range  $[-0.25:0.25]$ ; with  $\Delta[V/U_{\max}] = 0.025$ . . . . . 136
- 4.35 A sequence of phase-averaged non-dimensionalised  $U$  velocity contours, extracted over one motion period,  $T$ , at  $KC_t=6.28$ ,  $\beta_t=18$  in regime D. Positive and negative velocity contours are denoted by red and blue colours respectively.  $U$  velocity contours are evenly spaced over the range  $[-0.2:0.2]$ ; with  $\Delta[U/U_{\max}] = 0.02$ . . . . . 137
- 4.36 A sequence of phase-averaged velocity vector fields extracted over one motion period,  $T$ , at  $KC_t=6.28$ ,  $\beta_t=18$  in regime D. Positive and negative velocity contours are denoted by red and blue colours respectively. The arrow in image (f) shows the direction of the created jet flow. . . . 138
- 4.37 Contour of phase-averaged non-dimensionalised vorticity of regime D,  $KC_t=6.28$ ,  $\beta_t=18$ . This phase is corresponding to image (b) of figure 4.33. The dark cylinder shows the actual position of the cylinder in that phase of the motion and the grey cylinder is shown to clearly show one diameter location behind the cylinder. This shows the one order of magnitude difference in the magnitude of the  $\omega_z^*$ . . . . . 139

- 4.38 Patterns of instantaneous dimensionless vorticity,  $\omega_z^*$ , for the sinusoidally oscillating flow past the circular cylinder in regime E at  $KC_t=5$  and  $\beta_t=80$ . For dimensionless vorticity  $\omega_z^*$ ,  $\Delta[\omega_z^*]=0.3$ . The cylinder is oscillating horizontally from left to right, at its most left position in the cycle. (a) shows cycles before change in the direction, (b) transition in the change in the direction, and (c) cycles after transition. . . . . 142
- 4.39 A sequence of phase-averaged non-dimensionalised out-of-plane vorticity contours,  $\omega_z^*$ , extracted over one motion period,  $T$ , at  $KC_t=8.17$ ,  $\beta_t=30$  in regime F. Positive (counter-clockwise) and negative vorticity contours are denoted by red and blue colours respectively. Vorticity contours are evenly spaced over the range  $[-1.5:1.5]$ ; with  $\Delta[\omega_z^*] = 0.1$ . Thick line is image (a) shows the axis of oscillation. The angle between the shed vortices and the axis of oscillation is  $18^\circ$  in this case. . . . . 144
- 4.40 A sequence of phase-averaged non-dimensionalised  $V$  velocity contours, extracted over one motion period,  $T$ , at  $KC_t=8.17$ ,  $\beta_t=30$  in regime F. Positive and negative velocity contours are denoted by red and blue colours respectively.  $V$  velocity contours are evenly spaced over the range  $[-0.25:0.25]$ ; with  $\Delta[V/U_{\max}] = 0.025$ . . . . . 145
- 4.41 A sequence of phase-averaged non-dimensionalised  $U$  velocity contours, extracted over one motion period,  $T$ , at  $KC_t=8.17$ ,  $\beta_t=30$  in regime F. Positive and negative velocity contours are denoted by red and blue colours respectively.  $U$  velocity contours are evenly spaced over the range  $[-0.2:0.2]$ ; with  $\Delta[U/U_{\max}] = 0.02$ . . . . . 146
- 4.42 A sequence of phase-averaged velocity vector fields extracted over one motion period,  $T$ , at  $KC_t=8.17$ ,  $\beta_t=30$  in regime F. Positive and negative velocity contours are denoted by red and blue colours respectively. . . . 147

4.43	Distribution of absolute dimensionless peak vorticities, $ \omega_z^* $ , of three vortices A (solid red line, square), B (solid blue line, triangle), and C (dashed red line, circle) shown in figure 4.39. These data are for regime F, $KC_t=8.17$ and $\beta_t=30$ and are extracted from the phase-averaged PIV analysis. The lines are only showing the trend of distribution of $\omega_z^*$ . . .	148
5.1	Contours of vorticity around the cylinder undergoing combined translational and rotational oscillation at $KC = \pi$ , $\beta = 90$ , and (a) $\Phi = \pi$ , (b) $\Phi = \pi/2$ , (c) $\Phi = \pi/4$ , taken at $t/T = 0$ from numerical simulation explained in §5.4. The dashed lines (enclosing blue) correspond to clockwise direction of vorticity (negative). The solid lines (enclosing red) correspond to counterclockwise direction of vorticity (positive). . . . .	155
5.2	Outline of the 518-element $30D \times 30D$ domain, s, used for the swimming cylinder simulations. . . . .	157
5.3	Floquet multipliers for $KC_t = 2.75$ for the three-dimensional instability of regime B at $\beta_t = 80$ . The current results (solid line) are compared with those from Elston <i>et al.</i> (2006) (squares). . . . .	157
5.4	Spatial autocorrelation function for $\beta=90$ , based on streamwise vorticity.	161
5.5	Lines showing the positions where the spatial autocorrelations are calculated and the streamwise and $V$ velocity data are extracted. . . . .	161
5.6	(left): Wavelength histogram of spanwise structures resulted from autocorrelation of $\omega_x$ fields over 500 data sets. The red line illustrates a Gaussian fit to the histogram; (right): Distribution of wavelengths at different $y/D$ locations behind the cylinder; for $\beta = 90$ . . . . .	162



5.7 Vorticity contours around the cylinder undergoing combined translational and rotational oscillation at  $KC = \Phi = \pi$  and  $\beta = 90$ . The numerical result is presented on the left, and the experimental result on the right. The experimental result is a phase-average of 10 successive cycles. The phase shown corresponds to  $t = 0$ . The dashed lines (enclosing blue) correspond to clockwise direction of vorticity (negative), and the solid lines (enclosing red) correspond to counterclockwise direction of vorticity (positive). . . . . 162

5.8 Flow produced by a cylinder with combined oscillatory translation and rotation. This figure shows the sequence and development of the  $\omega_z$  vorticity for one complete cycle, (a)  $t = 0$  to (h)  $t = 7T/8$  at  $KC = \Phi = \pi$  and  $\beta = 90$  where  $T$  is the period of oscillation. The radial line shows the rotational displacement of the cylinder. The dashed lines (enclosing blue) correspond to clockwise direction of vorticity (negative), and the solid lines (enclosing red) correspond to counterclockwise vorticity (positive). 165

5.9 Schematic of the acceleration vectors at  $KC = \Phi = \pi$  and  $\beta = 90$ . The sequence and development of the  $\omega_z$  vorticity for the first three phases of oscillation, (a)  $t = 0$  to (b)  $t = 2T/8$ , is also shown. The radial line shows the rotational displacement of the cylinder. The dashed lines (enclosing blue) correspond to clockwise direction of vorticity (negative), and the solid lines (enclosing red) correspond to counterclockwise vorticity (positive). The green and purple vectors denote the translational and rotational components, respectively. The resultant vector is also shown in yellow. The phase at which the vectors are depicted is shown as well in this figure, with the red line showing the  $y(t)$  and the blue line  $\theta(t)$ . The crosshairs denote the fixed point that the cylinder is oscillating about. 166

5.10	Instantaneous experimental vorticity contours around the cylinder undergoing combined translational and rotational oscillation at $KC = \Phi = \pi$ and $\beta = 90$ . The phase shown corresponds to $t = 0$ . The dashed lines (enclosing blue) correspond to clockwise direction of vorticity (negative), and the solid lines (enclosing red) correspond to counterclockwise direction of vorticity (positive). The snapshots are taken after (a) 12 and (b) 68 cycles. . . . .	167
5.11	Contours of vorticity around the cylinder undergoing combined translational and rotational oscillation at $KC = \pi$ , $\beta = 90$ and $\Phi = \pi/2$ . (a) Numerical simulation, (b) Instantaneous PIV, (c) Phase-averaged PIV, taken at $t/T = 0$ from numerical simulation explained in §5.4. The blue corresponds to clockwise direction of vorticity (negative). The red corresponds to counterclockwise direction of vorticity (positive). . . . .	168
5.12	Experimental phase-averaged velocity vector and $V$ velocity distribution behind the swimming cylinder at $t/T = 0$ , $KC = \Phi = \pi$ and $\beta = 90$ . (a) Velocity vectors, (b) $V$ velocity distribution. . . . .	169
5.13	Experimental phase-averaged $V$ velocity distribution for three different locations, $x/D = 1.0$ (solid line), $x/D = 1.5$ (dashed line) and $x/D = 2.0$ (dashed double dot line), behind the swimming cylinder at $t/T = 0$ , $KC = \Phi = \pi$ and $\beta = 90$ . The jet-like flow is clearly seen in this figure. . . . .	170
5.14	Schematic of spanwise PIV imaging system. . . . .	171
5.15	Spanwise coordinate system with laser sheets. Double arrow indicates the direction of cylinder translational oscillation. . . . .	171
5.16	Schematic of camera positions in the $xy$ -plane (as shown in figure 5.15) for the spanwise PIV measurements. The thick green line denotes the laser sheets, the blue box shows the camera and the dashed red boxes represents the region of interest. . . . .	172

5.17	Experimental phase-averaged $\omega_x$ vorticity iso-contours for different $\beta$ values at $KC = \Phi = \pi$ . (a) $\beta = 45$ , (b) $\beta = 90$ , (c) $\beta = 120$ and (d) $\beta = 150$ . $\omega_x$ vorticity iso-contours; the dashed lines (enclosing blue) correspond to clockwise direction of vorticity (negative), and the solid lines (enclosing red) correspond to counterclockwise vorticity (positive). $\lambda$ in (a) denotes the characteristic wavelength. . . . .	173
5.18	Experimental phase-averaged $V, y$ -velocity fields results of the spanwise distribution of flow for different $\beta$ values at $KC = \Phi = \pi$ . (a) $\beta = 45$ , (b) $\beta = 90$ , (c) $\beta = 120$ and (d) $\beta = 150$ . . . . .	174
5.19	Spatial autocorrelation function for $\beta=90$ and 100 cycles, based on streamwise vorticity. The thin color lines show the autocorrelation curves for each of the cycles and the thick black line illustrates the average of them.	174
5.20	Experimental streamline results of the spanwise distribution of flow for $\beta = 20$ at $KC = \Phi = \pi$ . . . . .	175
5.21	Floquet multipliers for several Reynolds numbers for the spanwise instability at $KC = \Phi = \pi$ . (a) Floquet multipliers as a function of spanwise wavelength. The open (closed) symbols represent the shortest (longest) wavelength mode. Circles and black line: $Re = 377$ ; Squares and blue lines: $Re = 283$ ; Diamonds and red line: $Re = 226$ ; Triangles and magenta line: $Re = 141$ . (b) Comparison of the Floquet analysis predicted wavelength values as a function of Reynolds number with experimental measurements. The blue line corresponds to the wavelength range of the longest spanwise wavelength mode. The red dashed line corresponds to the extent of the shortest spanwise wavelength mode. The thick lines correspond to the predicted dominant wavelengths. The black circles represent experimental measurements with error bars reporting the standard deviation of the measurements. . . . .	178

5.22	Photographs of the cylinder showing the methods used to artificially force the wake at the predicted optimal shorter wavelength, <i>i.e.</i> $\lambda/D \approx 0.7$ . (a) Thin tape; (b) Thin and short wires; (c) Small O-rings. . . . .	179
5.23	Experimental instantaneous $V$ field results of the spanwise distribution of flow while artificially forcing the wake at the critical short wavelength, <i>i.e.</i> $\lambda/D \approx 0.7$ for $KC = \Phi = \pi$ and $\beta = 90$ . The results are obtained using forcing with O-rings. . . . .	179
5.24	Experimental instantaneous $V$ field taken at the $xz$ -plane (see figure 5.15) for $KC = \Phi = \pi$ and $\beta = 90$ . . . . .	180
5.25	Experimental instantaneous $V$ fields of the spanwise distribution of flow taken in a plane at $x/D = 0.5$ (left) and $x/D = 0.25$ (right) parallel to the $yz$ -plane (see figure 5.15) for $KC = \Phi = \pi$ and $\beta = 90$ . . . . .	180
5.26	Contours of streamwise perturbation vorticity taken at $KC = \Phi = \pi$ and $\beta = 90$ ( $Re \approx 283$ ) and when the cylinder is at $t = 0$ for: (left) $\lambda = 1.8D$ the long wavelength; (right) $\lambda = 0.7D$ the short wavelength. The dashed lines correspond to the base flow clockwise direction of vorticity (negative), and the solid lines correspond to the counterclockwise vorticity (positive). . . . .	180
6.1	Velocity vectors upstream of the cylinder, measured to capture the free-stream velocity prior each set of experiments. The flow is from left to right. . . . .	185
6.2	Instantaneous and phase-averaged contours of vorticity (top row), $U$ (middle row) and $V$ (bottom row) velocities measured at the downstream of the fixed cylinder. The flow direction is from left to right. The blue color in the top row shows negative vorticity and the red color shows positive vorticity being in the counter-clockwise direction. . . . .	186
6.3	A normalised power spectrum, against maximum power spectrum, extracted from FFT analysis of fluctuating $U$ velocity over 5000 images captured at 10Hz at the downstream of the fixed cylinder. . . . .	186

- 6.4 Motion phase-locked vorticity contours taken at the motion-phase of  $t = T$  for  $A_t = D/8$ ,  $f_N=0.6$  Hz,  $V_R=0.25$ ,  $F_R=1$  and  $Re=1291$ . The near-wake vorticity is shown for different phase angle differences between the two imposed oscillatory motions. Vorticity contours are evenly spaced over the range  $[-0.1 : 0.1]$ ; with  $\Delta\omega_z = 0.01$ . . . . . 188
- 6.5 Motion phase-locked vorticity contours (lines) and root-mean-square vorticity (gray-scale) contours taken at the motion-phase of  $t = T$  for  $A_t = D/8$ ,  $f_N=0.6$  Hz,  $V_R=0.25$ ,  $F_R=1$  and  $Re=1291$ . The near-wake rms vorticity is shown for different phase angle differences between the two imposed oscillatory motions. The flow direction is from left to right. Root-mean-square vorticity contours are evenly spaced over the range  $[0.02 : 0.1]$ ; with  $\Delta\omega_z = 0.02$ , and vorticity contours are evenly spaced over the range  $[-0.1 : 0.1]$ ; with  $\Delta\omega_z rms = 0.01$ . . . . . 189
- 6.6 Motion phase-locked  $U/U_\infty$  velocity contours taken at the motion-phase of  $t = T$  for  $A_t = D/8$ ,  $f_N=0.6$  Hz,  $V_R=0.25$ ,  $F_R=1$  and  $Re=1291$ . The velocity contours are shown for different phase angle differences between the two imposed oscillatory motions. The flow direction is from left to right.  $U/U_\infty$  velocity contours are evenly spaced over the range  $[-1 : 1.8]$ ; with  $\Delta(U/U_\infty) = 0.2$ . . . . . 190
- 6.7 Motion phase-locked  $V/U_\infty$  velocity contours taken at the motion-phase of  $t = T$  for  $A_t = D/8$ ,  $f_N=0.6$  Hz,  $V_R=0.25$ ,  $F_R=1$  and  $Re=1291$ . The velocity contours are shown for different phase angle differences between the two imposed oscillatory motions. The flow direction is from left to right.  $V/U_\infty$  velocity contours are evenly spaced over the range  $[-0.2 : 2.4]$ ; with  $\Delta(V/U_\infty) = 0.2$ . . . . . 191

- 6.8 Motion phase-locked vorticity contours taken at the motion-phase of  $t = T$  for  $A_t = D/4$ ,  $f_N=0.6$  Hz,  $V_R=0.5$ ,  $F_R=1$  and  $Re=1\ 274$ . The near-wake vorticity is shown for different phase angle differences between the two imposed oscillatory motions. The flow direction is from left to right. Vorticity contours are evenly spaced over the range  $[-0.1 : 0.1]$ ; with  $\Delta\omega_z = 0.01$ . . . . . 192
- 6.9 Motion phase-locked vorticity contours (lines) and root-mean-square vorticity (gray-scale) contours taken at the motion-phase of  $t = T$  for  $A_t = D/4$ ,  $f_N=0.6$  Hz,  $V_R=0.5$ ,  $F_R=1$  and  $Re=1\ 274$ . The near-wake rms vorticity is shown for different phase angle differences between the two imposed oscillatory motions. The flow direction is from left to right. Root-mean-square vorticity contours are evenly spaced over the range  $[0.02 : 0.1]$ ; with  $\Delta\omega_z = 0.02$ , and vorticity contours are evenly spaced over the range  $[-0.1 : 0.1]$ ; with  $\Delta\omega_{zrms} = 0.01$ . . . . . 193
- 6.10 Motion phase-locked  $U/U_\infty$  velocity contours taken at the motion-phase of  $t = T$  for  $A_t = D/4$ ,  $f_N=0.6$  Hz,  $V_R=0.5$ ,  $F_R=1$  and  $Re=1\ 274$ . The velocity contours are shown for different phase angle differences between the two imposed oscillatory motions. The flow direction is from left to right.  $U/U_\infty$  velocity contours are evenly spaced over the range  $[-1 : 1.8]$ ; with  $\Delta(U/U_\infty) = 0.2$ . . . . . 194
- 6.11 Motion phase-locked  $V/U_\infty$  velocity contours taken at the motion-phase of  $t = T$  for  $A_t = D/4$ ,  $f_N=0.6$  Hz,  $V_R=0.5$ ,  $F_R=1$  and  $Re=1\ 274$ . The velocity contours are shown for different phase angle differences between the two imposed oscillatory motions. The flow direction is from left to right.  $V/U_\infty$  velocity contours are evenly spaced over the range  $[-0.2 : 2.4]$ ; with  $\Delta(V/U_\infty) = 0.2$ . . . . . 195

6.12 Motion phase-locked vorticity contours taken at the motion-phase of  $t = T$  for  $A_t = D/2$ ,  $f_N=0.6$  Hz,  $V_R=F_R=1$  and  $Re=1322$ . The near-wake vorticity is shown for different phase angle differences between the two imposed oscillatory motions. Of particular interest is the asynchronous (unlocked) wake with the imposed translational motion for the phase  $\Phi = -90^\circ$  and  $\Phi = -120^\circ$ . The flow direction is from left to right. Vorticity contours are evenly spaced over the range  $[-0.1 : 0.1]$ ; with  $\Delta\omega_z = 0.01$ . . . . . 196

6.13 Motion phase-locked vorticity contours (lines) and root-mean-square vorticity (gray-scale) contours taken at the motion-phase of  $t = T$  for  $A_t = D/2$ ,  $f_N=0.6$  Hz,  $V_R=F_R=1$  and  $Re=1322$ . The near-wake rms vorticity is shown for different phase angle differences between the two imposed oscillatory motions. Of particular interest is the asynchronous (unlocked) wake with the imposed translational motion for the phase  $\Phi = -90^\circ$  and  $\Phi = -120^\circ$ . The flow direction is from left to right. Root-mean-square vorticity contours are evenly spaced over the range  $[0.02 : 0.1]$ ; with  $\Delta\omega_z = 0.02$ , and vorticity contours are evenly spaced over the range  $[-0.1 : 0.1]$ ; with  $\Delta\omega_z rms = 0.01$ . . . . . 197

6.14 Motion phase-locked  $U/U_\infty$  velocity contours taken at the motion-phase of  $t = T$  for  $A_t = D/2$ ,  $f_N=0.6$  Hz,  $V_R=F_R=1$  and  $Re=1322$ . The velocity contours are shown for different phase angle differences between the two imposed oscillatory motions. Of particular interest is the asynchronous (unlocked) wake with the imposed translational motion for the phase  $\Phi = -90^\circ$  and  $\Phi = -120^\circ$ . The flow direction is from left to right.  $U/U_\infty$  velocity contours are evenly spaced over the range  $[-1 : 1.8]$ ; with  $\Delta(U/U_\infty) = 0.2$ . . . . . 198

6.15 Motion phase-locked  $V/U_\infty$  velocity contours taken at the motion-phase of  $t = T$  for  $A_t = D/2$ ,  $f_N=0.6$  Hz,  $V_R=F_R=1$  and  $Re=1322$ . The velocity contours are shown for different phase angle differences between the two imposed oscillatory motions. Of particular interest is the asynchronous (unlocked) wake with the imposed translational motion for the phase  $\Phi = -90^\circ$  and  $\Phi = -120^\circ$ . The flow direction is from left to right.  $V/U_\infty$  velocity contours are evenly spaced over the range  $[-0.2 : 2.4]$ ; with  $\Delta(V/U_\infty) = 0.2$ . . . . . 199

6.16 Motion phase-locked vorticity contours taken at the motion-phase of  $t = T$  for  $A_t = 3D/4$ ,  $f_N=0.6$  Hz,  $V_R=1.5$ ,  $F_R=1$  and  $Re=1291$ . The near-wake vorticity is shown for different phase angle differences between the two imposed oscillatory motions. Of particular interest is the asynchronous (unlocked) wake with the imposed translational motion for the phase  $\Phi = -90^\circ$ ,  $\Phi = -120^\circ$ ,  $\Phi = -150^\circ$  and  $\Phi = \pm 180^\circ$ . The flow direction is from left to right. Vorticity contours are evenly spaced over the range  $[-0.1 : 0.1]$ ; with  $\Delta\omega_z = 0.01$ . . . . . 200

6.17 Motion phase-locked vorticity contours (lines) and root-mean-square vorticity (gray-scale) contours taken at the motion-phase of  $t = T$  for  $A_t = 3D/4$ ,  $f_N=0.6$  Hz,  $V_R=1.5$ ,  $F_R=1$  and  $Re=1291$ . The near-wake rms vorticity is shown for different phase angle differences between the two imposed oscillatory motions. Of particular interest is the asynchronous (unlocked) wake with the imposed translational motion for the phase  $\Phi = -90^\circ$ ,  $\Phi = -120^\circ$ ,  $\Phi = -150^\circ$  and  $\Phi = \pm 180^\circ$ . The flow direction is from left to right. Root-mean-square vorticity contours are evenly spaced over the range  $[0.02 : 0.1]$ ; with  $\Delta\omega_z = 0.02$ , and vorticity contours are evenly spaced over the range  $[-0.1 : 0.1]$ ; with  $\Delta\omega_z rms = 0.01$ . 201



6.18 Motion phase-locked  $U/U_\infty$  velocity contours taken at the motion-phase of  $t = T$  for  $A_t = 3D/4$ ,  $f_N=0.6$  Hz,  $V_R=1.5$ ,  $F_R=1$  and  $Re=1\,291$ . The velocity contours are shown for different phase angle differences between the two imposed oscillatory motions. Of particular interest is the asynchronous (unlocked) wake with the imposed translational motion for the phase  $\Phi = -90^\circ$ ,  $\Phi = -120^\circ$ ,  $\Phi = -150^\circ$  and  $\Phi = \pm 180^\circ$ . The flow direction is from left to right.  $U/U_\infty$  velocity contours are evenly spaced over the range  $[-1 : 1.8]$ ; with  $\Delta(U/U_\infty) = 0.2$ . . . . . 202

6.19 Motion phase-locked  $V/U_\infty$  velocity contours taken at the motion-phase of  $t = T$  for  $A_t = 3D/4$ ,  $f_N=0.6$  Hz,  $V_R=1.5$ ,  $F_R=1$  and  $Re=1\,291$ . The velocity contours are shown for different phase angle differences between the two imposed oscillatory motions. Of particular interest is the asynchronous (unlocked) wake with the imposed translational motion for the phase  $\Phi = -90^\circ$ ,  $\Phi = -120^\circ$ ,  $\Phi = -150^\circ$  and  $\Phi = \pm 180^\circ$ . The flow direction is from left to right.  $V/U_\infty$  velocity contours are evenly spaced over the range  $[-0.2 : 2.4]$ ; with  $\Delta(V/U_\infty) = 0.2$ . . . . . 203

6.20 Motion phase-locked vorticity contours taken at the motion-phase of  $t = T$  for  $A_t = D/4$ ,  $A_\theta = 0.5$  rad,  $f_N=0.6$  Hz,  $V_R=1.0$ ,  $F_R=1$  and  $Re=1\,366$ . The near-wake vorticity is shown for different phase angle differences between the two imposed oscillatory motions. The flow direction is from left to right. Vorticity contours are evenly spaced over the range  $[-0.1 : 0.1]$ ; with  $\Delta\omega_z = 0.01$ . . . . . 204

6.21	Motion phase-locked vorticity contours (lines) and root-mean-square vorticity (gray-scale) contours taken at the motion-phase of $t = T$ for $A_t = D/4$ , $A_\theta = 0.5$ rad, $f_N=0.6$ Hz, $V_R=1.0$ , $F_R=1$ and $Re=1\ 366$ . The near-wake rms vorticity is shown for different phase angle differences between the two imposed oscillatory motions. The flow direction is from left to right. Root-mean-square vorticity contours are evenly spaced over the range $[0.02 : 0.1]$ ; with $\Delta\omega_z = 0.02$ , and vorticity contours are evenly spaced over the range $[-0.1 : 0.1]$ ; with $\Delta\omega_{zrms} = 0.01$ . . . . .	205
6.22	Motion phase-locked $U/U_\infty$ velocity contours taken at the motion-phase of $t = T$ for $A_t = D/4$ , $A_\theta = 0.5$ rad, $f_N=0.6$ Hz, $V_R=1.0$ , $F_R=1$ and $Re=1\ 366$ . The velocity contours are shown for different phase angle differences between the two imposed oscillatory motions. The flow direction is from left to right. $U/U_\infty$ velocity contours are evenly spaced over the range $[-0.2 : 2.4]$ ; with $\Delta(U/U_\infty) = 0.2$ . . . . .	206
6.23	Motion phase-locked $V/U_\infty$ velocity contours taken at the motion-phase of $t = T$ for $A_t = D/4$ , $A_\theta = 0.5$ rad, $f_N=0.6$ Hz, $V_R=1.0$ , $F_R=1$ and $Re=1\ 366$ . The velocity contours are shown for different phase angle differences between the two imposed oscillatory motions. The flow direction is from left to right. $V/U_\infty$ velocity contours are evenly spaced over the range $[-0.2 : 2.4]$ ; with $\Delta(V/U_\infty) = 0.2$ . . . . .	207
6.24	Lissajous pattern defined horizontally with the translational forcing mechanism ( $y$ ) and vertically with lift ( $C_L$ and top) or drag ( $C_D$ and bottom) coefficient (case 5 of Table 6.1). . . . .	208
6.25	Typical flow features for different imposed phase differences. Top: single-row of vortices transitioning downstream to a double-row followed by a further secondary instability in the far-wake ( $\Phi = -170^\circ$ ). Centre: double-row of vortices followed by a <i>quasi-periodic</i> pattern ( $\Phi = -40^\circ$ ). Bottom: <i>chaotic</i> pattern of vortices ( $\Phi = -100^\circ$ ). The domain of the numerical simulation was extended to $100D$ downstream for these cases.	208

6.26 Poincaré map for two typical unlocked regimes for  $Re = 225$ . Left: quasi-periodic behaviour for  $\Phi = -80^\circ$ ; Right: Chaotic regime for  $\Phi = -130^\circ$ . The phase diagram shows the horizontal and the vertical velocities at  $7D$  downstream on the centreline. . . . . 209

6.27 Motion phase-locked vorticity contours taken at the motion-phase of  $t = T$  for  $A_t = D/4$ ,  $A_\theta = 0.5$  rad,  $f_N=0.6$  Hz,  $V_R=1.0$ ,  $\Phi = -90^\circ$  and  $Re=1\ 247$ . The near-wake vorticity is shown for different phase angle differences between the two imposed oscillatory motions. Of particular interest is the asynchronous (unlocked) wake with the imposed translational motion for the frequency ratios between the oscillatory motions and the natural vortex shedding of  $F_{RN} = 0.9$  to  $F_{RN} = 1.15$ . The flow direction is from left to right. Vorticity contours are evenly spaced over the range  $[-0.2 : 0.2]$ ; with  $\Delta\omega_z = 0.02$ . . . . . 210

6.28 Motion phase-locked vorticity contours (lines) and root-mean-square vorticity (gray-scale) contours taken at the motion-phase of  $t = T$  for  $A_t = D/4$ ,  $A_\theta = 0.5$  rad,  $f_N=0.6$  Hz,  $V_R=1.0$ ,  $\Phi = -90^\circ$  and  $Re=1\ 247$ . The near-wake rms vorticity is shown for different phase angle differences between the two imposed oscillatory motions. Of particular interest is the asynchronous (unlocked) wake with the imposed translational motion for the frequency ratios between the oscillatory motions and the natural vortex shedding of  $F_{RN} = 0.9$  to  $F_{RN} = 1.15$ . The flow direction is from left to right. Root-mean-square vorticity contours are evenly spaced over the range  $[0.02 : 0.1]$ ; with  $\Delta\omega_z rms = 0.02$ , and vorticity contours are evenly spaced over the range  $[-0.2 : 0.2]$ ; with  $\Delta\omega_z = 0.02$ . . . . . 211

6.29 Motion phase-locked  $U/U_\infty$  velocity contours taken at the motion-phase of  $t = T$  for  $A_t = D/4$ ,  $A_\theta = 0.5$  rad,  $f_N=0.6$  Hz,  $V_R=1.0$ ,  $\Phi = -90^\circ$  and  $Re=1247$ . The near-wake streamwise velocity is shown for different phase angle differences between the two imposed oscillatory motions. Of particular interest is the asynchronous (unlocked) wake with the imposed translational motion for the frequency ratios between the oscillatory motions and the natural vortex shedding of  $F_{RN} = 0.9$  to  $F_{RN} = 1.15$ . The flow direction is from left to right.  $U/U_\infty$  velocity contours are evenly spaced over the range  $[-0.5 : 1.5]$ ; with  $\Delta(U/U_\infty) = 0.1$ . . . . . 212

6.30 Motion phase-locked  $V/U_\infty$  velocity contours taken at the motion-phase of  $t = T$  for  $A_t = D/4$ ,  $A_\theta = 0.5$  rad,  $f_N=0.6$  Hz,  $V_R=1.0$ ,  $\Phi = -90^\circ$  and  $Re=1247$ . The near-wake transverse velocity is shown for different phase angle differences between the two imposed oscillatory motions. Of particular interest is the asynchronous (unlocked) wake with the imposed translational motion for the frequency ratios between the oscillatory motions and the natural vortex shedding of  $F_{RN} = 0.9$  to  $F_{RN} = 1.15$ . The flow direction is from left to right.  $V/U_\infty$  velocity contours are evenly spaced over the range  $[0.2 : 7.4]$ ; with  $\Delta(V/U_\infty) = 0.4$ . . . . . 213

6.31 Motion phase-locked vorticity contours taken at the motion-phase of  $t = T$  for  $A_t = D/2$ ,  $A_\theta = 1.0$  rad,  $f_N=0.6$  Hz,  $V_R=1$ ,  $F_R=0.5$  and  $Re=1251$ . The near-wake vorticity is shown for different phase angle differences between the two imposed oscillatory motions. Of particular interest is the asynchronous (unlocked) wake with the imposed translational motion for the phase  $\Phi = -90^\circ$ ,  $\Phi = -120^\circ$ ,  $\Phi = -150^\circ$  and  $\Phi = \pm 180^\circ$ . The flow direction is from left to right. . . . . 214

- 6.32 Motion phase-locked vorticity contours (lines) and root-mean-square vorticity (gray-scale) contours taken at the motion-phase of  $t = T$  for  $A_t = D/2$ ,  $A_\theta = 1.0$  rad,  $f_N=0.6$  Hz,  $V_R=1$ ,  $F_R=0.5$  and  $Re=1\ 251$ . The near-wake rms vorticity is shown for different phase angle differences between the two imposed oscillatory motions. Of particular interest is the asynchronous (unlocked) wake with the imposed translational motion for the phase  $\Phi = -90^\circ$ ,  $\Phi = -120^\circ$ ,  $\Phi = -150^\circ$  and  $\Phi = \pm 180^\circ$ . The flow direction is from left to right. . . . . 215
- 6.33 Motion phase-locked  $U$  velocity contours taken at the motion-phase of  $t = T$  for  $A_t = D/2$ ,  $A_\theta = 1.0$  rad,  $f_N=0.6$  Hz,  $V_R=1$ ,  $F_R=0.5$  and  $Re=1\ 251$ . The near-wake streamwise velocity is shown for different phase angle differences between the two imposed oscillatory motions. Of particular interest is the asynchronous (unlocked) wake with the imposed translational motion for the phase  $\Phi = -90^\circ$ ,  $\Phi = -120^\circ$ ,  $\Phi = -150^\circ$  and  $\Phi = \pm 180^\circ$ . The flow direction is from left to right. . . . . 216
- 6.34 Motion phase-locked  $V$  velocity contours taken at the motion-phase of  $t = T$  for  $A_t = D/2$ ,  $A_\theta = 1.0$  rad,  $f_N=0.6$  Hz,  $V_R=1$ ,  $F_R=0.5$  and  $Re=1\ 251$ . The near-wake transverse velocity is shown for different phase angle differences between the two imposed oscillatory motions. Of particular interest is the asynchronous (unlocked) wake with the imposed translational motion for the phase  $\Phi = -90^\circ$ ,  $\Phi = -120^\circ$ ,  $\Phi = -150^\circ$  and  $\Phi = \pm 180^\circ$ . The flow direction is from left to right. . . . . 217
- 6.35 Motion phase-locked vorticity contours taken at the motion-phase of  $t = T$  for  $A_t = D/2$ ,  $A_\theta = 1.0$  rad,  $f_N=0.6$  Hz,  $V_R=1$ ,  $F_R=2$  and  $Re=1\ 251$ . The near-wake vorticity is shown for different phase angle differences between the two imposed oscillatory motions. Of particular interest is the asynchronous (unlocked) wake with the imposed translational motion for the phase  $\Phi = -90^\circ$ ,  $\Phi = -120^\circ$ ,  $\Phi = -150^\circ$  and  $\Phi = \pm 180^\circ$ . The flow direction is from left to right. . . . . 218

6.36	Motion phase-locked vorticity contours (lines) and root-mean-square vorticity (gray-scale) contours taken at the motion-phase of $t = T$ for $A_t = D/2$ , $A_\theta = 1.0$ rad, $f_N=0.6$ Hz, $V_R=1$ , $F_R=2$ and $Re=1251$ . The near-wake rms vorticity is shown for different phase angle differences between the two imposed oscillatory motions. Of particular interest is the asynchronous (unlocked) wake with the imposed translational motion for the phase $\Phi = -90^\circ$ , $\Phi = -120^\circ$ , $\Phi = -150^\circ$ and $\Phi = \pm 180^\circ$ . The flow direction is from left to right. . . . .	219
6.37	Motion phase-locked $U$ velocity contours taken at the motion-phase of $t = T$ for $A_t = D/2$ , $A_\theta = 1.0$ rad, $f_N=0.6$ Hz, $V_R=1$ , $F_R=2$ and $Re=1251$ . The near-wake streamwise velocity is shown for different phase angle differences between the two imposed oscillatory motions. Of particular interest is the asynchronous (unlocked) wake with the imposed translational motion for the phase $\Phi = -90^\circ$ , $\Phi = -120^\circ$ , $\Phi = -150^\circ$ and $\Phi = \pm 180^\circ$ . The flow direction is from left to right. . . . .	220
6.38	Motion phase-locked $V$ velocity contours taken at the motion-phase of $t = T$ for $A_t = D/2$ , $A_\theta = 1.0$ rad, $f_N=0.6$ Hz, $V_R=1$ , $F_R=2$ and $Re=1251$ . The near-wake transverse velocity is shown for different phase angle differences between the two imposed oscillatory motions. Of particular interest is the asynchronous (unlocked) wake with the imposed translational motion for the phase $\Phi = -90^\circ$ , $\Phi = -120^\circ$ , $\Phi = -150^\circ$ and $\Phi = \pm 180^\circ$ . The flow direction is from left to right. . . . .	221
A.1	Schematics illustrating representative ways in which the two-dimensional symmetries of the basic state can be broken. The basic state, (a), has the three symmetries $K_x$ , $H_1$ , $H_2$ , while in (b – d), two out of three break, and the outcomes are labelled with their remaining symmetry.  <i>The images appeared in Elston (2005) and is reproduced by permission. .</i>	230

# Chapter 1

## Introduction

This thesis presents the results of an experimental investigation into the flows produced by a bluff body subjected to oscillatory motion in a Newtonian fluid. A bluff body can be defined as a body that, as a result of its shape, has separated flow over a substantial part of its surface. An important feature of a bluff body flow is that there is a very strong interaction between the viscous and inviscid regions. The traditional types of floating and fixed offshore, or man-made, structures used for oil recovery can expect waves and currents from any direction and they are designed using bluff cross sections, such as the circle and the square. The cylinder has geometric simplicity enabling models to be easily manufactured for basic experimental research (Bearman 1997). Hence, in this thesis a circular cylinder is used as the bluff body.

The structures formed by an oscillating cylinder are highly dependent upon the characteristics of the cylinder's oscillation and are additionally influenced by the presence of an external flow. In a quiescent fluid, at very low amplitudes and frequencies of translational oscillation, the flow about a circular cylinder is symmetric about its axis of oscillation and is two-dimensional (it has no variation along the span), attached and non-turbulent. However as either, or both, of these parameters increase, the flow structures produced by the cylinder change dramatically. The initial symmetry is lost and a number of two- and three-dimensional flow structures are seen in the cylinder's wake. An example of this is the "streaked flow" observed by Honji (1981) wherein regularly spaced chains of dye were seen to form along the cylinder span for a particular envelope of amplitudes and frequencies of oscillation (Elston 2005).

Driving this oscillating body research is the fact that, in nature, a number of oceanic animals have evolved a highly efficient propulsive mechanism that is, in its simplest form, a body subjected to both a lateral and twisting oscillatory motion. This means of

propulsion, known as Carangiform motion, involves the animals tail fin being subjected to a twisting motion at the extreme ends of the fins lateral oscillatory motion. It is a highly effective form of propulsion and is used by a number of the fastest swimming oceanic lifeforms such as dolphins, marlin and some families of sharks.

Studies on flow past an oscillating cylinder can be divided into the following three categories depending on the motion of the cylinder. In the first category, the cylinder oscillates translationally only, at an angle of  $0^\circ$  or  $90^\circ$ , or even in between these values, with respect to the free-stream. The  $0^\circ$  case is a purely in-line oscillation, and the  $90^\circ$  case is a purely transverse oscillation. Many researchers (such as Bishop & Hassan 1964; Koopmann 1967; Hamman & Dalton 1971; Sarpkaya 1976a; Taneda 1978b; Griffin & Hall 1991; Bearman & Currie 1979; Sarpkaya & Isaacson 1981; Bearman *et al.* 1981; Bearman 1984; Williamson 1985; Ongoren & Rockwell 1988a; Williamson & Roshko 1988; Hover *et al.* 1998; Konstantinidis *et al.* 2000; Carberry *et al.* 2001; Uzunoglu *et al.* 2001; Sarpkaya 2002; Konstantinidis *et al.* 2002; Carberry *et al.* 2005; Leontini *et al.* 2006a,b, 2007; Konstantinidis *et al.* 2007, and many more) have shown that the vortex shedding phenomenon can be dramatically altered for the cylinder undergoing in-line and transverse oscillation in a fluid stream. For in-line oscillations, vortex lock-on occurs when the oscillation frequencies are approximately twice the Strouhal frequency (the frequency of the vortex shedding from a stationary cylinder). For transverse oscillations, lock-on usually occurs near the Strouhal frequency (Griffin & Hall 1991; Meneghini & Bearman 1995).

In the second category, the cylinder performs a rotational oscillation about its axis in mean flow. Lock-on or resonance occurs when the body and wake oscillations have the same frequency, which is near one of the characteristic frequencies of the structures. Vortex lock-on can also be realized with rotational oscillations of a circular cylinder. However, in contrast to the large number of studies conducted in the first category, there is relatively little research carried out in this category (for example Wu *et al.* 1989; Tokumaru & Dimotakis 1991; Filler *et al.* 1991; Lu & Sato 1996; Fujisawa *et al.* 1998; Mahfouz & Badr 2000; Cheng *et al.* 2001a; Choi & Choi 2002; Du *et al.* 2003; Schmidt & Smith 2004; Thiria *et al.* 2006; Lo Jacono *et al.* 2010).

The third category, which is of a class of flow that has not received much attention until now, is created by a circular cylinder moving with combined oscillatory translational *and* rotational motion in quiescent fluid or free-stream. Blackburn *et al.* (1999)



found that a circular cylinder undergoing combined oscillation in a quiescent fluid has the capability to generate thrust. This phenomenon is the major interest of the present thesis. The primary aims of this thesis are to extend the numerical study of Blackburn *et al.* (1999) both experimentally and numerically, to examine the three-dimensional wake development experimentally, using the particle image velocimetry technique, and to determine the three-dimensional stability of the wake through Floquet stability analysis.

The results are compared to the only known available numerical results of Blackburn *et al.* (1999) to confirm the thrust generating ability of the cylinder. Placing the circular cylinder which is undergoing combined oscillatory motion in a free-stream has shown to generate intriguing wake modes and the potential of such flows to reduce synchronisation of the cylinder motion in the near-wake (Al-Mdallal 2004; Kocabiyik & Al-Mdallal 2005). The effect of phase difference and velocity ratio between the two oscillatory motions on the synchronisation in the near-wake of the cylinder were considered for the first time in this thesis.

The problem considered here involves a circular cylinder being subjected to one or more modes of oscillation while surrounded by either an externally imposed flow or by a quiescent fluid. Simple harmonic forms of translational and rotational oscillation were used for all the modes of imposed oscillation considered in this thesis.

The investigation is composed of three components:

1. An investigation of the near-wake produced by a circular cylinder oscillating only translationally in a quiescent fluid at low  $KC_t$  and  $\beta_t$  numbers in a quiescent fluid.
2. The mechanism resulting in the combined rotational and translational oscillation of a circular cylinder in a quiescent fluid producing a time-averaged thrust is experimentally examined and the thrust generation ability is confirmed, *i.e.* the “swimming cylinder”. Additionally the influence of phase difference between the two motions on the near-wake structure and three-dimensionality of flow along the span of the cylinder are investigated.
3. The effect of adding a cross flow to the swimming cylinder case on the synchronisation in the near-wake of the cylinder is also examined. The effect of the phase difference and velocity ratio between the two motions are investigated.

## Structure of the Thesis

The thesis is structured as follows:

**Chapter 2:** A review of the relevant literature is conducted in order to assess the current state of knowledge, and to highlight unanswered questions and gaps in the existing research.

**Chapter 3:** The experimental method used to measure the flows is outlined. The particle image velocimetry technique and flow visualisation are used for flow measurements.

**Chapter 4:** An investigation of the flow generated at very low amplitudes and frequencies of translational oscillation is made. This chapter provides quantitative measurements of flow around the cylinder oscillating in an initially quiescent fluid.

**Chapter 5:** The “swimming cylinder” problem of a cylinder in combined translational and rotational oscillatory motion is examined. The impact of the various parameters controlling the motion of the resultant flow is investigated.

**Chapter 6:** The addition of cross flow to the “swimming cylinder” is investigated. The impact of the various parameters controlling the motion of the resultant flow is investigated.

**Chapter 7:** The overall conclusions of the thesis, summarising the results obtained in the previous chapters, are presented. Potential future directions for research in this area are discussed.

**Appendix A:** A definition of spatial and/or temporal properties symmetry is given.

**Appendix B:** Copies of the papers published in the Physics of Fluids journal arising from Chapters 5 and 6 are provided.

**Appendix C:** During the candidature opportunity arose to conduct a series of experiments on a different topic than the aim of present thesis, a copy of the paper published recently in the Physics of Fluids journal from this work is provided here.

**Bibliography:** A bibliography that contains all the references cited throughout the body of this thesis.

## Chapter 2

# Literature Review

### 2.1 Introduction

In the following sections previous research into aspects of a cylinder oscillating in a fluid are examined. In particular two specific phenomena that, in part, provided the motivation for this research will be examined in greater detail. The first of these phenomena arises from the research of Honji (1981); Williamson (1985) and Tatsuno & Bearman (1990) who collectively observed that the translational oscillation of a circular cylinder at low amplitudes and frequencies of oscillation in a quiescent fluid, or equivalently a fixed cylinder in sinusoidally oscillating flow, can generate a set of intriguing flow structures. Tatsuno & Bearman (1990) defined a number of unique regimes, on the basis of the distinctive flow structures shed from the cylinder, that were observed to occur over a very small range of Keulegan-Carpenter and Stokes numbers.

The second phenomenon of interest is observed when a harmonic rotational oscillation is imposed upon the cylinder in addition to the aforementioned translational motion. It has been computationally shown by Blackburn *et al.* (1999) that, for particular phase angles between the two forms of oscillations, a net thrust can be produced by the cylinder which acts upon the surrounding fluid and results in a time-averaged flow past the cylinder. This motion combination has also been identified, (see for example Lighthill 1986), as being the propulsion mechanism used by the fastest deep sea marine animals. These animals, a small sample of which includes tuna, swordfish, sharks, whales and dolphins, utilise a form of tail-fin motion identified as carangiform motion that in its simplest form can be related back to a bluff body performing translational and rotary oscillation. Although in carangiform motion, the phase angle between the rotational and translational motions is the reverse of that found to produce a thrust by

Blackburn *et al.* (1999) with a circular cylinder.

To gain an insight into the effects that occur with the combined motion it is informative to review the body of knowledge surrounding the individual motion components. The following sections shed some light on the previous researches conducted on a circular cylinder in a free-stream, pure translational oscillatory motion and the combined oscillatory motions in either free-stream or quiescent fluid, *i.e.* stationary fluid. Initially we start by defining some fluid mechanic variables followed by definitions on flow instability and intrinsic flow transition. It is then followed by reviewing a stationary cylinder with no oscillation in a free-stream and then review the influence of the addition of either oscillatory motion types with or without the free-stream presence.

## 2.2 Flow past a fixed cylinder

Anagnostopoulos (1997) has introduced some researchers like Leonardo da Vinci, Strouhal or von Kármán as the pioneers in the vortex shedding behind the bluff body field. He said “in the fifteenth century Leonardo da Vinci sketched a double row of vortices in the wake of a bluff body. Strouhal (1878) demonstrated that the dimensionless frequency remains constant over a wide range of Reynolds number, while von Kármán (1911) replaced the actual vortex street with a double row of point vortices and proposed stability criteria for its existence.”

Flow around cylindrical structures is of relevance for many practical applications, *e.g.* offshore risers, bridge piers, periscopes, chimneys, towers, masts, stays, cables, antenna, and wires. Knowledge about flow-related unsteady loading on such structures is crucial for hydro- and aerodynamic design and control (Blevins 1977; Norberg 2003). For nearly a century research (see for example Strouhal 1878; von Kármán 1911) has been conducted on the flow past a fixed circular cylinder. A primary reason for this is that the geometry is easy to describe, being defined by only the cylinder diameter and length. In the limit of two-dimensional flow, this description requires the definition of only one term, the diameter. Other shapes share this feature, such as squares and equilateral triangles, however, these shapes possess sharp corners, or discontinuities. This means that the angle of attack of the flow needs to be considered for these other cross-sections, whereas it is unimportant for a circular cylinder (Leontini 2007). The dimensionless quantity describing the flow around a smooth stationary circular cylinder in a uniform stream of Newtonian fluid can be described by a single parameter, the

cylinder Reynolds number (Stokes 1851; Reynolds 1883; Munson *et al.* 2006):

$$Re = \frac{DU_\infty}{\nu}, \quad (2.1)$$

which represents the ratio of inertial to viscous forces.

The flow undergoes major changes as the Reynolds number is increased from zero to very high values and does not vary linearly, but a series of distinct transitions do occur. The flow moves from a two-dimensional creeping flow, to a two-dimensional separated flow, then to an unsteady flow, a three-dimensional flow and finally a fully-turbulent flow (Zdravkovich 1997; Leontini 2007). The flow regimes experienced with increasing  $Re$  are summarised in figure 2.2. Summations of the characteristics of these different flow regimes, particularly those after the transition to unsteady flow, can also be found in Roshko (1993); Williamson (1996c). While the wake extends over a distance which is comparable with the cylinder diameter, the boundary layer extends over a very small thickness, which is normally small compared with diameter. The most important feature of the flow regimes summarised in figure 2.2 is the vortex shedding phenomenon, which is common to all the flow regimes for  $Re > 40$ . For these values of  $Re$ , the boundary layer over the cylinder surface will separate due to the adverse pressure gradient imposed by the divergent geometry of the flow environment at the rear side of the cylinder. As a result of this, a shear layer is formed, as shown in figure 2.3 (Sumer & Fredsøe 1997). The boundary layer formed along the cylinder contains a significant amount of vorticity. Regular patterns of vortices can be formed in the wake, a classical and well known example being the von Kármán vortex street, see figure 2.1. The vortices are shed alternately from either side of the cylinder causing periodic forces to be experienced by the cylinder. The periodic force has a component in the direction normal to the free-stream, which oscillates at the shedding frequency (Bearman 1984), and a component in-line with a stream, which oscillates at twice the shedding frequency (see for example Sarpkaya & Isaacson 1981; Hurlbut *et al.* 1982; Lecointe & Piquet 1989). As the velocity of the free-stream varies the frequency of the shedding vortices also varies. This vortex shedding frequency, when normalised with the flow velocity and the cylinder diameter takes the form of

$$St = \frac{f_N D}{U_\infty} \quad (2.2)$$

The normalised vortex shedding frequency,  $St$ , is the Strouhal number. This dimen-



FIGURE 2.1: Kármán vortex street behind a circular cylinder at  $Re = 105$ . The image shows streaklines produced by electrolytic precipitation in water. *Photograph by Sadatoshi Taneda and is then reproduced from Van Dyke (1982)*

sionless group was first suggested by Rayleigh (1879), to collapse the data presented by Strouhal (1878) in a study of Aeolian tones from cylindrical strings.

### 2.2.1 Wake regimes: Variation with Reynolds number

The different flow regimes provide a natural delineation when describing the flow around a circular cylinder. Therefore, the following review of the literature pertaining to this flow is presented in sections relating to increasing  $Re$ . Of the main interest and most relevant to the present study is the effect of wake transition as  $Re$  increases. Figure 2.4 shows the variation of Strouhal number with Reynolds number for the cylinder wake. The figure is reproduced from Barkley & Henderson (1996). It should be mentioned that the  $Re$  number corresponding to the primary and secondary wake instability boundaries have varied from  $Re \approx 46$  (Barkley & Henderson 1996, for example) to  $Re \approx 49$  (Williamson 1989, for example) in the literature. In this part of thesis the experimental values from Williamson (1996c) are used.

#### 2.2.1.1 Laminar Steady Regime ( $0 < Re < 49$ )

For very small values of  $Re$  (where  $Re < 1$ ), viscous forces dominate the flow and no separation occurs. The flow does not separate from the surface of the cylinder, but stays completely attached, and the flow streamlines appear identical upstream and downstream of the cylinder. This flow is known as creeping or Stokes flow (Stokes 1851). A schematic example of such a flow is shown in figure 2.2a. This flow around a circular cylinder persists only at very small values of  $Re$ , until the first of a series of transitions occurs. The separation first appears when  $Re$  becomes 5. This is the transition to










a)		No separation. Creeping flow	$Re < 5$
b)		A fixed pair of symmetric vortices	$5 < Re < 40$
c)		Laminar vortex street	$40 < Re < 200$
d)		Transition to turbulence in the wake	$200 < Re < 300$
e)		Wake completely turbulent. A: Laminar boundary layer separation	$300 < Re < 3 \times 10^5$  Subcritical
f)		A: Laminar boundary layer separation B: Turbulent boundary layer separation; but boundary layer laminar	$3 \times 10^5 < Re < 3.5 \times 10^5$ Critical (Lower transition)
g)		B: Turbulent boundary layer separation; the boundary layer partly laminar partly turbulent	$3.5 \times 10^5 < Re < 1.5 \times 10^6$ Supercritical
h)		C: Boundary layer com- pletely turbulent at one side	$1.5 \times 10^6 < Re < 4 \times 10^6$ Upper transition
i)		C: Boundary layer com- pletely turbulent at two sides	$4 \times 10^6 < Re$ Transcritical

FIGURE 2.2: Regimes of flow around a smooth circular cylinder in steady current. *Reproduced from Sumer & Fredsøe (1997).*

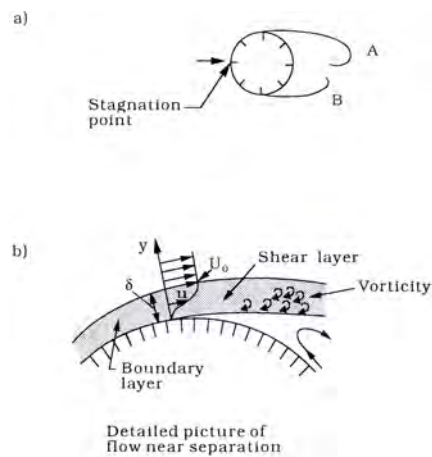


FIGURE 2.3: The shear layer. The shear layer on both sides roll up to form the lee-wake vortices, vortices A and B. *Reproduced from Sumer & Fredsøe (1997).*

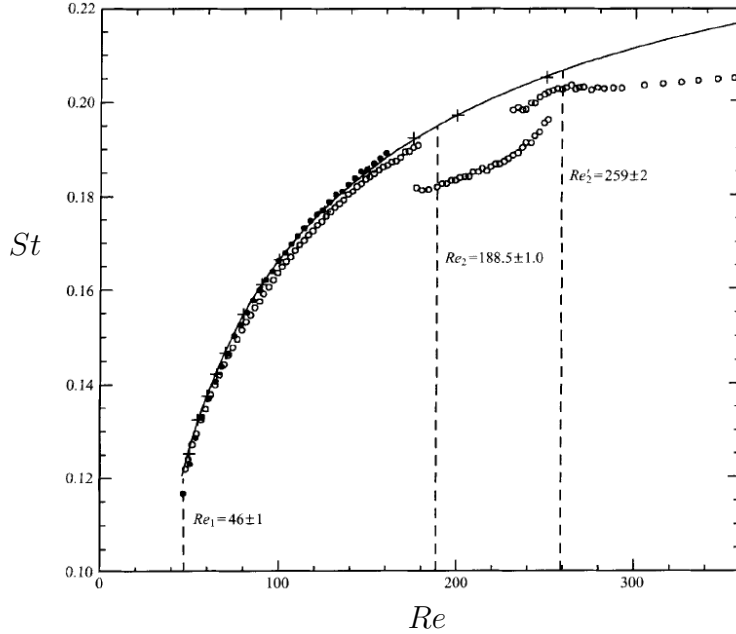


FIGURE 2.4: Variation of Strouhal number with Reynolds number for the cylinder wake. Shown are experimental results:  $\circ$ , Williamson (1989);  $\bullet$ , Hammache & Gharib (1991) and numerical results:  $+$ , Barkley & Henderson (1996). Wake instabilities up to  $Re = 300$  are labelled:  $Re_1$  (the primary instability),  $Re_2$  (the secondary instability) and  $Re_2'$  (a point of further three-dimensional instability; the trinary instability (Elston 2005)). *Reproduced from Barkley & Henderson (1996).*

separated flow, when small steady two-dimensional regions of recirculating flow form behind the cylinder. This wake region consists of two vortices symmetrically placed on either side of the wake centreline, which together form a symmetric recirculation region. Williamson (1996c) notes that the length of this region has been experimentally (Taneda 1956; Gerrard 1978; Coutanceau & Bouard 1977; Roshko 1993) and numerically (Dennis & Chang 1970) shown to increase as the Reynolds number increases. An schematic example of this steady, separated flow is shown in figure 2.2b. According to Taneda (1956) this occurs for  $Re \simeq 5$ .

### 2.2.1.2 Primary Wake Instability ( $Re \simeq 49$ )

As the Reynolds number is further increased it exceeds a critical value at which point an instability has been shown by Taneda (1956); Gerrard (1978) to manifest itself in the form of sinuous waves which propagate along the boundary of the wake recirculation in the downstream direction (Elston 2005). This trend continues until  $Re \simeq 49$  (Taneda 1956; Roshko 1993; Dušek *et al.* 1994; Williamson 1996c; Le Gal *et al.* 2001; Thompson & Le Gal 2004). At this limit, the flow undergoes its second major transition, this time



to an unsteady, time-periodic flow. This type of transition, from a steady flow to a time-periodic flow, is known as a Hopf bifurcation (Hopf 1942; Seydel 1994).

### 2.2.1.3 Laminar Vortex Shedding Regime ( $49 < Re < 140 - 190$ )

The transition from a steady flow to a time-periodic one is probably the most important transition in cylinder wakes with respect to VIV. As a consequence of the Hopf bifurcation, the primary instability, (Provansal *et al.* 1987) the wake in this regime oscillates periodically. As the Reynolds number is further increased within this regime, the amplitude of these oscillations increase. After this transition, laminar vortex shedding occurs, with vortices being shed in turn from alternate sides of the cylinder. This periodic shedding causes a periodic force on the cylinder. This force has been found to have components in the direction normal to the free-stream, which oscillates at the shedding frequency of the vortices, as noted in the review of Bearman (1984), and a component in-line with the stream, which oscillates at twice the shedding frequency, as noted in the review of Sarpkaya & Isaacson (1981). The vortices shed organise themselves into a two-row configuration, known as the Kármán vortex street. This is named after Theodore von Kármán because of his observation and analysis of the configuration (von Kármán 1911). von Kármán (1911)'s analysis was based on the earlier observation of this street of Bénard (1908). A classic example of the Kármán vortex street is shown in figures 2.1 and 2.2c. The frequency of this shedding, where the flow remains laminar and two-dimensional, is a unique function of the Reynolds number (see equation 2.2).

In an ideal case the cylinder is of infinite spanwise length, however in any laboratory experiment the cylinder is of a finite length and the experiment's spanwise boundary conditions have been shown to exert considerable influence over the flow. Williamson (1996c) observed that if the experimental spanwise boundary conditions are carefully manipulated then the flow is periodic and vortex shedding is parallel to the cylinder.

According to Williamson (1996c) the upper limit of this laminar shedding range has an enormous spread in the literature,  $Re = 140$  up to 194, although recent precise results now place the critical Reynolds number very close to 194. Barkley & Henderson (1996) found it to be  $188.5 \pm 1.0$ .

### 2.2.1.4 Secondary Instability ( $Re \simeq 190$ )

The transition from the Laminar vortex shedding regime is first observed in experiments as a sharp discontinuity of the Strouhal number, as shown in figure 2.4, where the

Strouhal number can be seen to drop rapidly at  $Re \simeq 180$ . This rapid experimental transition is characterised as the secondary instability of steady flow past a fixed circular cylinder. Williamson (1996c) observes that the upper-limit of the previous laminar vortex shedding regime has been found to vary considerably in experiments, from  $Re = 140 - 194$ . This large variation in the experimentally measured point of transition was ascribed by Williamson (1996c) to be a consequence of experimental sources of perturbation to the ideal flow. Cylinder roughness, free-stream turbulence amplitude, blockage and end effects are some of the perturbation sources cited which tended to have the effect of reducing the point of transition to a lower Reynolds number. Barkley & Henderson (1996) numerically investigated the secondary instability via numerical techniques, using a Floquet stability analysis, see §5.4, with the objective of quantifying the nature and location of the transitions to three-dimensionality. Their results showed the secondary instability transition to occur at  $Re = 188.5 \pm 1.0$ , as shown in figure 2.4. However, investigation of the location of the second instability will not be considered in this review as is not the focus of this study. A comprehensive review of this instability can be found in Barkley & Henderson (1996); Williamson (1996c); Zdravkovich (1997); Elston (2005).

#### **2.2.1.5 3-D Wake Transition Regime ( $190 < Re < 260$ )**

Williamson (1996c) describes this transition regime to be associated with two discontinuous changes in the wake formation as  $Re$  is increased. The discontinuities may be manifested by the change in base suction of the cylinder (Williamson & Roshko 1990), or by the variation in Strouhal number as the Reynolds number is increased Williamson (1988) as shown in figure 2.4. The transition to three-dimensionality begins with the onset of mode A Williamson (1988). At the first discontinuity near  $Re = 180 - 194$  (depending on experimental conditions), the inception of vortex loops (in a mode A instability) and the formation of streamwise vortex pairs due to the deformation of primary vortices as they are shed can be seen. This range has been attributed to end effects, and the “pure” transition is seen to occur very close to  $Re = 190$  (Williamson 1996c; Barkley & Henderson 1996). The mode is characterised by deformation of the vortex cores in the Kármán vortex street. The cores become wavy rather than straight, with a spatial wavelength of around 3–4 cylinder diameters. This waviness therefore turns some of the vorticity in the streamwise direction, and vortex loops are then drawn

out in the high-strain region between the primary vortices (Henderson 1997). This discontinuity is hysteretic and is labeled as a “hard” transition by Zhang *et al.* (1995). Experimental and numerical examples of the structure of the saturated mode A are shown in figure 2.5. The Floquet stability analysis of Barkley & Henderson (1996) provided predictions of both critical wavelengths and  $Re$  for three-dimensional modes arising from the two-dimensional Kármán vortex street. That study found that the first Floquet mode became unstable at  $Re = 188.5$ , and possessed a spatial wavelength of  $\lambda = 3.96D$ , corresponding to mode A. This linear analysis also indicated that mode A was at its strongest in the vortex cores, agreeing with the experimental observation of vortex core waviness. Leweke & Williamson (1998) also investigated the character of the mode A instability. The analysis returned a predicted wavelength for the instability of  $3D$ , in good agreement with the observed wavelength of mode A. Their analysis also indicated areas of the flow where the mode would be expected to grow. Leontini (2007) reported on the paper from Henderson (1997) which covered many phenomena relating to the transition to three-dimensionality and mode A. The symmetry properties of the mode were reported, and an investigation to the effect of the span of the cylinder was made. It was reported that for long cylinder spans, mode A led to the development of spatio-temporal chaos, or a disordered pattern and a lack of periodicity in the wake. This was distinguished from strong turbulence that occurs with increasing  $Re$  and the reducing impact of dissipative viscous forces. This spatio-temporal chaos offered an explanation for the spread in the data of earlier  $StRe$  curves (Roshko 1954). While mode A is the first three-dimensional mode to arise, it is not the most resilient. At the second discontinuous change in the  $St - Re$  relation, there is a gradual transfer of energy from mode A shedding to a finer-scaled mode, logically named mode B (Williamson 1988). Floquet stability analysis by Barkley & Henderson (1996) predicted mode B to first become unstable at  $Re = 259$ , but experimentally mode B is first detected anywhere in the range  $230 < Re < 250$  Williamson (1988, 1996a). With the onset of mode B, energy is gradually passed from mode A to mode B, until by  $Re \simeq 285$  there is effectively no evidence of mode A. Once mode B is established, it is very robust, with evidence of mode B still present in the wake at  $Re = 1000$  (Wu *et al.* 1996). Early three-dimensional simulations by Karniadakis & Triantafyllou (1992) indicated that mode B was the primary three-dimensional transition, and that it led to a period-doubling cascade as the route to turbulence. However, later simulations

from Zhang *et al.* (1995), and the extensive computations of Thompson *et al.* (1996) indicated that if a suitable spanwise domain was employed, mode A was resolved and the predicted period-doubling cascade did not occur, the route to turbulence instead being through spatio-temporal chaos. These findings highlighted that the suppression of particular three-dimensional modes could change the path to turbulence. Mode B comprises finer-scale streamwise vortices, with a spanwise length scale of around  $1D$  and is more or less focused in the braid shear layer that links successive primary vortices in the Kármán vortex street. Examples of the saturated mode B are shown in figure 2.5. Following the discovery of modes A and B, and their effect on the path to turbulence, few researchers investigated the possibility of other types of modes. As well as modes A and B, other modes have been shown to be theoretically possible. Marques *et al.* (2004) and Blackburn *et al.* (2005), using group theory (Rosen 1995), showed that for flows possessing the symmetries of the Kármán wake, only three generic bifurcations can arise from the two-dimensional base flow. One of which breaks the “time” part of the spatio-temporal symmetry, and is represented by a quasi-periodic mode, or a mode that has a different period to the two-dimensional base flow. Such a quasi-periodic mode can be found numerically in the fixed cylinder wake (Blackburn & Lopez 2003). It is predicted to occur around  $Re = 377$ , and so is not observed in experiments, as the base flow is far from two-dimensional by this stage. However, experiments by Zhang *et al.* (1995) with an upstream tripping wire excited a mode with a similar value of  $\lambda$  to this quasi-periodic mode, in the Reynolds number range  $170 \leq Re \leq 270$ . The experiments of Zhang *et al.* (1995) and the restricted-domain simulations of Karniadakis & Triantafyllou (1992) demonstrated that relatively passive measures could be used to affect the inception order of the three-dimensional modes, even if there is only a small number of possible modes involved (Marques *et al.* 2004; Blackburn *et al.* 2005; Leontini 2007).

### 2.2.1.6 Fine Scale 3-D Wake Regime ( $260 < Re < 1000 - 2000$ )

This regime initially consists of mode B shedding. Subsequent increases in  $Re$  towards the limits of our consideration ( $Re = 2000$ ) result in the flow becoming increasingly disordered, leading to a reduction in two-dimensional Reynolds stresses and an increasing length of the formation region. The flow in the range of  $Re$  between 1000 and 2000 also is experiencing the wake contraction and the wake regime is not changing

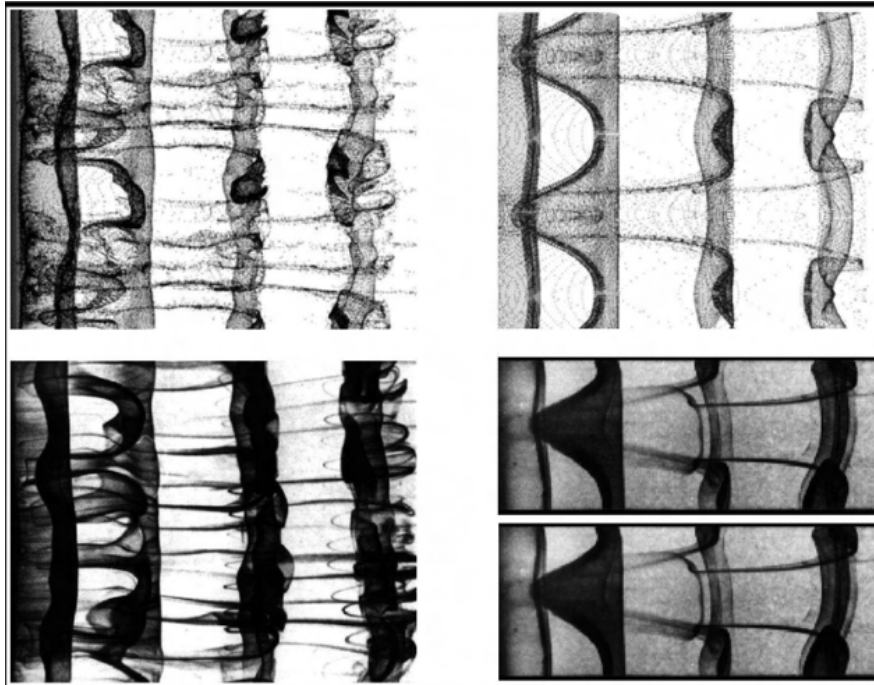


FIGURE 2.5: The saturated mode structure for mode B (left), and mode A (right). The bottom images were obtained through dye visualisation during experiments such as those by Williamson (1996c). The top images were obtained through particle tracking three-dimensional simulations such as those by Thompson *et al.* (1996). Both show the development of spanwise vortices. The waviness of the vortex cores in mode A is clear, as is the finer-scale structure of mode B. Flow is from left to right. *Reproduced from Thompson et al. (2006b).*

significantly. This regime is also equivalent with the sub-regime TrSL1 definition of Zdravkovich (1997).

### 2.3 Flow past a translationally oscillating cylinder

The focus of this thesis is on cylinders undergoing combined translational and rotational oscillatory motions mainly in quiescent fluid and to some extent in a free-stream. Therefore, the following sections of this literature review focus on the primary phenomena that occur in such flows and reviewing the few available sources of literature on the combined motion. To gain an insight into the effects that occur with the combined motion it is informative to review the body of knowledge surrounding the individual motion components. For this reason, the literature pertaining to purely translational or rotational oscillatory motion is also presented. The approaches to studying and understanding this problem have tended to fall into two categories; the study of the response of an elastically mounted cylinder in a free-stream or of a cylinder that has been subjected to forced oscillations in a free-stream or quiescent fluid. The present

review will primarily focus on the forced translational oscillations approach, as it is the most relevant to the current investigation. In forced translational oscillations the cylinder axis is translating along a linear path at some orientation relative to the incident flow. Here we primarily consider two particular orientations relative to the free-stream: transverse oscillation where the direction of cylinder oscillation is at right angles to the incident flow; and in-line oscillation where the direction of cylinder oscillation is aligned with the free-stream. A more detailed review of other orientations can be for example found in Elston (2005).

The study of VIV is important to a large number of disciplines such as fluid mechanics, structural vibrations, acoustics, offshore engineering, heat exchanger design, bridge design and aeronautical engineering. Accordingly, substantial research time and publications have been devoted to this phenomenon (Elston 2005). Before considering VIV, it is important to have an in-depth understanding of how the oscillation of a cylinder changes the behaviour of the flow from the limiting case of a fixed cylinder. Therefore, phenomena such as synchronisation, timing of vortex shedding, and wake modes will be presented. As mentioned above, with these concepts established, the literature on the flow past an oscillating cylinder will first be reviewed. In the following section the literature on the translational oscillation in a quiescent fluid will be presented. Finally, the flow around a combined oscillatory motions in either quiescent fluid or free-stream will be reviewed.

### **2.3.1 Transverse Oscillations**

The vibration of structures immersed in a fluid flow has received much experimental, analytical, and numerical study, as reported in review articles by Parkinson (1974); Savkar (1977); Sarpkaya (1979); King (1977); Williamson (1996c); Paidoussis (1998); Williamson & Govardhan (2004); Sarpkaya (2004), and textbooks of Blevins (1977); Sumer & Fredsøe (1997); Naudascher & Rockwell (1994). Numerical studies of vortex shedding have primarily addressed the flow of a uniform stream normal to a rigid circular cylinder, in either two- or three-dimensions. Since the cylinder is fixed, no information about vibration interaction is thus obtained. If the cylinder is vibrating, either in forced or natural motion, a nonlinear interaction occurs as the cylinder frequency approaches the vortex shedding frequency. This interaction has two major characteristics: First, the natural shedding frequency is suppressed and vortex shedding

occurs instead at the cylinder vibration frequency over a range of flow velocities. This is known as the lock-on or “wake capture” phenomenon. Second, the transverse or lift force increases greatly, with a maximum response occurring near the mid-point of the lock-on range. These effects occur when the cylinder is vibrating either in-line or transverse (The translational oscillations comprise a set of oscillations where the cylinder axis is translating in any orientation relative to the incident flow with the free-stream direction).

The large number of studies into a cylinder in simple harmonic cross-flow oscillation has identified a number of significant features of the fluid-cylinder interaction. The features most relevant to the present study are reviewed in the following sections.

### **2.3.1.1 Lock-on**

Vortex shedding results in periodic forcing of a body that under certain conditions induces large scale motion of the body. As flow interacts with the bluff body above a certain Reynolds number vortices are produced at the trailing edge of the body and shed at a given frequency. Vortices are regions of low pressures, consequently the pressure differences between the vortex cores and outside them exert a force on the body. As the vortices shed regularly the body experiences a periodic forcing. A significant feature of the fluid-structure interaction for a cylinder in transverse oscillation is the ability of the cylinder to capture the vortex shedding frequency ( $f_v$ ) so that it oscillates at the cylinder oscillation frequency ( $f_t$ ) instead of the natural frequency of shedding ( $f_N$ ) for a fixed cylinder. The terms “Synchronisation”, “Lock-in” or “Lock-on” are used to describe the wake when the periodic shedding of vortex structures and the resulting fluctuating forces are synchronised with the motion of the body. The frequency of vortex shedding can be quantified by measuring the velocity within the wake or the lift force on the body. If lock-on occurs the structure may experience resonance and, due to the periodic forcing induced by the flow the body, may exhibit large scale motion, compared to when the frequencies were not synchronised. The bounds of lock-on are generally defined to include all cases where the most energetic wake frequency coincides with the frequency of oscillation, see for example Bishop & Hassan (1964); Marris (1964); Koopmann (1967); Griffin & Ramberg (1974); Stansby (1976); Blevins (1977); Sarpkaya (1979); Karniadakis & Triantafyllou (1989); Cheng & Moretti (1991); Hall & Griffin (1993); Blackburn & Henderson (1999) and Balabani *et al.* (2007). When the vortex

shedding, or wake frequency has a strong spectral peak, lock-on can easily be identified. However, the definition of lock-on is somewhat subjective as it depends on how and where the wake frequency is measured, therefore the exact boundaries of lock-on are not rigorously defined. Lock-on can be demonstrated schematically using a phase plot of the displacement of the body versus lift or wake velocity/frequency. In cases where the flow is not locked-on, the most energetic shedding frequency is often close, or equal to the Strouhal shedding frequency of the stationary body (Carberry 2002). The lock-on range is somewhat dependent on the Reynolds number and cylinder amplitude and the maximum range is approximately  $\pm 40$  percent of the mid-point frequency (Hurlbut *et al.* 1982). Cylinder vibrations at frequencies far removed from the harmonics and sub-harmonics of the shedding frequency have only a small effect on the wake (Blevins 1977).

This lock-on, or synchronisation, effect was first documented by Hartog (1956) and later by Bishop & Hassan (1964) (Blevins 1977; Hall & Griffin 1993). In their experimental driven oscillation study, they found synchronisation occurred for driving frequencies close to, but both above and below, the natural shedding frequency. Therefore, a defining parameter was the ratio of the oscillation frequency to the Strouhal frequency,  $f_t/f_N$ . It was also noted that the range of synchronisation frequencies seemed to increase with increasing amplitude of oscillation. This was systematically studied by Koopmann (1967) with a series of low- $Re$  experiments. This flow regime has been found to occur for oscillations at various orientations to the incident flow (Hall & Griffin 1993) and for rotational oscillation as observed by Tokumaru & Dimotakis (1991). For lock-on to occur, a sufficiently large oscillation amplitude is required and once this threshold is exceeded the oscillations causing the lock-on can control the location and extent of the vortex formation region (Hall & Griffin 1993; Sarpkaya & Isaacson 1981). It was shown by Koopmann (1967) that the amplitude of oscillation increased, so did the range of frequencies resulting in synchronisation. This range always encompassed the Strouhal frequency for a fixed cylinder,  $f_N$ , but extended further for frequencies below  $f/f_N$  than for frequencies above it. This synchronisation dependence on  $A_t/D$  has been confirmed through the experiments of Griffin (1971); Griffin & Ramberg (1974); Stansby (1976) and Williamson & Roshko (1988), and the simulations of Hurlbut *et al.* (1982); Blackburn & Karniadakis (1993), and Meneghini & Bearman (1995) among others, at  $Re$  where the flow is both two- and three-dimensional.



Sometime later Cheng & Moretti (1991) showed that the vortex shedding frequency locks onto the cylinder forced frequency not only in the vicinity of the frequency of vortex shedding expected for a fixed cylinder, but also when the driving frequency is a multiple of the expected frequency. At very small amplitudes the phenomenon has been demonstrated to occur when the frequency ratio  $f_t/f_N$  is near 1.0. Subsequent increases of the amplitude of oscillation has been shown to increase the envelope of frequencies over which the primary lock-on regime will occur. A lock-on envelope derived from results presented in the reviews of Blevins (1977) and Sarpkaya (2004) can be seen in figure 2.6 which shows the boundaries of this region for low- $Re$  experiments. The comparison between the results of Koopmann (1967) and Cheng & Moretti (1991) shows that increasing the Reynolds number results in a widening of the lock-on envelope. Cheng & Moretti (1991) also showed that outside the lock-on regions, the frequency of vortex shedding gradually decreases with increasing forcing frequency and also with increasing amplitude. They speculated that this is related to a widening of the wake they have observed in their flow visualisation experiments. In the cases shown, the central frequency of the lock-on envelope is tilted towards the lower frequencies ( $< 1$ ). Additionally, the envelope of frequencies found by Cheng & Moretti (1991) exhibits a slanted onion-shaped region. According to Sarpkaya (2004), the Reynolds number has a strong influence on the upper frequency lock-on boundary. As the amplitude of oscillation approaches zero the lock-on envelope narrows such that  $f_t/f_N$  approaches 1.0. The results of Koopmann (1967), shown in figure 2.6, have a minimum amplitude at which lock-on was found to occur,  $A_t/D \approx 0.05$ . However, the results of Cheng & Moretti (1991), also presented in figure 2.6, show that much lower values of  $A_t/D$  in the lock-on regime can be achieved. Blackburn & Henderson (1999) suggested that the minimum amplitude was associated with the presence of oblique, instead of parallel, vortex shedding for the stationary circular cylinder. Further, they speculated that it is likely for three-dimensionally unstable flows that there does exist a limiting minimum amplitude for lock-on to occur in experiments due to the perturbation imposed by the cylinder on the flow being too small to control the turbulent wake. Karniadakis & Triantafyllou (1989) also qualitatively distinguished the upper and lower branch over a range of  $f_t/f_N$  and observed that the lock-on region was amplitude dependent and became larger (wider) with an increase of amplitude. Their experiment also displayed a region outside the lock-on boundaries where the flow is receptive to the oscillation

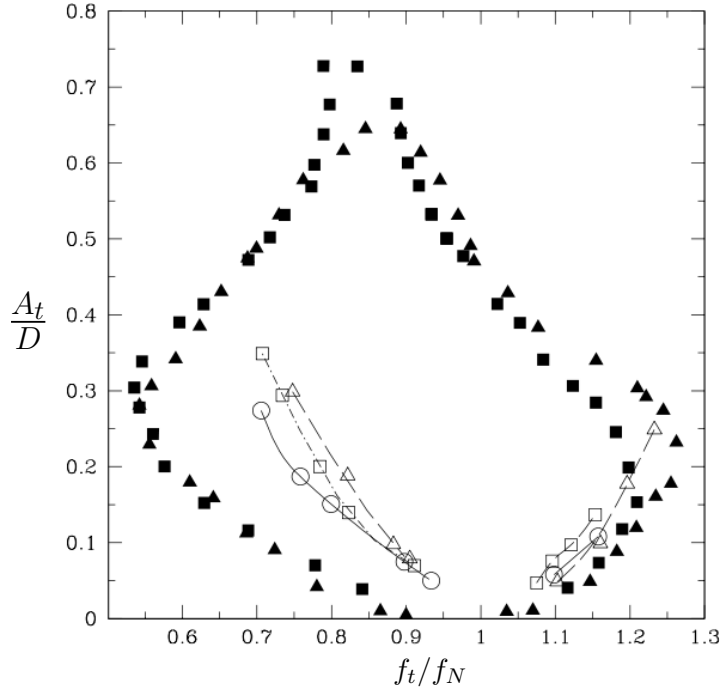


FIGURE 2.6: Primary lock-on regime. Shown are the boundaries of the lock-on regime as a function of the frequency ratio between the excitation and natural shedding frequency and the non-dimensionalised amplitude of oscillation. Low Reynolds number results from Koopmann (1967) are at:  $\triangle$ ,  $Re = 100$ ;  $\square$ ,  $Re = 200$  and  $\circ$ ,  $Re = 300$ . The experimental results of Cheng & Moretti (1991) were obtained at Reynolds numbers of 1500,  $\blacksquare$ , and 1650,  $\blacktriangle$ ; *The graph appeared in Elston (2005) and is reproduced by permission.*

frequency of the body. Bearman (1984) suggested that in driven cylinder experiments the cylinder oscillation also has the effect, during lock-on, of synchronising the moment (in time) of shedding along the span of the cylinder, so that parallel vortex shedding is universally observed, with no oblique modes present.

Other researchers also investigated the lock-on phenomenon for other applications like: rotationally oscillating cylinder (for example Chou 1997), pulsating flow (for example Konstantinidis & Balabani 2008), pulsating flow in tube arrays (for example Konstantinidis *et al.* 2000) and oscillating flow at high  $Re$  numbers (Barbi *et al.* 1986). As these are not the focus of this thesis they will not be covered here.

The applications of biomimetic motion proposed by Blackburn *et al.* (1999) and its application to the reduction of VIVs is of particular interest to the present study. As was explained so far there has been considerable research on the effects of transverse only motion on cylindrical wakes but there is not much studies on VIV of a circular cylinder undergoing combined translational and rotational oscillatory motion.

### 2.3.1.2 Vortex Shedding Structures and Wake modes

The general form of the fluid structures shed into the near-wake is often described in terms of the mode of vortex shedding. An oscillating cylinder can exhibit a number of different shedding modes. A systematic study of the wake modes of a driven oscillating cylinder was made by Williamson & Roshko (1988). They visualised the vortex wake patterns for a cylinder subjected to harmonic transverse motion in a uniform cross-flow over a Reynolds number range 300-1000. The shedding regimes are generally expected to persist over a wider range of Reynolds numbers (Carberry 2002). The non-dimensionalised oscillation parameters of amplitude,  $A_t/D$ , and wavelength,  $\lambda_{osc}/D$ , were used to characterise their study, where  $\lambda_{osc} = U_\infty T_t$  is equal to the product of the free-stream velocity,  $U_\infty$ , and the period of cylinder oscillation  $T_t$ . The parameters were varied over the range  $0 < A_t/D < 5.0$  and  $0 < \lambda_{osc}/D < 15.0$ . A number of different regimes were observed where each regime was characterised by the number of single vortices ( $S$ ) or vortex pairs ( $P$ ) formed on each side of the cylinder over each cycle of vortex shedding, *i.e.*, the classical antisymmetric Kármán vortex street is designated the  $2S$  mode using this notation, and a mode consisting of a pair of vortices shed each half-cycle, or a total of four vortex structures per oscillation, is designated the  $2P$  mode. Their results can be seen in figure 2.7, which shows the modes in the vicinity of the lock-on regime. In the regime of synchronisation, only the  $2S$  and  $2P$  modes were observed at amplitudes of relevance to VIV. Examples of the  $2S$  and  $2P$  mode, along with the asymmetric  $P + S$  mode, are also shown in figure 2.8. The Reynolds number was not held constant over the entire  $A_t/D - \lambda_{osc}$  plane, it being argued that the Strouhal number for a fixed cylinder does not vary over this range. However, significant changes do occur over this range, such as decreasing base-suction coefficient and formation length (Roshko 1993; Williamson 1996c). Therefore, the boundaries shown on this plot may have some built-in bias. Regardless, the modes present seem universal, even if the boundaries are not completely fixed (Leontini 2007)). Basic modes of vortex formation from the cylinder undergoing forced translational oscillations, in general at angle  $\eta$  with respect to the free-stream, are summarised in figure 2.9 (see Ongoren & Rockwell 1988b, p. 227). The same notation will be used throughout the thesis.

These VIV results, along with the driven oscillation results, do indicate that a relatively high amplitude is required to form the  $2P$  wake. Results from Govardhan

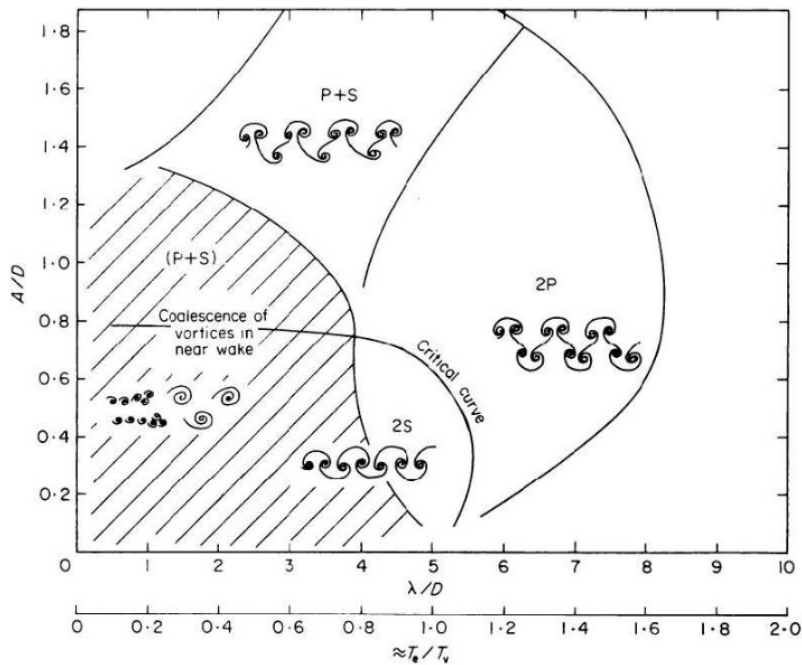


FIGURE 2.7: Map of vortex synchronisation patterns near the fundamental lock-on region. The critical curve marks the transition from one mode of vortex formation to another. *Reproduced from Williamson & Roshko (1988).*

& Williamson (2001) show a significant increase in the periodic Reynolds stress when the  $2P$  wake is present, as compared to the fixed cylinder Kármán wake. These results also show that the  $2P$  wake does not consist of four vortical structures being shed from the body; instead, one structure is shed per half-cycle that is then split into two under the influence of the high strain in the near-wake. The influence of Reynolds stress goes some way to explaining the phenomenon of the  $2P$  wake.

Blackburn *et al.* (2000) presented two-dimensional and three-dimensional simulations at the same  $Re$ , and showed that the  $2P$  wake was present for the three-dimensional flow, and the  $2S$  wake for two-dimensional flow. The only study that shows anything other than the  $2S$  wake for two-dimensional VIV is Singh & Mittal (2005), where the  $P + S$  wake was realised. However, this only occurred for  $Re > 300$  where the flow is assumed to be naturally three-dimensional, so that the assumption of the  $2S$  wake being the only configuration for two-dimensional VIV still seems to hold. Leontini (2007) investigated the conditions at which the two-dimensional assumption holds. As this is not the aim of this thesis will not be covered in the present review.

Blevins (1977) showed that lock-on increases the spanwise correlation of vortex shedding along the cylinder axis. Figure 2.10 shows the effects that cylinder oscillation can

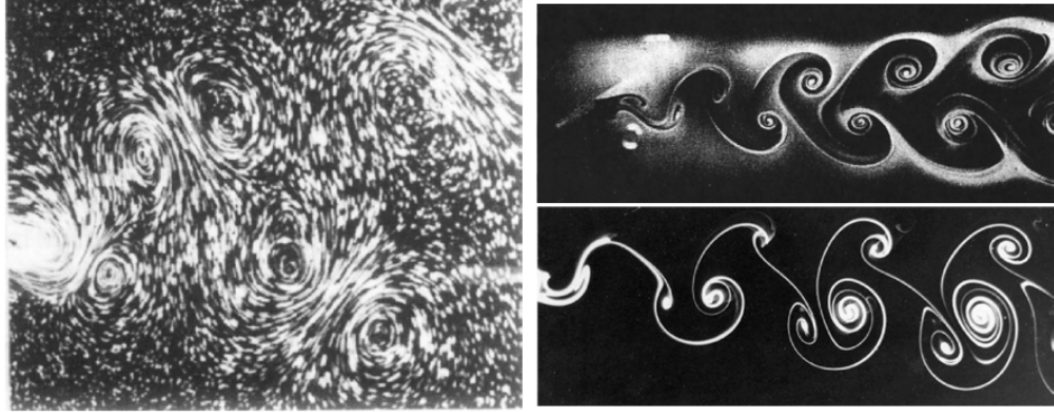


FIGURE 2.8: The major wake modes during synchronised VIV and driven oscillation. Left: the  $2P$  mode (Williamson & Roshko 1988). Top right: the  $2S$  mode (Koopmann 1967). Bottom right: the  $P + S$  mode (Williamson & Govardhan 2004). Flow is from left to right in all images. *The graph appeared in Leontini (2007) and is reproduced by permission.*

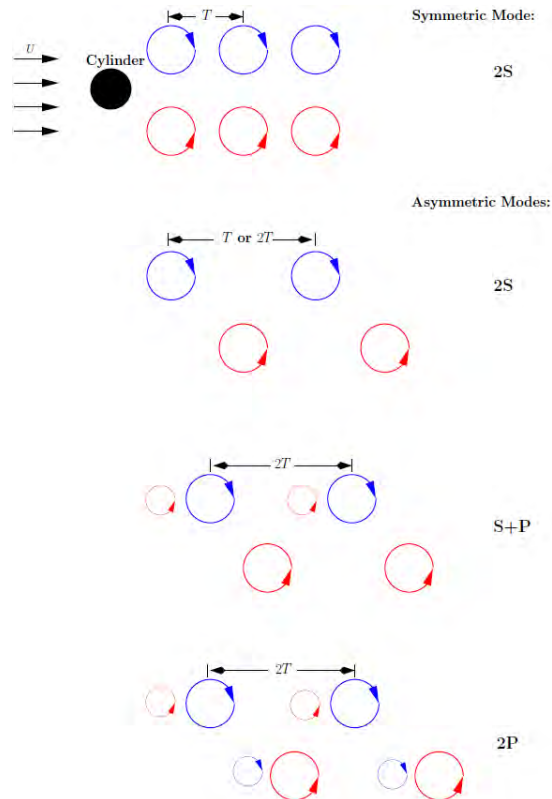


FIGURE 2.9: Representation of basic modes of vortex formation from cylinder oscillating translationally at angle  $\eta$  with respect to the free-stream. *The graph originally appeared in Ongoren & Rockwell (1988b) and then is reproduced from Al-Mdallal (2004) by permission.*

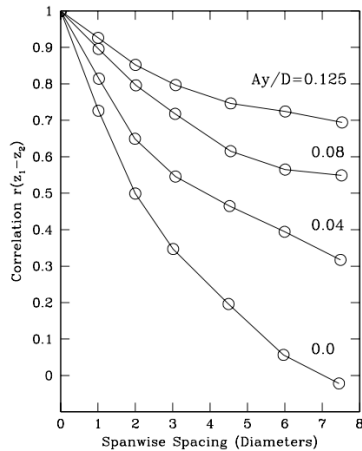


FIGURE 2.10: Spanwise correlation of vortex shedding for a rigid cylinder during lock-on. The graph originally appeared in Blevins (1977) and then is reproduced from Elston (2005) by permission.

have on the spanwise correlation, where a value of 1.0 corresponds to two-dimensional flow.

The investigations of Ongoren & Rockwell (1988a) and Gu *et al.* (1994) also considered the variation of the wake as the frequency ratio between the forced oscillation to the natural shedding,  $f_t/f_N$ , increased through unity, focusing on the changes in the phase referenced structure of the near-wake. In both these investigations the phase point at which the flow fields were compared corresponded to the maximum displacement of the cylinder. Carberry (2002) comprehensively investigated this problem and not being the aim of this thesis is not considered here.

### 2.3.2 In-line and Oblique Oscillations

The study of forced oscillations at angles other than transverse to the flow,  $\eta$ , ( $0^\circ \leq \eta \leq 90^\circ$ ) have received considerably less attention than the transverse case. Primarily this appears to have occurred because the forces arising from transverse oscillations are substantial greater than those arising from in-line oscillations. However Jauvtis & Williamson (2003, 2004) have observed significant alteration of the fluid-structure interactions when the mass ratio between the cylinder and surrounding fluid is reduced below 6. In this scenario, a new response branch was observed with much larger amplitudes of in-line oscillation and a vortex shedding mode that resulted in a triplet of vortices being formed in each half-cycle.

Ongoren & Rockwell (1988b) presented hydrogen bubble visualisations of a circular cylinder subjected to forced oscillations at angles to the cross-flow ranging from the in-

line case,  $\eta = 0^\circ$ , to the transverse case,  $\eta = 90^\circ$ . Visual observations were made in the Reynolds number and frequency ratio ranges  $584 \leq Re \leq 1300$  and  $0.5 \leq f_t/f_N \leq 4.0$ , respectively, at angle of inclination  $\eta = 0^\circ, 45^\circ, 60^\circ, 90^\circ$  of cylinder oscillation with respect to the free-stream. For most experiments, a constant value of dimensionless amplitude,  $A_t/D = 0.26$ , was chosen. They showed that if the cylinder is excited at an angle other than the cross-stream or streamwise direction, then there is mixed-mode excitation: the perturbation from the cylinder motion contains both symmetrical and anti-symmetrical contributions and the potential for exciting both types of modes. Moreover, these modes either can be synchronised, *i.e.* phase-locked, with the cylinder motion, or they can compete with each other. In their investigation, they addressed under which conditions these modes occur, for both synchronised and non-synchronised vortex formation. Particularly remarkable is the finding by Ongoren & Rockwell (1988b) of the occurrence of synchronised vortex formation in the asymmetric mode when the cylinder motion produces purely symmetrical perturbations of large amplitude.

According to the experimental work of Ongoren & Rockwell (1988b) symmetric modes can occur at any value of inclination angle to the free-stream except  $90^\circ$ . The asymmetric,  $2S$ ,  $P + S$  and  $2P$ , modes (a notation similar to that of Williamson & Roshko (1988) explained in the previous section §2.3.1.2 is used) over two oscillation cycles occur only for  $0^\circ \leq \eta < 90^\circ$  where there is a symmetrical component in the flow perturbation. In fact the effect of the symmetrical component of the perturbation is to double the period of the asymmetrical vortex formation. The asymmetric  $2S$  mode over two periods of the cylinder oscillation occurs only for  $\eta \neq 0^\circ$ . The asymmetric  $P + S$  and  $2P$  occur only for  $\eta = 0^\circ$ . We note that generalisation of occurrence of these modes are restricted to the relatively small amplitudes of cylinder oscillation. Ongoren & Rockwell (1988b) showed that the cylinder at an angle other than  $0^\circ$  or  $90^\circ$  can cause vortex lock-on. In their work it was reported that phase-locking of vortex shedding with the cylinder motion is possible for all the modes described earlier. Griffin & Ramberg (1976) in an in-line study only,  $\eta = 0^\circ$ , experimentally visualised two modes of vortex shedding. These modes correspond to the symmetric and antisymmetric observed by Ongoren & Rockwell (1988b).

Griffin & Ramberg (1976) and Ongoren & Rockwell (1988b) found the lock-on region for in-line oscillations was centred at a frequency which is double the Strouhal frequency

of shedding,  $2f_N$ , as compared to the lock-on region for transverse oscillations which is centred at the Strouhal frequency. Ongoren & Rockwell (1988b) also found that lock-on was possible for all the modes they observed. When the vortex shedding was not synchronised to the oscillation frequency a competition between the symmetrical and antisymmetrical modes was observed. It was found that the near-wake structure locks on to each mode for a number of cycles and then abruptly switches to the next mode.

## 2.4 Flow Past a Rotationally Oscillating Cylinder

Many attempts have been made to control the wake behind a circular cylinder in recent years. The rotation of a cylinder in various uniform flows is expected to modify wake flow pattern and vortex shedding configuration, which may reduce a flow-induced oscillation or augment a lift force. The basic rationale behind the rotation effect is that as a cylinder rotates the flow is accelerated on one side of the cylinder and decelerated on the other side. Hence, pressure on the accelerated side becomes smaller than that on the decelerated side, resulting in a mean lift force. Such a phenomenon is referred to as the “Magnus” effect. As a result, the rotation significantly alters the flow pattern, and probably has an effect on flow-induced oscillation. Most of such research performed to date can be classified into two categories, a rotary oscillation and a unidirectional rotation. There are a large number of papers investigating the latter, unidirectional rotation. Among them the most recent one is the experimental and numerical investigation of the wake behind a cylinder rolling on a wall at varying rotation rates by Stewart *et al.* (2010). As it is more relevant to this thesis the first, rotary oscillation, is reviewed here.

A brief survey of the experimental studies by Taneda (1978a); Wu *et al.* (1989); Tokumaru & Dimotakis (1991) and Filler *et al.* (1991) reveals that rotational oscillations can significantly alter the wake shedding pattern and can lead to dramatic decreases in the cylinder drag coefficient when the velocity of the rotation is large enough. Taneda (1978a) experimentally investigated the effects of rotary cylinder oscillations over a low Reynolds number range. He demonstrated that the wake structure can be substantially altered by rotary oscillation. Taneda (1978a) performed a series of visualisations, using aluminium dust and electrolytic precipitation techniques, for the Reynolds number range 30 to 300 and Strouhal numbers between 0 and 55. By altering the frequency and



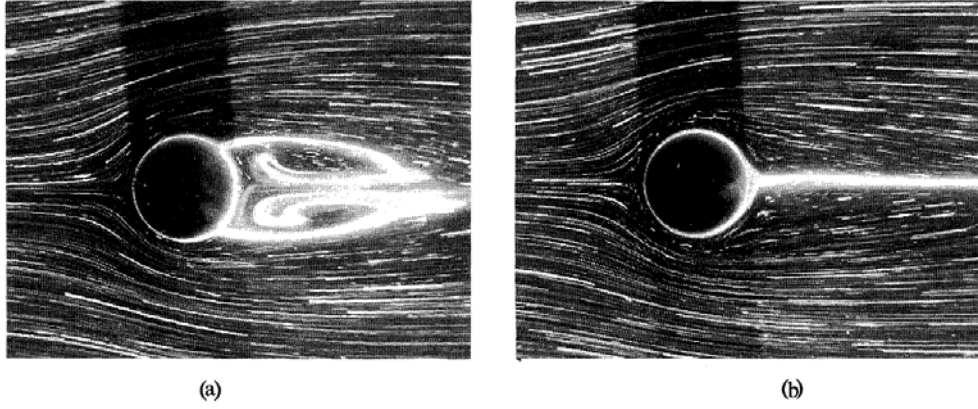


FIGURE 2.11: Streamline and streak-line patterns at  $Re = 33.7$ ,  $D = 1.0\text{cm}$ ,  $\theta = 45^\circ$ . (a)  $St_f = 0$ , (b)  $St_f = 3.4$ . At a critical frequency of oscillation the wake region behind the cylinder is much reduced. *Reproduced from Tameda (1978a)*.

amplitude of rotary oscillation he was able to determine a critical value of the Strouhal number where the dead water region behind the cylinder vanishes. In these experiments the Strouhal number was based on oscillation frequency,  $St_f$  ( $f_\theta =$  frequency of rotary oscillation) instead of the classical shedding frequency. The critical Strouhal number,  $St_c$ , was found to vary inversely with the oscillation amplitude but was independent of the Reynolds number over the range of values considered. Increasing  $St_f$  from zero was found to cause the separation points to move rearward until  $St_c$  was attained. At this point the recirculation region of the wake vanished and the wake was found to be narrow with no reverse flow. At values of  $St_f$  greater than  $St_c$ , the streamlines were found to converge at the back of the cylinder and approach a potential flow solution. Figure 2.11 shows clearly the effects mentioned for  $St_f = 0$  and  $St_f = 3.4$ , where  $St_c = 2.8$ .

Experiments at a higher Reynolds number of  $1.5 \times 10^4$  by Tokumaru & Dimotakis (1991) yielded related results. At this Reynolds number the rotational frequency (forcing Strouhal number,  $St_f$ ) and the normalised peak rotation rate of  $\Omega_1$  were varied, where the rotation rate,  $\Omega(t)$ , is defined as

$$\Omega(t) = \frac{\dot{\theta}D}{2U_\infty} = \Omega_1 \sin(\omega t) \quad (2.3)$$

and  $\dot{\theta}$  is the angular velocity of the cylinder. The drag coefficient,  $C_d$ , and the wake displacement area were evaluated at a single location,  $4.5D$  downstream of the cylinder. The results showed that the wake displacement area could be made substantially larger or smaller than in the unforced case by altering the rotary motion of the cylinder. It

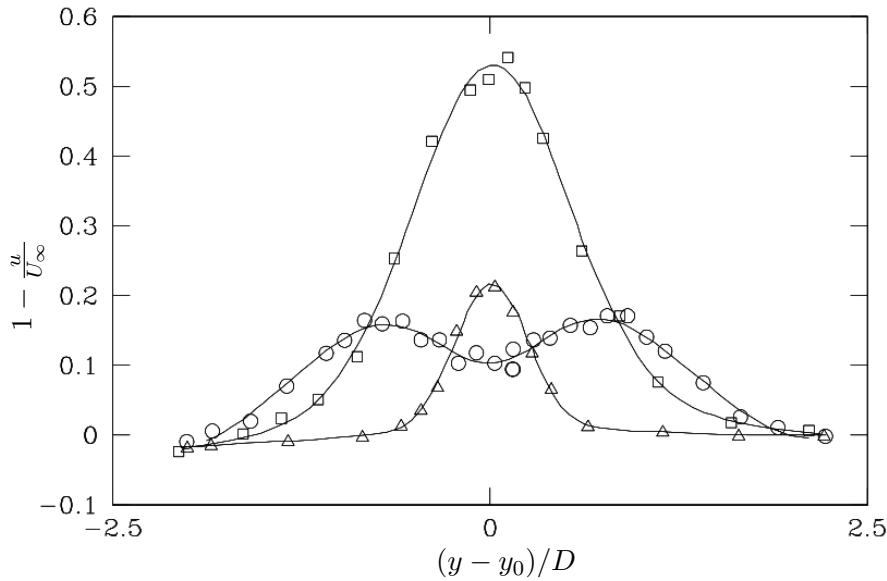


FIGURE 2.12: Cylinder wake mean velocity profiles, measured at midspan ( $\Omega_1 = 2$ ):  $\square$ , unforced;  $\circ$ ,  $St_f \approx 0.2$ ;  $\triangle$ ,  $St_f \approx 1$  (Tokumaru & Dimotakis 1991). The graph appeared in Elston (2005) and is reproduced by permission.

was found that the minimum wake displacement area occurred in the neighbourhood of  $St_f = 1$  and  $\Omega_1 = 3$ , where it was half the value for the unforced case (Tokumaru & Dimotakis 1991). The cylinder wake-mean velocity profiles in figure 2.12 clearly demonstrate the influence of the rotational frequency. The minimum  $C_d$  was found to approximately coincide with the minimum wake area. The rate of rotation affected the number of vortices shed per cycle and four distinct modes of vortex shedding per cycle were identified. It was concluded that when the forcing frequency is similar to the natural vortex shedding frequency, the greatest control can be exerted over the wake. In both studies there was no net circulation introduced by the rotary oscillation and consequentially there was no time-mean lift generated.

Lu & Sato (1996) and Chou (1997), in numerical studies of vortex shedding from a rotationally oscillating cylinder, recorded the transition and selection of different vortex shedding modes and the lock-on phenomenon. Lu & Sato (1996) conducted their experiments at  $Re = 200, 1000, \text{ and } 3000$  for a range of rotational velocities and frequencies and used a wide range of frequency ratios  $F_\theta = 0.5, 1, 2, 3, \text{ and } 4$  ( $F_\theta = f_\theta / f_v$ ) with no emphasis on the variation of frequency ratio in the neighbourhood of  $F_\theta = 1$  in order to give more details about the lock-on range, while Chou (1997) reported with the same approach but mainly at different Reynolds number ( $Re = 500 \text{ and } 1000$ ). The main objective of Chou (1997) was to study the flow structure in the wake as well as

the hydrodynamics associated with a circular cylinder performing rotational oscillation in a cross-stream.

More recently computational works by Baek & Sung (1998, 2000); Mahfouz & Badr (2000); Cheng *et al.* (2001a,b) and Dennis *et al.* (2000) have expanded upon these earlier experimental studies. The focus in this latter work has been on the lock-on behavior in the fluctuating forces acting on the cylinder, and while they have shown a sampling of the different locked-on wake states, they have not examined in great detail how the wake changes as the rotational forcing changes. Du *et al.* (2003) have also examined the effects of rotational oscillation on the vortex shedding mode and the spatial structure and strength of the shed vortices behind a circular cylinder at  $Re = 1750$ . Depending on the values of the rotational oscillation frequency and amplitude, they observed different vortex shedding modes. They found that the vortex wake expanded for oscillation frequencies less than the natural Kármán frequency while contracting for frequencies greater than the Kármán frequency. They also found out that the longitudinal spacing is decreased pronouncedly with increasing frequency and changed to a much lesser degree with an increase in the oscillation amplitude, while the lateral spacing of the shed vortices showed a weaker dependence on the cylinder oscillations.

Poncet (2002) investigated the three-dimensionality of flow behind a rotationally oscillating cylinder. He found that the flow around a rotational oscillation cylinder, like the translational oscillation, will change its behaviour from two-dimensional to three-dimensional in most of the flow regimes. The von Kármán streets generated in the wake of a circular cylinder are, at low Reynolds numbers, a time-periodic and two-dimensional flow. It is now well known from both experiments (Wu *et al.* 1996; Brede *et al.* 1996; Williamson 1996a,b) and numerical investigations (Thompson *et al.* 1996) that this nominally two-dimensional flow becomes three-dimensional when  $Re > 190$ .

Most recently Schmidt & Smith (2004); Thiria *et al.* (2006) and Al-Mdallal & Kocabiyik (2006) have investigated experimentally and numerically, respectively, in more detail the rotary oscillation of a circular cylinder. Schmidt & Smith (2004) explored the synchronising behaviour in the wake of a circular cylinder at  $Re = 125$  when the cylinder undergoes rotational oscillations about its longitudinal axis. They mostly focused on the changes observed in the vortex shedding pattern for different synchronised conditions, while in addition Thiria *et al.* (2006) studied the wake of a cylinder performing rotary oscillations around its axis at moderate Reynolds numbers. They observed

that the structure of the vortex shedding is strongly affected by the forcing parameters. The forced wake is characterised by a “lock-on” region where the vortices are shed at the forcing frequency and a region where the vortices are recognised to give a second frequency close to those observed for the unforced wake. They showed that these modifications of the wake structure change the dynamics of the fluctuations downstream from the cylinder. They conducted all of their experiments at  $Re = 150$ . The effect of forcing amplitude on the wake is shown in figures 2.13 (Thiria *et al.* 2006). Schmidt & Smith (2004) numerically investigated the laminar unsteady periodic flow motion in the wake of a rotationally oscillating circular cylinder at a Reynolds number of 855 over a wide range of oscillation amplitudes ( $15^\circ < A_\theta < 75^\circ$ ) and frequency ratios ( $f_\theta/f_N = 2, 3$ ). In general they found that at a given frequency ratio, increasing the rotational amplitude changes the wake synchronisation mode from non-synchronised to lock-on. They also concluded that the effect of increasing the amplitude of rotary oscillation is to reduce the period of vortex shedding modes whereas the effect of increasing the frequency ratio is to increase it. However, as the amplitude of oscillation increases the band of lock-on also increases.

Lo Jacono *et al.* (2010) also investigated the flow past an oscillatory rotating cylinder, where the frequency of oscillation was matched to the natural frequency of the vortex street generated in the wake of a stationary cylinder, at Reynolds number 300. Their focus was on the wake transition to three-dimensional flow and, in particular, the changes induced in this transition by the addition of the oscillatory rotation. Using Floquet stability analysis, they found that the fine-scale three-dimensional mode that typically dominates the wake at a Reynolds number beyond that at the second transition to three-dimensional flow (referred to as mode B) is suppressed for amplitudes of rotation beyond a critical amplitude, which is in agreement with past studies. However, the rotation does not suppress the development of three-dimensionality completely, as other modes are discovered that would lead to three-dimensional flow. In particular, the longer-wavelength mode that leads the three-dimensional transition in the wake of a stationary cylinder (referred to as mode A) is left essentially unaffected at low amplitudes of rotation. At higher amplitudes of oscillation, mode A is also suppressed as the two-dimensional near-wake changes in character from a single- to a double-row wake; however, another mode is predicted to render the flow three-dimensional, dubbed mode D (for double row). This mode has the same spatio-temporal symmetries as mode

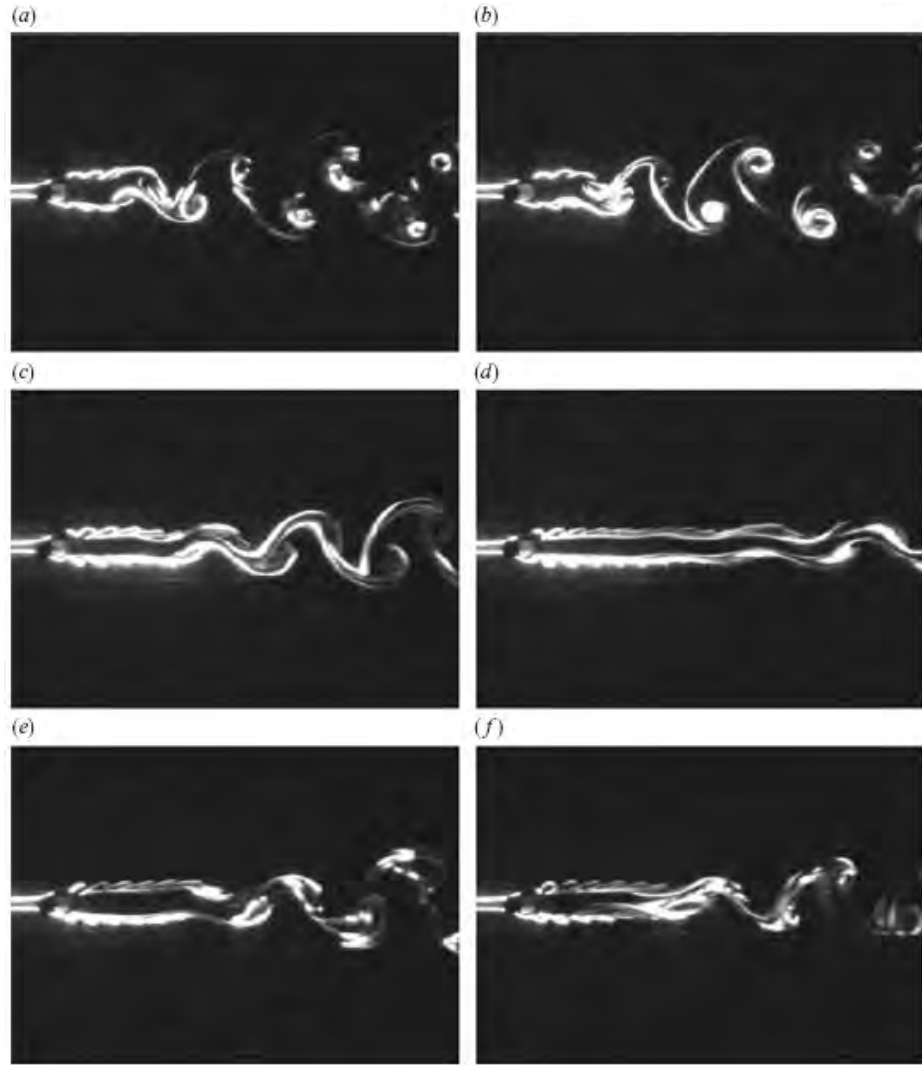


FIGURE 2.13: Effect of forcing amplitude on the wake. The forcing frequency is  $F_\theta = 5$  (low drag situation), the forcing amplitude is (a)  $\Omega = 1$ , (b)  $\Omega = 2$ , (c)  $\Omega = 4$ , (d)  $\Omega = 5$ , (e)  $\Omega = 7$  and (f)  $\Omega = 9$ . *Reproduced from Thiria et al. (2006).*

A. Figure 2.14 shows the contours of vorticity of the two-dimensional base flow past a cylinder undergoing several amplitudes of rotation at  $Re = 300$ .

There are also a number of references that theoretically, experimentally or numerically analysed and measured lift exerted on a rotational cylinder. The experiments of Tokumaru & Dimotakis (1993) have shown that higher cylinder aspect ratios yield higher maximum lift coefficients. The maximum lift coefficients in their experiments exceed that proposed by Prandtl (1926), possibly because Prandtl's arguments neglected unsteady effects. Recently Fujisawa *et al.* (2005) have extensively conducted experimental investigation on forces exerted on a rotating cylinder.

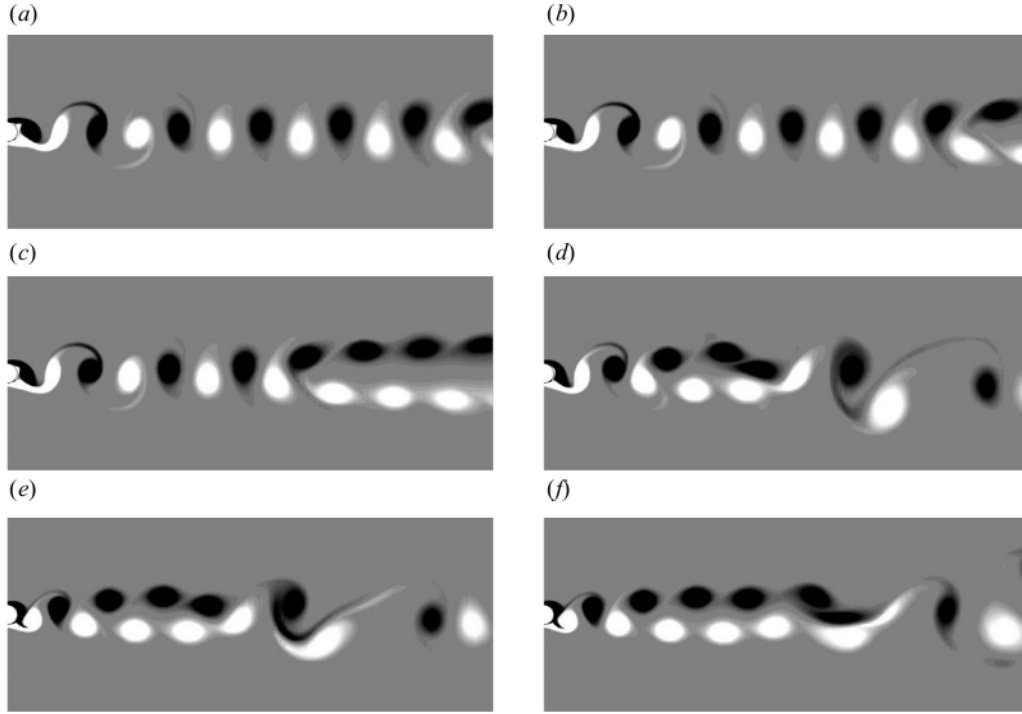


FIGURE 2.14: Contours of vorticity of the two-dimensional base flow past a cylinder undergoing several amplitudes of rotation at  $Re = 300$ . The flow is from left to right. The amplitudes of the imposed rotation are expressed in radians. Amplitude of rotation ( $A_\theta$ ) increases as:  $A_\theta = 0, 0.20, 0.40, 0.60, 0.80, 1.00$  from (a) to (f), respectively. All the images are taken at  $\theta = 0$ . White (black) represents positive (negative) vorticity. For all the cases considered the near-wake was synchronized to the forcing frequency. *Reproduced from Lo Jacono et al. (2010).*

## 2.5 Translational Oscillation in Quiescent Fluid

Vortex shedding behind a circular cylinder is a complicated flow phenomenon that has proved a challenging area for researchers over many years. Various investigators continued the research on vortex shedding behind bluff bodies, and many of them focused their attention on low Reynolds numbers, where the phenomenon is less complicated due to the absence of turbulence. Bodies oscillating in a stationary or unsteady fluid flow and stationary bodies in an oscillating unsteady flow are fluid-structure interaction problems of great practical and theoretical interest in the fields of aerospace, naval architecture, and offshore engineering. For example, as Uzunoğlu *et al.* (2001) mentioned, a ship or aircraft maneuvering, a submersible oscillating under prescribed experimental conditions to measure fluid actions, cylindrical tubular structures (*i.e.* offshore platforms, risers, etc.) subject to current and wave loads, etc. are practical illustrations of fluid-structure interactions, facets of which are discussed by Duncan (1959); Hamman & Dalton (1971); Burcher (1972); Etkin (1972); Sarpkaya & Isaacson (1981); Faltinsen

(1990) and Naudascher & Rockwell (1994). The study of the oscillating flow around circular cylinders is of importance in off-shore engineering because it is an idealised representation of the wave-induced loads on cylindrical structures (Bearman 1997; Nehari *et al.* 2004), while oscillation of the cylinder in quiescent fluid, or the converse situation of oscillating flow pass a stationary cylinder, are effective representations of wave-cylinder interaction in the area of the ocean engineering (Lin & Rockwell 1997). Consequently, sinusoidally oscillating flow about a circular cylinder has been extensively researched in the past century. However, most of the research into these applications involves flow with high Keulegan-Carpenter and Stokes numbers, which are not the focus of this study, and consequentially is not considered here. A wide variety of vortex patterns are attainable, as described in the insightful works and assessments of Maull & Milliner (1978); Sarpkaya & Isaacson (1981); Williamson (1985); Bearman *et al.* (1985); Obasaju *et al.* (1988) and Tatsuno & Bearman (1990). Of primary interest to the current investigation are the flow visualisation studies of Honji (1981); Williamson (1985) and Tatsuno & Bearman (1990), which were conducted at low  $KC$  and  $\beta$ . There are not much studies at low  $KC$  and  $\beta$  which investigated such flows quantitatively.

Earlier laboratory studies employed a U-tube to produce an oscillating water flow in which a stationary circular cylinder was placed in the flow. Dye-streak and other flow visualisation techniques were used in later studies to observe the vortex patterns around the cylinder (Williamson 1985; Obasaju *et al.* 1988; Tatsuno & Bearman 1990). Some of these studies employed a similar laboratory situation of a cylinder oscillating with a sinusoidal motion in an otherwise still fluid (Lam & Dai 2002). Simulation of loading due to long waves can also be accomplished by subjecting a stationary cylinder to unidirectional oscillatory flow or, conversely, oscillating the cylinder in quiescent fluid (Yang & Rockwell 2002). Based on the results of these studies, different regimes of the flow have been classified, each with a distinct pattern of vortices and fluid forces. The flow regimes are determined mainly by the Keulegan-Carpenter number (Keulegan & Carpenter 1958) which is defined by

$$KC = \frac{U_{\max}T}{D}. \quad (2.4)$$

In the situation of a cylinder oscillating in quiescent water, the cylinder movement can

be described by

$$y(t) = A_t \sin(2\pi f_t t) \quad (2.5)$$

$$\theta(t) = A_\theta \sin(2\pi f_\theta t + \Phi). \quad (2.6)$$

The flow is weakly dependent on a second parameter,  $\beta$ , which is sometimes known as the Stokes number (or viscous scale parameter: Sarpkaya (1976b, 2005)) defined by

$$\beta = \frac{fD^2}{\nu}. \quad (2.7)$$

A Reynolds number can be defined for this type of flow as

$$Re = KC.\beta \quad (2.8)$$

It is well known that when a bluff body is oscillated in a still fluid or a fixed body is placed in an oscillating flow, secondary streaming is generated around the body owing to the influence of nonlinear effects (see for example Tatsuno 1973, 1981). The resulting secondary flow is symmetrical about the axis of oscillation and has been visualised by many studies (*e.g.* the visualisations of Schlichting (1932) and later by M. Tatsuno as shown in figure 2.15). When the Keulegan-Carpenter or Stokes number exceeds a critical value the flow is altered by the formation and subsequent separation of vortices on the cylinder surface, leading to a loss of this symmetry and the formation of three-dimensional flow (Bearman *et al.* 1981; Elston 2005).

The flow at very small  $KC$  has been studied analytically first by Stokes (1851) and then by Wang (1968) who developed an asymptotic theory assuming that the flow remains attached. It is well established, however, that as  $KC$  is increased the flow will separate and eventually become asymmetrical (Sarpkaya 1986; Bearman *et al.* 1985; Justesen 1991). Experimental investigations of the oscillatory flow around a circular cylinder at small  $KC$  have shown that the flow can be classified into a number of different flow regimes governed mainly by  $KC$  and with a weak dependency on  $Re$  (Bearman *et al.* 1981; Williamson 1985; Sarpkaya 1986).

Williamson (1985) performed experiments, using a combination of two-dimensional flow visualisations and force measurements. He investigated the different patterns of vortex shedding for a cylinder in relative sinusoidal oscillatory motion for  $KC_t < 60$  and two  $\beta_t$  values of 255 and 730. Using two-dimensional visualisations of the repeatable patterns produced on the water tank surface, a set of flow regimes were identified as a



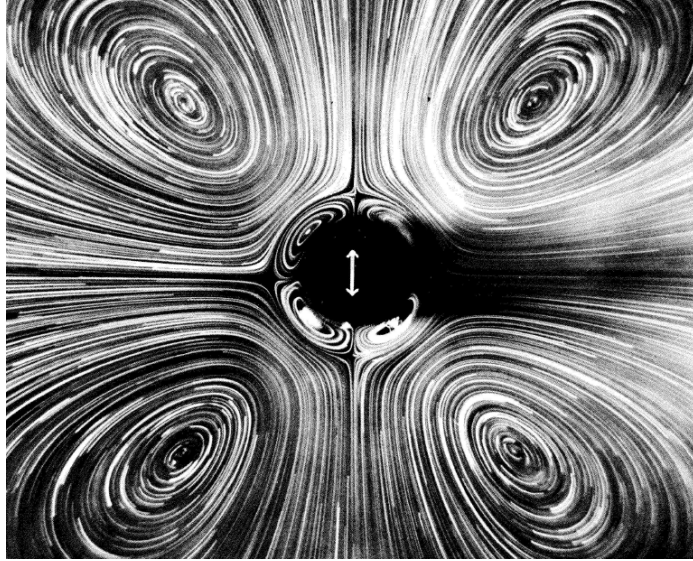


FIGURE 2.15: Secondary streaming induced by an oscillating cylinder. This image was produced by illuminating glass beads with a stroboscope. The image was taken at an oscillation amplitude of  $A_t/D = 0.085$  and at  $Re = 70$  (based on frequency). *Reproduced from Van Dyke (1982). Photograph by Masakazu Tatsuno.*

function of  $KC$ . The modes observed were found to be a function of the  $KC$  number. A common element of all modes identified was the pairing of vortices from a previous half-cycle with those in the present half-cycle. He did not examine, however, the three-dimensional structure of the flow along the cylinder axis. The approximate relationship between the observed flow patterns and the  $KC$  number is shown in figure 2.16.

The regular lift force fluctuations were shown to be directly related to the repeatable vortex shedding patterns observed in the cylinder wake. It was found that the lift force fluctuation frequency was a multiple of the forcing frequency and that this was directly tied to the shedding of a specific number of vortices in each half-cycle. In each of the regimes identified in figure 2.16 a specific number of vortices was shed in each half-cycle. The subsequent pairing of vortices shed in the present half-cycle with those of the preceding half-cycle was identified as being a core feature leading to the formation of the repeatable vortex patterns. In the first regime identified ( $0 < KC_t < 7$ ) a pair of attached vortices are formed in the wake in each half-cycle. These are shed from the cylinder as it reverses direction and are symmetrical about the axis of oscillation up to  $KC \approx 4$ , where it was observed that the vortices formed are no longer equal in magnitude and are not shed at the time of cylinder reversal. This led to the detection of a lift force varying with the oscillation frequency. This regime could reasonably be subdivided into two sub-regimes which are distinguished by the breaking of the symmetry

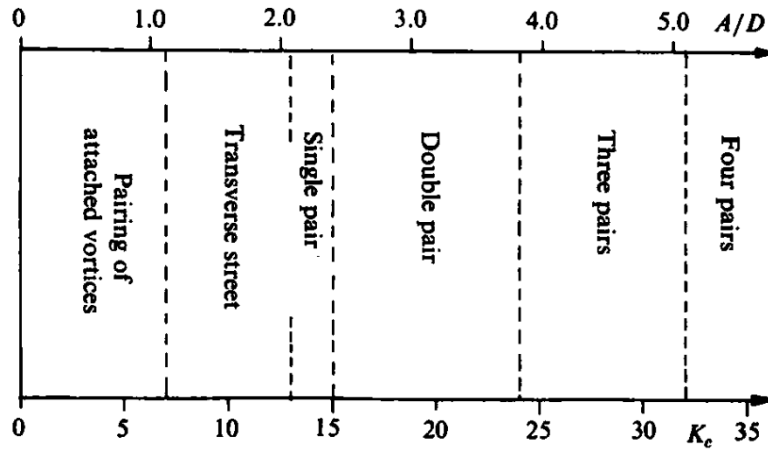


FIGURE 2.16: An approximate guide to the flow patterns from an oscillating cylinder as a function of the  $KC$  number. Annotations describe the number of vortices shed per oscillation half-cycle. Regimes are based on observations conducted for  $\beta$  values of 255 and 730. *Reproduced from Williamson (1985).*

about the oscillation axis.

In the transverse street/single pair regime ( $7 < KC_t < 15$ ), see figure 2.17, a single vortex is shed per half-cycle which pairs up with the shed vortex from the previous half-cycle. A series of cycles results in a number of pairs being formed and shed on the same side of the cylinder. These pairs form a transverse street which convect away from the cylinder. In the lower end of the range ( $7 < KC_t < 13$ ), namely double pair, the direction of the street was observed to be approximately perpendicular to the oscillation axis, as shown in figure 2.17, while in the upper end of the range ( $13 < KC_t < 15$ ), namely three or more pairs, the direction of the street was observed to be at an angle of approximately  $45^\circ$  to the oscillation axis. Initial conditions were thought to determine which side of the cylinder the street formed on, although it was also observed that the shedding could intermittently change sides. Higher regimes (Double pair, Three pairs and Four pairs) were distinguished by the formation of more vortices per cylinder oscillation cycle. In each case the process of pairing of the shed vortices was fundamental to the pattern formed.

Visualisations of Williamson (1985) provide a good deal of insight into the flow dynamics despite the inherent limitation due to their two-dimensional nature. A prior study by Honji (1981) produced visualisations of the three-dimensional structures that can arise in the same  $(KC_t, \beta_t)$  parameter space. Honji (1981) visualised the flow around a transversely oscillating cylinder in a quiescent fluid for  $68.8 < \beta_t < 700$  and  $KC_t < 7.5$ . He has shown that a three-dimensional instability of the flow occurs around

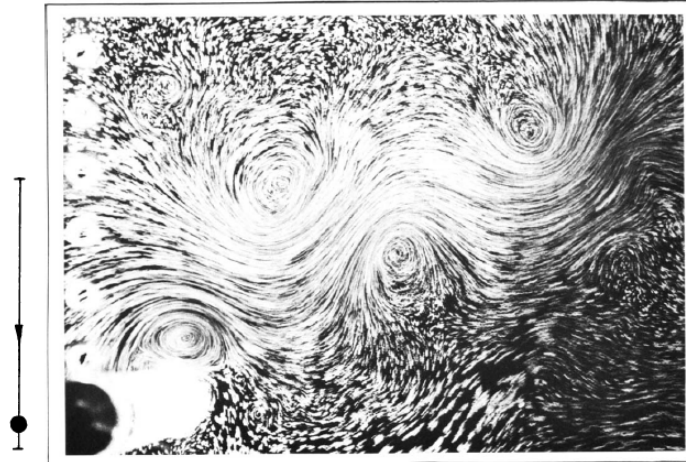


FIGURE 2.17: Transverse street wake for  $KC = 12.0$ . The cylinder is approaching its lowest point of its oscillation. This regime is delineated by the distinctive trail of vortices which convects away at around  $90^\circ$  to the oscillation axis. *Reproduced from Williamson (1985).*

a circular cylinder oscillating in a quiescent fluid at small  $KC$ . Honji (1981) observed that in a certain range of  $KC_t$  an instability of the flow developed that resulted in the appearance of streaks which arrange alternately in a double row along the cylinder axis, which he attributed to the onset of turbulence. These structures were named the “Honji Instability” by Sarpkaya (1986) although Honji simply referred to the patterns formed as “streaked flow”. Honji (1981) also observed the presence of mushroom shaped vortices, in a plane normal to the direction of cylinder motion, which were arranged alternately along each side of the cylinder span in a double row. The spanwise streak spacing was found to only weakly depend on the Stokes number and increased as the Keulegan–Carpenter number was increased. Honji suggested that the instability mechanism leading to this flow pattern was “a kind of centrifugal one”. While Honji does not explicitly state that this was a Taylor–Görtler instability, it is possible that he was referring to this form of instability, which arises from the centrifugal forces induced by the curvature of the boundary layer (Elston 2005).

The usual view, implicit in most experimental and numerical studies, is that the process of vortex formation from the oscillating cylinder involves a layer of distributed vorticity feeding into a large-scale vortex. Most relevant to the present study is the flow visualisation of Tatsuno & Bearman (1990). They further extended the previous works explained above and produced a control-space map, classifying the flows into eight separate flow regimes each with a two- and three-dimensional flow structure and vortex shedding characteristics. Tatsuno & Bearman (1990) comprehensively investigated

translational harmonic oscillation in a quiescent fluid at various independent variables, *e.g.* the amplitude and frequency of oscillations corresponding to  $KC_t$  and  $\beta_t$  numbers, respectively. They covered a wide range of  $KC_t$  and  $\beta_t$  numbers using flow visualization but without the availability of such experimental techniques at the time their results are qualitative in nature. Their experiments were carried out at  $KC_t$  numbers between 1.6 and 15 and  $\beta_t$  numbers between 5 and 160. They observed the wake vortices' formation and some asymmetry in the flow separation and the associated vortex development behind the cylinder for different cases. Their flow regimes were identified within the above mentioned ranges of  $KC_t$  and  $\beta_t$  numbers. Like Williamson (1985) and Honji (1981), they observed symmetrical flow separation and vortex development about the oscillation axis of the cylinder for very low Keulegan-Carpenter numbers. However, as the Keulegan-Carpenter number was increased, and eventually exceeded a critical value, the onset of an asymmetry in the vortex development and flow separation was observed.

The reduced version of the  $(KC_t-\beta_t)$ -space map they produced, which classified the unique flows identified into regimes, is shown in figure 2.18. Their nomenclature for labelling these regimes, A\*–G, will be used for clarity from this point forward. The boundary between regimes A\* and A was not explicitly delineated in the original diagram of Tatsuno & Bearman (1990) while in their graph reproduction, figure 2.18, it is shown as a dashed line.

These regimes match well with the observations of Honji (1981) and Williamson (1985). Results of Honji (1981) were obtained for an overlapping region,  $68.8 < \beta_t < 700$ , within which Tatsuno & Bearman (1990) observations closely agree. Williamson (1985)'s results were obtained at a larger Stokes number,  $\beta_t \approx 255$ , and due to the two-dimensional limitation of Williamson (1985)'s visualisations no observation of “streaked flow” was made. However, the two-dimensional characteristics observed for  $KC_t < 7$  resemble those identified by Honji (1981) and Tatsuno & Bearman (1990) for  $\beta_t > 60$ . A sample of the cross-sectional images that appeared in Tatsuno & Bearman (1988, 1990) illustrating these different regimes is shown in figure 2.19. Flows of regime A\* were found to have no vortex shedding. They observed no flow along the span of the cylinder (*i.e.* two-dimensional flow) and found the flow to be symmetrical about the oscillation axis as shown in figure 2.19. Regime A is distinguished from A\* due to the formation and shedding of vortices which was not observed in regime A\*. In

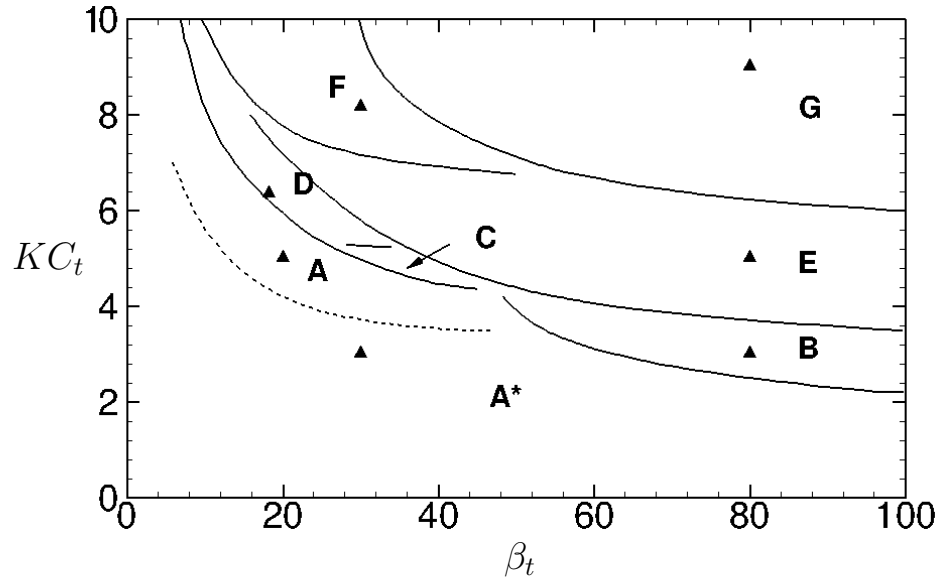


FIGURE 2.18: Parameter-space map created by Tatsuno & Bearman (1990) identifying eight different flow regimes in the  $(KC_t-\beta_t)$  plane indicated. A: symmetric with vortex shedding, two-dimensional; A: symmetric and attached, two-dimensional; B: longitudinal vortices, three-dimensional streaked flow; C: rearrangement of large vortices, three-dimensional; D: transverse street, three-dimensional; E: transverse street with irregular switching, three-dimensional; F: diagonal double-pair, three-dimensional; G: transverse vortex street, three-dimensional. The triangles indicate the cases investigated here. *Reproduced from Tatsuno & Bearman (1990) by permission.*

other respects it retains the same characteristics of regime  $A^*$ . The lack of a distinct boundary was attributed by Tatsuno & Bearman (1990) to it being very difficult to determine the onset of vortex shedding and a consequence of the visual means used to evaluate this. In figure 2.19(A) the concentrations of dye that could be mistaken as the presence of vortices actually represent a periodic mass convection away from the cylinder. Tatsuno & Bearman (1990) stated that the vortices formed and shed in each half-cycle of cylinder motion are convected back towards the cylinder in the subsequent half-cycle and are then annihilated by mixing with vorticity in the boundary layer.

The structure of flow in regime B differs remarkably from that of other regimes seen so far. Regime B is defined by Tatsuno & Bearman (1990) as the onset of three-dimensional instability and longitudinal vortices. The flow in this regime is characterised by the presence of spanwise, periodic structures in the induced flow due to a three-dimensional instability. Both Honji (1981) and Tatsuno & Bearman (1990) visualised the formation of streaked flow, as shown in figures 2.20(a-c), which was formed and shed alternately along the cylinder span at regular intervals. From figures 2.20(a-c) and with reference to the work of Honji, it may be concluded that in regime B pairs

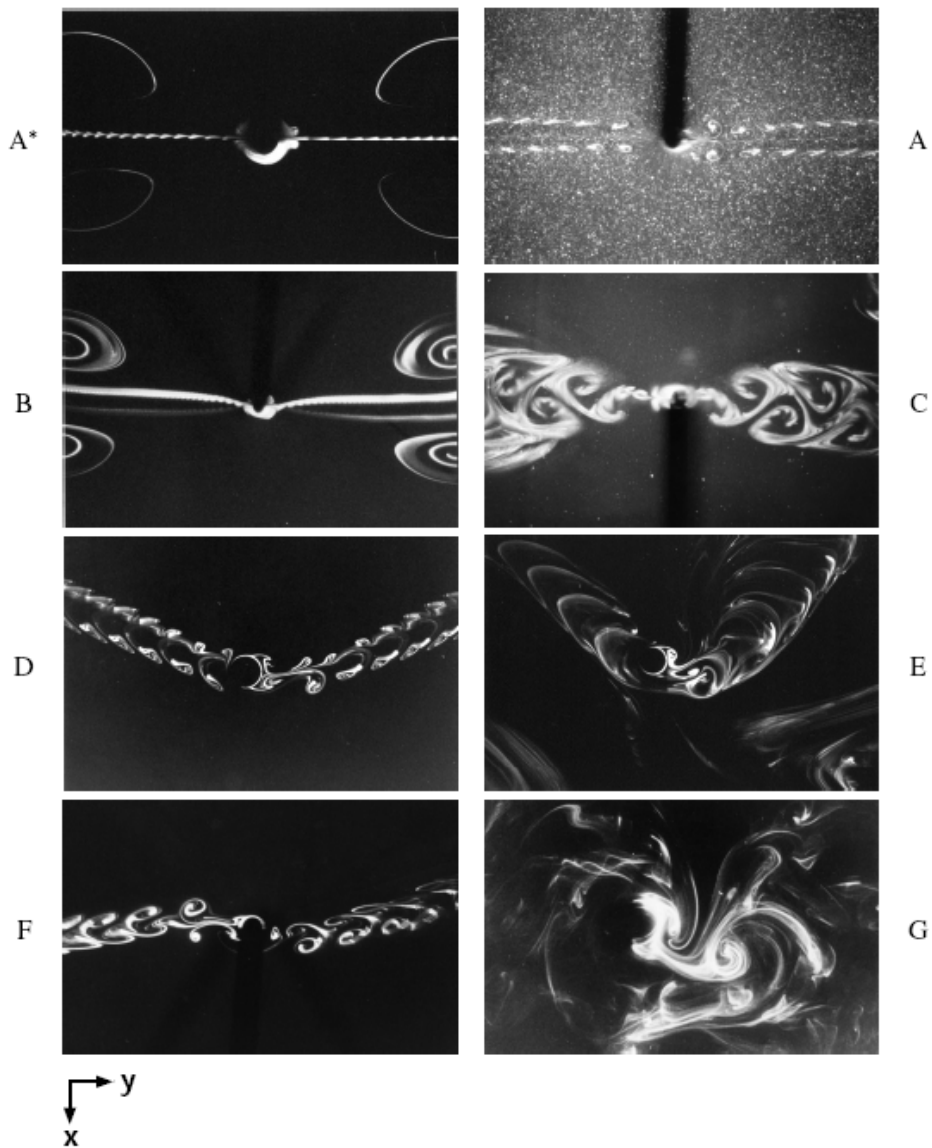


FIGURE 2.19: Two-dimensional visualisations of the vortex shedding patterns found for Regimes A\*–G. The cylinder is shown oscillating along the horizontal axis of the page. The image for regime F appeared in Tatsuno & Bearman (1988), while the others are from Tatsuno & Bearman (1990); *All images are reproduced with their permission.*

of contra-rotating longitudinal vortices are formed alternately along the cylinder axis and extend in the direction of cylinder oscillation. The boundaries for this regime almost exactly match those identified by Honji (1981) for the formation of “streaked flow”. Through measurements of the streak spacing, these vortices were found to have a spanwise wavelength ratio ( $\lambda/D$ ) that increased as the KeuleganCarpenter number also increased. Despite the onset of a three-dimensional instability the spanwise average of the flow in regime B was found to preserve symmetry, as shown in figure 2.19(B). This tendency is similar to that found by Honji (1981) in the range  $200 < \beta_t < 400$ . One of

the defining characteristics of regime B is the presence of structures which vary along the span of the cylinder. In that respect this case has broken a symmetry property and is no longer considered to be fully two-dimensional.

The flow of regime C was found to be three-dimensional but appeared to have no periodic spanwise structure as shown in figures 2.20(d,e). In the cross-sectional plane the vortices initially shed from the cylinder were seen to roll up into large vortices, figure 2.19(C), and form a street of vortices similar to that of the von Kármán street, although in this case the sense of rotation of the vortices was opposite to that of the von Kármán street, *i.e.* jet-like. It was noted by Tatsuno & Bearman (1990) that the large vortices are formed in succession for equal numbers of oscillation cycles, however it is unclear how many oscillation cycles are required for the formation of a large vortex. Due to reasons highlighted above this regime was not considered as part of this thesis.

Apart from the two-dimensionality and symmetry of flow with respect to the axis of oscillation in regimes A\* , A and to some extent B, the flow characteristic will change as  $KC_t$  increases at relatively lower  $\beta_t$ . Regime D flows were found to break a symmetry that characterised the previously discussed flows; in this regime the induced flow no longer convected along the axis of oscillation, as it did for regimes A\*-C, but at an angle to the axis of oscillation as shown in figure 2.19(D). No mention was made of the actual angle to the oscillation axis that the flow initially convected along, however from the figures presented it can be estimated to be approximately  $25^\circ$ . While the resultant flow breaks symmetry about the axis of oscillation (the  $x$ -axis), it was observed that the time-periodic symmetry about the  $y$ -axis was retained, *i.e.* the flow was still synchronous with the cylinder oscillation. Along the span the formation of regular “tubes” was found, see figure 2.20(f), within which the fluid was observed to be travelling faster than the surrounding fluid. The spanwise spacing between the tubes was found to be independent of  $KC_t$  and only weakly to decrease with increasing Stokes numbers.

The flow in regime E exhibited spatial patterns in the cross-section similar to that of regime D see figure 2.19(E), but it was found that the direction to which the flow convected intermittently changed between the  $+x$  and  $-x$  side of the cylinder. According to the classification of Tatsuno & Bearman (1990) the resulting flow belongs to regime E representing temporarily stable V-type vortex streets. The irregular switching to either side is in contrast to regime D where the direction was fixed. Along the span there was evidence of some three-dimensional structures, see figure 2.20(g), although

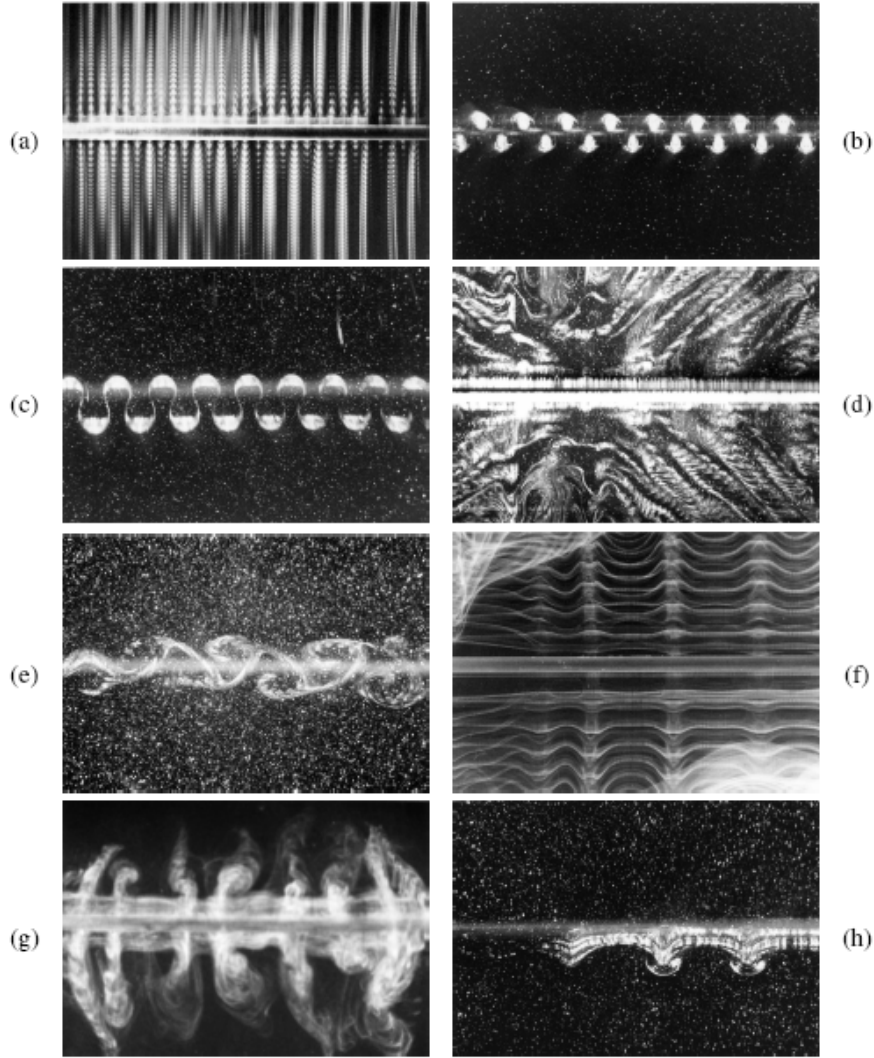


FIGURE 2.20: Visualisations of the three-dimensional structures observed in Regimes B to F. The images were produced using an electrostatic precipitation method and show the variation in the flow along the cylinder span. The span of the cylinder ( $z$ -axis) is orientated horizontally in all these images with the cylinder oscillating along the  $y$ -axis. Images (a), (d), (f), (g) and (h) are taken in the  $y - z$  plane while images (b), (c) and (e) are taken in the  $x - z$  plane. Presented are Regime B [(a), (b) & (c)], Regime C [(d) & (e)], Regime D [(f)], Regime E [(g)] and Regime F [(h)]. *All the images appeared in Tatsuno & Bearman (1990) and are reproduced with their permission.*

no periodic wavelength could be established. The structures that were present were found to be obscured by the switching of the flow convection direction.

Regime F is a double-pair diagonal regime, in which vorticity is shed diagonally with respect to the axis of oscillation (see figure 2.19(F)). Along the span, a periodic structure was found with pairs of counter rotating vortices observed to form at regular intervals along the span as shown in figure 2.20(h). The spacing between these structures was found to vary in the same manner as it did for its neighbouring regime, D.



A circulatory streaming motion around the cylinder was observed to occur in regime G, figure 2.19(G). Increases in  $KC_t$  or  $\beta_t$  within this region resulted in the onset of turbulent motion and the streaming flow generated by the cylinder motion was observed to irregularly change direction. No regular formation of structures along the span was observed.

Yang & Rockwell (2002) observed sinusoidal spanwise variations in the flow about a cylinder subjected to wave loading at a relatively low  $KC_t = 4.5$ . Along the span of the cylinder regular patterns of streamwise vorticity were observed. The spanwise wavelength between vorticity of like sign ranged from  $1 \lesssim \lambda/D \lesssim 4.5$ , which at this  $\lambda/D$  value of  $KC_t$  is compatible with the observations of Tatsuno & Bearman (1990). At larger values of  $KC_t$  (10 and 18) larger scale regular variations along the span were observed. These variations were of the order  $10 \lesssim \lambda/D \lesssim 110$  which was greater than the distances between individual concentrations of streamwise vorticity.

Using a two-dimensional finite-difference numerical technique Justesen (1991) was able to predict the transverse street and other vortex shedding regimes, as found by Williamson (1985) and shown in figure 2.7. Despite this study being under-resolved in some regions of its parameter space, it was conducted for  $\beta_t$  in the range 196 – 1035 and  $KC_t$  between 0 and 26, and being restricted to two-dimensions they were able to obtain good agreement between calculated drag and inertia coefficients and experimental data. The onset of an asymmetry in the flow was found to occur at  $KC_t \approx \pi$  for  $\beta_t = 196$  and to decrease slightly for higher Stokes numbers.

Dütsch *et al.* (1998) performed a series of experiments using LDA and compared it with their two-dimensional computations for three regimes: A, E and F. In regime A they found good agreement between the velocity fields produced by both techniques. These data are used to validate our experimental technique and apparatus, see §4.4.1. In regime F they found that the flow was asynchronous using both techniques. As a consequence of the formation of a vortex pair that was unequal in magnitude a vortex street was observed to form that convected away from the cylinder at an angle of approximately  $27^\circ$ . This again matches previous results, *e.g.* see figure 2.19(F), but is interesting because it was achieved by both LDA and two-dimensional computation suggesting that the breaking of symmetry about the oscillation axis and the asynchronous behaviour are largely two-dimensional phenomena. In the last regime studied, E, they presented vorticity contours which matched the flow fields generated by Tatsuno &

Bearman (1990) in figure 2.19(E). However, they found that their simulations were stable after 15 cycles and that periodic shedding resulted. This is in direct contrast to Tatsuno & Bearman (1990) who observed an irregular switching of the direction of vorticity shedding between the  $+x$  and  $-x$  sides of the cylinder. The computed lift force history of Dütsch *et al.* (1998) showed that the vortex shedding was first symmetric to the plane of oscillation and then became unstable involving a strong increase of the lift force and a slight decrease of the in-line force.

Iliadis & Anagnostopoulos (1998) used a finite-element study to locate a boundary in  $(KC_t, \beta_t)$ -space where the two-dimensional symmetric flow became asymmetric. They conducted their study over the range  $KC_t \leq 15$  and  $6 \leq \beta_t \leq 100$  and found good agreement with the experimental boundaries presented in figure 2.18 for  $\beta_t > 40$ , but in the low Stokes number region the match was poorer. At a low Stokes number (regime D) their vorticity contours match experimental visualisations both in their spatial and temporal (synchronous) nature. Investigations of flows in regimes E and F yielded results that showed no intermittent switching of the shedding direction as found in experiments. This led them to conclude that the switching of the flow direction is associated with the three-dimensional nature of the flow.

The characteristics of the flow regimes defined by Tatsuno & Bearman (1990) can also be described in terms of their symmetry properties. At the boundaries between these regimes a transition in the symmetry properties occurs. A more relevant study to the present study is the more recent work of Elston (2005) and Elston *et al.* (2006), which investigated the two- and three-dimensional instabilities and symmetry breaking within the parameter space map of Tatsuno & Bearman (1990). They used a Floquet analysis (for definition refer to §5.4) and direct numerical simulation to study the instability of such flows. Their study isolated and classified the symmetry-breaking instabilities from these two-dimensional basic states as functions of the control parameters. They found that while the initial bifurcations produced by increasing the parameters can be due to three-dimensional flows, much of the behaviour can be explained in terms of two-dimensional symmetry-breaking instabilities. These have two primary manifestations: at low Stokes numbers, the instability was synchronous with the imposed oscillation, and gave rise to a “boomerang-shaped” mode, while at higher Stokes numbers, the instability was quasi-periodic, with a well-defined second period, which became infinite as Stokes numbers were reduced along the marginal stability boundary, “freezing”

the quasi-periodic mode into a synchronous one. Elston *et al.* (2006) found that these two-dimensional modes are, with further small increase in control parameter, unstable to three-dimensional secondary instabilities. In contrast, the mode first reported by Honji (1981), which arises at high Stokes numbers, and lower Keulegan–Carpenter numbers than the two-dimensional quasi-periodic mode, has a three-dimensional primary instability arising directly from the symmetrical two-dimensional basic state. The outcomes of the investigation of Elston *et al.* (2006) are summarised in figure 2.21. In general, within the range of control parameters ( $0 < \beta_t < 100$  and  $0 < KC_t < 10$ ), they found that there are two fundamentally different types of symmetry-breaking instability in this flow: two-dimensional and three-dimensional. Flows for which two-dimensional symmetry breaking is the primary instability are almost immediately unstable to three-dimensional secondary instabilities, and these secondary regimes are the ones that have been observed in experiments, *e.g.* regimes C and D. Like their underlying two-dimensional equivalents, regime D flows are synchronous with the forcing, while flows of regime C are quasi-periodic. There is also a direct primary breakage to three-dimensional instability at Stokes numbers  $\beta \gtrsim 50$ ; this produces regime B flow, another synchronous mode. Elston *et al.* (2006) also found that the fundamental distinction between the flows of regimes C and D, on the one hand, and those of regime B on the other, is that the spanwise average flows of regime B have the two-dimensional symmetries of the base flows, while those of regimes C and D do not. Elston *et al.* (2006) concluded, based on the detail of their findings, that the regime map presented by Tatsuno & Bearman (1990), while a very good guide to the terrain to be encountered in such a study, is, like many early maps, to be interpreted with care.

Most recently Lam *et al.* (2010) performed a series of experiments using time-resolved PIV to investigate the development of vortex patterns around a circular cylinder oscillating in a quiescent fluid. Experiments were conducted at  $KC_t$  between 8 and 36 with Reynolds number kept constant at 2400 (consequently  $67 \lesssim \beta_t < 300$ ). Similar to previous studies, they identified three modes and denoted as modes I, II, and III (characterised by one, two and three (or more) vortices generated in each half cycle, respectively). Lam *et al.* (2010) classified the modes based on the development mechanism of shear layers around the cylinder, the number of vortices shed in each half cycle, and the characteristics of the vortex street. Figure 2.22 illustrates the flow of fluid associated with the vortex patterns in each mode. They found that vortex shedding in

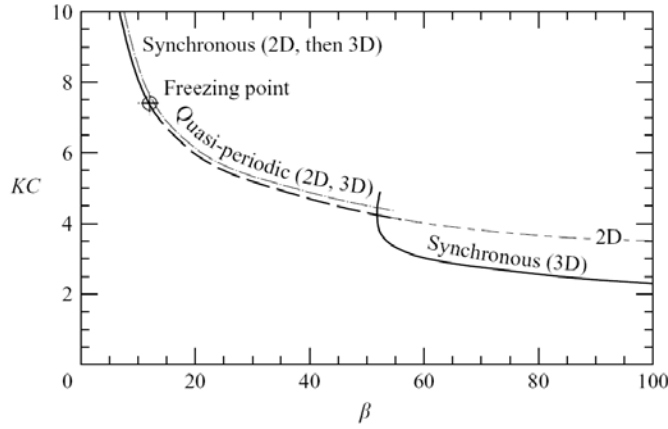


FIGURE 2.21: Locations and characteristics of the primary and secondary symmetry-breaking bifurcations. *Reproduced from Elston et al. (2006).*

mode I occurred only on one side of the line of cylinder motion. This mode which occurs at  $8 \leq KC_t \leq 16$ , was observed to have two submodes with different orientations of the vortex street to the line of cylinder motion. Similar vortex patterns to mode I has also been reported in the literature as the transverse vortex street or single vortex pair (Williamson 1985; Obasaju *et al.* 1988; Tatsuno & Bearman 1990). They also observed that the vortex street intermittently swaps from one side to the other. It has been found that below a critical  $KC_t$  number of  $\approx 8$ , no large-scale vortices can be completely shed from the cylinder. It was also seen by Lam *et al.* (2010) that the vortex street is not necessarily always perpendicular to the line of cylinder motion. Sometimes, the vortex street is aligned at about  $45^\circ$  to the line of cylinder motion, shown in figure 2.22b. They have noticed that this submode was occurred more often at  $KC_t > 12$ . The same submode was reported in Williamson (1985) as the single (vortex) pair. Mode II occurred at  $KC_t$  between 16 and 24 and the vortex street extended to both sides of the line of cylinder motion and lies at about  $45^\circ$  to the line. At mode III ( $KC_t > 24$ ) vortices are shed behind the moving cylinder similar to the case of a towed cylinder. Mode III features one longitudinal vortex street, similar to a limited-length von-Kármán street, which consists of at least three vortices. One more vortex is produced in each half cycle with the increase in  $KC_t$  by approximately 8. At  $KC_t$  between 24 and 32, three vortices are shed in each cylinder stroke but were found not to be exactly in pairs. Instead, the first vortex shed in each stroke has the same sense of rotation as the third and last vortex shed in the previous stroke. In general, they found that each vortex pattern was associated with the typical secondary flow stream. As mentioned above,

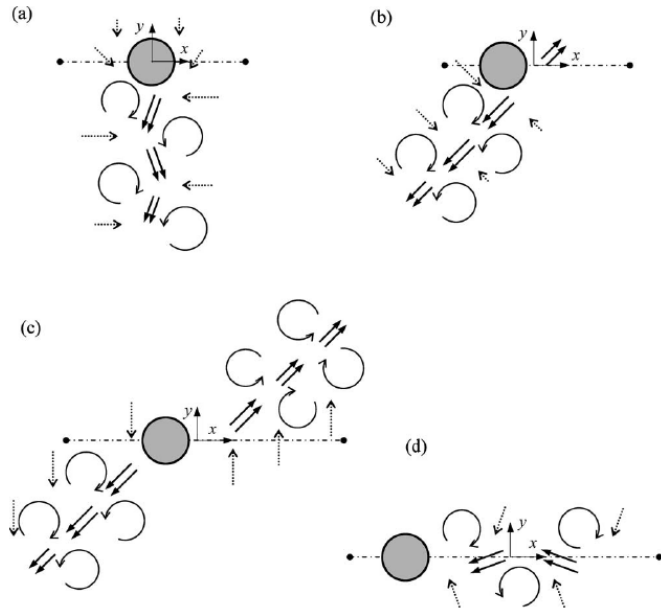


FIGURE 2.22: Interrelation of vortex pattern with secondary flow stream. (a) Mode I, lateral vortex street; (b) mode I, inclined vortex street; (c) mode II; (d) mode III. Bold arrows: secondary flow stream; dotted arrows: ambient water flow; dot-dashed lines: typical length of cylinder stroke. *Reproduced from Lam et al. (2010).*

these secondary flow streams have been noted by Williamson (1985) and Tatsuno & Bearman (1990). Also, the results of Lam *et al.* (2010) showed that  $KC_t$  number, or equivalently, the stroke length of cylinder motion, and the secondary flow stream are the key factors responsible for the different vortex patterns.

Three-dimensional numerical investigations of this parameter space have been more sparse. An investigation into the onset of three-dimensionality by Zhang & Dalton (1999) using a numerical technique at  $\beta_t = 196$  yielded a set of results that agreed with experimental results. The onset of three-dimensionality was observed for  $KC_t = 2$  and separation was subsequently observed to occur at  $KC_t = 3.2$  before the flow became chaotic at  $KC_t = 4$ . Nehari *et al.* (2004) examined two three-dimensional states, both at  $\beta_t = 20$ ; one at  $KC_t = 6.5$  (Regime D) and the other at  $KC_t = 8.5$  (Regime F). They found that in both cases irregular switching of the vortex streets between the  $+x$  and  $-x$  directions was observed. This behaviour could be reproduced using purely two-dimensional simulations and therefore it was concluded that this is related to a two-dimensional instability, a finding in direct contrast to that of Iliadis & Anagnostopoulos (1998). It was noted that three-dimensionality appears after the underlying two-dimensional symmetry has been broken. Thus was speculated to be due to switching of the vortex shedding direction in combination with the onset of

three-dimensionality, which would contribute to the formation of the sinuous S-mode witnessed by Yang & Rockwell (2002).

Table 2.1 briefly summarises the flow patterns observed in previous investigations reviewed above. Only the most relevant papers to the present study are listed in the table. There are many high quality research studies available in the literature but many are not relevant to this thesis because their focus is on high  $KC_t$  and  $\beta_t$  numbers. The development of new measuring techniques that provide detailed information about the time variations of local flow properties are stirring this new interest in a field which has seen active research efforts for many decades. Despite a huge number of visualisations on low amplitude and frequency cases (Tatsuno & Bearman 1990), and some other translational research in quiescent flow, either experimentally or numerically, like: Hamman & Dalton (1971); Justesen (1991); Lin & Rockwell (1997); Dütsch *et al.* (1998); Iliadis & Anagnostopoulos (1998); Zhang & Dalton (1999); Uzunoğlu *et al.* (2001); Lam & Dai (2002); Elston *et al.* (2004); Elston (2005); Elston *et al.* (2006), there are few quantitative experimental investigations (*i.e.* PIV) especially at low values of translational amplitudes and frequencies. Therefore this is one of the aims of the present study - to provide an insight into this problem using high resolution PIV.

## 2.6 Combined Rotational and Translational Oscillation Motion

A circular cylinder undergoing a combination of oscillatory translation and rotation in either quiescent fluid or external flow has received little attention until now. It was shown in §2.5 that when a bluff body is oscillating translationally in a quiescent fluid, secondary streaming is generated around the body because of nonlinear effects (Bearman *et al.* 1981). However, the combination of two oscillatory forcing mechanisms, under specific conditions detailed later, results in a net thrust being experienced by the circular cylinder in a direction normal to the translational axis (Blackburn *et al.* 1999). The cylinder experiencing thrust, while undergoing a series of pitch and plunge, has been labeled the “*swimming cylinder*”. When the circular cylinder was permitted to move in response to the average force, a terminal velocity approximately one third of the peak translational velocity was predicted (Blackburn *et al.* 1999). The forces experienced by the circular cylinder had only been examined in detail for the particular case of a zero phase angle between the oscillatory motions, although according to Blackburn

Reference	Method	$KC_t$	$\beta_t$	$Re_t$	TB Regime
Williamson (1985)	Visualisations	Below 4	255	Below 1020	
		4-7	255	1020-1785	
		12	255	3060	
Obasaju <i>et al.</i> (1988)	Visualisations	7	416	2912	
		10	416	4160	
		1.6-15	5-160	Mostly < 600	A*-G
Tatsuno & Bearman (1990)	Visualisations	2.2	250	550	
Justesen (1991)	CFD	4	250, 1020	1000, 4080	
		8	196	1568	
		12	196	2352	
		18	196	3528	
		26	196	5096	
		10	378	3780	
		4	196, 730	784, 2920	
		6.28	22.1	139	
		5	20	100	A
		10	20	200	F
Lin & Rockwell (1997) Zhang & Zhang (1997)	PIV	6	35	210	E
		2	100	200	A*
		4	50	200	A
		10	378	3780	
		3.14	52.8	165.79	A*
		11.0	7.4	81.4	A
		6.0	35.0	320.0	E
		4.25	1290	5500	
		6.28	940	5900	
		12	200	2400	
Lam & Dai (2002)	PIV	0-10	0-100		All regimes
		8-36	67-300	2400	
Elston <i>et al.</i> (2006) Lam <i>et al.</i> (2010)	CFD	0-10	0-100		All regimes
		8-36	67-300	2400	

TABLE 2.1: Flow patterns observed in previous investigations, TB=Tatsuno & Bearman (1990).

*et al.* (1999) instantaneous vorticity contours at other angles would suggest a similar forcing. The results of the Blackburn *et al.* (1999) are all numerical and, up until now, there has been no experimental investigation of the swimming cylinder reported.

A set of preliminary studies into the effect of combining rotational and translational oscillations of a circular cylinder by Elston (1997); Blackburn *et al.* (1998, 1999) have demonstrated a number of interesting results (Figure 2.23). In a series of two-dimensional numerical simulations conducted by Elston (2005) the phase angle,  $\Phi$ , between the two motions was found to have a significant effect upon the near-wake structure, as shown in figure 2.23. Indeed, previous interesting results on purely transverse oscillation in free-stream (Leontini *et al.* 2006a) have also indicated that the phase difference between the two motions is of considerable importance and this is the focus of the research discussed here. The phase angle between the motions seems to influence the degree to which cross-annihilation of vorticity occurs and the distance from the cylinder at which vorticity persists. Elston (1997); Blackburn *et al.* (1998, 1999) have shown that the “in-phase” or “opposing-phase” ( $\Phi = 0, \pi$ , respectively) motion in the combined oscillation would produce the most thrust effective jet stream. In these cases a net force was found to act on the surrounding fluid at an angle perpendicular to the oscillation axis. In the results shown, figure 2.23, the computational domain has periodic boundaries and for  $\Phi = \pi/4, 3\pi/8$  and  $\pi/2$  this permitted vortex pairs to leave the domain and re-enter on the opposite side. Blackburn *et al.* (1999) and Elston (2005) examined two scenarios for this case: firstly where the cylinder was held fixed in the horizontal plane and secondly where the cylinder was permitted to freely move in the horizontal plane. The translational oscillation had the parameters  $KC_t = \pi$  and  $\beta_t = 90$  which was shown to result in a regime B (refer to §2.5 and Tatsuno & Bearman (1990)) flow with no rotary oscillation present. The frequency of the rotary oscillation was set to be synchronous with the translational oscillation and the amplitude of oscillation was one radian (Elston 2005).

Elston (2005) mentioned that for the first scenario where the cylinder was fixed in the horizontal direction, see figure 2.24, a streaming flow along this axis is apparent in the vorticity contours. A corresponding simulation of particles being shed from the cylinder surface further illustrates the jet that results. A wake velocity profile at  $x/D = 2.0$  downstream revealed this jet to have a double-peaked nature as suggested by the particle transport map. In the second scenario, where the cylinder was allowed



to move in response to the forces exerted by the jet, *i.e.* the swimming cylinder case, a terminal velocity approximately one third of the magnitude of the maximum translational velocity was achieved. The instantaneous vorticity contour and particle transport maps are shown in figure 2.25. In these maps the high-speed pulsating nature of the jet is shown as discrete “puffs” of particles.

The combined translational and rotational oscillation of the cylinder can result in one side of the cylinder having a greater relative acceleration to the fluid than the opposite side. The greater tangential surface acceleration results in a corresponding increase in vorticity production from the surface. Only in certain cases the motion of the cylinder thus acts to produce vorticity more strongly from one side of the cylinder while retaining an overall zero production of vorticity from the cylinder. The net production of vorticity in one motion cycle is theoretically zero due to the symmetry of the motion. In practice this might not occur because the fluid motion around the cylinder will not remain symmetrical. The thrusting effect appears to occur in a lock-on regime and as reported by Blackburn *et al.* (1999) for this to occur a threshold amplitude of oscillation is required (Figure 2.23).

Elston (2005) had no physical experiments against which to compare his numerical simulations to confirm these effects. To date no detailed studies, especially experimental, into the effects of combining an oscillatory rotational and translational motion of a circular cylinder in either quiescent fluid or in external flow are known. The only available studies on the combined oscillatory motion in external flow are Al-Mdallal (2004) and Kocabiyik & Al-Mdallal (2005). There are also no three-dimensional experimental and numerical studies of the flow available. The three-dimensionality potentially could have a significant impact on the thrust observed by Blackburn *et al.* (1999) as the flow for a cylinder in purely translational motion at this point in the  $(KC_t, \beta_t)$ -parameter space has been proven to be three-dimensional (Elston 2005). Al-Mdallal (2004) has also explicitly mentioned that “*despite the large number of papers dedicated to the problem of a cylinder vibrating transverse to a fluid flow there is only one paper which also allows the body to perform rotational oscillations about its axis in a quiescent fluid (swimming motion): Blackburn et al. (1999)*”.

On the other hand, there exists a similar form of motion in nature that is a combination of rotational and translational motion, which is used as a propulsion mechanism. This motion will be discussed in §2.6.1.

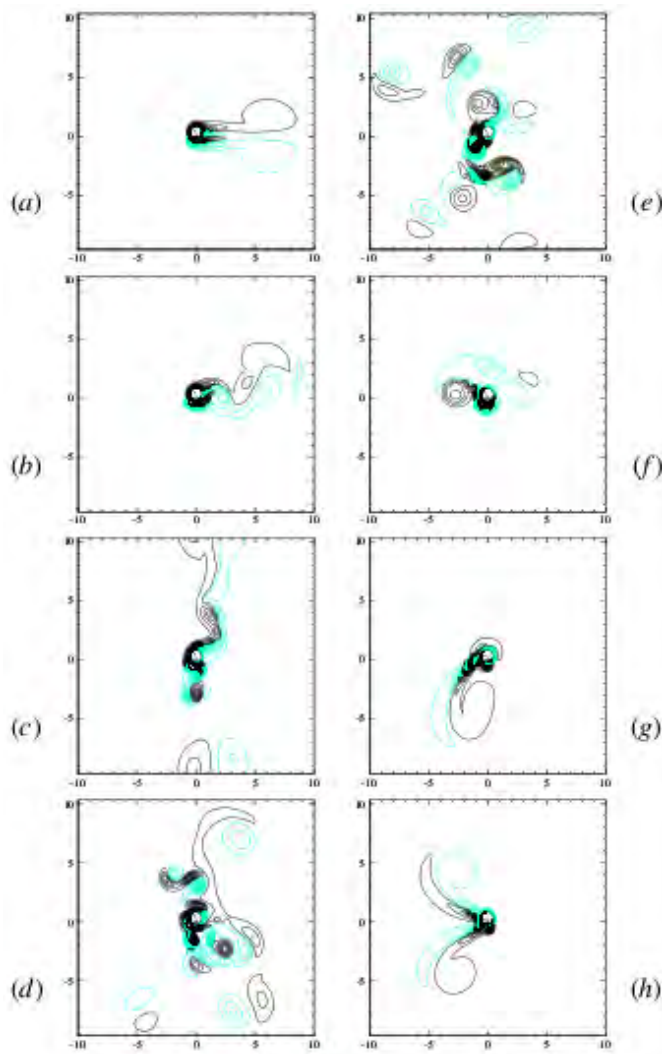


FIGURE 2.23: Instantaneous vorticity contours for a cylinder with both translational and rotational oscillation, shown at  $t/T = 45.75$  for a range of phase angles: (a),  $\Phi = 0^\circ$ ; (b),  $\Phi = 22.5^\circ$ ; (c),  $\Phi = 45^\circ$ ; (d),  $\Phi = 67.5^\circ$ ; (e),  $\Phi = 90^\circ$ ; (f),  $\Phi = 112.5^\circ$ ; (g),  $\Phi = 135^\circ$ ; (h),  $\Phi = 157.5^\circ$ . The graph originally appeared in Blackburn *et al.* (1998) and then is reproduced from Elston (2005) by permission.

Similarities can be found between the study of oscillating cylinders, and oscillating foils. Triantafyllou *et al.* (1991) experimentally investigated the wake mechanics of thrust generated by oscillating foils, and noted that the vortex structure produced in the wake of an oscillating foil resembles that produced by a bluff-body, but with reverse rotational direction. The wake dynamics were dominated by the non-dimensional parameter, the Strouhal number. Streitlien *et al.* (1996) used a similar definition of efficiency as it was used by Triantafyllou *et al.* (1991) in analysing the oscillating foil numerically but required an altered definition to examine the effects of ambient vorticity, because efficiencies of greater than 100% could be achieved by manipulating vorticity

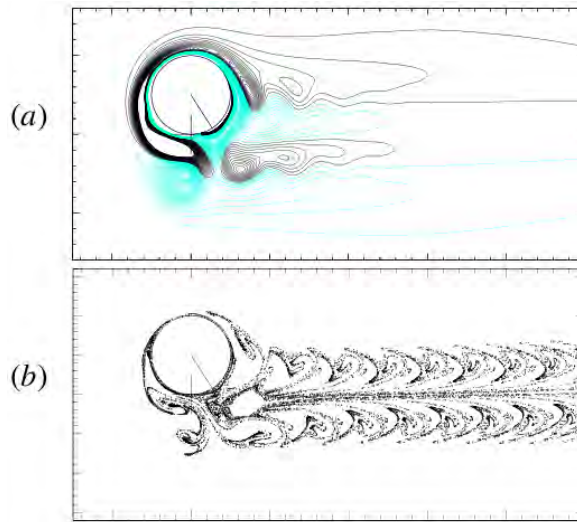


FIGURE 2.24: Flows produced by a cylinder with oscillatory translation and rotation: (a) instantaneous vorticity contours; (b) fluid particle transport. The cylinder is at its maximum vertical position and most negative angular displacement at the instant shown. The rest position of the cylinder is indicated by cross-hairs, and the radial line shows the radial displacement of the cylinder from the horizontal. *The graph originally appeared in Blackburn et al. (1999) and then is reproduced from Elston (2005) by permission.*

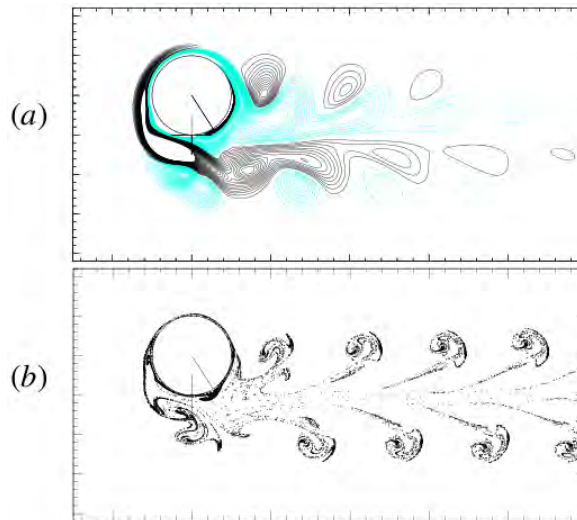


FIGURE 2.25: Flows produced by a cylinder with oscillatory translation and rotation with no restraints applied in the horizontal direction: (a) instantaneous vorticity contours; (b) fluid particle transport. The cylinder is moving at terminal speed in the  $-x$  direction. *The graph originally appeared in Blackburn et al. (1999) and then is reproduced from Elston (2005) by permission.*

present in the stream. Anderson *et al.* (1998) performed further practical investigations into oscillating foils and were able to achieve efficiencies as high as 87% under optimal conditions. The critical factors influencing thrust optimisation were Strouhal number, amplitude of heave motion-to-chord ratio, angle of attack and phase angle between pitch and heave.

As mentioned above the only available studies on the combined translation and rotation oscillatory motions in a free-stream are Al-Mdallal (2004) and Kocabiyik & Al-Mdallal (2005). They dealt with this class of wake flows to analyse the vortex formation modes and synchronisation (lock-on) phenomena behind the cylinder (in the near-wake region) as well as the fluid forces acting on the cylinder. They conducted a series of numerical simulations assuming the flow to be incompressible and two-dimensional, with harmonic translational and rotational oscillations. Their numerical simulations were carried out at only one Reynolds number,  $Re = 855$ , under the same oscillation conditions as the experimental study of Ongoren & Rockwell (1988b) for the case of a cylinder undergoing purely forced translational oscillations at angles of  $0^\circ, 60^\circ, 90^\circ$  with respect to the uniform free-stream.

For the combined forced translational and rotational cylinder oscillation case the numerical simulations of Al-Mdallal (2004) were carried out for combined phase-locked translation and rotation with only a single frequency, *i.e.*,  $f = f_t = f_\theta$ . They also assumed that the instantaneous translation and rotation start at the same moment and the development of the flow was studied in a coordinate frame which moved with the cylinder but did not rotate. Al-Mdallal (2004) considered two types of forced translational oscillation of the circular cylinder in their numerical simulations. In the first, the cylinder was forced to move by combined transverse (cross-stream) and rotational oscillation ( $\eta = 90^\circ, A_\theta \neq 0$ ). In the second, the cylinder was forced to move by combined in-line (streamwise) and rotational oscillation ( $\eta = 0^\circ, A_\theta \neq 0$ ). Calculations were carried out for values of Reynolds number,  $Re = 855$ , and amplitude of translational (in-line or transverse) oscillatory motion,  $A_t/D = 0.26$ , respectively, in the cases  $f/f_N = 0.5, 1, 2, 3, 4$  and  $A_\theta = 15^\circ, 30^\circ, 60^\circ, 75^\circ$ . The effects of  $f/f_N$  and  $A_\theta$  on the vortex formation modes as well as the fluid forces acting on the cylinder were examined. Results of Al-Mdallal (2004) show that five basic asymmetric modes of vortex formation synchronised with the body motions in the near-wake region. Four of these asymmetric modes showed period doubling; doubling or tripling; tripling and

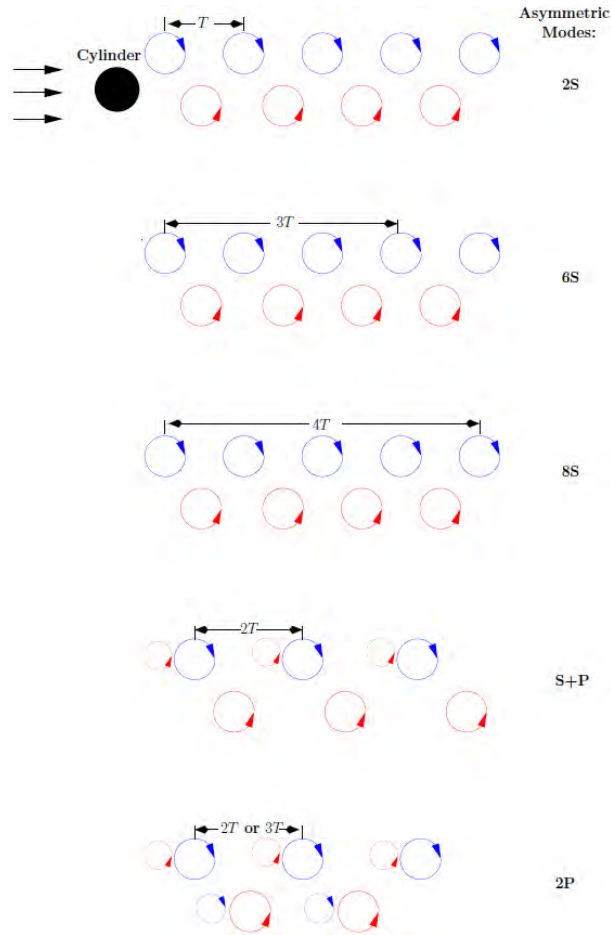


FIGURE 2.26: Representation of basic modes of vortex formation from cylinder undergoing combined translational and rotational oscillation. *Reproduced from Al-Mdallal (2004) by permission.*

quadrupling relative to the classical Kármán mode. These modes are schematically shown in figure 2.26. The asymmetric  $2S$  and  $P + S$  modes occur for both types of forced combined oscillation; the asymmetric  $6S$ ,  $8S$  and  $2P$  modes occur only for combined transverse and rotational oscillation case. The following summarises an overview of wake modes and fluid forces calculated by Al-Mdallal (2004) for the transverse and in-line cases separately:

*Combined transverse and rotational cylinder oscillations:*

When the forcing frequency is  $f/f_N = 1$ , the classical asymmetric  $2S$  mode over one oscillation cycle was the dominant mode for all values of  $A_\theta$  since the maximum oscillatory speeds of both motions are less than the uniform flow speed. Figure 2.27 shows a sample of Al-Mdallal (2004)'s results of combined transverse and rotational cylinder oscillation when  $f/f_N = 1$ . In the range of the frequency ratios when  $f/f_N \geq 2$ , the vortex shedding becomes more complicated due to the strong interaction between

the cylinder motion and the shed vortices. Breaking up of the near-wake vortices and coalescence of these vortices occurred in the region very close to the cylinder surface. This coalescence phenomenon produced interesting repeatable patterns in the near-wake region. They found that the translational oscillation plays an important role in activating the periodic coalescence phenomenon at high values of the frequency ratio. The asymmetric  $P + S$  mode occurred over two oscillation cycles only for  $f/f_N = 2$ :  $A_\theta = 15^\circ$ . The asymmetric  $2P$  mode occurred over two and three cycles of oscillation when  $f/f_N = 2$ :  $A_\theta = 30^\circ$  and  $f/f_N = 3$ :  $A_\theta = 15^\circ$ , respectively. The asymmetric  $6S$  and  $8S$  modes occurred over three and four oscillation cycles for  $f/f_N = 3$ :  $A_\theta = 30^\circ$ ;  $f/f_N = 4$ :  $A_\theta = 60^\circ$  and  $f/f_N = 4$ :  $A_\theta = 15^\circ, 30^\circ$ , respectively. Period doubling; tripling; quadrupling relative to the classical Kármán mode occurred in the cases  $f/f_N = 2$ :  $A_\theta = 15^\circ, 30^\circ$ ;  $f/f_N = 3$ :  $A_\theta = 30^\circ$  and  $f/f_N = 4$ :  $A_\theta = 60^\circ$ ;  $f/f_N = 4$ :  $A_\theta = 15^\circ, 30^\circ$ , respectively. Thus, the vortex shedding period was found to increase proportionally with  $f/f_N$ . Al-Mdallal (2004) also found that the time-averaged drag coefficient reached its maximum value at  $f/f_N = 1$  for all values of the rotational oscillation amplitude. Al-Mdallal (2004) found that the effect of increasing the rotational oscillation amplitude is to reduce the vortex shedding period. The location of the developing vortices increased vertically on the cylinder surface as  $A_\theta$  increases. Thus, the angle of separation is increasing as  $A_\theta$  increases which was consistent with their results observed for rotational-only oscillations case.

Based on the results of Al-Mdallal (2004), the vortex lock-on phenomenon was observed for all values of  $f/f_N \geq 1$ , when  $15^\circ \leq A_\theta \leq 75^\circ$ . An interesting result related to the lock-on phenomenon was observed at  $f/f_N = 4$  and  $A_\theta = 15^\circ$  in which the vortex shedding in both purely transverse and rotational oscillation cases was not locked-on while it produced vortex lock-on for the case of combined translational and rotational oscillations.

*Combined in-line and rotational cylinder oscillations:*

The classical asymmetric  $2S$  mode over one period of oscillation cycle was the dominant mode for all values of  $f/f_N$  and  $A_\theta$  except  $f/f_N = 2$ :  $A_\theta = 15^\circ, 30^\circ$ . They found that this vortex shedding mode was consistent with the in-line-only oscillation case at  $f/f_N = 2, 3$ . Figure 2.28 shows a sample of Al-Mdallal (2004)'s results of combined transverse and rotational cylinder oscillation when  $f/f_N = 1$ . In the first one, they observed a small counter-rotating vortex accompanying the large shed vortex

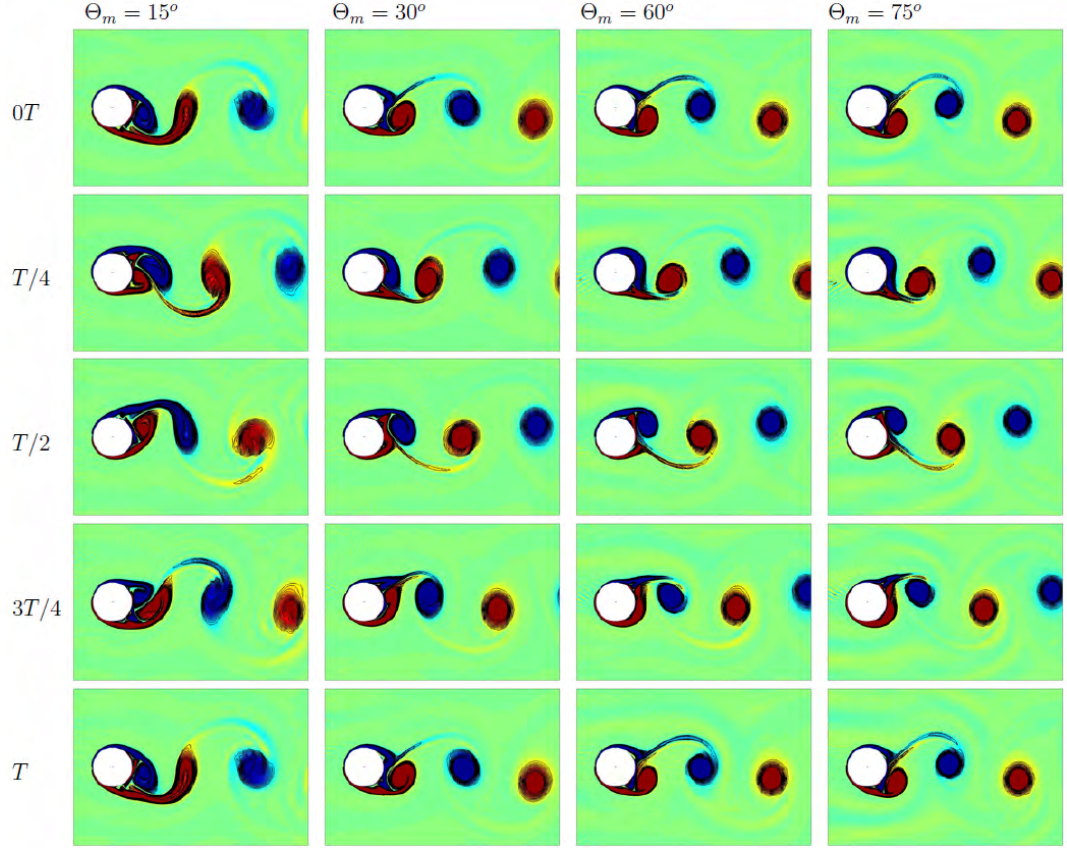


FIGURE 2.27: Equivorticity lines over one period of oscillation,  $T$ , for the combined transverse and rotational oscillation case ( $\eta = 90^\circ$ ,  $15^\circ \leq A_\theta \leq 75^\circ$ ) when  $Re = 855$ ,  $A_t/D = 0.26$ :  $f/f_N = 1$  ( $T = 9.09, 81.82 \leq t \leq 90.91$ ). *Reproduced from Al-Mdallal (2004) by permission.*

from the upper side of the cylinder for a limited distance in the downstream direction. In the second occurrence this counter-rotating vortex accompanies the shed vortex from the bottom of the cylinder. Finally, in the third occurrence each shed vortex was accompanied by a counter-rotating vortex. Moreover, the existence of the asymmetric  $P + S$  mode which was observed at  $f/f_N = 2$  when  $A_\theta \leq 30^\circ$  is consistent with the results of previous experimental and numerical studies for the case of in-line-only oscillation at the same value of  $f/f_N$ .

All of the above are the results of numerical simulations. There is no available experimental investigation on the combined oscillatory motion either in quiescent fluid or free-stream. It therefore seems worthwhile investigating not only the near-wake structure of such a combination of forcing mechanisms, but also to extend this to examine the three-dimensional nature of the wake, which is yet to receive any attention. These are the aims of this thesis.

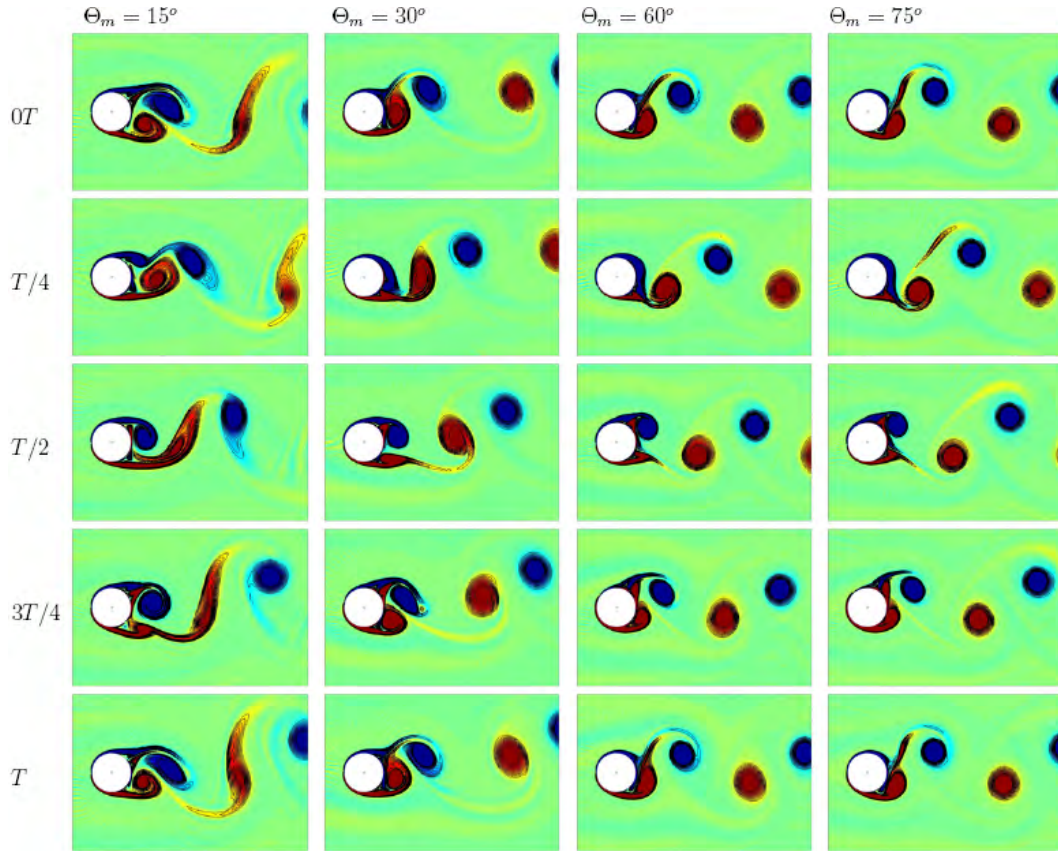


FIGURE 2.28: Equivorticity lines over one period of oscillation,  $T$ , for the combined in-line and rotational oscillation case ( $\eta = 0^\circ$ ,  $15^\circ \leq A_\theta \leq 75^\circ$ ) when  $Re = 855$ ,  $A_t/D = 0.26$ :  $f/f_N = 1$  ( $T = 9.09, 81.82 \leq t \leq 90.91$ ). *Reproduced from Al-Mdallal (2004) by permission.*

### 2.6.1 Carangiform Motion

In the animal kingdom, the process of evolution has led to highly efficient methods of propulsion being developed. Of particular relevance to the combined motion outlined earlier is the means of propulsion developed by animals of three distinct groups that include all of the fastest, continuously swimming animals in the ocean. These animals, such as tuna, marlin, sharks, whales and dolphins, all have an identical means of propulsion which is based upon their fins (tails) being given a characteristic combination of rectilinear and rotational oscillation. This mode of oscillation, which is called Carangiform motion, utilises a twist of the animal's wing-like surface at the extreme ends of the fins translational oscillation. This mode of oscillation, carangiform (after the horse-mackerel Caranax), necessitates a twist at each extreme of the oscillation to give backward inclination to the moving winglike surface, that is to a vertically oscillating cetacean tail, or to a fish's horizontally oscillating caudal fin, see figure 2.29 (Lighthill 1986).



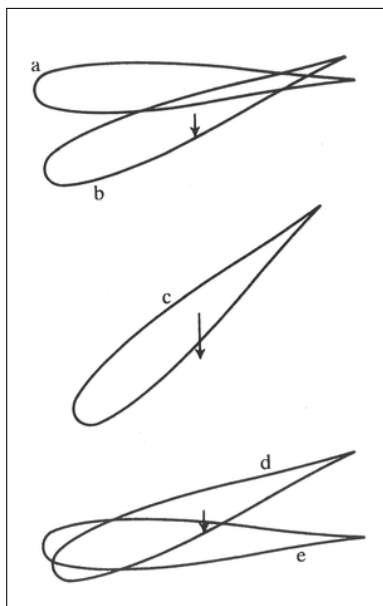


FIGURE 2.29: Carangiform motion involves a twist at each extreme of the oscillation. Successive positions a, b, c, d and e, assumed by a lunate tail's airfoil cross-section at equal time-intervals, are sketched for half of the cycle of oscillation. The other half of the cycle is a mirror image of that shown. *Reproduced from Lighthill (1989).*

In comparison, the results for the circular cylinder have the change in rotational velocity at the midpoint of the cylinders translation. The propulsive jet that is produced from carangiform motion occurs when the oscillations are in-phase, in contrast to the preliminary results for the swimming cylinder, which occurred when the translational and rotational oscillations were out of phase (Blackburn *et al.* 1999; Elston 2005). It has been suggested that this disparity in the phase angle between carangiform motion and the numerical results could be linked to the features which act to influence and control the fin's wake. The magnitude of thrust from the fin is also much larger than that from the oscillating cylinder, but it is likely that much of the thrust comes from the aerodynamics shape of the fin. It is possible that the oscillatory motion of the fin could serve as a drag reduction mechanism (Elston 2005).

## 2.7 Summary

There have been many studies investigating the translational and rotational oscillatory motions in different flow regimes and characteristics. These research studies have focussed on the flow structures and force measurements. However, research into the effects of combining the two oscillatory motions is at a preliminary stage. A number of interesting features have been shown to occur as a result of combining the motions. In

particular, the apparent jet of fluid produced by the cylinder, for a specific phase relationship between motions, has been shown to propel the cylinder. To date, no physical experiments exist to verify these results. The mechanism that results in the cylinder producing a thrust is yet to be investigated. How the relationship between the two motions affects the resulting wake structure has also not been investigated extensively. The combination of oscillatory motions has been shown to be capable of producing a wide variety of vorticity wake patterns. Based on the reviewed literature outlined in this chapter, the aim of the present thesis is first: to quantify the flow around a pure translational oscillating cylinder in a quiescent fluid at low values of  $KC_t$  and  $\beta_t$  in more detail; second: for the first time to experimentally investigate the addition of rotational oscillatory motion to the translational motion in a quiescent fluid, *i.e.* the swimming cylinder; third: to investigate the effect of a free-stream past the swimming cylinder and the effect of a change of phase difference between translational and rotational oscillation on the synchronisation behaviour.

## Chapter 3

# Experimental Methodology

### 3.1 Introduction

This chapter describes the experimental apparatus, facilities, procedures and techniques used in this research/study. This includes the post processing techniques and calculations used to evaluate the data. The chapter is divided into three parts; the first deals with the experiments on the pure translational oscillation in a quiescent fluid (a description of the PIV measurement technique is provided here); the second looks at the combined translational and rotational oscillations in a quiescent fluid *i.e.* the swimming cylinder; the third looks at the combined translational and rotational oscillations in a free-stream flow. Due to the need for specialised design of the experimental instrumentation for the individual experiments, the description of those aspects of the experiment that were not common to all experiments is given in the relevant results chapters. This is particularly the case for the cameras, particles used, number of vectors and number of images acquired and used for phase-averaging.

### 3.2 Problem definition and Parameter Space

In the case where a cylinder is exposed to an oscillatory flow, or equivalently is driven by unidirectional simple harmonic (translational oscillatory) motion in a quiescent fluid, the dimensionless quantities representative of amplitude and frequency of the motion are usually defined as (Sumer & Fredsøe 1997):

$$KC = \frac{U_{\max}}{fD}, \quad (3.1)$$

$$\beta = \frac{fD^2}{\nu}, \quad (3.2)$$

where  $KC$  is the Keulegan–Carpenter number (Keulegan & Carpenter 1958) and  $\beta$  is the Stokes number (for example see Sarpkaya 2005). If the flow is sinusoidal with the

equation of motion defined by:

$$y(t) = A_t \sin(2\pi f_t t) \quad (3.3)$$

then the maximum (peak) translational velocity will be:

$$U_{\max_t} = 2\pi A_t f_t. \quad (3.4)$$

For sinusoidal oscillation the  $KC_t$  number will therefore be identical to:

$$KC_t = \frac{2\pi A_t}{D} \quad (3.5)$$

A Reynolds number, although less commonly used in the published literature than  $KC$  and  $\beta$ , can alternatively be defined as a combination of two of these dimensionless parameters. The associated Reynolds number,  $Re_t$ , is then

$$Re_t = \frac{U_{\max_t} D}{\nu} = KC_t \beta_t. \quad (3.6)$$

When rotational oscillation is added to the translational oscillation of a circular cylinder in a quiescent fluid, a similar but separate set of dimensionless quantities representative of amplitude and frequency of the rotational oscillatory motion can be defined as:

$$KC_\theta = \frac{U_{\max_\theta}}{f_\theta D}, \quad (3.7)$$

$$\beta_\theta = \frac{f_\theta D^2}{\nu}, \quad (3.8)$$

where  $KC_\theta$  and  $\beta_\theta$  are the rotational Keulegan–Carpenter and Stokes numbers, respectively. If the equation for the rotational sinusoidal motion is defined as:

$$\theta(t) = A_\theta \sin(2\pi f_\theta t + \Phi) \quad (3.9)$$

then the maximum (peak) rotational velocity and  $KC_\theta$  number will be:

$$U_{\max_\theta} = 2\pi A_\theta f_\theta, \quad (3.10)$$

$$KC_\theta = \frac{2\pi A_\theta}{D}. \quad (3.11)$$

The experimental arrangement allowed independent variation of the translational and rotational  $KC$  and  $\beta$  numbers.

## 3.3 Experimental Set-up

### 3.3.1 Flow System

This section explains the two different flow systems used in this research, quiescent (stationary) fluid and free-stream.

#### 3.3.1.1 Quiescent Fluid

The experiments were performed in an adjustable size tank in a recirculating free-surface water channel at Monash University, Melbourne, Australia. Two transparent walls made of Perspex were inserted into the test section of the water channel that fitted within and were a snug fit with the glass side walls and the other two walls of the box were perpendicular to this. The insertion of the box combined with the water channel being turned off during the quiescent flow experiments ensured zero velocity flow in the channel. The inserted tank was sealed using small round cross section tubes that were attached on the edges of the walls. To ensure stability of the walls a horizontal flat plate was mounted at the end of the walls to sit on the bottom of the water channel. These movable walls were used to set different tank sizes, if necessary. The tank width was limited by the width of the water channel test section, this being 600mm or  $30D$ . The use of the tank also allowed heavy seeding levels during the PIV experiments.

The water channel was equipped with a PIV measurement system. This could direct a laser sheet from either underneath or through the side wall of the working section. The laser sheet could be either parallel or perpendicular to the direction of flow/fluid by adjusting the reflection mirror and lens under or next to the working section. Figures 3.1 and 3.2 show the photo of the experimental rig and schematic of the water tank, with details of the location of the walls, respectively.

#### 3.3.1.2 Streaming Flow

Some of the experiments were conducted in the recirculating free-surface water channel test section with water recirculating through the channel. A centrifugal pump controlled by an electronic controller was used to give flows with free-stream velocities in the working section between  $0.047$  and  $0.456 \text{ m s}^{-1}$  (corresponding to the pump frequency range between 5 and 50 Hz). For a cylinder with a diameter of 20mm, this range of flow speed gives a Reynolds number range between 1000 and 9200,  $Re$  based on the cylinder diameter (this range can vary slightly due to water properties varying with the

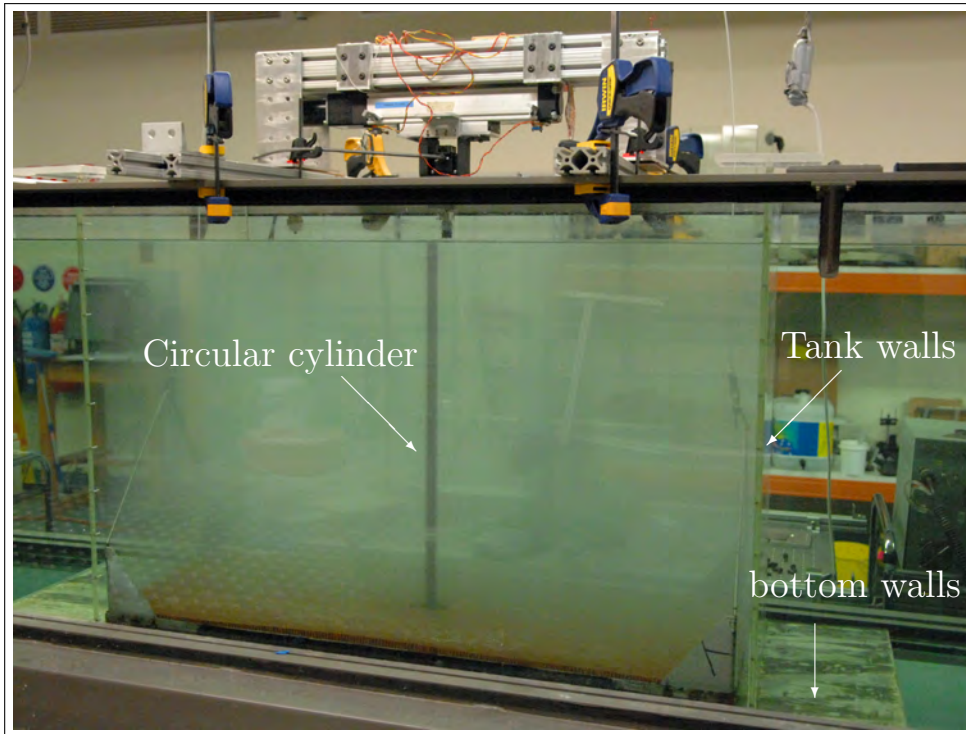


FIGURE 3.1: A photograph showing cylinder and oscillation system in the tank working section.

slight changes in temperature). The test section had a width of 600mm (transverse), depth of 800mm (vertical, free-surface) and was 4000mm long (downstream). The channel's test section was positioned between two large tanks of water. Upstream of the working section, water flows through a distribution manifold followed by flow conditioning honeycombs and screens before going through a 3:1 contraction to the working section. This combination of flow conditioning and contraction act to straighten the flow and yield a free-stream turbulence level of less than 1.0%. The maximum angle between measured velocity vectors and the downstream direction was less than  $1^\circ$ . Of course, these values only apply when there was a mean flow in the water channel, *i.e.* not quiescent cases. More details of the flow quality in the water channel have been reported by Leweke (2002).

### 3.3.2 Experimental Apparatus

To generate the harmonic oscillatory movement of the cylinder within the tank or test section of the water channel, a rig was designed that could accurately translate and/or rotate the cylinder at specific amplitudes and frequencies of oscillations with an adjustable phase difference between the two motions. The rig was designed such that

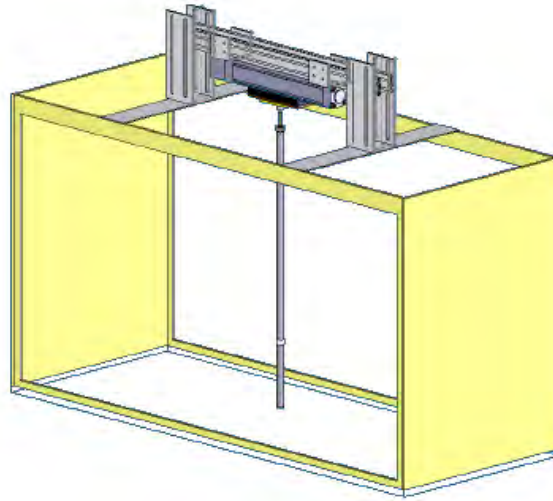


FIGURE 3.2: Water tank assembly.

it can hold the weight of the actuator, the stepper motors, the sting, the vertically-mounted cylinder, and digital scale. Figure 3.1 shows the experimental rig on top of the test section of the water channel during a quiescent fluid experiment. The following sections describe the individual parts of the experimental apparatus.

### 3.3.2.1 Cylinder Model and Coordinates

The experimental model used for the experiments was a hollow circular cylinder machined to smooth outside diameter of 20mm and a length of 800mm, giving an aspect ratio of 40 (see Figure 3.3). This value has been shown by several researchers to be adequate not to affect the two-dimensionality of the flow (Norberg 1994; Williamson 1989; König *et al.* 1990; Lee & Budwig 1991; Szepessy & Bearman 1992; Williamson 1996c; Carberry 2002). The effect of aspect ratio has also been discussed in §2.2.1.3. The cylinder was made of carbon fibre and suspended vertically by a sting from an in-line actuator placed above the water and controlled by a micro-stepping stepper motor. The cylinder was vertically mounted such that its spanwise axis was perpendicular to the free-surface as shown in Figure 3.1 and Figure 3.4. A small section of the cylinder (17mm long and located at a distance of 180mm from the end of cylinder) was replaced by a thin-walled transparent cylinder, whose interior was filled with distilled water. This window minimises shadow effects arising from refractive distortion of the laser light sheet that was generated for acquisition of the PIV images. Figure 3.3 shows a schematic view of the cylinder and its dimensions.

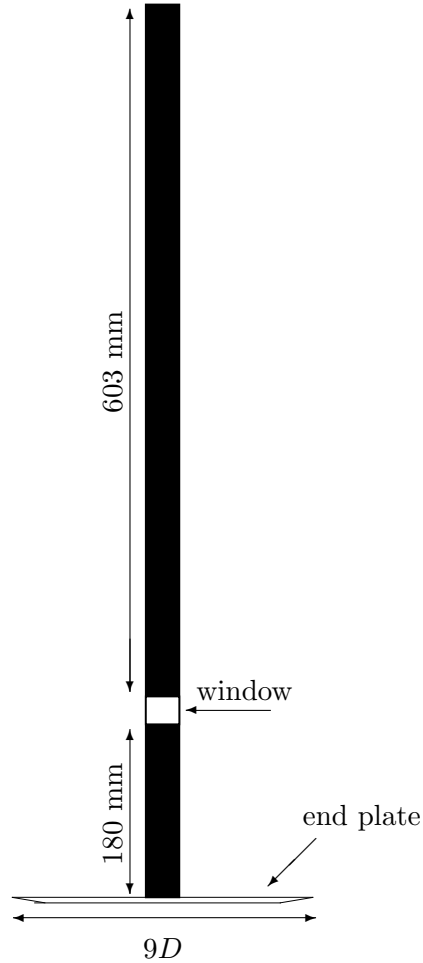


FIGURE 3.3: Schematic showing dimensions of the circular cylinder model.

The cylinder used was fitted with an end plate to reduce end effects. End plates are frequently employed (see for example Nishioka & Sato (1974); Mair & Stansby (1975); Gerich & Eckelmann (1982); Fox & West (1990); Hammache & Gharib (1991); Szepessy & Bearman (1992); Szepessy (1993); Norberg (1994, 2003); Parnaudeau *et al.* (2008)) in wind tunnel or water channel studies in an attempt to ensure that “two-dimensional” flow conditions occur around nominally two-dimensional bluff bodies. Despite the widespread use of end plates with circular cylinders, there is only limited information available on the recommended specific design criteria to be met for their adoption. Stansby (1974) conducted series of experiments with different rectangular shaped end plates and established the basic requirements through measuring the mean base pressure of circular cylinders for designing end plates.

Here, we used the Stansby criteria (Stansby 1974) to reduce the end effects; an end plate was designed and used following the recommendations by Stansby (1974).



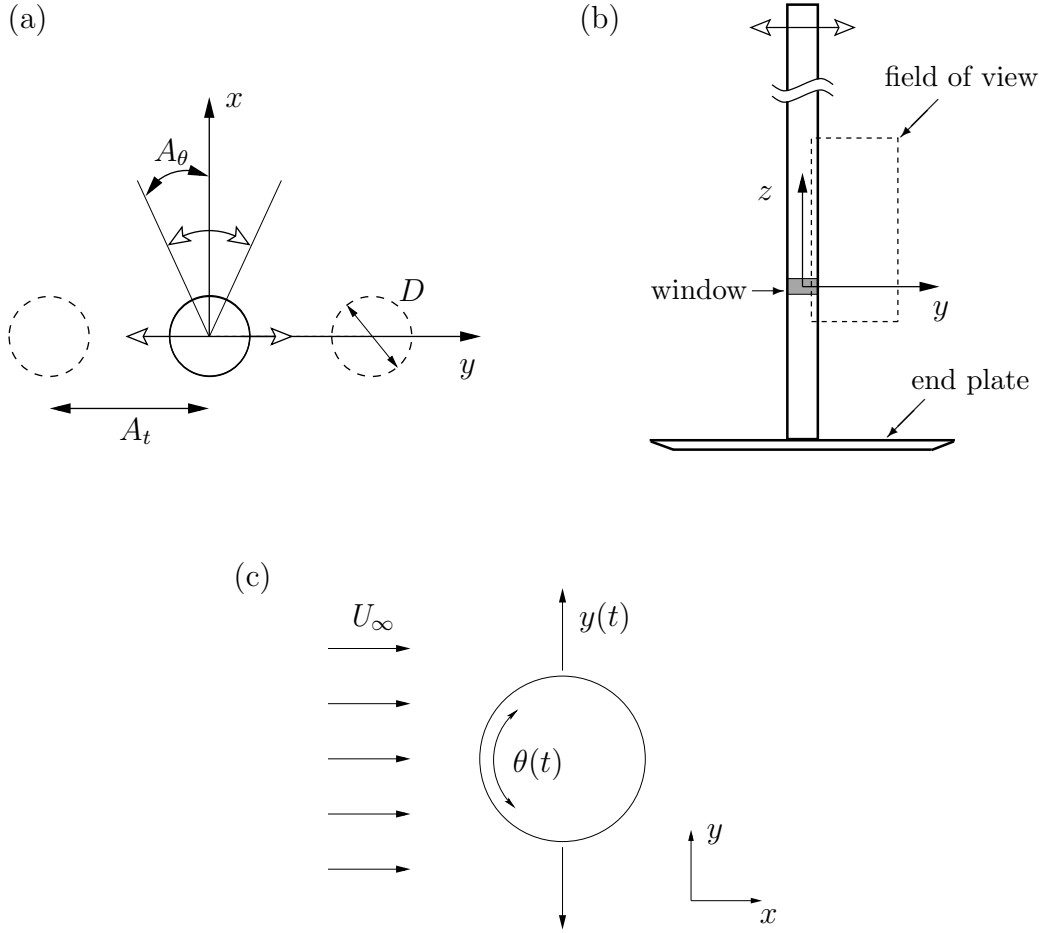


FIGURE 3.4: Schematic of the problem geometry and important parameters relevant to the oscillatory forcing motions. (a): the two-dimensional overview ( $xy$ -plane) of the cylinder and the sinusoidal motions parameters, (b): spanwise view of the cylinder ( $yz$ -plane) with end plate and field of view (PIV), (c): the two-dimensional overview of the cylinder and the sinusoidal motion parameters in a free-stream.

However, in this case we did not use rectangular plates, as recommended by Stansby (1974), circular end plates were used instead. This was done based on the fact that the vertical cylinder must remain axisymmetric along the vertical axis when rotated. The circular end plates were made of Perspex with a diameter of  $9D$  and a thickness of 3mm. An end plate was mounted on the bottom end of the cylinder. Special care was taken to ensure the gap between the end plate and the bottom glass of the test section was always less than 2mm.

The Cartesian coordinate system used was defined such that the origin is located at the centre of the circular cylinder (at  $t = 0$ ) at the above-mentioned window. Figure 3.4 illustrates the definitions of the variables used in equation 3.3 and equation 3.9. The  $x$ -direction is referred to as streamwise, the  $y$ -direction as transverse and the  $z$ -direction

as spanwise (see figure 3.4). To verify the frequency and amplitude of oscillation a digital scale was used to measure the oscillation displacement of the actuator which was attached to the cylinder. This also provide a means of tracking the motion with an oscilloscope.

### 3.3.2.2 Motion Controller and Stepper Motors

In a number of previously published studies of related flows a Scotch Yoke mechanism (for example see Tatsuno & Bearman 1990; Dütsch *et al.* 1998; Kishnamoorthy *et al.* 2001; Sarpkaya 2002, and many more) was widely used as the means of generating sinusoidal oscillatory motion. However, for these experiments it was felt that the approach could have difficulties for the detailed examination of the phase relationship between the different oscillatory motions. U-tubes have also previously been used for related flow and has been found to work particularly well for flow visualisation experiments (for example see Williamson 1985).

The high efficiency and versatility of modern high resolution micro-stepping stepper motors and controllers, encouraged us to use this technology to generate a wide range of motion profiles. Using high resolution stepper motors (here the maximum resolution was  $50800 \text{ steps rev}^{-1}$ ) provides more control of the independent variables of a harmonic oscillation motion. They were used here to generate the required sinusoidal oscillatory motions. This was achieved by using a 2-axis controller (Parker Compumotor 6K2); two independent drivers (Parker OEM650 and E-DC) for driving translational and rotational motions, respectively; two independent high resolution stepper motors (Parker S-series and LV231-02-10-EC); a rodless in-line mounting actuator (Parker ERS50-B02LA20-FSR150-A) and a desktop personal computer (PC).

The vertically mounted cylinder was directly connected to a high resolution stepper motor that generates the rotational motion. The motor was housed in a bracket (see Figure 3.5) and connected to the sliding plate underneath the rodless in-line mounting actuator through shafts and bearings. The second high resolution stepper motor was connected to one end of the in-line actuator and generates the translational oscillatory motion. The 2-axis controller allows the stepper motors to be controlled independently, allowing the generation of the two motions with any combination of frequency, amplitude and phase angle difference. A desktop PC was used to program the controller, using the “Motion Planner” software provided by the Parker company.

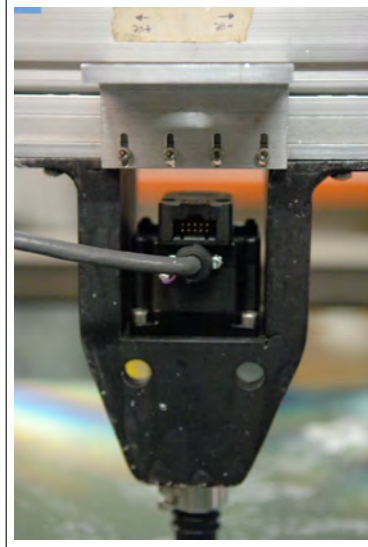


FIGURE 3.5: A photograph showing the rotational stepper motor housed in a bracket, where the circular cylinder is vertically mounted to.

One of the options of the controller was used to generate a sine wave for driving the cylinder's motion. It was possible to produce sinusoidally oscillating motions, with control of the phase angle, amplitude, and centre of oscillation. One sine wave was produced per axis, each using the variable count frequency of that axis to increase or decrease the frequency of motion, up to a maximum angular frequency of 40 Hz. For each set of experiments, the motion was controlled such that, after started, the controller sent signals to the drivers of both axes. These then drove the stepper motors at preselected resolutions, which here were set to the maximum resolution *i.e.* 50800 steps  $\text{rev}^{-1}$ .

The control software was programmed such that the output profile incorporated triggering (TTL-signal) signals to acquire images from the camera acquisition and fire the laser. In this way the PIV images could be captured at pre-selected phase angles in the oscillation cycle (phase-locked), see figure 3.13c. Figures 3.6 and 3.7 show the schematic and a photo of the controller system, respectively.

A digital scale (150mm vertical type) was used to obtain position feedback of the translational motion as an analog signal. An interface box was made to take serial digital position data from the digital scale and convert it to an analog voltage. The scale sample rate could be changed from its default mode of about 3 Hz to the fast mode of about 40 Hz. Figure 3.8 shows a schematic of the digital scale mounted to the actuator rig.

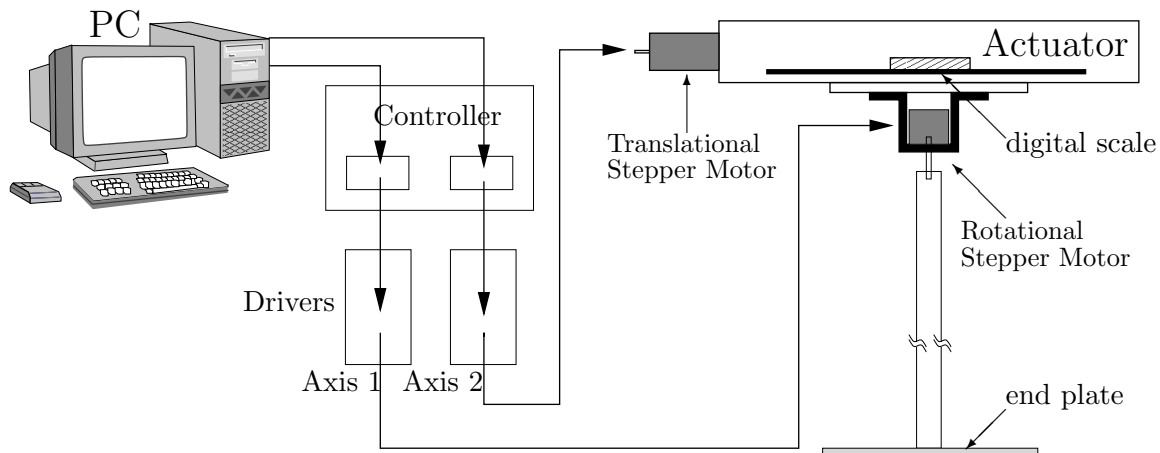


FIGURE 3.6: Schematic of the 2-axis controller, drivers, digital scale and PC used.

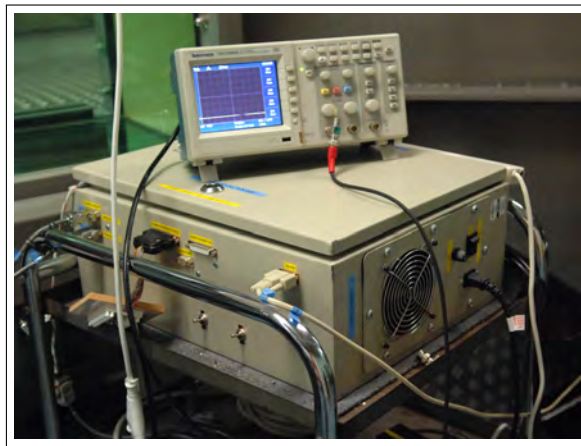


FIGURE 3.7: A photograph showing the controller and the oscilloscope inside the box!.

### 3.3.2.3 Means of obtaining Quiescent Flow

The experiments for the first two parts of this study were conducted in a fluid initially at rest, *i.e.* *quiescent*. The experiments were conducted in a laboratory with no temperature control, meaning special care was required to ensure the quiescency of the flow because the temperature difference between the water and the room could result in undesirable motion of the water inside the tank. Following each experiment, the cylinder held stationary in the tank for at least one hour to allow the flow to become stationary again. During the course of experiments, the water and room temperatures were monitored and recorded hourly using an ebro TFX430 thermometer. Figure 3.9 shows a typical variation of room and water temperature for different times of a day and different days throughout a year.

Due to temperature differences between the water and room, for most of the exper-

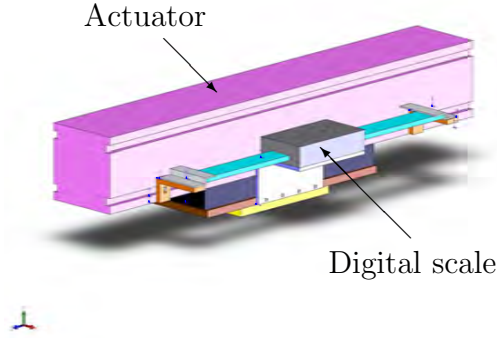


FIGURE 3.8: Schematic of the digital scale.

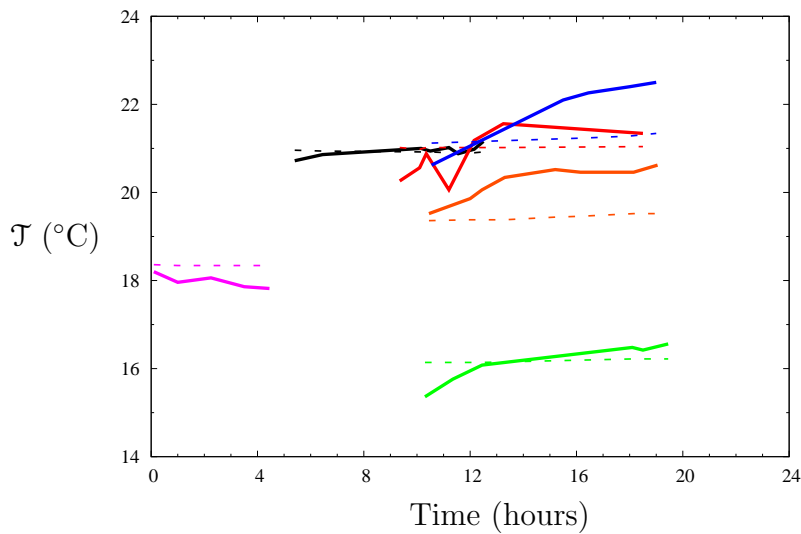


FIGURE 3.9: Room and water temperature variation during the course of experiment for different days throughout the year. The horizontal axis shows time in hour and the vertical axis shows the temperature. The solid line denotes the room temperature, whereas the dashed line denotes water temperature.

iments there was unwanted fluid motion inside the tank due to the resultant natural convection. To minimise, and preferably eliminate these a sheet of honeycomb, 30mm thick, was suspended above the tank (see Figure 3.10) and moved in and out of the tank very slowly before each set of experiments. This reduced the waiting period between the experiments by breaking any large-scale flow structures into small-scales, which consequently dissipated more rapidly. This resulted in less unwanted motion and reduced background noise. Typically, the background noise amplitude, measured with the norm of velocity magnitude was in the order of  $0.1\text{mm s}^{-1}$ . Figure 3.11 shows a sample of these measurements before starting the main experiment. Special care was also taken to make sure both the norm of velocity magnitudes and the norm of stan-

standard deviation of the velocity magnitudes converged to a satisfactorily low value. This starting criterion was found to be less than 0.1% of  $U_{\max}$  of the experiment.



FIGURE 3.10: A photograph showing the honeycomb used to settle the flow for the quiescency experiments.

Figure 3.12 shows a typical comparison between the quiescency of the water in the tank with and without the use of the honeycomb. Clearly this shows the effect of the honeycomb in damping the large-scale motions. The honeycomb in this particular case reduced the waiting time by at least 50%, from about an hour to 30 minutes.

### 3.3.3 Experimental measurement systems

The primary visualisation method used in this study was particle image velocimetry, PIV (Adrian 1991). PIV is now a well known and accepted technique and so only a brief overview is presented here.

The software used to perform the PIV analysis was an in-house developed algorithm written primarily by Dr. Andreas Fouras of Monash University (for example see Fouras & Soria 1998; Fouras *et al.* 2008). It incorporates a number of error correction algorithms previously discussed in the literature.

Particle Streaked Visualisation was also used, and will be briefly described in the following sections.

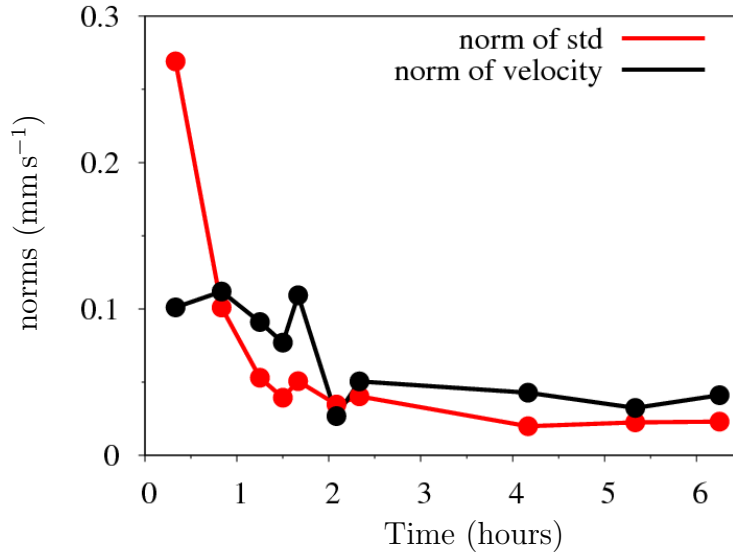


FIGURE 3.11: This figure shows a sample quiescency case,  $KC=5$ ,  $\beta=20$  and  $U_{\max}=5.56$   $\text{mm s}^{-1}$ . The vertical axis shows the norms of either standard deviation of the velocity fields (red color) or the velocity fields (black color). The horizontal axis is showing the time in hours. The average room temperature during the quiescency experiments is  $18.1^{\circ}\text{C}$ .

### 3.3.3.1 Flow Visualisation

Flow visualisation techniques were mainly used for the quiescent fluid experiments. In acquiring the flow visualisation images, the water inside the tank was seeded with polymer sphere particles (VESTOSINT 2157 natural color) having a mean diameter of  $56\mu\text{m}$ . Particles were poured into the water tank, while stirring the water well to distribute the particles homogeneously across the box. The system was then allowed to settle as discussed above in § 3.3.2.3. Preliminary experiments showed that the particles can remain buoyant for at least 45–60 minutes after the flow settled down; all experiments were conducted during this time. The flow visualisation was performed with the same hardware and techniques used to obtain PIV images but with different camera and software settings, *e.g.* longer exposure times (due to using video PIV mode). The main difference between the flow visualisation methods in this study and PIV were in the use of a continuous light sheet instead of a pulsed laser sheet, and the camera settings, as the flow visualisation didn't need an expensive PIV camera. Two apertured 1200W stage-lamps as light sources, one on each side of the water channel, were used to ensure the light sheet passed through the water window of the model (see Figure 3.3). The thickness of the light-sheet was controlled to be about 3mm. Visualisation images were captured on a high performance digital CCD camera system (Cooke Pixelfly) with a maximum resolution of  $1376 \times 1040$  pixels. The stepper motor has the capability of

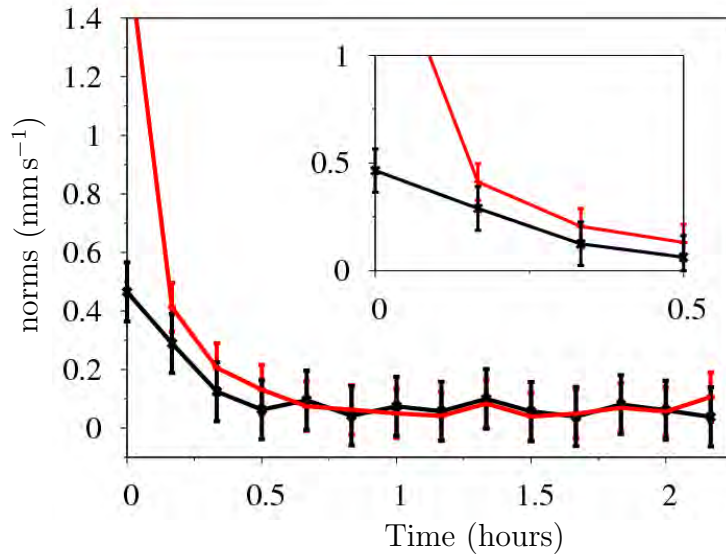


FIGURE 3.12: Comparison of quiescency with (black color) and without (red color) honeycomb,  $KC=5$ ,  $\beta=20$  and  $U_{\max}=5.56 \text{ mm s}^{-1}$ . The vertical axis shows the velocity norms of the measurement field. The horizontal axis is showing the time in hours. The average room temperature for the cases with and without honeycomb are  $21.4^\circ\text{C}$  and  $22.0^\circ\text{C}$ , respectively

delivering triggering TTL pulses to the CCD PIV camera. Consequently the stepper motor triggers the CCD camera at pre-selected phase angles. The flow visualisation results were useful in revealing vortex structures in the flow and also to make sure that the system was giving results comparable with the flow visualisation results of Tatsuno & Bearman (1990).

### 3.3.3.2 PIV - Particle Image Velocimetry imaging system

The PIV technique provides instantaneous velocity vectors,  $\mathbf{u}$ , of a fluid in a region of interest of the flow illuminated by a sheet of laser light. This method determines particle displacement  $(\Delta x, \Delta y)$  in a flow over a known time,  $\Delta t$ . PIV gives quantitative and non-intrusive flow measurements with high spatial resolution, advantages of this technique over other visualisation techniques. In these experiments flow fields around a sinusoidally oscillating circular cylinder were measured using PIV.

Particles are used to seed the flow and two consecutive images acquired in a plane of interest in the flow that is illuminated by a laser sheet. The images are taken a time  $\Delta t$  apart. In general, particles made from different materials such as Polystyrene, Aluminium flakes, hollow glass spheres, granules for synthetic coatings or polyamide can be used (Raffel *et al.* 2007). If the particles in a region of the flow field move by an amount  $\Delta x$  in the  $x$ -direction and  $\Delta y$  in the  $y$ -direction in time  $\Delta t$ , the velocities



of the particles in  $x$  and  $y$ -directions are

$$u = \frac{\Delta x}{\Delta t} \quad (3.12)$$

and

$$v = \frac{\Delta y}{\Delta t}. \quad (3.13)$$

In each pair of images, a small sub-region of the image is interrogated with a cross-correlation algorithm that identifies where the group of particles in the first frame have moved to in the second frame. A vector is then drawn in the centre of the first image interrogation window with a length and direction corresponding to the offset (to sub-pixel accuracy) of the particle group. Then, by knowing the image resolution and the time between images ( $\Delta t$ ), the vector can be linearly scaled to give a fluid velocity in that region (using the magnification factor,  $\mathcal{M}$ ). The magnification factor can be measured by placing a ruler or grid with known spacing in the plane of interest and convert the pixels to required unit length. In this study a ruler was used to calculate the  $\mathcal{M}$  factor prior to experiments. This process is repeated over the whole image, resulting in a grid of velocity vectors, typically presented as the horizontal and vertical components of the resultant velocity vector. Further information on the PIV method can for example be found in Adrian (1991) and Raffel *et al.* (2007).

The in-house algorithm used here also determined a bound on the velocity results of the experimental interrogation (Fouras & Soria 1998; Fouras *et al.* 2008). At each interrogation location, theoretical velocity vectors were determined using a deconvolution of a simplified Navier–Stokes equation fit through surrounding vectors. Erroneous vectors were detected and replaced using an algorithm incorporated into the PIV processing software. Any experimental measurements that were not within two pixels of that predicted value at that location were then replaced with the theoretical vector. This vector is then known as *filled*, and a count of the number of filled vectors in any given image gave an estimate of the adequacy of the experimental data. Any data set that had more than 5% of vectors filled was discarded and all the efforts have been made to reduce this value as much as possible prior to any experiment.

From the sequence of images obtained, *i.e.* the instantaneous results, an averaged flow field was required for each parameter setting in the phase-locked experiments. The simplest method of doing this is by averaging the vectors at each interrogation location for all the PIV images in a given sequence. A more accurate technique that has also

been incorporated was developed by Meinhart *et al.* (2000), who showed that greater accuracy could be obtained by averaging the correlation space peaks of the same interrogation region of each image before determining the real-space vector. However, this method assumes that the flow is steady in time as any temporal variation in the flow will be smoothed out by this procedure and hence was not used for the majority of data analysis here. Also included in the PIV algorithm used in this investigation was a technique developed by Hart (2000) to improve the accuracy of cross-correlation by successively reducing the interrogation window size. In this technique, an initial interrogation is performed on all images in a sequence with a large interrogation window size. The velocity vectors produced by this method were then used as a first approximation to a second interrogation using a window size reduced by half. This process is repeated for successively smaller window sizes and can be repeated theoretically until the window size matches a particle size. However, to minimise noise, this is usually limited in practice to a window size that includes at least 7 to 8 particles. This multi-pass technique has been used to analyse the PIV images. It was finally found that an initial  $32 \times 32$  pixel interrogation window size on a  $16 \times 16$  pixel grid with 50% overlap would produce good balance between accurate results as in less than 5% filled vectors and computational times in comparison with an initial approximation using a window size of  $64 \times 64$  pixels. Other combinations of the multi-pass interrogation window sizes have also been tested but none of the larger ones fulfilled the less than 5% of filled vectors criterion explained above. Smaller initial interrogation window sizes than what is used have also been tested and due to the longer computational times in comparison with the accuracy of the results were not used. It should be noted that in order to achieve more accurate results a 50% overlap between the interrogation windows was always used (Raffel *et al.* 2007), hence while testing smaller initial window sizes of  $16 \times 16$  pixel a grid size of  $8 \times 8$  pixel was used. Larger initial sizes significantly increased the processing time with no great improvement in accuracy (Atvars 2007). Most of the results presented in the following chapters are phase-averaged. For this purpose, the images were taken at pre-selected phases in the oscillating cycle for a series of time and then the displacement fields were temporally averaged as can be seen in equations 3.14 and 3.15. Equation 3.14 shows the instantaneous velocity and 3.15 the phase-averaged velocity over  $n$  number of cycles.

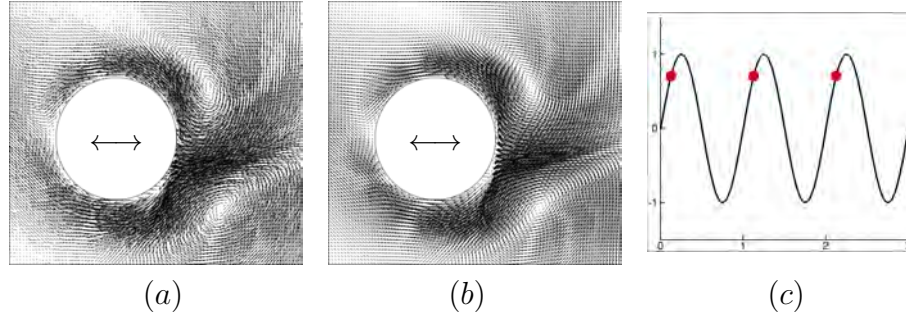


FIGURE 3.13: A sample of (a) instantaneous and (b) phase-averaged PIV results. (c) shows a typical harmonic motion of the cylinder and the circles on the curve show the pre-selected phase in the cycle at which the PIV images were taken. The measurement has been taken over a translationally oscillating cylinder at  $KC_t=6.25$ ,  $\beta_t=18$  corresponding to regime D of Tatsuno & Bearman (1990), refer to §2.3 and §4.4.6 for further information. The arrows represent the direction of the oscillation.

$$\mathbf{u} = \mathbf{u}\left(\frac{nt}{T}\right) \quad (3.14)$$

$$\langle \mathbf{u} \rangle = \frac{1}{n} \sum_{k=0}^n \mathbf{u}\left(\frac{kt}{T}\right) \quad (3.15)$$

Figures 3.13a and 3.13b show a sample of instantaneous and phase-averaged PIV results for a translationally oscillating cylinder, respectively. In order to identify the statistically sufficient number of frames to average, prior to experiments for a very long series of data the root-mean-square (rms) of the velocities in the  $x$  and  $y$ -directions were recorded. In a long enough series of data the rms values of the velocities will reach an asymptotic value, from which the optimum and sufficient number of cycles to average was extracted for each case. The same test was repeated once one of the independent variables was changed to make sure sufficient number of frames were used for averaging.

A schematic diagram of the PIV set-up can be seen in Figure 3.14. The PIV set-up, using digital double exposure cameras and illustrated in Figure 3.14, was based on that originally described by Adrian (1986, 1991) and developed over the past decades (see for example Rockwell & Lin 1993; Rockwell *et al.* 1993; Westerweel 1997).

As mentioned previously, the primary output of PIV is a 2D velocity vector, these were converted into vorticity normal to the flow field, given by

$$\omega_z = \frac{\partial v}{\partial x} - \frac{\partial u}{\partial y} \quad (3.16)$$

Spatial displacement gradients were derived by  $\chi^2$  fitting a second-order interpolator

curve through the vectors surrounding the interrogation point, rather than by a discrete finite difference approach. Fouras & Soria (1998) measured the gains in accuracy resulting from this approach when calculating quantities requiring velocity gradients, for example shear stress and vorticity. More detailed information can be found in Dusting (2006).

In this research, a twenty one-point 2D local fit to the discrete velocity data, based on what is explained in Fouras & Soria (1998), was used. The additional bias and random error introduced by this approximation into the vorticity value have also been investigated by Fouras & Soria (1998). The accuracy of the  $\omega_z$  field measurement depends primarily on the spatial sampling distance between each velocity data point and the accuracy of resolved velocity vector field, as is discussed in detail by Fouras & Soria (1998).

Subsequent processing was undertaken using scripts written with the MATLAB<sup>®</sup> (Octave) data manipulation and programming tool. Additional scripts were used to calculate the circulations and other important flow properties.

The circulation of vortices was calculated by integrating the vorticity in the longitudinal direction over the cross-section of the vortices in the wake of the cylinder.

The edge of the vortices was defined to be the contour of the points of about 10% of the local extreme value of the vorticity, as defined by McWilliams (1990). Eventually the spacing between vorticity concentrations was determined.

The vorticity is non-dimensionalised by the maximum velocity of the cylinder motion,  $U_{\max}$ , and the cylinder diameter by

$$\omega_z^* = \frac{\omega_z D}{U_{\max}}. \quad (3.17)$$

The circulation is also non-dimensionalised by  $U_{\max}$  and  $D$  so that

$$\Gamma^* = \frac{\Gamma}{\pi D U_{\max}}. \quad (3.18)$$

From the computed vorticity distribution, vortex shedding and vortex motion could easily be recognised and was used to determine the time-dependent vortex dynamics induced by the oscillating cylinder. The phase averaged velocity and vorticity fields were also calculated to examine the repeatable features of the flow field.

### 3.3.4 Experimental procedures

The PIV processes used in the experiments are described below. Here only a generic procedure is described. Other parameters specific to individual sets of experiment are included when they are described in the results section.

#### 3.3.4.1 PIV measurement procedure

The method for capturing PIV data was described in §3.3.3.2. PIV was used to investigate the wake behind a purely translational oscillatory circular cylinder in a quiescent fluid (the first part of the present study) and combined translational and rotational sinusoidally oscillating circular cylinder in a quiescent fluid and free-stream (the second and third part of this study, respectively).

Figure 3.14 shows a schematic of the PIV imaging system. For the  $xy$ -plane measurements the camera was mounted underneath the water channel test section facing up and the laser was mounted horizontally on the side of test section. The laser sheet was set such that it passed through the window in the circular cylinder model. The laser was then triggered at certain phases of the motion. For the  $yz$ -plane or spanwise measurements the location of the camera and the laser was switched. The camera was now mounted on the side of the test section and the laser was fired from underneath the channel. For both cases, the laser beam was passing through a plano-concave lens to generate the laser sheet.

The flow was then seeded with spherical polyamide particles of specific gravity of 1.016. A range of particle sizes have been used depending on the specifications of each of experiment. The size of particles varied from  $11\mu\text{m}$  to  $56\mu\text{m}$  in diameter (VESTOSINT 2159, 2158 and 2157 natural color, respectively). The particles were illuminated using two miniature Nd:YAG laser sources (Continuum Minilite II Q-Switched) of a wavelength of  $532\text{nm}$  and maximum energy output of  $25\text{ mJ pulse}^{-1}$ . The thickness of the laser sheet was measured to be less than  $2\text{mm}$ . Pairs of images were captured on a high resolution CCD camera (either Cooke pco2000 or Cooke pco4000) with a maximum resolution of  $4008 \times 2672$  pixels. An interrogation window of  $32 \times 32$  pixels was used for the parts of this study (with an initial window size of  $64 \times 64$  pixels) and was found to give satisfactory results with 50% overlap. More than 98% of the vectors were valid for all the experiments. At a particular phase of the oscillation cycle, a number of image pairs over successive cycles were taken and stored for further processing. The timing

of the laser and camera triggering was controlled by a special in-house designed timing unit, with an estimated accuracy of  $1\mu\text{s}$ . The camera and the laser were triggered by a TTL-signal, which was delivered from the stepper motor once during each laser shot. Using predefined timing sequences, the first and then second laser were triggered and fired by the timing unit. The time difference between image pairs,  $\Delta t$ , was calculated for each case based on the values of  $KC$  and  $\beta$  to give a displacement of at least 8px in each pair. The timing between the triggering pulses and the signals from the stepper motors were also monitored and checked using a Tektronix TDS2002B oscilloscope for all the times. For each set of measurements unbiased images were taken of a ruler next to the cylinder to give the spatial calibration of the PIV images (magnification factor,  $\mathcal{M}$ ). Figure 3.15 shows the PIV set-up during capturing an image while the laser fires.

It should be noted that particles with different diameter sizes were used in this thesis. Regardless of the diameter size of the particles, according to the manufacturer's user manual (Vestosint 2010), the specific gravity (1.016) is identical among all of them. Based on the Stokes' law (Happel & Brenner 1983) a terminal velocity for a particle travelling in the  $z$ -axis direction at low  $Re$  number can be calculated by (Rhodes 2008):

$$w_p = \frac{2(\rho_p - \rho_f)gr_p^2}{9\mu}. \quad (3.19)$$

For the  $20\mu\text{m}$  particle case,  $w_p$  is found to be  $3.67 \times 10^{-6} \text{ m s}^{-1}$ , hence the settling time of the particles for travelling from the water surface to the bottom of the channel test section (800mm) can take up to  $\approx 90$  hours. This value in comparison with the range of oscillation period experienced in this thesis ( $1.6 \leq T \leq 20 \text{ sec}$ ) is negligible.

To ensure that the particles were following the streamlines a Stokes number defined as:

$$Stk = \frac{t_{relax}}{T}, \quad (3.20)$$

is required to be  $Stk \ll 1$ , where  $t_{relax}$  is the relaxation time. The Stokes number corresponds to the behaviour of particles suspended in a fluid. For  $Stk \gg 1$ , particles will continue in a straight line as the fluid turns around the obstacle therefore impacting on the obstacle. For  $Stk \ll 1$ , particles will follow the fluid streamlines closely. A relaxation time for particles is defined as the time required for a particle to adjust or relax its velocity to a new condition of forces. It is an indication of the particle's ability to quickly adjust to a new environment or condition. It depends on the mass and mechanical mobility of the particle, and is not affected by the external forces acting on

the particle. The particle relaxation time can be obtained from the following equation (Hinds 1999):

$$t_{relax} = \frac{(\rho_p - \rho_f)d_p^2}{18\mu}. \quad (3.21)$$

In the present study depending on the size of the particles used, relaxation time can be calculated to be in the range  $1.14 \times 10^{-7} \leq t_{relax} \leq 2.94 \times 10^{-6}$  sec, where the limits correspond to  $11\mu\text{m}$  and  $56\mu\text{m}$  particles, respectively. Consequently, the ratio between the relaxation time and oscillation period is calculated to be in the range  $1.875 \times 10^{-8} \leq Stk \leq 2.34 \times 10^{-7}$ . As it can be seen for all the cases the  $Stk \ll 1$ , meaning that the particles are following the streamlines in all the experiments and the flow and vorticity paths are not affected by particles.

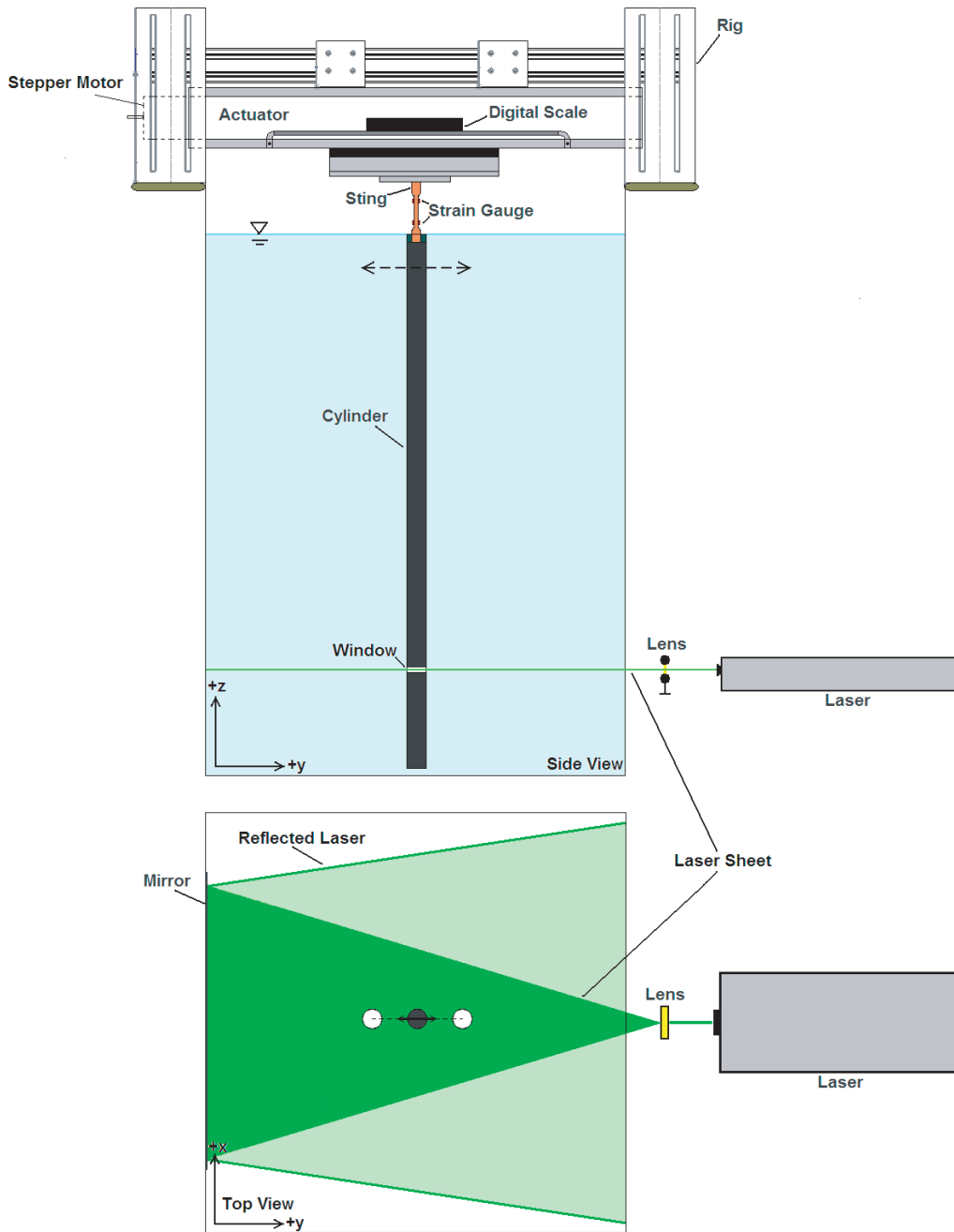


FIGURE 3.14: Schematic of PIV imaging system.



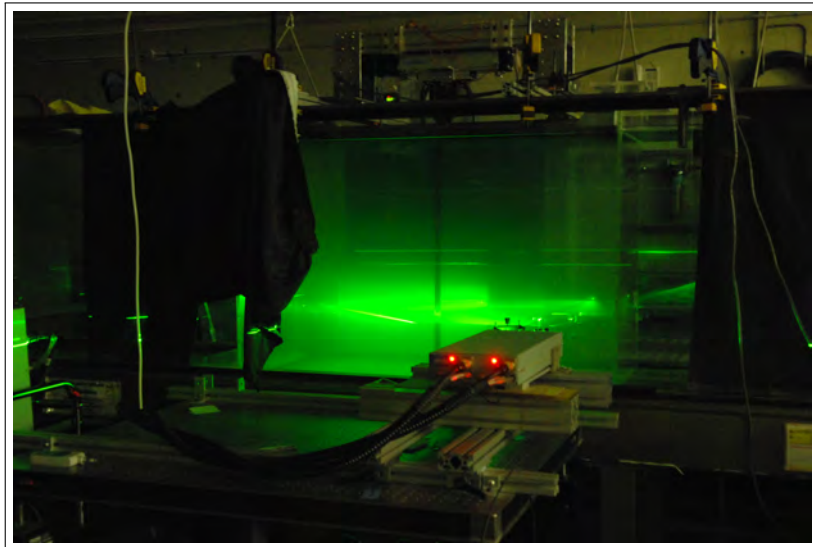


FIGURE 3.15: A photograph showing the experimental PIV set-up and the laser sheet.



## Chapter 4

# Translationally oscillating cylinder in quiescent fluid

### 4.1 Introduction

The oscillatory motion of a cylinder relative to the surrounding fluid gives rise to a large number of different flow regimes that affect the forces that the body experiences during its motion. Of primary interest in this thesis is the combination of forced simple harmonic (sinusoidal) translational and rotational oscillation of a circular cylinder in either a quiescent fluid or free-stream flow. Numerical research into the effects of combining these motions has demonstrated that a number of interesting features arise, however there have been few detailed, particularly experimental, research studies done on these findings to date (see for example Elston 1997; Blackburn *et al.* 1998, 1999; Al-Mdallal 2004; Kocabiyik & Al-Mdallal 2005). To gain an insight into the effects that occur with the combined motion it is informative to review and investigate the body of knowledge surrounding the individual motion components. This chapter deals only with the pure translational oscillatory motion in quiescent fluid (see §2.5).

There have been many excellent visualisations of the flow in an otherwise quiescent fluid resulting from low amplitude rectilinear motion at a range of frequencies by Tatsuno & Bearman (1990) and others, such as Lin & Rockwell (1996, 1997); Dütsch *et al.* (1998); Blackburn *et al.* (1998); Uzunoglu *et al.* (2001); Lam & Dai (2002); Elston *et al.* (2004); Elston (2005); Elston *et al.* (2006). However, there has been a lack of quantitative experimental investigations at low values of translational amplitudes and frequencies. In this work PIV was used as it has the potential to examine vorticity fields, their evolution and transitions between different resulting wake structures.

Most relevant to the present study is the flow visualisation of Tatsuno & Bearman

Case	Regime	$KC_t$	$\beta_t$	$Re$
1	A*	$\pi$	53	166
2	A	8.16	8.18	67
3	B	$\pi$	63.1	198
4	C	4.40	44.44	195
5	D	8.17	11.00	90
6	E	$2\pi$	26.23	165
7	F	12.57	38.68	486
8	G	8.25	38.68	319

TABLE 4.1: Flow Visualisation test cases conducted in this chapter. One value of  $KC_t$  and  $\beta_t$  was chosen as a representative of each regime.

(1990). Using qualitative techniques they comprehensively investigated translational harmonic oscillation in a quiescent fluid at  $KC_t$  numbers between 1.6 and 15 and  $\beta_t$  numbers between 5 and 160. They produced a control space map, classifying the parameter space into eight flow regimes that were identified within the above mentioned ranges of  $KC_t$  and  $\beta_t$  numbers (see figure 2.18). Each regime was identified based on the two- or three-dimensionality of flow structure and vortex shedding characteristics. Many of these regimes have a spatially periodic pattern, providing the basis of phase-averaging.

The major objective of this part of the study was to quantitatively investigate the structure and dynamics of the flow induced by a circular cylinder performing pure rectilinear sinusoidal oscillations in a fluid initially at rest, *quiescent*, for  $KC_t < 15$  and  $\beta_t < 160$ , the same parameter range as of Tatsuno & Bearman (1990). All of the two- and three-dimensional regimes of the Tatsuno & Bearman (1990) map except regime C (the quasi-periodic regime), were investigated (see §2.5). The nomenclature of Tatsuno & Bearman (1990) for labelling the flow regimes, A\*–G, was used for clarity throughout this thesis (see figure 2.18).

In the next section, the experimental arrangements and apparatus is explained first. The results of flow visualisations which provided qualitative information on the nature of these flow and the resulting wake structures are then presented. In the following sections, the two- and three-dimensional regimes are analysed. Finally, a quantitative comparison between the different regimes is presented.

## 4.2 Experimental Arrangement and Parameters

As described in chapter 3, the technique of high-image-density particle image velocimetry was employed to determine the flow physics. This technique allows quantitative space-time imaging and thereby whole-field representations of the flow structure. For these particular experiments for the flow visualisation and PIV the flow was seeded with spherical polyamide particles with a mean diameter of  $56\mu\text{m}$  and  $11\mu\text{m}$ , respectively, with specific gravity of 1.016. In the PIV system, the particles were illuminated using two miniature Nd:YAG laser sources (Continuum Minilite II Q-Switched). The planes of interest for these experiments were the  $yz$ - and  $xy$ -planes, being the spanwise and streamwise directions, as was shown in figure 3.4. The thickness of the laser sheet was measured to be less than 2mm. Pairs of images were captured on a high resolution CCD camera (Cooke pco4000) with a maximum resolution of  $4008 \times 2672$  pixels. The camera was equipped with two Nikkor (Nikon Corporation, Japan) lenses of focal lengths of 105mm and 200mm. An interrogation window of  $32 \times 32$  (with an initial window size of  $64 \times 64$ ) pixels was found to give satisfactory results with 50% overlap. More than 98% of the vectors were valid for all the experiments. The interrogation window size used for this part of experiments corresponds to an average interrogation window of  $0.156D \times 0.156D$  and  $0.0615D \times 0.0615D$  for 105mm and 200mm lenses, respectively. It was possible to obtain a measurement resolution of  $124 \times 82$  (total of 10168) vectors in each field of view. The overall field of view was  $2000 \times 1336$  pixels ( $9.76D \times 6.52D$  and  $3.84D \times 2.56D$  for the 105mm and 200mm lenses, respectively). All the images were captured at pre-selected phase angles in the oscillation cycle (phase-locked). Phase-averaged vorticity and velocity fields are presented using 30 or more instantaneous measurements unless otherwise mentioned. The vorticity fields were calculated with the technique developed by Fouras & Soria (1998). The velocity and spatial coordinates are non-dimensionalised by the maximum velocity of the translational cylinder motion,  $U_{\max_t}$ , and the cylinder diameter,  $D$ , respectively.

In the following sections the results of seven of the eight regimes of Tatsuno & Bearman (1990) are presented. The points in the  $(KC_t, \beta_t)$ -map were selected on the basis of their being representative of the regimes they lie in. Tables 4.1 and 4.2 show the selected points for the flow visualisation and PIV experiments, respectively.

## 4.3 Flow Visualisation

The flow visualisation undertaken as part of the current study is in agreement with the work of Tatsuno & Bearman (1990). It was undertaken to ensure the experimental apparatus gave results comparable with their flow visualisations. The Tatsuno & Bearman (1990) work was taken as a benchmark for the flow visualisations given its quality and the extensive explorations of the relevant parameter space. This was further confirmed by the excellent agreement with the extensive numerical study of Elston *et al.* (2006). Flow visualisation was also undertaken as a means of examining the dynamics of the flow and focussing the PIV experiments. Based on the method explained in §3.3.3.1, a series of images were taken for all of the regimes listed in table 4.1.

### 4.3.1 Validation

The results of regime D were used for detailed validation but flow visualisation results of the other regimes also matched well with the results of Tatsuno & Bearman (1990). They will be presented and explained in the following sections. Figure 4.1 shows a comparison of the flow around the translationally oscillating cylinder at the same position of the cylinder between the present results and Tatsuno & Bearman (1990) in regime D. The similar vortices and vortex paths, shown by red arrows in figure 4.1, are denoted as vortices A & B, and trail C & D, respectively in the figure. The inset in figure 4.1b shows the direction of movement and the phase at which the images were taken. It is clearly seen from the figure that the location of the flow structures and flow pattern around the cylinder match well with the results of Tatsuno & Bearman (1990). The present flow visualisation technique enabled capturing of the vortex structures of A and B more clearly, even though the exposure time for capturing the images was shorter than that of Tatsuno & Bearman (1990) (figure 4.1b).

### 4.3.2 Results

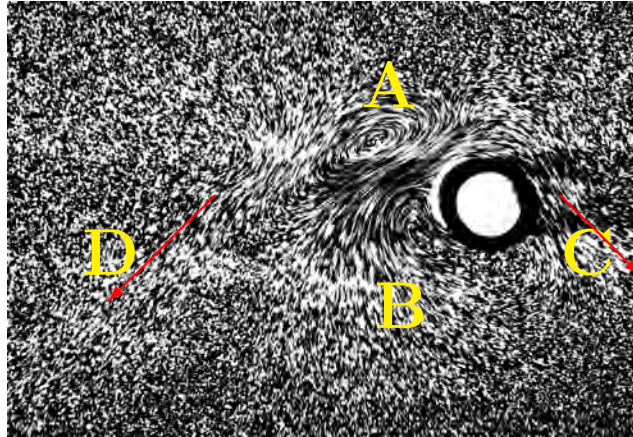
This section presents the results obtained from flow visualisation experiments conducted during the course of research. The results are presented separately for each regime of Tatsuno & Bearman (1990) listed in table 4.1.

Case	Regime	$KC_t$	$\beta_t$	$Re$	$A_t$ (mm)	$f_t$ (Hz)	$U_{\max}$ (mm s <sup>-1</sup> )
1	A*	3	30	90	9.55	0.075	4.50
2	A	5	20	100	16	0.05	5.00
3	B	3	80	240	9.55	0.2	12.00
4	D	6.28	18	113	20	0.045	5.65
5	E	5	80	400	15.92	0.2	20.00
6	F	8.17	30	245	26	0.075	12.25
7	G	9	80	720	28.64	0.2	36.00

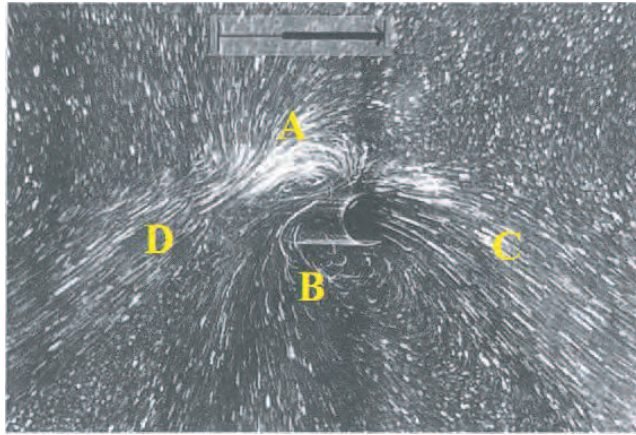
TABLE 4.2: Experimental (PIV) test cases conducted in this chapter. One value of  $KC_t$  and  $\beta_t$  was chosen as a representative of each regime.

#### 4.3.2.1 Case I: Regime A\*, Two-dimensional patterns without vortex shedding and flow separation

Figure 4.2 shows a sequence of instantaneous flow visualisation images and the vortex patterns around a translationally oscillating circular cylinder in regime A\* ( $KC_t=\pi$  and  $\beta_t=53$ ) over a half period of oscillation. The figure shows that the structure of the vortices are symmetrical with respect to the axis of oscillation, shown as arrow in image (a) of figure 4.2. They also show that no vortex shedding occurs for this regime, as there is no evidence of trailing vortices behind the cylinder in the direction of oscillation away from the cylinder. The same trend was observed at even longer exposure times, not shown here. The vortex structures are always attached to the cylinder and, as Tatsuno & Bearman (1990) suggested, do not break away from the boundary layer on the body surface. The two counter-rotating vortices, denoted as vortices A and B in figure 4.2a, which are formed each half cycle do not survive into the next half cycle. As the cylinder is oscillated at low values of  $KC_t$  and  $\beta_t$  and the cylinder is not moving much relative to the size of diameter, once they will be cancelled because of cross-annihilation with opposite-sign vorticity generated at the wall (boundary layer around the body surface), as seen in figures 4.2b and 4.2c. By looking at figure 4.2 it can be seen that as the cylinder moves from left to right, figure 4.2a to figure 4.2h, by approaching the middle of motion two new vortices are generated one at the top and one at the bottom of the cylinder, shown as vortices C and D in figures 4.2c-h. When the cylinder approaches the end of its first half cycle motion, the generated vortices remain attached to the cylinder and are not shed from the top and bottom surfaces of the cylinder. Figures 4.2g and 4.2h clearly show how close the vortices are to the surface of the cylinder. These vortices are the ones which will disappear due to cross-



(a)



(b)

FIGURE 4.1: Comparison of the flow visualisation of the present study with Tatsuno & Bearman (1990), Regime D: (a) Present study:  $KC=8.17$ ,  $\beta=11.11$ , exposure time=1.6 sec; (b) Tatsuno & Bearman (1990):  $KC_t=8.16$ ,  $\beta_t=11.0$ , exposure time=2 sec.

annihilation with the opposite-sign vortices generated at the beginning of the next half cycle, same as vortices A and B shown in figure 4.2a which are from the previous half cycle.

The flow visualisation images also revealed that the flow streams move away from the cylinder along the oscillation axis, figures 4.2c and 4.2d, though only up to  $1D$  behind the cylinder. There are no far-field concentrations of vorticity seen in figure 4.2. This finding is in agreement with the lack of vortex shedding observed by Tatsuno & Bearman (1990) and the numerical results of Elston (2005). Elston (2005) showed that the vorticity contours from his numerical simulations for this regime are all connected back to the near cylinder region and that there are no far-field concentrations of vorticity. On the other hand Tatsuno & Bearman (1990), §2.5, observed a jet of particles moving away from the cylinder along the axis of oscillation. This far-field traces of flow



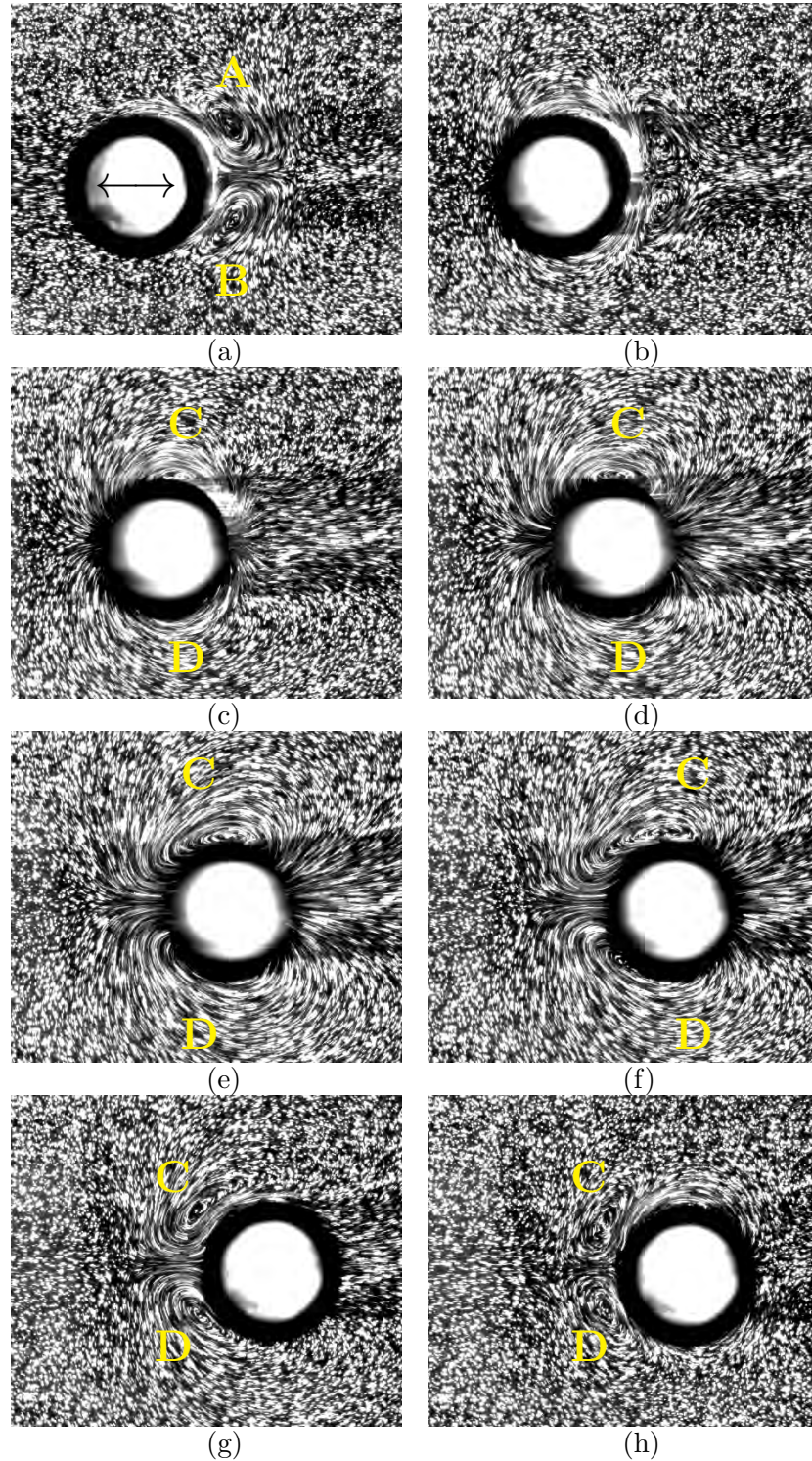


FIGURE 4.2: Plane views of flows at various stages of motion in regime A\* (case 1 in table 4.1) showing flow patterns and structures for over half a cycle: Flow visualisation method,  $A_t = 10$  mm,  $f_t = 0.132$  Hz (equivalent to  $KC_t = \pi$ ,  $\beta_t = 53$ , respectively), exposure time=0.6 sec. (a) is showing the cylinder at its left most position and starting its motion from left to right and (h) is showing the cylinder at the most right end of its motion, the end of first half cycle. The arrow in image (a) shows the direction of oscillation.

were not observed in the present flow visualisation and Elston (2005)'s results. The results of Elston (2005) showed that all the particles remained in the near vicinity of the cylinder, which is also consistent with the present flow visualisations. Figure 4.3, directly reproduced from Elston (2005), shows the numerical particle-track plot of flow for this regime. The image was created by placing ten sources of massless particles equally around the cylinder circumference at a very small distance from the cylinder surface and evolving the flow using two-dimensional DNS. The image clearly shows how all the particles remain in the near vicinity of the cylinder which contrasts with the results of Tatsuno & Bearman (1990) and is in favour with the present study for regime A\*. The reason for the discrepancy observed is not clearly known. It may be because of using dye in Tatsuno & Bearman (1990)'s experiments or the artifact of their experiments. Dye flow visualisations are normally more sensitive than particle flow visualisations. Dyes diffuse further away from the body than particles. It is also true that the particles used are not massless so cannot travel away from the body as dyes can. However, the numerical massless particle visualisations of Elston (2005), see figure 4.3, showed that the particles are not convected away from the body too. The fact that for low  $KC$  and  $Re$  ( $\beta$ ) numbers, the vorticity decaying effect is dominant in the flow field, whereas at higher  $Re$  numbers vorticity convection becomes stronger (Zhang & Zhang 1997) may in addition explain why the streams of flow moving away from the cylinder were not observed experimentally. The spanwise measurements also confirmed the two-dimensionality of the flow in this regime (discussed in §4.4.3). The flow observed by Elston (2005) is symmetrical and two-dimensional which is in agreement with the results of Tatsuno & Bearman (1990). Elston (2005) saw no evidence of three-dimensional spanwise structures in regime A\*. More detailed quantitative measurements of the flow in regime A\* are presented in §4.4.3.

#### **4.3.2.2 Case II: Regime A, Symmetrical patterns with vortex shedding; two-dimensional**

Figure 4.4 shows a sequence of instantaneous flow visualisation images and vortex patterns around a translationally oscillating circular cylinder in regime A over a half period of motion. The other half period is the mirror image of what is shown in the figure. It can be seen that the structure of the vortices, like regime A\* are symmetrical with respect to the axis of oscillation, shown as arrow in image (a) of figure 4.4.

It is clear that two vortices, with rotations of opposite signs, are formed symmetri-

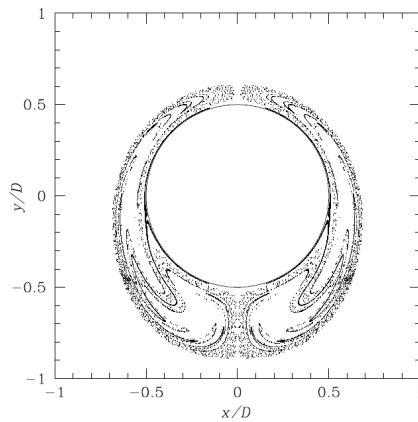


FIGURE 4.3: Numerically generated particle shedding image. Over 15 periods of motion conducted at  $KC_t=2$ ,  $\beta_t=80$ , with two-dimensional DNS, ten equally spaced points on the cylinder surface released massless particles into the surrounding fluid; *the image appeared in Elston (2005) and reproduced by permission.*

cally behind the cylinder in each half cycle (figure 4.4a). At the end of the half cycle the two vortices stay behind the cylinder and as the cylinder reverses it moves through the previously generated vortices (figure 4.4h). It should be noted that these vortices do not survive into the next half cycle and as Tatsuno & Bearman (1990) suggested, based on the delineations of Bearman *et al.* (1981), the vortices may be cancelled by cross-annihilation of the opposite-sign vortices in the cylinder boundary layer. Tatsuno & Bearman (1990) characterised regime A as to having the same vortex generation sequence as regime A\* except the existence of vortex shedding and flow separation in regime A. Tatsuno & Bearman (1990) defined separation as “*breaking away of vortices which moves the vortices away from the body surface*”. Based on this no evidence of vortex shedding was observed in the present flow visualisation results. Figure 4.4 clearly shows that the flow remains attached to the cylinder, it does not move away from the cylinder and so no vortex shedding is observed. This finding is in agreement with the numerical simulations of Elston (2005) and in contrast to the flow visualisations of Tatsuno & Bearman (1990). Tatsuno & Bearman (1990) identified this case,  $KC_t = 8.16$  &  $\beta_t = 8.18$ , as belonging to regime A with its definitive characteristic, in relation to the flows of regime A\*, being the presence of vortex shedding. Elston (2005)’s results suggested that this location in  $(KC_t, \beta_t)$ -map should belong to regime A\*, which appears consistent with the present findings.

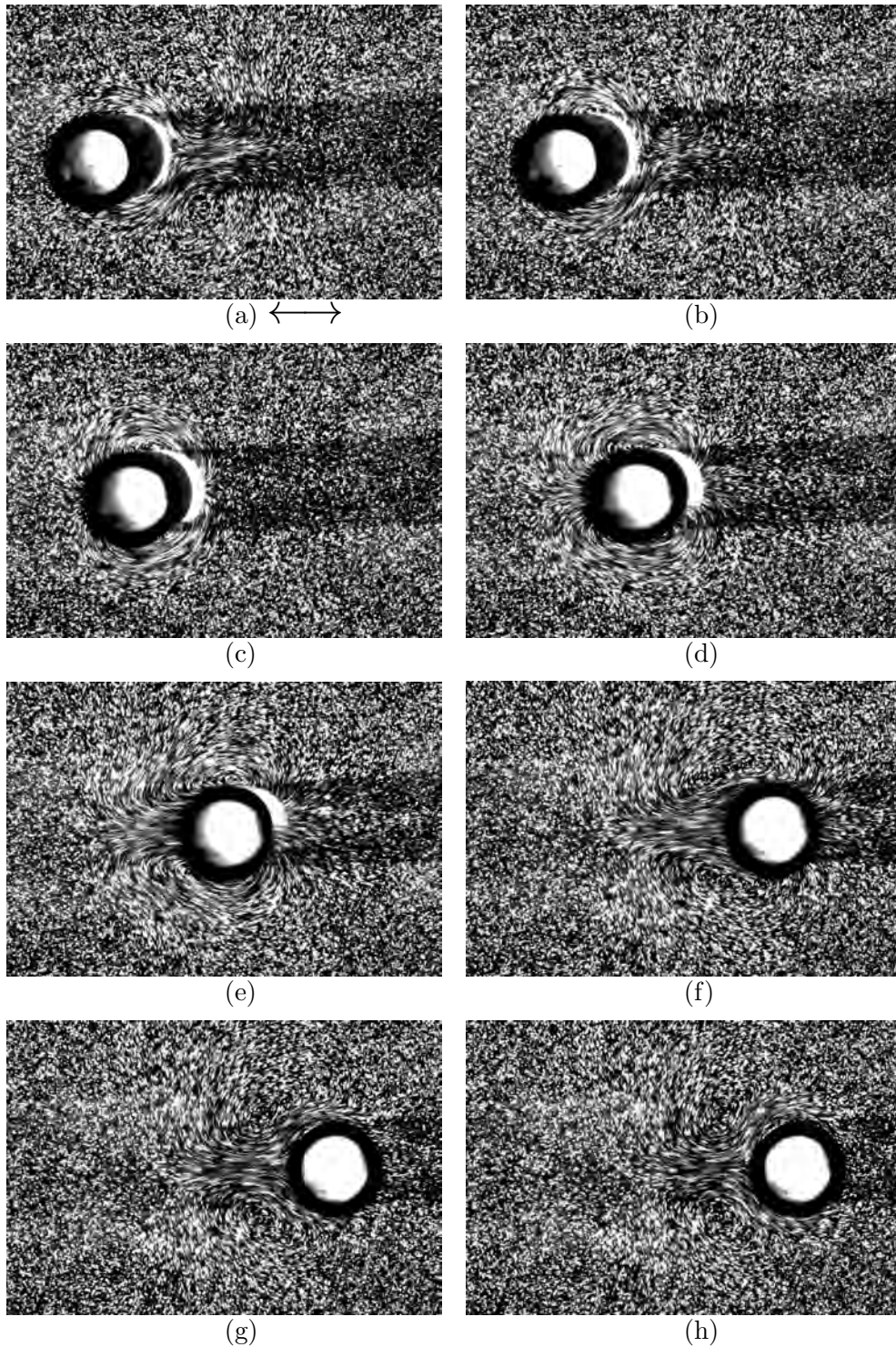


FIGURE 4.4: Plane views of flows at various stages of motion in regime A (case 2 in table 4.1) showing flow patterns and structures for over half a cycle: Flow visualisation method,  $A_t = 26$  mm,  $f_t = 0.02$  Hz (equivalent to  $KC_t = 8.17$ ,  $\beta_t = 8.11$ , respectively), exposure time=1.1 sec. (a) is showing the cylinder at its left most position and starting its motion from left to right and (h) is showing the cylinder at the most right end of its motion, the end of the first half of the cycle. The arrow in image (a) shows the direction of oscillation.

#### 4.3.2.3 Case III: Regime B, Onset of three-dimensional instability; longitudinal vortices

The third case examined is at  $KC_t = \pi$ ,  $\beta = 63.1$ . This point lies in regime B of the Tatsuno & Bearman (1990)  $(KC_t, \beta_t)$ -map. One of the defining characteristics of regime B is the presence of structures which regularly vary along the span of the cylinder. In this respect this case has broken a symmetry property and is no longer considered two-dimensional. In regime B the onset of a regular spanwise variation in the structures visualised was first experimentally observed by Honji (1981) and later by Tatsuno & Bearman (1990).

It should be noted that the present flow visualisation results of regime B appeared different from the results of Tatsuno & Bearman (1990) for this regime. However, the present PIV results, see §4.4.5, clearly showed the three-dimensionality effect. This may be because of the artifact of our experiments for regime B. A comparison between the three regimes of A\*, A and B is also provided in §4.4.5.

#### 4.3.2.4 Case IV: Regime C, Rearrangement of large vortices; three-dimensional

Regime C is a three-dimensional and quasi-periodic regime of very narrow parameter space and as mentioned in §2.5 was not of interest in this thesis. In the interests of completeness the flow visualisation of this regime is shown in figure 4.5. Large vortices are formed in succession for equal numbers of oscillation cycles, however it is unclear how many oscillation cycles are required for the formation of a large vortex. The arrangement of these vortices is similar to that in a Kármán vortex street behind a cylinder in uniform flow. However the sense of rotation of the vortices is opposite to that found in a unidirectional flow wake and the vortices convect themselves away from the oscillating cylinder, *i.e.* jet-like flow.

#### 4.3.2.5 Case V: Regime D, Flow convected obliquely to one side of the axis of oscillation; three-dimensional

Apart from the two-dimensionality and symmetry of flow with respect to the axis of oscillation in regimes A\*, A and to some extent B, the flow characteristics will change as  $KC_t$  increases at relatively lower  $\beta_t$ . According to the argument of Tatsuno & Bearman (1990), and based on the present flow visualisations, the flow characteristics in regime D change dramatically compared to those of regimes A\*–C. In this regime the induced flow is no longer convected along the axis of oscillation, as it did for

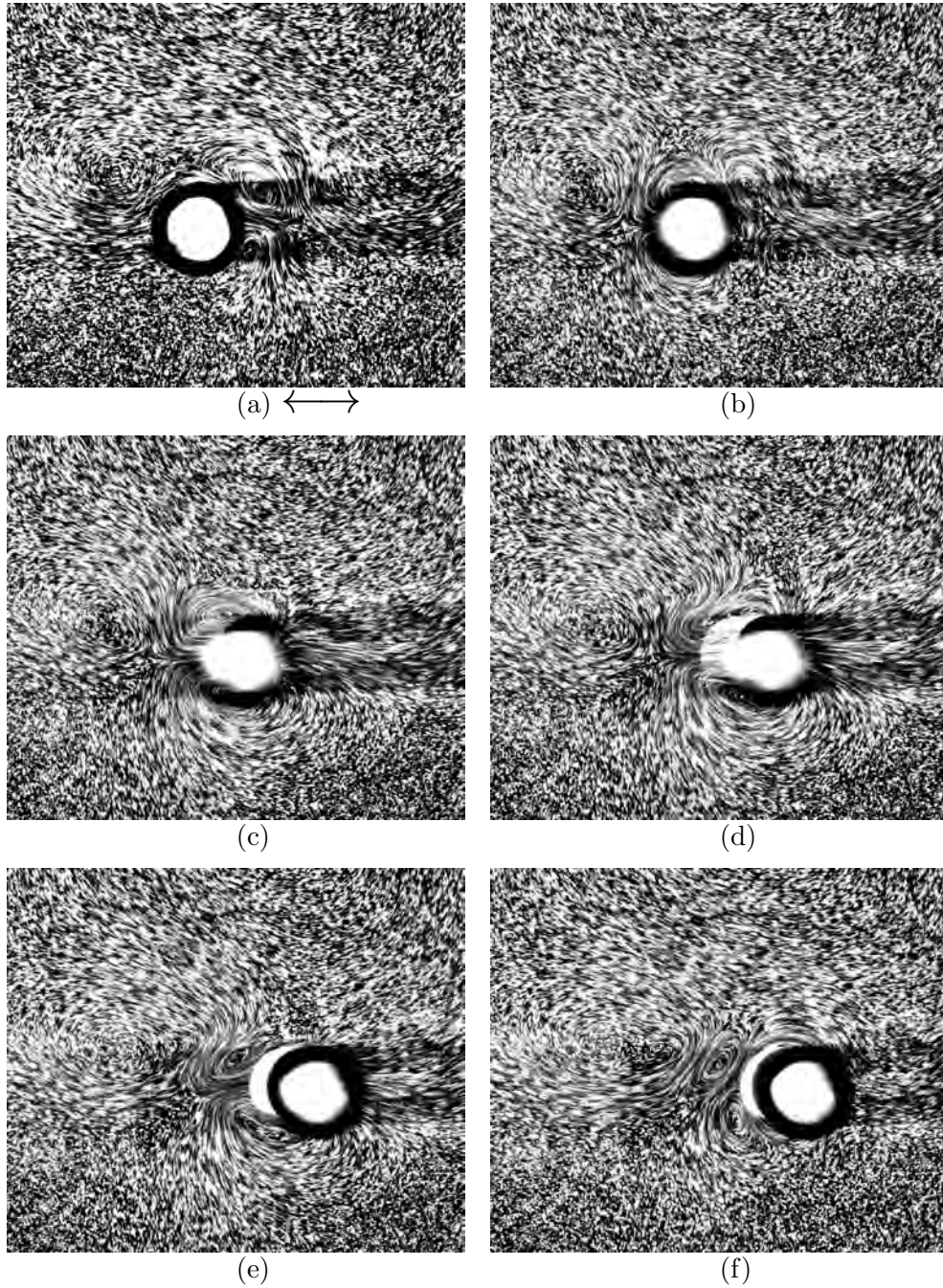


FIGURE 4.5: Plane views of flows at various stages of motion in regime C (case 4 in table 4.1) showing flow patterns and structures for over half a cycle: Flow visualisation method,  $A_t = 14$  mm,  $f_t = 0.11$  Hz (equivalent to  $KC_t = 4.40$ ,  $\beta_t = 44.44$ , respectively), exposure time=1.0 sec. (a) is showing the cylinder at its left most position and starting its motion from left to right and (e) is showing the cylinder at the most right end of its motion, the end of first half cycle. The arrow in image (a) shows the direction of oscillation.

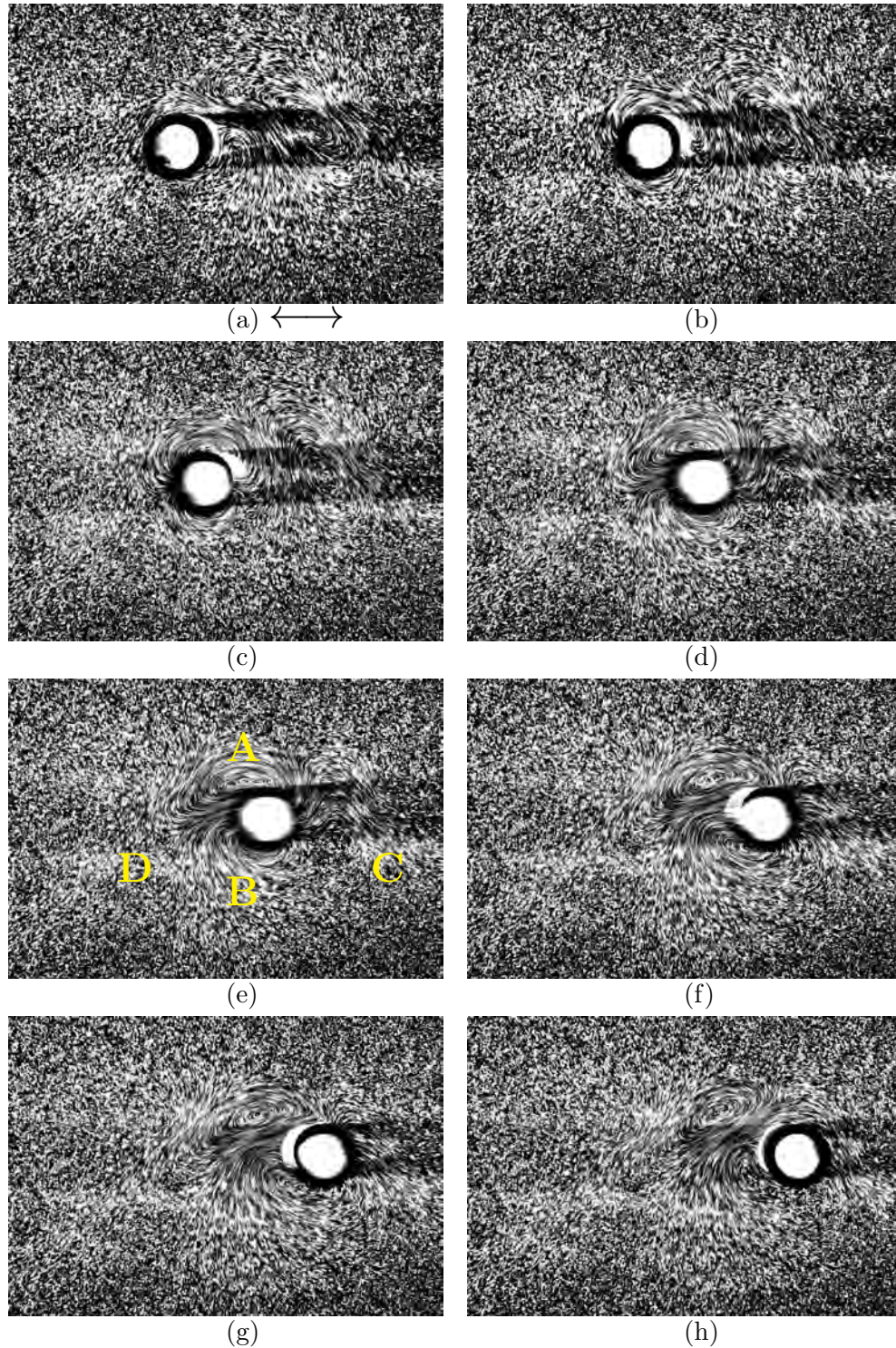


FIGURE 4.6: Plane views of flows at various stages of motion in regime D (case 5 in table 4.1) showing flow patterns and structures for over half a cycle: Flow visualisation method,  $A_t = 26$  mm,  $f_t = 0.0275$  Hz (equivalent to  $KC_t = 8.17$ ,  $\beta_t = 11$ , respectively), exposure time=1.6 sec. (a) is showing the cylinder at its left most position and starting its motion from left to right and (h) is showing the cylinder at the most right end of its motion, the end of first half cycle. The arrow in image (a) shows the direction of oscillation.

regimes A\*-C. As  $KC_t$  increases some asymmetry appears in the vortex development and induced flows are now convected at an angle to the axis of oscillation. At higher  $KC_t$ , than those for which two-dimensional flow regimes are found, an asymmetry develops in the direction of flow convection around the cylinder. Regime D is the onset of this symmetry breaking in a sense that the flow will not convect along the direction of cylinder oscillation anymore. This feature was attributed to an asymmetry in the development of a vortex pair in each half-cycle. It should be noted that while the resultant flow breaks symmetry about the axis of oscillation, it was observed that the time-periodic symmetry about the vertical axis,  $x$ -axis, was retained, *i.e.* the flow was still synchronous with the cylinder oscillation (Elston 2005, and §4.4.6). The flow along the span of the cylinder is now three-dimensional and, as noted by Tatsuno & Bearman (1990), regular “tubes” form along the span of the cylinder (see figure 2.20). In these tubes the fluid was observed by Tatsuno & Bearman (1990) to be travelling faster than the surrounding fluid. The spanwise spacing between the tubes was found to be independent of  $KC_t$  and only weakly to decrease with increasing  $\beta_t$ .

Figure 4.6 shows a sequence of instantaneous flow visualisation images and the vortex patterns around a translationally oscillating circular cylinder in regime D over a half period of motion. Generally speaking, in regime D, asymmetrical vortices, with opposite sense of rotation, are formed on the top and bottom sides of the cylinder when the cylinder translates from left to right. In this case, the negative (clockwise) vortex is developed on the lower side of the cylinder, vortex B in figure 4.6e, whereas the positive (counter-clockwise) vortex on the upper side, vortex A in figure 4.6e. The vortices formed during previous cycles are convected towards the streamwise direction as paths of vortices denoted as C and D in figure 4.6e. During the visualisation experiments it was observed that vortex A, on the upper side of the cylinder, appears to grow stronger than vortex B. As described by Tatsuno & Bearman (1990), Iliadis & Anagnostopoulos (1998) and Elston (2005), this clockwise rotating vortex in the upper part of the cylinder appears in elongated form compared with that formed at the lower side and is tilted downwards. It is seen from figures 4.6a and 4.6b that the positive vortex formed during the previous half-cycle below the cylinder starts to split into two parts, a process leading to the formation of two equal sign vortices in subsequent images. The negative vortex formed during the previous half-cycle above the cylinder is swept downstream and pairs up with the opposite-signed vortex forming above the cylinder.



In addition, two relatively parallel rows of opposite sign vortices exist on both sides of the cylinder, inclined to the horizontal. The strength of these vortices decreases with increasing distance from the cylinder by almost one order of magnitude within one diameter from the cylinder, as is shown in §4.4.6. When the cylinder reaches its zero velocity position at the rightmost part of the cycle, the negative sign vortex has moved further downstream, while the positive vortex forming above the cylinder appears in elongated form with respect to the vortex forming below the cylinder, as shown in figure 4.6h. It was also observed by Tatsuno & Bearman (1990) that as the value of  $\beta_t$  is increased the flow becomes more curved.

When the cylinder reaches at the rightmost part of its cycle, figure 4.6h, the elongated positive vortex core, from previous snapshots, has already commenced convecting downstream. The motion of the cylinder prior to this snapshot has drawn this positive vortex core downstream and in the negative  $y$ -direction, such that it is now directly behind the cylinder. The negative vortex core, shed from lower surface of the cylinder, is stretched around the small positive vortex core created adjacent to the body in the lower half, and the body. A jet of fluid can be seen to be formed between the two vortex cores. The jet travels both in the upstream and negative  $y$ -direction.

As the cylinder reverses, the vortices shed during the previous half-cycle are swept back towards the cylinder. Also, though not shown in the sequence of frames in figure 4.6, the stronger vortex is convected back along the cylinder surface and shed obliquely across the axis of oscillation. Hence, the direction of the flow induced by the cylinder oscillation deviates from the direction of oscillation. In consequence, a strong vortex is developed on only one side of the axis of oscillation in each half cycle and the fluid mass accompanying the vortex is convected obliquely to the other side of the axis of oscillation, as also discussed by Tatsuno & Bearman (1990). By starting the cylinder's motion from right to left, the negative vortex structure mentioned earlier (vortex B) wraps around the small positive vortex core and the cylinder, moving towards the upper side of the cylinder. This negative vortex starts strengthening significantly, due to the solid surface interaction. It is also clear from the sequence of images in figure 4.6 that one vortex is shed during each half-cycle. Examining the visualisations over a large number of oscillation cycles, and also from further measurements by PIV (discussed in §4.4.6), revealed that the vortices are phase-locked to the motion of the cylinder. This periodicity enabled phase-averaging when taking PIV data. This

phase-lock phenomenon was also mentioned by Iliadis & Anagnostopoulos (1998).

It is also noted that, depending on small disturbances in the fluid prior to the beginning of the motion, the flow was convected to either side of the cylinder. Once the motion started and the flow deflected it remained on that side and never changed its direction to the other side of the cylinder.

#### **4.3.2.6 Case VI: Regime E, Irregular switching of flow convection direction; three-dimensional**

Figure 4.7 shows a sequence of instantaneous and temporarily stable flow visualisation images around a translationally oscillating circular cylinder in regime E over a half period of motion. The flow pattern of this regime resembles that in regime D, §4.3.2.5, with the flow being convected to one side of the axis of oscillation and forming a V-shape vortex streets pattern around the cylinder. In the flow visualisations of Tatsuno & Bearman (1990) it was observed that the direction of convection of the flow intermittently changed between the  $+x$  and  $-x$  side of the cylinder. Tatsuno & Bearman (1990) noted that this switching of the flow is likely to be triggered by small disturbances. As discussed in §2.5, Dütsch *et al.* (1998) and Iliadis & Anagnostopoulos (1998) were not able to confirm the change in convection of the flow from one side to the other side of the cylinder. This may be due to two-dimensional nature of their numerical studies. The present experiments confirmed that the flow does irregularly switches from one side to the other side of the cylinder. The results of change of direction of the convected flow is discussed in §4.4.7 in more detail. Figure 4.7 is for one instance of the flow and hence does not show the change of direction.

Moreover, results of Tatsuno & Bearman (1990) revealed that this flow regime has significant three-dimensional structures along the span, see figures 2.18, 2.19 and 2.20, although no periodic wavelength could be established. The structures that were present were found to be obscured by the switching of the flow convection direction (Tatsuno & Bearman 1990). Further discussion about this regime and the observation of switching of the flow is presented in §4.4.7.

#### **4.3.2.7 Case VII: Regime F Flow convected diagonally; three-dimensional**

Regime F is defined as a double-pair diagonal regime, in which vorticity is shed diagonally with respect to the axis of oscillation (Tatsuno & Bearman 1990). The mechanism of vortex shedding has been described in detail by several authors (see for example Tat-

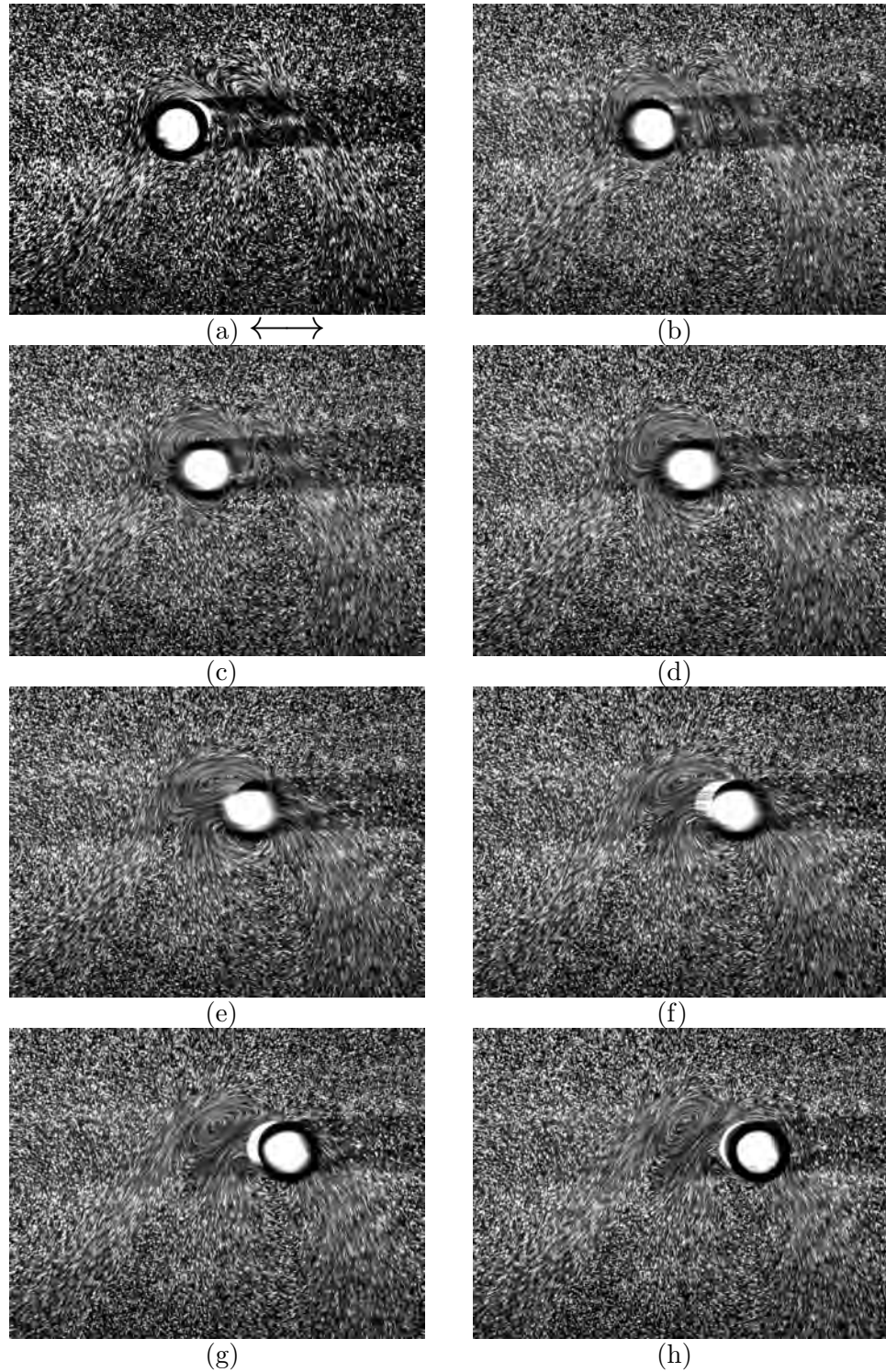


FIGURE 4.7: Plane views of flows at various stages of motion in regime E (case 6 in table 4.1) showing flow patterns and structures for over half a cycle: Flow visualisation method,  $A_t = 20$  mm,  $f_t = 0.0655$  Hz (equivalent to  $KC_t = 2\pi$ ,  $\beta_t = 26.23$ , respectively), exposure time=1.0 sec. (a) is showing the cylinder at its left most position and starting its motion from left to right and (h) is showing the cylinder at the most right end of its motion, the end of first half cycle. The arrow in image (a) shows the direction of oscillation.

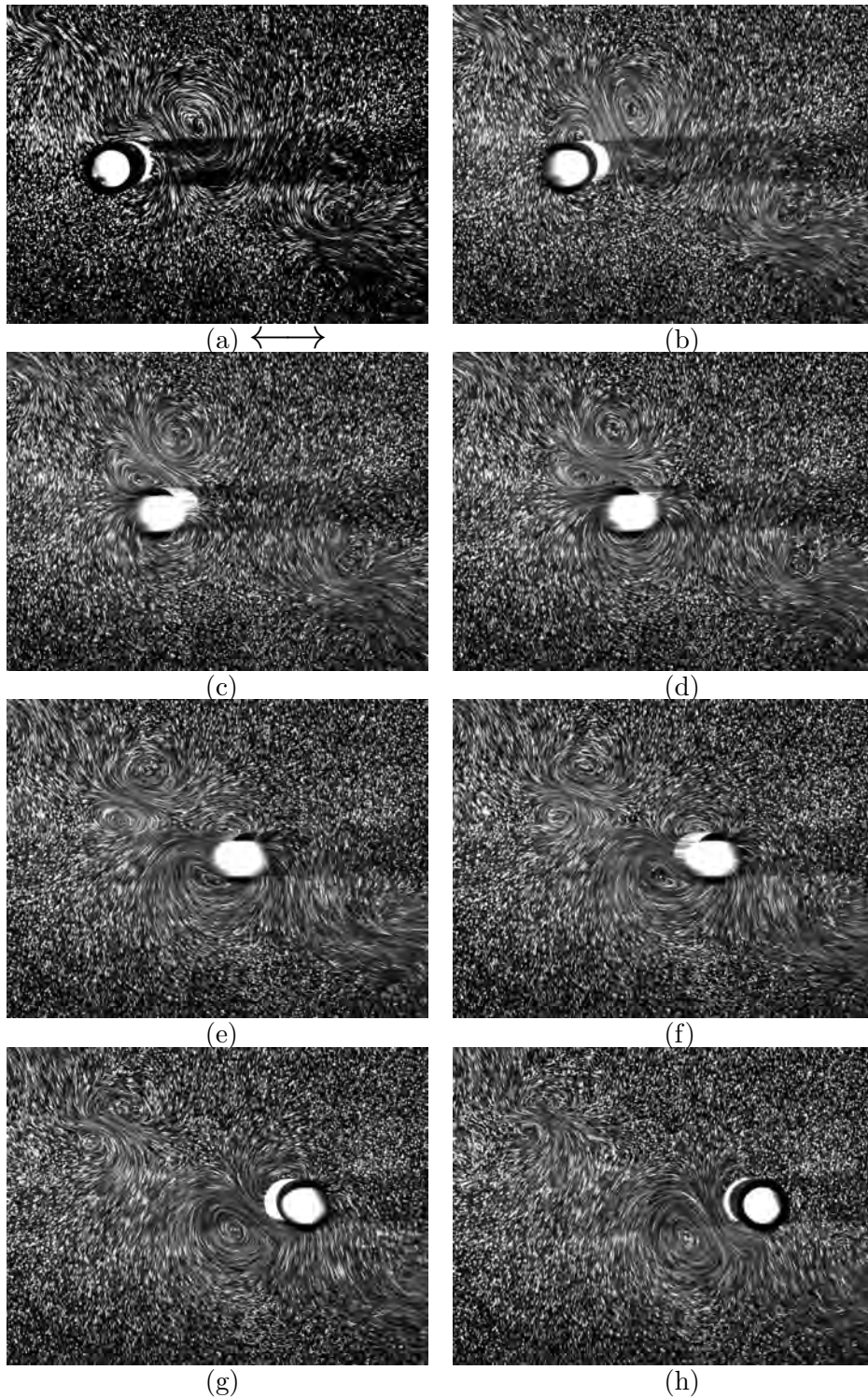


FIGURE 4.8: Plane views of flows at various stages of motion in regime F (case 7 in table 4.1) showing flow patterns and structures for over half a cycle: Flow visualisation method,  $A_t = 40$  mm,  $f_t = 0.454$  Hz (equivalent to  $KC_t = 12.57$ ,  $\beta_t = 18.16$ , respectively), exposure time=1.0 sec. (a) shows the cylinder at its left most position and starting its motion from left to right and (h) is showing the cylinder at the most right end of its motion, the end of first half cycle. The arrow in image (a) shows the direction of oscillation.

suno & Bearman 1990; Dütsch *et al.* 1998; Iliadis & Anagnostopoulos 1998; Elston *et al.* 2006), as discussed in §2.5. Figure 4.8 shows a sequence of instantaneous and temporarily stable flow patterns of flow visualisation images around a translationally oscillating circular cylinder in regime F over a half period of motion.

When the cylinder starts its motion from rest, symmetric vortex shedding occurred first in roughly the same way as described in §4.3.2.2. However, after a few cycles of oscillation, the symmetric flow pattern ceased to exist. The symmetric vortex formation became unstable, resulting in the occurrence of a stronger vortex on one side of the cylinder and a weaker one on the other. Both vortices that were formed did not cross this axis, but moved away from it.

Two related features of the shedding wake distinguish the flow past an oscillating cylinder in regime F. First, the wake sheds at an angle to the flow. Second, the fluid structures are shed in vortex pairs. These structures induce a jet of fluid to travel in the positive  $y$ -direction when the cylinder is moving from left to right and in the reverse of this when moving from right to left. This induces the angle at which the wake is shed. The motion of the cylinder is responsible for inducing the vortex pairing, as is clearly reflected in figure 4.8 and in more detail in §4.4.8

In the present investigation, similar to other investigations mentioned above, it was observed that two vortex pairs are shed during each oscillation cycle. It was also seen that a single vortex, in this particular configuration, with positive sign is also shed in the same direction as that of the pairs in each half cycle, but with much less concentration. Examination of Elston (2005)'s numerical results reveals that the single vortex shed from the cylinder can also be identified and it is clearly present (figure 4.9). This has not been discussed by other researchers including Elston (2005) so far. However, it can clearly be observed in the flow visualisations shown here. Figure 4.9 shows the instantaneous vorticity contours for two-dimensional flow in regime F shown at  $y = y_{max}$  at two different locations in the regime F of the Tatsuno & Bearman (1990)  $(KC_t, \beta_t)$ -map from the two-dimensional numerical simulation of Elston (2005). In the figure arrows show the above mentioned single vortex. Tatsuno & Bearman (1990) mentioned that the convection of vortices away from the body at large angles to the oscillation direction seems to be similar to the formation of two vortex pairs per cycle at larger  $\beta_t$ , which has been described as the  $2P$  pattern by Williamson (1985). It is proposed from the present study that this regime could be characterised as the  $2P + 2S$

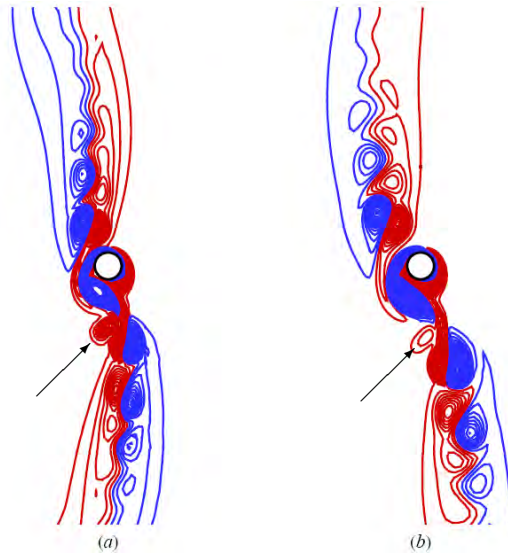


FIGURE 4.9: Instantaneous vorticity contours for two-dimensional flow in regime F shown at  $y = y_{max}$ . The flows were computed at: **(a)**  $KC_t = 8$ ,  $\beta_t = 25.0$ ; and **(b)**  $KC_t = 10$ ,  $\beta_t = 20.0$ . The arrows in the figure shows the single vortex shed per cycle. *The image appeared in Elston (2005) and reproduced by permission.*

pattern using the same shedding nomenclature, introduced in §2.3.1.2, as described by Williamson (1985). Further information on this regime is presented in §4.4.8.

#### 4.3.2.8 Case VIII: Regime G, Transverse vortex street; three-dimensional

In this regime the majority of the vortex activity leading to vortex shedding occurs either above or below the cylinder. Figure 4.10 shows a sequence of instantaneous and temporarily stable flow patterns of flow visualisation images around a translationally oscillating circular cylinder in regime G over a half period of motion. Two vortices are formed per half cycle; when the cylinder moves from right to left one vortex is attached to the cylinder and the other seems to have just been shed from the cylinder. This vortex, with a counter-clockwise rotation, is shed downwards halfway through a cycle. In the next half cycle from left to right, a clockwise vortex is shed downwards. As such a process is repeated, a circulatory streaming is generated.

As Tatsuno & Bearman (1990) suggested, this regime appears to be similar to the transverse vortex street observed by Bearman *et al.* (1981) and Williamson (1985) at higher values of  $\beta_t$ . By increasing  $KC_t$  or  $\beta_t$ , turbulent motion appears and the direction of flow may change intermittently. They also suggested that the flow may have a three-dimensional structure, but this structure is not regular along the cylinder axis. This was not seen in the present flow visualisation results shown in figure 4.10.

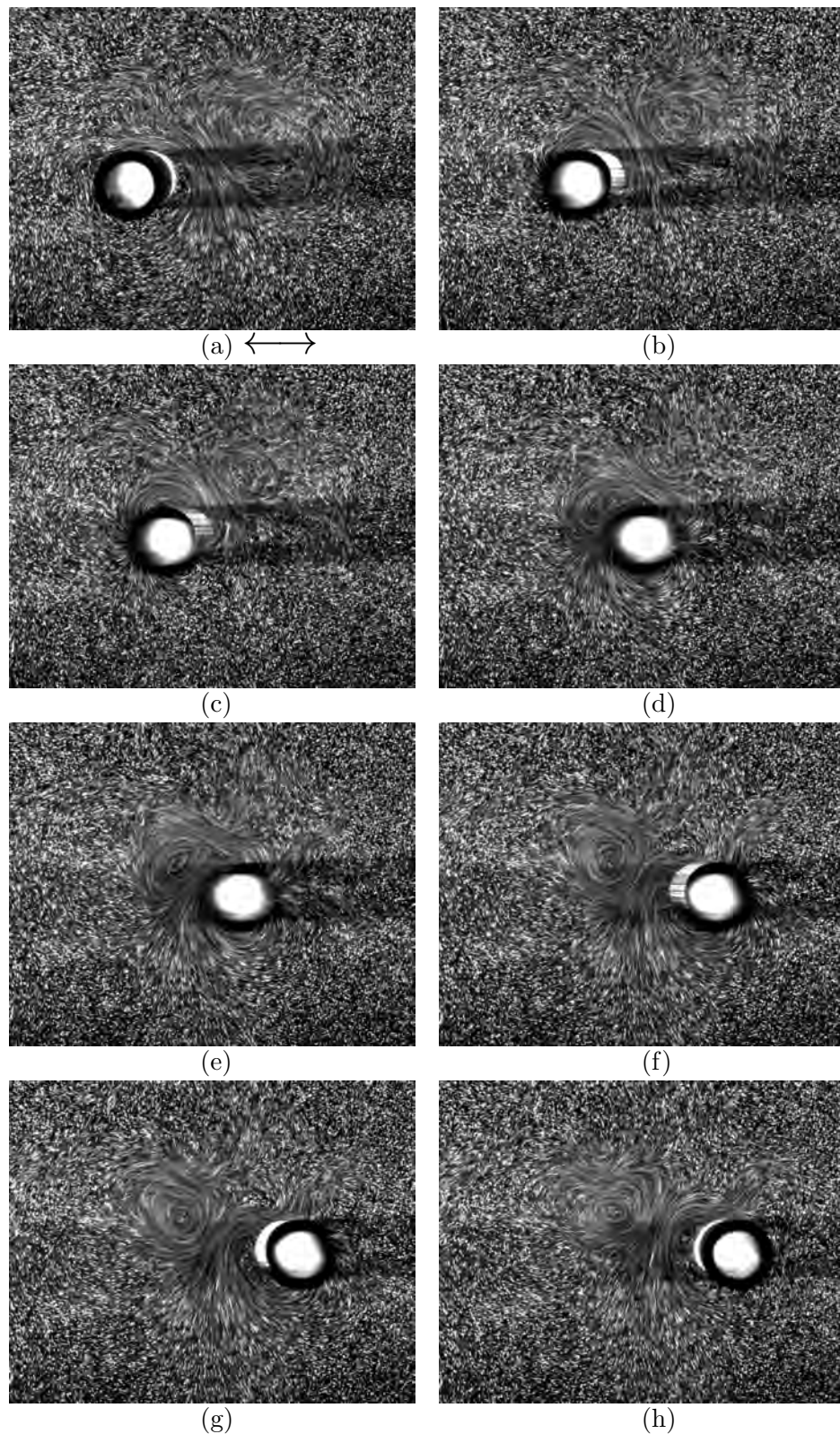


FIGURE 4.10: Plane views of flows at various stages of motion in regime G (case 8 in table 4.1) showing flow patterns and structures for over half a cycle: Flow visualisation method,  $A_t = 26.25$  mm,  $f_t = 0.967$  Hz (equivalent to  $KC_t = 8.25$ ,  $\beta_t = 38.68$ , respectively), exposure time=0.5 sec. (a) is showing the cylinder at its left most position and starting its motion from left to right and (h) is showing the cylinder at the most right end of its motion, the end of first half cycle. The arrow in image (a) shows the direction of oscillation.

## 4.4 PIV results

This section presents the results obtained from PIV experiments conducted during the course of research. The results are presented separately for each regime of Tatsuno & Bearman (1990) listed in table 4.2. First validation of the PIV set-up and apparatus is presented. The next section explains briefly the mechanisms of vortex generation and decay based on the arguments of Morton (1984) and Reynolds & Carr (1985). This arguments are used from this point onwards. The following sections are followed by detailed results of each of the regimes mentioned above.

### 4.4.1 Validation

This section compares the PIV results of the present thesis with the previous experimental and numerical results of other researchers in the literature (for example Dütsch *et al.* 1998; Tatsuno & Bearman 1990) for  $xy$ - and  $yz$ -plane measurements. The validation case studied is for a purely translational oscillation of the cylinder in a quiescent fluid. Other researchers such as Uzunoglu *et al.* (2001), Guilmineau & Queutey (2002) and Nehari *et al.* (2004) also used the numerical and experimental results of Dütsch *et al.* (1998) to validate their numerical codes. Dütsch *et al.* (1998) was found to be the main article available in the literature containing quantitative experimental results at low  $KC_t$  and  $\beta_t$  numbers.

Initially, the experimental results were validated qualitatively against the available results in the literature. This was done to ensure, as was done for the flow visualisations in §4.3, that the results are similar to those expected and also to confirm the flow patterns. Figure 4.11 shows the qualitative comparison between the present study and that of Iliadis & Anagnostopoulos (1998) for dimensionless vorticity contours at two different phase angles, at each end of the oscillation cycle. Figure 4.11a is a phase-averaged vorticity contour at the same two phases of the cycle from the results of Iliadis & Anagnostopoulos (1998). The location of the vortex concentration cores and the flow pattern around the cylinder is seen to be in an excellent agreement. The direction of movement of the cylinder is from left to right and right to left for positions  $t = 0$  and  $t = 4T/8$ , respectively. The positive values of the vorticity contours are shown as full lines and the negative values as broken lines in the figure.

To further validate our PIV set-up and increase confidence in our experimental results, the data were processed to yield local phase-averaged information on two velocity



components, the streamwise ( $U$ ) and transverse ( $V$ ) velocities. These were compared with measurements taken by Dütsch *et al.* (1998). Figure 4.12 demonstrates the excellent agreement between the experimental results of Dütsch *et al.* (1998), the present experimental measurements and our numerical study conducted for this purpose, which further confirms the accuracy of our experimental apparatus and PIV set-up. The numerical computational method is described in §5.4. The comparisons were performed at different cross-sections in the flow measured from the centre of the cylinder, *i.e.*  $y/D = -0.6, 0.0, 0.6$  and  $1.2$ .

The flow in the spanwise direction,  $z$ -direction, of the cylinder was also validated with the measurements of Tatsuno & Bearman (1990) to make sure the experimental apparatus is capable of capturing the three-dimensional structures along the span of the cylinder irrespective of whether the regime was three-dimensional or not. Regime B was chosen, as the onset of three-dimensionality and breaking the symmetry, to validate the results. Figure 4.13, reproduced from Tatsuno & Bearman (1990), shows the distance between two streaked flows along one side of the cylinder in regime B for different  $KC_t$  numbers. The vertical axis shows the wavelength along the  $z$ -axis. The point selected to conduct the experiments was  $KC_t = 2.51$  and  $\beta_t = 142$  ( $Re_t = 356$ ). Tatsuno & Bearman (1990) using flow visualisation techniques measured the wavelength to be  $\lambda = 1.0D$ , whereas it was found from our measurements the wavelength to be  $\lambda = 1.04D$ . This was found to be within 4% of the previously reported value. Tatsuno & Bearman (1990)'s results for various  $\beta_t$  and  $KC_t$  is depicted in figure 4.13. The measurements have been conducted for more than 300 oscillation cycles. The wavelength extraction method from velocity and vorticity fields along the span of the cylinder is described in detail in §5.5.

In the following sections, results from seven of the eight investigated regimes of Tatsuno & Bearman (1990) are presented. The data points selected are representative of each of the Tatsuno & Bearman (1990)'s regimes except regime C (refer to table 4.2).

#### 4.4.2 Generation and decay of vorticity

During the past few years, researchers like Morton (1984) and Reynolds & Carr (1985) tried to either physically or analytically investigate the generation and decay of vorticity. As Morton (1984) has expressed vorticity, although not the primary variable of fluid dynamics, is an important derived variable playing both mathematical and physical

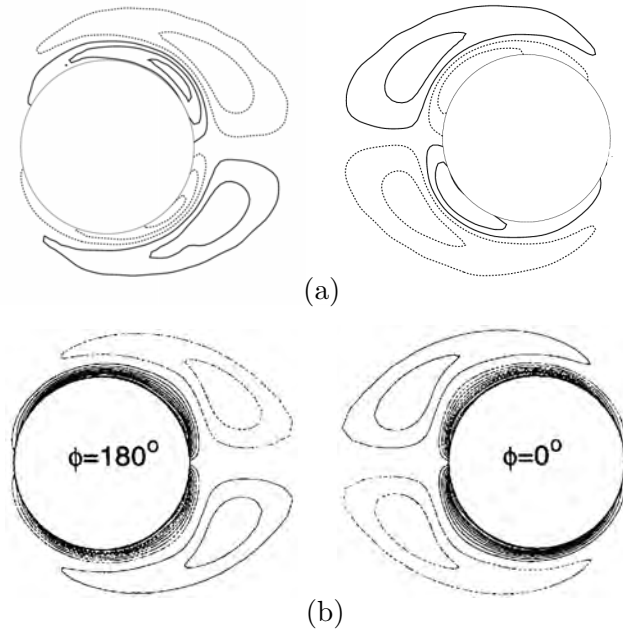


FIGURE 4.11: Comparison of the present PIV results with numerical results of Iliadis & Anagnostopoulos (1998) in regime A\*. The full lines represent positive (counter-clockwise) and the broken lines negative (clockwise) values of vorticity. (a) Present study,  $KC_t = 3$  &  $\beta_t = 30$ ; (b) Iliadis & Anagnostopoulos (1998)'s study,  $KC_t = 2$  &  $\beta_t = 100$ .

roles in the solution and understanding of fluid mechanics problems. Morton (1984) showed the rate of generation of vorticity to be the relative tangential acceleration of fluid and boundary without taking viscosity into account and the generating mechanism therefore involves the tangential pressure gradient within the fluid and the external acceleration of the boundary only. The mechanism is inviscid in nature and independent of the no-slip condition at the boundary, although viscous diffusion acts immediately after generation to spread vorticity outward from boundaries. He also showed that the vorticity diffuses neither out of boundaries nor into them, and the only means of decay is by cross-diffusive annihilation within the fluid. Morton (1984) classified the vortex generation mechanism from oscillating plates to be slow. He also identified in detail a number of properties that must be taken into account in developing any comprehensive treatment of the generation and decay of vorticity. Even though the detailed discussion can be seen in Morton (1984), it is worthwhile summarising and highlighting the important and more relevant ones to the present study as follows:

- *generation results from tangential acceleration of a boundary, from tangential initiation of boundary motion and from tangential pressure gradients acting along a boundary;*

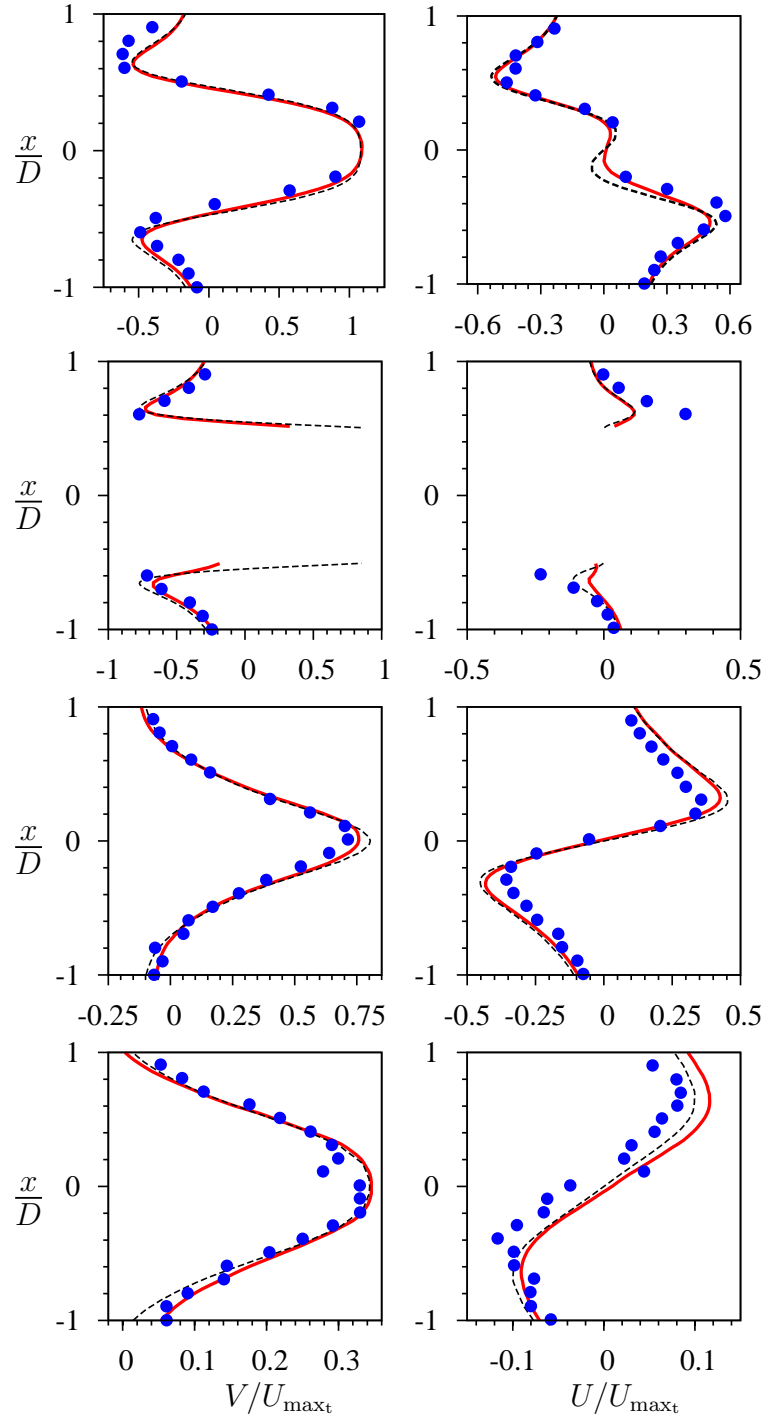


FIGURE 4.12: Comparison of the velocity components at three cross-sections of the translationally oscillating cylinder in a quiescent fluid at constant  $y/D$  values. The  $y/D$  values from the top to bottom rows are  $-0.6$ ,  $0.0$ ,  $0.6$  and  $1.2$ , respectively. The measurements are taken at  $KC_t = 5$  and  $\beta_t = 20$ , similar to previous numerical and experimental results (Dütsch *et al.* 1998). This places the flow generated from the cylinder in two-dimensional regime A (see figure 2.18). The left column depicts the  $V/U_{\max_t}$  and the right column  $U/U_{\max_t}$ . The solid lines (red) show the present experiment, the dashed lines (black) the present numerical simulation and the filled circle points (blue) the experimental results of Dütsch *et al.* (1998).

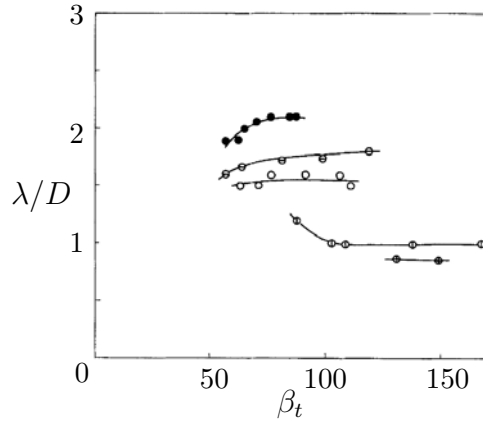


FIGURE 4.13: Distance between the two streaked flows on one side of a cylinder in regime B (wavelength,  $\lambda/D$ ).  $\bullet$ ,  $KC_t=3.77$ ;  $\ominus$ ,  $KC_t=3.35$ ;  $\circ$ ,  $KC_t=3.14$ ;  $\oplus$ ,  $KC_t=2.51$ ;  $\oplus$ ,  $KC_t=2.09$ ; the image appeared in Tatsuno & Bearman (1990) and is reproduced by permission.

- *generation is instantaneous;*
- *vorticity once generated cannot subsequently be lost by diffusion to boundaries;*
- *wall stress relates to the presence of vorticity but is not a cause of its generation;*
- *the generation process is independent of the prior presence of vorticity;*
- *walls play no direct role in the decay or loss of vorticity;*
- *vorticity decay results from cross-diffusion of two fluxes of opposite sense and takes place in the fluid interior; i.e. vorticity is not lost by diffusion to boundaries other than in circumstances in which vorticity of counter-sign is being generated and suffering immediate cross-diffusive annihilation with pre-existing vorticity.*

In the following results sections/chapters the above mentioned properties will be used to explain and interpret the experimental results of this thesis.

#### 4.4.3 Regime A\*

The comprehensive flow visualisations of Tatsuno & Bearman (1990) revealed that no vortex shedding occurred in regime A\*. They also observed that large regions of contra-rotating crescent-like flow structures, *i.e.* streaming flow, are formed on both sides of the cylinder, whereas in this research due to the small field of view of the camera in the two-dimensional cases, *i.e.* regimes A\*, A and B, the areas far around the cylinder were not observed. Uzunoglu *et al.* (2001) and other researchers (see for example Lam

& Dai 2002; Elston 2005) observed the same vortex pattern for this two-dimensional and symmetrical regime.

Figures 4.14, 4.15, 4.16, 4.17 and 4.18 show a cross-sectional view and sequence of phase-averaged PIV results of out-of-plane vorticity ( $\omega_z^*$ ),  $V/U_{\max}$  and  $U/U_{\max}$  velocity contours and velocity vector fields extracted over one motion period,  $T$ , in regime A\*. These figures focus on the region near the surface of the cylinder. Furthermore, it should be noted that the image sequence over one cycle of the cylinder oscillation extends from image (a),  $t = 0$ , of each figure to image (h),  $t = 7T/8$ . The same sequence is used throughout this chapter. This helps to clearly see and compare the mirror image of each phase. The images in figure 4.14 indicate the formation of positive (counter-clockwise) and negative (clockwise) concentrations of vorticity around the surface of the cylinder. It is clearly seen from the results of dimensionless vorticity contours,  $\omega_z^*$ , that the flow around the cylinder during one cycle is symmetrical with respect to the axis of oscillation,  $y$ -axis. The instantaneous, dimensionless spanwise velocity vector field along the vertical axis of the cylinder after about 50 cycles is shown in figure 4.19. The figure reveals the two-dimensionality of the flow along the cylinder vertical axis. This verifies the results of Elston (2005) which showed no variation along the span in regimes A\* as well as A. Apart from the secondary streaming, the main characteristics of this regime discussed by Tatsuno & Bearman (1990) were all observed in this research, *i.e.* no flow separation; two-dimensionality; no vortex shedding (see figures 4.14 to 4.19).

By looking at the concentrations of vortices generated in each oscillation cycle, it can be seen that the vortices remain in the vicinity of the surface of the cylinder. They are not shed, in the sense of being separated from the cylinder and moving away from it. They do not survive to their next half cycle. Compared with the results of the other 2D regime, *i.e.* regime A (see §4.4.4), it can be seen that the vortices generated in each half cycle, *i.e.* vortices C and D in image (a), are not separated from the surface. They are just elongated in the opposite direction to the cylinder's motion, as the cylinder continues its motion to the right and accelerates toward the other end of the motion. This clearly shows that, based on the above argument, there is no vortex shedding in regime A\*.

From images (a) to (h) of figure 4.14, previously created concentrations of vorticity, arising during the preceding oscillation cycle, are evident; they are designated as A' and B' in images (a) to (c), and vanish as the cylinder reaches to the mid-point of its

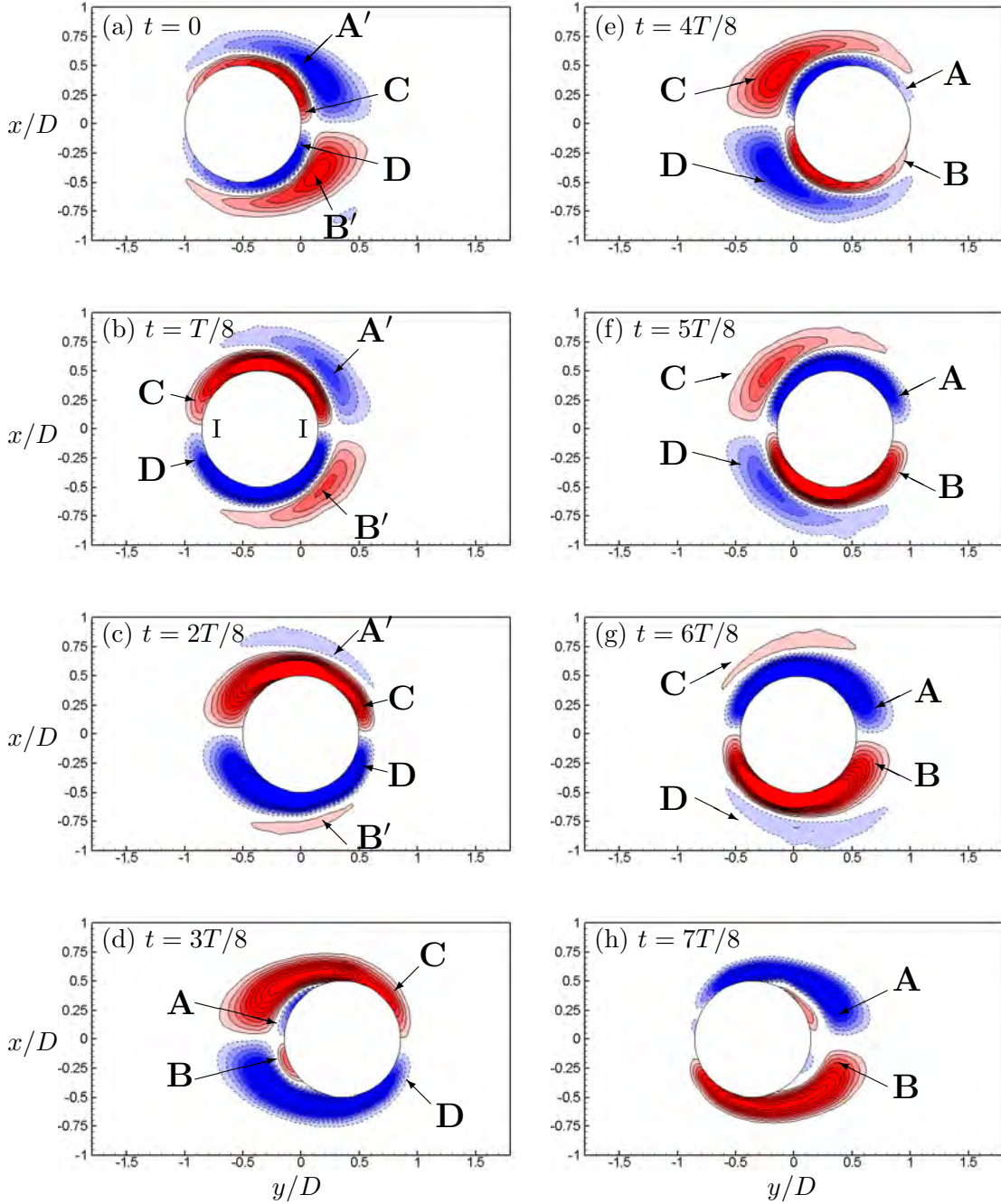


FIGURE 4.14: A sequence of phase-averaged non-dimensionalised out-of-plane vorticity contours,  $\omega_z^*$ , extracted over one motion period,  $T$ , at  $KC_t = 3$ ,  $\beta_t = 30$  in regime  $A^*$ . Positive (counter-clockwise) and negative vorticity contours are denoted by red and blue colours, respectively. Vorticity contours are evenly spaced over the range  $[-6.0:6.0]$ ; with  $\Delta[\omega_z^*] = 0.6$ .

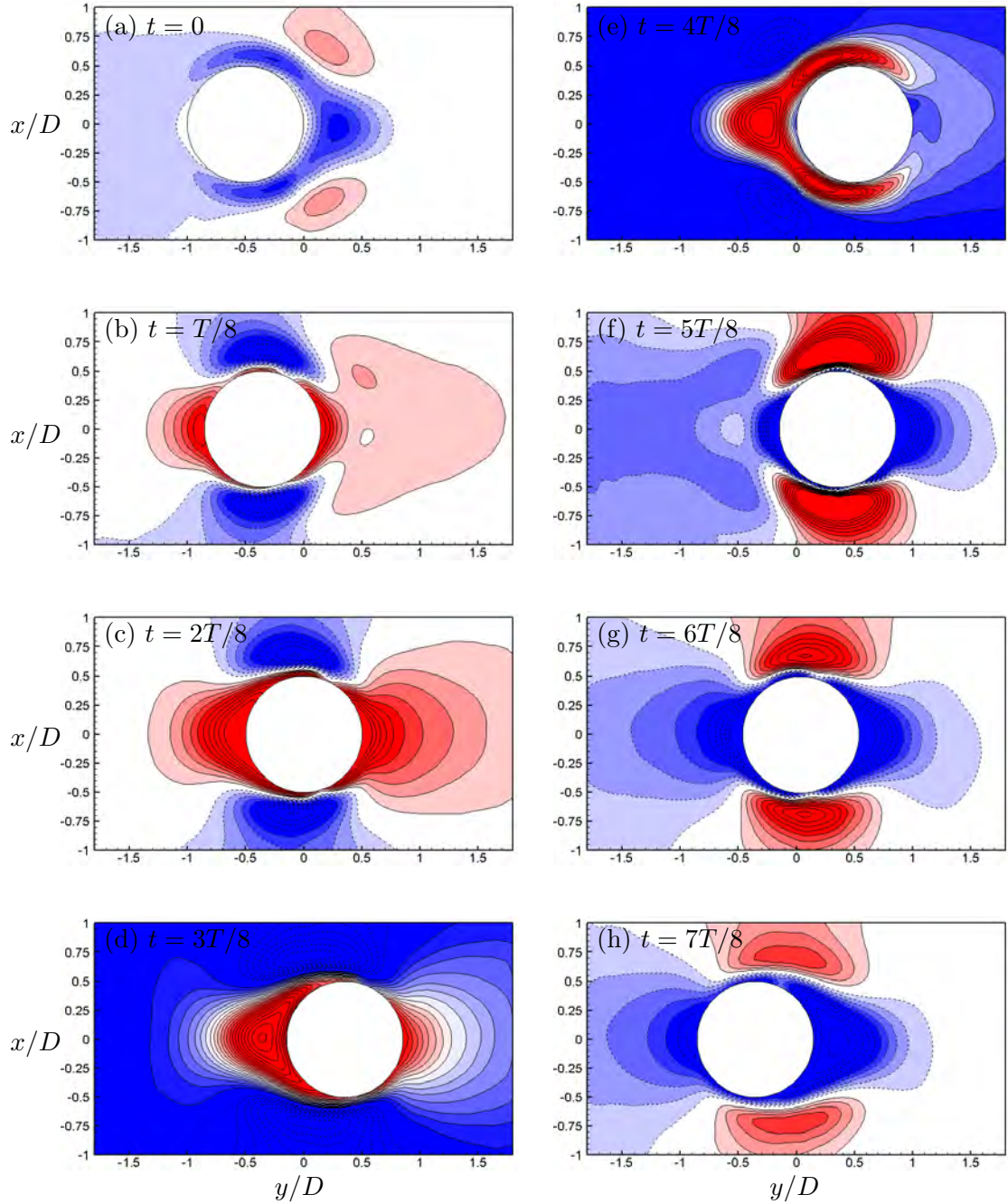


FIGURE 4.15: A sequence of phase-averaged non-dimensionalised  $V$  velocity contours, extracted over one motion period,  $T$ , at  $KC_t = 3$ ,  $\beta_t = 30$  in regime A\*. Positive and negative velocity contours are denoted by red and blue colours respectively.  $V$  velocity contours are evenly spaced over the range  $[-0.8:0.8]$ ; with  $\Delta[V/U_{\max}] = 0.08$ .

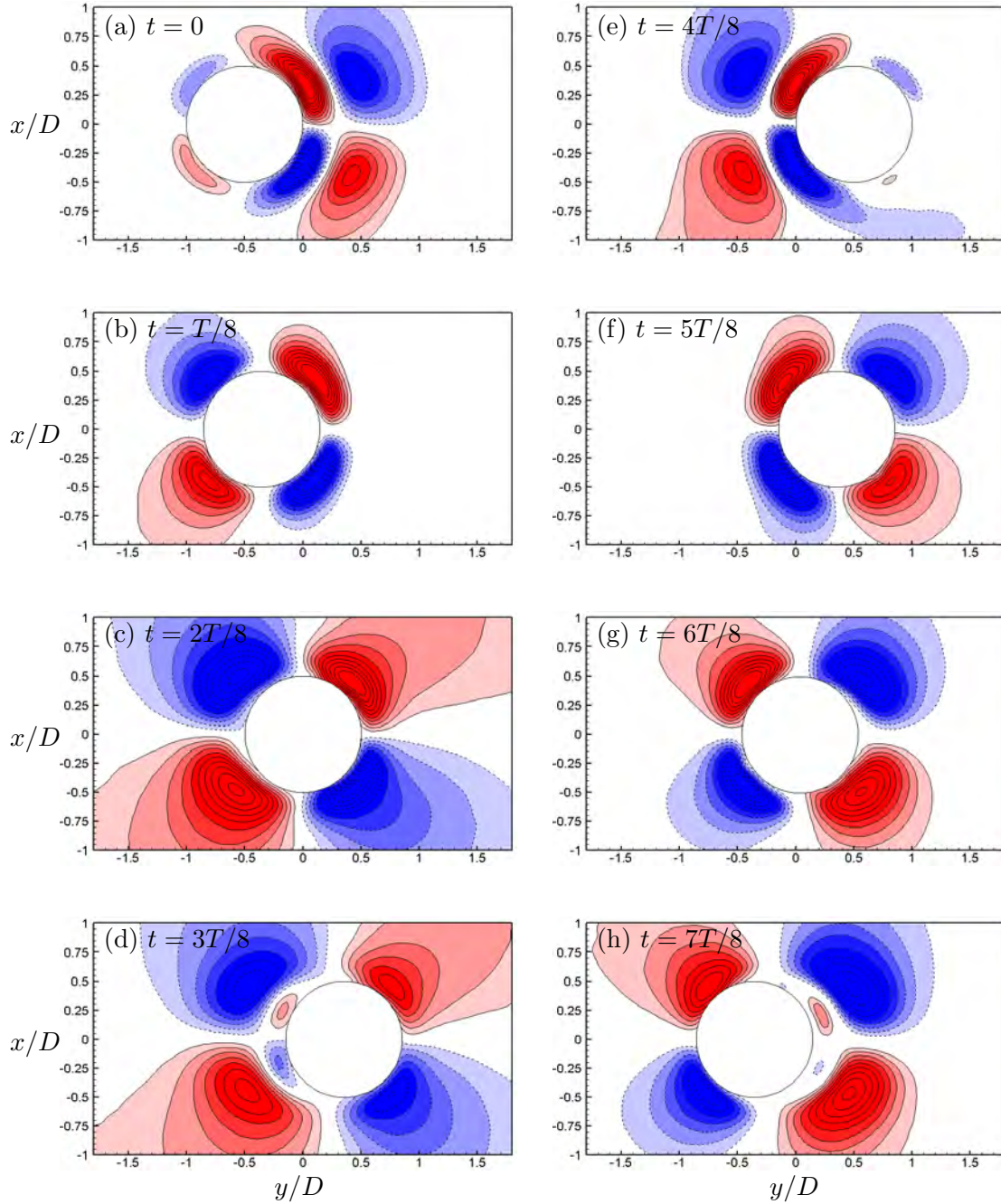


FIGURE 4.16: A sequence of phase-averaged non-dimensionalised  $U$  velocity contours, extracted over one motion period,  $T$ , at  $KC_t = 3$ ,  $\beta_t = 30$  in regime A\*. Positive and negative velocity contours are denoted by red and blue colours respectively.  $U$  velocity contours are evenly spaced over the range  $[-0.6:0.6]$ ; with  $\Delta[U/U_{\max}] = 0.06$ .



amplitude to the right, *i.e.* image (d). This happens due to the cross-annihilation of the opposite-sign vortices  $A'$  and  $C$  on the upper and  $B'$  and  $D$  on the lower side of the cylinder. Concentrations  $C$  and  $D$  are from the present cycle of the cylinder motion. As the cylinder starts its motion from left to right (or the converse situation when the flow passes over the cylinder from right to left), *i.e.* image (a), small positive and negative concentrations of vorticity grow in size. These are the vortices that started forming adjacent to the body surface of the cylinder from the previous cycle, *i.e.* image (h) of the previous cycle not shown here. These are the symmetric upper and lower boundary layers designated as  $C$  and  $D$  in images (a) to (g). Concentrations  $C$  and  $D$  can almost survive during one complete oscillation cycle, starting from position (h),  $t = 7T/8$ , of the previous cycle and disappearing in the  $t = 7T/8$  position of the present cycle, *i.e.* image (h) of figure 4.14. Two fixed stagnation points, shown as points  $I$  in image (b), at the front and the back of the cylinder, exist in all the cylinder positions shown. It is evident that at all the instants of figure 4.14 the concentrations are all not shed and remain in the vicinity of the surface of the cylinder. Again this confirms the characteristics of the flow in regime  $A^*$  as defined by Tatsuno & Bearman (1990) and numerically by Elston (2005). As the cylinder moves to the right, the concentrations  $A'$  and  $B'$ , from the previous cycle, experience a decrease of peak vorticity level, as well as leaving behind the cylinder as it passes them. As the cylinder continues the motion to the right, concentrations  $A'$  and  $B'$  are no longer detectable from images (d) onwards and concentrations  $C$  and  $D$  continue to accumulate vorticity, as well as experiencing an increase of peak vorticity level in the vicinity of the cylinder. The direction of motion of the cylinder will eventually drag concentrations  $C$  and  $D$ , such that they wrap around the body and remain attached to the surface until the cylinder approaches zero velocity, at the end of its right-most end of motion, image (e).

Before the cylinder reaches its right-most end of motion, image (d), two counter-rotating concentrations of vorticities of the opposite direction to the concentrations  $C$  and  $D$ , *i.e.* concentrations  $A$  and  $B$ , are formed. These are the onset of formation of a narrow shear layer adjacent to the body of cylinder. These two newly created vortices,  $A$  and  $B$ , will grow in size as the cylinder reaches its peak amplitude at the right-most of its oscillation cycle, and also will remain attached to the cylinder body surface as the cylinder reverses its oscillation direction from right to left, becoming larger in size and in their values of vorticity. Changing the direction of the cylinder

motion and movement of the cylinder breaks up concentrations C and D, which force them to move past the cylinder to the opposite side. As the cylinder continues the motion, concentrations C and D, as previously happened to concentrations A' and B' in the previous half cycle, experienced a decrease in the peak vorticity level. In time they vanish, due to cross-diffusive annihilation, and concentrations A and B dominate the flow. Figure 4.20 clearly shows how the peak vorticity level changes for regime A\* (as well as regimes A and B, this will be explained in §4.4.4 and §4.4.5). It should be noted that no convection of the vortices was observed as they are created adjacent to the body, *i.e.* in the attached shear layer, or vanish in the vicinity of the cylinder, *i.e.* in the separated shear layer.

Figure 4.21 shows the time history of dimensionless circulation,  $\Gamma^*$ , of concentrations of vorticity C and D, adjacent to the cylinder surface for regimes A\*, A and B at different phase positions in a cycle. The comparison between the regimes will be described in §4.4.5. At the instant corresponding to figure 4.14a ( $t = 0$ ), the identifiable symmetric concentrations of vorticity C and D each have average dimensionless circulation values of about 0.5. It should be noted that the points are connected by lines to give an easier visual identification of the changes in  $\Gamma^*$ , not to indicate a continuous time history. Each point is an average over more than 30 cycles. As the cylinder reaches the end of the cycle, *i.e.* images (g) and (h),  $\Gamma^*$  values decrease until they reach values of approximately 0.26 at  $t = 6T/8$  and nearly zero for  $t = 7T/8$ . This is speculated to be due to the cross-diffusive annihilation of the vortices with the newly generated vortices A and B. As was mentioned above, simultaneously concentrations C and D become clearly defined in images (b) to (f), and on top and bottom of the cylinder surface, distributed trails of positive (solid line) and negative (dashed line) vorticity clusters persist, respectively. These vortices will gradually grow in size and circulation due to the motion of the cylinder until they reach their maximum  $\Gamma^*$  values of 1.76 at (c), which corresponds to the middle of oscillation cycle and the maximum velocity of the cylinder in the cycle ( $U_{\max}$ ).

The velocity patterns of figures 4.15 and 4.16 as well as velocity distributions of figure 4.22 clearly show the symmetry of the flow around the oscillating cylinder in this regime, in an appropriate sense. Figure 4.15a indicates substantial levels of negative  $V/U_{\max}$ . This relates to the direction of the motion of the cylinder prior to this location from the previous cycle. As the cylinder reverses, image (b) onwards, the substantial

levels of  $V/U_{\max}$  change sign to positive. This trend continues until the cylinder reverses at image (e). It can be seen from figure 4.15 and figure 4.16 that the patterns of  $V/U_{\max}$  and  $U/U_{\max}$ , respectively do not lose their symmetry with respect to the axis of oscillation.

Figure 4.17 and figure 4.18 show the velocity vector fields and streamline topology of the flow in a frame of reference moving with the instantaneous velocity of the cylinder in regime A\*. Figure 4.18 shows that the flow is steady and there is no evidence of separation, except images (d) and (h) which corresponds to the onset of the formation of concentrations A and B in figure 4.14d and h, respectively. This does not imply full separation of the flow from the cylinder surface, but shows that part of the elongated concentrations of C and D are lifted from the surface due to the generation of vortices A and B, see for example figure 4.14d.

Figure 4.22 shows the  $V/U_{\max}$  phased-averaged velocity and  $\omega_z^*$  distribution at  $y/D=0.0$  for four different phases of the motion in one cycle. The four phases chosen here are at the middle (figures 4.15c,g and figures 4.14c,g) and at the ends (figures 4.15a,e and figures 4.14a,e) of the oscillation cycle, *i.e.* the cylinder maximum and zero velocity locations, respectively. This figure clearly shows the symmetry of the flow with respect to the axis of oscillation,  $y$ -axis, and also the  $x$ -axis. As expected, the results are the mirror image of each other. These results further confirm the symmetry suggested by Tatsuno & Bearman (1990) in regime A\*.

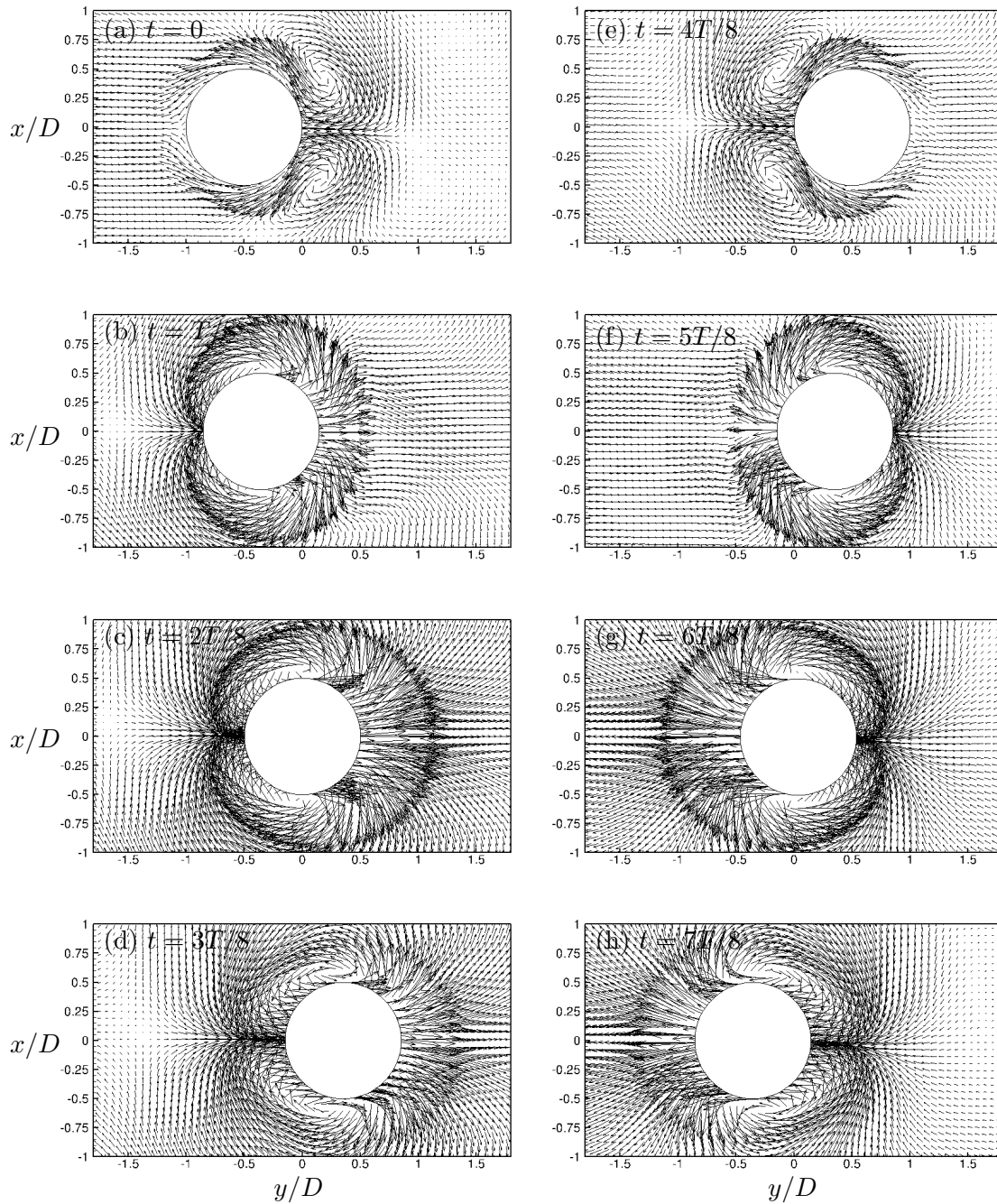


FIGURE 4.17: A sequence of phase-averaged velocity vector fields, extracted over one motion period,  $T$ , at  $KC_t = 3$ ,  $\beta_t = 30$  in regime A\*.

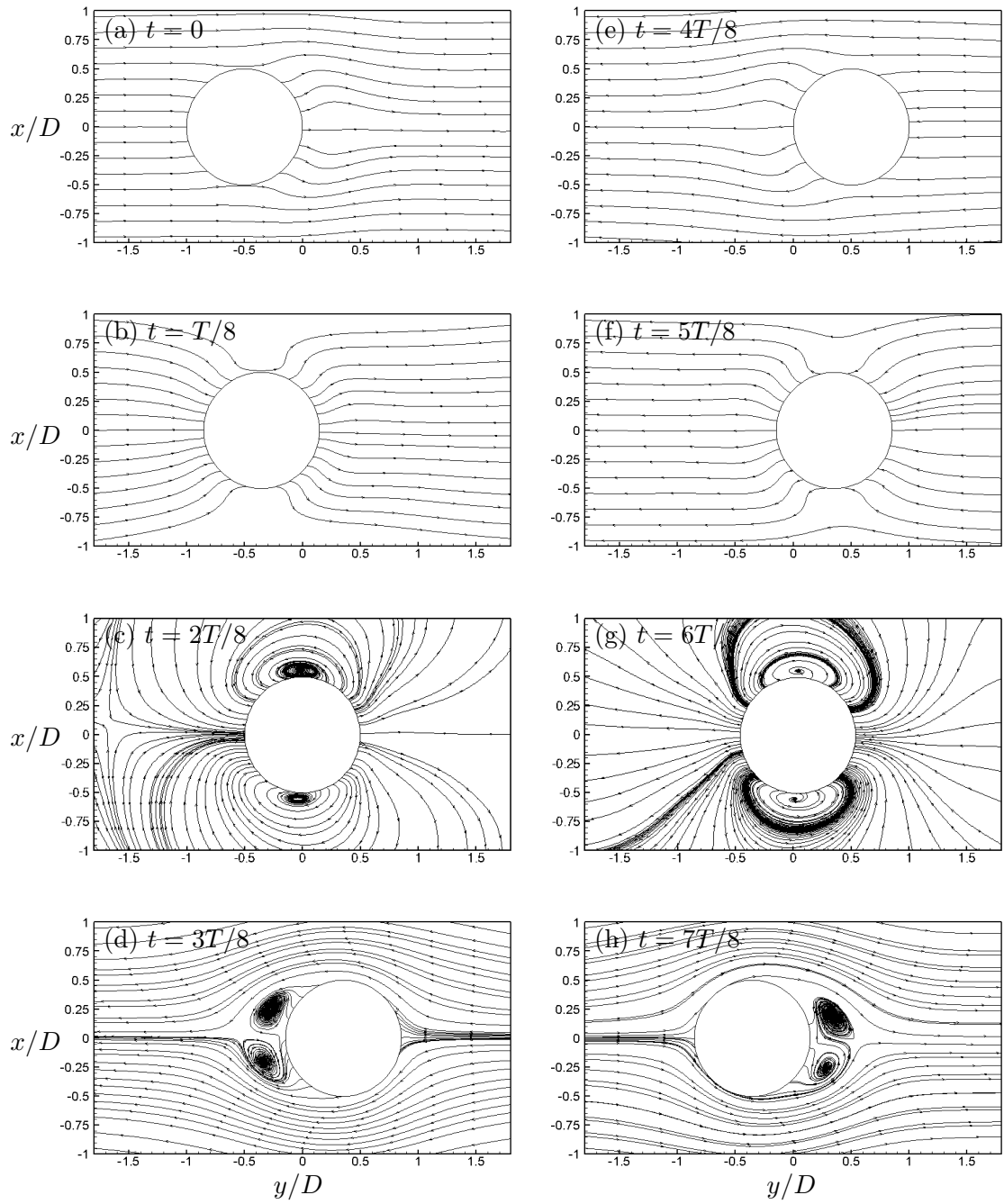


FIGURE 4.18: Phase-averaged streamline patterns extracted over one motion period,  $T$ , at  $KC_t = 3$ ,  $\beta_t = 30$  in regime A\*. Images are in a frame moving with instantaneous velocity of the cylinder.

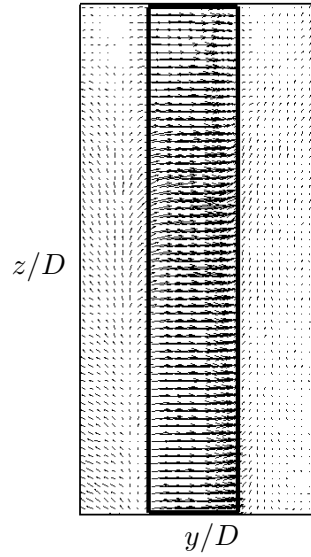


FIGURE 4.19: Two-dimensionality of flow along the cylinder axis in regime A\* ( $KC_t = 3$  &  $\beta_t = 30$ ); Instantaneous dimensionless velocity vectors after 50 cycles. The solid rectangle lines denote the position of the cylinder in this phase.

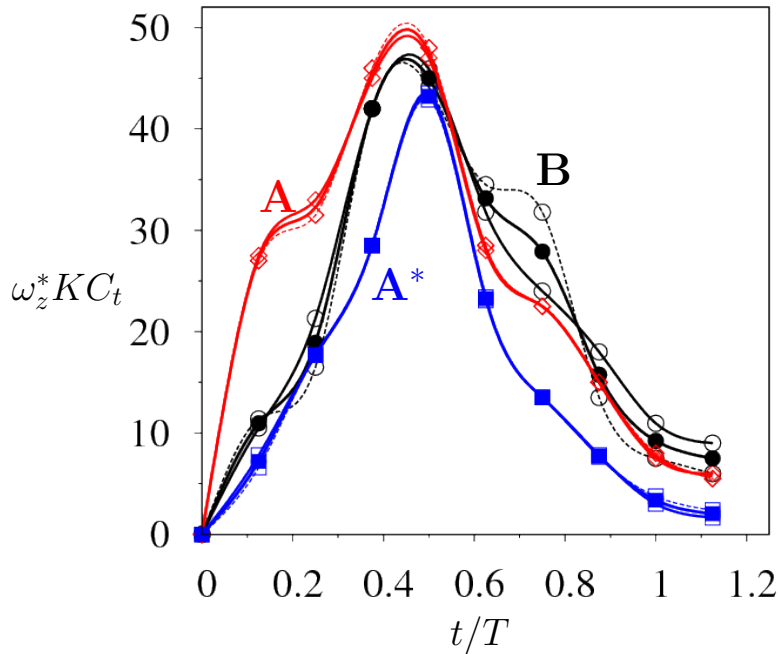


FIGURE 4.20: Comparison of time history of dimensionless peak vorticity of vortices C (narrow solid lines) and D (dotted lines), labelled in figure 4.29, adjacent to the cylinder body surface for regimes A\*(squares), A (diamonds) and B(circles) at different phase locations. Thick solid lines/symbols indicate the average peak vorticity value for both vortices C and D.

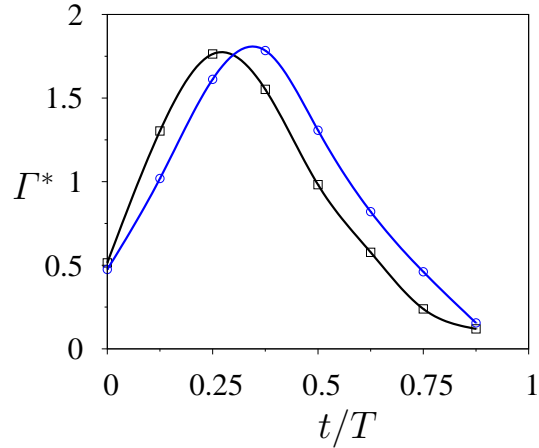


FIGURE 4.21: Time history of dimensionless circulation of vortices C and D, adjacent to the cylinder body surface for regimes A\* (black color) and A (blue color) at different phase positions. The vortices C and D are symmetric with respect to the axis of oscillation. This results the absolute value of dimensionless circulation of vortices C and D coincides in this figure.

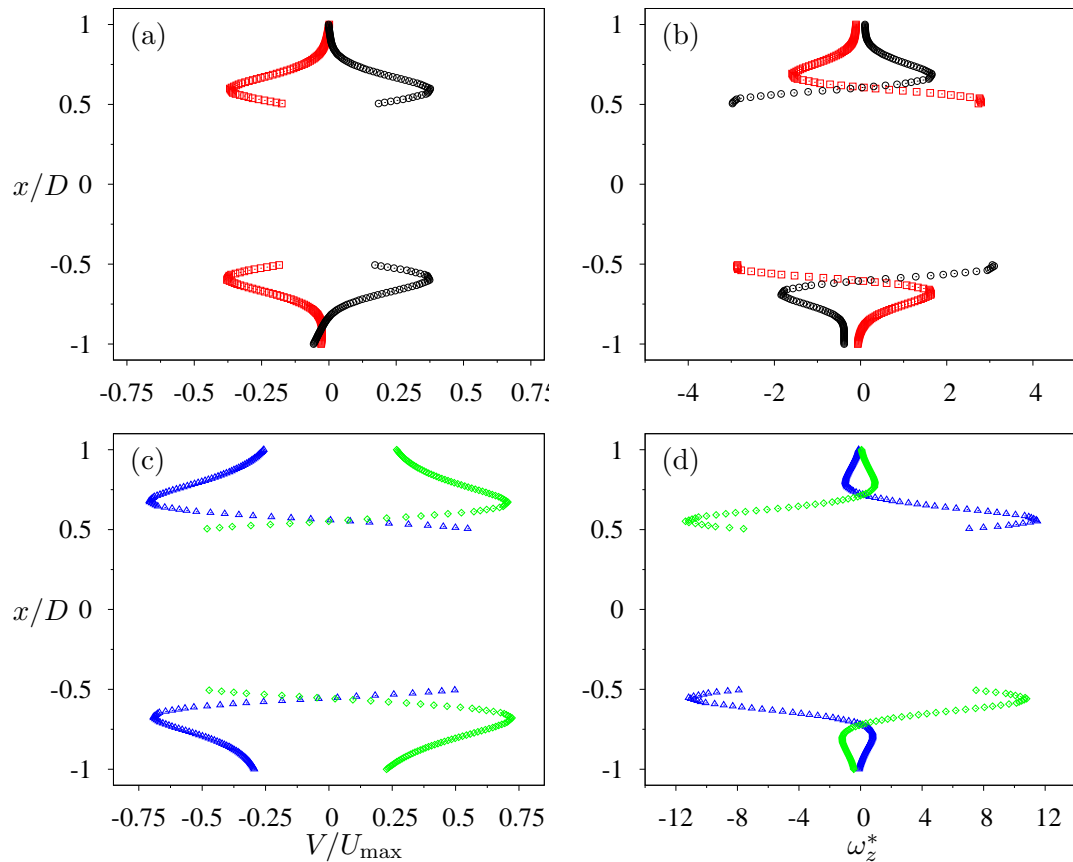


FIGURE 4.22:  $V/U_{\max}$  velocity component and  $\omega_z^*$  distribution of flow at the cross-section  $y/D=0.0$  for four different phases of flow in the cycle in regime A\*,  $KC_t=3$  and  $\beta_t=30$ . The phases are selected to locate at the middle and the end of the cycle where the velocity of the cylinder is maximum and zero, respectively. The square symbols show the  $t=0$  (figure 4.14a and 4.15a) phase, the circle  $t=4T/8$  (figure 4.14e and 4.15e) phase, the triangle  $t=2T/8$  (figures 4.15c and 4.15c) and the diamond shape  $t=6T/8$  (figures 4.15g and 4.15g).

#### 4.4.4 Regime A

Based on the observations of Tatsuno & Bearman (1990) the flow in regime A is characterised by stable, symmetric and periodic vortex shedding. It is two-dimensional and two vortices are shed symmetrically per half cycle. The flow is also symmetric with respect to the axis of motion of the oscillating cylinder, the  $y$ -axis. At values of  $KC_t$  larger than that of regime A\* for  $\beta_t < 50$ , vortices are formed and the flow, according to Tatsuno & Bearman (1990), is composed of secondary streaming and flows due to vortices resulting from separation. The point selected for this regime is case 2 of table 4.2, *i.e.*  $KC_t=5$  and  $\beta_t=20$ . This regime was used in the validation section (§4.4.1) to compare our results against that of Dütsch *et al.* (1998). The flow pattern in regime A was found to be similar to that of regime A\*(Tatsuno & Bearman (1990) and §4.3.2.1). Tatsuno & Bearman (1990) characterised this regime to have periodic vortex shedding, which they declared was the main difference between this regime and regime A\*. As was discussed in §4.3.2.1, based on the flow visualisation results previously presented and Elston (2005)'s numerical results, no evidence of vortex shedding for this regime was observed. The vortices did not appear to be shed nor did they convect away from the cylinder. The main differences between the present regime and regime A\* observed to be:

- the vortices and shear layers generated in regime A are larger in size and also stronger (see figures 4.14, 4.20 and 4.23) than that of regime A\*;
- the elongated concentrations of vorticity C and D (labelled in figures 4.14 and 4.23)) travel slightly further away from the cylinder surface in regime A;
- the separation of the elongated vortices which wrap around the cylinder surface (vortices C and D) occurs only in the vicinity of the cylinder. The vortices are not moved away from the vicinity of the cylinder, and based on the separation definition of Tatsuno & Bearman (1990), noted in §4.3.2.2, the flow is not separated in regime A, same as what was observed in regime A\*.

This was observed to be the case both in the PIV and flow visualisation results. It was found that the separated vortices remained within a distance of a maximum of one cylinder diameter away from the oscillating surface. Referring to figure 4.20, it can be seen from the non-dimensionalised  $\omega_z^*$  that the peak vorticity values of regime A are



always greater than that of regime A\*. This implies that since the emergence of the vortices the same vortices generated in regime A, during one cycle, are always stronger than regime A\*.

A sequence of regime A's periodic flow patterns caused by the forward and backward motion and explained above is shown in figures 4.23, 4.24, 4.25 and 4.26. As was presented in §4.4.3 two fixed stagnation points (points I in image (c)), at the front and the back of the cylinder, exist for all positions. The resulting vortex dynamics can be described as follows. As the oscillating cylinder moves in the forward direction, *e.g.* left to right starting from image (a) or conversely from right to left from image (e) in figure 4.23, symmetric upper and lower boundary layers develop at the front of the cylinder (shear layers C-D or A'-B' in (a)-(d) or (e)-(h), respectively); these layers locally/partially separate at a symmetric upper and lower position on the cylinder wall (points II in image (d)) creating two symmetrical counter-rotating vortices of the same strength behind the cylinder. At the end of the half cycle the two vortices remain behind the cylinder and as the cylinder reverses the vortices are convected towards the cylinder. This is an indication of no vortex shedding for this regime, otherwise the vortices separated from the surface of the cylinder would be expected to travel away. In addition, the backward motion of the cylinder causes a splitting of the vortex pair (vortices C-D in image (g) for example), which is produced by the forward motion, and finally wake reversal occurs. Consequently, these vortices do not survive into the next half cycle and may be cancelled by mixing with vorticity of opposite sign in the cylinder boundary layer. As the cylinder approaches the end of its full cycle, the pair A-B, which moves slowly towards the cylinder, is still detectable at image (g) and amalgamates with the vorticity generated on the cylinder at image (h), A'-B'. Similarly the pair C-D of image (h) persists and is still detectable. The only difference is that this pair decreases in size from the interaction with the vorticity generated on the cylinder as it convects downstream.

As was found in regime A\* the flow here is observed to be two-dimensional along the span of the cylinder with the same pattern as in figure 4.19. Figure 4.27 shows the phase-averaged  $V/U_{\max}$  velocity vectors along the span of the cylinder in regime A. The solid line in the figure denotes the position of the cylinder at that particular phase of measurement. As can be seen from the figure, the flow is parallel to the bottom surface of the channel test section (or the  $y$ -axis). This confirms the two-dimensionality of the

flow in this regime.

#### 4.4.5 Regime B

The structure of the flow in regime B differs remarkably from that of the regimes at lower amplitude or frequency. Those regimes, *i.e.* A\* and A (refer to figure 2.18), are two-dimensional and spatially symmetric with respect to the axis of oscillation. Regime B, however, is defined by Tatsuno & Bearman (1990) as the onset of three-dimensional instability and longitudinal vortices. As discussed in §2.5, Honji (1981) investigated this flow in detail and named it the “streaked flow”. Figure 4.28 shows the three-dimensionality of the flow along the span of the cylinder. Section §4.4.1 showed the comparison of the measured distance ( $\lambda/D$ ) between the centres of the two “streaked flows” adjacent to each other on one side of the cylinder for a sample point in regime B. Unlike regimes A\* and A, regime B is no longer symmetric with respect to the axis of oscillation. Figure 4.29 shows this asymmetry, at  $x/D = 0$ . The results are phase-averaged over more than 30 cycles.

Figure 4.29 shows a sequence of phase-averaged  $\omega_z^*$  contours. Figures 4.30, 4.31 and 4.32 show a sequence of phase-averaged  $V/U_{\max}$  and  $U/U_{\max}$  velocity contours and velocity vector fields, respectively. All of the sequences are extracted over one motion period,  $T$  at  $KC_t=3$ ,  $\beta_t=80$  in regime B. Again, these figures clearly show the asymmetry of the flow with respect to the axis of oscillation. As the cylinder starts its motion from left to right, two initially symmetric vortices, vortices C and D in figure 4.29, emerging from the previous cycle, start growing in size while retaining their circulation as the cylinder moves to right. They become stronger, relatively symmetric and also stretch as the cylinder passes the middle of its motion. Once the cylinder reaches the end of its half cycle motion, image (e) of figure 4.29, the vortices become asymmetric with respect to the axis of oscillation, but they still hold their  $T/2$  reflection symmetry about  $y/D = 0$  axis. This symmetry breaking about the  $x/D = 0$  axis of regime B can clearly be seen in figures 4.30 and 4.32 as well. It should be noted that regimes A\* and A, as was shown in §4.4.3 and §4.4.4, were found to keep their symmetry about the axis of oscillation as well as the axis of  $y/D$ . These results are consistent with the previous results of Tatsuno & Bearman (1990) and Elston (2005). Appendix A explains the definition of different types of symmetries based on what was introduced by Elston (2005).

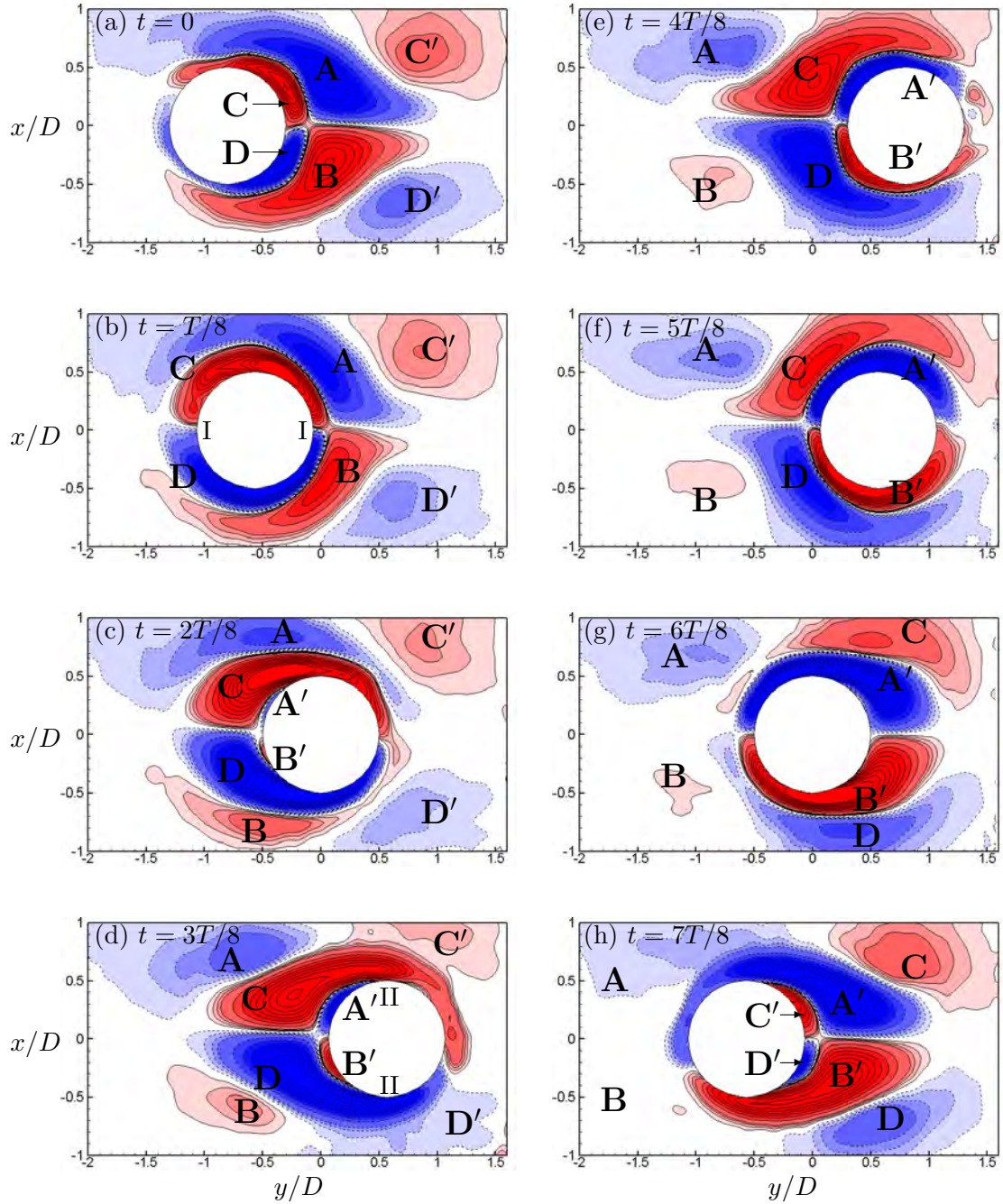


FIGURE 4.23: A sequence of phase-averaged non-dimensionalised out-of-plane vorticity contours,  $\omega_z^*$ , extracted over one motion period,  $T$ , at  $KC_t=5$ ,  $\beta_t=20$  in regime A. Positive (counter-clockwise) and negative vorticity contours are denoted by red and blue colours respectively. Vorticity contours are evenly spaced over the range  $[-6.0;6.0]$ ; with  $\Delta[\omega_z^*] = 0.15$ .

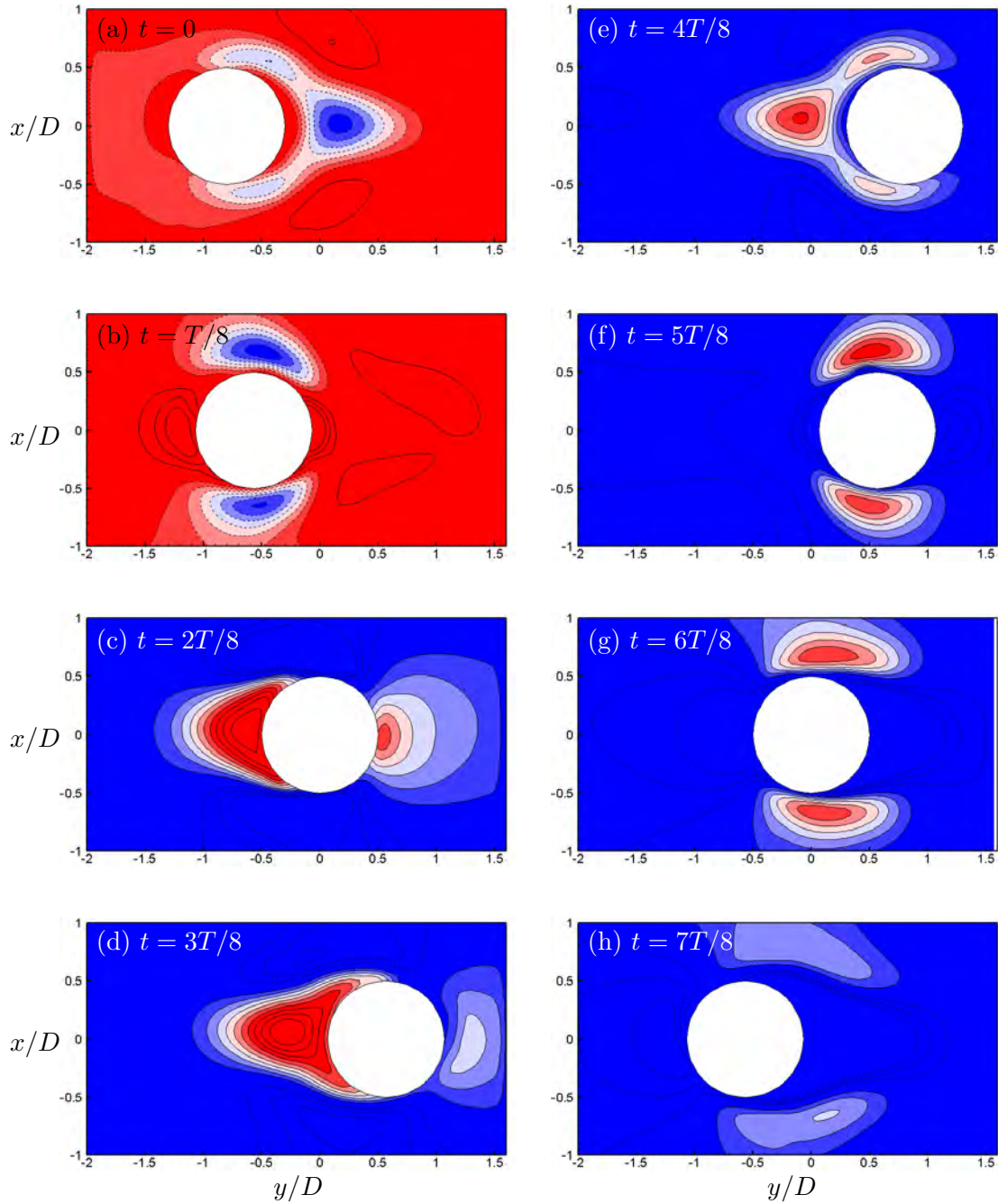


FIGURE 4.24: A sequence of phase-averaged non-dimensionalised  $V$  velocity contours, extracted over one motion period,  $T$ , at  $KC_t=5$ ,  $\beta_t=20$  in regime A. Positive and negative velocity contours are denoted by red and blue colours respectively.  $V$  velocity contours are evenly spaced over the range  $[-0.3:1.0]$ ; with  $\Delta[V/U_{\max}] = 0.1$ .

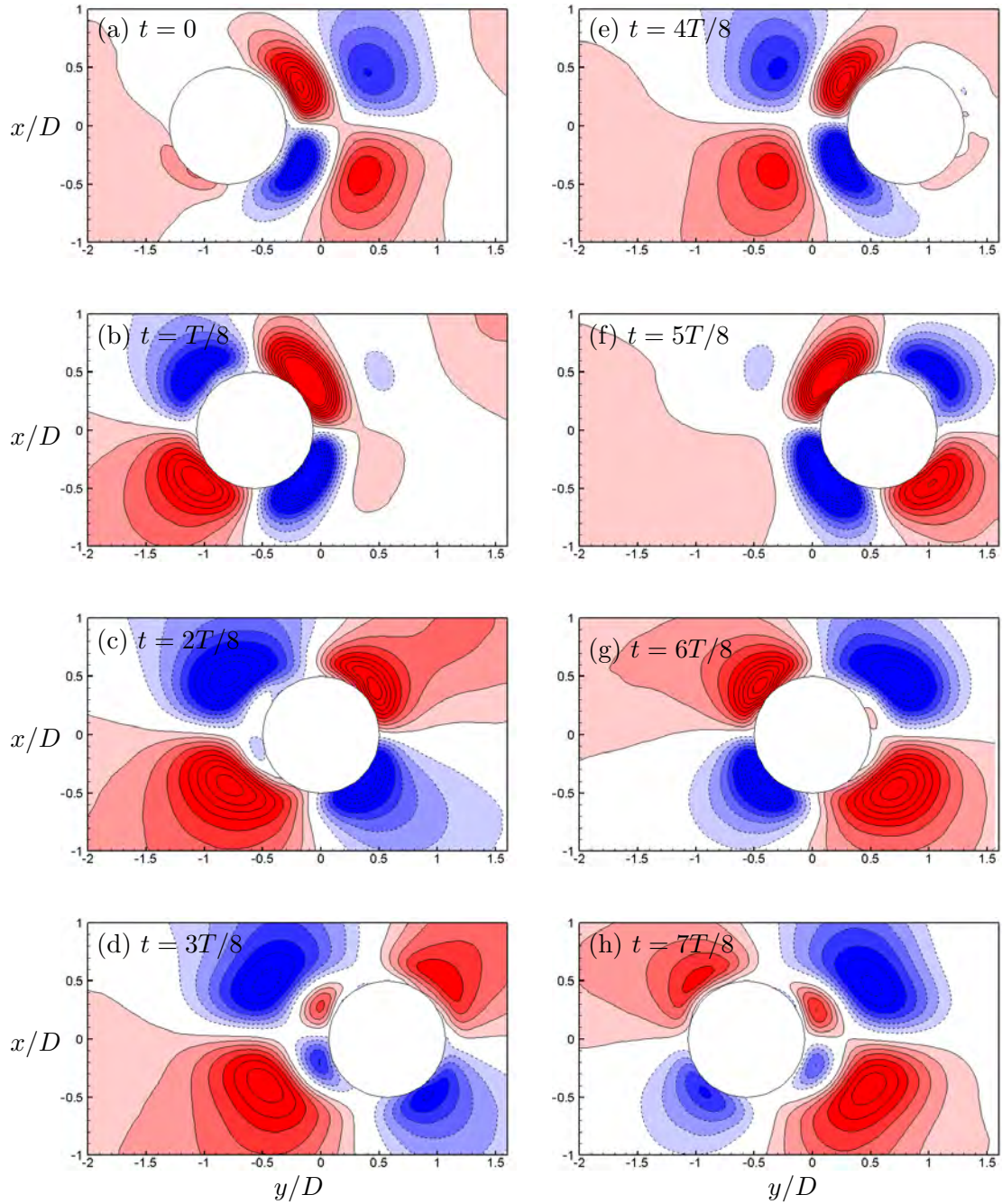


FIGURE 4.25: A sequence of phase-averaged non-dimensionalised  $U$  velocity contours, extracted over one motion period,  $T$ , at  $KC_t=5$ ,  $\beta_t=20$  in regime A. Positive and negative velocity contours are denoted by red and blue colours respectively.  $U$  velocity contours are evenly spaced over the range  $[-0.6:0.6]$ ; with  $\Delta[U/U_{\max}] = 0.06$ .

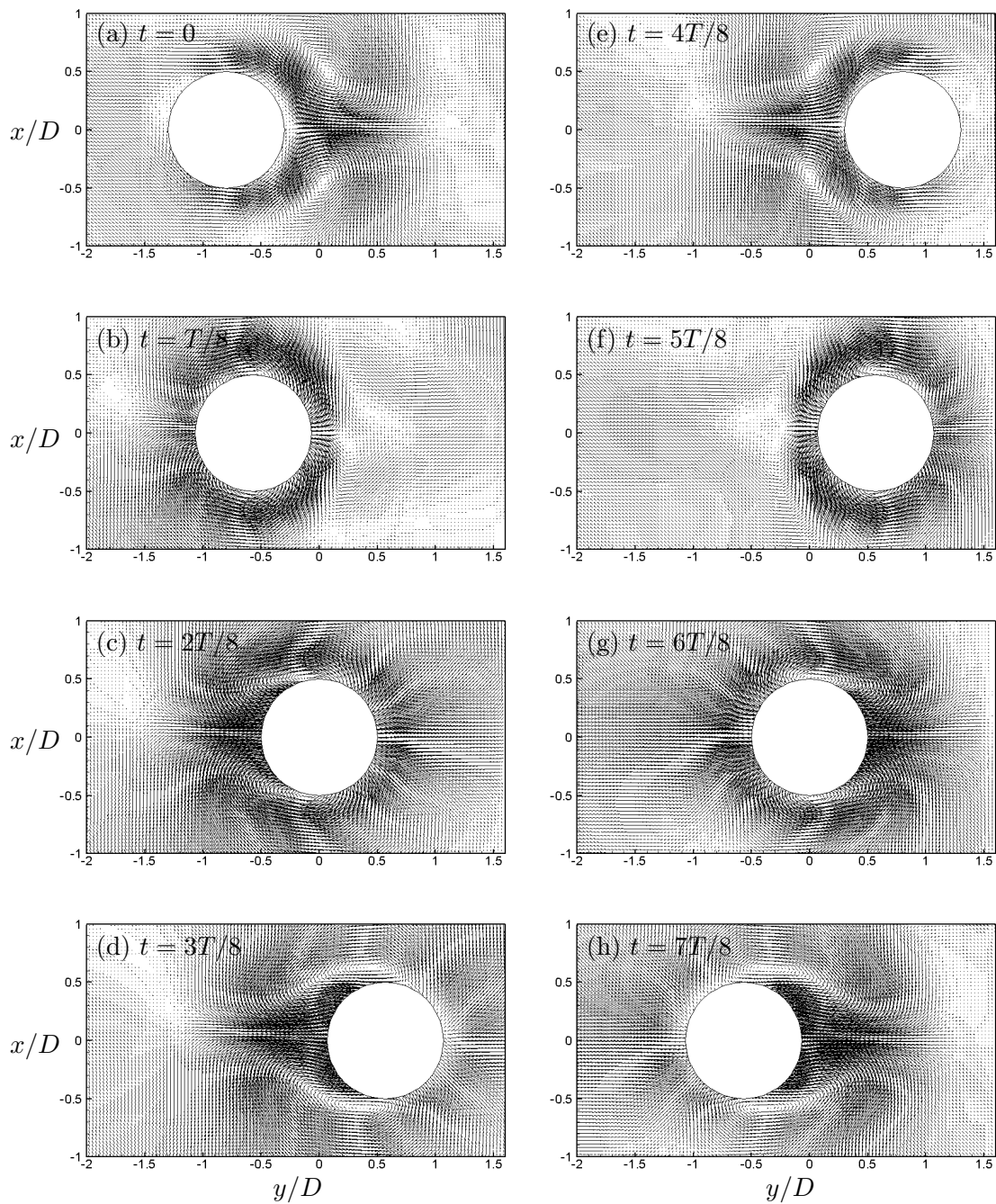


FIGURE 4.26: A sequence of phase-averaged velocity vector fields extracted over one motion period,  $T$ , at  $KC_t=5$ ,  $\beta_t=20$  in regime A. Positive and negative velocity contours are denoted by red and blue colours respectively.

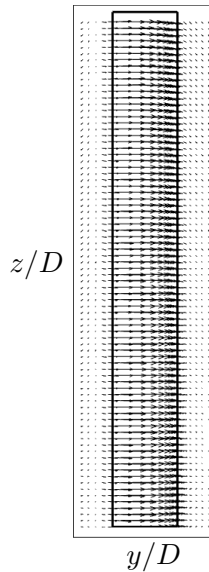


FIGURE 4.27: Two-dimensionality of flow along the cylinder axis in regime A ( $KC_t=5$  &  $\beta_t=20$ ); Instantaneous dimensionless velocity vectors after 50 cycles. The solid rectangle lines denote the position of the cylinder in this phase.

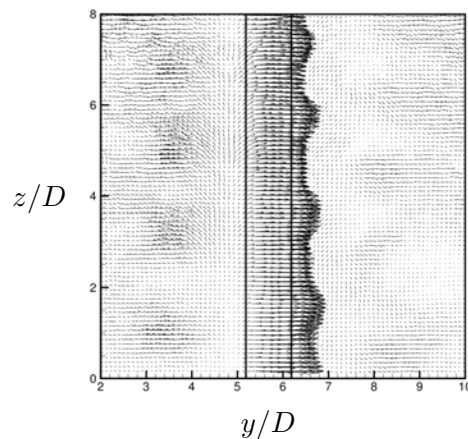


FIGURE 4.28: Three-dimensionality of flow along the cylinder axis in regime B ( $KC_t = 3$  &  $\beta_t = 80$ ); Instantaneous spanwise dimensionless velocity vector at the 36<sup>th</sup> cycle and phase angle of 270°. The solid rectangle lines denote the position of the cylinder in this phase which moves from right to left.

The cylinder shown in image (e) of figure 4.29 is at its right-most position in the oscillation cycle and is starting its motion from right to left. Vortices C and D are now those generated in the previous half-cycle, originating from the interaction of the flow and body. Vortices A' and B' have just been created, image (d), and are almost symmetrical relative to the axis of oscillation. These are the vortices which are close to the surface of the cylinder and remain attached to the cylinder until the cylinder reverses. As with vortices C and D at the beginning of their creation, they are also more symmetrical in shape than vortices C and D which were created and separated from the body in the previous cycle and have lost their symmetry with respect to the

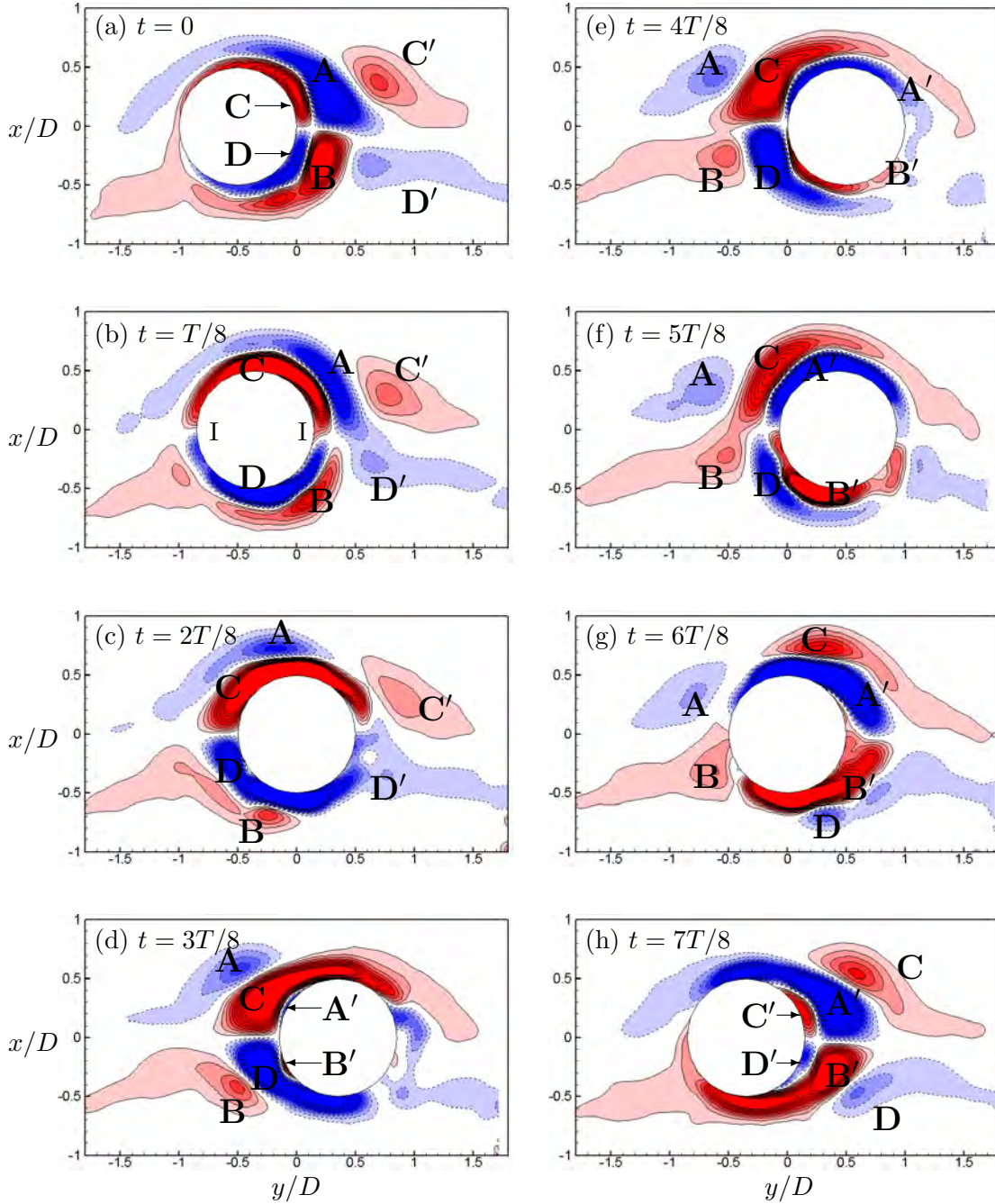


FIGURE 4.29: A sequence of phase-averaged non-dimensionalised out-of-plane vorticity contours,  $\omega_z^*$ , extracted over one motion period,  $T$ , at  $KC_t=3$ ,  $\beta_t=80$  in regime B. Positive (counter-clockwise) and negative vorticity contours are denoted by red and blue colours respectively. Vorticity contours are evenly spaced over the range  $[-5.0:5.0]$ ; with  $\Delta[\omega_z^*] = 0.5$ .



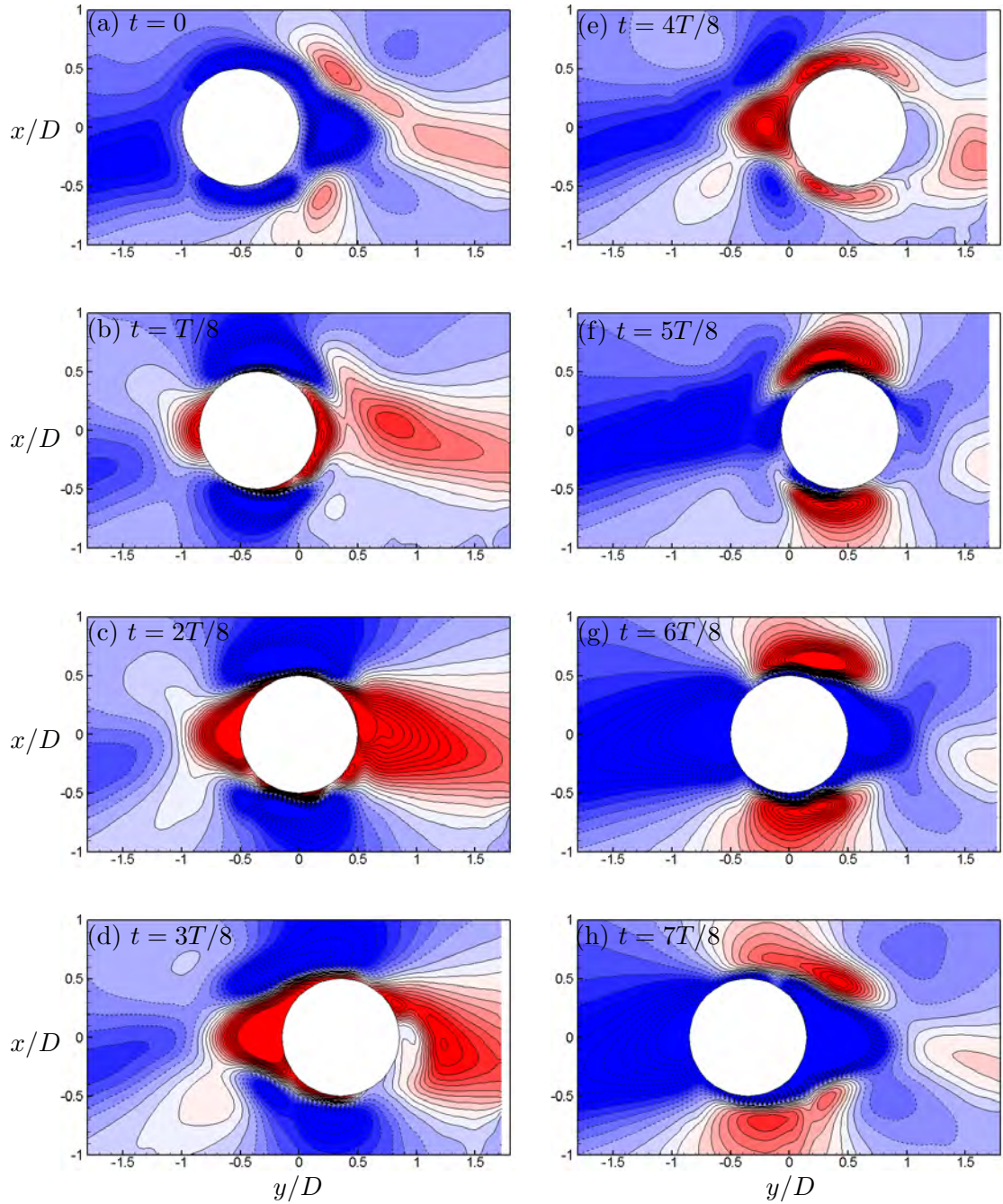


FIGURE 4.30: A sequence of phase-averaged non-dimensionalised  $V$  velocity contours, extracted over one motion period,  $T$ , at  $KC_t=3$ ,  $\beta_t=80$  in regime B. Positive and negative velocity contours are denoted by red and blue colours respectively.  $V$  velocity contours are evenly spaced over the range  $[-0.5:0.7]$ ; with  $\Delta[V/U_{\max}] = 0.04$ .

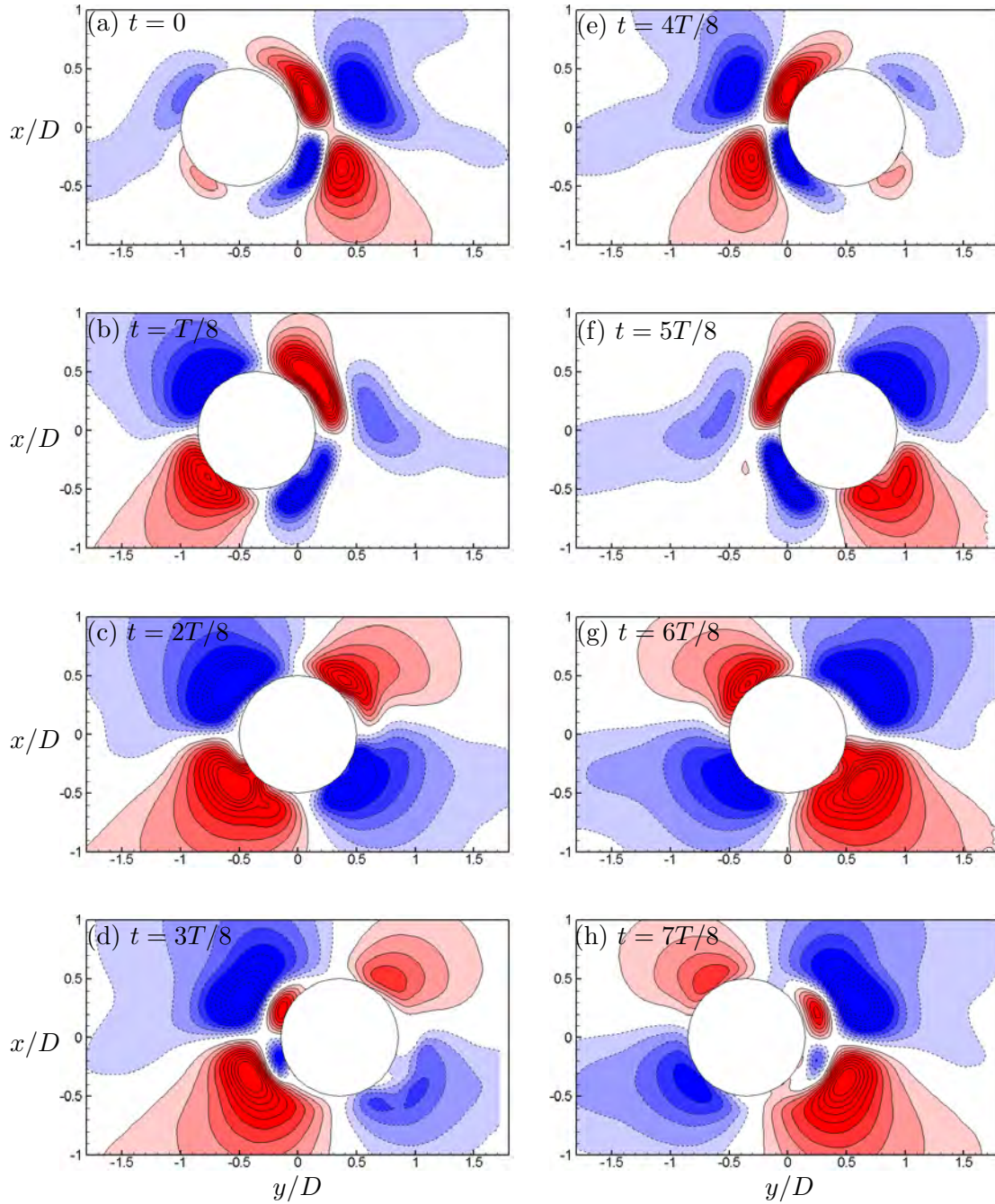


FIGURE 4.31: A sequence of phase-averaged non-dimensionalised  $U$  velocity contours, extracted over one motion period,  $T$ , at  $KC_t=3$ ,  $\beta_t=80$  in regime B. Positive and negative velocity contours are denoted by red and blue colours respectively.  $U$  velocity contours are evenly spaced over the range  $[-0.6:0.6]$ ; with  $\Delta[U/U_{\max}] = 0.06$ .

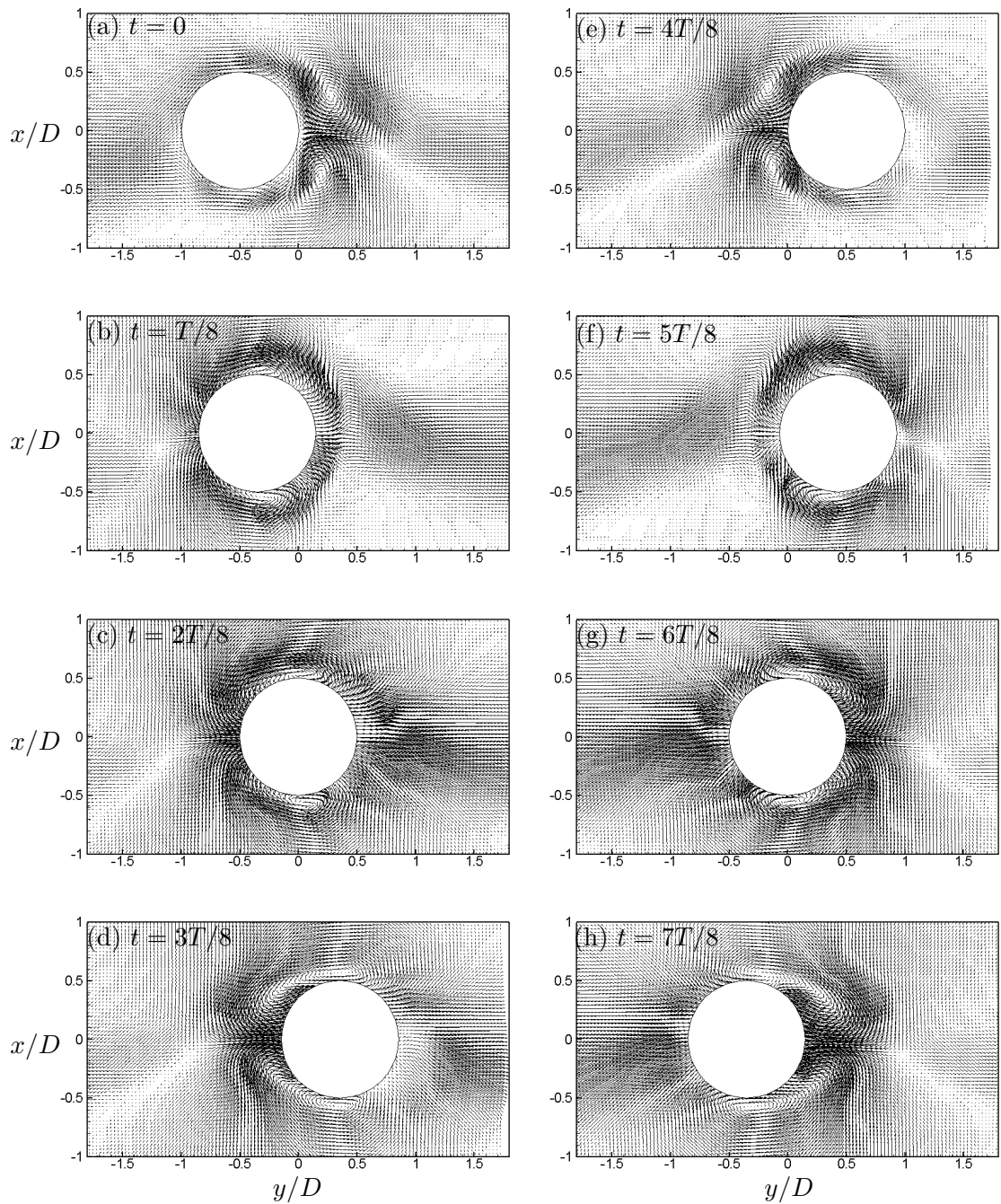


FIGURE 4.32: A sequence of phase-averaged velocity vector fields extracted over one motion period,  $T$ , at  $KC_t=3$ ,  $\beta_t=80$  in regime B. Positive and negative velocity contours are denoted by red and blue colours respectively.

axis of oscillation. This asymmetry can also be seen in figure 4.20. As the cylinder reverses and continues to complete its motion and finish one cycle, the vortices C and D wrap around the cylinder. As the cylinder continues its motion they will be directed to the other side of the cylinder.

Since the three regimes A\*, A and B exhibit similar vortex patterns the peak vorticity of a pair of vortices (C and D) is compared between these regimes in figure 4.20, where normalised peak vorticity,  $\omega_z^* K C_t$ , is plotted against  $t/T$ . The narrow solid lines indicate the time evolution of vortex C with positive sign and the dotted lines denote the time history evolution of vortex D with negative sign. The thick solid lines, the average value of the normalised peak vorticity of both vortices, are also shown for comparison purposes. Positive vorticity is defined as counter-clockwise rotation. In this figure, the blue lines represent regime A\* and red lines regime A.

The peak vorticity values for both vortices C and D are similar for regimes A\* and A and exhibit symmetry whereas for regime B the distributions of peak vorticity values only for the first half of motion coincide. The second half of motion exhibit asymmetry in peak vorticity values. The asymmetry of the vorticity pattern of regime B with respect to the oscillation axis in figure 4.20 is clearly shown at  $t/T = 0.875$ , corresponding to image (h) of figure 4.29. As the absolute magnitude of the vorticity of vortex C is higher than that of vortex D, the flow between these two vortices tends to tilt towards the axis of oscillation leading to an asymmetry in the flow. This causes the breaking of the reflection symmetry about the  $x/D = 0$  axis, as can be seen in figure 4.29, but yet keeping the  $T/2$  reflection symmetry about the  $y/D = 0$  axis.

For all these experiments the camera was held fixed at the bottom of the test section, in the case of the 2D measurements. In some cases, due to the larger amplitude of oscillation and the perspective effects of the cylinder in the PIV images, a small region of shadow was seen around the cylinder. This affected the results around the cylinder as for example can be seen in the middle right hand side of the cylinder in image (c) of figure 4.29. Special care was taken to reduce or even eliminate the shadow effect at all times but in some cases it was inevitable that we would lose a small region of the data. Primarily, this affected the front and rear parts of the cylinder.

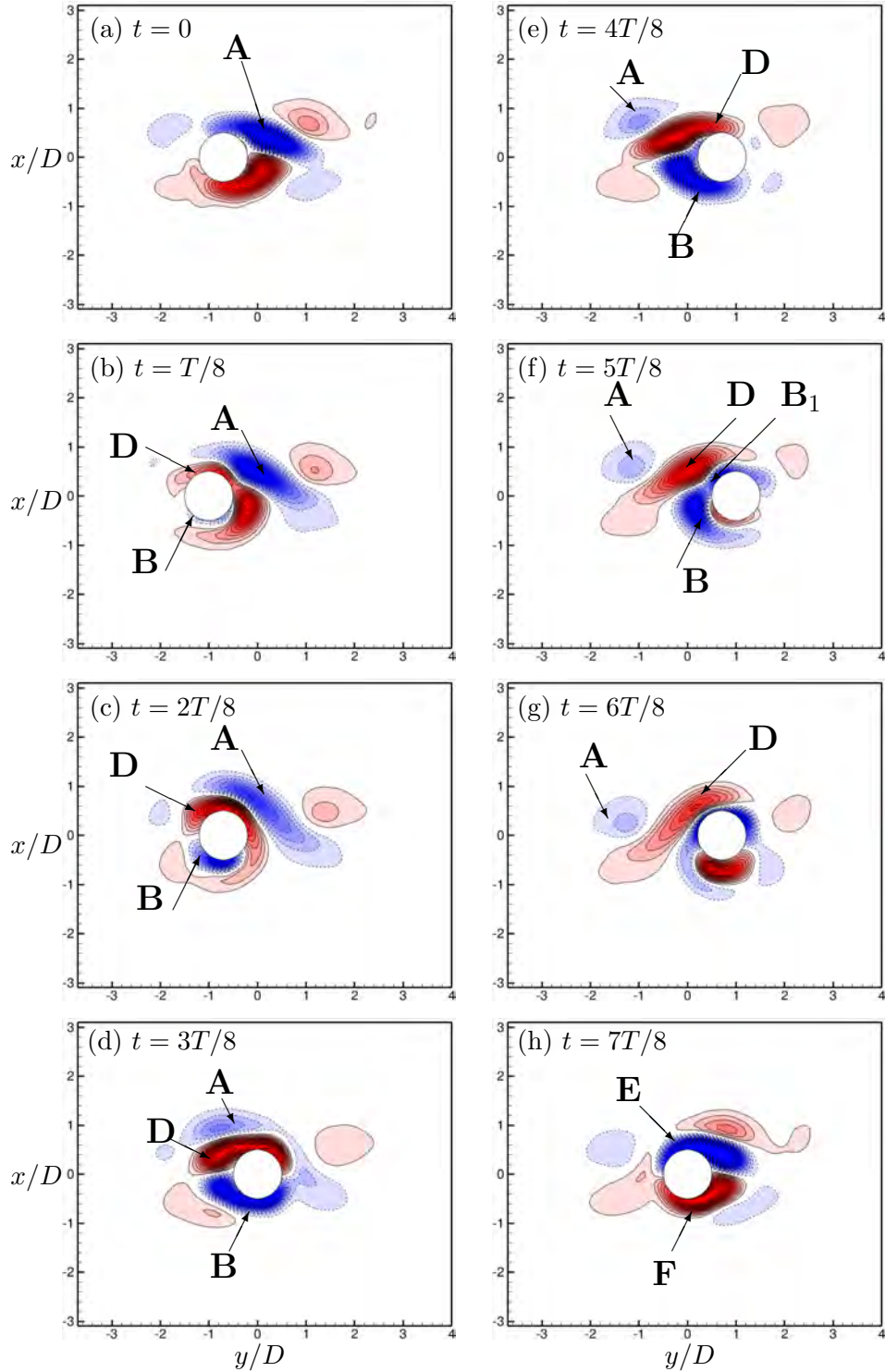


FIGURE 4.33: A sequence of phase-averaged non-dimensionalised out-of-plane vorticity contours,  $\omega_z^*$ , extracted over one motion period,  $T$ , at  $KC_t=6.28$ ,  $\beta_t=18$  in regime D. Positive (counter-clockwise) and negative vorticity contours are denoted by red and blue colours respectively. Vorticity contours are evenly spaced over the range  $[-1.5;1.5]$ ; with  $\Delta[\omega_z^*] = 0.1$ .

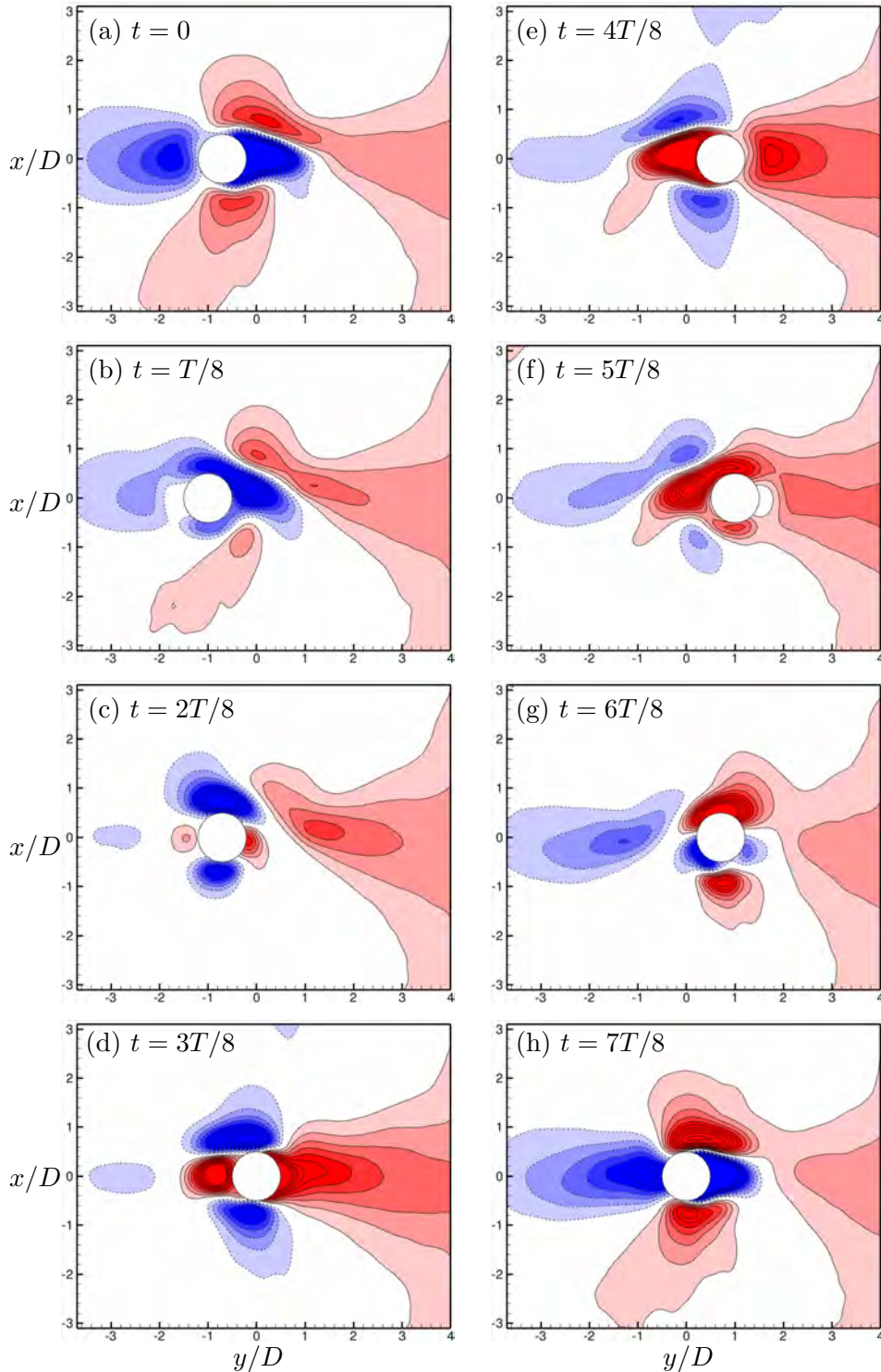


FIGURE 4.34: A sequence of phase-averaged non-dimensionalised  $V$  velocity contours, extracted over one motion period,  $T$ , at  $KC_t=6.28$ ,  $\beta_t=18$  in regime D. Positive and negative velocity contours are denoted by red and blue colours respectively.  $V$  velocity contours are evenly spaced over the range  $[-0.25:0.25]$ ; with  $\Delta[V/U_{\max}] = 0.025$ .

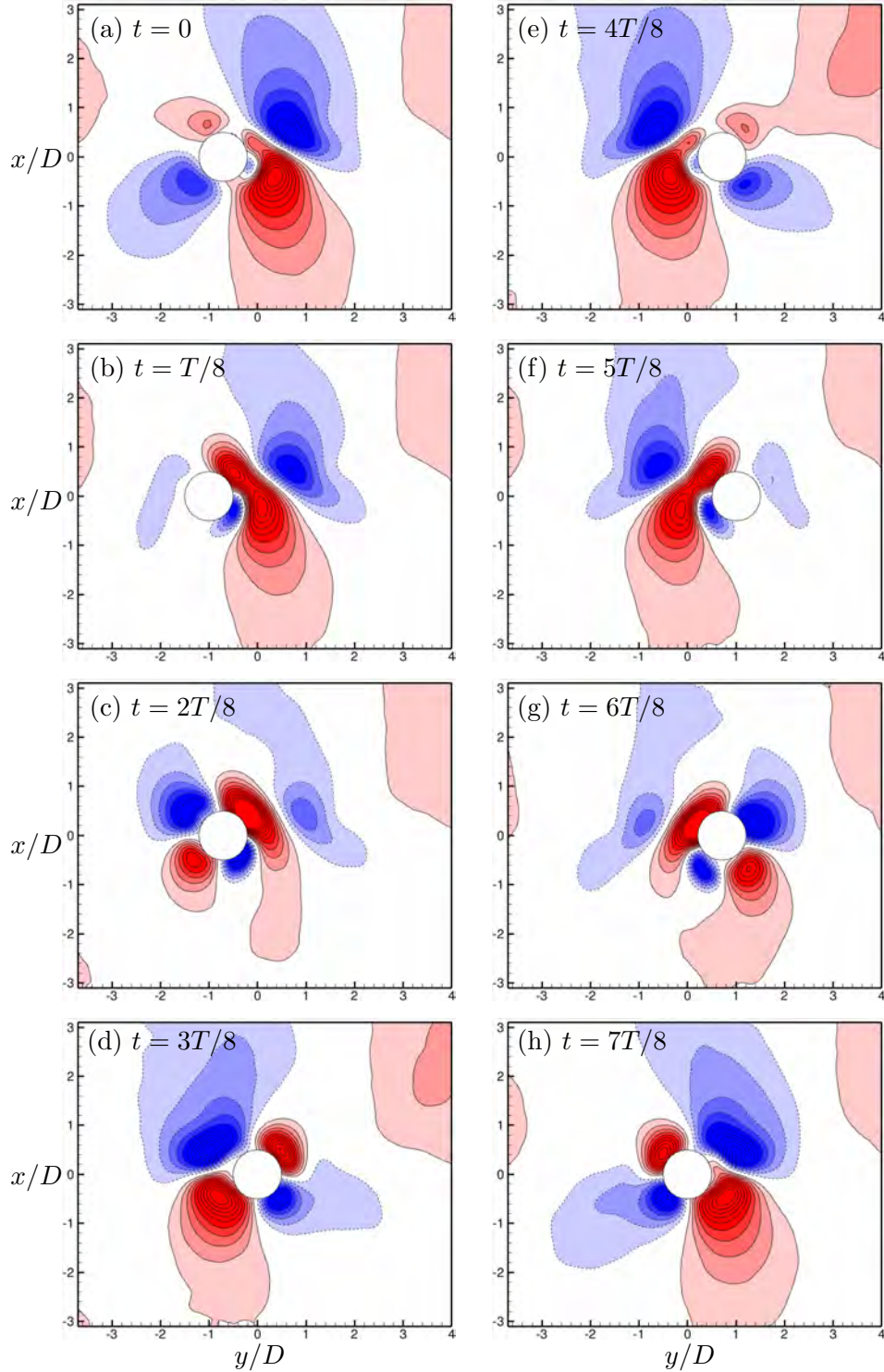


FIGURE 4.35: A sequence of phase-averaged non-dimensionalised  $U$  velocity contours, extracted over one motion period,  $T$ , at  $KC_t=6.28$ ,  $\beta_t=18$  in regime D. Positive and negative velocity contours are denoted by red and blue colours respectively.  $U$  velocity contours are evenly spaced over the range  $[-0.2:0.2]$ ; with  $\Delta[U/U_{\max}] = 0.02$ .

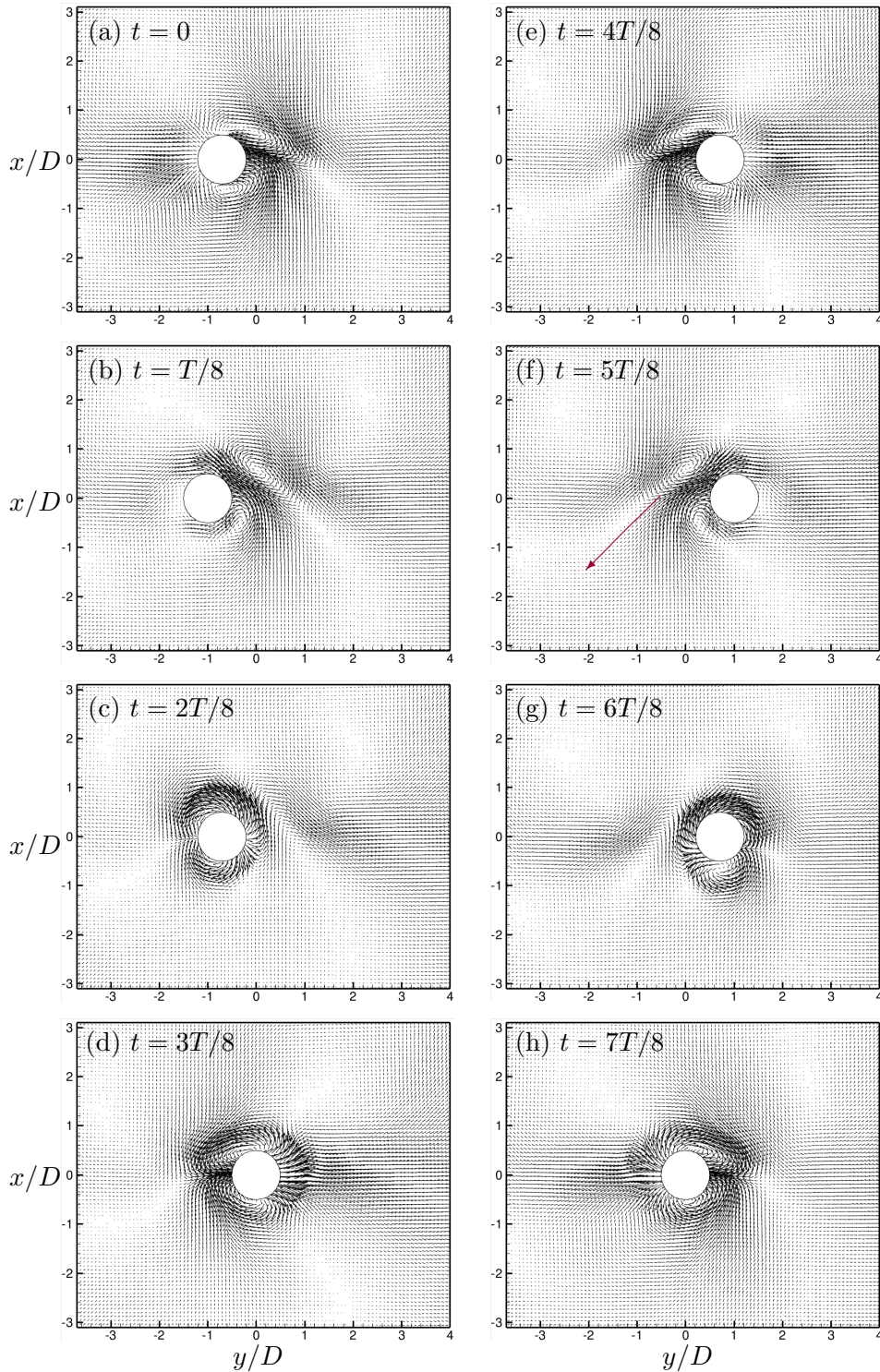


FIGURE 4.36: A sequence of phase-averaged velocity vector fields extracted over one motion period,  $T$ , at  $KC_t=6.28$ ,  $\beta_t=18$  in regime D. Positive and negative velocity contours are denoted by red and blue colours respectively. The arrow in image (f) shows the direction of the created jet flow.



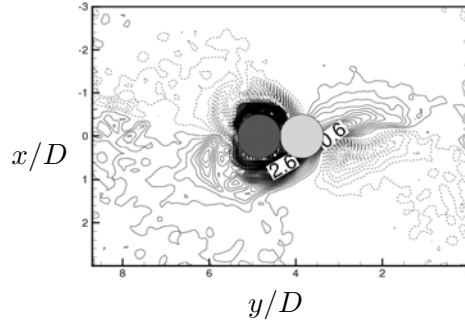


FIGURE 4.37: Contour of phase-averaged non-dimensionalised vorticity of regime D,  $KC_t=6.28$ ,  $\beta_t=18$ . This phase is corresponding to image (b) of figure 4.33. The dark cylinder shows the actual position of the cylinder in that phase of the motion and the grey cylinder is shown to clearly show one diameter location behind the cylinder. This shows the one order of magnitude difference in the magnitude of the  $\omega_z^*$ .

#### 4.4.6 Regimes D

Apart from the two-dimensionality and symmetry of flow with respect to the axis of oscillation in regimes A\*, A and to some extent B, the flow characteristics will change as  $KC_t$  increases at relatively low  $\beta_t$ . Contrary to what was observed in the previous regimes, where the flow induced by the cylinder convects along the direction of cylinder oscillation (Tatsuno & Bearman 1990), the flow characteristics in regime D changes dramatically. At higher values of  $KC_t$ , than that of the two-dimensional regimes, an asymmetry develops in the direction of flow convection around the cylinder. Regime D is the onset of this symmetry breaking in a sense that the flow will no longer convect along the direction of cylinder oscillation. The flow has been characterised by Tatsuno & Bearman (1990) to eventually form a V-shaped vortex pattern.

Figures 4.33, 4.34, 4.35 and 4.36 show the patterns of phase-averaged vorticity and velocity contours for the flow in regime D. Image (a) of figure 4.33 shows the vortices pre-existing from the previous cycles. Generally speaking, in regime D, when the cylinder translates from left to right, asymmetrical vortices, with opposite signs of rotation, are formed on the top and bottom sides of the cylinder. In this case a negative vortex is developed on the lower side of the cylinder and a positive vortex on the upper side as shown in images (a)-(e) of figure 4.33 (vortices B and D in image (b) of figure 4.33, respectively). As the cylinder continues its motion to the right the newly generated vortices from the surface of the cylinder grow in size the break through the vortices formed during the previous cycles. The interaction between the newly generated vortices and the ones from the previous one cause the vortices to cross-annihilate and diffuse (vortex D in image (d)) as the cylinder moves through

them. The negative vortex A which is now weakened due to the diffusion pairs up with the positive vortex D, hence generating a jet flow which can be clearly seen in image (f) of figure 4.36, as the cylinder reaches its end of half cycle. The arrow in image (f) of figure 4.36 shows the direction of the created jet flow. In this instance (images (e) and (f)) vortex D has not yet interacted with any other vortices nor the motion of the cylinder has moved through it yet, hence it is stronger than vortex A. As the vortex D is stronger than vortex A at this stage the jet flow is now convected towards the stronger vortex, *i.e.* vortex D. This jet flow is now creating the left tail of the V-shaped vortex pattern mentioned above as being the characteristic of flow in regime D. The same mechanism is applied to the right tail of this V-shaped vortex pattern. On the other hand while the cylinder is still in its movement from left to right, the negative vortex (vortex B of image (b) in figure 4.33) becomes larger and as the cylinder approaches the end of the mid-point of the motion to the right (image (e)) the vortex wraps around the cylinder. As the cylinder reverses, a stronger part of the vortex remains around the cylinder, vortex B in image (f), while the weaker part of the same vortex, vortex B<sub>1</sub> in image (f), sheds on the opposite direction of the cylinder motion joining the weak positive vortex being created at the same time on the lower surface of the cylinder. As described by Tatsuno & Bearman (1990) and Iliadis & Anagnostopoulos (1998), this negative sign vortex, vortex E in image (h), in the upper part of the cylinder appears in elongated form compared with the one formed at the lower side, vortex F in image (h), and is tilted downwards, in this case.

In addition, two relatively parallel rows of opposite sign vortices exist on both sides of the cylinder, inclined to the horizontal. The strength of these vortices decreases with increasing distance from the cylinder by almost one order of magnitude within one diameter from the cylinder (shown in figure 4.37). When the cylinder reaches its zero velocity position at the right-most point of the cycle, the negative sign vortex has moved further downstream while the positive vortex forming above the cylinder appears in an elongated form with respect to that forming below the cylinder, as shown in image (e) of figure 4.33. It was also observed by Tatsuno & Bearman (1990) that as the value of  $\beta_t$  is increased the flow sheds at larger angles with respect to the axis of oscillation, hence more curvature is visible around the cylinder.

When the cylinder reaches this right-most point of its cycle, the elongated positive vortex core has already commenced convecting downstream, as shown previously.

The motion of the cylinder prior to this snapshot has drawn this positive vortex core downstream and in the negative  $y$ -direction, such that it is now directly behind the cylinder. The negative vortex core, shed from the lower surface of the cylinder, is stretched around the small positive vortex core created adjacent to the body in the lower half, and the body itself. From the velocity vectors it can be seen that a jet of fluid has formed between the two vortex cores (figure 4.36). The jet is travelling in the upstream and positive  $y$ -direction.

As the cylinder reverses, images (e) and (f) of figure 4.33 show that the vortices shed during the previous half-cycle are swept back towards the cylinder. Also, as the sequence of frames in images (e)–(h) of figure 4.33 shown, the stronger vortex (vortex A) is convected back along the cylinder surface and shed obliquely across the axis of oscillation. Hence, the direction of the flow induced by the cylinder oscillation deviates from the direction of oscillation. In consequence, a strong vortex is developed on only one side of the axis of oscillation in each half cycle and the fluid mass accompanying the vortex is convected obliquely to the other side of the axis of oscillation (Tatsuno & Bearman 1990). As the cylinder starts its motion from right to left, starting from image (e) of figure 4.33, the negative vortex structure mentioned earlier wraps around the small positive vortex core and the cylinder towards the upper side of the cylinder. This negative vortex starts strengthening significantly. It is also clear from the sequence of images in figure 4.33 that one vortex is shed during each half-cycle. The same trend can be seen in figures 4.34 and 4.35. The solution over a large number of oscillation cycles revealed the absolute periodicity of the phenomenon, which made it possible to do phase-averaging. These results are similar to that of Tatsuno & Bearman (1990) and Iliadis & Anagnostopoulos (1998).

#### 4.4.7 Regime E

According to the classification of Tatsuno & Bearman (1990) the flow patterns belonging to regime E represent temporally stable V-type vortex streets. Figure 4.38 shows typical examples of the behaviour of the flow in this regime, in which the flow changes with time. As the flow in this regime is not phase-locked the instantaneous results are presented. The instantaneous non-dimensionalised vorticity contours in figure 4.38 were taken in a sequence during one run. Tatsuno & Bearman (1990) discuss how the flow pattern in this regime temporarily resembles that in regime D (refer to §4.4.6). Here,

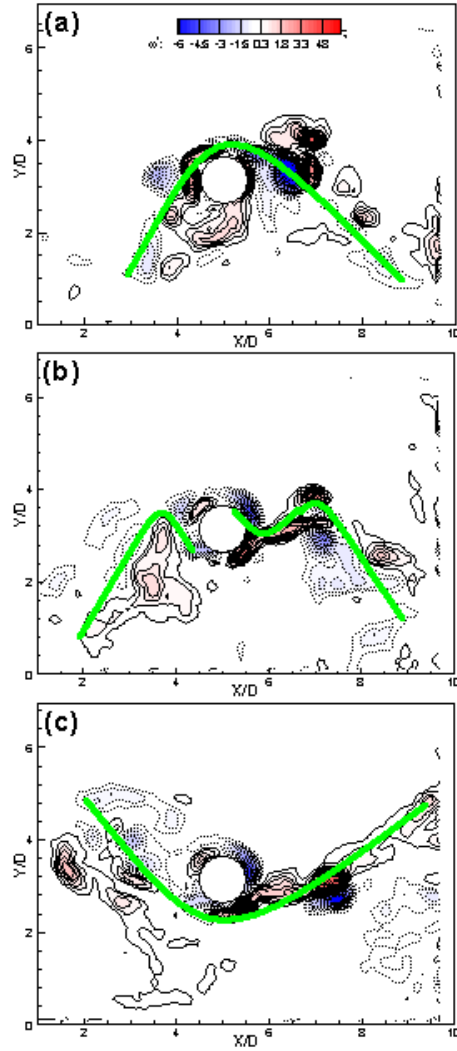


FIGURE 4.38: Patterns of instantaneous dimensionless vorticity,  $\omega_z^*$ , for the sinusoidally oscillating flow past the circular cylinder in regime E at  $KC_t=5$  and  $\beta_t=80$ . For dimensionless vorticity  $\omega_z^*$ ,  $\Delta[\omega_z^*]=0.3$ . The cylinder is oscillating horizontally from left to right, at its most left position in the cycle. (a) shows cycles before change in the direction, (b) transition in the change in the direction, and (c) cycles after transition.

however, the flow that convects to one side of the axis of oscillation intermittently changes direction to the other side. This switching of the flow occurs at irregular intervals and is presumably triggered by small disturbances. Elston (2005) speculated that the onset of regime E may be caused by the onset of an instability of the quasi-periodic mode, which leads to an intermittency in the direction of the vorticity shed from the cylinder. Figures 4.38a and c show temporally stable flow patterns, whereas figure 4.38b shows the transient flow changing from one side to the other. Previous experimental and numerical studies by Dütsch *et al.* (1998), Iliadis & Anagnostopoulos (1998) on flow in regime E, have failed to capture this intermittent change. Although

Nehari *et al.* (2004) have also investigated regime D and observed the switching in their three-dimensional simulation at  $KC_t=6.5$  and  $\beta_t=20$ , Elston (2005) has shown that their simulation might be better categorised as being of regime E, rather than D. The present results reveal this intermittent change in the direction of the V-shape vortex in regime E experimentally, which has only been observed previously on a few occasions, see for example Tatsuno & Bearman (1990). The flow in this regime has a strong three-dimensional structure.

#### 4.4.8 Regimes F

Figures 4.39, 4.40, 4.41 and 4.42 show a cross-sectional view and sequence of phase-averaged PIV results of out-of-plane vorticity ( $\omega_z^*$ ),  $V/U_{\max}$  and  $U/U_{\max}$  velocity contours and velocity vector fields extracted over one motion period,  $T$ , in regime F. Regime F is characterised by Tatsuno & Bearman (1990) to be a double-pair diagonal regime, in which vorticity is shed diagonally with respect to the axis of oscillation. When starting the cylinder from rest, symmetric vortex shedding first occurred in much the same way as described in §4.4.4. However, after a few cycles of oscillation, the symmetric flow pattern ceased to exist. The symmetric vortex formation became unstable, resulting in the occurrence of a stronger vortex on one side of the cylinder and a weaker one on the other side. Both vortices that were formed did not cross the axis of oscillation, but moved away from it (Dütsch *et al.* 1998).

According to Tatsuno & Bearman (1990) two related features of the shedding wake distinguish the flow past an oscillating cylinder in regime F. First, the wake is shedding at an angle to the in-flow or axis of oscillation. Second, the fluid structures are shed in vortex pairs. As it was discussed in §4.3.2.7 based on observations of the results of Elston (2005) and present flow visualisations it was proposed that this regime could be characterised as a  $2P + 2S$  pattern instead of the so-called  $2P$  shed per cycle. The PIV results of the present section also confirm and support this proposal. Vortex C labelled in figure 4.39 is the single vortex shed per cycle.

The vortex pair structures induce a jet of fluid travelling in the positive  $y$ -direction, as the cylinder moves from left to right, or the negative  $y$ -direction, when the motion is reversed; the same jet is responsible for the angle the wake is shed. Figure 4.43 compares the absolute values of peak dimensionless vorticity,  $|\omega_z^*|$ , between the individual vortices in the vortex pairs (A-B) and the single vortex (C) in each cycle. Clearly, the magnitude

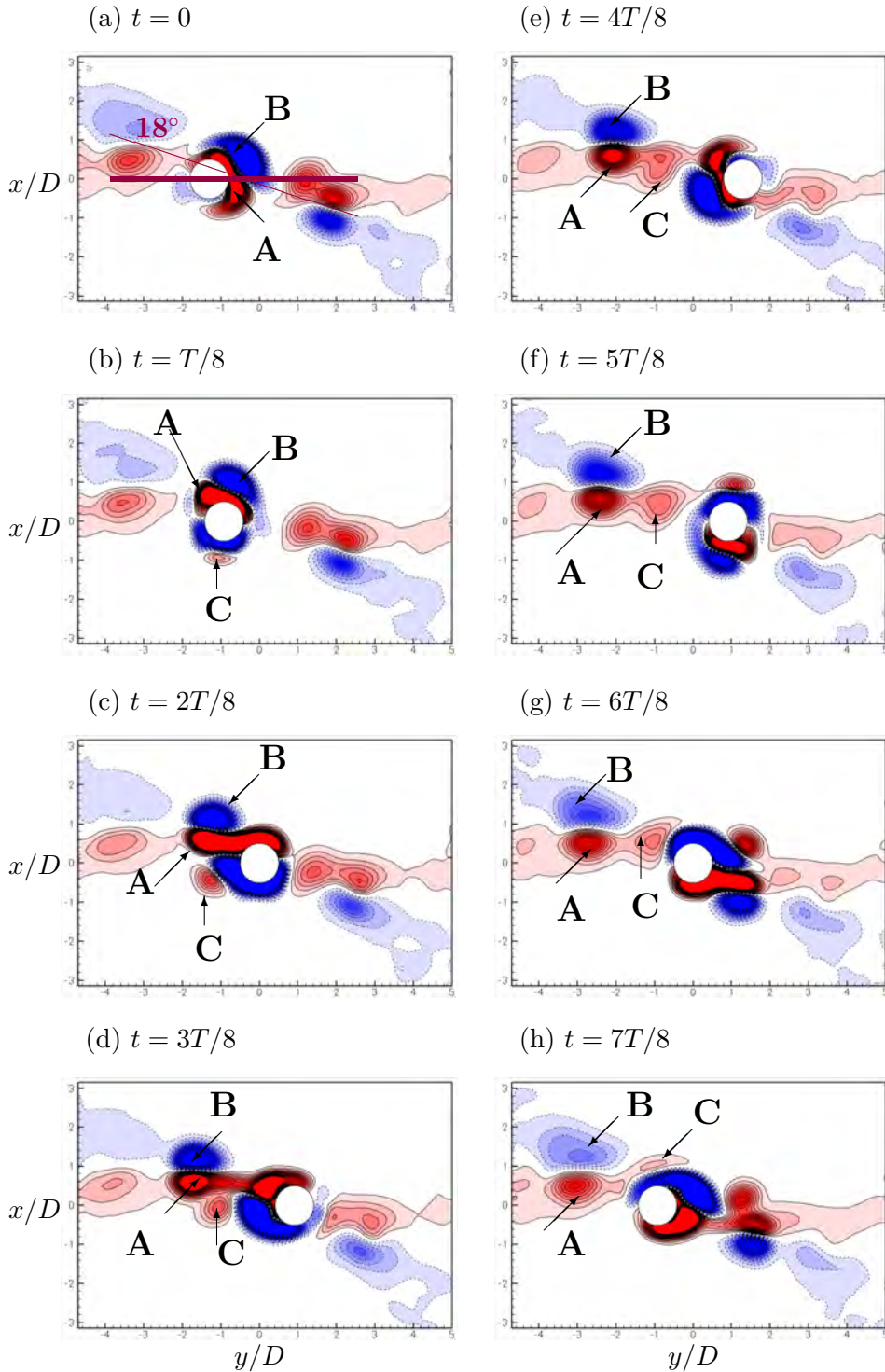


FIGURE 4.39: A sequence of phase-averaged non-dimensionalised out-of-plane vorticity contours,  $\omega_z^*$ , extracted over one motion period,  $T$ , at  $KC_t=8.17$ ,  $\beta_t=30$  in regime F. Positive (counter-clockwise) and negative vorticity contours are denoted by red and blue colours respectively. Vorticity contours are evenly spaced over the range  $[-1.5:1.5]$ ; with  $\Delta[\omega_z^*] = 0.1$ . Thick line in image (a) shows the axis of oscillation. The angle between the shed vortices and the axis of oscillation is  $18^\circ$  in this case.

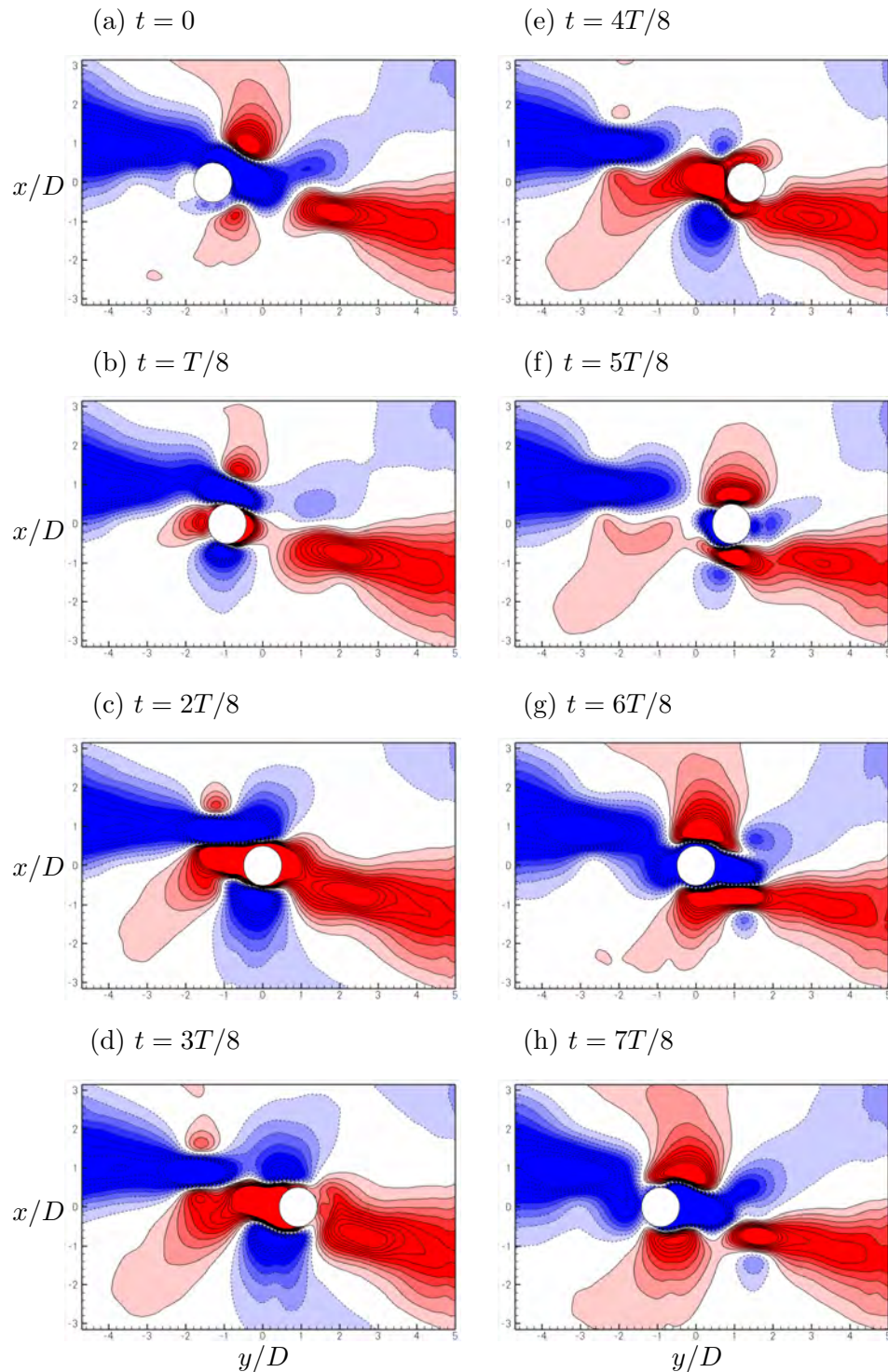


FIGURE 4.40: A sequence of phase-averaged non-dimensionalised  $V$  velocity contours, extracted over one motion period,  $T$ , at  $KC_t=8.17$ ,  $\beta_t=30$  in regime F. Positive and negative velocity contours are denoted by red and blue colours respectively.  $V$  velocity contours are evenly spaced over the range  $[-0.25:0.25]$ ; with  $\Delta[V/U_{\max}] = 0.025$ .

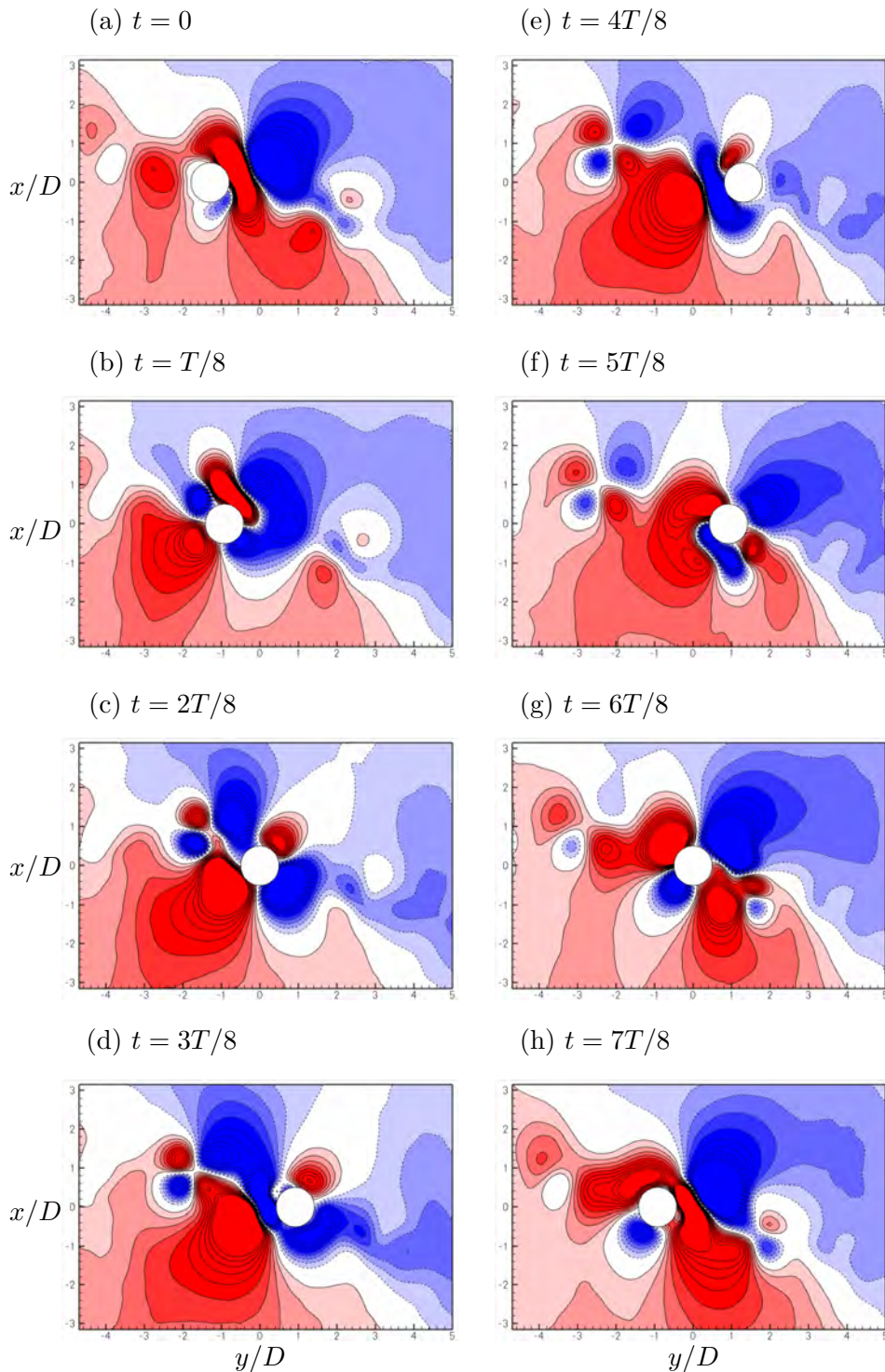


FIGURE 4.41: A sequence of phase-averaged non-dimensionalised  $U$  velocity contours, extracted over one motion period,  $T$ , at  $KC_t=8.17$ ,  $\beta_t=30$  in regime F. Positive and negative velocity contours are denoted by red and blue colours respectively.  $U$  velocity contours are evenly spaced over the range  $[-0.2:0.2]$ ; with  $\Delta[U/U_{\max}] = 0.02$ .



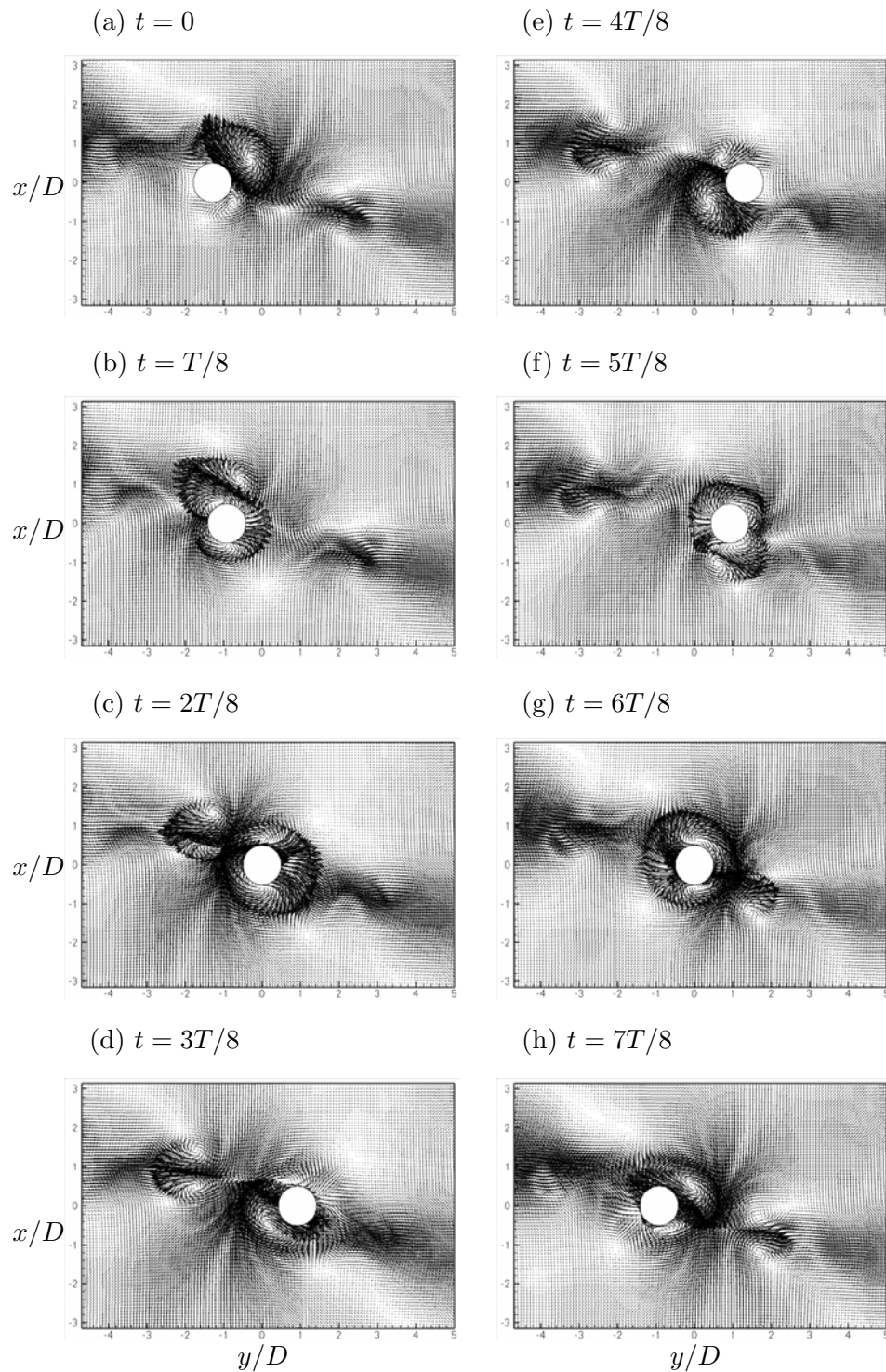


FIGURE 4.42: A sequence of phase-averaged velocity vector fields extracted over one motion period,  $T$ , at  $KC_t=8.17$ ,  $\beta_t=30$  in regime F. Positive and negative velocity contours are denoted by red and blue colours respectively.

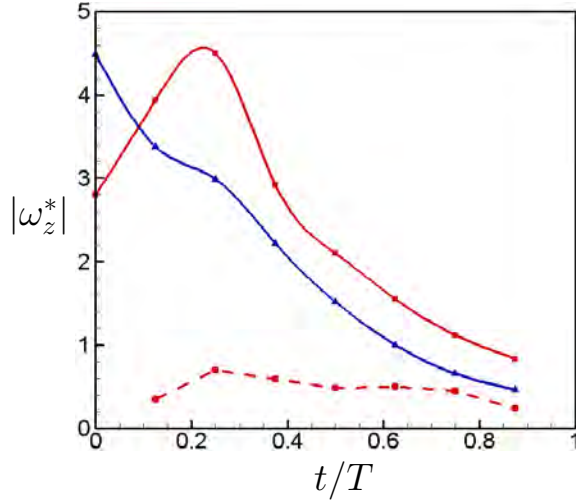


FIGURE 4.43: Distribution of absolute dimensionless peak vorticities,  $|\omega_z^*|$ , of three vortices A (solid red line, square), B (solid blue line, triangle), and C (dashed red line, circle) shown in figure 4.39. These data are for regime F,  $KC_t=8.17$  and  $\beta_t=30$  and are extracted from the phase-averaged PIV analysis. The lines are only showing the trend of distribution of  $\omega_z^*$ .

of the single vortex, denoted as C in images (b)–(h) of figure 4.39, is approximately less than half of the value of the pairs vortices A and B. This figure also shows that the magnitude of the positive vortex of the pair (vortex A) over most of the phases is greater than that of the negative vortex of the pair (vortex B), except at the beginning of the motion. Since vortex B is stronger than vortex A at the beginning of the motion, the relatively strong jet flow between these two vortices will be tilted towards vortex B. Once the cylinder starts its motion from left to right, images (b–e), it breaks through vortex B, and due to diffusive cross-annihilation of vortex B and the newly opposite-sign generated vortex from the cylinder surface and vortex A, vortex B becomes weaker in comparison with its strength in image (a). This implies that the direction of the jet flow is now deflected towards vortex A rather than vortex B and is also determined by the strength of vortex pair A-B.

As already mentioned the motion of the cylinder is responsible for inducing the vortex pairing. This is clearly reflected in figure 4.39, which indicates that the difference in the magnitude of the two vortices resulted in a motion of the vortices away from the cylinder at an angle of approximately  $18^\circ$  with respect to the axis along which the cylinder oscillated. Elston (2005) indicated that the above-mentioned angle is  $25^\circ$ , but Tatsuno & Bearman (1990) did not provide any measured values of this angle. However, Nehari *et al.* (2004) mentioned in their article that the angle of inclination of the diagonal pattern with respect to the longitudinal axis increases with  $KC_t$ . The results

of the flow visualisations of Tatsuno & Bearman (1990) showed that for  $KC_t < 10$  the angle of inclination of the diagonal vortex pattern is small, and, in the far field, the pattern tends to be parallel to the longitudinal axis. As  $KC_t$  increases ( $KC_t > 10$ ) the angle of inclination of the pattern increases, and vorticity is convected along a straight line that, in the far-field, maintains its angle of inclination. Consequently as the value of  $KC_t$  in this study was less than those used by Elston (2005) and Nehari *et al.* (2004), which were 10 and 8.5 respectively, the smaller values of inclination angle observed in this investigation appear reasonable. It should also be mentioned that although it has not been examined in this research, but Tatsuno & Bearman (1990) have observed that at larger  $\beta_t$  the convection of vortices away from the body occurs at large angles to the oscillation direction.

## 4.5 Chapter Summary

In this chapter the flow around a translationally oscillating circular cylinder at low  $KC_t$  and  $\beta_t$  numbers was investigated experimentally. PIV and flow visualisation techniques were used to quantify and qualitatively investigate the flow around a sinusoidally oscillating circular cylinder in water initially at rest for the ranges of system parameters  $1.6 < KC_t < 15$  and  $5 < \beta_t < 160$ , respectively. A number of measures were used to establish the properties of the flow which included examining the vorticity field over a period of cylinder motion and the long exposure particle visualisation images.

An interesting feature that was also clarified was the absence of vorticity shedding observed in regime A. Tatsuno & Bearman (1990) delineated the difference between regimes A\* and A as the presence of vorticity shedding in regime A. In the observation of flows in both regimes, no far-field concentrations of vorticity were observed to occur and it is concluded that there is no difference between the flows of either regime in terms of the vorticity contours. One difference that was observed was that the particles shed for low Keulegan–Carpenter numbers remained in the near cylinder region, up to  $1D$  from the cylinder surface. The difference between regimes A\* and A might better be defined by the size and strength of the generated vortices.

The results for regime B, as was first discussed by Tatsuno & Bearman (1990), reveal the onset of three-dimensionality in this type of flow. The spanwise velocity vectors distribution clearly shows this feature.

Contrary to the two-dimensional numerical investigations of Iliadis & Anagnos-

topoulos (1998) and Dütsch *et al.* (1998) and the results of Nehari *et al.* (2004), the intermittent switching in the direction of the V-shaped vortex pattern in regime E has been observed. However, this switching was observed irregularly and its cause has not been yet determined, but as mentioned by Tatsuno & Bearman (1990) this is presumably triggered by small disturbances in the flow.

Tatsuno & Bearman (1990) mentioned that the convection of vortices away from the body at large angles to the oscillation direction seems to be similar to the formation of two vortex pairs per cycle at larger  $\beta_t$ , which has been described as the  $2P$  pattern by Williamson (1985). It was proposed in the present study that this regime could be characterised as the  $2P + 2S$  pattern shed per cycle.

## Chapter 5

# The ‘Swimming’ Cylinder

### 5.1 Introduction

Previous two-dimensional numerical studies have shown that a circular cylinder undergoing both oscillatory rotational and translational motion can generate thrust so that it will actually self-propel through a stationary fluid, the so-called “*swimming cylinder*”. This was shown by Blackburn *et al.* (1999) to happen only at certain phase angle differences between the two motions,  $\Phi$ . Although a cylinder undergoing a single oscillation has been thoroughly studied, see Chapter 4, the combination of the two oscillations has not received much attention until now. So far, only the investigations by Blackburn *et al.* (1999), Elston (2005), and more recent the ones by Al-Mdallal (2004), Kocabiyik & Al-Mdallal (2005), Elston (2005), Nazarinia *et al.* (2009) have reported on the combined oscillatory motion of a circular cylinder. Among them the work by Blackburn *et al.* (1999) and Elston (2005) are the only ones on the swimming cylinder (*i.e.* the quiescent fluid case).

A number of interesting features have been shown to occur as a result of combining the two motions. Of principal interest is the jet flow produced by the cylinder when the two imposed motions are in opposition of phase. The propulsive force produced by the cylinder causes it to accelerate until eventually reaching a terminal speed of 33% of the peak translational speed (Blackburn *et al.* 1999). Naturally, the above mentioned phenomena are true when the two motions are in-phase, the difference is that the jet flow appears on the opposite side.

The results of Blackburn *et al.* (1999) were obtained via numerical simulations but to date no experimental studies into the effect of combining an oscillatory rotational and translational motion of a circular cylinder in either quiescent fluid or in external flow are known. However, a similar form of motion, *Carangiform motion*, is observed in

nature, for example, the motion used by a tuna fish to propel through water. This mode of oscillation necessitates a twist at each extreme of the oscillation to give backward inclination to the moving wing-like surface, that is, to a vertically oscillating cetacean tail, or to a fish's horizontally oscillating caudal fin. However, the propulsive jet that is produced from Carangiform motion only occurs when the oscillations are in-phase (Lighthill 1986), see §2.6.1.

The purpose of the present study is to investigate not only the near-wake structure of the combination of the two forcing mechanisms, but also to extend this to examine the three-dimensional nature of the wake, which is yet to receive any attention. The results of the present chapter incorporate both experimental and numerical studies, although the main focus is on the experimental investigations. The numerical simulations, *i.e.* Floquet stability analysis and DNS, are used as tools to provide further insights into the wake flows produced. To characterise the experimental flows, as discussed in Chapter 3, PIV was employed.

In the next sections a description of the experimental and numerical methods, and the parameter range under investigation, are given. An overview of the linear Floquet stability analysis is given. This is followed by a presentation of results confirming the thrust generation. The three-dimensionality of the flow around the swimming cylinder is also established, and the three-dimensional transition characterised. Following on from the study by Blackburn *et al.* (1999), the following questions arise:

- What is the behaviour of flow around a swimming cylinder? Does the 2D model capture the main features of real 3D flows?
- Is there any three-dimensional instability involved?
- At what  $Re$  does the transition to three-dimensional flow occur?
- What three-dimensional modes occur and how do they influence the wake and swimming ability?

PIV measurements along with Floquet stability analysis have been employed to answer these questions in this chapter.

The next chapter, Chapter 6, reports on the combined oscillatory motion of a cylinder in a free-stream. The current chapter extends the numerical study of Blackburn

*et al.* (1999) and Elston (2005) both experimentally and numerically: recording detailed vorticity fields in the wake and using these to elucidate the underlying physics; examining the three-dimensional wake development experimentally; and determining the three-dimensional stability of the wake. Experiments conducted in the laboratory are presented for a given parameter range, confirming the results from Blackburn *et al.* (1999).

## 5.2 Experimental Arrangement and Parameters

The motion profiles and the parameters defining the combined translational and rotational oscillatory motion of a circular cylinder in a quiescent fluid were given in Chapter 3 and §3.2, and also shown schematically in figure 3.4. Equations 3.3 and 3.9 defined the harmonic motions of the cylinder translationally and rotationally, respectively. It is seen from the equations that addition of the rotational oscillation to the translational oscillatory motion, mentioned in Chapter 4, adds three more independent variables to the problem. These are the rotational amplitude, the frequency and the phase difference between the two oscillatory motions, in addition to translational amplitude and frequency. This results in five dimensionless variables that in combination specify uniquely the state of the system. These five variables are repeated below:

- The translational Keulegan–Carpenter number:

$$KC_t = \frac{U_{\max_t}}{f_t D} = \frac{2\pi A_t}{D} \quad (5.1)$$

- The translational Stokes number:

$$\beta_t = \frac{f_t D^2}{\nu} \quad (5.2)$$

- The rotational Keulegan–Carpenter number ( $A_\theta$  in radians):

$$KC_\theta = \frac{U_{\max_\theta}}{f_\theta D} = \pi A_\theta \quad (5.3)$$

- The rotational Stokes number:

$$\beta_\theta = \frac{f_\theta D^2}{\nu} \quad (5.4)$$

- The phase angle between translation and rotation motions:

$$\Phi. \quad (5.5)$$

The velocity ratio, taken at the surface of the cylinder, between the translational and rotational motions is expressed as:

$$V_R = \frac{U_{\max_t}}{U_{\max_\theta}} = \frac{\beta_t KC_t}{\beta_\theta KC_\theta}. \quad (5.6)$$

In the previous studies of Blackburn *et al.* (1999) and Elston (2005), referred to previously in Chapter 2, the translational and rotational Keulegan–Carpenter numbers were specified as  $KC_t = KC_\theta = \pi$ , and the translational Stokes number as  $\beta_t = 90$ . As Elston (2005) also points out, on a purely translational oscillation basis, this places the flow generated from the cylinder in three-dimensional regime B on the  $(KC_t, \beta_t)$ -space map (see figures 2.18, 2.19 and 2.20). The rotational Stokes number was also fixed to a single value, that of the translational Stokes number, such that  $\beta_t = \beta_\theta = 90$ . The phase angle between the motions was fixed at  $\Phi = \pi$ , which has been shown in Blackburn *et al.* (1999) to result in net thrust on the cylinder along the axis perpendicular to the axis of oscillation. The final parameter required to determine the motion of the cylinder was the rotational Keulegan–Carpenter number,  $KC_\theta$ . In Blackburn *et al.* (1999) and Elston (2005) this was set to the value  $KC_\theta = \pi$ .

In the present study, in analogy with the studies of Blackburn *et al.* (1999) and Elston (2005), *i.e.* the swimming cylinder case, the frequency ratios were held to be the same, *i.e.*  $\beta_t = \beta_\theta = \beta$ , and the phase difference between the two motions was set to  $\Phi = \pi$ . Some preliminary investigations were conducted into the effect of varying the phase difference between two motions, both experimentally and numerically. The combination of oscillatory motions was found to produce a wide range of flow patterns depending on the phase difference between the two motions. Figure 5.1 shows an example of the near-wake structure for three phase differences. It can be seen that by changing the phase angle, the flow field around the cylinder changes dramatically. Notably, it is clear that only the in-phase or opposing phase cases ( $\Phi = 0, \pi$ ) produce a jet-like flow (The results for  $\Phi = 0$  are not shown in figure 5.1). The other phases result in a flow with a somewhat preferred direction without the jet-like feature and dramatically different from the  $\Phi = 0, \pi$  cases. It should be noted that Elston (1997) showed in his numerical simulations that the phase differences within  $\pm 30^\circ$  also generate jet-like flow, but the flow convected at an angle and is not perpendicular to the axis of oscillation anymore. Additionally for all of the experiments in this chapter, the associated translational and rotational Keulegan–Carpenter numbers are  $KC_t = KC_\theta = \pi$ . The non-dimensional frequency was chosen to cover the range  $45 \leq \beta \leq 200$ , consequently the range of Reynolds



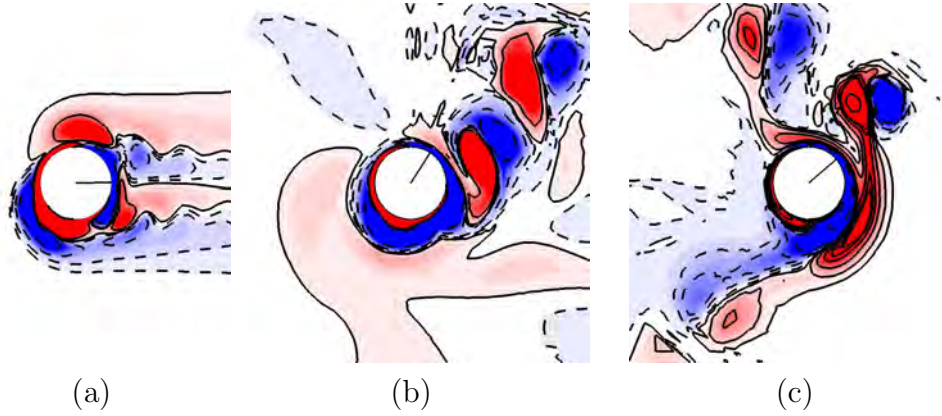


FIGURE 5.1: Contours of vorticity around the cylinder undergoing combined translational and rotational oscillation at  $KC = \pi$ ,  $\beta = 90$ , and (a)  $\Phi = \pi$ , (b)  $\Phi = \pi/2$ , (c)  $\Phi = \pi/4$ , taken at  $t/T = 0$  from numerical simulation explained in §5.4. The dashed lines (enclosing blue) correspond to clockwise direction of vorticity (negative). The solid lines (enclosing red) correspond to counterclockwise direction of vorticity (positive).

number covered was  $141 \leq Re \leq 628$ . As a result of fixing the above parameters the equation for the velocity ratio for all the present experiments was held constant at the value  $V_R = 1$ . The effect of varying this ratio was not investigated in this thesis as was the case in Elston (2005).

The experimental technique used here is the same as that described in Chapter 3 and used for Chapter 4. For these particular experiments the flow was seeded with spherical polyamide particles with a mean diameter of  $20\mu\text{m}$  and specific gravity of 1.016. In this system, the particles were illuminated using two miniature Nd:YAG laser sources (Continuum Minilite II Q-Switched). The planes of interest for these experiments were the  $yz$ - and  $xy$ -planes, being the spanwise and streamwise directions, as was shown in figure 3.4. The thickness of the laser sheet was measured to be less than 2mm. Pairs of images were captured on a high resolution CCD camera (Cooke pco4000) with a maximum resolution of  $4008 \times 2672$  pixels. The camera was equipped with a Nikkor 105mm lens (Nikon Corporation, Japan). An interrogation window of  $32 \times 32$  (with an initial window size of  $64 \times 64$ ) pixels was found to give satisfactory results with 50% overlap. More than 98% of the vectors were valid for all the experiments. This window size corresponds to an average interrogation window of  $0.064D \times 0.064D$ . It was possible to obtain a measurement resolution of  $249 \times 166$  (total of 41334) vectors in each field of view. The overall field of view was  $4008 \times 2672$  pixels ( $8.0D \times 5.3D$ ). Phase-averaged vorticity and velocity fields are presented using 500 or more instantaneous measurements. It should also be noted that the cylinder was fitted with an end

plate to reduce the end effects. The end plate was designed following recommendations by Stansby (1974), and consisted of a circular plate with a diameter of  $9D$ ; schematics are shown in figures 3.3 and 3.4. All the images were captured at pre-selected phase angles in the oscillation cycle (phase-locked). Phase-averaged vorticity and velocity fields are presented using 30 or more instantaneous measurements. The vorticity fields were calculated with the technique developed by Fouras & Soria (1998). The velocity and spatial coordinates are non-dimensionalised by the maximum velocity of the translational cylinder motion,  $U_{\max_t}$ , and the cylinder diameter,  $D$ , respectively.

Same as for other quiescent experiments outlined in Chapter 4, special care was always taken to ensure near quiescency of the flow. Prior to each set of experiments, a honeycomb device was drawn through the working volume to break up large-scale flow structures into smaller scales, minimising the time required to reach the background noise level. Typically, this background level, measured by the norm of velocity magnitude, was kept less than 1.41% of  $U_{\max_t}$  ( $0.1\text{mm s}^{-1}$  or less).

### 5.3 Validation

In this section the results for the swimming cylinder case, *i.e.*  $\Phi = \pi$ , are compared with numerical simulations to provide confidence in the experimental predictions before other cases are examined. This proceeds in three stages: The validation case applied first with the two individual oscillatory motions and then with the combined motion. As was mentioned in §4.4.1 a useful validation case for the purely translational oscillation of a cylinder in a quiescent fluid is the experimental study of Dütsch *et al.* (1998). This is combined with our numerical simulations at  $KC_t = 5$  and  $\beta_t = 20$  (see figure 4.12). These parameters place the wake flow in two-dimensional regime A (see figures 2.18, 2.19 and 2.20). Other researchers, *e.g.* Uzunoglu *et al.* (2001), Guilmineau & Queutey (2002) and Nehari *et al.* (2004) also used the numerical and experimental results of Dütsch *et al.* (1998) to validate their numerical codes against. The numerical results (explained in the next section) also match well with those of Dütsch *et al.* (1998). Dütsch *et al.* (1998) was found to be a key article containing quantitative experimental results at low  $KC_t$  and  $\beta_t$  numbers.

To provide some validation for the experiments in the 3D regime, the spanwise wavelength was measured (using the technique explained in §5.5). This was for  $KC_t = 2.51$  and  $\beta_t = 142$  ( $Re_t = 356$ ), corresponding to regime B from Tatsuno & Bearman

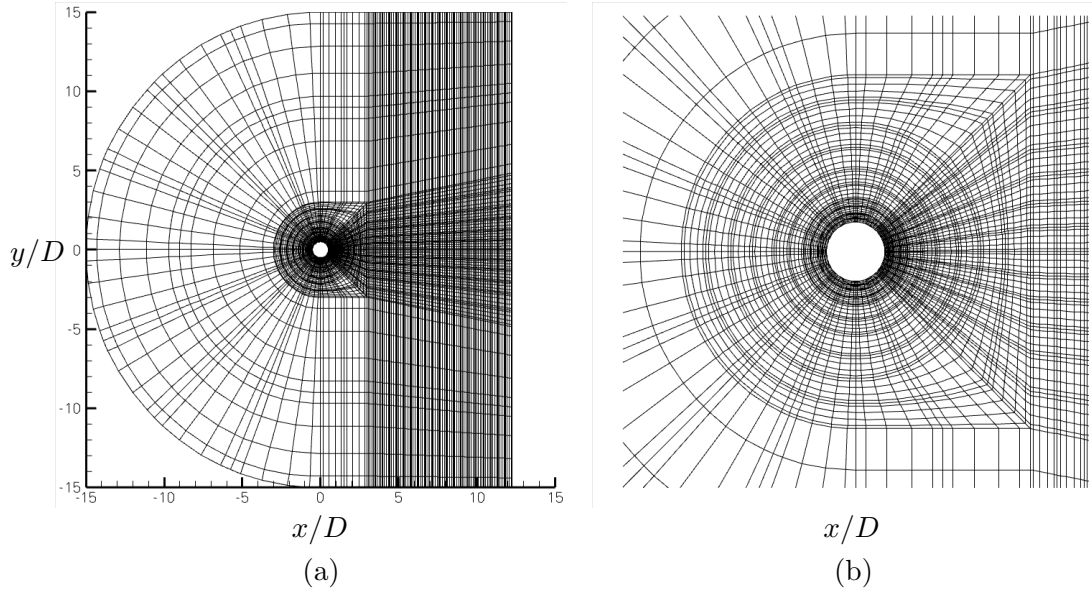


FIGURE 5.2: Outline of the 518-element  $30D \times 30D$  domain,  $s$ , used for the swimming cylinder simulations.

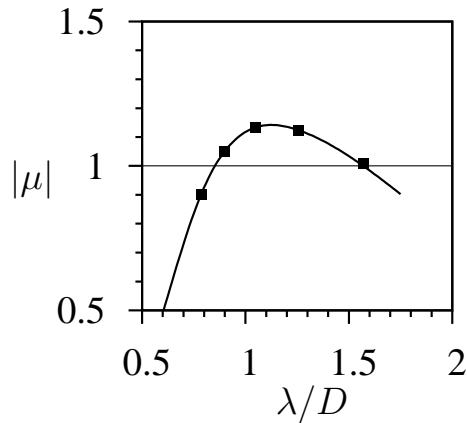


FIGURE 5.3: Floquet multipliers for  $KC_t = 2.75$  for the three-dimensional instability of regime B at  $\beta_t = 80$ . The current results (solid line) are compared with those from Elston *et al.* (2006) (squares).

(1990) (figure 12, Tatsuno & Bearman (1990)). It was found to be within 4% of the previously reported value from Tatsuno & Bearman (1990) ( $\lambda = 1.04D$  cf.  $1.0D$ ).

## 5.4 Numerical formulation

As outlined earlier in the thesis the main focus of the present study is the experimental measurement of the flow around an oscillating cylinder, and in particular the swimming cylinder. Two-dimensional DNS and Floquet stability analysis were used to help further understand the experimental results and to provide alternative insights into the physics of the flow, but they are not a main focus. In this regard, the description of the methodology is purposefully brief. Comprehensive descriptions of the methods have

been given in previous articles. Details of the method in general are given by Karniadakis & Sherwin (2005), and the implementation used here by Thompson *et al.* (1996). The code employed has been well-proven for use in bluff-body problems, and Floquet stability analysis. There are a large number of papers available using the present numerical code, *e.g.* Sheard *et al.* (2003); Ryan *et al.* (2005); Leontini *et al.* (2007); Leontini (2007); Griffith (2007); Lo Jacono *et al.* (2008). However, a brief outline of the method is provided here.

The 2D base flows (*i.e.* the time dependent wake flows) for the present study were calculated by solving the incompressible, time-dependent Navier–Stokes equations. The discretisation method employed was a spectral-element method, using seventh-order Lagrange polynomials associated with Gauss–Lobatto–Legendre quadrature points. The time integration was executed using a three-step splitting scheme (Canuto *et al.* 1990; Karniadakis *et al.* 1991; Thompson *et al.* 2006a). A computational domain extending  $30D \times 30D$  was split into 518 elements, the majority of which were concentrated in the boundary layer and wake region. Figure 5.2 shows the mesh used. The resolution, element distribution and domain size are consistent with those used successfully in the previous similar studies. At the cylinder surface, a time-dependent Dirichlet condition was utilised that varied sinusoidally in time according to the driven rotational oscillation. To account for the translational oscillation, the calculations were performed in an accelerating frame of reference attached to the cylinder. The frame acceleration was added to the Navier–Stokes equations to account for this. The method employed is second-order in time with the Courant condition controlling the timestep. The unit time step employed was 0.010 ( $\approx 1250$  timestep/cycle) for  $\beta \leq 70$  and 0.005 ( $\approx 2500$  timestep/cycle) for  $\beta \geq 70$ .

For the Floquet stability analysis, perturbation equations were formed by decomposing the flow into base and perturbation components, subtracting the base flow, and linearising the result. These equations were then integrated forward in time using the same spectral-element technique as outlined above. Floquet multipliers were calculated using the change to the perturbation field at successive instances one period apart. The dominant multiplier is obtained by taken the ratio of (a norm of) the perturbation field and the field one period before. This ratio converges to the dominant multiplier after many periods. It is possible for the multiplier to oscillate. This is an indication that the Floquet multiplier does not have the same period as the base flow. In this case

the dominant multipliers are complex conjugate pair. The complex multipliers were resolved using Arnoldi decomposition.

Figure 5.3 shows a validation of our technique with previous numerical simulations of Elston *et al.* (2006). Here, the magnitude of the dominant Floquet multiplier as a function of wavelength is shown. The validation case studied is a pure translational motion with  $KC_t = 2.75$  and  $\beta_t = 80$  ( $Re_t = 220$ ), corresponding to regime B of Tatsuno & Bearman (1990). The agreement was found to be excellent throughout the range tested.

## 5.5 Experimental technique: Spanwise wavelength measurement

The technique used to extract the dominant spanwise wavelength,  $\lambda$ , from the experimental measurements is based on spatial autocorrelation. The spatial autocorrelation function contain a peak, which corresponds to the regular spacing of vorticity or velocity variations along the span. This gives the so-called wavelength. In the following sections a brief mathematical definition of the autocorrelation is given, which is followed by the explanation of how the technique is implemented.

### 5.5.1 Autocorrelation

Autocorrelation is the cross-correlation of a signal with itself. Informally, it gives the similarity between observations as a function of the time or space separation between them. It is a mathematical tool for finding repeating patterns, such as the presence of a periodic signal which has been buried under noise, or identifying the missing fundamental frequency in a signal implied by its harmonic frequencies. It is often used in signal processing for analysing functions or series of values, such as time domain signals (Fouras 1997). In this chapter the autocorrelation function is used to identify the spanwise wavelengths of the vortex structures along the span of the cylinder.

In statistics, the autocorrelation of a random process describes the correlation between values of the process at different points in time, as a function of the two times or of the time difference. Let  $X$  be some repeatable process, and  $i$  be some point in time after the start of that process ( $i$  may be an integer for a discrete-time process or a real number for a continuous-time process). Then  $X_i$  is the value (or realisation) produced by a given run of the process at time  $i$ . Suppose that the process is further known to

have defined values for mean  $\mu_i$  and variance  $\sigma_i^2$  for all times  $i$ . Then the definition of the autocorrelation between any two times  $s$  and  $t$  can be defined as

$$R(s, t) = E[(X_t - \mu_t)(X_s - \mu_s)], \quad (5.7)$$

where “E” is the expected value operator.

If  $X_t$  is a second-order stationary process, a stochastic process whose joint probability distribution only applied to pairs of random variables from the time-series does not change when shifted in time or space, then the mean  $\mu$  and the variance  $\sigma^2$  are time-independent, and further the autocorrelation depends only on the difference between  $t$  and  $s$ : the correlation depends only on the time-distance between the pair of values but not on their position in time. This further implies that the autocorrelation can be expressed as a function of the time-lag, and that this would be an even function of the lag  $\tau = t - s$ . This gives the more familiar form

$$R(\tau) = E[(X_t - \mu)(X_{t+\tau} - \mu)], \quad (5.8)$$

and the fact that this is an even function can be stated as

$$R(\tau) = R(-\tau). \quad (5.9)$$

Note that the above discussion focuses on time as the independent variable. For the current context, the method can be used to extract spatial wavelength by replacing time by a spatial variable, in this case the spanwise distance. The spatial autocorrelation function will contain a peak at the origin and two symmetrical secondary peaks, as shown in figure 5.4. The distance between the peak at the origin and the secondary peak corresponds to the distance, here spanwise wavelength ( $\lambda/D$ ), between the velocity or vorticity distribution peaks.

### 5.5.2 Wavelength Extraction

In order to be able to extract the wavelengths of the spanwise vortex structures along the span of the cylinder, the  $V$  velocity and  $\omega_x$  vorticity contours were extracted from the instantaneous results at 16 positions behind the cylinder with an interval of  $0.5D$  from the surface of the cylinder, *i.e.*  $x/D = 0.5$ . Figure 5.5 shows the positions of lines along which data were extracted. Then, at each position behind the cylinder the spatial autocorrelation is evaluated for each set of  $V$  velocity and  $\omega_x$  vorticity fields,

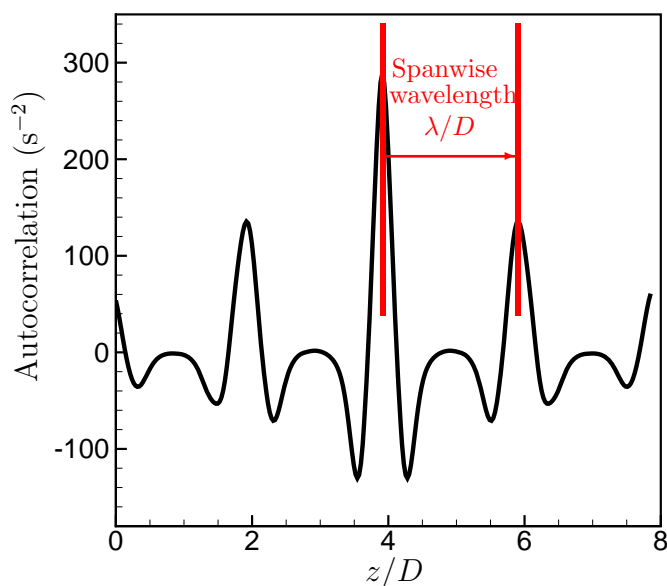


FIGURE 5.4: Spatial autocorrelation function for  $\beta=90$ , based on streamwise vorticity.

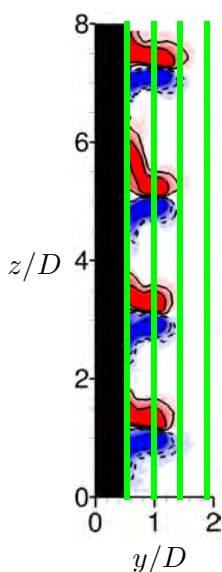


FIGURE 5.5: Lines showing the positions where the spatial autocorrelations are calculated and the streamwise and  $V$  velocity data are extracted.

separately. Figure 5.4 shows a sample of the autocorrelation curve obtained for the  $\omega_x$  vorticity data. The distance between the central peak and dominant side peaks of the autocorrelation curve corresponds to the predominant wavelength of the wake at that position/time, *i.e.*  $\lambda$ . Finally a histogram of all of the wavelengths extracted for each position (for more than 500 temporal samples) is prepared. Using the probability frequency distribution, the standard deviation and the dominant wavelength of the spanwise variations corresponding to the peak of the probability distribution, are

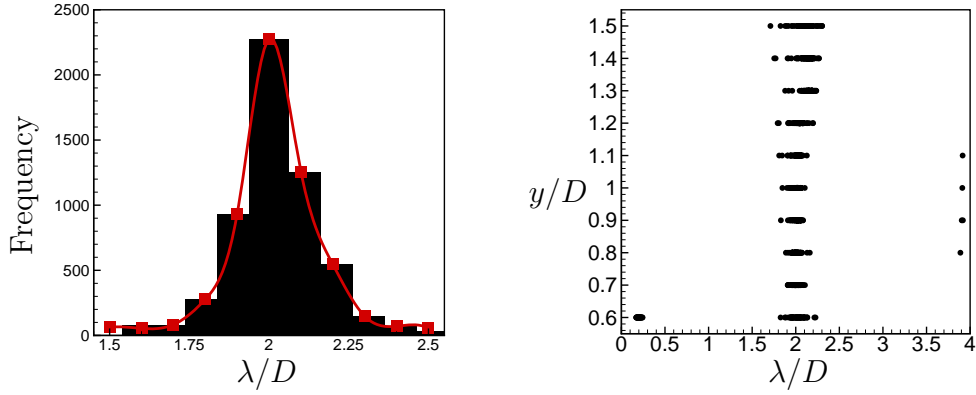


FIGURE 5.6: (left): Wavelength histogram of spanwise structures resulted from autocorrelation of  $\omega_x$  fields over 500 data sets. The red line illustrates a Gaussian fit to the histogram; (right): Distribution of wavelengths at different  $y/D$  locations behind the cylinder; for  $\beta = 90$ .

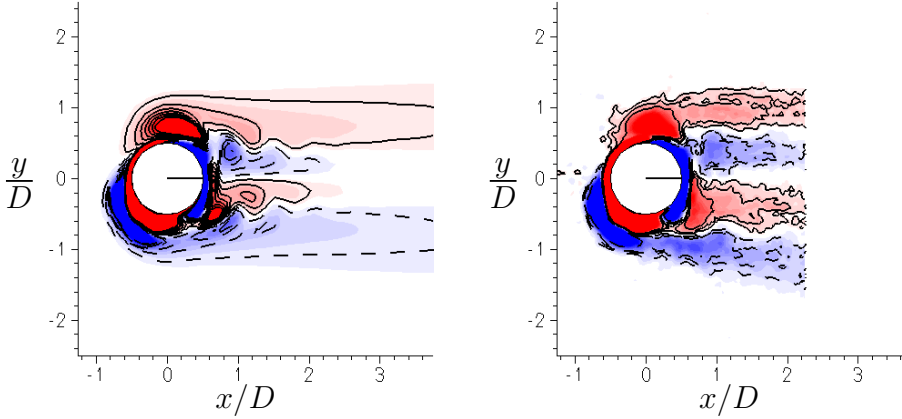


FIGURE 5.7: Vorticity contours around the cylinder undergoing combined translational and rotational oscillation at  $KC = \Phi = \pi$  and  $\beta = 90$ . The numerical result is presented on the left, and the experimental result on the right. The experimental result is a phase-average of 10 successive cycles. The phase shown corresponds to  $t = 0$ . The dashed lines (enclosing blue) correspond to clockwise direction of vorticity (negative), and the solid lines (enclosing red) correspond to counterclockwise direction of vorticity (positive).

identified. Figure 5.6a shows a sample of the histogram prepared for the  $\omega_x$  vorticity data. Figure 5.6b shows the density distribution of the spanwise wavelengths at each position for more than 500 sets. All the wavelength results in the following sections are extracted using this method.

## 5.6 Results and discussions

In this section the results are presented in two parts. In the first part, the wake profiles around the cylinder in the streamwise direction ( $xy$ -plane) for  $KC = \Phi = \pi$  and  $\beta = 90$  are examined, and the second part investigates the three-dimensionality of such flows for  $KC = \Phi = \pi$  for the range of  $20 < \beta < 200$  (corresponding to  $62.8 < Re_t < 628$ ).



### 5.6.1 Wake profile in the streamwise direction

It has previously been found by Blackburn *et al.* (1999) that for the case with  $KC = \Phi = \pi$  and  $\beta = 90$ , and vertical cylinder translation, vorticity transport is predominantly in the horizontal direction. Figure 5.7 clearly shows this vorticity transport to one side of the cylinder as well as a direct comparison between results from the present experimental and numerical investigation. Figure 5.7 also shows the excellent qualitative agreement between the two methods used. Figure 5.8 depicts the sequence of one complete cycle of translational and rotational oscillation, from the numerical simulations. Experimental results of figure 5.7 clearly shows the transportation of wake vorticity in the perpendicular direction to the axis of oscillation.

The cylinder motion, based on equations 3.3 and 3.9, starts from the centre towards the top of the page, *i.e.* the positive direction of  $y$ -axis, and at the same time starts rotating clockwise, *i.e.* the negative direction of rotation angle,  $\theta$ . Figure 5.8c shows the instant when the cylinder is at its maximum  $y$ -displacement position and most negative angular displacement.

As the oscillations are in opposing phase, the maximum surface-tangential component of cylinder acceleration is located on the left-hand side of the cylinder, *i.e.* the accelerations in that location are additive rather than in opposition. This is shown schematically in figure 5.9. The acceleration vectors on the right-hand side of the cylinder cancel each other, whereas on the left-hand side they add together. This is in fact the effect of rotary oscillation that increases accelerations on one side of the cylinder and decreases them on the other side during one half cycle. This leads to the formation of a vortex pair which is unbalanced. The yellow vector in figure 5.9 shows the resultant acceleration vector tangent to the cylinder surface. This sequence is only shown for the first three phases of the oscillation. Morton (1984) has shown that this combination of accelerations will result in (kinematic) generation of vorticity on that side of the cylinder while the cancellation of accelerations on the other side results in little direct vorticity generation on the right-hand side. In this figure it can clearly be seen that the regions of highest vorticity formation, vortex pairs, are concentrated on the left-hand side of the cylinder. The direction of rotation of the vortices will result in their being strained and directed to only one side of the cylinder and perpendicular to its translation axis. On the other hand this pair of vortices moves away from the cylinder in the direction of cylinder translational and rotational oscillation, due to one of the vortices

being stronger, which acts to cause the trajectory of the pair to bend. Because two pairs are being shed in a complete cycle of motion, the cylinder trajectory components are cancelled out leaving a vortex path that is directed away from the oscillating cylinder. The vortex sheets formed as a result of the oscillations rapidly cross-annihilate and diffuse in the wake, as can be seen in the vorticity contours on the right in figure 5.8, so that with increasing distance from the cylinder the vortex sheets rapidly weaken. As Elston (2005) has also stated, at a distance of approximately five diameters downstream the vorticity has cross-annihilated to a level below the magnitude of the smallest contour. Based on the vorticity fields, this will necessarily result in thrust generation in this direction, but it has not been effectively measured experimentally. Elston (2005) showed the  $H_1$  symmetry (refer to Appendix A) about the wake centreline, as can also be clearly seen in figures 5.7 and 5.8. The thrusting effect appears to occur in a lock-in regime and, as reported earlier by Blackburn *et al.* (1999), and would be expected to occur for all cases where the flow structure is as shown in figure 5.1a. However, it may be the case that there is a threshold set of amplitudes required to establish this but this has not been determined to date. The phase angle between the motions influence the degree to which cross-annihilation of vorticity occurs and the distance from the cylinder at which vorticity persists (as was shown in figure 5.1).

It should be noted that the experimental result shown in figure 5.7 is phase-averaged over just few cycles. It was observed that the vorticity concentrations convected to the right-hand side of the cylinder started flapping after few cycles, hence making it impossible to phase-average. This flapping is shown in figure 5.10. It can be seen that the shed vortices are at an angle to the  $x$ -axis and not parallel to it as was shown in figure 5.7. The developing unsteadiness of the flow didn't allow averaging over larger number of cycles. The experiments were repeated several times and identical results were obtained. This difference between the experimental and numerical flows suggested that although this flow has been investigated previously by two-dimensional numerical codes and has initially been examined here experimentally in a 2D plane, it may not be two-dimensional, and may undergo transition to three-dimensionality soon after startup. This suggested scrutinising the flow in the spanwise direction to find an answer to why the flows don't completely match. In §5.6.2 the three-dimensionality of the flow is addressed.

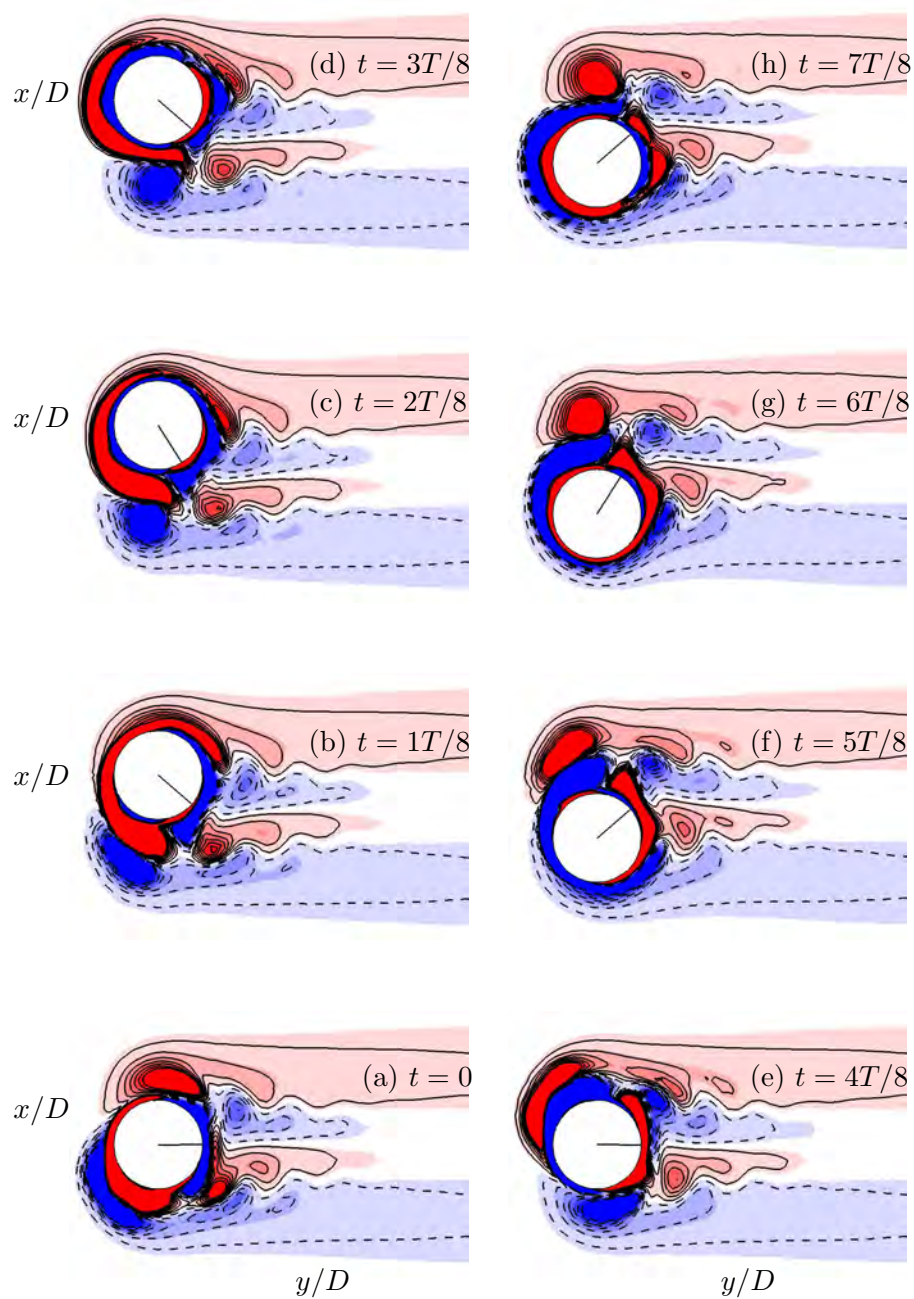


FIGURE 5.8: Flow produced by a cylinder with combined oscillatory translation and rotation. This figure shows the sequence and development of the  $\omega_z$  vorticity for one complete cycle, (a)  $t = 0$  to (h)  $t = 7T/8$  at  $KC = \Phi = \pi$  and  $\beta = 90$  where  $T$  is the period of oscillation. The radial line shows the rotational displacement of the cylinder. The dashed lines (enclosing blue) correspond to clockwise direction of vorticity (negative), and the solid lines (enclosing red) correspond to counterclockwise vorticity (positive).

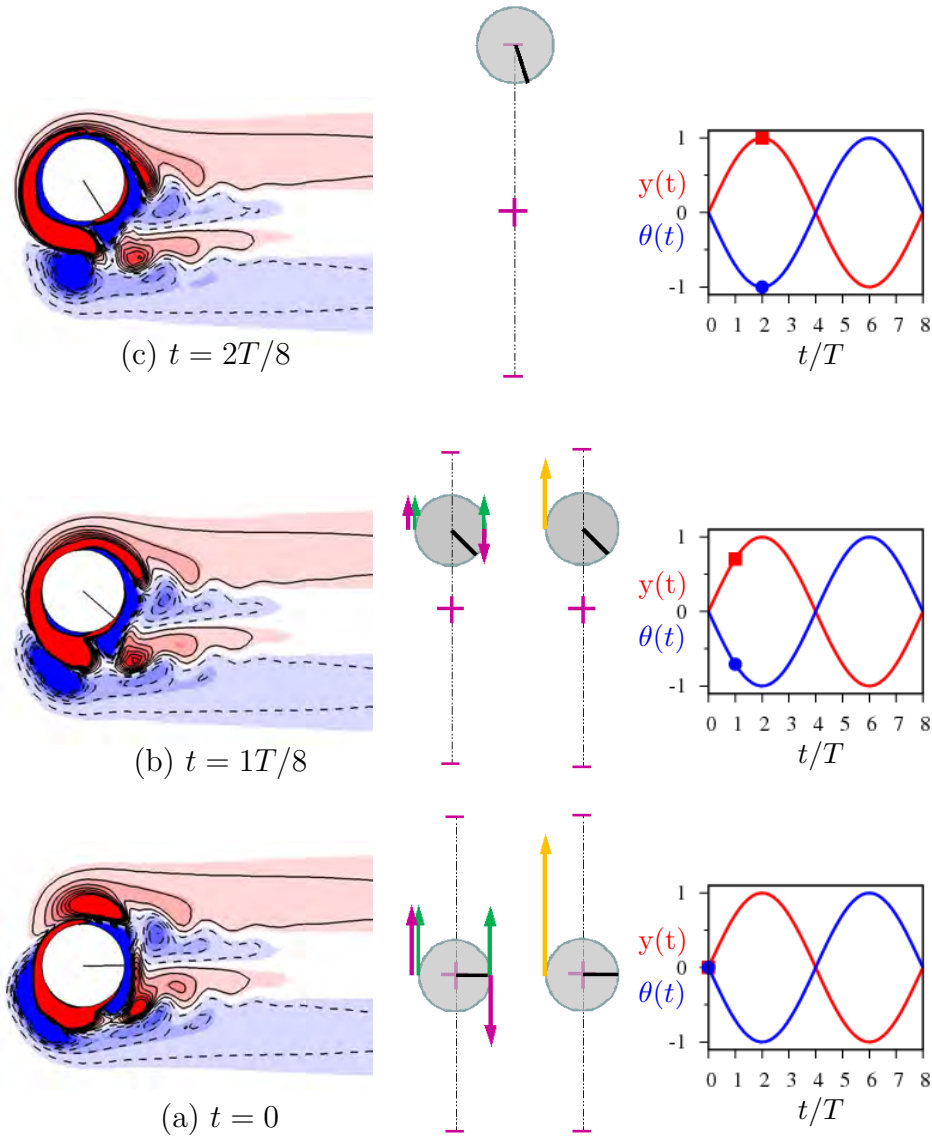


FIGURE 5.9: Schematic of the acceleration vectors at  $KC = \Phi = \pi$  and  $\beta = 90$ . The sequence and development of the  $\omega_z$  vorticity for the first three phases of oscillation, (a)  $t = 0$  to (b)  $t = 2T/8$ , is also shown. The radial line shows the rotational displacement of the cylinder. The dashed lines (enclosing blue) correspond to clockwise direction of vorticity (negative), and the solid lines (enclosing red) correspond to counterclockwise vorticity (positive). The green and purple vectors denote the translational and rotational components, respectively. The resultant vector is also shown in yellow. The phase at which the vectors are depicted is shown as well in this figure, with the red line showing the  $y(t)$  and the blue line  $\theta(t)$ . The crosshairs denote the fixed point that the cylinder is oscillating about.

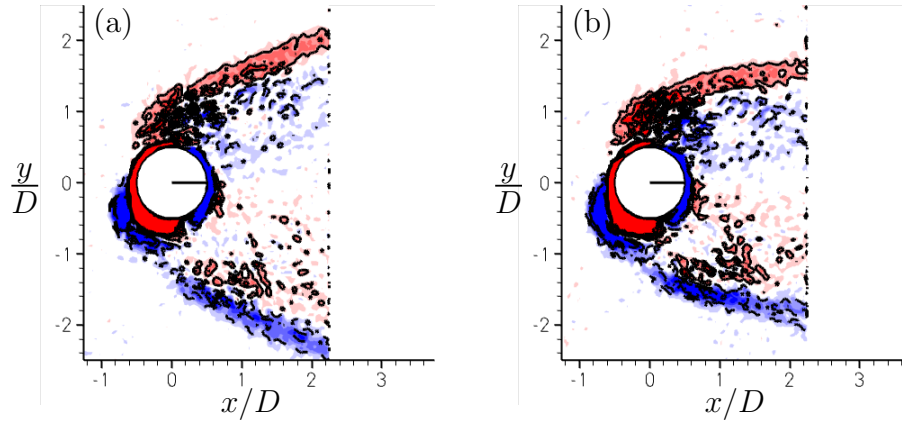


FIGURE 5.10: Instantaneous experimental vorticity contours around the cylinder undergoing combined translational and rotational oscillation at  $KC = \Phi = \pi$  and  $\beta = 90$ . The phase shown corresponds to  $t = 0$ . The dashed lines (enclosing blue) correspond to clockwise direction of vorticity (negative), and the solid lines (enclosing red) correspond to counterclockwise direction of vorticity (positive). The snapshots are taken after (a) 12 and (b) 68 cycles.

#### 5.6.1.1 Comparison between experimental and numerical results: Effect of varying $\Phi$

As discussed above, figure 5.1 shows the effect of varying phase difference angles. It is seen that by changing the phase angle, the flow pattern around the cylinder changes dramatically. As the phase angle deviates from the swimming cylinder case,  $\Phi = \pi$ , the vorticity concentrations are not convected to one side of the cylinder perpendicular to the direction of the axis of oscillation. For the first time the effect of varying phase angle difference is investigated experimentally. Figure 5.11 shows the comparison between the experimental and numerical results for a phase difference angle other than the swimming cylinder case.

Figure 5.7 shows the flow around the combined oscillatory cylinder at  $\Phi = \pi$ . This phase angle results in a net force in the  $x$ -direction. The vortex pair shown in figures 5.7 and 5.11 causes a fluid velocity through its centre that is from left to right. This vortex pair is then carried downstream from the cylinder by the flow. The detailed mechanism by which the flow is generated at the  $\Phi = \pi$  case is discussed in §5.6.1. This fluid jet is clearly depicted in figures 5.12 and 5.13. Figure 5.12a shows the flow direction on the right-hand of the cylinder being from left to right. The same pattern can also be seen in figure 5.12b. Figure 5.12b also shows the unbalanced flow around the cylinder as was discussed in §5.6.1. By moving away from the cylinder and advecting downstream the effect of cross-annihilation of vortices can directly be seen here. Moving away from the body decreases and eventually eliminates the unbalanced vortices. Figure 5.13

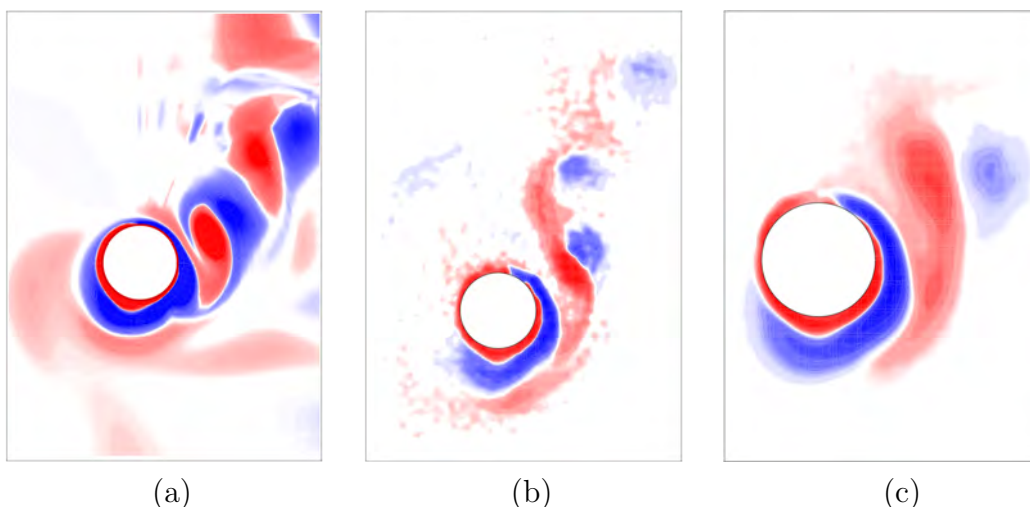


FIGURE 5.11: Contours of vorticity around the cylinder undergoing combined translational and rotational oscillation at  $KC = \pi$ ,  $\beta = 90$  and  $\Phi = \pi/2$ . (a) Numerical simulation, (b) Instantaneous PIV, (c) Phase-averaged PIV, taken at  $t/T = 0$  from numerical simulation explained in §5.4. The blue corresponds to clockwise direction of vorticity (negative). The red corresponds to counterclockwise direction of vorticity (positive).

shows the distribution of  $V$  velocity behind the cylinder at three different locations of  $x/D = 1.0, 1.5$  and  $2.0$ . This figure also shows the unbalanced flow around the swimming cylinder also with the jet-type flow generated at the right-hand side of the cylinder. Figure 5.13 also shows that the jet strength decreases as it moves away from the cylinder. It should be mentioned that the wake vortex structure for  $\Phi = 0$  is identical to that of the  $\Phi = \pi$  case described above, except that wake appears on the opposite side. This is due to the symmetry of the oscillating functions. This has been shown by Blackburn *et al.* (1999).

As shown in figures 5.1, 5.7 and 5.11, when  $\Phi$  varies from the swimming cylinder case, the flow patterns also changes from that of the swimming cylinder case. At  $\Phi = \pi/4$ , for example, the shed vortices are no longer forming into consistent vortex sheets to one side of the cylinder. This is clearly seen in figure 5.1, where recently shed vortices are located both above and below the cylinder. The vortices at this phase angle still retain some connection with the cylinder.

Figure 5.11 shows the wake flow structure for the  $\Phi = \pi/2$  case. The formation of vortex pairs that move off into the fluid appear to be the dominant characteristic of this phase angle. There appears, in comparison to other cases, to be less cross-annihilation of the vorticity, presumably due to the greater distance between vorticity concentrations.

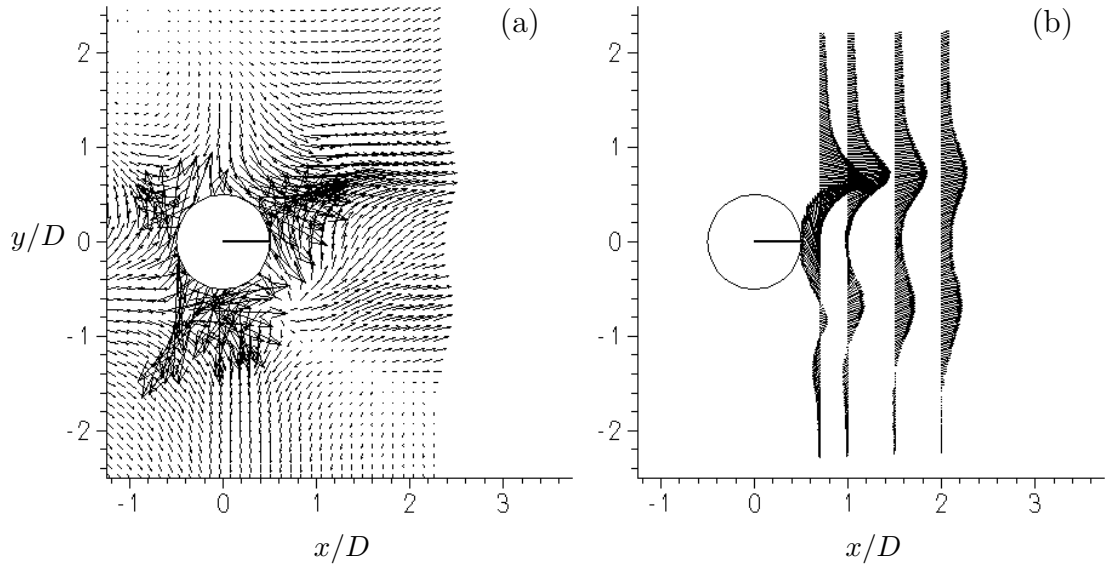


FIGURE 5.12: Experimental phase-averaged velocity vector and  $V$  velocity distribution behind the swimming cylinder at  $t/T = 0$ ,  $KC = \Phi = \pi$  and  $\beta = 90$ . (a) Velocity vectors, (b)  $V$  velocity distribution.

## 5.6.2 Wake profile in the spanwise direction

This section describes the results obtained for the wake profile of the swimming cylinder along the span of the cylinder. As it was mentioned earlier, the flow in the streamwise direction for the swimming cylinder case was quasi-periodic and for a given phase in time only few cycles could be averaged, see §5.6.1. In order to investigate this in more detail a series of experiments were conducted in the spanwise direction of the cylinder as well. Section §3.3.3.2 and figure 3.4 described and showed the PIV set-up in the streamwise direction and provided a schematic of the geometry of the cylinder, respectively. In this section the PIV set-up and regions of interest along the span of the cylinder, and location of the cameras are discussed. In the following sections, the results of the PIV measurements, including extracted wavelengths, are revealed. At the end of the section, DNS and linear Floquet stability analysis are used to interpret the experimental results in more detail.

### 5.6.2.1 Spanwise PIV set-up

This section describes the position of the laser sheets and camera used in the spanwise PIV experiments. The coordinate system used in this study is comprehensively defined in §3.3.2.1 and thus is not to be covered here. The only notable differences in the PIV set-up for the spanwise direction measurements,  $xz$  and  $yz$ -planes, in comparison

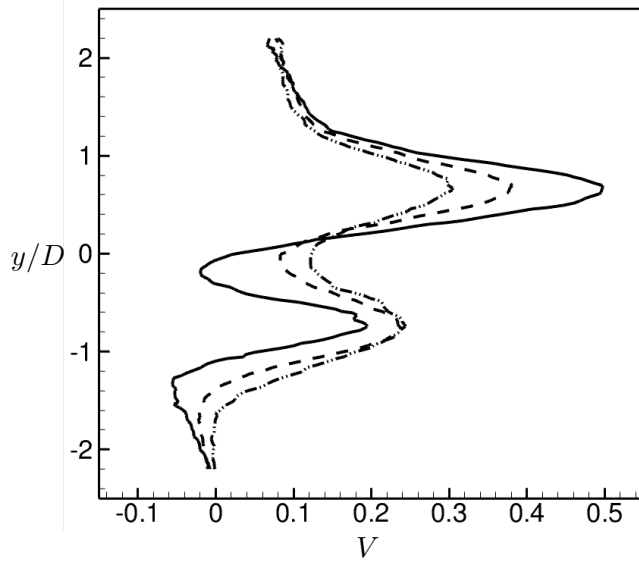


FIGURE 5.13: Experimental phase-averaged  $V$  velocity distribution for three different locations,  $x/D = 1.0$  (solid line),  $x/D = 1.5$  (dashed line) and  $x/D = 2.0$  (dashed double dot line), behind the swimming cylinder at  $t/T = 0$ ,  $KC = \Phi = \pi$  and  $\beta = 90$ . The jet-like flow is clearly seen in this figure.

to the streamwise direction measurements,  $xy$ -plane, are the position of the camera and laser sheet. Figure 5.14 shows the schematic of the PIV imaging system used for the spanwise measurements. As shown in figure 5.14 the camera in this case was mounted on the side of the channel/tank and the laser was fired from underneath the test section. Figure 5.15 shows the spanwise coordinate system with laser sheets. The  $yz$  and  $xz$ -planes were used for the spanwise measurements in the present study. Most of the experiments were conducted in the  $yz$ -plane. Figure 5.16 shows different camera positions used in this study. In order to ensure the reliability and repeatability of the experiments, experiments with different camera positions were conducted, however position (a) of figure 5.16 was used for most of the experiments.

### 5.6.2.2 Effect of varying Reynolds number

The non-periodicity of flow around the swimming cylinder which was seen in the streamwise direction and already discussed in §5.6.1, suggested three-dimensionality of the flow for the swimming cylinder case at least at higher  $\beta$  ( $Re$ ). In order to investigate the possible three-dimensionality, spanwise flow measurements using the PIV technique, were conducted.

Figures 5.17b and 5.18b show the vorticity field contours ( $\omega_x$ ) and  $y$ -velocity fields ( $V$ ) along the span of the cylinder, when  $\beta = 90$ , *i.e.* the swimming cylinder case. Clearly, as can be seen from these figures, the flow is three-dimensional with regular



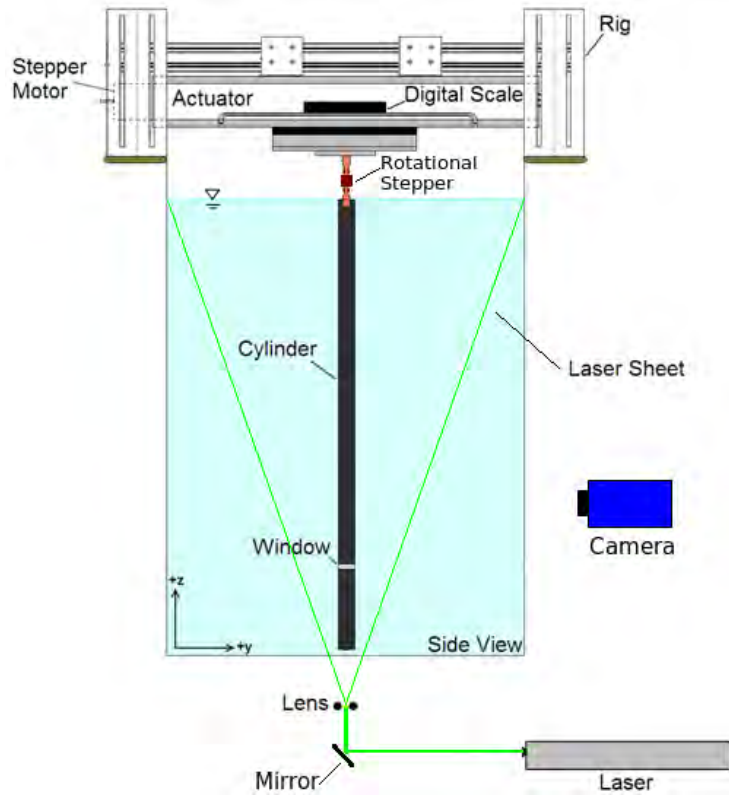


FIGURE 5.14: Schematic of spanwise PIV imaging system.

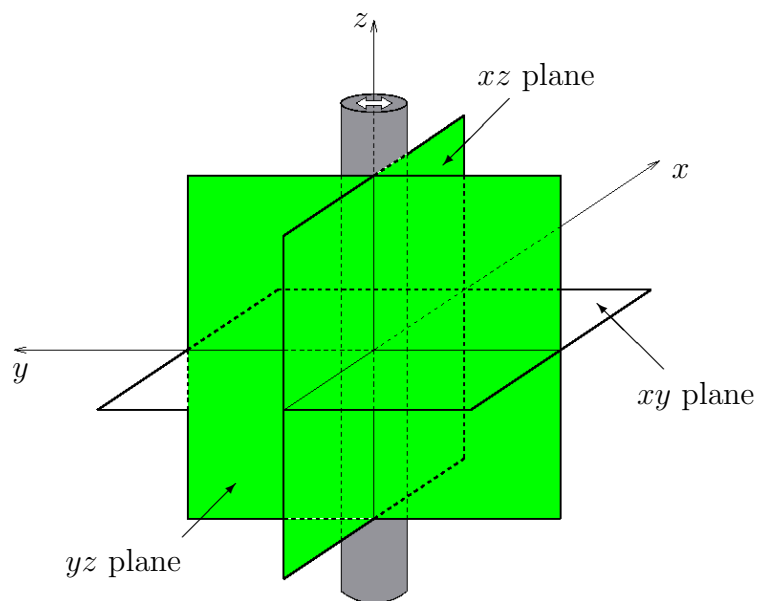


FIGURE 5.15: Spanwise coordinate system with laser sheets. Double arrow indicates the direction of cylinder translational oscillation.

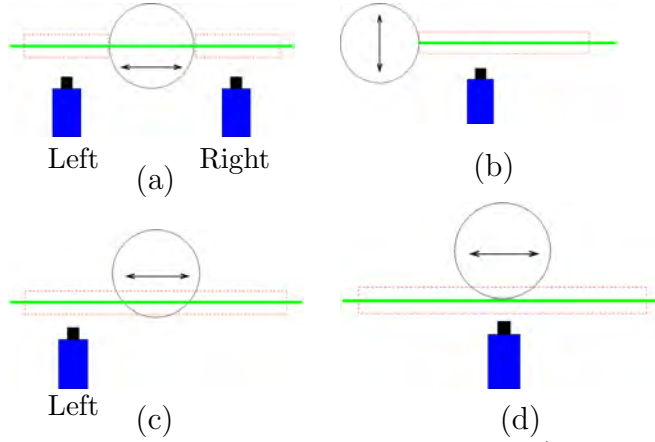


FIGURE 5.16: Schematic of camera positions in the  $xy$ -plane (as shown in figure 5.15) for the spanwise PIV measurements. The thick green line denotes the laser sheets, the blue box shows the camera and the dashed red boxes represents the region of interest.

and stable mushroom-shape structures distributed along the span of the cylinder, having an apparently constant characteristic wavelength ( $\lambda$ ). These structures are found to be steady and fixed in position after just a few cycles from the beginning of the motion. The results shown in figures 5.17 and 5.18 are all phased-averaged results over at least 500 cycles. The three-dimensionality of the flow along the span of the cylinder indicates a transition from two-dimensional to three-dimensional flow, as discussed in Chapter 2.

Next the effect of varying Reynolds number on three-dimensionality of the flow is investigated. The  $KC$  number and the  $\Phi$  angle were held constant and the same as the swimming cylinder case for all the spanwise experiments. The independent variable varied was  $\beta$ , which is equivalent to varying the Reynolds number (refer to equation 3.6). As for §5.6.1, the non-dimensional frequency was set to be the same for both the translational and rotational oscillation, *i.e.*  $\beta_t = \beta_\theta = \beta$ . The non-dimensional frequency was chosen to cover the range  $45 \leq \beta \leq 200$ , consequently the range of Reynolds number covered was  $141 \leq Re \leq 628$ .

Figures 5.17 and 5.18 show the experimental spanwise distribution of flow for different values of  $\beta$  at  $KC = \Phi = \pi$ . They show the vorticity field ( $\omega_x$ ) contours and the  $y$ -velocity field ( $V$ ) along the span of the cylinder, respectively. The measurements are taken in the  $yz$ -plane shown in figure 5.15 and the position of the camera is the right-hand side shown in figure 5.16a. The three-dimensional structures shown appear regular and stable, with a constant characteristic wavelength. Further analysis of the experimental data, using autocorrelation, as discussed previously and shown in figure 5.19, shows this to be the case.

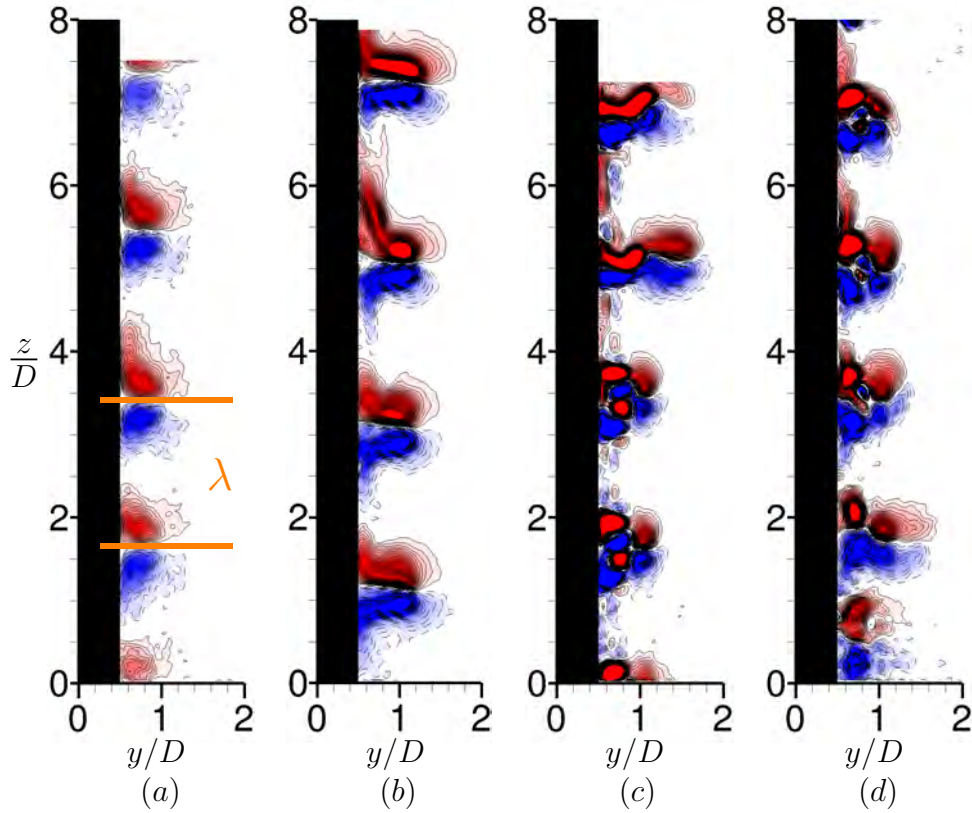


FIGURE 5.17: Experimental phase-averaged  $\omega_x$  vorticity iso-contours for different  $\beta$  values at  $KC = \Phi = \pi$ . (a)  $\beta = 45$ , (b)  $\beta = 90$ , (c)  $\beta = 120$  and (d)  $\beta = 150$ .  $\omega_x$  vorticity iso-contours; the dashed lines (enclosing blue) correspond to clockwise direction of vorticity (negative), and the solid lines (enclosing red) correspond to counterclockwise vorticity (positive).  $\lambda$  in (a) denotes the characteristic wavelength.

Figures 5.17 and 5.18 show that as the Reynolds number increases the spanwise variation changes slightly. The structures are found to remain reasonably regular but are not as stable as for the lower Reynolds number cases. Despite the increasing irregularity the discrete wavelength is preserved and remains approximately the same. A series of experiments at lower Reynolds numbers have also been conducted. The experiments show that at Reynolds numbers less than about 100, the flow is two-dimensional and there is no evidence of three-dimensional structures along the span of the cylinder. Figure 5.20 shows approximately parallel streamlines indicating two-dimensional vortex shedding around the cylinder,  $Re \approx 63$ . In order to scrutinise and understand the instability and three-dimensionality of such flow in more detail, linear Floquet analysis has been used.

Figure 5.21 shows the Floquet multipliers,  $|\mu|$ , for several Reynolds numbers for a spanwise instability at  $KC = \Phi = \pi$ . Figure 5.21a shows the value of  $|\mu|$  as a function of the spanwise wavelength,  $\lambda/D$ . This figure clearly depicts the emergence of two distinct

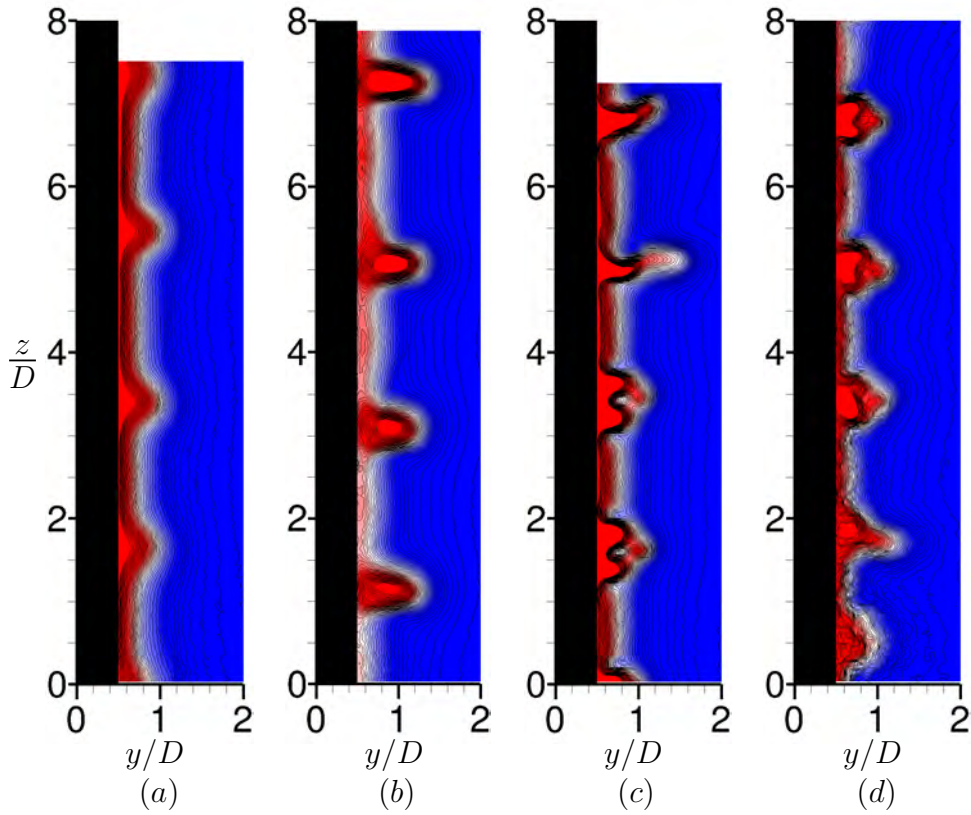


FIGURE 5.18: Experimental phase-averaged  $V$ ,  $y$ -velocity fields results of the spanwise distribution of flow for different  $\beta$  values at  $KC = \Phi = \pi$ . (a)  $\beta = 45$ , (b)  $\beta = 90$ , (c)  $\beta = 120$  and (d)  $\beta = 150$ .

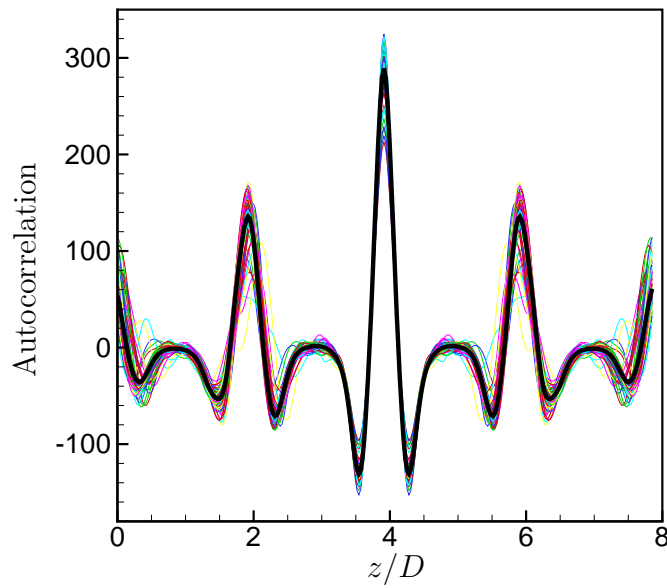


FIGURE 5.19: Spatial autocorrelation function for  $\beta=90$  and 100 cycles, based on streamwise vorticity. The thin color lines show the autocorrelation curves for each of the cycles and the thick black line illustrates the average of them.

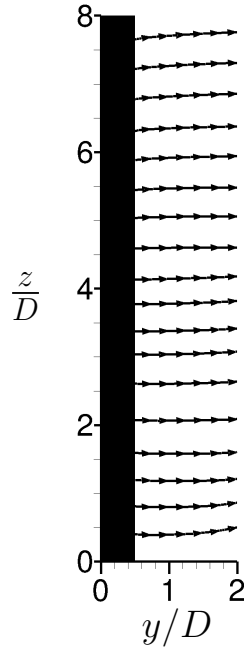


FIGURE 5.20: Experimental streamline results of the spanwise distribution of flow for  $\beta = 20$  at  $KC = \Phi = \pi$ .

instability modes, a short and a long wavelength mode. The longer wavelength mode has a critical Reynolds number of  $Re_c \approx 100$ , at a critical wavelength of  $\lambda \approx 1.8D$ , figure 5.21b. The second instability first occurs at a much higher Reynolds number of  $Re_c \approx 226$ , the peak of red curve in figure 5.21b, for a wavelength of  $\lambda \approx 0.7D$ . The experiments show that the spanwise wavelength observed in the wakes at various Reynolds numbers was close to  $2D$  at onset, decreasing to about  $1.5D$  at  $Re = 600$ . These values are broadly consistent with the wavelengths corresponds to the fastest growing modes. The thick red and blue solid lines in figure 5.21b corresponds to the fastest growing wavelength for the short and long wavelength modes respectively, as the Reynolds number is varied. Figure 5.21b also shows the unstable Reynolds number range for each mode as function of the preferred wavelength. The experimental wavelength variation with Reynolds number is marked on this figure by the symbols. This matches the predicted preferred wavelength very well.

These long and short wavelength modes have the same spatio-temporal symmetries as the mode A and B wake modes for a stationary circular cylinder in a uniform flow (see Williamson 1988), respectively. These two symmetry breaking bifurcations are the only ones possible with the same period as the base flow, as was shown using group theory arguments by Blackburn *et al.* (2005). It is interesting to note that the symmetry breaking transitions occur in the same order as for a circular cylinder,

even though the two-dimensional base wake flow and perturbation field distributions are completely different. Note that for different body geometries, the transition order can be different, such as for an elongated streamlined cylinder with a leading-edge and a square trailing-edge, for which the transition order is reversed (Ryan *et al.* 2005). Perhaps of even more interest is that for a circular cylinder wake, the saturated second critical mode, mode B, dominates the flow dynamics as the Reynolds number is increased above the two transitions (Wu *et al.* 1996); in fact, for Reynolds numbers close to 300, the wake appears to be in an almost pure mode B state (Williamson 1996b). Notably, this corresponds to the Reynolds number at which the mode B growth rate grows to exceed that of mode A. This is not the case here. Despite examining the wakes experimentally at Reynolds numbers up to 640, there was no evidence of the shorter wavelength instability in the wake. There was also an attempt to artificially force the wake at the predicted optimal shorter wavelength, *i.e.*  $\lambda/D \approx 0.7$ . This also failed to generate any long term change to the wake, *i.e.*, the shorter wavelength mode was visible initially but the wake quickly reverted to the longer wavelength state, similar to that shown in figures 5.17 and 5.18 for the unperturbed case. For that investigation, the wake was artificially forced by placing either thin tapes, thin wires or small O-rings on the cylinder. Figure 5.22 shows the images depicting the methods used for forcing the wake at the critical short wavelength. Figure 5.23 also shows the instantaneous  $y$ -velocity component fields of the flow along the span of the cylinder for three different cycles at  $KC = \Phi = \pi$  and  $\beta = 90$ . The results clearly show that initially the shorter wavelength mode is visible but after few cycles it reverts to the longer wavelength state. The same results were achieved by using the thin wires and tapes (not shown here). The experimental runs continued for more than 500 cycles and were repeated several times on different days. The longer wavelength mode was always the result after sufficient time. In order to more completely investigate the existence of the shorter wavelength mode, different spanwise planes were also examined. These planes are shown in figures 5.16b, c and d. Figure 5.24 shows the  $V$  field in the plane shown in figure 5.16b. The result for the  $xz$ -plane showed no evidence of any short wavelength instability. The observed wavelength corresponds to the long wavelength mode. Figure 5.25 also shows the  $V$  field along the span in planes corresponding to positions in figures 5.16c and d, respectively. None of the cases examined showed evidence of the shorter wavelength instability for long times.

Figure 5.21a clearly shows that linear theory predicts that the growth rate of the shorter wavelength mode quickly overtakes the longer wavelength mode, so this is somewhat surprising. Of course, the growth and nonlinear saturation of the long wavelength mode changes the base flow, so the result is not inconsistent.

Figure 5.26 shows the perturbation  $\omega_z$  vorticity contours of the short and long wavelength modes. This clearly shows the spatio-temporal symmetries of the two modes in terms of the perturbation vorticity, for the long wavelength mode. For the long wavelength mode the flow reflects about the centreline and reverses in sign; for short wavelength mode the sign reversal does not occur. These symmetries are the same as for modes A and B, respectively. The mode structure of both modes is quite complex, with substantial mode amplitude both near the cylinder and in the wake.

## 5.7 Chapter Summary

In this chapter the development of three-dimensionality of flow around a cylinder undergoing a combined translation and rotation oscillatory motion has been considered, both experimentally and numerically. The study is restricted to the case with the phase angle set to  $\Phi = \pi$ , and for large amplitude oscillations, corresponding to a *swimming cylinder*. Because of this phase difference, the oscillation velocities at the cylinder surface cancel on one side and reinforce on the other. This leads to preferential vorticity generation and transport on one side, and the cylinder rotational motion sweeps this vorticity around to the other side producing a thrust wake. Although previous two-dimensional simulations have shown that this mechanism leads to self propulsion orthogonal to the translational oscillatory motion, the question of whether this will be effective at higher Reynolds numbers remains. This work shows that the wake becomes three-dimensional at a Reynolds number of approximately 100 due to a three-dimensional instability with a spanwise wavelength of approximately 2 cylinder diameters. The Floquet analysis shows that the two-dimensional base flow is also unstable to another three-dimensional instability with a shorter wavelength ( $\lambda \approx 0.7D$ ) for  $Re \geq 226$ ; however, the experimental results, even at much higher Reynolds numbers do not show any sign of the occurrence of this mode. The experimental results indicate that the development of three-dimensionality in the wake leads to significant distortion of the previously two-dimensional wake. The effect on the self-propulsion is yet to be determined.

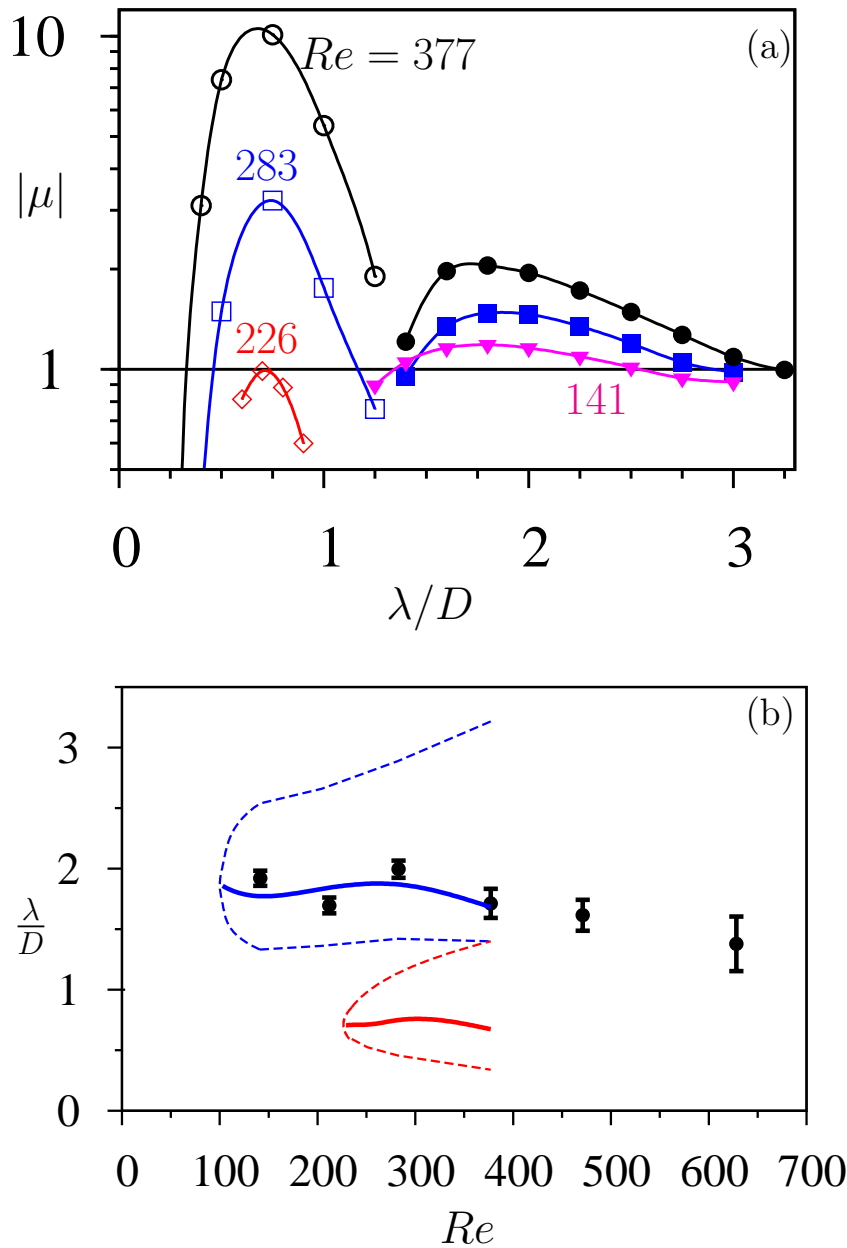


FIGURE 5.21: Floquet multipliers for several Reynolds numbers for the spanwise instability at  $KC = \Phi = \pi$ . (a) Floquet multipliers as a function of spanwise wavelength. The open (closed) symbols represent the shortest (longest) wavelength mode. Circles and black line:  $Re = 377$ ; Squares and blue lines:  $Re = 283$ ; Diamonds and red line:  $Re = 226$ ; Triangles and magenta line:  $Re = 141$ . (b) Comparison of the Floquet analysis predicted wavelength values as a function of Reynolds number with experimental measurements. The blue line corresponds to the wavelength range of the longest spanwise wavelength mode. The red dashed line corresponds to the extent of the shortest spanwise wavelength mode. The thick lines correspond to the predicted dominant wavelengths. The black circles represent experimental measurements with error bars reporting the standard deviation of the measurements.



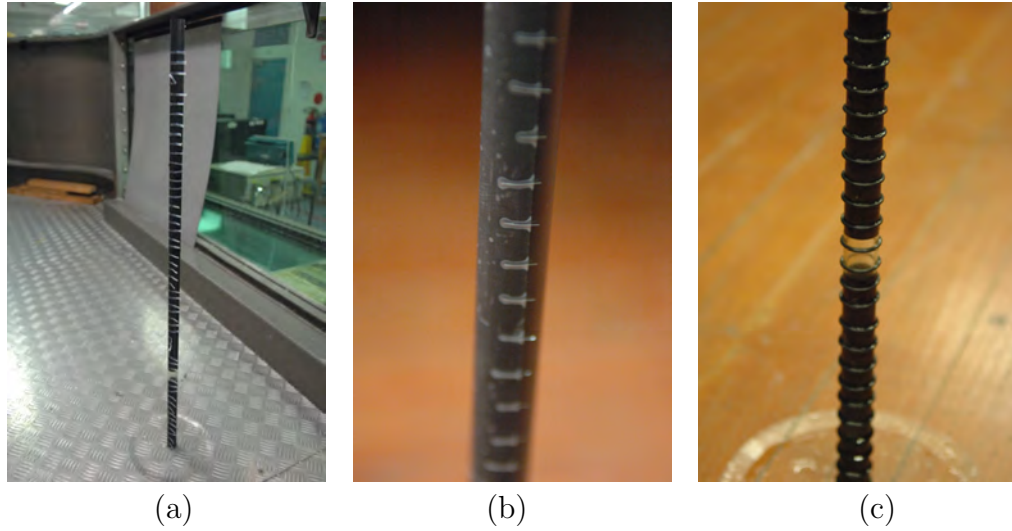


FIGURE 5.22: Photographs of the cylinder showing the methods used to artificially force the wake at the predicted optimal shorter wavelength, *i.e.*  $\lambda/D \approx 0.7$ . (a) Thin tape; (b) Thin and short wires; (c) Small O-rings.

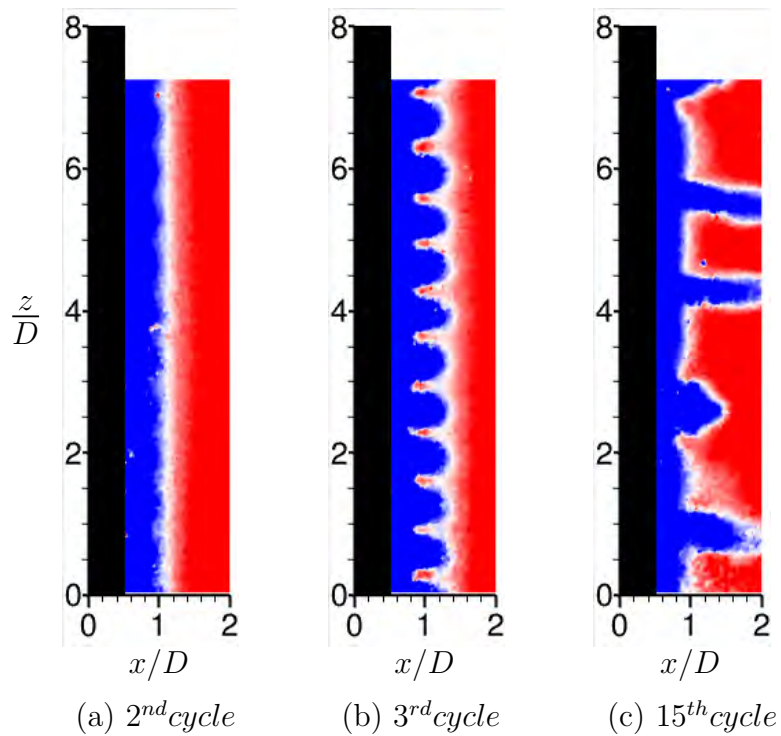


FIGURE 5.23: Experimental instantaneous  $V$  field results of the spanwise distribution of flow while artificially forcing the wake at the critical short wavelength, *i.e.*  $\lambda/D \approx 0.7$  for  $KC = \Phi = \pi$  and  $\beta = 90$ . The results are obtained using forcing with O-rings.

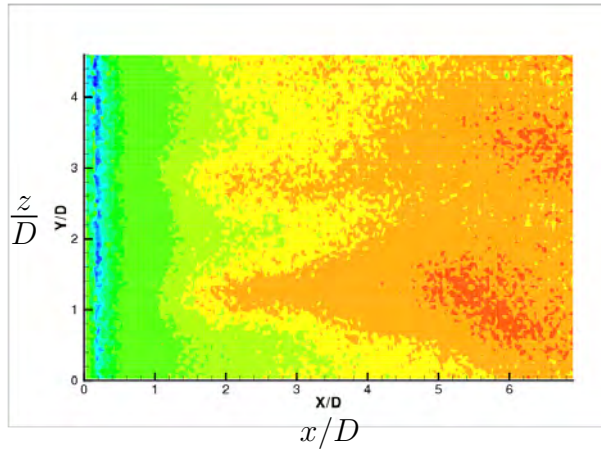


FIGURE 5.24: Experimental instantaneous  $V$  field taken at the  $xz$ -plane (see figure 5.15) for  $KC = \Phi = \pi$  and  $\beta = 90$ .

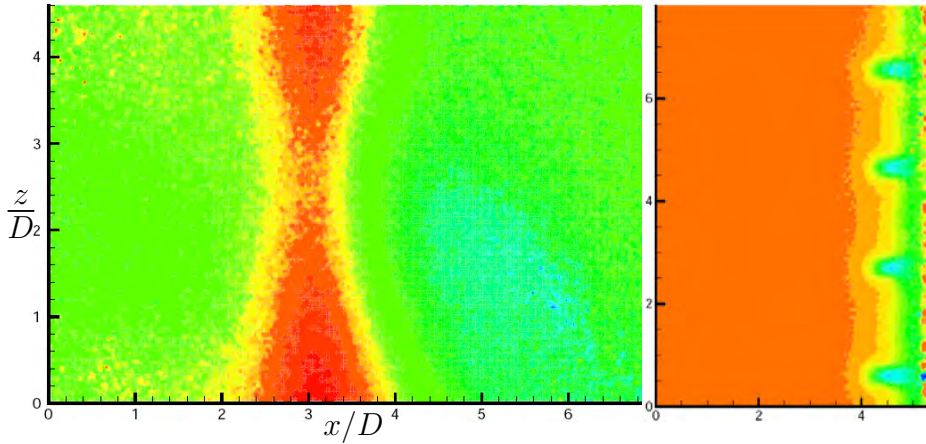


FIGURE 5.25: Experimental instantaneous  $V$  fields of the spanwise distribution of flow taken in a plane at  $x/D = 0.5$  (left) and  $x/D = 0.25$  (right) parallel to the  $yz$ -plane (see figure 5.15) for  $KC = \Phi = \pi$  and  $\beta = 90$ .

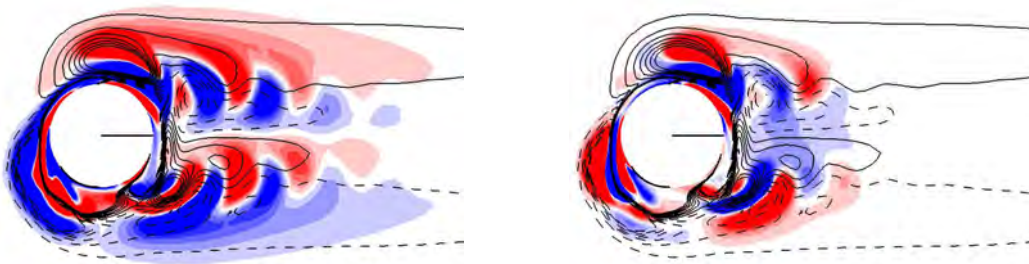


FIGURE 5.26: Contours of streamwise perturbation vorticity taken at  $KC = \Phi = \pi$  and  $\beta = 90$  ( $Re \approx 283$ ) and when the cylinder is at  $t = 0$  for: (left)  $\lambda = 1.8D$  the long wavelength; (right)  $\lambda = 0.7D$  the short wavelength. The dashed lines correspond to the base flow clockwise direction of vorticity (negative), and the solid lines correspond to the counterclockwise vorticity (positive).

## Chapter 6

# Combined translational and rotational oscillatory motion in free-stream

In this chapter, the focus is on the experimental investigation and numerical results of the wake flow created in a free-stream behind a cylinder undergoing forced combined oscillatory motions. The motion consists of two independent oscillations: cross-stream translation and rotation. The previous chapter investigated the combined oscillatory motion in a quiescent fluid, here the effect of another independent variable, *i.e.* Reynolds number, is investigated. Previous studies have extensively investigated the effect of both motions individually on cylinder wakes; however, the investigation of their combined effect is new. The motivation lies in its application to vortex-induced vibration (VIV) and its possible suppression, and to bio-mimetic motion (refer to Chapter 2). The primary focus here is on the effect of the phase angle difference between the two motions. The effect of change of translational amplitude has also been briefly investigated. In general, the results show that there is an unexpected loss of synchronisation of the wake for a finite range of phase differences at a given Reynolds number. This chapter takes the form of first briefly describing the problem to be solved, followed by the experimental arrangements and parameters, then the results are presented, including a comparison with numerical results. The numerical methods used to acquire these are the same as those described in §5.4.

### 6.1 Introduction

Offshore structures are often subjected to VIV; if the structure's motion becomes synchronised with the vortex shedding the resulting resonance may cause its premature

structural failure. In an effort to explore ways of suppressing VIV here we investigate the effect of the Reynolds number and the phase angle difference between the rotational and translational motions,  $\Phi$ . Our aim is to understand the influence of these parameters on the synchronisation of a cylinder wake under forced combined oscillatory motion. With an in-depth understanding of the flow physics it may be possible to propose novel means of actively or passively suppressing the lock-on between vortex shedding and transverse oscillation. Also, we are interested in the application to bio-mimetic motions and in particular to carangiform motion (Blackburn *et al.* 1999). There has been considerable research on the effect of either transverse or rotational oscillations on cylinder wakes, as reviewed by Williamson & Govardhan (2004); Sarpkaya (2004) and Chapter 2. These primarily focused on the translational oscillation due to their focus on VIV. There have also been studies of the effect of rotational oscillation on wakes, such as Tokumaru & Dimotakis (1991) and Filler *et al.* (1991). Previous numerical work has also examined the effect of the combined motions in quiescent fluids (Blackburn *et al.* 1999) and when there is flow past the cylinder (Kocabiyik & Al-Mdallal 2005). Kocabiyik & Al-Mdallal (2005) didn't examine the effect of the phase angle difference between the two motions in the free-stream. Previous results of Elston (2005) and Leontini *et al.* (2006a) indicate that the phase angle difference between the two motions is important and this is the primary focus of the research discussed here.

## 6.2 Experimental Arrangement and Parameters

The motion profiles and the parameters involved in combined translational and rotational oscillatory motion of a circular cylinder in a free-stream were described in Chapter 3 and §3.2, as shown in figure 3.4. Equations 3.3 and 3.9 defined the harmonic motions of the cylinder, translationally and rotationally. It is seen from the equations that adding the rotational oscillation to the translational motion adds three more independent variables to the problem; these are the rotational amplitude, frequency and the phase angle difference between the two oscillatory motions. These are in addition to the translational amplitude and frequency and free-stream velocity, *i.e.* Reynolds number. This results in the six dimensionless variables given below, which combine to determine the state of the cylinder at any time:

- The translational Keulegan-Carpenter number:

$$KC_t = \frac{U_{\max_t}}{f_t D} = \frac{2\pi A_t}{D} \quad (6.1)$$

- The translational frequency ratio:

$$F_{Rt} = \frac{f_t}{f_N} \quad (6.2)$$

- The rotational Keulegan-Carpenter number ( $A_\theta$  in radian):

$$KC_\theta = \frac{U_{\max_\theta}}{f_\theta D} = \pi A_\theta \quad (6.3)$$

- The rotational frequency ratio:

$$F_{R\theta} = \frac{f_\theta}{f_N} \quad (6.4)$$

- The phase angle between translation and rotation motions:

$$\Phi \quad (6.5)$$

- The Reynolds number:

$$Re = \frac{U_\infty D}{\nu}, \quad (6.6)$$

The cylinder's velocity ratio, between the translational and rotational motions is expressed as:

$$V_R = \frac{U_{\max_t}}{U_{\max_\theta}} = \frac{\beta_t KC_t}{\beta_\theta KC_\theta}, \quad (6.7)$$

and the frequency ratio between the translational and rotational motions as:

$$F_R = \frac{f_t}{f_\theta}. \quad (6.8)$$

The experiments were conducted in the same water channel and with the same cylinder model as discussed previously (see Chapter 3). The averaged fixed upstream velocity was  $U_\infty = 60.6\text{mm/s}$  giving  $Re_{avg} = 1322$ . The frequencies of the oscillations were fixed to be close to the natural frequency ( $T^{-1} = f_t = f_\theta = 0.6\text{Hz} \approx f_N$ ). Due to the change in the temperature of the water the actual  $Re$  number of each set of experiments might be marginally different from the averaged value, which is presented for each set of experiments in the relevant figure. The natural frequency was found to be  $f_N \approx 0.625\text{Hz}$ . The Strouhal number based on this frequency is  $St \approx f_N D / U_\infty = 0.203$  and the Strouhal number of the forcing is  $St_t \approx f_t D / U_\infty = 0.198$ .

Case	$A_t$	$A_\theta(\text{rad})$	$V_R$	$U_{\max_t}(\text{mms}^{-1})$	$U_{\max_t}/U_\infty$
1	$D/8$	0.25	1.0	9.4	0.16
2	$D/8$	1.0	0.25	9.4	0.16
3	$D/4$	0.5	1.0	18.8	0.31
4	$D/4$	1.0	0.5	18.8	0.31
5	$D/2$	1.0	1.0	37.7	0.62
6	$5D/8$	1.25	1.0	47.1	0.78
7	$3D/4$	1.0	1.5	56.5	0.93

TABLE 6.1: Summary of the values of  $A_t$  and  $A_\theta$  used when  $F_R=1.0$ .

A range of translational and rotational amplitudes have been used. These amplitudes when combined with the equal frequencies used result in equal maximum velocities from the translational and rotational motions, *i.e.*  $V_R=1$ . When  $A_t$  was varied  $A_\theta$  was also varied to provide equal maximum velocities from the translational and rotational motions. The effect of varying  $V_R$  was also investigated. A summary of these values is given in Table 6.1. The maximum velocity from the forcing is equal to  $U_{\max} = 2\pi f_t A_t = 37.7\text{mms}^{-1}$ , which corresponds to a ratio of  $U_{\max}/U_\infty = 0.62$ . All of the experiments started after at least 20 cycles from the start of the motion to ensure that the flow had reached its steady state condition.

Prior each set of experiments the flow approximately  $10D$  upstream and downstream of the fixed cylinder was measured. The upstream results were used to accurately obtain the Reynolds number of each case and the downstream results were used to measure the most accurate as possible of the natural vortex shedding frequency. Figure 6.1 shows a sample of velocity vectors taken at the upstream of the cylinder. More than 100 frames were measured in every set, then the instantaneous results were averaged temporally and spatially to find the averaged displacement vector in the  $x$ - and  $y$ -directions. Hence using the magnification factor,  $\mathcal{M}$ , the free-stream velocity was calculated. Figure 6.2 also shows instantaneous and phase-average contours of vorticity,  $U/U_\infty$  and  $V/U_\infty$  velocities taken downstream of the fixed cylinder.

In order to obtain the most accurate results for the natural vortex shedding frequency PIV measurements at different small regions of interest, mainly located at the shear layer or downstream of the cylinder in the near-wake where most of velocity fluctuations occur, were performed. Measurements of flow in small regions of interest allowed us to capture PIV images at higher frame rates, slightly more than 10 frames per second. For each set of experiments 5000 images were captured and analysed. Once

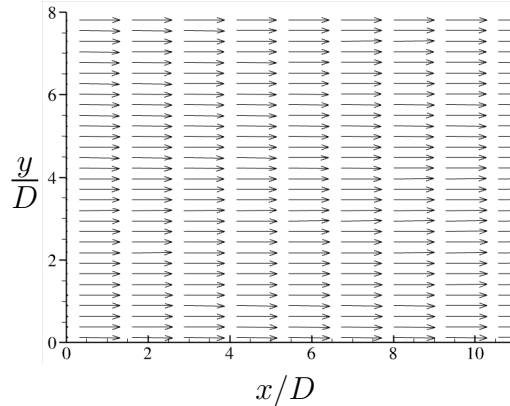


FIGURE 6.1: Velocity vectors upstream of the cylinder, measured to capture the free-stream velocity prior each set of experiments. The flow is from left to right.

the displacement vectors for 5000 image pairs were obtained, the velocity vectors were temporally averaged and the fluctuating  $U$ -velocity were calculated. They were then analysed using a Fast Fourier Transform (FFT) technique to obtain the power spectra and hence the natural vortex shedding frequency. Figure 6.3 shows a sample of the normalised power spectrum, against maximum power spectrum, where a natural frequency of 0.63 Hz is extracted. This method was applied once prior each set of experiments on the combined oscillatory motion and once at the end of the experiments. This was to ensure the natural frequency measurement was as accurate as possible with our existing equipment, *i.e.* PIV technique.

The results presented here primarily show the effect of the phase difference,  $\Phi$ , between the translational and rotational motion on the wake. This parameter was chosen as its variation had led to interesting behaviour in a quiescent fluid. The mechanisms and variety of such flows has been extensively explained in Chapter 5 and is purposely brief here. If the maximum velocities of the oscillatory motions are equal,  $V_R = 1.0$ , it can be shown that there will be an uneven distribution of velocity at the surface of the cylinder depending on the phase imposed. Indeed, for opposing phases ( $\Phi = 180^\circ$ ) the two velocities will cancel on one side (orthogonal to the translational motion) and add on the other side. This creates a vorticity difference between the two halves of the cylinder, resulting in a wake flow orthogonal to the translational movement. This mechanism is based on Morton (1984) who explained the vorticity generation mechanism that depends on the acceleration of the surface relative to the fluid. This has been extensively explained and discussed in §5.6.1. The experimental method used here to characterise the wake of this forced cylinder is the same as described previously,

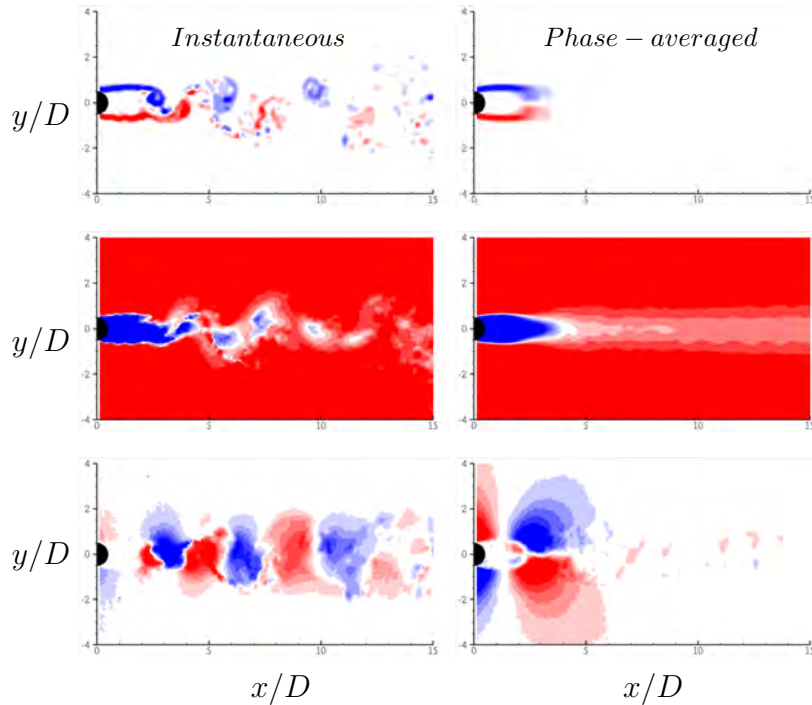


FIGURE 6.2: Instantaneous and phase-averaged contours of vorticity (top row),  $U$  (middle row) and  $V$  (bottom row) velocities measured at the downstream of the fixed cylinder. The flow direction is from left to right. The blue color in the top row shows negative vorticity and the red color shows positive vorticity being in the counter-clockwise direction.

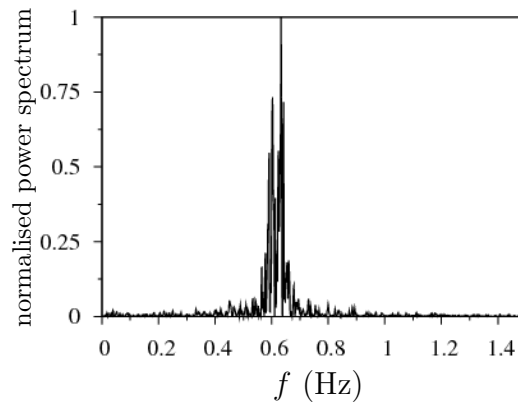


FIGURE 6.3: A normalised power spectrum, against maximum power spectrum, extracted from FFT analysis of fluctuating  $U$  velocity over 5000 images captured at 10Hz at the downstream of the fixed cylinder.

Chapters 4 and 5, with the exception of particle size and field-of-view dimensions. The experiments of the present study were conducted using  $56\mu\text{m}$  diameter particles and the experimental set-up provided a field-of-view of approximately  $6D \times 6D$ . It was possible to obtain a measurement resolution of  $127 \times 127$  (total of 16129) vectors in each field of view.

It should be noted that the same PIV set-up, experimental apparatus and numerical techniques and codes were used here, hence was as outlined the same validation cases



as those described in sections §4.3.1, §4.4.1, §5.3 and §5.4 hold here as well.

## 6.3 Results

In the following sections, the results are presented in four parts. Firstly, the effect of varying the velocity ratio between the two oscillatory motions at a given Reynolds number and equal frequency of harmonic oscillations is investigated. Secondly, a comparison between our experimental and numerical results at a lower  $Re$  number is made. Thirdly, the effect of varying the frequency ratio between the oscillatory motions and natural vortex shedding frequency of the cylinder,  $F_{RN}$ , for the  $F_R=1.0$  case is explained in brief. Fourthly, the effect of varying the frequency ratio between the rotational and translational oscillatory motions is presented. The same sign conventions as before have been used for the vorticity; red color represents positive or counter-clockwise vorticities and blue color shows negative or clock-wise vorticities.

### 6.3.1 Effect of varying $V_R$

Figures 6.4, 6.5, 6.6 and 6.7 present the near-wake phase-locked vorticity, root-mean-square (rms) vorticity,  $U$  and  $V$  velocity contours, respectively, taken at  $t = T$  for various phase angle differences at  $A_t = D/8$  and  $V_R = 0.25$  (case 2 of Table 6.1). It should be noted that the field-of-view does not allow us to see the flow structures that occur further downstream, the near-wake flow structures are the main focus of this study. The image at the top left of figures 6.4 and 6.5 shows the case where the two motions are of opposite phase ( $\Phi = 180^\circ$ ). In this case we observe a  $2S$  mode (2 single vortices shed per period) in a single-row aligned in the medial plane but with a slight offset from the centreline. The field-of-view does not allow us to see the double-row that should occur further downstream (see for example Lamb 1932; Cimbala *et al.* 1988; Johnson *et al.* 2004). The classification of the different vortex modes is given by Williamson & Roshko (1988) and was presented in Chapter 2 (see figure 2.7). As the phase angle difference decreases, the spacing between the vortices and the cylinder body also decreases while the offset of the vortices from the centreline slightly increases. The vortices are not separated widely and remain less than  $1D$  from the centreline. The positive vorticity generated on the lower part of the cylinder also approaches the cylinder until  $\Phi = 60^\circ$  where it becomes attached to the cylinder. Once the phase angle difference decreases below than the in-phase case ( $\Phi = 0^\circ$ ) the positive vortex becomes

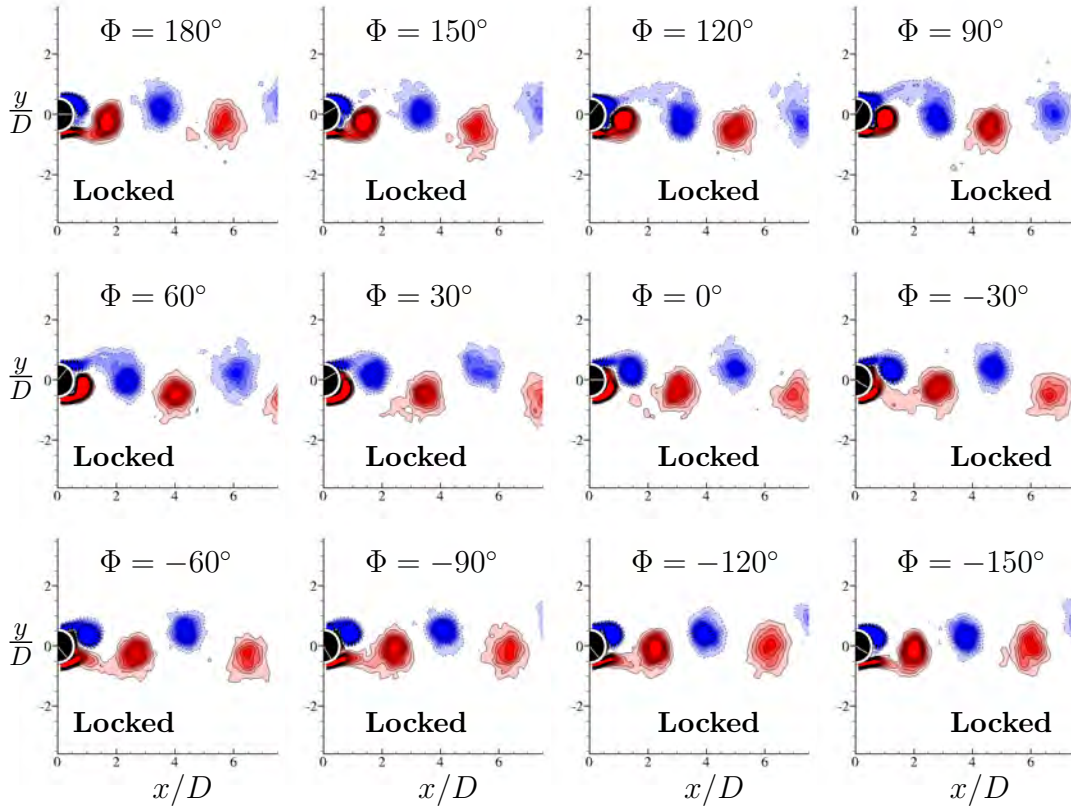


FIGURE 6.4: Motion phase-locked vorticity contours taken at the motion-phase of  $t = T$  for  $A_t = D/8$ ,  $f_N=0.6$  Hz,  $V_R=0.25$ ,  $F_R=1$  and  $Re=1291$ . The near-wake vorticity is shown for different phase angle differences between the two imposed oscillatory motions. Vorticity contours are evenly spaced over the range  $[-0.1 : 0.1]$ ; with  $\Delta\omega_z = 0.01$ .

detached again. Interestingly, no transition to different wake modes is observed over the range of  $\Phi$  angles studied, with the vortices being shed in a  $2S$  configuration in a single-row mode. Throughout the observations it can be seen that the near-wake vortices remain coherent and are synchronised with the translational motion, at least up to  $6D$  downstream. This synchronisation is characterised by a repeatable vortex shedding pattern. Figure 6.5 also shows the existence of the coherent vortex structures in the near-wake. It can be seen that the velocity distribution is not altered. This suggests that over this range of  $\Phi$  angles examined at  $A_t = D/8$  and  $V_R = 0.25$  the vortices are synchronised with the translational motion, *i.e.* locked. Note that setting the  $V_R$  to such a small value means the rotational oscillatory speed is much faster than the translational. A possible explanation for the lock-on is that the rotational oscillation adds momentum to the flow. In all the sets of experiments in which the phase angle difference was varied, the last case  $\Phi = -180^\circ$  is identical with the  $\Phi = 180^\circ$  case.

Figures 6.8, 6.9, 6.10 and 6.11 present the near-wake motion phase-locked vorticity,

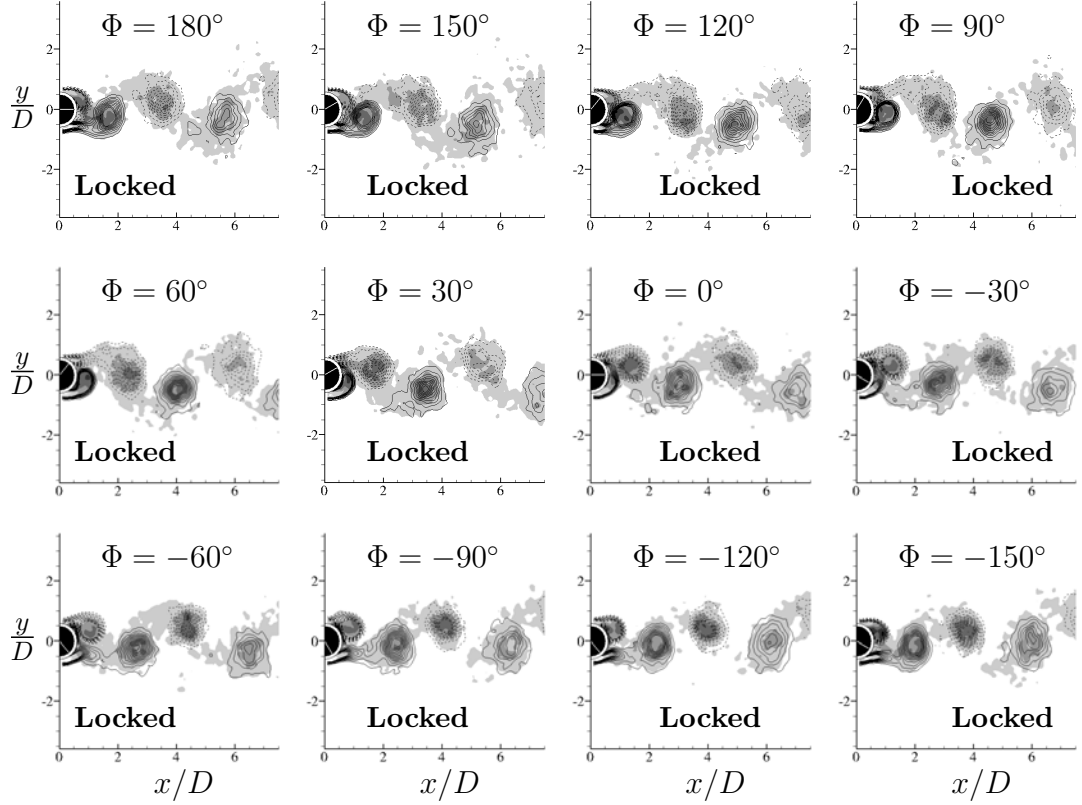


FIGURE 6.5: Motion phase-locked vorticity contours (lines) and root-mean-square vorticity (gray-scale) contours taken at the motion-phase of  $t = T$  for  $A_t = D/8$ ,  $f_N = 0.6$  Hz,  $V_R = 0.25$ ,  $F_R = 1$  and  $Re = 1291$ . The near-wake rms vorticity is shown for different phase angle differences between the two imposed oscillatory motions. The flow direction is from left to right. Root-mean-square vorticity contours are evenly spaced over the range  $[0.02 : 0.1]$ ; with  $\Delta\omega_z = 0.02$ , and vorticity contours are evenly spaced over the range  $[-0.1 : 0.1]$ ; with  $\Delta\omega_{zrms} = 0.01$ .

rms vorticity,  $U$  and  $V$  velocity contours, respectively, taken at  $t = T$  for various phase angle differences at  $A_t = D/4$  and  $V_R = 0.5$  (case 4 of Table 6.1). At the beginning of the phase angle range,  $\Phi = 180^\circ$ , nearly the same trend as in the previous case can be observed. The vortices are shed in a  $2S$  single-row mode. The vortices at this phase are at a closer distance to the cylinder than that of figure 6.4. The vortices are also located at a slight offset of the centreline. The same trend exists for up to  $\Phi = 60^\circ$  case. As the phase angle difference angle is reduced to  $\Phi = 30^\circ$ , in the direction towards being in-phase, the vortices are arranged towards each other and are less well-aligned with the medial plane, suggesting an earlier double-row transition. The vorticity pattern remains a  $2S$  mode but is changed to a double-row configuration. The vortices are now shed widely apart (nearly  $2D$ ). This trends continues as the phase angle difference passes  $\Phi = -60^\circ$ . Reducing the phase angle difference beyond this point causes the

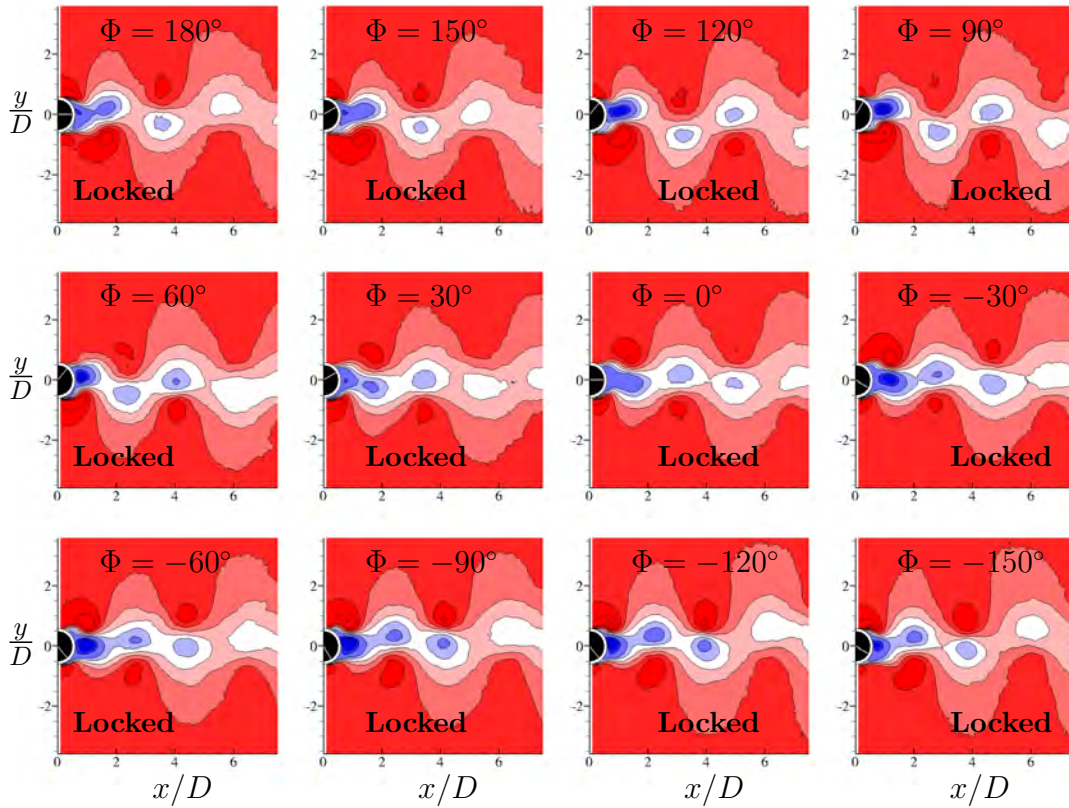


FIGURE 6.6: Motion phase-locked  $U/U_\infty$  velocity contours taken at the motion-phase of  $t = T$  for  $A_t = D/8$ ,  $f_N = 0.6$  Hz,  $V_R = 0.25$ ,  $F_R = 1$  and  $Re = 1291$ . The velocity contours are shown for different phase angle differences between the two imposed oscillatory motions. The flow direction is from left to right.  $U/U_\infty$  velocity contours are evenly spaced over the range  $[-1 : 1.8]$ ; with  $\Delta(U/U_\infty) = 0.2$ .

vortices to come closer to the centreline and form a single-row configuration. The rms vorticity, shown in figure 6.9, along with the  $U$  and  $V$  velocity contours (figures 6.10 and 6.11) have similar trend and configuration to the previously discussed case, confirming that the near-wake still synchronises with the combined motion. However, we do see a change of shedding mode from single-row to double-row.

Figures 6.12, 6.13, 6.14 and 6.15 present near-wake motion phase-locked vorticity, rms vorticity,  $U$  and  $V$  velocity contours, respectively, taken at  $t = T$  for various phase angle differences at  $A_t = D/2$  and  $V_R = 1.0$  (case 5 of Table 6.1). The image at the top left shows the case where the two motions are of opposite phase ( $\Phi = 180^\circ$ ); the  $2S$  mode can be observed with vortices in a single row. The field-of-view does not allow us to see the double-row that should occur further downstream (see for example Lamb 1932; Cimbala *et al.* 1988; Johnson *et al.* 2004). The structure of a double-row wake is shown for the  $\Phi = -30^\circ$  case, in which alternate vortices align in two rows offset from

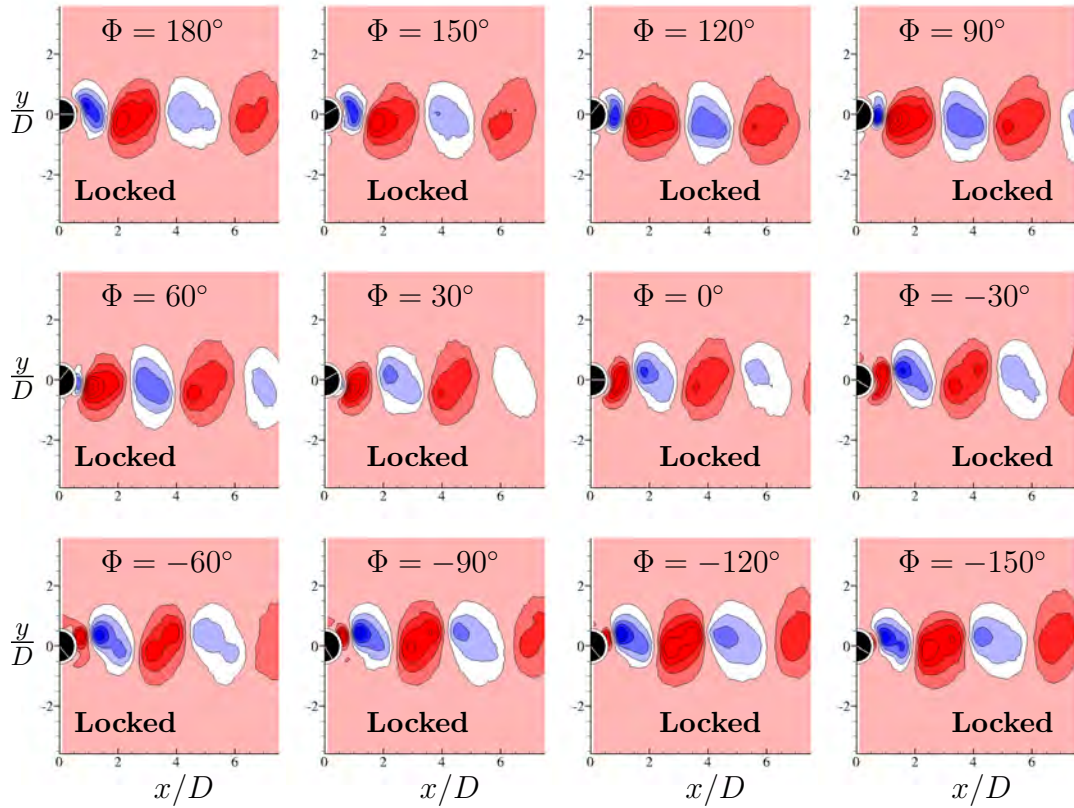


FIGURE 6.7: Motion phase-locked  $V/U_\infty$  velocity contours taken at the motion-phase of  $t = T$  for  $A_t = D/8$ ,  $f_N = 0.6$  Hz,  $V_R = 0.25$ ,  $F_R = 1$  and  $Re = 1291$ . The velocity contours are shown for different phase angle differences between the two imposed oscillatory motions. The flow direction is from left to right.  $V/U_\infty$  velocity contours are evenly spaced over the range  $[-0.2 : 2.4]$ ; with  $\Delta(V/U_\infty) = 0.2$ .

the centreline. As the phase angle difference is reduced, from  $\Phi = 180^\circ$ , towards being in-phase,  $\Phi = 0^\circ$ , the vortices are arranged closer to each other and are less well-aligned with the medial plane, suggesting an earlier double-row transition. The in-phase case,  $\Phi = 0^\circ$ , presents the signature of a  $P+S$  mode (a single vortex and a vortex pair formed per cycle), at least in the near-wake. For this in-phase case, the vortices are shed widely apart (nearly  $4D$ ), readily explained by the rotational oscillation adding momentum to the translational motion. The resulting strain favours a transition to the  $P+S$  wake (Leontini *et al.* 2006b). Reducing the phase difference to  $\Phi = -30^\circ$  and  $\Phi = -60^\circ$ , the vorticity pattern returns to a  $2S$  mode in a double-row configuration. It should be noted that the spacing between the two rows reduces (from  $2.5D$  to  $2D$ ) as we decrease  $\Phi$ . The cases of  $\Phi = -90^\circ$  and  $\Phi = -120^\circ$  are of particular interest: contrary to the other experimental cases, these two cases were not synchronised with the translational motion beyond  $2D$  downstream. The effect of this loss of synchronisation can be seen in the

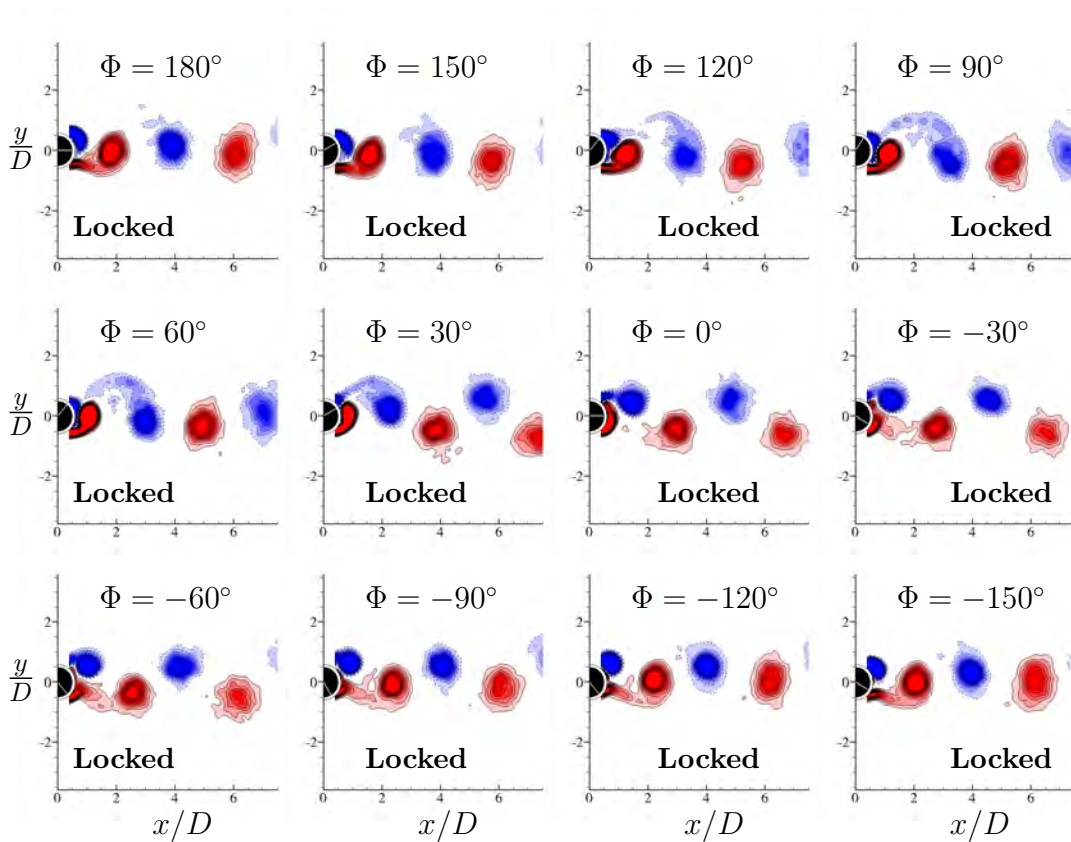


FIGURE 6.8: Motion phase-locked vorticity contours taken at the motion-phase of  $t = T$  for  $A_t = D/4$ ,  $f_N = 0.6$  Hz,  $V_R = 0.5$ ,  $F_R = 1$  and  $Re = 1274$ . The near-wake vorticity is shown for different phase angle differences between the two imposed oscillatory motions. The flow direction is from left to right. Vorticity contours are evenly spaced over the range  $[-0.1 : 0.1]$ ; with  $\Delta\omega_z = 0.01$ .

rapid downstream dissipation of the mean vortex structures. Only the two vortices near the cylinder remain coherent. This *a priori* surprising phenomenon might be explained by the fact that the separation between the two rows of vortices is smaller and that this arrangement of vortices is not stable. Similar behaviour can be found behind elliptical cylinders (Johnson *et al.* 2004). The last case  $\Phi = -150^\circ$  (and necessarily the first case,  $\Phi = \pm 180^\circ$ ) displays vortices in a single-row.

Comparing the  $U$  and  $V$  velocity contours of this case (figures 6.14 and 6.15) with the previous two cases, shows that there is a dramatic change of patterns in the velocity distribution between the synchronised and desynchronised cases. The dominant velocity contribution for the synchronised cases ( $\Phi = -90^\circ$  and  $\Phi = -120^\circ$ ) is the  $U$  velocity. Beyond  $4D$  downstream, the  $V$  velocities become much smaller than those found in the near-wake structures. The synchronised velocity patterns are all well organised and qualitatively similar to each other. A gradual change in the velocity patterns can be

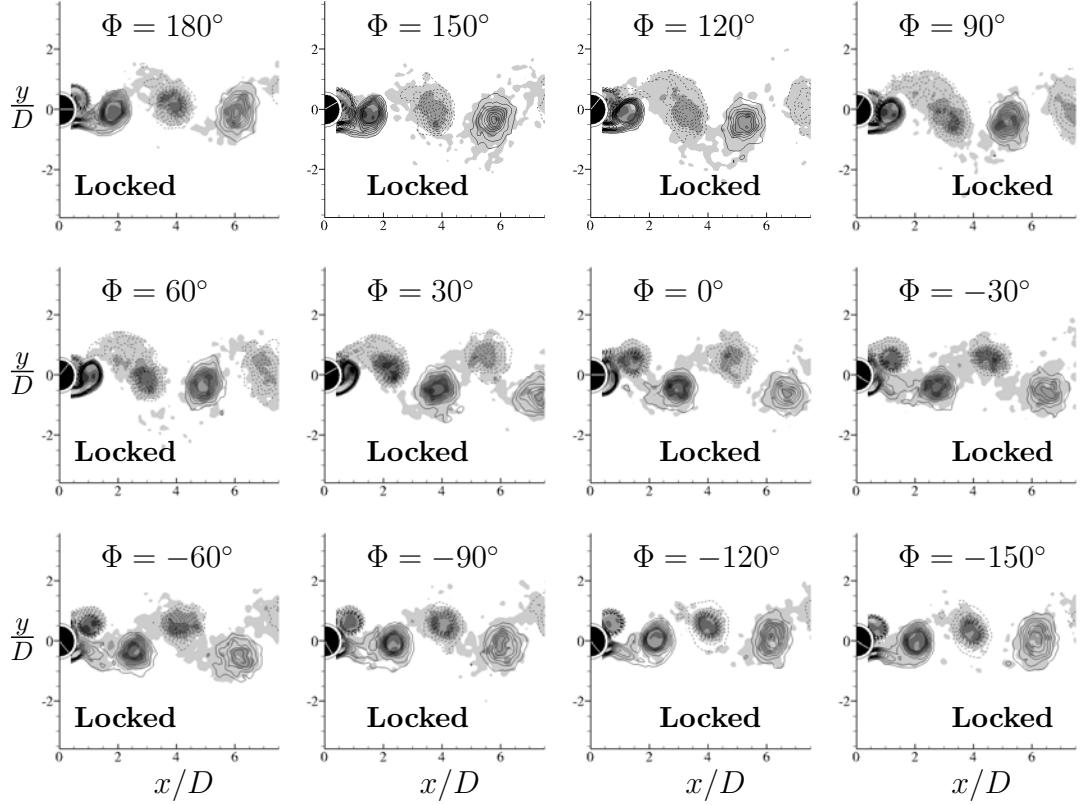


FIGURE 6.9: Motion phase-locked vorticity contours (lines) and root-mean-square vorticity (gray-scale) contours taken at the motion-phase of  $t = T$  for  $A_t = D/4$ ,  $f_N = 0.6$  Hz,  $V_R = 0.5$ ,  $F_R = 1$  and  $Re = 1274$ . The near-wake rms vorticity is shown for different phase angle differences between the two imposed oscillatory motions. The flow direction is from left to right. Root-mean-square vorticity contours are evenly spaced over the range  $[0.02 : 0.1]$ ; with  $\Delta\omega_z = 0.02$ , and vorticity contours are evenly spaced over the range  $[-0.1 : 0.1]$ ; with  $\Delta\omega_{zrms} = 0.01$ .

seen as we move away from the in-phase case,  $\Phi = 0^\circ$  towards the  $\Phi = -60^\circ$  until the flow becomes desynchronised (unlocked). No similar trends in the near-wake to the previous two cases,  $A_t = D/8$  and  $A_t = D/4$  were observed.

Figures 6.16, 6.17, 6.18 and 6.19 present motion phase-locked vorticity, rms vorticity,  $U$  and  $V$  velocity contours, respectively, taken at  $t = T$  for various phase angle differences at  $A_t = 3D/4$  and  $V_R = 1.5$  in the near-wake (case 7 of Table 6.1). By looking at the top left image of figure 6.16, *i.e.*  $\Phi = 180^\circ$ , it can be seen that the near-wake flow is already unlocked. There are no well-defined vortex structures in the near-wake and also vortices are dissipated at a close distance downstream of the cylinder. As the phase angle difference is reduced the vortices are seen to no longer be shed in a single-row as seen in the previous cases. The shedding mode for  $\Phi = 150^\circ$  is  $2S$ , whereas it becomes  $P + S$  when the phase angle difference is reduced to the in-phase

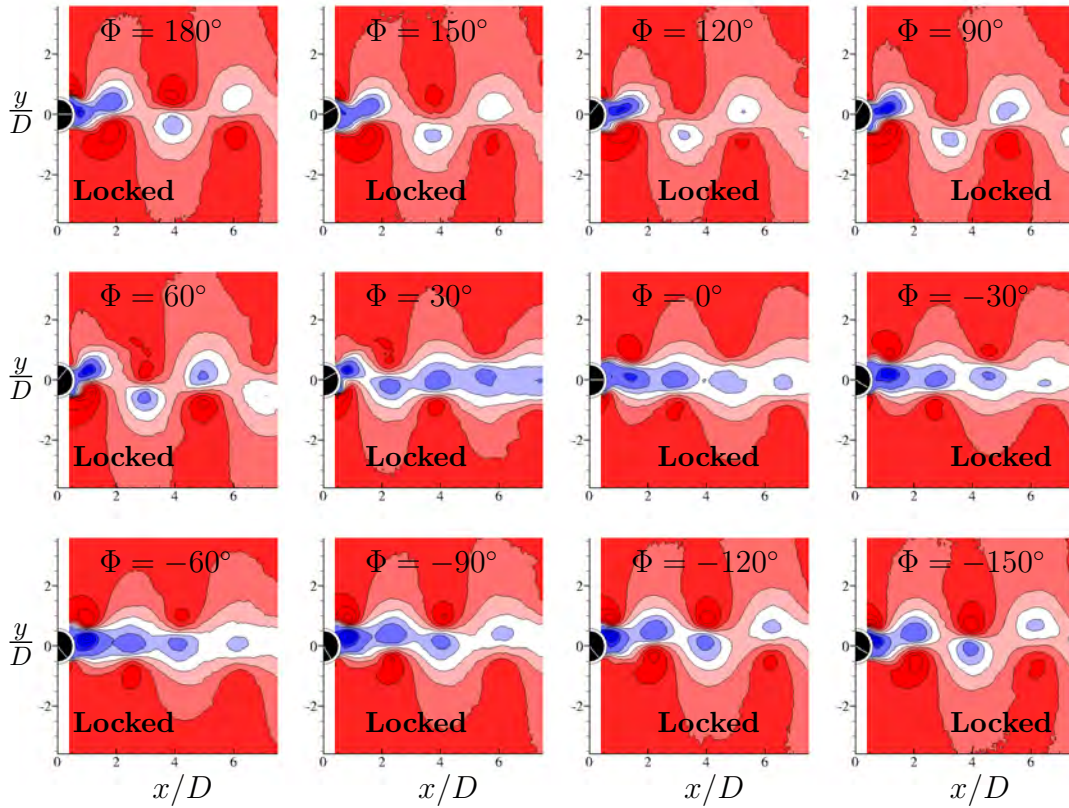


FIGURE 6.10: Motion phase-locked  $U/U_\infty$  velocity contours taken at the motion-phase of  $t = T$  for  $A_t = D/4$ ,  $f_N = 0.6$  Hz,  $V_R = 0.5$ ,  $F_R = 1$  and  $Re = 1274$ . The velocity contours are shown for different phase angle differences between the two imposed oscillatory motions. The flow direction is from left to right.  $U/U_\infty$  velocity contours are evenly spaced over the range  $[-1 : 1.8]$ ; with  $\Delta(U/U_\infty) = 0.2$ .

case,  $\Phi = 0^\circ$ . Over the phase angle difference range of  $\Phi = 120^\circ$  to  $\Phi = 0^\circ$  the vortex shedding pattern does not change significantly as the phase angle difference is reduced further. The vortices are more defined in the vortex street and are observed to be synchronised with the motion. While the spacing of the vortices remains the same, the near-wake flow pattern changes from the  $P + S$  configuration to a  $2S$  in a double-row mode. The difference between the  $2S$  mode over the range of  $\Phi = -30^\circ$  to  $\Phi = -90^\circ$  compared with the larger  $\Phi$  is that the vortices for this range are located further apart ( $\approx 4D$ ) as opposed to those seen at  $\Phi = 150^\circ$  case, where the spacing is typically  $2D$ . All the cases mentioned so far are synchronised with the motion except for the  $\Phi = 180^\circ$  case. From  $\Phi = -90^\circ$  onward reducing the phase angle difference makes the flow desynchronised; the vortices not well-defined anymore and are dissipated at a closer distance to the cylinder. Confirmation of this pattern can also be seen in figure 6.17 by looking at the rms vorticity contours. The phase-averaged rms vorticity patterns for



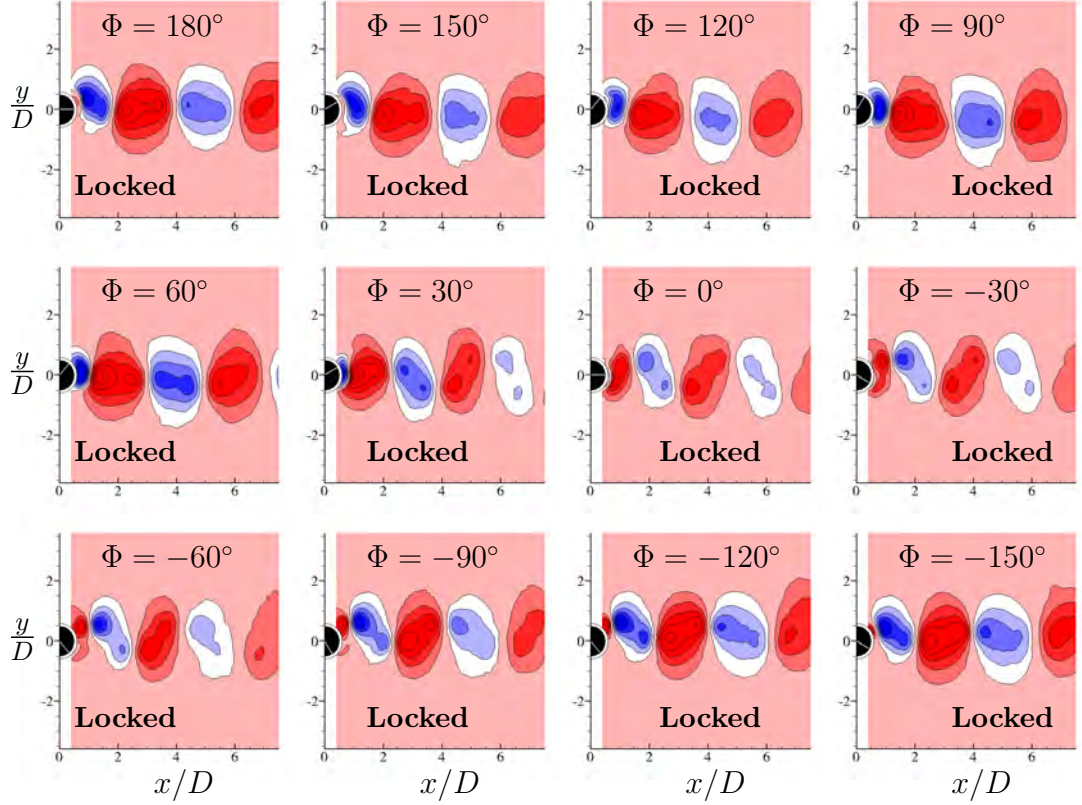


FIGURE 6.11: Motion phase-locked  $V/U_\infty$  velocity contours taken at the motion-phase of  $t = T$  for  $A_t = D/4$ ,  $f_N = 0.6$  Hz,  $V_R = 0.5$ ,  $F_R = 1$  and  $Re = 1274$ . The velocity contours are shown for different phase angle differences between the two imposed oscillatory motions. The flow direction is from left to right.  $V/U_\infty$  velocity contours are evenly spaced over the range  $[-0.2 : 2.4]$ ; with  $\Delta(V/U_\infty) = 0.2$ .

the  $\Phi = \pm 180^\circ, -90^\circ, -120^\circ$  and  $-150^\circ$  cases are similar to the unlocked phases of the  $V_R = 1$  case. The vorticity patterns are not well formed and their structures are not coherent. This pattern shows that the flow is not synchronised and the perturbations are clearly visible in those regions and hence the vortices are all unlocked.

Figures 6.18 and 6.19 also confirms the changes through the  $U$  and  $V$  velocity contour patterns. Figure 6.19 clearly shows that the  $V$  velocity contour pattern has changed dramatically for the unlocked cases and for distances further downstream than approximately  $3D$  the dissipation of vortices is more apparent.

Figures 6.20, 6.21, 6.22 and 6.23 present motion phase-locked vorticity, rms vorticity,  $U$  and  $V$  velocity contours, respectively, taken at  $t = T$  for various phase angle differences at  $A_t = D/4$ ,  $A_\theta = 0.5$  and  $V_R = 1.0$  in the near-wake (case 3 of Table 6.1). Keeping the  $V_R = 1.0$  and reducing the translational amplitude necessitates reducing the rotational amplitude also. It can be observed from the figures that the vortices in

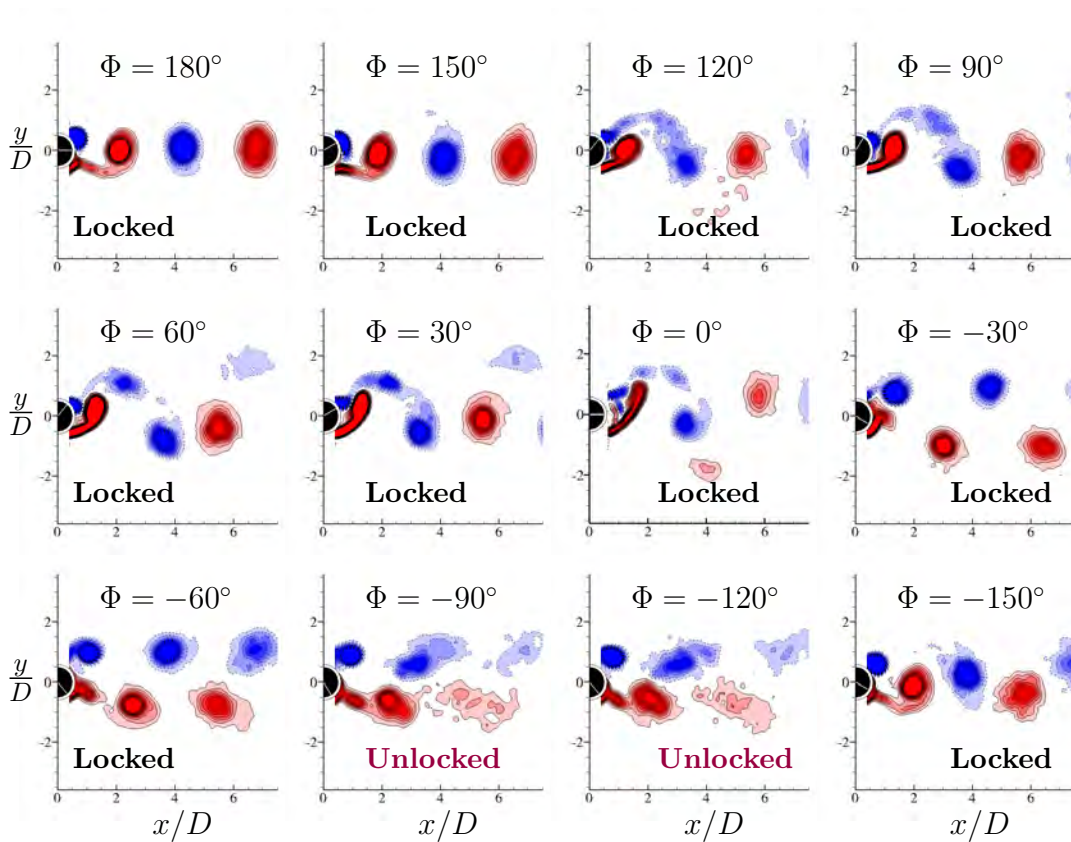


FIGURE 6.12: Motion phase-locked vorticity contours taken at the motion-phase of  $t = T$  for  $A_t = D/2$ ,  $f_N = 0.6$  Hz,  $V_R = F_R = 1$  and  $Re = 1322$ . The near-wake vorticity is shown for different phase angle differences between the two imposed oscillatory motions. Of particular interest is the asynchronous (unlocked) wake with the imposed translational motion for the phase  $\Phi = -90^\circ$  and  $\Phi = -120^\circ$ . The flow direction is from left to right. Vorticity contours are evenly spaced over the range  $[-0.1 : 0.1]$ ; with  $\Delta\omega_z = 0.01$ .

this case are all larger than that of figure 6.8 and well formed. The near-wake for all of the  $\Phi$ s is synchronised with the translation motion and the shedding mode is  $2S$ . It can be seen that even though the  $V_R = 1.0$  is the same for the two cases 3 and 4 of Table 6.1 the near-wake structure is completely different. No transition between shedding modes can be observed as  $\Phi$  is varied. As shown in table 6.1, in case 3 the rotational amplitude is half that of case 4. Thus, the rotational motion has the capacity to add more momentum into the flow, making the vortices more compact and meaning that the phase angle difference cannot influence the synchronisation of the near-wake nor the vortex shedding mode. This means the vortices are now harder to disturb. The rms vorticity and velocity contours of figures 6.21, 6.22 and 6.23 confirm the synchronisation of the near-wake. The velocity patterns are qualitatively similar to the previous locked cases and no evidence of transition between states can be observed.

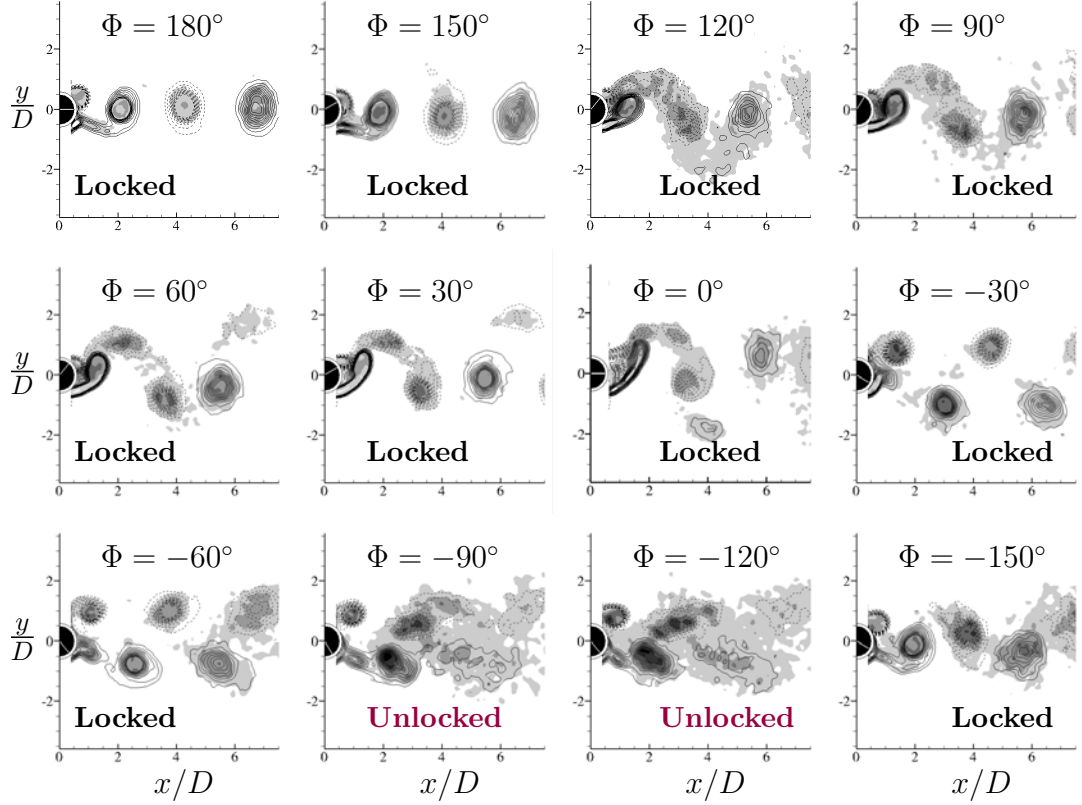


FIGURE 6.13: Motion phase-locked vorticity contours (lines) and root-mean-square vorticity (gray-scale) contours taken at the motion-phase of  $t = T$  for  $A_t = D/2$ ,  $f_N = 0.6$  Hz,  $V_R = F_R = 1$  and  $Re = 1322$ . The near-wake rms vorticity is shown for different phase angle differences between the two imposed oscillatory motions. Of particular interest is the asynchronous (unlocked) wake with the imposed translational motion for the phase  $\Phi = -90^\circ$  and  $\Phi = -120^\circ$ . The flow direction is from left to right. Root-mean-square vorticity contours are evenly spaced over the range  $[0.02 : 0.1]$ ; with  $\Delta\omega_z = 0.02$ , and vorticity contours are evenly spaced over the range  $[-0.1 : 0.1]$ ; with  $\Delta\omega_z rms = 0.01$ .

### 6.3.2 Comparison with numerical simulations

The comparison which was previously made between the phase-locked vorticity and rms vorticity contours does not however give an indication of how locked or unlocked the flow is. In addition to the experiments, numerical simulations have been undertaken to elucidate the flow synchronisation behaviour and to confirm certain aspects of the unlocked regime. The numerical simulations are conducted based on the methods explained and discussed in §5.4. Although these (two-dimensional) numerical simulations are performed at a much lower Reynolds number, the near-wake predictions are predominantly consistent with the experimental results (*e.g.* the vorticity pattern). This is likely to be sufficient to match against experiments, provide insight into the mechanisms by which transitions occur and also due to the strong forcing, to partially override the

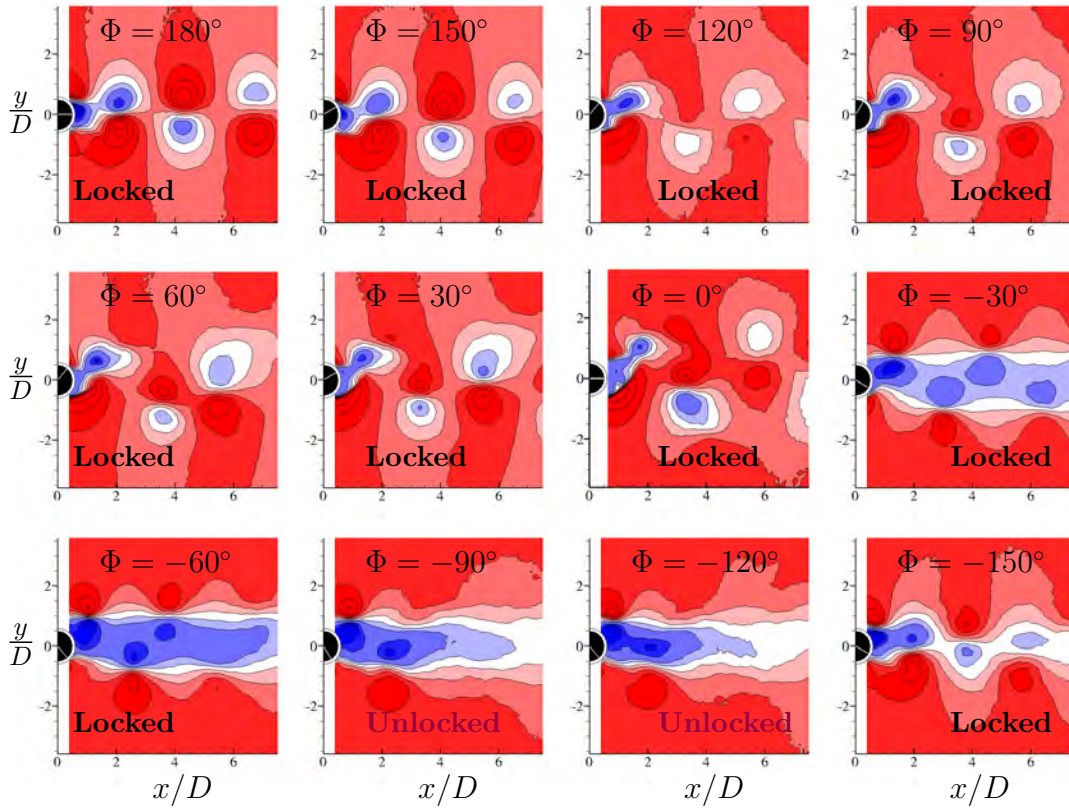


FIGURE 6.14: Motion phase-locked  $U/U_\infty$  velocity contours taken at the motion-phase of  $t = T$  for  $A_t = D/2$ ,  $f_N=0.6$  Hz,  $V_R=F_R=1$  and  $Re=1322$ . The velocity contours are shown for different phase angle differences between the two imposed oscillatory motions. Of particular interest is the asynchronous (unlocked) wake with the imposed translational motion for the phase  $\Phi = -90^\circ$  and  $\Phi = -120^\circ$ . The flow direction is from left to right.  $U/U_\infty$  velocity contours are evenly spaced over the range  $[-1 : 1.8]$ ; with  $\Delta(U/U_\infty) = 0.2$ .

modifying effect of three-dimensional transition, at least for the near-wake. Due to the time constraint of this part of research the numerical simulations were only performed for the conditions of figure 6.12.

The description of the numerical methodology will be brief because it has been adequately described in §5.4 and also in previous papers and is not the focus of this thesis. Details of the general method and its implementations can be found in Karniadakis & Sherwin (2005); Thompson *et al.* (1996). The code employed has been well-proven for use in bluff-body problems (Ryan *et al.* 2005; Leontini *et al.* 2007; Lo Jacono *et al.* 2008) and is the same as the one used for the “swimming cylinder” case in Chapter 5. The time-asymptotic wake flows for the present study were calculated by solving the incompressible, time-dependent Navier–Stokes equations in a translating accelerating frame-of-reference attached to the cylinder. The discretisation method employed was a spectral-element method, using seventh-order Lagrange polynomials associated with

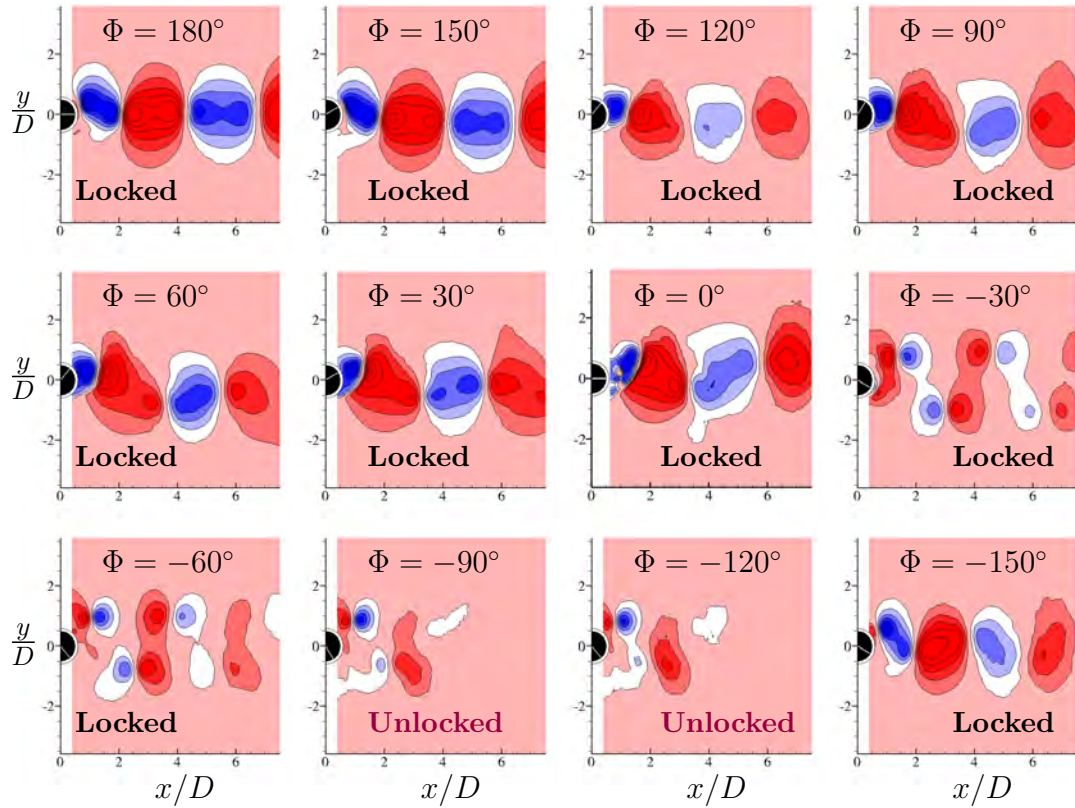


FIGURE 6.15: Motion phase-locked  $V/U_\infty$  velocity contours taken at the motion-phase of  $t = T$  for  $A_t = D/2$ ,  $f_N=0.6$  Hz,  $V_R=F_R=1$  and  $Re=1322$ . The velocity contours are shown for different phase angle differences between the two imposed oscillatory motions. Of particular interest is the asynchronous (unlocked) wake with the imposed translational motion for the phase  $\Phi = -90^\circ$  and  $\Phi = -120^\circ$ . The flow direction is from left to right.  $V/U_\infty$  velocity contours are evenly spaced over the range  $[-0.2 : 2.4]$ ; with  $\Delta(V/U_\infty) = 0.2$ .

Gauss–Lobatto–Legendre quadrature points. The computational domain, consisting of a semicircular upstream section and a rectangular downstream section, extended at least  $30D$  in all directions. This was split into 518 elements, the majority of which were concentrated in the cylinder boundary layer and wake regions. At the cylinder surface, a time-dependent Dirichlet condition was used that varied sinusoidally in time according to the driven rotational oscillation. In all cases the numerical simulations were performed for more than 200 cycles and started at rest. This was found to be sufficient for the asymptotic state to be achieved.

Various methods were used to analyse and characterise the predictions. Lissajous figures of the lift and drag coefficients against the transverse forcing mechanism for each phase angle difference have been produced. From these one can assess whether the flow was periodic, quasi-periodic or highly irregular (or chaotic). Examples for two different cases are given in figure 6.24. The left-hand figures show *quasi-periodic*

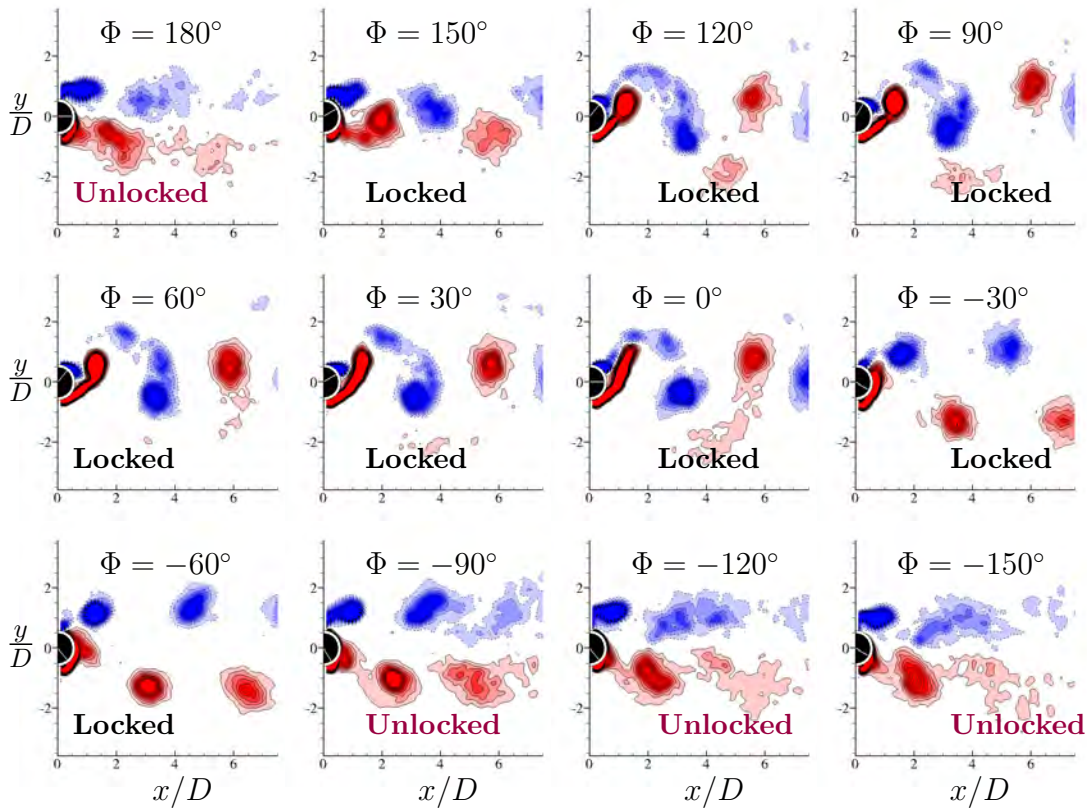


FIGURE 6.16: Motion phase-locked vorticity contours taken at the motion-phase of  $t = T$  for  $A_t = 3D/4$ ,  $f_N = 0.6$  Hz,  $V_R = 1.5$ ,  $F_R = 1$  and  $Re = 1291$ . The near-wake vorticity is shown for different phase angle differences between the two imposed oscillatory motions. Of particular interest is the asynchronous (unlocked) wake with the imposed translational motion for the phase  $\Phi = -90^\circ$ ,  $\Phi = -120^\circ$ ,  $\Phi = -150^\circ$  and  $\Phi = \pm 180^\circ$ . The flow direction is from left to right. Vorticity contours are evenly spaced over the range  $[-0.1 : 0.1]$ ; with  $\Delta\omega_z = 0.01$ .

behaviour with the phase plots repeating after 5 forcing periods. The right-hand figures indicate chaotic behaviour since the trajectories do not repeat.

To understand the flow in the far-wake of the cylinder, some representative base flows are displayed in figure 6.25. Despite the Reynolds number difference (simulations  $Re = 225$ , experiments  $Re \approx 1322$ ) these qualitatively reproduce the near-wake behaviour of the PIV results. For  $\Phi > -20^\circ$  a single-row of vortices is displayed. For  $-30^\circ \leq \Phi \leq -20^\circ$  a double-row of vortices appears after a single-row of vortices. The number of vortices in a single-row diminishes as we approach  $\Phi = -30^\circ$ . For  $-70^\circ \leq \Phi \leq -30^\circ$ , the wake no longer displays an initial single-row but instead immediately forms a double-row. These vortex rows interact further downstream to form a quasi-periodic far-wake. The number of vortices forming the double-row diminishes as  $\Phi$  diminishes. For  $-130^\circ \leq \Phi \leq -80^\circ$  the wake immediately transitions to a fully chaotic state. For  $\Phi < -130^\circ$  the flow undergoes a succession of double-row, to sin-

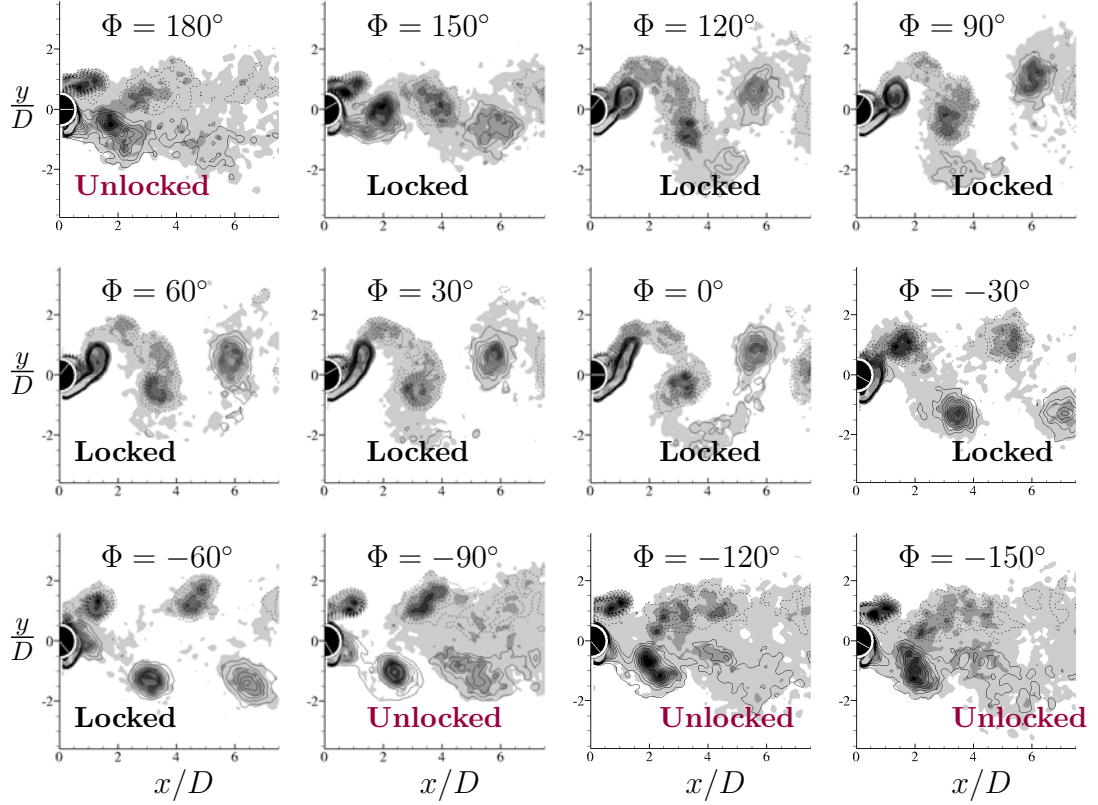


FIGURE 6.17: Motion phase-locked vorticity contours (lines) and root-mean-square vorticity (gray-scale) contours taken at the motion-phase of  $t = T$  for  $A_t = 3D/4$ ,  $f_N = 0.6$  Hz,  $V_R = 1.5$ ,  $F_R = 1$  and  $Re = 1291$ . The near-wake rms vorticity is shown for different phase angle differences between the two imposed oscillatory motions. Of particular interest is the asynchronous (unlocked) wake with the imposed translational motion for the phase  $\Phi = -90^\circ$ ,  $\Phi = -120^\circ$ ,  $\Phi = -150^\circ$  and  $\Phi = \pm 180^\circ$ . The flow direction is from left to right. Root-mean-square vorticity contours are evenly spaced over the range  $[0.02 : 0.1]$ ; with  $\Delta\omega_z = 0.02$ , and vorticity contours are evenly spaced over the range  $[-0.1 : 0.1]$ ; with  $\Delta\omega_z rms = 0.01$ .

gle then double-row, until a unique single-row pattern. See the top wake pattern of figure 6.25 as representative of this final case.

Table 6.2 reports the experimental and numerical behaviour of the wake flow for the same set of parameters *but* with  $Re = 225$  for the numerical results. It can be seen that the discrepancy in the value of the Reynolds number does not have an impact on the synchronisation for  $\Phi$  values close to the loss of synchronisation. The numerical simulations confirm the loss of synchronisation for qualitatively the same region as the experiments. Given this agreement between experimental and numerical predictions of the lock-in regions the numerical simulations were then used to deduce the synchronisation of the near-wake from the experimental results of other cases. Note that the numerical simulations revealed that the unlocked regime contains quasi-periodic and chaotic patterns. The chaotic regime appears to be surrounded by quasi-periodicity.

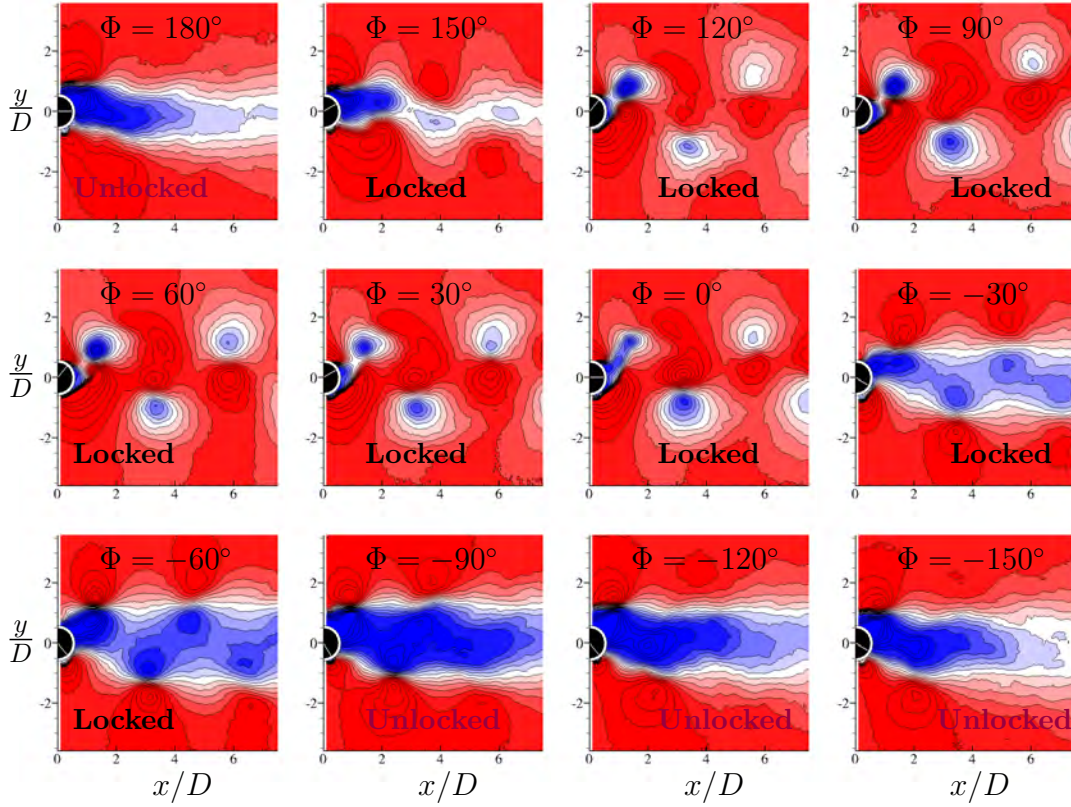


FIGURE 6.18: Motion phase-locked  $U/U_\infty$  velocity contours taken at the motion-phase of  $t = T$  for  $A_t = 3D/4$ ,  $f_N = 0.6$  Hz,  $V_R = 1.5$ ,  $F_R = 1$  and  $Re = 1291$ . The velocity contours are shown for different phase angle differences between the two imposed oscillatory motions. Of particular interest is the asynchronous (unlocked) wake with the imposed translational motion for the phase  $\Phi = -90^\circ$ ,  $\Phi = -120^\circ$ ,  $\Phi = -150^\circ$  and  $\Phi = \pm 180^\circ$ . The flow direction is from left to right.  $U/U_\infty$  velocity contours are evenly spaced over the range  $[-1 : 1.8]$ ; with  $\Delta(U/U_\infty) = 0.2$ .

$\Phi$ [°]	$f_t/f_N$			
	Exp $\approx 1$	0.9	1.0	1.1
-30	L	L	L	L
-40		QP	L	L
-50		QP	L	QP
-60	L	QP	QP	QP
-70	UL	QP	QP	C
-80	UL	QP	QP	C
-90	UL	QP	C	C
-100	UL	QP	C	C

$\Phi$ [°]	$f_t/f_N$			
	Exp $\approx 1$	0.9	1.0	1.1
-110	UL	L	C	C
-120	UL	L	C	C
-130		L	C	C
-140		L	QP	C
-150	L	L	L	C
-160		L	L	L
-170		L	L	L
-180	L	L	L	L

TABLE 6.2: Summary of the synchronisation around the unlocked regime. L (light green), QP (orange) and C (dark red) stands for locked-on, quasi-periodic and chaotic respectively. The unlocked regime (UL, dark red) for the experimental results are likely to be chaotic.  $f_t$  and  $f_N$  stands for forced frequency and natural frequency for a fixed cylinder.



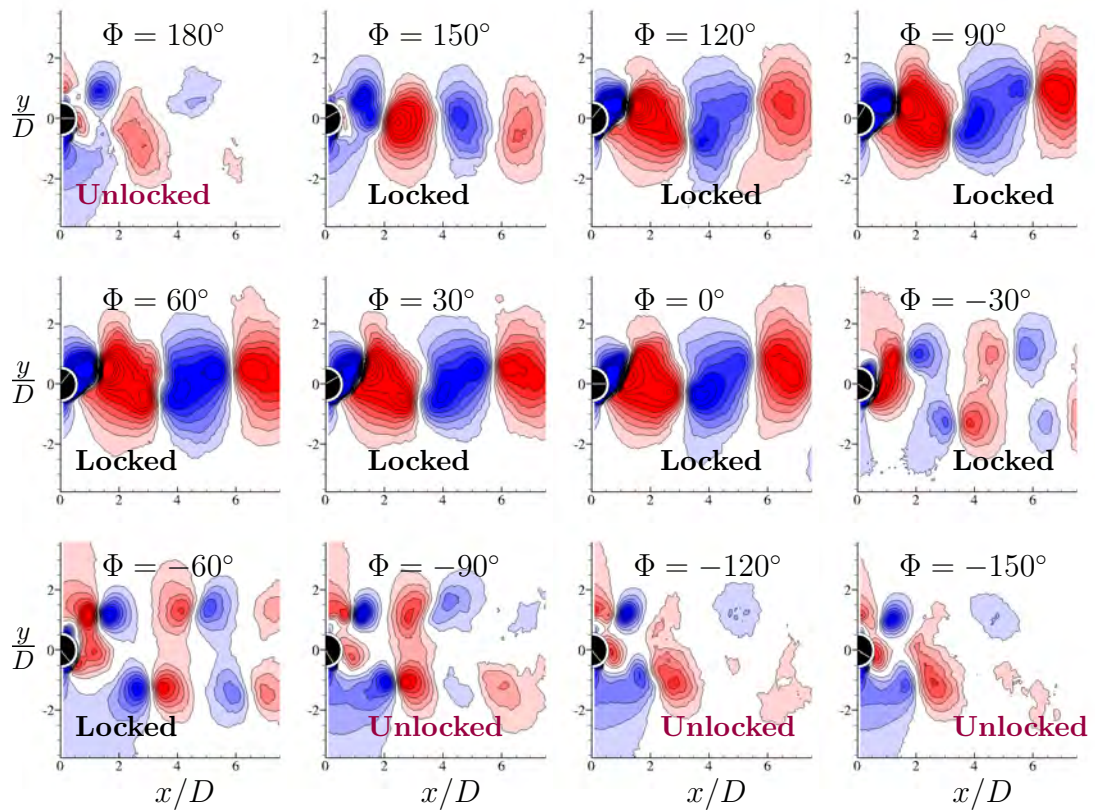


FIGURE 6.19: Motion phase-locked  $V/U_\infty$  velocity contours taken at the motion-phase of  $t = T$  for  $A_t = 3D/4$ ,  $f_N = 0.6$  Hz,  $V_R = 1.5$ ,  $F_R = 1$  and  $Re = 1291$ . The velocity contours are shown for different phase angle differences between the two imposed oscillatory motions. Of particular interest is the asynchronous (unlocked) wake with the imposed translational motion for the phase  $\Phi = -90^\circ$ ,  $\Phi = -120^\circ$ ,  $\Phi = -150^\circ$  and  $\Phi = \pm 180^\circ$ . The flow direction is from left to right.  $V/U_\infty$  velocity contours are evenly spaced over the range  $[-0.2 : 2.4]$ ; with  $\Delta(V/U_\infty) = 0.2$ .

Also the likelihood of an unlocked regime is greater when the ratio  $F_{RN}$  is higher than unity.

To further examine this behaviour, Poincaré maps have been constructed for each phase angle difference. The horizontal and vertical velocities are sampled at a pre-chosen point downstream,  $(x, y) = (7D, 0)$ , at the end of each forcing period  $T$ . For example, figure 6.26 illustrates the quasi-periodicity of the case where  $\Phi = -80^\circ$ . Here the periodicity of the flow is of  $5T$  as can be seen from the distribution of 5 distinct islands of points in the phase diagram. The chaotic nature of the regime in the case of  $\Phi = -130^\circ$  can be readily seen, with the distribution of points in the phase diagram showing no preferred region or cycle.

It appears that *synchronisation* may be a more complex process than at first thought. Both the experimental and numerical results show that the size of the nearly periodic

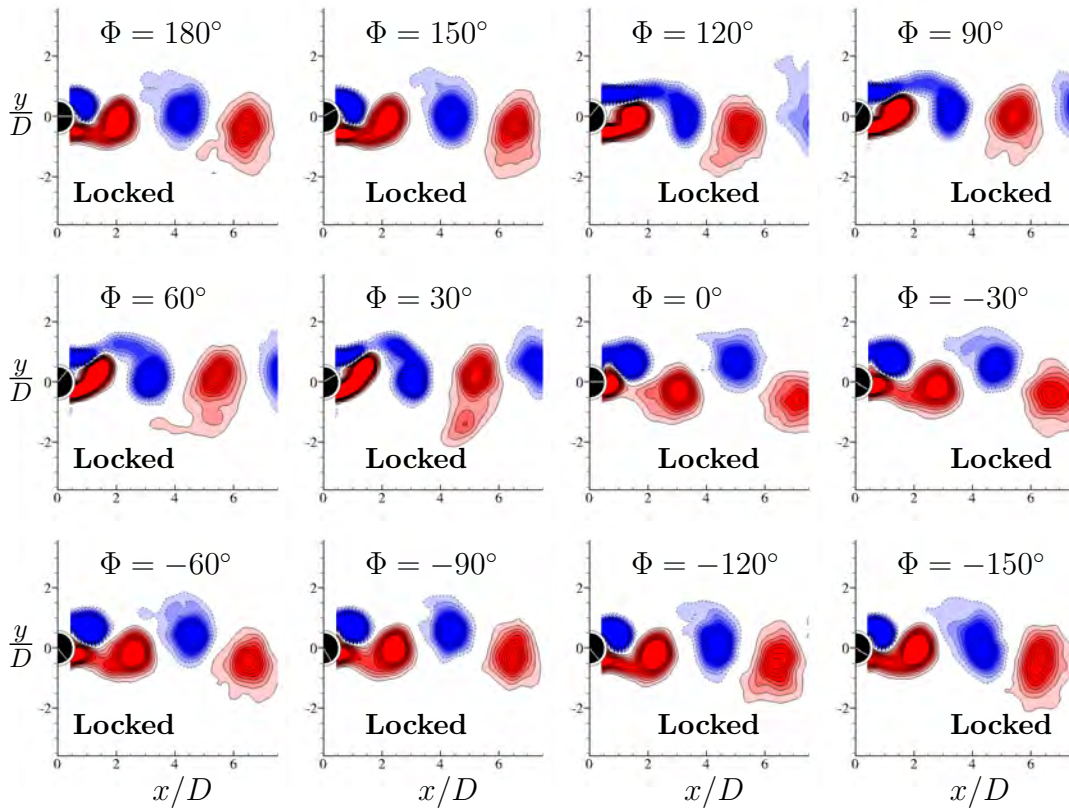


FIGURE 6.20: Motion phase-locked vorticity contours taken at the motion-phase of  $t = T$  for  $A_t = D/4$ ,  $A_\theta = 0.5$  rad,  $f_N = 0.6$  Hz,  $V_R = 1.0$ ,  $F_R = 1$  and  $Re = 1366$ . The near-wake vorticity is shown for different phase angle differences between the two imposed oscillatory motions. The flow direction is from left to right. Vorticity contours are evenly spaced over the range  $[-0.1 : 0.1]$ ; with  $\Delta\omega_z = 0.01$ .

near-wake region is very much a function of the phase angle difference. Both sets of results show that this section of the wake becomes very short for  $\Phi \simeq -100^\circ$ . Further downstream the wake undergoes a rapid transition to a chaotic state. For other phase angle difference ranges, the ordered near-wake persists further downstream but still can be subject to secondary transitions resulting in a quasi-periodic or chaotic far wake. If one measures the wake response using integral measures such as the lift or drag coefficient, then these will be affected to some extent by the far-wake behaviour, even though they primarily respond to the wake state near the cylinder. If the ordered near-wake region is long, then these global measures should indicate synchronisation. As the near-wake is reduced in length, the far-wake behaviour can influence the signal recorded at the cylinder so that it contains low frequency components, or even increase the frequency content to such an extent that the behaviour is chaotic. Interestingly, quasi-periodic and chaotic far-wake behaviour can be observed for elliptical shaped

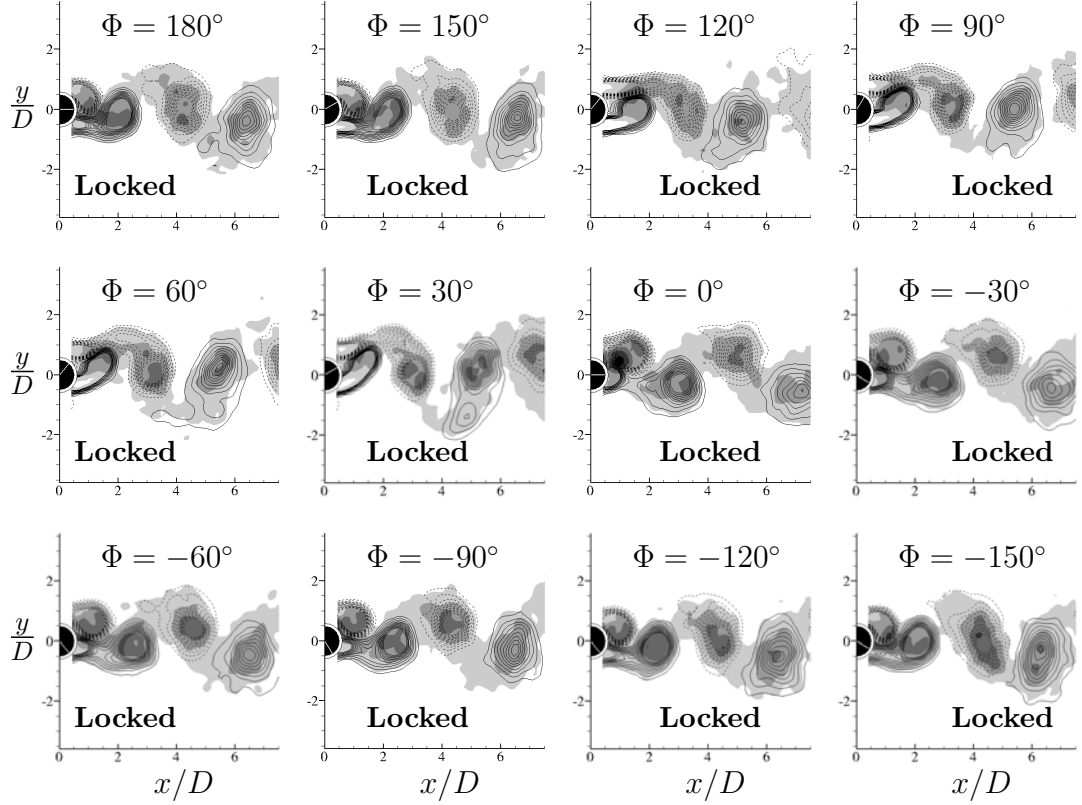


FIGURE 6.21: Motion phase-locked vorticity contours (lines) and root-mean-square vorticity (gray-scale) contours taken at the motion-phase of  $t = T$  for  $A_t = D/4$ ,  $A_\theta = 0.5$  rad,  $f_N = 0.6$  Hz,  $V_R = 1.0$ ,  $F_R = 1$  and  $Re = 1366$ . The near-wake rms vorticity is shown for different phase angle differences between the two imposed oscillatory motions. The flow direction is from left to right. Root-mean-square vorticity contours are evenly spaced over the range  $[0.02 : 0.1]$ ; with  $\Delta\omega_z = 0.02$ , and vorticity contours are evenly spaced over the range  $[-0.1 : 0.1]$ ; with  $\Delta\omega_{zrms} = 0.01$ .

cylinders (Johnson *et al.* 2004) and the normal flat plate (Najjar & Balachandar 1998), even in the unforced case. Experiments and numerical simulations (not shown here) suggest that the suppression mechanism also holds for smaller amplitudes of motion ( $A_\theta$  and  $A_t$ ).

### 6.3.3 Effect of varying $F_{RN}$

Figures 6.27, 6.28, 6.29 and 6.30 present near-wake motion phase-locked vorticity, rms vorticity,  $U$  and  $V$  velocity contours, respectively, taken at  $t = T$  for various  $F_{RN}$  at  $A_t = D/4$ ,  $A_\theta = 0.5$ ,  $V_R = 1.0$  and  $\Phi = -90^\circ$ . It was seen from figure 6.12 that the near-wake becomes unlocked at  $\Phi = -90^\circ$ . This happened at the case where the two motions were oscillating at the same frequency, *i.e.*  $F_R = F_{RN} = 1.0$ . Now the question of how sensitive the synchronisation of the near wake to  $F_{RN}$  is investigated.

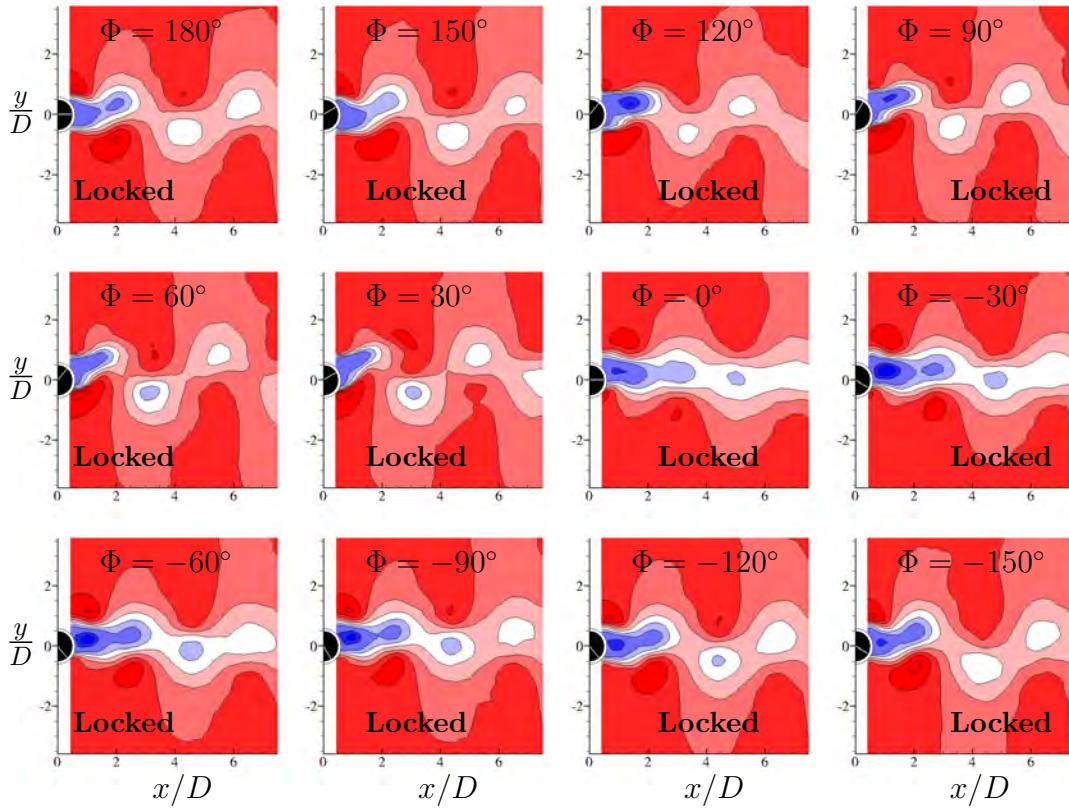


FIGURE 6.22: Motion phase-locked  $U/U_\infty$  velocity contours taken at the motion-phase of  $t = T$  for  $A_t = D/4$ ,  $A_\theta = 0.5$  rad,  $f_N = 0.6$  Hz,  $V_R = 1.0$ ,  $F_R = 1$  and  $Re = 1366$ . The velocity contours are shown for different phase angle differences between the two imposed oscillatory motions. The flow direction is from left to right.  $U/U_\infty$  velocity contours are evenly spaced over the range  $[-0.2 : 2.4]$ ; with  $\Delta(U/U_\infty) = 0.2$ .

The frequency ratio between the imposed oscillatory motions and the natural vortex shedding frequency was varied from  $F_{RN} = 0.85$  to  $F_{RN} = 1.15$  in increments of 0.05. The top left image of figure 6.27 shows the vorticity contours for  $F_{RN} = 0.85$ . The very near-wake vortex structures are coherent, well defined and synchronised. As the  $F_{RN}$  ratio is increased the region where the near-wake vortices are coherent and well defined becomes shorter and gets closer to the cylinder. The very far-wake starts to dissipate. Increasing the  $F_R$  ratio to 0.95 and 1.0, shows that the dissipation region becomes shorter and get closer to the near-wake region. The near-wake vortices are all still locked which can also be seen from figures 6.28, 6.29 and 6.30. Once the frequency ratio becomes greater than unity, the near-wake also starts to become desynchronised and by increasing the  $F_{RN}$  ratio this desynchronisation region becomes smaller and smaller towards the cylinder. This can also be clearly seen in figure 6.30. It was possible through observing the dynamics of the wake as recorded in animation. The

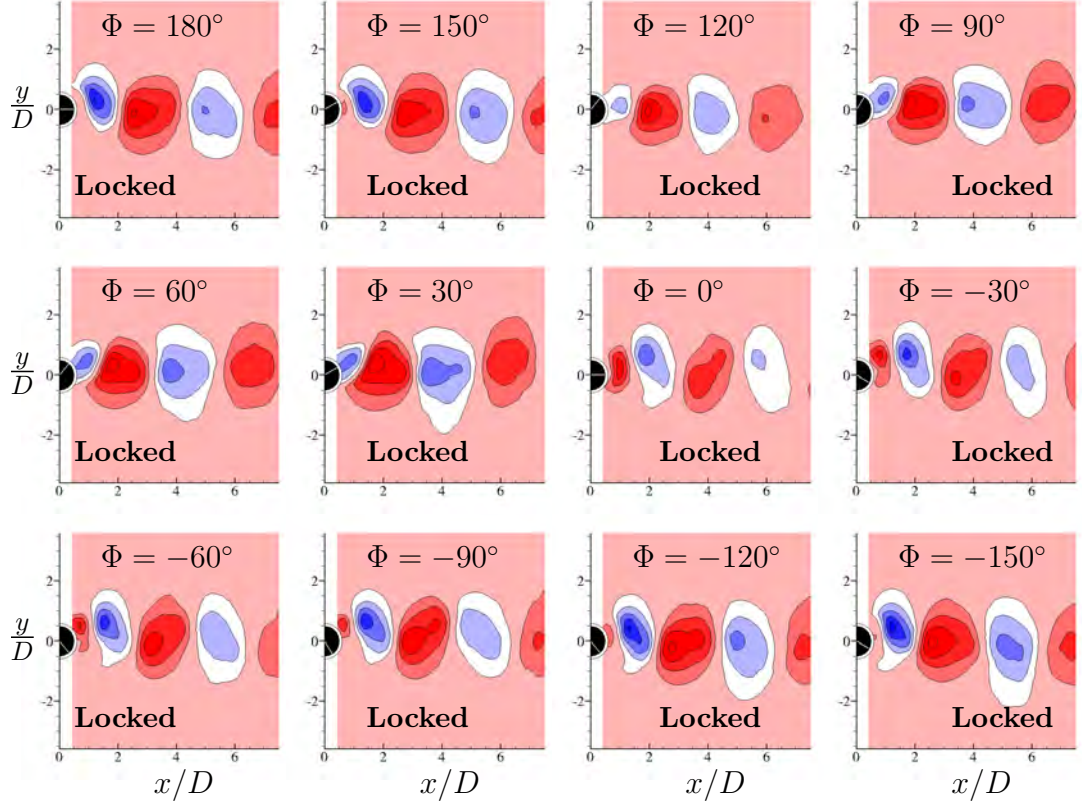


FIGURE 6.23: Motion phase-locked  $V/U_\infty$  velocity contours taken at the motion-phase of  $t = T$  for  $A_t = D/4$ ,  $A_\theta = 0.5$  rad,  $f_N = 0.6$  Hz,  $V_R = 1.0$ ,  $F_R = 1$  and  $Re = 1366$ . The velocity contours are shown for different phase angle differences between the two imposed oscillatory motions. The flow direction is from left to right.  $V/U_\infty$  velocity contours are evenly spaced over the range  $[-0.2 : 2.4]$ ; with  $\Delta(V/U_\infty) = 0.2$ .

recorded animations clearly showed the lock-on behaviour and this is not as clear in the presented figures. This is also evident in figures 6.28, 6.29 and 6.30.

### 6.3.4 Effect of varying $F_R$

All the results presented in the previous sections were obtained when the frequencies of the translational and rotational oscillations were the same, *i.e.*  $F_R = 1$ . This section deals with the case where the frequencies are different. Two cases with  $F_R = 0.5$  and  $F_R = 2$  are investigated. Figures 6.31, 6.32, 6.33 and 6.34 present near-wake motion phase-locked vorticity, rms vorticity,  $U$  and  $V$  velocity contours, respectively, taken at  $t = T$  for various phase differences at  $A_t = D/2$ ,  $A_\theta = 0.5$ ,  $V_R = 1.0$ ,  $F_R = 0.5$  and  $Re = 1251$ . The top left image of figure 6.31 shows the  $\Phi = 120^\circ$  case; similar to previous cases we observe a  $2S$  mode in a single-row. Interestingly and contrary to all the previous cases, the vortices are not shed in the medial plane. They are shed with an angle to the centreline. This is seen in all the cases investigated at  $F_R = 0.5$ . It can also

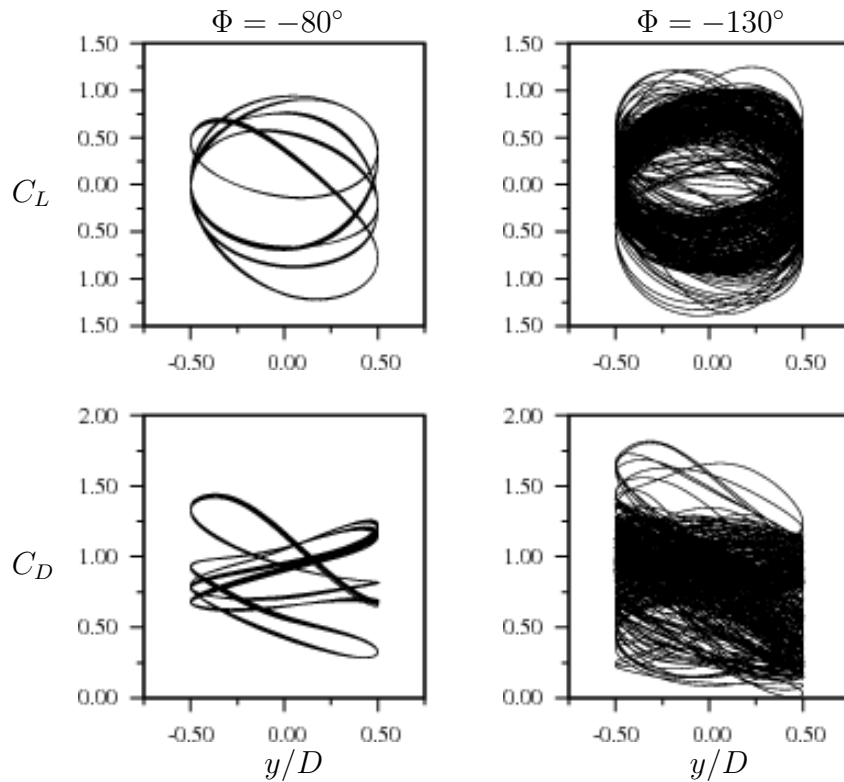


FIGURE 6.24: Lissajous pattern defined horizontally with the translational forcing mechanism ( $y$ ) and vertically with lift ( $C_L$  and top) or drag ( $C_D$  and bottom) coefficient (case 5 of Table 6.1).

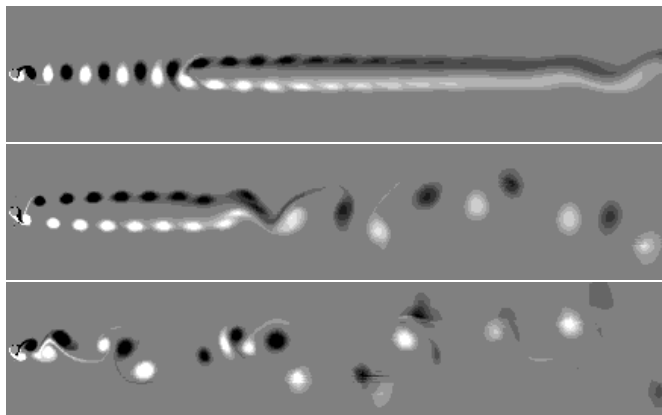


FIGURE 6.25: Typical flow features for different imposed phase differences. Top: single-row of vortices transitioning downstream to a double-row followed by a further secondary instability in the far-wake ( $\Phi = -170^\circ$ ). Centre: double-row of vortices followed by a *quasi-periodic* pattern ( $\Phi = -40^\circ$ ). Bottom: *chaotic* pattern of vortices ( $\Phi = -100^\circ$ ). The domain of the numerical simulation was extended to  $100D$  downstream for these cases.

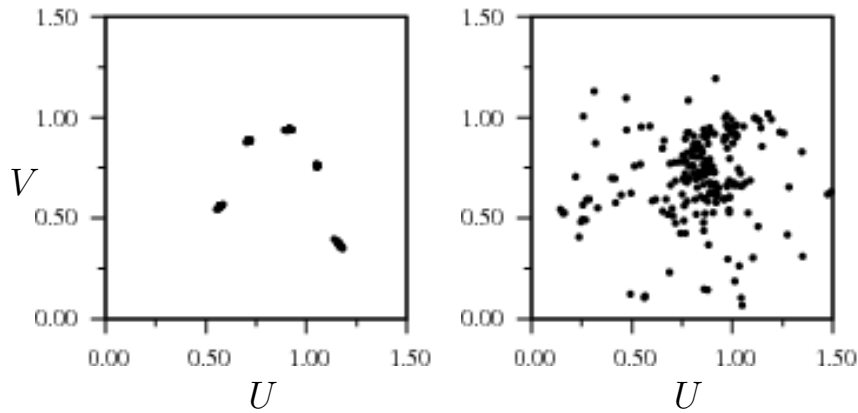


FIGURE 6.26: Poincaré map for two typical unlocked regimes for  $Re = 225$ . Left: quasi-periodic behaviour for  $\Phi = -80^\circ$ ; Right: Chaotic regime for  $\Phi = -130^\circ$ . The phase diagram shows the horizontal and the vertical velocities at  $7D$  downstream on the centreline.

be seen that all the vortices are well defined and coherent. They are also located widely apart from each other. As the phase angle difference reduces the vortices approach each other and the cylinder. The angled shedding of the vortices can be observed for all the phase angle differences studied. Figures 6.32, 6.33 and 6.34 clearly show that there is no transition between modes in the rms,  $U$  and  $V$  velocity contours. As it can be seen from figures 6.35, 6.36, 6.37 and 6.38 all the  $\Phi$  cases are unlocked for the case of  $F_R=2.0$ . It was observed that only the negative sign vortex attached to the cylinder is synchronised and once shed it cannot pick the natural shedding frequency and becomes desynchronised. As the translational motion is oscillating at a higher frequency than the rotational motion in this case the rotational motion doesn't add as much momentum into the shed vortices as it does for the  $F_R < 1$  cases. The vortices dissipate quickly beyond  $3D$  downstream of the cylinder, they are not as well-defined and coherent as in the  $F_R < 1$  cases. The rms vorticity and velocity contours also confirm the patterns related to unlocked cases, similar to what was seen in previous unlocked cases like  $\Phi = -90^\circ$  of figure 6.12.

## 6.4 Chapter Summary

In this chapter we presented, for the first time, experimental results of a cylinder near-wake when the cylinder is experiencing combined rotary and translational oscillation. The effect of phase angle difference between the two forced motions for a given Reynolds number and combination of  $V_R$  and  $F_R$  reveals that regular shedding can be suppressed for particular phase angle differences. The range of phase difference the suppression

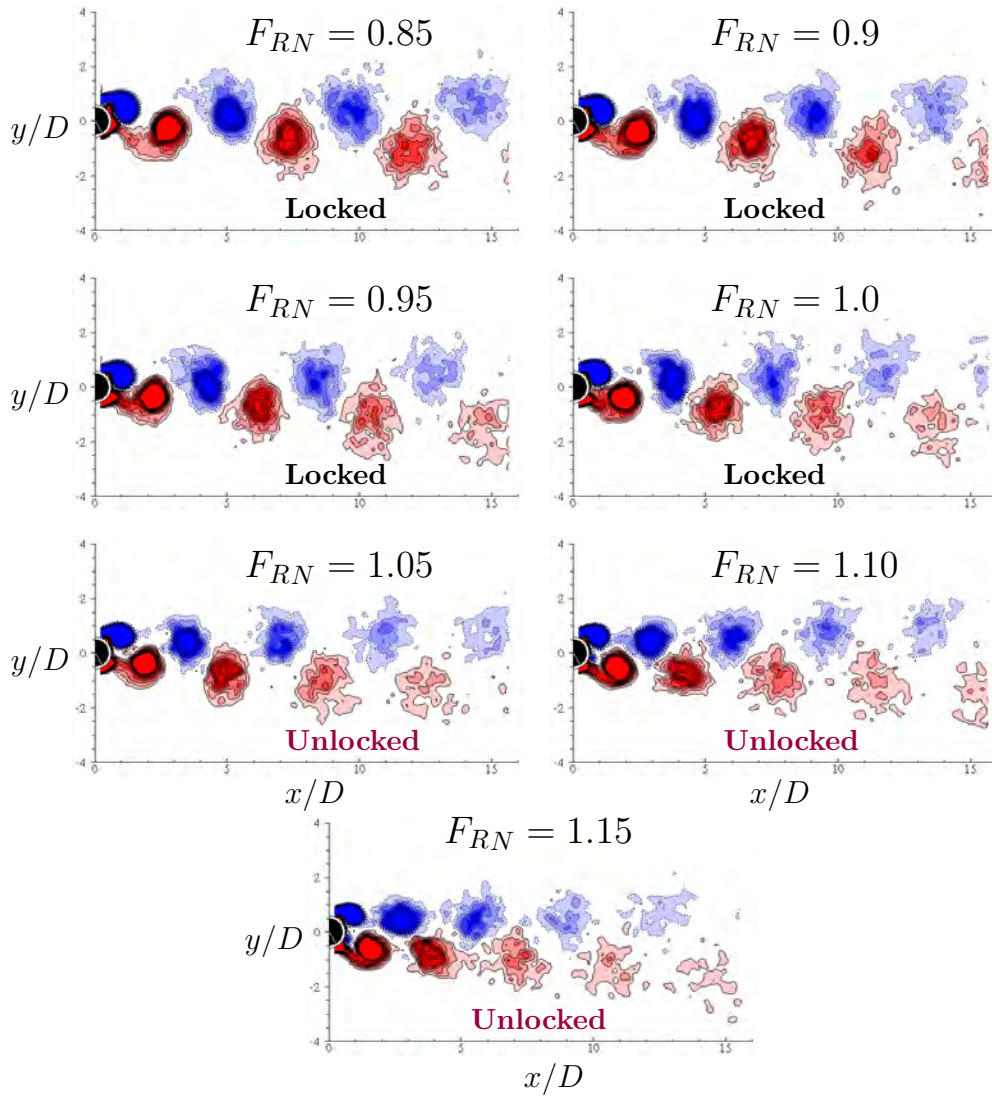


FIGURE 6.27: Motion phase-locked vorticity contours taken at the motion-phase of  $t = T$  for  $A_t = D/4$ ,  $A_\theta = 0.5$  rad,  $f_N = 0.6$  Hz,  $V_R = 1.0$ ,  $\Phi = -90^\circ$  and  $Re = 1247$ . The near-wake vorticity is shown for different phase angle differences between the two imposed oscillatory motions. Of particular interest is the asynchronous (unlocked) wake with the imposed translational motion for the frequency ratios between the oscillatory motions and the natural vortex shedding of  $F_{RN} = 0.9$  to  $F_{RN} = 1.15$ . The flow direction is from left to right. Vorticity contours are evenly spaced over the range  $[-0.2 : 0.2]$ ; with  $\Delta\omega_z = 0.02$ .

occurs depends on the  $V_R$  and  $F_R$  of the oscillations and the oscillation frequency ratio to natural vortex shedding frequency of a fixed cylinder. This experimental study raised several interesting features that were further investigated with the aid of numerical simulations.



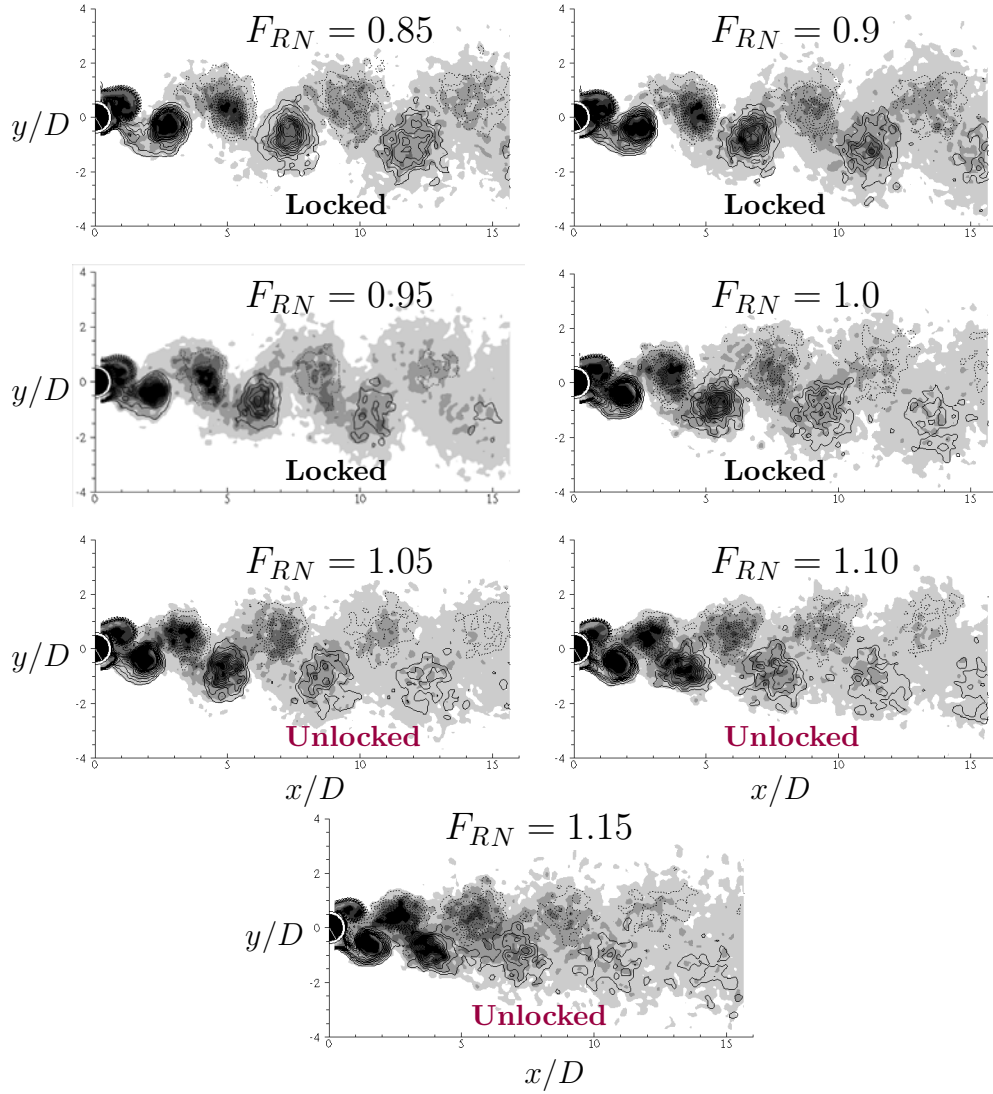


FIGURE 6.28: Motion phase-locked vorticity contours (lines) and root-mean-square vorticity (gray-scale) contours taken at the motion-phase of  $t = T$  for  $A_t = D/4$ ,  $A_\theta = 0.5$  rad,  $f_N = 0.6$  Hz,  $V_R = 1.0$ ,  $\Phi = -90^\circ$  and  $Re = 1247$ . The near-wake rms vorticity is shown for different phase angle differences between the two imposed oscillatory motions. Of particular interest is the asynchronous (unlocked) wake with the imposed translational motion for the frequency ratios between the oscillatory motions and the natural vortex shedding of  $F_{RN} = 0.9$  to  $F_{RN} = 1.15$ . The flow direction is from left to right. Root-mean-square vorticity contours are evenly spaced over the range  $[0.02 : 0.1]$ ; with  $\Delta\omega_{z,rms} = 0.02$ , and vorticity contours are evenly spaced over the range  $[-0.2 : 0.2]$ ; with  $\Delta\omega_z = 0.02$ .

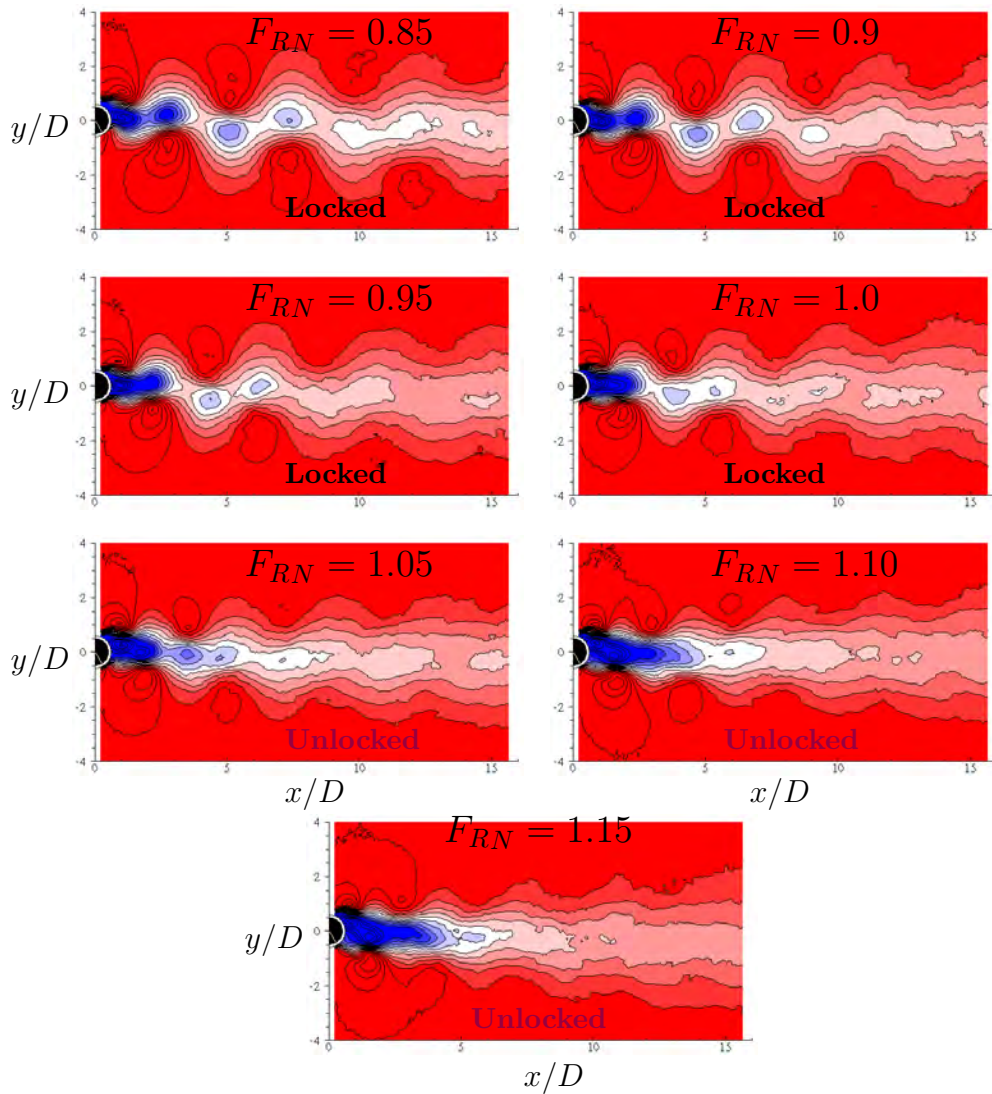


FIGURE 6.29: Motion phase-locked  $U/U_\infty$  velocity contours taken at the motion-phase of  $t = T$  for  $A_t = D/4$ ,  $A_\theta = 0.5$  rad,  $f_N = 0.6$  Hz,  $V_R = 1.0$ ,  $\Phi = -90^\circ$  and  $Re = 1247$ . The near-wake streamwise velocity is shown for different phase angle differences between the two imposed oscillatory motions. Of particular interest is the asynchronous (unlocked) wake with the imposed translational motion for the frequency ratios between the oscillatory motions and the natural vortex shedding of  $F_{RN} = 0.9$  to  $F_{RN} = 1.15$ . The flow direction is from left to right.  $U/U_\infty$  velocity contours are evenly spaced over the range  $[-0.5 : 1.5]$ ; with  $\Delta(U/U_\infty) = 0.1$ .

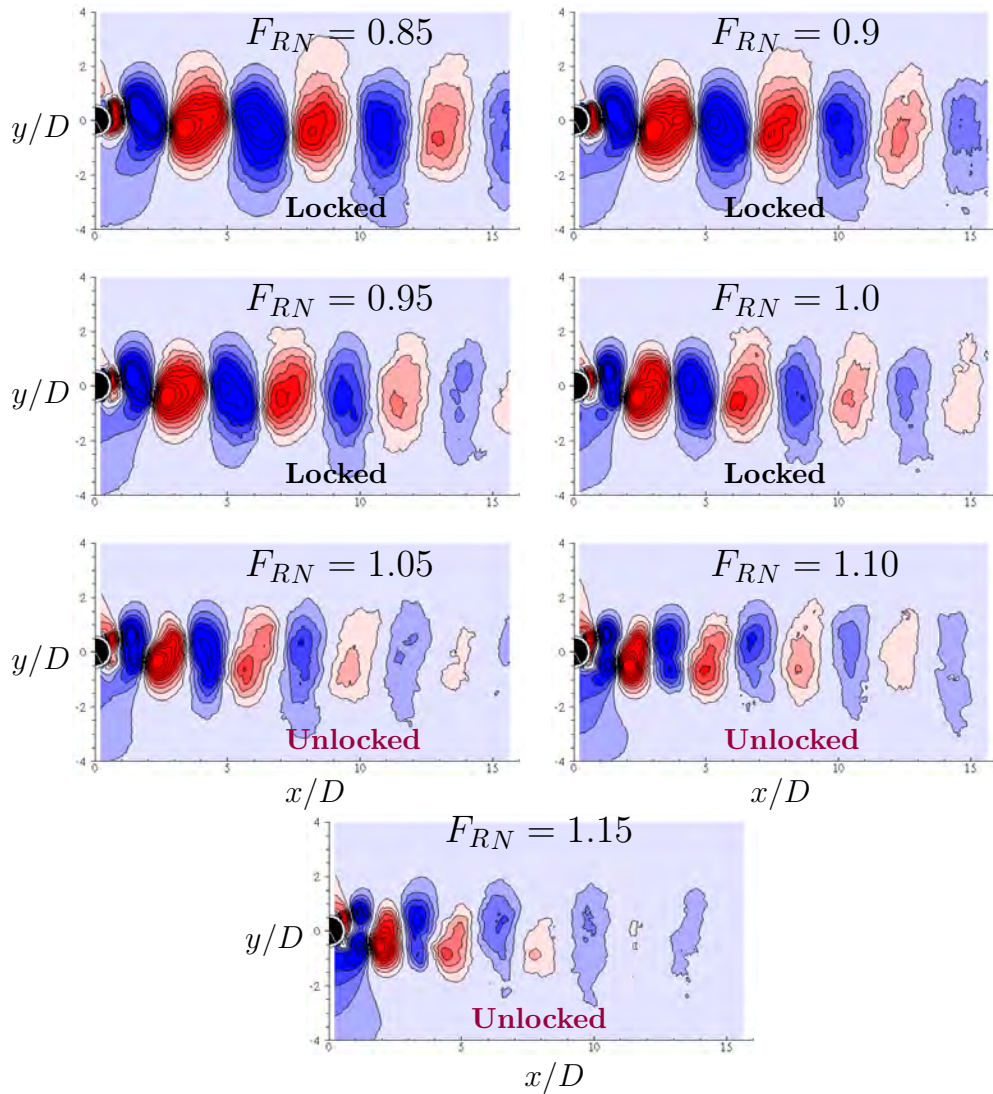


FIGURE 6.30: Motion phase-locked  $V/U_\infty$  velocity contours taken at the motion-phase of  $t = T$  for  $A_t = D/4$ ,  $A_\theta = 0.5$  rad,  $f_N = 0.6$  Hz,  $V_R = 1.0$ ,  $\Phi = -90^\circ$  and  $Re = 1247$ . The near-wake transverse velocity is shown for different phase angle differences between the two imposed oscillatory motions. Of particular interest is the asynchronous (unlocked) wake with the imposed translational motion for the frequency ratios between the oscillatory motions and the natural vortex shedding of  $F_{RN} = 0.9$  to  $F_{RN} = 1.15$ . The flow direction is from left to right.  $V/U_\infty$  velocity contours are evenly spaced over the range  $[0.2 : 7.4]$ ; with  $\Delta(V/U_\infty) = 0.4$ .

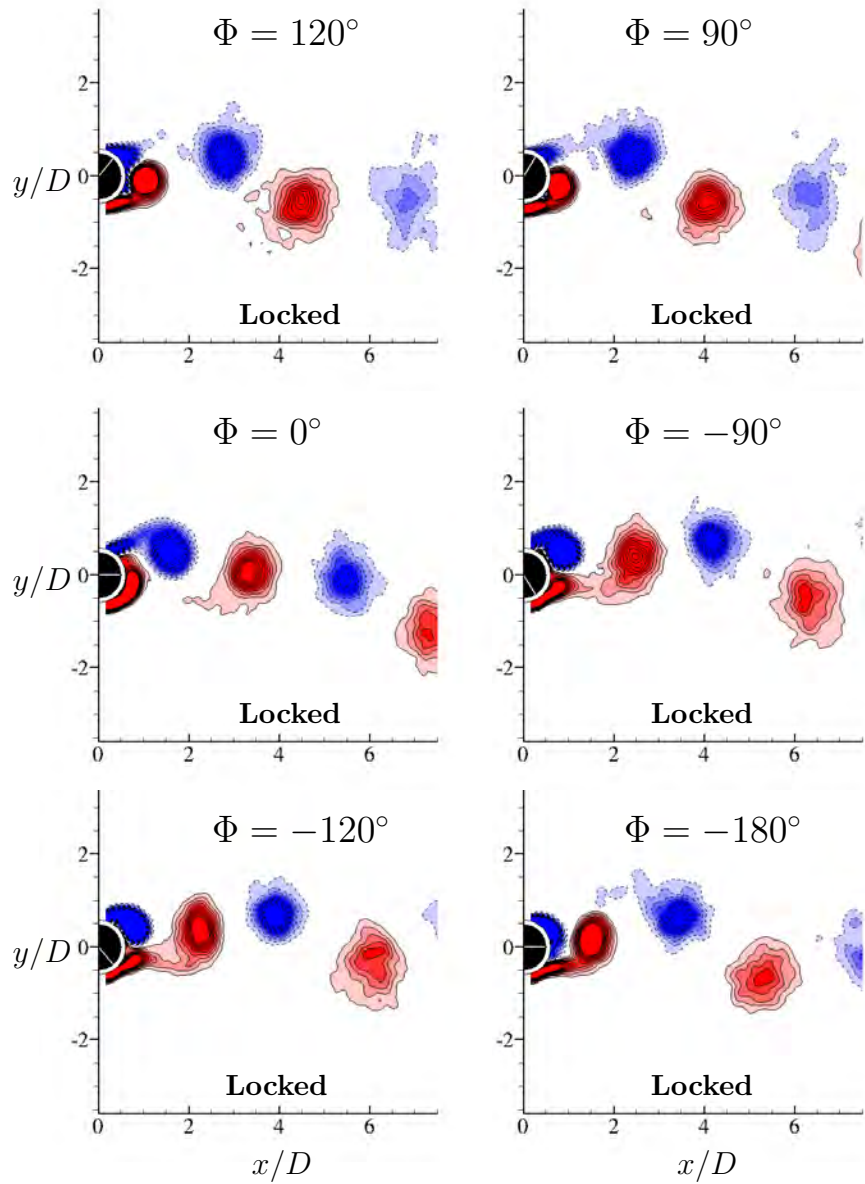


FIGURE 6.31: Motion phase-locked vorticity contours taken at the motion-phase of  $t = T$  for  $A_t = D/2$ ,  $A_\theta = 1.0$  rad,  $f_N = 0.6$  Hz,  $V_R = 1$ ,  $F_R = 0.5$  and  $Re = 1251$ . The near-wake vorticity is shown for different phase angle differences between the two imposed oscillatory motions. Of particular interest is the asynchronous (unlocked) wake with the imposed translational motion for the phase  $\Phi = -90^\circ$ ,  $\Phi = -120^\circ$ ,  $\Phi = -150^\circ$  and  $\Phi = \pm 180^\circ$ . The flow direction is from left to right.

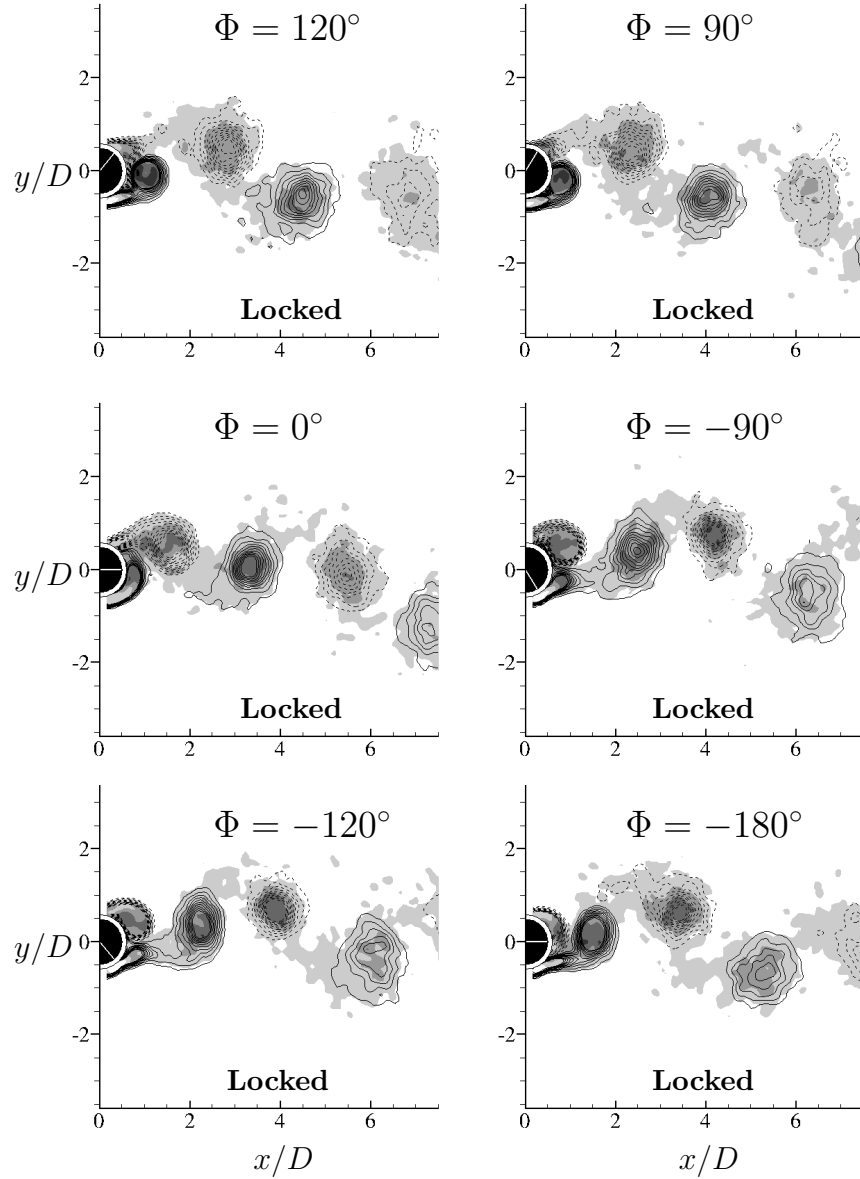


FIGURE 6.32: Motion phase-locked vorticity contours (lines) and root-mean-square vorticity (gray-scale) contours taken at the motion-phase of  $t = T$  for  $A_t = D/2$ ,  $A_\theta = 1.0$  rad,  $f_N = 0.6$  Hz,  $V_R = 1$ ,  $F_R = 0.5$  and  $Re = 1251$ . The near-wake rms vorticity is shown for different phase angle differences between the two imposed oscillatory motions. Of particular interest is the asynchronous (unlocked) wake with the imposed translational motion for the phase  $\Phi = -90^\circ$ ,  $\Phi = -120^\circ$ ,  $\Phi = -150^\circ$  and  $\Phi = \pm 180^\circ$ . The flow direction is from left to right.

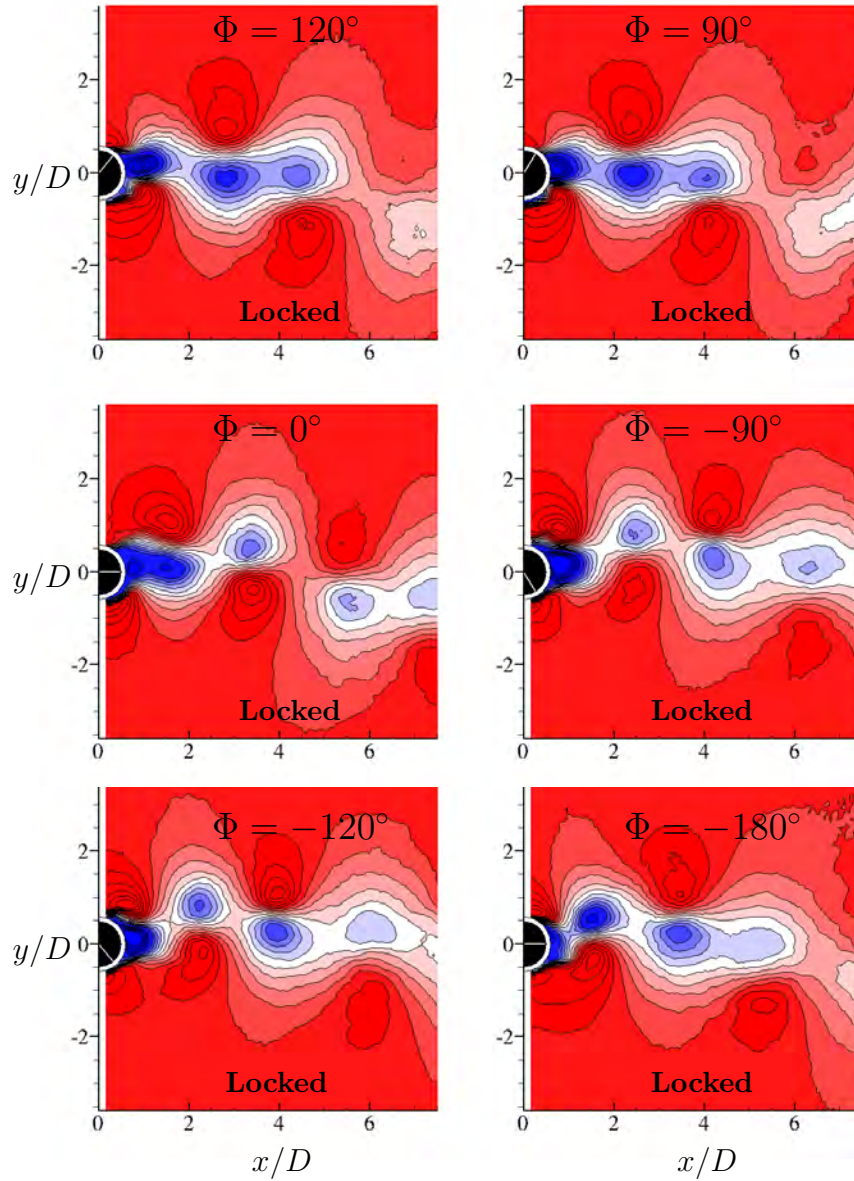


FIGURE 6.33: Motion phase-locked  $U$  velocity contours taken at the motion-phase of  $t = T$  for  $A_t = D/2$ ,  $A_\theta = 1.0$  rad,  $f_N = 0.6$  Hz,  $V_R = 1$ ,  $F_R = 0.5$  and  $Re = 1251$ . The near-wake streamwise velocity is shown for different phase angle differences between the two imposed oscillatory motions. Of particular interest is the asynchronous (unlocked) wake with the imposed translational motion for the phase  $\Phi = -90^\circ$ ,  $\Phi = -120^\circ$ ,  $\Phi = -150^\circ$  and  $\Phi = \pm 180^\circ$ . The flow direction is from left to right.

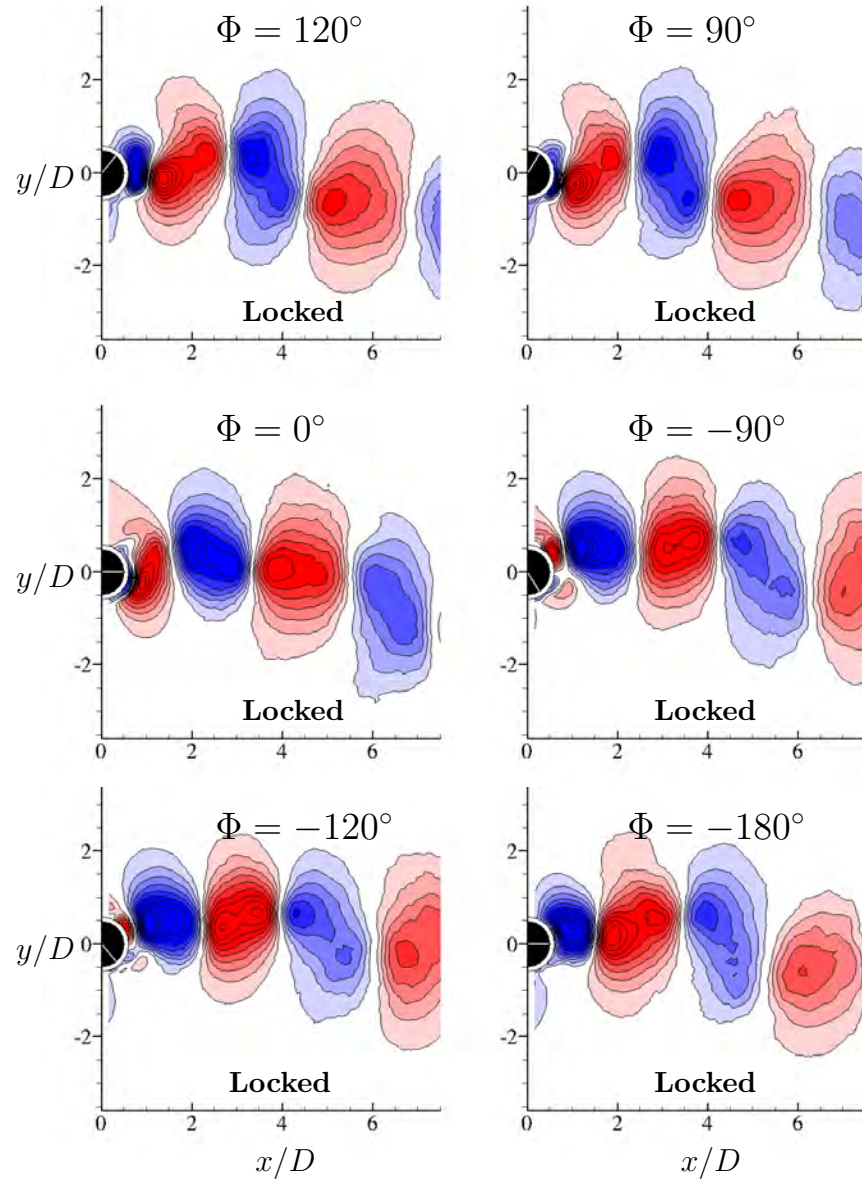


FIGURE 6.34: Motion phase-locked  $V$  velocity contours taken at the motion-phase of  $t = T$  for  $A_t = D/2$ ,  $A_\theta = 1.0$  rad,  $f_N = 0.6$  Hz,  $V_R = 1$ ,  $F_R = 0.5$  and  $Re = 1251$ . The near-wake transverse velocity is shown for different phase angle differences between the two imposed oscillatory motions. Of particular interest is the asynchronous (unlocked) wake with the imposed translational motion for the phase  $\Phi = -90^\circ$ ,  $\Phi = -120^\circ$ ,  $\Phi = -150^\circ$  and  $\Phi = \pm 180^\circ$ . The flow direction is from left to right.

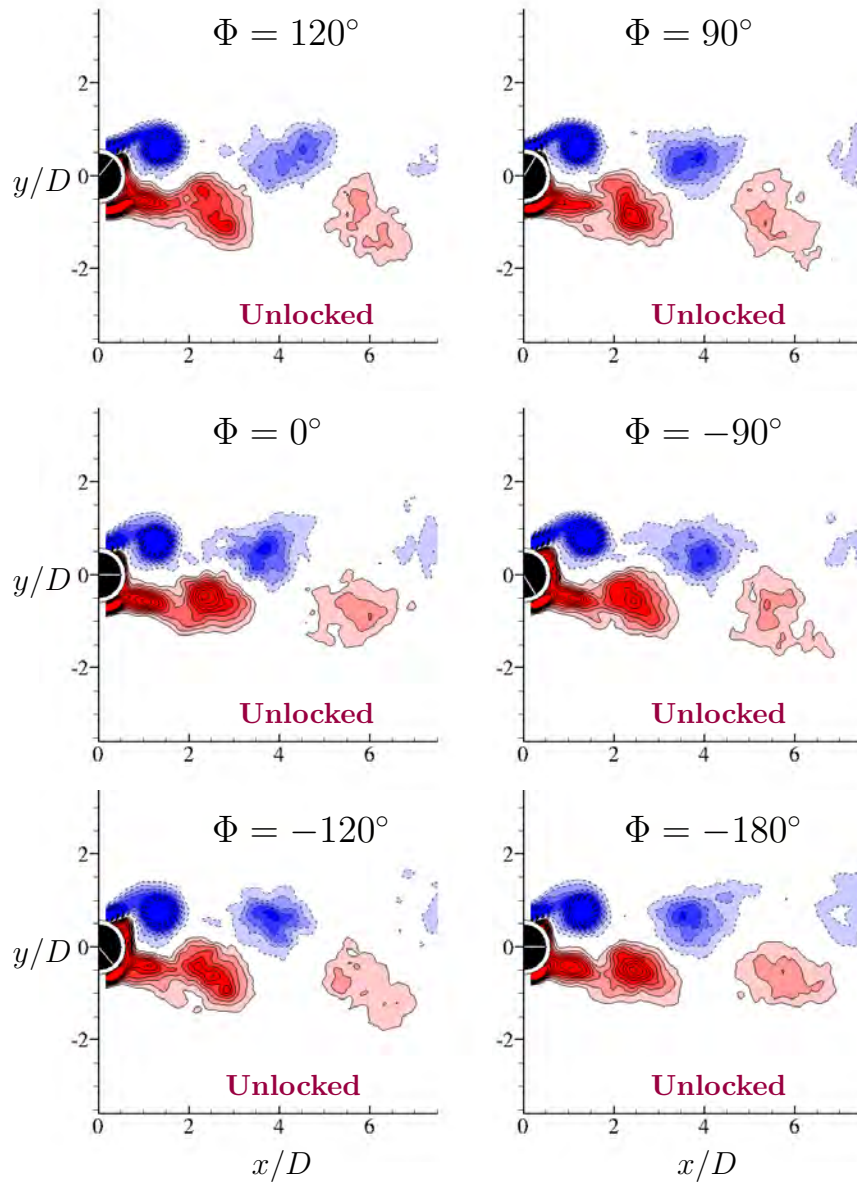


FIGURE 6.35: Motion phase-locked vorticity contours taken at the motion-phase of  $t = T$  for  $A_t = D/2$ ,  $A_\theta = 1.0$  rad,  $f_N = 0.6$  Hz,  $V_R = 1$ ,  $F_R = 2$  and  $Re = 1251$ . The near-wake vorticity is shown for different phase angle differences between the two imposed oscillatory motions. Of particular interest is the asynchronous (unlocked) wake with the imposed translational motion for the phase  $\Phi = -90^\circ$ ,  $\Phi = -120^\circ$ ,  $\Phi = -150^\circ$  and  $\Phi = \pm 180^\circ$ . The flow direction is from left to right.



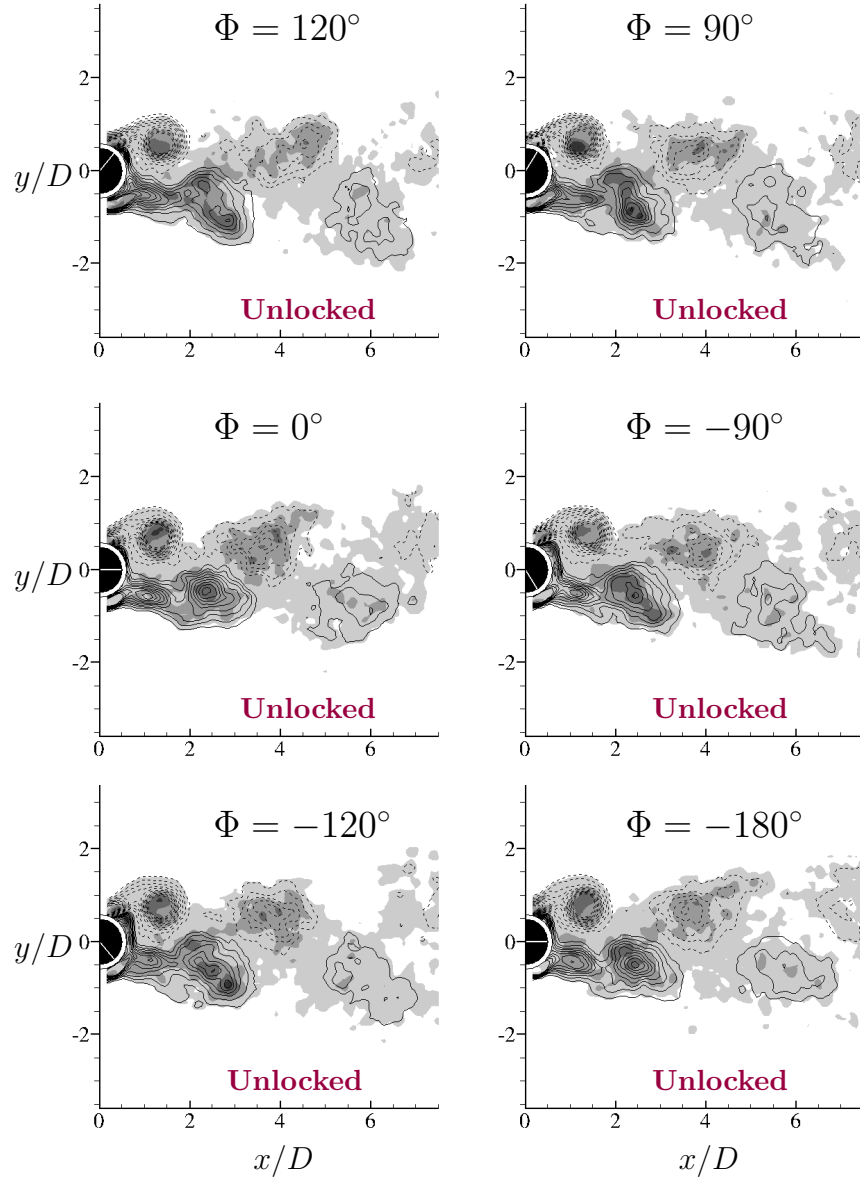


FIGURE 6.36: Motion phase-locked vorticity contours (lines) and root-mean-square vorticity (gray-scale) contours taken at the motion-phase of  $t = T$  for  $A_t = D/2$ ,  $A_\theta = 1.0$  rad,  $f_N = 0.6$  Hz,  $V_R = 1$ ,  $F_R = 2$  and  $Re = 1251$ . The near-wake rms vorticity is shown for different phase angle differences between the two imposed oscillatory motions. Of particular interest is the asynchronous (unlocked) wake with the imposed translational motion for the phase  $\Phi = -90^\circ$ ,  $\Phi = -120^\circ$ ,  $\Phi = -150^\circ$  and  $\Phi = \pm 180^\circ$ . The flow direction is from left to right.

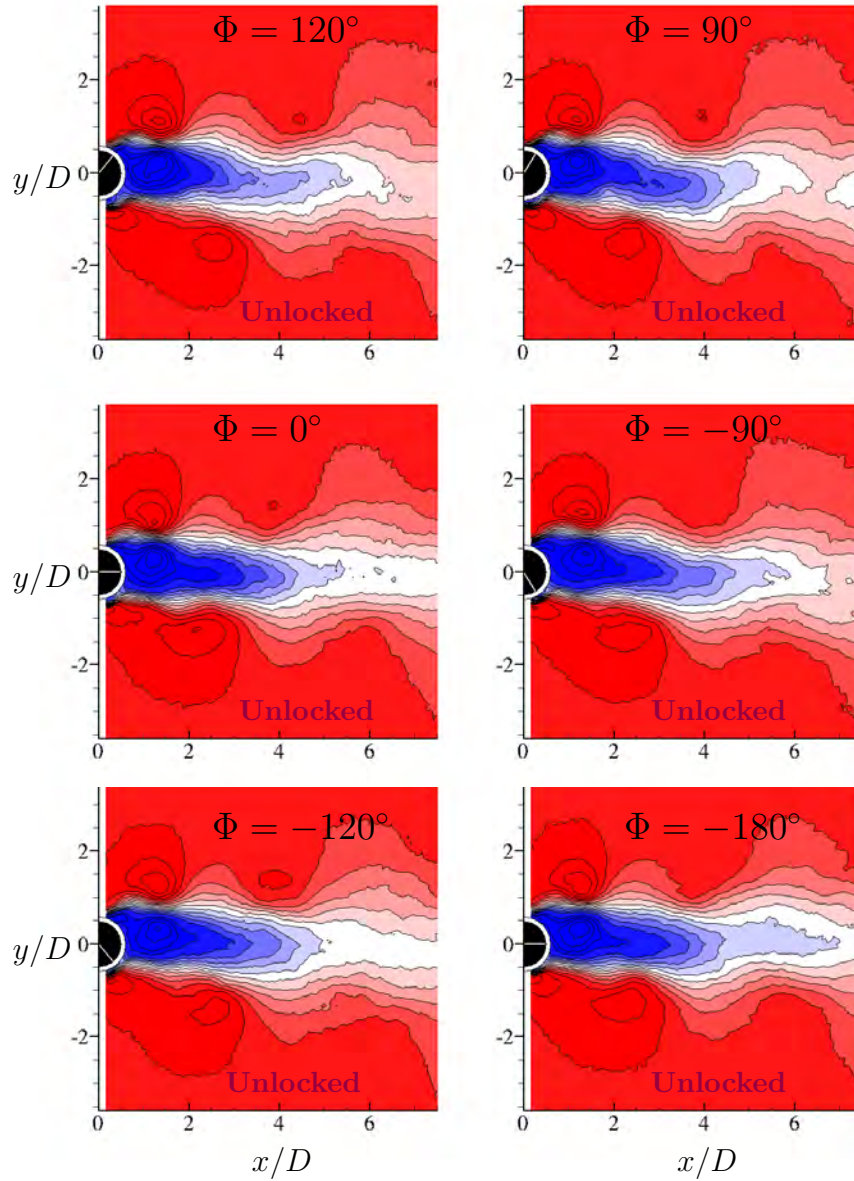


FIGURE 6.37: Motion phase-locked  $U$  velocity contours taken at the motion-phase of  $t = T$  for  $A_t = D/2$ ,  $A_\theta = 1.0$  rad,  $f_N=0.6$  Hz,  $V_R=1$ ,  $F_R=2$  and  $Re=1251$ . The near-wake streamwise velocity is shown for different phase angle differences between the two imposed oscillatory motions. Of particular interest is the asynchronous (unlocked) wake with the imposed translational motion for the phase  $\Phi = -90^\circ$ ,  $\Phi = -120^\circ$ ,  $\Phi = -150^\circ$  and  $\Phi = \pm 180^\circ$ . The flow direction is from left to right.

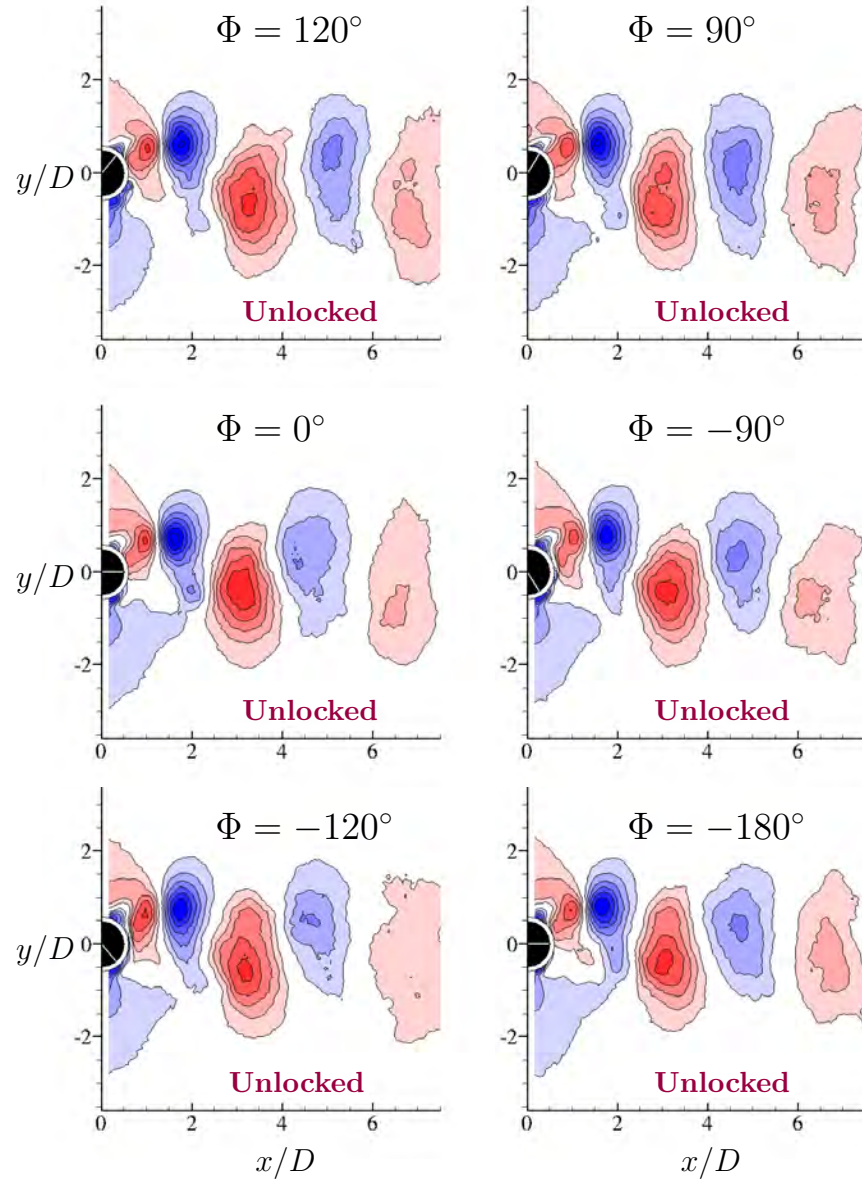


FIGURE 6.38: Motion phase-locked  $V$  velocity contours taken at the motion-phase of  $t = T$  for  $A_t = D/2$ ,  $A_\theta = 1.0$  rad,  $f_N = 0.6$  Hz,  $V_R = 1$ ,  $F_R = 2$  and  $Re = 1251$ . The near-wake transverse velocity is shown for different phase angle differences between the two imposed oscillatory motions. Of particular interest is the asynchronous (unlocked) wake with the imposed translational motion for the phase  $\Phi = -90^\circ$ ,  $\Phi = -120^\circ$ ,  $\Phi = -150^\circ$  and  $\Phi = \pm 180^\circ$ . The flow direction is from left to right.



## Chapter 7

# Conclusions and recommended future work

This thesis deals with analysis and experimental investigation of a new class of wake flows generated by the combined translational and rotational oscillation of a circular cylinder. Numerical simulation was also used as a tool to provide further insight into the wake flows produced. The translational and rotational oscillations are harmonic and specifically the translational and rotational oscillatory amplitudes have the form  $y(t) = A_t \sin(2\pi f_t t)$  and  $\theta(t) = A_\theta \sin(2\pi f_\theta t + \Phi)$ , respectively. In general, there have been three related themes of study presented in the preceding chapters. The majority of the investigation focused on an examination of the flow around combined translational and rotational oscillatory motions of a circular cylinder. In the following sections the major conclusions arrived at for each theme are stated.

### 7.1 Translational Oscillations of a Circular Cylinder

The major objective of this study was to quantitatively investigate the structure and dynamics of the flow induced by a circular cylinder performing pure translational oscillations in a quiescent fluid within the range of control parameters  $0 \leq KC_t \leq 10$ ,  $0 \leq \beta_t \leq 100$ , the same parameter range as that of Tatsuno & Bearman (1990). All of the two- and three-dimensional regimes of the Tatsuno & Bearman (1990) map except regime C (the quasi-periodic regime), were investigated. The results were obtained using flow visualisation and PIV techniques. The following summarises the important findings of the second part of this research:

- We quantified the flow around a purely translational oscillating cylinder in a quiescent fluid for the ranges of  $1.6 < KC_t < 15$  and  $5 < \beta_t < 160$ .

- The results for regime B, reveal the onset of three-dimensionality and symmetry breaking, as was suggested by Tatsuno & Bearman (1990).
- The two-dimensionality of the flow for regimes A\* and A was confirmed and investigated.
- Contrary to the two-dimensional numerical investigations of Iliadis & Anagnostopoulos (1998) and Dütsch *et al.* (1998) and the results of Nehari *et al.* (2004), the intermittent switching in the direction of the V-shaped vortex pattern in regime E was observed. However, this switching was observed to be irregular and its cause has not been yet determined but, as mentioned by Tatsuno & Bearman (1990), this is presumably triggered by small disturbances in the flow.
- Tatsuno & Bearman (1990) defined regime F as a double-pair diagonal regime, in which vorticity is shed diagonally with respect to the axis of oscillation. Elston (2005) also performed a series of numerical simulations on this regime. Examination of Elston (2005)'s numerical results reveal that a single vortex shed from the cylinder can also be identified and it is clearly present in his results (figure 4.9). It is proposed from the present study that this regime could be characterised as the  $2P + S$  pattern, so regime F should be defined as a double-pair and single vortex diagonal regime instead.

## 7.2 The “Swimming” Cylinder

The purpose of this part of the research was to investigate not only the near-wake structure of the combination of the two forcing mechanisms, but also to extend this to examine the three-dimensional nature of the wake, which is yet to receive any attention. The results of the present chapter incorporate both experimental and numerical studies, although the main focus is on the experimental investigations. The numerical simulations, *i.e.* Floquet stability analysis and DNS, were used as tools to provide further insights into the wake flows produced. To characterise the experimental flows, as discussed in Chapter 3, PIV was employed. The study is restricted to the case with the phase angle set to  $\Phi = \pi$ , and for large amplitude oscillations, corresponding to a *swimming cylinder*. The following summarises the important findings of the second part of this research:

- The previous numerical study (Blackburn *et al.* 1999) showed that for the *swimming cylinder* case, because of the phase difference, the oscillation velocities at the cylinder surface cancel on one side and reinforce on the other. This eventually leads to preferential vorticity generation and transport on one side, and the cylinder rotational motion sweeps this vorticity around to the other side producing a thrust wake. For the first time the present experimental investigation of such flows confirms the transportation of generated vorticities to only one side of the cylinder, hence generation of the thrust wake. The present study also shows that the flow around the swimming cylinder is unsteady and not two-dimensional, undergoing transition to three-dimensionality soon after startup.
- This work shows that the wake becomes three-dimensional at a Reynolds number of approximately 100 due to a three-dimensional instability with a spanwise wavelength of approximately 2 cylinder diameters (long wavelength mode).
- The Floquet analysis also shows that the two-dimensional base flow is also unstable to another three-dimensional instability with a shorter wavelength ( $\lambda \approx 0.7D$ ) for  $Re \geq 226$ ; however, the experimental results, even at much higher Reynolds numbers do not show any sign of the occurrence of this mode.
- The two long (observed and confirmed experimentally) and short (only observed numerically) wavelength modes are broadly analogous to the three-dimensional wake transition mode for a circular cylinder, despite the distinct differences in wake/mode topology. The stability of the long wavelength mode was confirmed by experimental measurements.
- The experimental results indicate that the development of three-dimensionality in the wake leads to significant distortion of the previously two-dimensional wake.

### 7.3 Combined translational and rotational oscillatory motion in free-stream

The focus of this part of the study was on the experimental investigation and numerical results of the wake flow created in a free-stream behind a cylinder undergoing forced combined oscillatory motions. The motion consists of two independent oscillations: cross-stream translation and rotation. In this study the effect of another independent

variable, *i.e.* Reynolds number, was investigated. The primary focus here was on the effect of the phase difference between the two motions. The effect of change of translational amplitude has also been briefly investigated. In general, the results show that there is an unexpected loss of synchronisation of the wake for a finite range of phase differences at a given Reynolds number. The following summarises the important findings of the third part of this research:

- For the first time, experimental results of a cylinder near-wake when the cylinder is experiencing combined rotary and translational oscillation are presented.
- The effect of the phase differences between the two forced motions for a given Reynolds number and combination of  $V_R$  and  $F_R$  reveals that regular shedding can be suppressed for particular phase differences. At lower values of  $V_R$ , over the range of phase difference angle studied, no transition to different wake modes is observed. All the vortices in the near-wake region of the cylinder are synchronised and coherently shed in the  $2S$  mode. Increasing the  $V_R$  value beyond a certain value changes the wake modes and synchronisation effect of the vortices in the near-wake. The vortices become unlocked and less coherent as  $V_R$  is increasing further for a range of  $\Phi$ .
- The effect of changing translational and rotational amplitudes for a given  $V_R$ , *i.e.*  $V_R=1.0$ , was also investigated. It seems that at higher  $A_t$  and lower  $A_\theta$  the vortices in the near-wake are more compact and larger in size. Changing the  $A_t$  and  $A_\theta$  did not seem to have any effect on the synchronisation of the vortices and the wake modes.
- The experimental and numerical results were compared successfully. The results reveal that the discrepancy in the value of the Reynolds number does not have an impact on the synchronisation for  $\Phi$  values close to the loss of synchronisation. The numerical simulations confirm the loss of synchronisation for the same region as the experiments.
- The numerical simulations revealed that the unlocked regime contains quasi-periodic and chaotic patterns. The chaotic regime appears to be surrounded by quasi-periodicity. Also the likelihood of an unlocked regime is greater when the ratio  $F_{RN}$  is higher than unity. It appears that synchronisation may be a



more complex process than at first thought. Both the experimental and numerical results show that the size of the nearly periodic near-wake region is very much a function of the phase difference. Both sets of results show that this section of the wake becomes very short for  $\Phi \simeq -100^\circ$ . Further downstream the wake undergoes a rapid transition to a chaotic state. For other phase difference ranges, the ordered near-wake persists further downstream but still can be subject to secondary transitions resulting in a quasi-periodic or chaotic far-wake.

- The range of phase difference over which the suppression occurs depends on the  $V_R$  and  $F_R$  of the oscillations and the oscillation frequency ratio to natural vortex shedding frequency of a fixed cylinder. The results show that the vortices are synchronised in the near-wake at  $F_{RN}$  values less than unity and unlocked when  $F_{RN} > 1.0$ .

## 7.4 Recommendations for Future Work

It is hoped that the present investigation has provided some additional understanding of the dynamics of flows created by oscillating bluff bodies. However it has also raised a number of issues that warrant further investigation. In relation to a cylinder performing translational oscillations some of these include:

- Further examination of the flow transition close to boundaries between the regimes experimentally.
- Simultaneous force measurements can give more insight into the physics of flow at low  $KC_t$  and  $\beta_t$ .

Because the ‘‘Swimming’’ cylinder problem has been studied so little in the past there is a great deal of further work which could be done. At this stage, one of the pieces of work might be to investigate the effect of frequency and amplitude ratios between the two forcing motions on the three-dimensionality of the flow.

Other factors which could be examined are listed below:

- As was mentioned several times previously, because of the phase difference, the oscillation velocities at the cylinder surface cancel on one side and reinforce on the other. Although previous two-dimensional simulations have shown that this mechanism leads to self propulsion orthogonal to the translational oscillatory

motion, the question of whether this will be effective at higher Reynolds numbers remains.

- The experimental results indicate that the development of three-dimensionality in the wake leads to significant distortion of the previously two-dimensional wake. The effect on the self-propulsion is yet to be determined.
- The forces experienced by the cylinder have not yet experimentally examined. Measuring forces exerted on the cylinder can give more insight into understanding the physics of flow.
- The experimental and numerical results of the present research revealed that a thrust wake is generated around the swimming cylinder. This thrust has not yet experimentally been measured. This can be used to understand the thrust generating ability of the swimming cylinder and find an optimum thrust.

The combined translational and rotational oscillatory motion in free-stream problem also raises a number of questions that have not been addressed in this initial study:

- The present study only investigated the cross-stream translational oscillatory motion. Al-Mdallal (2004) and Kocabiyik & Al-Mdallal (2005) showed that the in-line translational oscillation also has strong effect on the synchronisation of vortices, this is yet to be investigated thoroughly experimentally.
- If one measures the wake response using integral measures such as the lift or drag coefficient, then these will be affected to some extent by the far-wake behaviour, even though they primarily respond to the wake state near the cylinder. If the ordered near-wake region is long, then these global measures should indicate synchronisation. So it is highly recommended to measure forces exerted on the cylinder to further investigate the synchronisation effect.
- The effect of various independent variables like  $F_{RN}$ ,  $F_R$  and  $V_R$  was investigated experimentally for the first time. All the experiments need to be further investigated for a wider parameter range of independent variables.

# Appendix A

## Symmetry Definitions

The following defines the spatial and/or temporal properties of flow. The characteristics of the two-dimensional symmetric state can be summarised as (Elston 2005):

1.  $T$ -periodic flow.
2. A reflection symmetry about the axis of oscillation,  $x/D = 0$ .
3. A  $T/2$  reflection symmetry about  $y/D = 0$ .
4. A spanwise invariance of the flow.

With the coordinate system fixed to the cylinder axis the two spatial symmetries for the velocity fields of the base flow can be written as:

$$x\text{-reflection : } K_x(u, v, w)(x, y, z, t) = (-u, v, w)(-x, y, z, t), \quad (\text{A.1})$$

$$z\text{-translation : } R_\alpha(u, v, w)(x, y, z, t) = (u, v, w)(x, y, z + \alpha, t), \quad (\text{A.2})$$

$$z\text{-reflection : } K_z(u, v, w)(x, y, z, t) = (u, v, -w)(x, y, -z, t). \quad (\text{A.3})$$

With some advance knowledge from the visualisations of Tatsuno & Bearman (1990), about the way in which the flow states change, the spatio-temporal symmetries can be written accordingly. The  $T/2$  reflection symmetry about  $y = 0$  and the  $T$ -periodicity are written as two spatio-temporal symmetry forms:

$$H_1(u, v, w)(x, y, z, t) = (u, -v, w)(x, -y, z, t + T/2), \quad (\text{A.4})$$

$$H_2(u, v, w)(x, y, z, t) = (-u, -v, w)(-x, -y, z, t + T/2). \quad (\text{A.5})$$

These two forms together define the spatiotemporal symmetry. In figure A.1 the ways in which the two-dimensional symmetry can be broken are illustrated in schematic form. The reflection symmetry,  $K_x$ , when applied twice returns the original starting point.

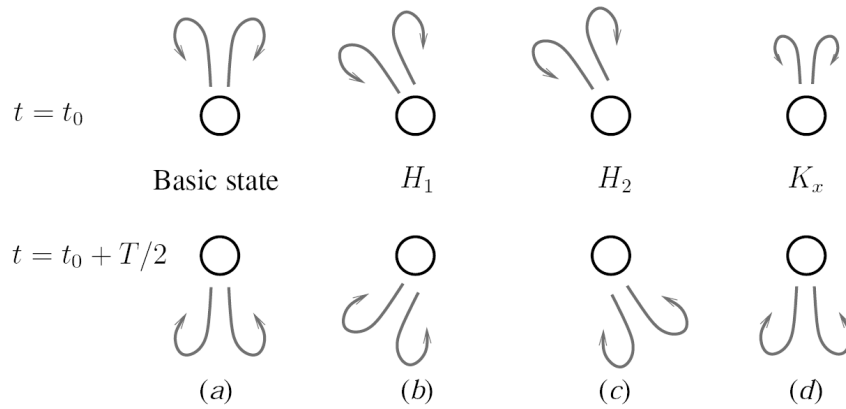


FIGURE A.1: Schematics illustrating representative ways in which the two-dimensional symmetries of the basic state can be broken. The basic state, (a), has the three symmetries  $K_x$ ,  $H_1$ ,  $H_2$ , while in (b – d), two out of three break, and the outcomes are labelled with their remaining symmetry. *The images appeared in Elston (2005) and is reproduced by permission.*

## Appendix B

# Journal publications arising from research reported in this thesis

This chapter presents copies of the two papers as were appeared in the *Physics of Fluids* journal arising from the results and findings of Chapters 5 and 6. The reference for the papers are:

1. NAZARINIA, M., LO JACONO, D., THOMPSON, M. C. & SHERIDAN, J. 2009  
The three-dimensional wake of a cylinder undergoing a combination of translational and rotational oscillation in a quiescent fluid. *Physics of Fluids* **21** (6), 064101.
2. NAZARINIA, M., LO JACONO, D., THOMPSON, M. C. & SHERIDAN, J. 2009  
Flow behind a cylinder forced by a combination of oscillatory translational and rotational motions. *Physics of Fluids* **21**, (5), 051701.

## The three-dimensional wake of a cylinder undergoing a combination of translational and rotational oscillation in a quiescent fluid

M. Nazarinia, D. Lo Jacono, M. C. Thompson, and J. Sheridan

*Department of Mechanical and Aerospace Engineering, Fluids Laboratory for Aeronautical and Industrial Research (FLAIR), Monash University, P.O. Box 31, Melbourne, Victoria 3800, Australia*

(Received 18 February 2009; accepted 5 May 2009; published online 4 June 2009)

Previous two-dimensional numerical studies have shown that a circular cylinder undergoing both oscillatory rotational and translational motions can generate thrust so that it will actually self-propel through a stationary fluid. Although a cylinder undergoing a single oscillation has been thoroughly studied, the combination of the two oscillations has not received much attention until now. The current research reported here extends the numerical study of Blackburn *et al.* [Phys. Fluids **11**, L4 (1999)] both experimentally and numerically, recording detailed vorticity fields in the wake and using these to elucidate the underlying physics, examining the three-dimensional wake development experimentally, and determining the three-dimensional stability of the wake through Floquet stability analysis. Experiments conducted in the laboratory are presented for a given parameter range, confirming the early results from Blackburn *et al.* [Phys. Fluids **11**, L4 (1999)]. In particular, we confirm the thrust generation ability of a circular cylinder undergoing combined oscillatory motions. Importantly, we also find that the wake undergoes three-dimensional transition at low Reynolds numbers ( $Re \approx 100$ ) to an instability mode with a wavelength of about two cylinder diameters. The stability analysis indicates that the base flow is also unstable to another mode at slightly higher Reynolds numbers, broadly analogous to the three-dimensional wake transition mode for a circular cylinder, despite the distinct differences in wake/mode topology. The stability of these flows was confirmed by experimental measurements. © 2009 American Institute of Physics. [DOI: 10.1063/1.3147935]

### I. INTRODUCTION

A circular cylinder undergoing a combination of oscillatory translation and rotation in quiescent fluid has not received much attention until now. It is well known that when a bluff body is oscillating translationally in a quiescent fluid, secondary streaming is generated around the body because of nonlinear effects.<sup>1</sup> However, the combination of two oscillatory forcing mechanisms, under specific conditions detailed later, results in a net thrust being experienced by the circular cylinder in a direction normal to the translational axis.<sup>2</sup> The cylinder experiencing thrust, while undergoing a series of pitch and plunge, has been labeled the *swimming cylinder*.

Numerous studies involving pure oscillatory motions, either translational or rotational, exist for different flow conditions.<sup>3–13</sup> Among them Honji<sup>3</sup> for the first time produced visualizations of the three-dimensional structures of such flows. Honji<sup>3</sup> visualized the flow around a transversely oscillating cylinder in a quiescent fluid, and produced excellent visualizations of a three-dimensional flow instability. The presence of mushroom shaped vortices was observed, in a plane normal to the direction of cylinder motion, which was arranged alternately along each side of the cylinder span in a double row. These structures were named the “Honji instability” by Sarpkaya<sup>14</sup> although Honji simply referred to the patterns formed as “streaked flow.” Also Tatsuno and Bearman<sup>5</sup> produced a control space map, classifying the space into eight flow regimes each with a two- or three-

dimensional flow structure and vortex shedding characteristics. Using two different flow visualization techniques, they comprehensively investigated translational harmonic oscillation in a quiescent fluid over a range of two independent variables, e.g., the amplitude and frequency of oscillation.

More recent numerical works<sup>15–17</sup> studied the instability of such flows, as well as Nehari *et al.*<sup>18</sup> who numerically looked at three dimensionality of the flow at low amplitudes and frequencies. Elston *et al.*<sup>15,16</sup> investigated the wakes using direct numerical simulation with Floquet analysis. They isolated and classified the symmetry breaking instabilities from the two-dimensional basic states as a function of Tatsuno and Bearman’s<sup>5</sup> control parameters.

Although not strictly relevant to the present study being in a quiescent fluid, the flows around a rotationally oscillating cylinder have also been investigated thoroughly.<sup>9–13,19,20</sup> Taneda<sup>9</sup> experimentally investigated the effects of rotary cylinder oscillations over a low Reynolds number range ( $Re = [30–300]$ ) using flow visualization. Experiments at a higher Reynolds number<sup>10</sup> of  $1.5 \times 10^4$  have yielded related results to those of Taneda.<sup>9</sup> Numerical studies of vortex shedding from a rotationally oscillating cylinder,<sup>19,20</sup> recorded the transition and selection of different vortex shedding modes and the lock-on phenomenon. More recently, Poncet<sup>11</sup> looked at the three dimensionality of flow around a cylinder undergoing rotational oscillation.

So far, to the best knowledge of the authors, only the investigations by Blackburn *et al.*<sup>2</sup> and more recent ones<sup>21–24</sup>

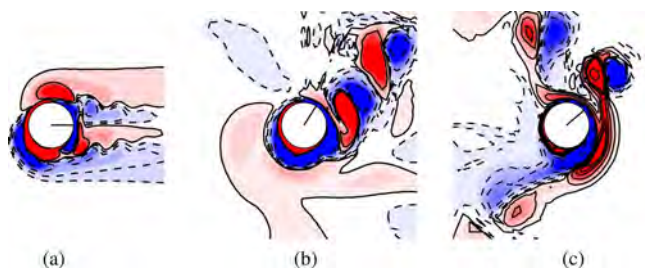


FIG. 1. (Color online) Contours of vorticity around the cylinder undergoing combined translational and rotational oscillation at  $KC=\pi$ ,  $\beta=90$ , and (a)  $\Phi=\pi$ , (b)  $\Phi=\pi/2$ , (c)  $\Phi=\pi/4$ , taken at  $t/T=0$  from numerical simulation. The dashed lines (enclosing blue) correspond to clockwise direction of vorticity (negative). The solid lines (enclosing red) correspond to counterclockwise direction of vorticity (positive).

reported on the combined oscillatory motion of a cylinder. Among them the work by Blackburn *et al.*<sup>2</sup> is the only one on the swimming cylinder (i.e., the quiescent case). A number of interesting features have been shown to occur as a result of combining the two motions. Of principal interest is the jet flow produced by the cylinder when the two imposed motions are in opposition of phase. The propulsive force produced by the cylinder causes it to accelerate until eventually reaching a terminal speed of 33% of the peak translational speed.<sup>2</sup> Naturally, the above mentioned phenomena is also true when the two motions are in phase, the difference being the side where the jet flow is produced. The combination of oscillatory motions has also been shown to be capable of producing a wide variety of flow patterns depending on the phase. Figure 1 shows an example of the near wake structure for a different phase. It can be seen that by changing the phase angle, the flow field around the cylinder changes dramatically. Notably it is clear that only the in phase or opposing phase cases ( $\Phi=0, \pi$ ) produce a jetlike flow. The other phases result in a flow with a somewhat preferred direction without the jetlike feature. The results by Blackburn *et al.*<sup>2</sup> were obtained via numerical simulations but to date, no detailed experimental studies into the effect of combining an oscillatory rotational and translational motion of a circular cylinder in either quiescent fluid or in external flow are known. However, a similar form of motion, *Carangiform motion*, is observed in nature. This mode of oscillation necessitates a twist at each extreme of the oscillation to give backward inclination to the moving winglike surface, that is, to a vertically oscillating cetacean tail, or to a fish's horizontally oscillating caudal fin. However, the propulsive jet that is produced from Carangiform motion only occurs when the oscillations are in phase.<sup>25</sup> The purpose of the present study is to investigate not only the near wake structure of such a combination of forcing mechanisms, but also to extend this to examine the three-dimensional nature of the wake, which is yet to receive any attention. The present study incorporates both experimental and numerical results. To characterize the experimental flows, the authors employed particle image velocimetry (PIV). Direct numerical simulation and Floquet analysis are also used to provide further insight in the wake flows produced. In Secs. II–IV, after defining the problem under investigation, the experimental and numerical tech-

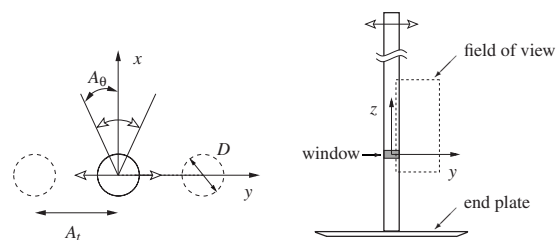


FIG. 2. Schematic of the problem geometry and important parameters relevant to the combined forcing. Left: the two-dimensional overview ( $xy$ -plane) of the cylinder. Right: spanwise view of the cylinder ( $yz$ -plane) with end plate and field of view (PIV).

niques utilized are described. Some validation with previous studies is then presented. The results and discussion sections follow, ending with conclusions.

## II. PROBLEM DEFINITION

When the relative flow past a cylinder is undergoing combined sinusoidal translational and rotational oscillations, the structure of the flow generated by the cylinder depends mainly on five independent parameters. The equations of the forcing motion are defined as

$$y(t) = A_t \sin(2\pi f_t t), \quad (1)$$

$$\theta(t) = A_\theta \sin(2\pi f_\theta t + \Phi), \quad (2)$$

where  $A_t$  ( $A_\theta$ ) is the amplitude of the translational (rotational) motion,  $f_t$  ( $f_\theta$ ) is the frequency of translational (rotational) oscillation, and  $\Phi$  is the phase between rotational and translational motions.

The dimensionless quantities representative of amplitude and frequency of each motion are usually defined as follows:

$$KC_t = \frac{U_{\max_t}}{f_t D} = \frac{2\pi A_t}{D}, \quad KC_\theta = \frac{U_{\max_\theta}}{f_\theta D} = \pi A_\theta, \quad (3)$$

$$\beta_t = \frac{f_t D^2}{\nu}, \quad \beta_\theta = \frac{f_\theta D^2}{\nu}, \quad (4)$$

where  $KC_t$  ( $KC_\theta$ ) and  $\beta_t$  ( $\beta_\theta$ ) are the translational (rotational) Keulegan–Carpenter number and Stokes number, respectively;  $U_{\max_t}$  ( $U_{\max_\theta}$ ) is the maximum translational (rotational) velocity of the cylinder motion,  $D$  is the cylinder diameter, and  $\nu$  is the kinematic viscosity of the fluid.

A Reynolds number can also be defined as a combination of two of the above dimensionless parameters. The associated translational Reynolds number,  $Re_t$ , is then

$$Re_t = \frac{U_{\max_t} D}{\nu} = KC_t \beta_t. \quad (5)$$

Figure 2 shows a schematic of the problem studied with some relevant notations and features. The Cartesian coordinate system in use is defined such that the origin is located at the center of the circular cylinder (at  $t=0$ ) at the window shown in Fig. 2, with  $x$ ,  $y$ , and  $z$  representing the streamwise, transverse, and spanwise directions, respectively (see Fig. 2).

### III. METHODS AND TECHNIQUES

#### A. Experimental setup

The experiments were conducted in the FLAIR free-surface closed-loop water channel at the Department of Mechanical and Aerospace Engineering, Monash University. Experiments were performed for a particular set of parameters which was shown earlier to be that of a swimming cylinder.<sup>2</sup> The frequency ratios were held to be the same  $\beta_t = \beta_\theta = \beta$  and the phase difference between the two motions set to  $\Phi = \pi$ . The associated translational and rotational Keulegan–Carpenter numbers are  $KC_t = KC_\theta = \pi$ . The nondimensional frequency was chosen to cover the range  $45 \leq \beta \leq 200$ , consequently the range of  $Re_t$  covered was  $141 \leq Re_t \leq 628$ .

The experimental model used for these experiments was a hollow circular cylinder of length 800 mm and outer diameter 20 mm, giving an aspect ratio of 40, see Fig. 2. The cylinder was made of carbon fiber and suspended vertically from an actuator that was controlled by a microstepping stepper motor. The cylinder was fitted with an end plate to reduce the end effects. The end plate was designed following recommendations by Stansby<sup>26</sup> and consisted of a circular plate with a diameter of  $9D$ . For PIV purposes, a small section of the cylinder was replaced by a thin-walled transparent cylinder, whose interior was filled with distilled water. The results shown later in the  $xy$ -plane are taken through this window.

The cylinder was oscillated translationally and rotationally by using two high-resolution stepper motors. The translational stepper motor actuated the rodless in-line mounting actuator and the rotational stepper motor was connected directly to the vertically mounted cylinder. The stepper motors were controlled using a two-axis indexer and two high-resolution drivers (running at 50 800 steps  $rev^{-1}$ ). A pure sinusoidal profile, as defined in Eqs. (1) and (2), was used throughout the paper. A TTL-signal triggered other devices (camera and laser), thus images could be captured at preselected phase angles in the oscillation cycle (phase locked).

During each set of experiments the fluid was initially at rest, i.e., it was *quiescent*. Special care was always taken to ensure near quiescency of the flow. Prior to each set of experiments, a honeycomb device was drawn through the working volume to break up large-scale flow structures into smaller scales, minimizing the time required to reach the background noise level. Typically, this background level, measured by the norm of velocity magnitude, was kept less than 1.41% of  $U_{max}$  (0.1 mm  $s^{-1}$  or less).

#### B. Experimental techniques

The velocity vector fields around the combined oscillating circular cylinder were measured using PIV. The PIV setup, illustrated schematically in Fig. 2, was based on that originally described by Adrian<sup>27</sup> and developed in-house over the past decades. The flow was seeded with spherical polyamide particles with a mean diameter of 20  $\mu m$  and specific weight of 1.016 g  $cm^{-3}$ . In this system, the particles were illuminated using two miniature Nd:YAG (yttrium aluminum garnet) laser sources (Continuum Minilite II

$Q$ -Switched). The planes of interest for these experiments were the  $yz$ - and  $xy$ -planes, being the spanwise and streamwise directions, as shown in Fig. 2. The thickness of the laser sheet was measured to be approximately less than 2 mm. Pairs of images were captured on a high-resolution charge coupled device camera with a maximum resolution of  $4008 \times 2672$  pixels. The camera was equipped with a 105 mm lens (Nikon Corporation, Japan). At a particular phase of the oscillation cycle, a number of image pairs over successive cycles were taken and stored for further processing. The timing of the laser and camera triggering was controlled by a special in-house designed timing unit, with an estimated accuracy of 1  $\mu s$ .

Each image pair was processed using in-house PIV software.<sup>28</sup> This software uses a double-frame, cross-correlation multiwindow algorithm to extract a grid of displacement vectors from the PIV images. An interrogation window of  $32 \times 32$  (with an initial window size of  $64 \times 64$ ) pixels was found to give satisfactory results with 50% overlap. More than 98% of the vectors were valid for all the experiments. This window size corresponds to an average interrogation window of  $0.064D \times 0.064D$ . It was possible to obtain a measurement resolution of  $249 \times 166$  (total of 41334) vectors in each field of view. The overall field of view was  $4008 \times 2672$  pixels ( $8.0D \times 5.3D$ ).

Phase-averaged vorticity and velocity fields are presented using 30 or more instantaneous measurements. The vorticity fields were calculated with the technique described previously.<sup>29</sup> The velocity and spatial coordinates are nondimensionalized by the maximum velocity of the translational cylinder motion,  $U_{max}$ , and the cylinder diameter,  $D$ , respectively.

Our PIV setup and technique have been validated against the previous numerical and experimental results<sup>5,8</sup> for the  $xy$ - and  $yz$ -plane measurements. The validation case studied is for a purely translational oscillation in a quiescent fluid. Figure 3 demonstrates an excellent agreement with the experimental and numerical study by Dütsch *et al.*<sup>8</sup> The numerical results (explained in Sec. III C) also match well with those of Dütsch *et al.*<sup>8</sup> Other profiles (not shown) at different locations are also in good agreement. For three-dimensional validation, the measured spanwise wavelength ( $\lambda = 1.04D$ ) for the  $KC_t = 2.51$  and  $\beta_t = 142$  ( $Re_t = 356$ ) case, corresponding to regime B of Tatsuno and Bearman<sup>5</sup> control parameter map (Fig. 12 of Ref. 5), was found to be within 4% of the previously reported value<sup>5</sup> ( $\lambda \approx 1.0D$ ), where  $\lambda$  is the wavelength along the span of the cylinder.

#### C. Numerical formulation

The description of the methodology will be purposefully brief because of descriptions given in previous papers. Details of the method in general,<sup>30</sup> and details of the implementation used here<sup>31</sup> can be found elsewhere. The code employed has been well proven for use in bluff-body problems, and Floquet stability analysis.<sup>17,32–34</sup> However, a brief outline of the method is given. The base flows for the present study were calculated by solving the incompressible, time-dependent Navier–Stokes equations. The discretization



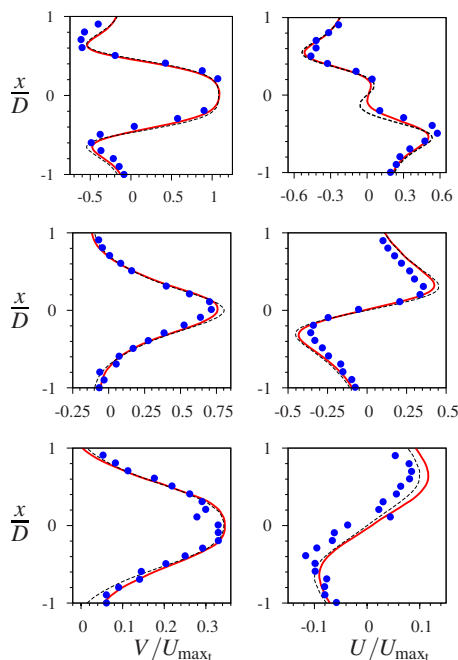


FIG. 3. (Color online) Comparison of the velocity components at three cross sections of the translationally oscillating cylinder in a quiescent fluid at constant  $y/D$  values. The  $y/D$  values from the top to bottom rows are  $-0.6$ ,  $0.6$ , and  $1.2$ , respectively. The measurements are taken at  $KC_t=5$  and  $\beta_t=20$ , similar to previous numerical and experimental results (Ref. 8). The left column depicts the  $V/U_{\max_t}$  and the right column  $U/U_{\max_t}$ . The solid lines (red) show the present experiment, the dashed lines (black) the present numerical simulation and the filled circle points (blue) the experimental results of Dütch *et al.* (Ref. 8).

method employed was a spectral-element method, using seventh-order Lagrange polynomials associated with Gauss–Lobatto–Legendre quadrature points. The time integration was executed using a three-step splitting scheme.<sup>35–37</sup> A computational domain extending  $30D \times 30D$  was split into 518 elements, the majority of which were concentrated in the boundary layer. The resolution, element distribution and domain size are consistent with those used successfully in previous similar studies. At the cylinder surface, a time-dependent Dirichlet condition was utilized that varied sinusoidally in time according to the driven translational and rotational oscillations. The calculations were performed in an accelerating frame of reference attached to the cylinder. The frame acceleration was added to the Navier–Stokes equations to account for this. The method employed is second order in time and time stepping is governed by the Courant condition on the explicit convective substep. The unit time step employed was  $0.010$  ( $\approx 1250$  time step/cycle) for  $\beta \leq 70$  and  $0.005$  ( $\approx 2500$  time step/cycle) for  $\beta > 70$ .

Floquet stability analysis employing a power method to resolve the most dominant Floquet mode (and the magnitude of the largest Floquet multiplier) has been used. Floquet stability analysis is a linear method designed to deduce the stability of periodic systems. The stability is deduced by calculating the Floquet multiplier,  $\mu$ , which can be thought of as the ratio of growth in amplitude of a perturbation from one period to the next, for a perturbation of a given spanwise wavelength,  $\lambda/D$ . If this ratio is such that  $|\mu| > 1$ , then the

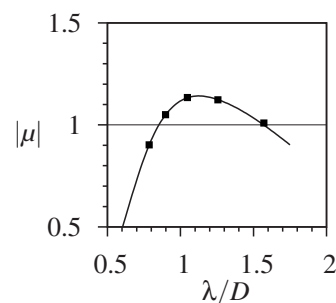


FIG. 4. Floquet multipliers for  $KC_t=2.75$  for the three-dimensional instability of regime B at  $\beta_t=80$ . The current results (solid line) are compared to those from Elston *et al.* (Ref. 16) (squares).

perturbation grows each period, and the two-dimensional base flow is said to be unstable to three-dimensional perturbations. Conversely, if  $|\mu| < 1$ , the perturbation decays each period, and will eventually die away, meaning the base flow is stable. Generally, this relies on the fact that a random perturbation of a given wavelength can be decomposed into a summation of eigen- or Floquet modes, each of which grows or decays at a certain rate. It is the fastest-growing or slowest decaying Floquet mode—the dominant mode—which dominates asymptotically with time. That is, after a certain amount of time, a perturbation decays to the dominant Floquet mode, with the size of the Floquet multiplier relative to unity determining the stability of the base flow. Details of the formulation can be found elsewhere.<sup>38</sup>

Figure 4 shows a validation of our technique with previous numerical simulations.<sup>16</sup> The validation case studied is a pure translational motion with  $KC_t=2.75$  and  $\beta_t=80$  ( $Re_t=220$ ), corresponding to regime B.<sup>5</sup> The agreement was found to be excellent throughout the range tested.

## IV. RESULTS AND DISCUSSION

In this section the results are presented in two parts. For the first, the wake profiles around the cylinder in the streamwise direction ( $xy$ -plane) for  $KC=\Phi=\pi$  and  $\beta=90$  are examined, and the second part investigates the three dimensionality of such flows for  $KC=\Phi=\pi$  and a range of  $20 < \beta < 200$  (corresponding to  $62.8 < Re_t < 628$ ).

### A. Wake profile in the streamwise direction

It has previously been found that for the case where  $KC=\Phi=\pi$  and  $\beta=90$ , while the cylinder translation axis is vertical, vorticity transport is predominantly in the horizontal direction.<sup>2</sup> Figure 5 clearly shows this vorticity transport to one side of the cylinder as well as comparing the same flow between the present experimental and numerical investigation. Figure 5 also shows the excellent qualitative agreement between the two methods used. Figure 6 depicts the sequence of one complete cycle of translational and rotational oscillation. The cylinder motion, based on Eqs. (1) and (2), starts from the center toward the top of the page, the positive direction of  $y$ , and at the same time starts rotating clockwise, the negative direction of rotation angle,  $\theta$ . Figure 6(c) shows the instant when the cylinder is at its maximum vertical po-

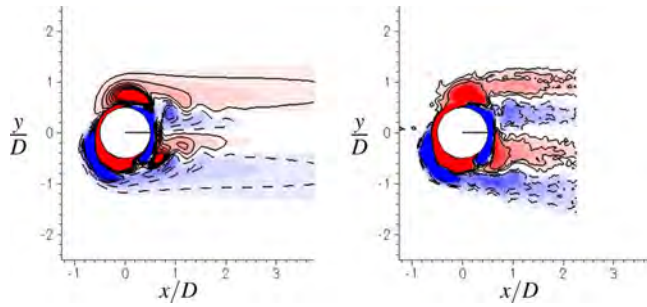


FIG. 5. (Color online) Vorticity contours around the cylinder undergoing combined translational and rotational oscillation at  $KC=\Phi=\pi$  and  $\beta=90$ . The numerical result is presented at the left, and the experimental result at the right. The experimental result is a phase-average of ten successive cycles. The phase shown corresponds to  $t=0$ . The dashed lines (enclosing blue) correspond to clockwise direction of vorticity (negative), and the solid lines (enclosing red) corresponds to counterclockwise direction of vorticity (positive).

sition and most negative angular displacement. As the oscillations are in opposition of phase, the maximum surface-tangential component of cylinder acceleration is located on the left-hand side of the cylinder, i.e., it is where the accelerations are additive rather than in opposition. Morton<sup>39</sup> showed that this combination of accelerations will result in the (kinematic) generation of vorticity on that side of the cylinder while the cancellation of accelerations on the other side results in little direct vorticity generation on the right side. The direction of rotation of the vortices will result in their being strained and directed to only one side of the cylinder and perpendicular to its translation axis. Based on the vorticity fields, this will necessarily result in thrust generation in this direction, but it has not been effectively measured experimentally. The thrusting effect appears to occur in a lock-in regime and, as reported earlier,<sup>2</sup> would be expected to occur for all cases where the flow structure is as shown in Fig. 1(a). However, it may be the case that there is a threshold set of amplitudes required to establish this but that has not been determined to date. The phase angle between the motions influences the degree to which cross annihilation of vorticity occurs and the distance from the cylinder at which vorticity persists (as was shown in Fig. 1).

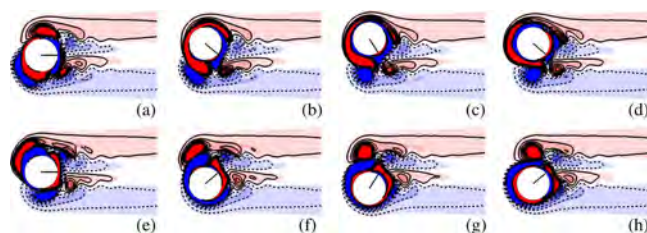


FIG. 6. (Color online) Flow produced by a cylinder with combined oscillatory translation and rotation. This figure shows the sequence and development of the  $\omega_z$  vorticity for one complete cycle, (a)  $t=0$  to (h)  $t=7T/8$  at  $KC=\Phi=\pi$  and  $\beta=90$ , where  $T$  is the period of oscillation. The radial line shows the rotational displacement of the cylinder. The dashed lines (enclosing blue) correspond to clockwise direction of vorticity (negative), and the solid lines (enclosing red) correspond to counterclockwise vorticity (positive).

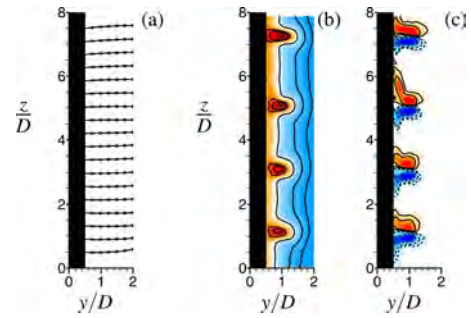


FIG. 7. (Color online) Experimental results of the spanwise distribution of flow for two values of  $\beta$  at  $KC=\Phi=\pi$ : (a)  $\beta=20$ , streamlines; (b)  $\beta=90$ ,  $u_y$  velocity isocontours; (c)  $\beta=90$ ,  $\omega_x$  vorticity isocontours; the dashed lines (enclosing blue) correspond to clockwise direction of vorticity (negative), and the solid lines (enclosing red) correspond to counterclockwise vorticity (positive).

### B. Wake profile in the spanwise direction

Figure 7 shows the experimental spanwise distribution of flow for two values of  $\beta$  at  $KC=\Phi=\pi$ . Figure 7(a) shows approximately parallel streamlines indicating two-dimensional vortex shedding around the cylinder. Here  $Re \approx 63$ , which the Floquet analysis, discussed later, shows to be a two-dimensional flow regime. Figures 7(b) and 7(c) present the  $y$ -velocity field ( $u_y$ ) and vorticity field ( $\omega_x$ ) contours along the span of cylinder, respectively. These are for  $Re \approx 283$ . The spanwise three-dimensional structures are clearly seen from these two depictions. The three-dimensional structures shown appear regular and stable, with a constant characteristic wavelength. Further analysis of the experimental data, not presented here, shows this to be the case.

Figure 8 shows the Floquet multipliers,  $|\mu|$ , for several Reynolds numbers for a spanwise instability at  $KC=\Phi=\pi$ . Figure 8(a) shows the value of  $|\mu|$  as a function of the spanwise wavelength,  $\lambda/D$ . This figure clearly depicts the emergence of two distinct instability modes, a short and a long

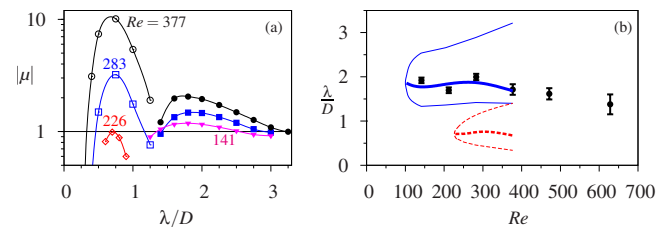


FIG. 8. (Color online) Floquet multipliers for several Reynolds numbers for the spanwise instability at  $KC=\Phi=\pi$ . (a) Floquet multipliers as a function of spanwise wavelength. The open (closed) symbols represent the shortest (longest) wavelength mode. The circles and black line represent results for  $Re=377$ ; the squares and blue line represent results for  $Re=283$ ; the diamonds and red line represent results for  $Re=226$ ; the lower triangles and magenta line represent results for  $Re=141$ . (b) Comparison of the Floquet analysis predicted wavelength values as a function of Reynolds number with experimental measurements. The blue dashed line corresponds to the wavelength range of the longest spanwise wavelength mode. The red dashed line corresponds to the extent of the shortest spanwise wavelength mode. The thick blue and red lines correspond to the predicted values of the long and short wavelengths, respectively. The black circles represent the present experimental measurements with error bars reporting the standard deviation of the measurements.

wavelength mode. The longer wavelength mode has a critical Reynolds number of  $Re_c \approx 100$ , at a critical wavelength of  $\lambda \approx 1.8D$ . The second instability first occurs at a much higher Reynolds number of  $Re_c \approx 226$  for a wavelength of  $\lambda \approx 0.7D$ . The experiments show that the spanwise wavelength observed in the wakes at various Reynolds numbers was close to  $2D$  at onset, decreasing to about  $1.5D$  at  $Re=600$ . These values are consistent with the wavelengths corresponding to the fastest-growing modes as the Reynolds number is varied. This is clearly depicted in Fig. 8(b), which shows the unstable Reynolds number range for each mode as a function of Reynolds number and the preferred wavelength. The experimental wavelength variation with Reynolds number matches the predicted preferred wavelength reasonably well.

These long and short wavelength modes have the same spatiotemporal symmetries as modes *A* and *B* wake modes for a stationary circular cylinder in a uniform flow,<sup>40</sup> respectively. These symmetry breaking bifurcations are the only ones possible with the same period as the base flow, as shown using group theory arguments by Blackburn *et al.*<sup>41</sup> It is interesting to note that the symmetry breaking transitions occur in the same order as for a circular cylinder, even though the two-dimensional base wake flow and perturbation field distributions are completely different. Of course, for different body geometries, the transition order can be different, such as for an elongated streamlined leading-edge square trailing-edge cylinder, for which the transition order is reversed.<sup>33</sup> Perhaps of even more interest is that for a circular cylinder wake, the saturated second critical mode, mode *B*, dominates the flow dynamics as the Reynolds number is increased above the two transitions;<sup>42</sup> in fact, for Reynolds numbers close to 300, the wake appears to be in an almost pure mode *B* state.<sup>43</sup> Notably this corresponds to the Reynolds number at which mode *B* growth rate grows to exceed that of mode *A*. This is not the case here. Despite examining the wakes experimentally at Reynolds numbers up to 640, there was no sign of any evidence of the shorter wavelength instability in the wake. There was also an attempt to artificially force the wake at this wavelength by placing thin tapes on the cylinder spaced at the predicted optimal shorter wavelength. This also failed to generate any long term change to the wake, i.e., the shorter wavelength mode was visible initially but the wake quickly reverted to the longer wavelength state, similar to that shown in Fig. 7 for the unperturbed case. Figure 8(a) clearly shows that linear theory predicts the growth rate of the shorter wavelength mode quickly overtakes the longer wavelength mode, so this is somewhat surprising. Of course, the growth and nonlinear saturation of the long wavelength mode changes the base flow so this result is not inconsistent.

Figure 9 shows the perturbation  $\omega_z$  vorticity contours of the short and long wavelength modes associated with the spanwise instability. This clearly shows the spatiotemporal symmetries of the two modes: In terms of the perturbation vorticity, for the long wavelength mode, the field repeats on passage in time through half a period, reflection about the centerline and reversal of sign, while for the shorter wavelength mode the sign reversal is not required. These symme-

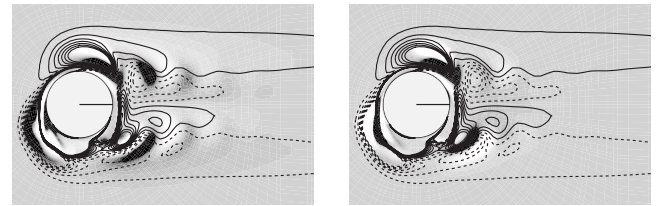


FIG. 9. Contours of streamwise perturbation vorticity taken at  $KC=\Phi=\pi$  and  $\beta=90$  ( $Re \approx 283$ ) and when the cylinder is at  $t=0$  for the following: (left)  $\lambda=1.8D$  the long wavelength; (right)  $\lambda=0.7D$  the short wavelength. The dashed lines correspond to the base flow clockwise direction of vorticity (negative), and the solid lines correspond to the counterclockwise vorticity (positive).

tries are the same as for modes *A* and *B*, respectively. The mode structure of both modes is quite complex, with substantial mode amplitude both near the cylinder and in the wake.

## V. CONCLUSIONS

In this work we have experimentally and numerically considered the development of three dimensionality of flow around a cylinder undergoing a combined translation and rotation oscillatory motion. The study is restricted to the case with the phase angle set to  $\pi$ , and large amplitude oscillations—corresponding to a *swimming cylinder*. Because of this phase difference, the oscillation velocities at the cylinder surface cancel on one side and reinforce on the other. This leads to preferential vorticity generation and transport on one side, and the cylinder rotational motion sweeps this vorticity around to the other side producing a thrust wake. Although previous two-dimensional simulations have shown this mechanism leads to self-propulsion orthogonal to the translational oscillatory motion, the question of whether this will be effective at higher Reynolds numbers remains. This work shows that the wake becomes three dimensional at a Reynolds number of approximately 100 due to a three-dimensional instability with a spanwise wavelength of approximately two cylinder diameters. The Floquet analysis shows that the two-dimensional base flow is also unstable to another three-dimensional instability with a shorter wavelength ( $\lambda \approx 0.7D$ ) for  $Re \geq 226$ ; however, the experimental results, even at much higher Reynolds numbers do not show any sign of the occurrence of this mode. The experimental results indicate that the development of three dimensionality in the wake leads to significant distortion of the previously two-dimensional wake. The effect on the self-propulsion is yet to be determined.

## ACKNOWLEDGMENTS

M.N. would like to acknowledge the support of a Monash Graduate Scholarship (MGS) and a Monash International Postgraduate Research Scholarship (MIPRS). D.L. acknowledges support from ARC Discovery under Grant No. DP0774525 and computing time from the Australian Partnership for Advanced Computing (APAC).

- <sup>1</sup>P. W. Bearman, J. M. R. Graham, P. Naylor, and E. D. Obasaju, "The role of vortices in oscillatory flow about bluff cylinders," *International Symposium on Hydrodynamics in Ocean Engineering* (Norwegian Hydrodynamics Laboratories, Trondheim, 1981), pp. 621–635.
- <sup>2</sup>H. M. Blackburn, J. R. Elston, and J. Sheridan, "Bluff-body propulsion produced by combined rotary and translational oscillation," *Phys. Fluids* **11**, 4 (1999).
- <sup>3</sup>H. Honji, "Streaked flow around an oscillating cylinder," *J. Fluid Mech.* **107**, 509 (1981).
- <sup>4</sup>C. H. K. Williamson, "Sinusoidal flow relative to circular cylinders," *J. Fluid Mech.* **155**, 141 (1985).
- <sup>5</sup>M. Tatsuno and P. W. Bearman, "A visual study of the flow around an oscillating circular cylinder at low Keulegan–Carpenter numbers and low Stokes numbers," *J. Fluid Mech.* **211**, 157 (1990).
- <sup>6</sup>P. Justesen, "A numerical study of oscillating flow around a circular cylinder," *J. Fluid Mech.* **222**, 157 (1991).
- <sup>7</sup>G. Iliadis and G. Anagnostopoulos, "Viscous oscillatory flow around a circular cylinder at low Keulegan–Carpenter numbers and frequency parameters," *Int. J. Numer. Methods Fluids* **26**, 403 (1998).
- <sup>8</sup>H. Dütsch, F. Durst, S. Becker, and H. Lienhart, "Low-Reynolds-number flow around an oscillating circular cylinder at low Keulegan–Carpenter numbers," *J. Fluid Mech.* **360**, 249 (1998).
- <sup>9</sup>S. Taneda, "Visual observations of the flow past a circular cylinder performing a rotary oscillation," *J. Phys. Soc. Jpn.* **45**, 1038 (1978).
- <sup>10</sup>P. T. Tokumaru and P. E. Dimotakis, "Rotary oscillation control of a cylinder wake," *J. Fluid Mech.* **224**, 77 (1991).
- <sup>11</sup>P. Poncet, "Topological aspects of three-dimensional wakes behind rotary oscillating cylinders," *J. Fluid Mech.* **517**, 27 (2004).
- <sup>12</sup>B. Thiria, S. Goujon-Durand, and J. E. Wesfreid, "The wake of a cylinder performing rotary oscillations," *J. Fluid Mech.* **560**, 123 (2006).
- <sup>13</sup>S. J. Lee and J. Y. Lee, "Temporal evolution of wake behind a rotationally oscillating circular cylinder," *Phys. Fluids* **19**, 105104 (2007).
- <sup>14</sup>T. Sarpkaya, "Force on a circular cylinder in viscous oscillatory flow at low Keulegan–Carpenter numbers," *J. Fluid Mech.* **165**, 61 (1986).
- <sup>15</sup>J. R. Elston, J. Sheridan, and H. M. Blackburn, "Two-dimensional Floquet stability analysis of the flow produced by an oscillating circular cylinder in quiescent fluids," *Eur. J. Mech. B/Fluids* **23**, 99 (2004).
- <sup>16</sup>J. R. Elston, H. M. Blackburn, and J. Sheridan, "The primary and secondary instabilities of flow generated by an oscillating circular cylinder," *J. Fluid Mech.* **550**, 359 (2006).
- <sup>17</sup>J. S. Leontini, M. C. Thompson, and K. Hourigan, "Three-dimensional transition in the wake of a transversely oscillating cylinder," *J. Fluid Mech.* **577**, 79 (2007).
- <sup>18</sup>D. Nehari, V. Armenio, and F. Ballio, "Three-dimensional analysis of the unidirectional oscillatory flow around a circular cylinder at low Keulegan–Carpenter and  $\beta$  numbers," *J. Fluid Mech.* **520**, 157 (2004).
- <sup>19</sup>X.-Y. Lu and J. Sato, "A numerical study of flow past a rotationally oscillating circular cylinder," *J. Fluids Struct.* **10**, 829 (1996).
- <sup>20</sup>M.-H. Chou, "Synchronization of vortex shedding from a cylinder under rotary oscillation," *Comput. Fluids* **26**, 755 (1997).
- <sup>21</sup>Q. M. Al-Mdallal, "Analysis and computation of the cross-flow past an oscillating cylinder with two degrees of freedom," Ph.D. thesis, Memorial University of Newfoundland, 2004.
- <sup>22</sup>S. Kocabiyik and Q. M. Al-Mdallal, "Bluff-body flow created by combined rotary and translational oscillation," in *Fluid Structure Interaction and Moving Boundary Problems*, WIT Transactions on the Built Environment, Vol. 84, edited by S. Chakrabarti (WIT, Southampton, 2005), p. 195.
- <sup>23</sup>M. Nazarinia, D. Lo Jacono, M. C. Thompson, and J. Sheridan, "Flow behind a cylinder forced by a combination of oscillatory translational and rotational motions," *Phys. Fluids* **21**, 051701 (2009).
- <sup>24</sup>J. R. Elston, "The structures and instabilities of flow generated by an oscillating circular cylinder," Ph.D. thesis, Monash University, 2005.
- <sup>25</sup>J. Lighthill, "Fundamentals concerning wave loading on offshore structures," *J. Fluid Mech.* **173**, 667 (1986).
- <sup>26</sup>P. K. Stansby, "The effect of end plates on the base pressure coefficient of a circular cylinder," *Aeronaut. J.* **78**, 36 (1974).
- <sup>27</sup>R. J. Adrian, "Particle-imaging techniques for experimental fluid mechanics," *Annu. Rev. Fluid Mech.* **23**, 261 (1991).
- <sup>28</sup>A. Fouras, D. Lo Jacono, and K. Hourigan, "Target-free stereo PIV: A novel technique with inherent error estimation and improved accuracy," *Exp. Fluids* **44**, 317 (2008).
- <sup>29</sup>A. Fouras and J. Soria, "Accuracy of out-of-plane vorticity measurements derived from in-plane velocity field data," *Exp. Fluids* **25**, 409 (1998).
- <sup>30</sup>G. E. Karniadakis and S. J. Sherwin, *Spectral/hp Methods for Computational Fluid Dynamics* (Oxford University Press, Oxford, 2005).
- <sup>31</sup>M. C. Thompson, K. Hourigan, and J. Sheridan, "Three-dimensional instabilities in the wake of a circular cylinder," *Exp. Therm. Fluid Sci.* **12**, 190 (1996).
- <sup>32</sup>G. Sheard, M. C. Thompson, and K. Hourigan, "From spheres to circular cylinders: The stability and flow structures of bluff ring wakes," *J. Fluid Mech.* **492**, 147 (2003).
- <sup>33</sup>K. Ryan, M. C. Thompson, and K. Hourigan, "Three-dimensional transition in the wake of bluff elongated cylinders," *J. Fluid Mech.* **538**, 1 (2005).
- <sup>34</sup>D. Lo Jacono, J. N. Sørensen, M. C. Thompson, and K. Hourigan, "Control of vortex breakdown in a closed cylinder with a small rotating rod," *J. Fluids Struct.* **24**, 1278 (2008).
- <sup>35</sup>G. E. Karniadakis, M. Israeli, and S. A. Orszag, "High-order splitting methods of the incompressible Navier–Stokes equations," *J. Comput. Phys.* **97**, 414 (1991).
- <sup>36</sup>M. C. Thompson, K. Hourigan, A. Cheung, and T. Leweke, "Hydrodynamics of a particle impact on a wall," *Appl. Math. Model.* **30**, 1356 (2006).
- <sup>37</sup>C. Canuto, M. Hussaini, A. Quarteroni, and T. Zang, *Spectral Methods in Fluid Dynamics*, 2nd ed. (Springer-Verlag, Berlin, 1990).
- <sup>38</sup>D. Barkley and R. D. Henderson, "Three-dimensional Floquet stability analysis of the wake of a circular cylinder," *J. Fluid Mech.* **322**, 215 (1996).
- <sup>39</sup>B. R. Morton, "The generation and decay of vorticity," *Geophys. Astrophys. Fluid Dyn.* **28**, 277 (1984).
- <sup>40</sup>C. H. K. Williamson, "The existence of two stages in the transition to three-dimensionality of a circular cylinder wake," *Phys. Fluids* **31**, 3165 (1988).
- <sup>41</sup>H. M. Blackburn, F. Marques, and J. M. Lopez, "Symmetry breaking of two-dimensional time-periodic wakes," *J. Fluid Mech.* **522**, 395 (2005).
- <sup>42</sup>J. Wu, J. Sheridan, M. C. Welsh, and K. Hourigan, "Three-dimensional vortex structures in a cylinder wake," *J. Fluid Mech.* **312**, 201 (1996).
- <sup>43</sup>C. H. K. Williamson, "Three-dimensional wake transition," *J. Fluid Mech.* **328**, 345 (1996).

## Flow behind a cylinder forced by a combination of oscillatory translational and rotational motions

M. Nazarinia, D. Lo Jacono,<sup>a)</sup> M. C. Thompson, and J. Sheridan

*Department of Mechanical and Aerospace Engineering, Fluids Laboratory for Aeronautical and Industrial Research (FLAIR), Monash University, Melbourne, 3800 Victoria, Australia*

(Received 3 February 2009; accepted 28 April 2009; published online 20 May 2009)

The flow behind a cylinder undergoing forced *combined* oscillatory motion has been studied. The motion consists of two independent oscillations: cross-stream translation and rotation. Previous studies have extensively investigated the effect of these motions individually on cylinder wakes; however, the investigation of their combined effect is new. The motivation lies in its application to vortex-induced vibration and its suppression and to biomimetic motion. The focus is on the effect of the phase difference between the two motions. The results show that there is an unexpected loss of synchronization of the wake for a finite range of phase differences. © 2009 American Institute of Physics. [DOI: 10.1063/1.3139184]

The primary goal of this research is to understand the physical mechanisms behind the response of a cylinder wake to the combined forcing mechanisms of cross-stream translation and rotational oscillations. With an in-depth understanding of the flow physics it may be possible to propose a novel means of actively or passively suppressing the lock-on between vortex shedding and transverse oscillation. Also, we are interested in the application to biomimetic motions and, in particular, to carangiform motion.<sup>1</sup> There has been considerable research on the effect of either transverse or rotational oscillations on cylinder wakes, as discussed in the extensive reviews.<sup>2,3</sup> Primarily, these have focused on the translational oscillation due to their focus on vortex-induced vibration. There have also been studies of the effect of rotational oscillation on wakes.<sup>4,5</sup> Previous numerical work has also been performed on the effect of the combined motions in quiescent fluids<sup>6</sup> and when there is a flow past the cylinder;<sup>7</sup> however, the influence of an important parameter was not considered. Indeed, previous interesting results<sup>6,8</sup> indicate that the phase difference between the two motions is of considerable importance and this is the focus of the research discussed here. This work is part of a more extensive set of experiments that considers the full range of independent variables.

The experiments were conducted in the FLAIR free-surface closed-loop water channel at Monash University. A schematic of the problem is given in Fig. 1. The cylinder used was 800 mm in length and with an outer diameter of  $D=20$  mm, giving an aspect ratio of 40. The experiments were performed for a fixed upstream velocity  $U_\infty=0.0606$  m/s giving  $Re=U_\infty D/\nu=1322$ . Two sinusoidal motions were imposed, namely, translational (cross stream), given by  $y(t)=A_t \sin(2\pi f_t t)/D$ , and rotational, given by  $\theta(t)=A_\theta \sin(2\pi f_\theta t + \Phi)$ . The frequencies are fixed close to that of the natural frequency ( $T^{-1}=f_t=f_\theta=0.6$  s<sup>-1</sup>  $\approx f_N$ ). The natural frequency was found to be equal to  $f_N \approx 0.6154$  s<sup>-1</sup>.

The Strouhal number based on this frequency is about  $St \approx f_N D/U_\infty=0.203$  and the Strouhal number of the forcing is  $St_t \approx f_t D/U_\infty=0.198$ . The experiments presented are for fixed amplitudes of oscillation,  $A_t=D/2$  and  $A_\theta=1$ . These amplitudes combined with the equal frequencies provide equal maximum velocities from the translational and rotational motions. The maximum velocities from the forcing are equal to  $U_{\max}=2\pi f_t A_t=0.0377$  m/s which correspond to a ratio of  $U_{\max}/U_\infty=0.62$ .

As mentioned earlier, the results presented here show the effect of the phase difference ( $\Phi$ ) between the translational and rotational motions on the wake. This parameter was chosen as its variation led to interesting behavior in a *quiescent* fluid. Only a brief outline of that case will be given; a more detailed discussion can be found in Refs. 1 and 6. If the maximum velocities of the oscillatory motions are equal, it can easily be shown that there will be an uneven distribution of velocity at the surface of the cylinder depending on the phase imposed. Indeed, for opposing phases ( $\Phi=180^\circ$ ) the two velocities will cancel on one side (orthogonal to the translational motion) and add on the other side. This creates a vorticity difference between the two halves of the cylinder, resulting in a wake flow orthogonal to the translational movement. The method used here to characterize the wake of this forced cylinder is via particle image velocimetry (PIV). The flow was seeded with spherical granular polyamide particles having a mean diameter of 55  $\mu\text{m}$  and specific gravity of 1.016. The particles were illuminated using two mini yttrium aluminum garnet laser sources. The plane of interest for these experiments was orthogonal to the cylinder's axis ( $xy$  plane) and downstream ( $x$  direction) of the cylinder. A small section of the cylinder is replaced by a thin-walled transparent cylinder, whose interior is filled with distilled water. It is located at about  $9D$  from the end of cylinder. The measured  $xy$  plane is located through the center of this window. The experimental setup provided a field of view of approximately  $6D \times 6D$ .

Figure 2 presents motion phase-locked vorticity isocontours taken at  $t=T$  for various phase differences. The image

<sup>a)</sup>Electronic mail: david.lojacono@eng.monash.edu.au.

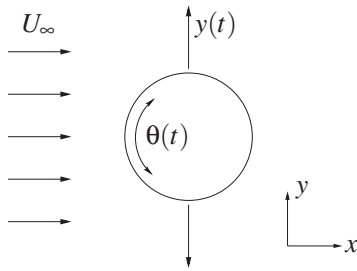


FIG. 1. Schematic showing the problem geometry and important parameters relevant to the combined forced oscillation and the circular cylinder model. The streamwise direction is the  $x$  direction.

at the top left shows the case where the two motions are of opposite phase ( $\Phi = 180^\circ$ ); we observe a  $2S$  mode (two single vortices shed per period) in a single row aligned in the medial plane. The field of view does not allow us to see the double row that should occur further downstream.<sup>9–11</sup> The structure of a double-row wake is shown for the  $\Phi = -30^\circ$  case, in which alternate vortices align in two rows offset from the centerline. As the phase difference is reduced toward being in phase,  $\Phi = 30^\circ$ , the vortices are arranged closer to each other and are less well aligned with the medial plane, suggesting an earlier double-row transition. The in-phase case,  $\Phi = 0^\circ$ , presents the signature of a  $P+S$  mode (a single vortex and a vortex pair formed per cycle), at least in the near wake. The classification of the different vortex modes is given in Ref. 12. For this in-phase case, the vortices are shed widely apart (nearly  $4D$ ), readily explained by the rotational oscillation adding momentum to the translational motion. The resulting strain favors a transition to the  $P+S$  wake.<sup>13</sup> Reducing the phase difference to  $\Phi = -30^\circ$  and  $\Phi = -60^\circ$ , the vorticity pattern returns to a  $2S$  mode in a double-row configuration. It should be noted that the spacing between the two rows reduces (from  $2.5D$  to  $2D$ ) as we decrease  $\Phi$ . The cases of  $\Phi = -90^\circ$  and  $\Phi = -120^\circ$  are of particular interest:

Contrary to the other experimental cases, these two cases were not synchronized with the translational motion beyond  $2D$  downstream. The effect of this loss of synchronization can be seen in the rapid downstream dissipation of the mean vortex structures due to averaging. Only the two vortices near the cylinder remain coherent. This *a priori* surprising phenomenon might be explained by the fact that the separation between the two rows of vortices is smaller and that this arrangement of vortices is not stable. Similar behavior can be found behind elliptical cylinders.<sup>11</sup> The last case  $\Phi = -150^\circ$  (and necessarily the first case,  $\Phi = \pm 180^\circ$ ) displays vortices in a single row.

In addition to the experiments, numerical simulations have been undertaken to elucidate certain behavior and to confirm certain aspects of the unlocked regime. Although these (two-dimensional) numerical simulations are performed at a much lower Reynolds number, the near-wake predictions are predominantly consistent with the experimental results (e.g., the vorticity pattern). This is likely due to the strong forcing, partially overriding the modifying effect of three-dimensional transition, at least for the near wake.

The description of the numerical methodology will be brief because it has been adequately described in previous papers. Details of the general method and its implementation can be found elsewhere.<sup>14,15</sup> The code employed has been well proven for use in bluff-body problems.<sup>16–18</sup> The time-asymptotic wake flows for the present study were calculated by solving the incompressible, time-dependent Navier–Stokes equations in a translating accelerating frame of reference attached to the cylinder. The discretization method employed was a spectral-element method using seventh-order Lagrange polynomials associated with Gauss–Lobatto–Legendre quadrature points. The computational domain, consisting of a semicircular upstream section and a rectangular downstream section, extended at least  $30D$  in all directions. This was split into 518 elements, the majority of which were

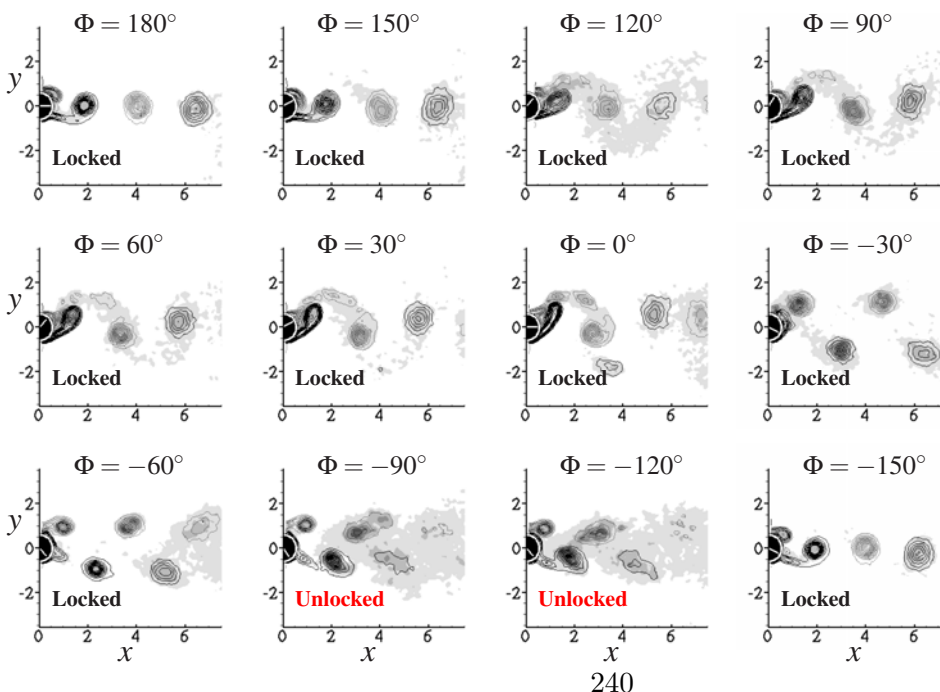


FIG. 2. (Color online) Motion phase-locked vorticity isocontours (lines) and root mean square vorticity (gray-scale) taken at the motion phase  $t=T$ . The near-wake vorticity is shown for different phase differences between the two imposed oscillatory motions. Of particular interest is the asynchronous (unlocked) wake with the imposed translational motion for the phases  $\Phi = -90^\circ$  and  $\Phi = -120^\circ$ .

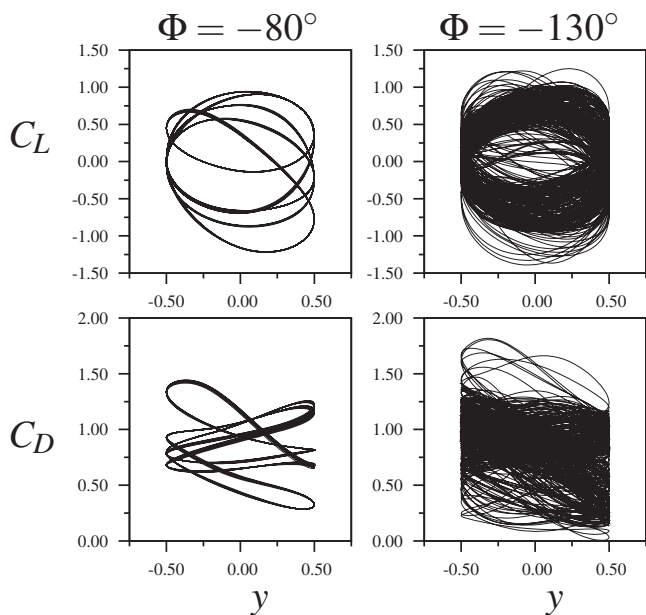


FIG. 3. Lissajous pattern defined horizontally with the translational forcing mechanism ( $y$ ) and vertically with lift (top) or drag (bottom) coefficient.

concentrated in the cylinder boundary layer and wake regions. At the cylinder surface, a time-dependent Dirichlet condition was used that varied sinusoidally in time according to the driven rotational oscillation. In all cases the numerical simulations were performed for more than 200 cycles and started at rest. This was found to be sufficient for the asymptotic state to be achieved.

Various methods were used to analyze and characterize the predictions. Lissajous figures of the lift and drag coefficients against the transverse forcing mechanism for each phase difference have been produced. From these one can assess whether the flow was periodic, quasiperiodic, or highly irregular (or chaotic). Examples for two different cases are given in Fig. 3. The left-hand figures show *quasi-periodic* behavior with the phase plots repeating after five forcing periods. The right-hand figures indicate chaotic behavior since the trajectories do not repeat.

Some representative base flows are displayed in Fig. 4. Despite the Reynolds number difference (simulations  $Re = 225$ , experiments  $Re = 1322$ ) these qualitatively reproduce the near-wake behavior of the PIV results. For  $\Phi > -20^\circ$  a single row of vortices is displayed. For  $-30^\circ \leq \Phi \leq -20^\circ$  a double row of vortices appears after a single row of vortices. The number of vortices in a single row diminishes as we approach  $\Phi = -30^\circ$ . For  $-70^\circ \leq \Phi \leq -30^\circ$ , the wake no longer displays an initial single row but instead immediately forms a double row. These vortex rows interact further downstream to form a quasiperiodic far wake. The number of vortices forming the double row diminishes as  $\Phi$  diminishes. For  $-130^\circ \leq \Phi \leq -80^\circ$  the wake immediately transitions to a fully chaotic state. For  $\Phi < -130^\circ$  the flow undergoes a succession of double row, to single row, then double row, until a unique single row pattern. See the top wake pattern of Fig. 4 as representative of this final case.

Table I reports the experimental and numerical behaviors

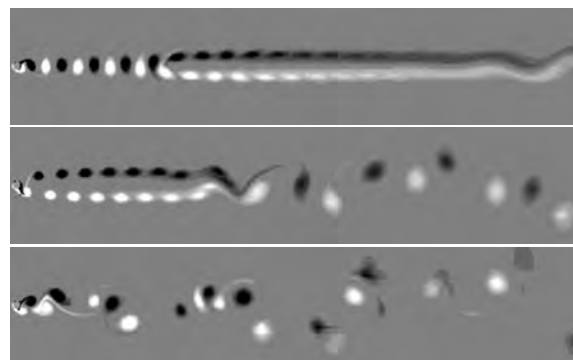


FIG. 4. Typical flow features for different imposed phase differences. Top: single row of vortices transitioning downstream to a double row followed by a further secondary instability in the far wake ( $\Phi = -170^\circ$ ). Center: double row of vortices followed by a quasiperiodic pattern ( $\Phi = -40^\circ$ ). Bottom: *chaotic* pattern of vortices ( $\Phi = -100^\circ$ ). The domain of the numerical simulation was extended to  $100D$  downstream for these cases.

of the wake flow for the same set of parameters *but* with  $Re = 225$  for the numerical results. As we will see the discrepancy in the value of the Reynolds number does not have an impact on the synchronization for  $\Phi$  values close to the loss of synchronization. The numerical simulations confirm the loss of synchronization for qualitatively the same region as the experiments. The numerical simulations reveal that the unlocked regime contains quasiperiodic and chaotic patterns. It appears that the chaotic regime is surrounded by quasiperiodicity. Also the likelihood of an unlocked regime is greater when the ratio  $f_i/f_{st}$  is higher than unity.

TABLE I. Summary of the synchronization around the unlocked regime. L, QP, and C stand for locked on, quasiperiodic, and chaotic, respectively. The unlocked regimes (UL) for the experimental results are likely to be chaotic.  $f_i$  and  $f_{st}$  stand for forced frequency and natural frequency for a fixed cylinder.

$\Phi$ (deg)	Expt. $\approx 1$	$f_i/f_{st}$		
		Numerical		
		0.9	1.0	1.1
-30	L	L	L	L
-40		QP	L	L
-50		QP	L	QP
-60	L	QP	QP	QP
-70	UL	QP	QP	C
-80	UL	QP	QP	C
-90	UL	QP	C	C
-100	UL	QP	C	C
-110	UL	L	C	C
-120	UL	L	C	C
-130		L	C	C
-140		L	QP	C
-150	L	L	L	C
-160		L	L	L
-170		L	L	L
-180	L	L	L	L

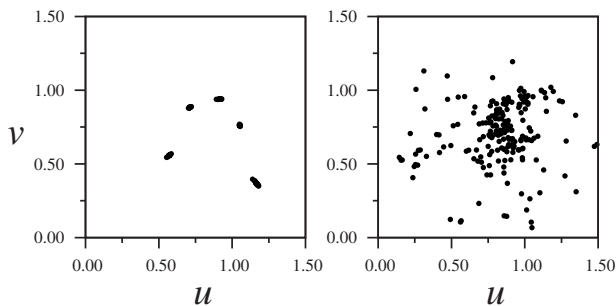


FIG. 5. Poincaré map for two typical unlocked regimes for  $Re=225$ . Left: quasiperiodic behavior for  $\Phi=-80^\circ$ . Right: chaotic regime for  $\Phi=-130^\circ$ . The phase diagram shows the horizontal and the vertical velocities at  $7D$  downstream on the centerline.

To further examine the behavior, Poincaré maps have been constructed for each phase difference. The horizontal and vertical velocities are sampled at a prechosen point downstream,  $(x, y) = (7D, 0)$ , at the end of each forcing period  $T$ . For example, Fig. 5 illustrates the quasiperiodicity of the case where  $\Phi = -80^\circ$ . Here the periodicity of the flow is of  $5T$  as can be seen from the distribution of five distinct islands of points in the phase diagram. The chaotic nature of the regime in the case of  $\Phi = -130^\circ$  can be readily seen by inspection, with the distribution of points in the phase diagram showing no preferred region or cycle.

It appears that *synchronization* may not be a clear concept. Both the experimental and numerical results show that the size of the nearly periodic near-wake region is very much a function of the phase difference. Both sets of results show that this section of the wake becomes very short for  $\Phi \approx -100^\circ$ . Further downstream the wake undergoes a rapid transition to a chaotic state. For other phase difference ranges, the ordered near-wake persists further downstream but still can be subject to secondary transitions resulting in a quasiperiodic or chaotic far wake. If one measures the wake response using integral measures such as the lift or drag coefficient, then these will be affected to some extent by the far-wake behavior, even though they primarily respond to the wake state near the cylinder. If the ordered near-wake region is long, then these global measures should indicate synchronization. As the near-wake is reduced in length, the far-wake behavior can influence the signal recorded at the cylinder so that it contains low frequency components or even increases the frequency content to such an extent that the behavior is chaotic. Interestingly, quasiperiodic and chaotic far-wake behaviors can be observed for elliptical shaped cylinders<sup>11</sup> and the normal flat plate,<sup>19</sup> even in the unforced case.

Experiments and numerical simulations (not shown here) suggest that the suppression mechanism also holds for smaller amplitudes of motion ( $A_\theta$  and  $A_t$ ). For the first time experiments have been carried out on a cylinder wake when the cylinder is experiencing combined rotary and transla-

tional oscillations. The effect of the phase differences between the two forced motions reveals that regular shedding can be suppressed for particular phase differences. This experimental study raised interesting features that were interpreted with the aid of numerical simulations, which qualitatively capture the near-wake behavior.

M.N. would like to acknowledge the support of a Monash Graduate Scholarship (MGS) and Monash International Postgraduate Research Scholarship (MIPRS). D.L. acknowledges support from ARC Discovery Grant No. DP0774525 and the Australian Partnership for Advanced Computing (APAC). We are also grateful to Alexis Cuquel for having helped with the numerical simulations.

- <sup>1</sup>H. M. Blackburn, J. R. Elston, and J. Sheridan, "Bluff-body propulsion by combined rotary and translational oscillation," *Phys. Fluids* **11**, 4 (1999).
- <sup>2</sup>C. H. K. Williamson and R. Govardhan, "Vortex-induced vibration," *Annu. Rev. Fluid Mech.* **36**, 413 (2004).
- <sup>3</sup>T. Sarpkaya, "A critical review of the intrinsic nature of vortex-induced vibrations," *J. Fluids Struct.* **19**, 389 (2004).
- <sup>4</sup>P. T. Tokumaru and P. E. Dimotakis, "Rotary oscillation control of a cylinder wake," *J. Fluid Mech.* **224**, 77 (1991).
- <sup>5</sup>J. R. Filler, P. L. Marston, and W. C. Mih, "Response of the shear layers separating from a circular cylinder to small amplitude rotational oscillations," *J. Fluid Mech.* **231**, 481 (1991).
- <sup>6</sup>J. R. Elston, "The structures and instabilities of flow generated by an oscillating circular cylinder," Ph.D. thesis, Monash University, 2006.
- <sup>7</sup>S. Kocabayik and Q. M. Al-Mdallal, "Bluff-body flow created by combined rotary and translational oscillation," in *Fluid Structure Interaction and Moving Boundary Problems*, WIT Transactions on the Built Environment, Vol. 84, edited by S. Chakrabarti (WIT, Southampton, UK, 2005), p. 195.
- <sup>8</sup>J. S. Leontini, B. E. Stewart, M. C. Thompson, and K. Hourigan, "Predicting vortex-induced vibration from driven oscillation results," *Appl. Math. Model.* **30**, 1096 (2006).
- <sup>9</sup>H. Lamb, *Hydrodynamics* (Dover, New York, 1932).
- <sup>10</sup>J. M. Cimbalá, H. M. Nagib, and A. Roshko, "Large structure in the far wakes of two-dimensional bluff bodies," *J. Fluid Mech.* **190**, 265 (1988).
- <sup>11</sup>S. A. Johnson, M. C. Thompson, and K. Hourigan, "Predicted low frequency structures in the wake of elliptical cylinders," *Eur. J. Mech. B/Fluids* **23**, 229 (2004).
- <sup>12</sup>C. H. K. Williamson and A. Roshko, "Vortex formation in the wake of an oscillating cylinder," *J. Fluids Struct.* **2**, 355 (1988).
- <sup>13</sup>J. S. Leontini, B. E. Stewart, M. C. Thompson, and K. Hourigan, "Wake state and energy transitions of an oscillating cylinder at low Reynolds number," *Phys. Fluids* **18**, 067101 (2006).
- <sup>14</sup>G. E. Karniadakis and S. J. Sherwin, *Spectral/hp Methods for Computational Fluid Dynamics* (Oxford University Press, Oxford, 2005).
- <sup>15</sup>M. C. Thompson, K. Hourigan, and J. Sheridan, "Three-dimensional instabilities in the wake of a circular cylinder," *Exp. Therm. Fluid Sci.* **12**, 190 (1996).
- <sup>16</sup>K. Ryan, M. C. Thompson, and K. Hourigan, "Three-dimensional transition in the wake of bluff elongated cylinders," *J. Fluid Mech.* **538**, 1 (2005).
- <sup>17</sup>J. S. Leontini, M. C. Thompson, and K. Hourigan, "Three-dimensional transition in the wake of a transversely oscillating cylinder," *J. Fluid Mech.* **577**, 79 (2007).
- <sup>18</sup>D. Lo Jacono, J. N. Sørensen, M. C. Thompson, and K. Hourigan, "Control of vortex breakdown in a closed cylinder with a small rotating rod," *J. Fluids Struct.* **24**, 1278 (2008).
- <sup>19</sup>F. M. Najjar and S. Balachandar, "Low-frequency unsteadiness in the wake of a normal flat plate," *J. Fluid Mech.* **370**, 101 (1998).



## Appendix C

# Other publications during candidature

During the course of my candidature an opportunity arose for me to conduct a series of experiments on a topic not related to my PhD thesis. The outcome of the research, conducted in collaboration with my supervisor Dr. David Lo Jacono and Professor Morten Brøns, was published in the journal of *Physics of Fluids*. This chapter presents a copy of the paper as it appeared in the journal. The reference for the paper is:

1. LO JACONO, D., NAZARINIA, M. & BRØNS, M. 2009 Experimental vortex breakdown topology in a cylinder with a free surface. *Physics of Fluids* **21**, (11), 111704.

## Experimental vortex breakdown topology in a cylinder with a free surface

David Lo Jacono,<sup>1,2,3,a)</sup> Mehdi Nazarinia,<sup>3</sup> and Morten Brøns<sup>4</sup>

<sup>1</sup>INPT, UPS, IMFT (Institut de Mécanique des Fluides de Toulouse), Université de Toulouse, Allée Camille Soula, F-31400 Toulouse, France

<sup>2</sup>CNRS, IMFT, F-31400 Toulouse, France

<sup>3</sup>Department of Mechanical and Aerospace Engineering, Fluids Laboratory for Aeronautical and Industrial Research (FLAIR), Monash University, Melbourne, 3800 Victoria, Australia

<sup>4</sup>Department of Mathematics, Technical University of Denmark, 2800 Kongens Lyngby, Denmark

(Received 21 July 2009; accepted 20 October 2009; published online 30 November 2009)

The free surface flow in a circular cylinder driven by a rotating bottom disk is studied experimentally using particle image velocimetry. Results are compared with computational results assuming a stress-free surface. A dye visualization study by Spohn *et al.* [“Observations of vortex breakdown in an open cylindrical container with a rotating bottom,” *Exp. Fluids* **14**, 70 (1993)], as well as several numerical computations, has found a range of different vortex breakdown structures in this flow. We confirm the existence of a transition where the top of the breakdown bubble crosses from the axis to the surface, which has previously only been found numerically. We employ a technique by Brøns *et al.* [“Topology of vortex breakdown bubbles in a cylinder with rotating bottom and free surface,” *J. Fluid Mech.* **428**, 133 (2001)] to find the corresponding bifurcation curve in the parameter plane, which has hitherto only been used on numerical data. The bifurcation curve located here agrees well with previous numerical simulations. For low values of the Reynolds number we find a regime with vortex breakdown that has not been previously identified. Experiments deviate substantially from computations, indicating the importance of surface effects in this regime. © 2009 American Institute of Physics. [doi:10.1063/1.3265718]

The flow in a circular cylinder driven by a rotating bottom disk has proven to be a most useful setup to study secondary structures on a main vortex. Both experimental and computational studies have shown that one or more vortex breakdown zones or bubbles may occur in this flow. We refer the reader to previous reviews for a summary of the central features of vortex breakdown.<sup>1,2</sup> In this letter we report experimental and computational results for the flow in a cylinder with a free surface. The first comprehensive experimental study of the closed cylindrical container case was undertaken by Escudier<sup>3</sup> to obtain a map of vortex breakdown transitions with respect to aspect ratio and Reynolds number. Numerous computational studies<sup>4–7</sup> have reproduced the transitions very accurately. The first experimental study of the open cylindrical container case with a free surface on the top was undertaken by Spohn *et al.*<sup>8</sup> Several computational studies of the flow assuming a stress-free, clean, and flat free surface are available.<sup>5,9–12</sup> Comparing numerical and experimental results<sup>11</sup> shows discrepancies not present in the closed cylinder case. Several flow topologies which are predicted numerically are not found experimentally, and the quantitative agreement between the numerical and computational results is generally poorer. It appears that physical effects such as surface deformation and surface contamination not included in this simple model influences the flow structure. Progress in the modeling of the flow has recently been obtained by Bouffanais and Lo Jacono<sup>13,14</sup> who presented the results of a full numerical simulation in which the laminar, unsteady, and transitional flow regimes have been modeled without resort-

ing to any symmetry property. Still, many challenges remain in modeling free surface flows<sup>15</sup> making experimental studies of this problem especially important. There is currently a technological interest in the cylinder flow with a free surface as it provides a promising model for bioreactors. The steady flow within a vortex breakdown zone has a low stress level, making it appropriate for growth of organic tissue.<sup>16–18</sup> Understanding the topology of the flow—the number and shape of the breakdown bubbles—as it depends on the system parameters clearly becomes important.

In the present letter we examine the topology of vortex breakdown flow experimentally in a cylinder with a free surface using the particle image velocimetry (PIV) technique. We compare the results with numerical simulations assuming a flat stress-free surface. In the parameter regime we explore there is a unique, steady stable flow. It is the variation in the structures in this flow we explore.

The experimental setup consists of a transparent cylinder of diameter  $D=2R=65$  mm that was filled with water and placed in the center of a water filled octagonal shaped container. The octagonal shape allows the exterior faces of the rig to be flat in order to reduce refraction effects. A similar experimental setup was successfully used elsewhere.<sup>19,20</sup> The temperature of the water in the surrounding tank was controlled and kept at 20 °C (Huber minitstat) with a resolution of 0.1 °C. The rotating flat circular disk was located at the bottom of the device. The shaft of this rotating plate was connected through a gear box (gear ratio of 40:1) to a high resolution stepper motor. The stepper motor was computer controlled via a high-performance motion controller at a resolution of 51 200 steps  $\text{rev}^{-1}$  (National Instrument MID-

<sup>a)</sup>Electronic mail: david.lojacono@imft.fr.

7604). The tracer particles used were spherical granular shaped polyamide particles with a nominal diameter of 20  $\mu\text{m}$  and specific weight of 1.016  $\text{gr cm}^{-3}$ . The particles were illuminated by a 2.0 mm thick laser sheet powered by two miniature Nd:yttrium aluminum garnet lasers (Continuum Minilite II) at a wavelength of 532 nm and maximum energy output of 25  $\text{mJ pulse}^{-1}$ . Pairs of images were captured on a high resolution camera with a maximum resolution of  $4008 \times 2672$  pixel. The camera was equipped with a 200 mm lens. This setup gave a range of field of view which varied between  $2672 \times 2170$  and  $2672 \times 3800$  pixel ( $1.232 \times 1.000R$  and  $1.232 \times 1.750R$ , respectively) for an aspect ratio of  $\Gamma = H/R = 1$  and  $\Gamma = 1.75$ , respectively. The accuracy of the aspect ratio was estimated to be about 3 pixel at each end, equating to  $1.38 \times 10^{-3}R$  at each end. It is worth noting that special care was taken to align the objectives, laser sheet, and camera, as any slight misalignment produces a non-negligible bias in the results. Each image pair was processed using in-house PIV software.<sup>19</sup> A final interrogation window of  $32 \times 32$  pixel ( $0.48 \times 0.48$  mm corresponding to  $1.475 \times 1.475 \times 10^{-2}R$ ) was found to give satisfactory results with a 50% overlap (grid spacing of  $16 \times 16$  pixels corresponding to  $7.375 \times 7.375 \times 10^{-3}R$ ). Thus, the maximum measurement resolution obtained was  $236 \times 166$  vectors for each field. A total number of 50 image pairs, taken at a 1.5 Hz, were acquired. Measurements were started after 100–150 cycles after the beginning of motion, allowing sufficient time to achieve steady state. These states display a high degree of symmetry which allows the determination of the axis of rotation. For a horizontal line at height  $z$  which is parametrized by a variable  $x$  we determine the point of intersection with the axis as the value of  $x$  which minimizes the following measure of asymmetry:

$$D(x) = \int [w(x + \xi) - w(x - \xi)]^2 d\xi. \quad (1)$$

For a large region in the middle of the container this value of  $x$  is well defined and is independent of  $z$  and hence identifies the axis.

As the main quantity to identify changes in flow topology we use the axial velocity at the axis  $w_0(z)$ . We use dimensionless variables where the velocity is scaled by  $R\Omega$ , where  $\Omega$  is the angular velocity of the bottom disk. The distance is scaled by  $R$  such that  $z$  varies from 0 at the bottom to  $\Gamma$  at the free surface. Furthermore, we show streamlines of the flow from the isocurves of the streamfunction  $\psi$  satisfying

$$u = \frac{1}{r} \frac{\partial \psi}{\partial z}, \quad w = -\frac{1}{r} \frac{\partial \psi}{\partial r}. \quad (2)$$

We find  $\psi$  by integrating the second equation radially and choosing the level  $\psi=0$  for the axis and the free surface. This method avoids using the radial velocity which is very small close to the axis and has a high relative uncertainty here. Away from the axis we have checked  $\psi$  by comparing the measured  $u$  with the one computed from Eq. (2) and found good agreement.

The incompressible Navier–Stokes equations were solved numerically using a spectral-element technique. The discretization method employed used seventh-order Lagrange polynomials associated with Gauss–Lobatto–Legendre quadrature points. The simulations were undertaken on a 400 macroelement mesh carefully concentrated toward the solid boundaries. Details of the implementation used here can be found in Ref. 21. The code employed has been well proven for use in bluff-body problems.<sup>22,23</sup> Axisymmetry and no-slip boundary conditions were applied on the appropriate sides of the computational domain.<sup>20</sup>

Figure 1 shows a typical sequence of flow structures for fixed  $\Gamma$  and increasing  $\text{Re}$ . A corner bubble is present if  $w_0 < 0$  in a region just below the surface. The bubble attaches to the axis at the point where  $w_0 = 0$ . In all cases there is good agreement between experiments and computations in the lower part of the cylinder, in particular, for the Ekman layer close to the rotating disk. Close to the free surface there are some discrepancies between experiments and computations, most prominently at the  $\text{Re}$  close to the corner crossing bifurcation. Experimentally, the flow topology can be clearly identified except for  $\text{Re} = 1850$  where the sign of  $w_0$  just below the surface cannot be determined unambiguously. Figure 2 summarizes our results for the corner crossing bifurcation. The existence of the bifurcation is clearly verified experimentally, and the precise location of it is in good agreement with computations, the maximal difference being around 100 in  $\text{Re}$  at the highest values of  $\Gamma$ , with better agreement at lower  $\Gamma$ . From the experimental data an estimate of the bifurcation curve can be found as follows. Let  $G(\Gamma, \text{Re}) = w_0'(0)$ , i.e., the axial derivative of the axial velocity evaluated at the axis on the free surface. If  $G > 0$  a corner bubble is present, if  $G < 0$  it is not, see Fig. 1. Hence, the bifurcation can be located by the condition  $G = 0$ . From the experimental data a series of values of  $G$  can be obtained and a bifurcation function  $\bar{G}$  is found by fitting these numbers using a second-order polynomial in  $\Gamma$  and  $\text{Re}$ . The bifurcation line  $\bar{G} = 0$  is shown as the dashed line in Fig. 2. The same procedure was used on numerical data.<sup>6</sup> While it is to be expected that numerical data will depend smoothly on parameters such that the procedure will result in unambiguous results, it is less evident that the same holds for experimental data. However, this is the case for the present dataset. The bifurcation function  $\bar{G}$  can be generated from a subset of the available data, and it turns out that the bifurcation curve is quite robust with respect to that choice. In particular, one may avoid data very close to the bifurcation line where the axial velocities close to the surface are very small, and hence  $\partial w / \partial z$  is poorly defined. In fact, for the curve in Fig. 2 we have only used the data from the maximal and the minimal  $\text{Re}$  at each  $\Gamma$ . We now turn to the flow at low  $\text{Re}$ . Both previous computations<sup>11</sup> and experiments<sup>8</sup> indicate that as  $\text{Re}$  is decreased the corner bubble turns into a detached bubble which then shrinks and disappears. Figure 3 shows, however, some quantitative differences in the location of the two curves. Our experiments reproduce the first experimental bifurcation curve with good agreement. For decreasing  $\text{Re}$  we do find that the detached bubble shrink but does not disappear com-

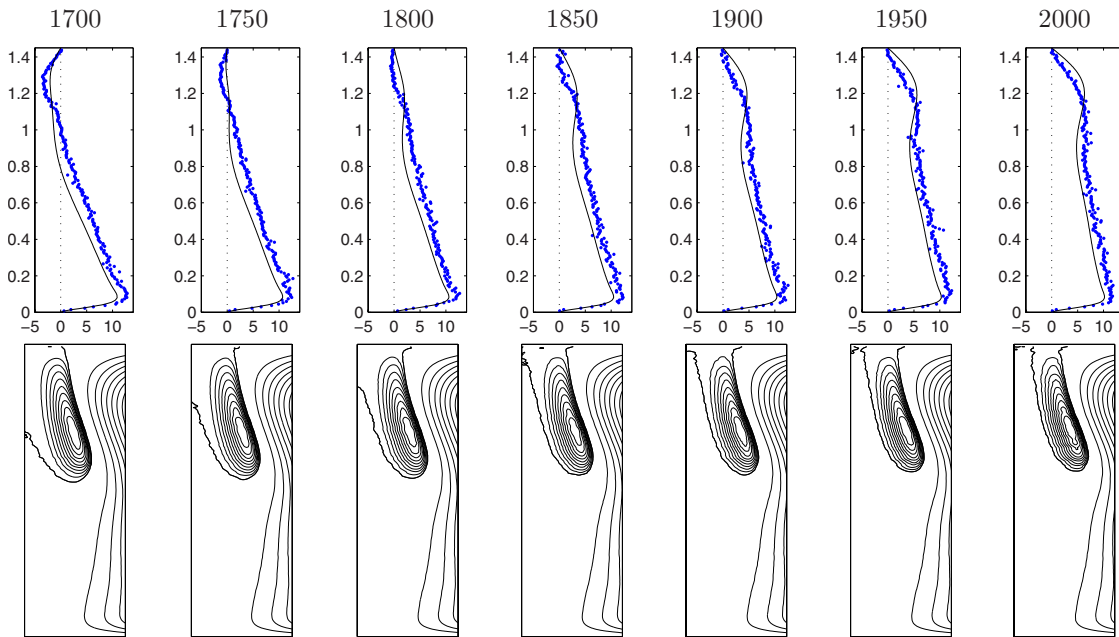


FIG. 1. (Color online) Transition from a corner bubble through a corner crossing bifurcation to an attached bubble at  $\Gamma = 1.45$  for increasing values of  $Re$ . The top row shows cylinder height vs  $w_0(z) \times 10^3$ . The markers are experimental results and the full curves are numerical results. Downward pointing velocities are positive. The bottom row shows corresponding isolines of  $\psi$  obtained from the experimental data. The left edge is the cylinder axis, the right edge is located at  $R/2$ .

pletely. At the same time the agreement with computations deteriorates, and at the lowest  $Re$  we find quite large breakdown bubbles with inner structures and an axial velocity profile which is completely different from the one obtained computationally, see Fig. 4. This behavior is consistent for all values of  $\Gamma$ . To the best of our knowledge, no experimental result in this regime is available in the literature. We attribute this discrepancy to surface effects which are not included in the computational model. We have taken great care to eliminate error sources such as vibrations and transients, but control of the surface properties is very difficult. Surface tension variations can give rise to stagnation points<sup>24</sup> and the flow topology is consequently very sensitive to sur-

face effects. This effect is dominating at low  $Re$ , since at high  $Re$  we get good agreement with computations assuming a stress-free surface.

In conclusion, we have shown that the present experimental technique allows a robust and reliable determination of vortex breakdown structures. We have confirmed the existence of a topological bifurcation where the topology changes from a corner bubble to an attached bubble through a corner crossing bifurcation that has previously only been found numerically. We have provided a proof of concept for a technique to determine a topological bifurcation curve

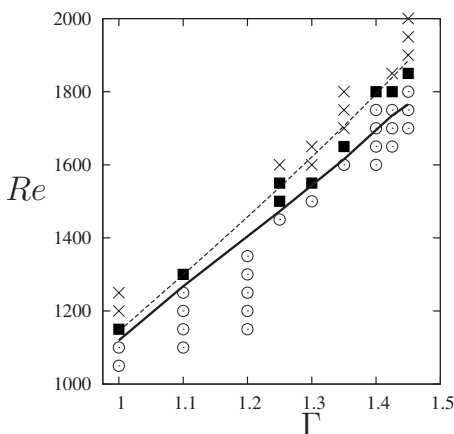


FIG. 2. Topological bifurcation diagram for the corner crossing bifurcation at high  $Re$ . The markers are experimental results.  $\circ$ : Corner bubble;  $\times$ : attached bubble;  $\blacksquare$ : topology indeterminate. The full line is the numerically predicted corner crossing curve. The dashed line is the corner crossing curve determined from the experimental bifurcation function  $\bar{G}$ .

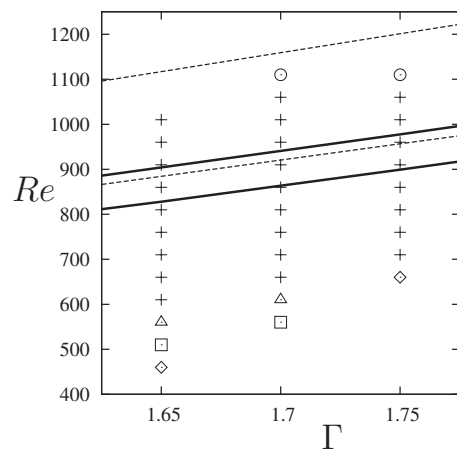


FIG. 3. Bifurcation diagram at low  $Re$ . The markers show experimental results.  $+$ : Detached bubble;  $\circ$ : corner bubble;  $\times$ : attached bubble;  $\Delta$ : detached+corner bubble;  $\diamond$ : detached bubble with inner structure;  $\square$ : corner bubble with inner structure. The full lines are bifurcation curves obtained from simulations. The lower curve is the creation of a detached bubble while the top curve is the corner crossing bifurcation to a corner bubble. The dashed lines are the corresponding experimental curves found by Spohn *et al.* (Ref. 8).

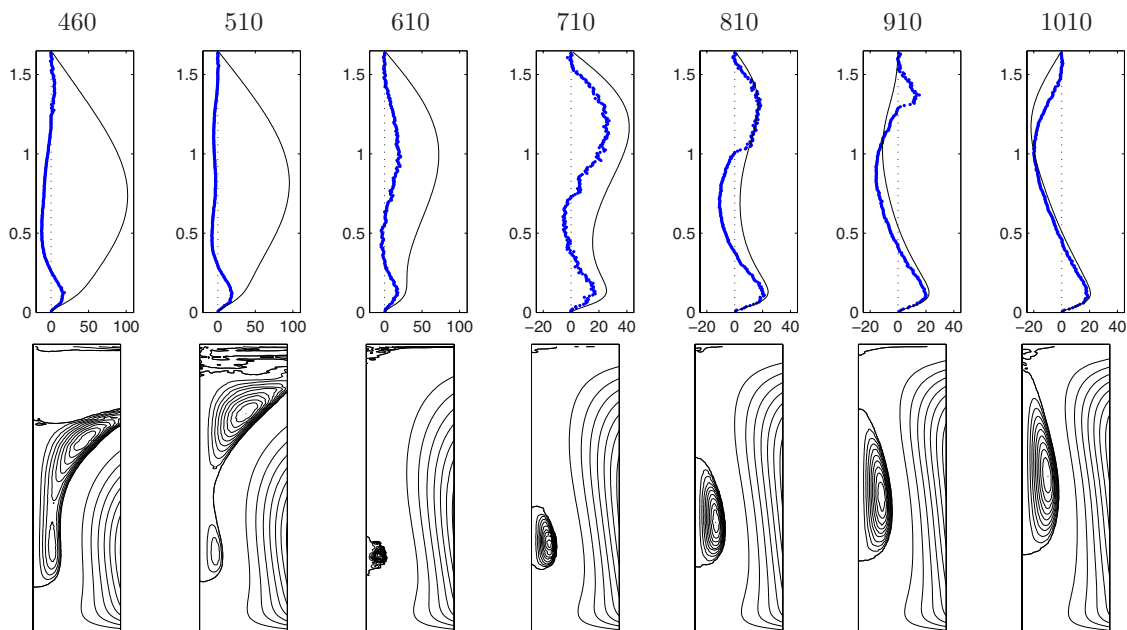


FIG. 4. (Color online) Flow topologies at  $\Gamma=1.65$  and varying  $Re$ . Legend as in Fig. 1. Note the larger velocity range for the lowest  $Re$ .

from the quantitative data obtained experimentally. Finally, we have explored a new region of the parameter space where we have found vortex breakdown bubbles hitherto not observed nor found computationally. The existence of these bubbles indicate that surface effects are very important for the overall flow at low  $Re$ .

Parts of this research was conducted while M.B. was on a sabbatical leave at Monash University. The hospitality and excellent working conditions provided are gratefully acknowledged. M.N. would like to acknowledge the support of a Monash Graduate Scholarship MGS and a Monash International Postgraduate Research Scholarship MIPRS. D.L.J. acknowledges support from ARC Discovery (DP0774525) as well as Swiss National Science Fellowships (PBEL2-112259).

<sup>1</sup>M. G. Hall, "Vortex breakdown," *Annu. Rev. Fluid Mech.* **4**, 195 (1972).

<sup>2</sup>S. Leibovich, "Vortex breakdown," *Annu. Rev. Fluid Mech.* **10**, 185 (1978).

<sup>3</sup>M. P. Escudier, "Observations of the flow produced in a cylindrical container by a rotating endwall," *Exp. Fluids* **2**, 189 (1984).

<sup>4</sup>J. M. Lopez, "Axisymmetric vortex breakdown Part 1. Confined swirling flow," *J. Fluid Mech.* **221**, 533 (1990).

<sup>5</sup>A. Y. Gelfgat, P. Z. Bar-Yoseph, and A. Solan, "Steady states and oscillatory instability of swirling flow in a cylinder with rotating top and bottom," *Phys. Fluids* **8**, 2614 (1996).

<sup>6</sup>M. Brøns, L. K. Voigt, and J. N. Sørensen, "Streamline topology of steady axisymmetric vortex break-down in a cylinder with co- and counter-rotating end-covers," *J. Fluid Mech.* **401**, 275 (1999).

<sup>7</sup>M. Brøns and A. V. Bisgaard, "Bifurcation of vortex breakdown patterns in a circular cylinder with two rotating covers," *J. Fluid Mech.* **568**, 329 (2006).

<sup>8</sup>A. Spohn, M. Mory, and E. J. Hopfinger, "Observations of vortex breakdown in an open cylindrical container with a rotating bottom," *Exp. Fluids* **14**, 70 (1993).

<sup>9</sup>D. T. Valentine and C. C. Jahnke, "Flows induced in a cylinder with both end walls rotating," *Phys. Fluids* **6**, 2702 (1994).

<sup>10</sup>J. M. Lopez, "Unsteady swirling flow in an enclosed cylinder with reflectional symmetry," *Phys. Fluids* **7**, 2700 (1995).

<sup>11</sup>M. Brøns, L. K. Voigt, and J. N. Sørensen, "Topology of vortex breakdown bubbles in a cylinder with rotating bottom and free surface," *J. Fluid Mech.* **428**, 133 (2001).

<sup>12</sup>R. Iwatsu, "Numerical study of flows in a cylindrical container with rotating bottom and top flat free surface," *J. Phys. Soc. Jpn.* **74**, 333 (2005).

<sup>13</sup>R. Bouffanais and D. Lo Jacono, "Transitional cylindrical swirling flow in presence of a flat free surface," *Comput. Fluids* **38**, 1651 (2009).

<sup>14</sup>R. Bouffanais and D. Lo Jacono, "Unsteady transitional cylindrical swirling flow in presence of a moving free surface," *Phys. Fluids* **21**, 064107 (2009).

<sup>15</sup>T. Sarpkaya, "Vorticity, free surface, and surfactants," *Annu. Rev. Fluid Mech.* **28**, 83 (1996).

<sup>16</sup>P. Yu, T. S. Lee, Y. Zeng, and H. T. Low, "Effect of vortex breakdown on mass transfer in a cell culture bioreactor," *Mod. Phys. Lett. B* **19**, 1543 (2005).

<sup>17</sup>J. Dusting, J. Sheridan, and K. Hourigan, "A fluid dynamics approach to bioreactor design for cell and tissue culture," *Biotechnol. Bioeng.* **94**, 1196 (2006).

<sup>18</sup>Y. D. Cui, J. M. Lopez, T. T. Lim, and F. Marques, "Harmonically forced swirling flow," *Phys. Fluids* **21**, 034106 (2009).

<sup>19</sup>A. Fouras, D. Lo Jacono, and K. Hourigan, "Stereo PIV: A novel technique with inherent error estimation and improved accuracy," *Exp. Fluids* **44**, 317 (2008).

<sup>20</sup>D. Lo Jacono, J. N. Sørensen, M. C. Thompson, and K. Hourigan, "Control of vortex breakdown in a closed cylinder with a small rotating rod," *J. Fluids Struct.* **24**, 1278 (2008).

<sup>21</sup>M. C. Thompson, K. Hourigan, and J. Sheridan, "Three-dimensional instabilities in the wake of a circular cylinder," *Exp. Therm. Fluid Sci.* **12**, 190 (1996).

<sup>22</sup>M. Nazarinia, D. Lo Jacono, M. C. Thompson, and J. Sheridan, "Flow behind a cylinder forced by a combination of oscillatory translational and rotational motions," *Phys. Fluids* **21**, 051701 (2009).

<sup>23</sup>M. Nazarinia, D. Lo Jacono, M. C. Thompson, and J. Sheridan, "The three-dimensional wake of a cylinder undergoing a combination of translational and rotational oscillation in a quiescent fluid," *Phys. Fluids* **21**, 064101 (2009).

<sup>24</sup>M. Brøns, "Topological fluid dynamics of interfacial flows," *Phys. Fluids* **6**, 2730 (1994).



# Bibliography

- ADRIAN, R. J. 1986 Image shifting technique to resolve directional ambiguity in double-pulsed velocimetry. *Appl. Optics* **25** (21), 3855–3858.
- ADRIAN, R. J. 1991 Particle-imaging techniques for experimental fluid mechanics. *Annu. Rev. Fluid Mech.* **23**, 261–304.
- AL-MDALLAL, Q. M. 2004 Analysis and computation of the cross-flow past an oscillating cylinder with two degrees of freedom. PhD thesis, Memorial University of Newfoundland.
- AL-MDALLAL, Q. M. & KOCABIYIK, S. 2006 Rotational oscillations of a cylinder in cross-flow. *Int. J. Comput. Fluid D.* **20** (5), 293–299.
- ANAGNOSTOPOULOS, P. 1989 Numerical solution for laminar two-dimensional flow about a fixed and transversely oscillating cylinder in a uniform stream. *J. Comp. Phys.* **85**, 434–456.
- ANAGNOSTOPOULOS, P. 1997 Computer-aided flow visualization and vorticity balance in the laminar wake of a circular cylinder. *J. Fluid. Struct.* **11**, 33–72.
- ANAGNOSTOPOULOS, P. & BEARMAN, P. W. 1992 Response characteristics of a vortex-excited cylinder at low Reynolds numbers. *J. Fluid. Struct.* **6**, 39–50.
- ANDERSON, J. M., STREITLIEN, K., BARRETT, D. S. & TRIANTAFYLLOU, M. S. 1998 Oscillating foils of high propulsive efficiency. *J. Fluid Mech.* **360**, 41–72.
- ATVARIS, K. 2007 Vortex breakdown control using a bluff body. PhD thesis, Monash University.
- BAEK, S.-J. & SUNG, H. J. 1998 Numerical simulation of the flow behind a rotary oscillating circular cylinder. *Phys. Fluids* **10**, 869–876.
- BAEK, S.-J. & SUNG, H. J. 2000 Quasi-periodicity in the wake of a rotationally oscillating cylinder. *J. Fluid Mech.* **408**, 275–300.
- BALABANI, S., KONSTANTINIDIS, E., LIANG, C. & PAPADAKIS, G. 2007 Numerical study of the effect of velocity perturbations on the mechanics of vortex shedding in

- synchronised bluff-body wakes. In *BBVIV5 (5th Conferece on Bluff Body Wakes and Vortex Induced Vibrations, Costa do Sauipe, Bahia, Brazil)*.
- BARBI, C., FAVIER, D. P., MARESCA, C. A. & TELIONIS, D. P. 1986 Vortex shedding and lock-on of a circular cylinder in oscillatory flow. *J. Fluid Mech.* **170**, 527–544.
- BARKLEY, D. & HENDERSON, R. D. 1996 Three-dimensional Floquet stability analysis of the wake of a circular cylinder. *J. Fluid Mech.* **322**, 215–241.
- BEARMAN, P. W. 1984 Vortex shedding from oscillating bluff bodies. *Annu. Rev. Fluid Mech.* **16** (1), 195–222.
- BEARMAN, P. W. 1997 Bluff body hydrodynamics. In *21st Symposium on Naval Hydrodynamics*, pp. 561–579. Naval Studies Board, National Research Council.
- BEARMAN, P. W. & CURRIE, I. G. 1979 Pressure fluctuation measurements on an oscillating circular cylinder. *J. Fluid Mech.* **91**, 661–677.
- BEARMAN, P. W., DOWNIE, M. J., GRAHAM, J. M. R. & OBASAJU, E. D. 1985 Forces on cylinders in viscous oscillatory flow at low Keulegan–Carpenter numbers. *J. Fluid Mech.* **154**, 337–356.
- BEARMAN, P. W., GRAHAM, J. M. R., NAYLOR, P. & OBASAJU, E. D. 1981 The role of vortices in oscillatory flow about bluff cylinders. In *International Symposium on Hydrodynamics in Ocean Engineering*, pp. 621–635. Trondheim Norway.
- BÉNARD, H. 1908 Formation de centres de giration a l’arriere d’un obstacle en mouvement. *C.R. Acad. Sci. Paris* **147**, 839.
- BISHOP, R. E. D. & HASSAN, A. Y. 1964 The lift and drag forces on a circular cylinder oscillating in a flowing fluid. *Proceedings of the Royal Society of London, series A* **277** (1368), 51–75.
- BLACKBURN, H. M., ELSTON, J. R. & SHERIDAN, J. 1998 Flows created by a cylinder with oscillatory translation and spin. In *FED’98 - ASME Fluids Engineering Division Summer Meeting*. Washington, DC, USA.
- BLACKBURN, H. M., ELSTON, J. R. & SHERIDAN, J. 1999 Bluff-body propulsion produced by combined rotary and translational oscillation. *Phys. Fluids* **11** (1), 4–6.
- BLACKBURN, H. M., GOVARDHAN, R. N. & WILLIAMSON, C. H. K. 2000 A complementary numerical and physical investigation of vortex-induced vibration. *J. Fluid. Struct.* **15**, 481–488.
- BLACKBURN, H. M. & HENDERSON, R. D. 1996 Lock-in behaviour in simulated vortex-induced vibration. *Exp. Therm. Fluid Sci.* **12**, 184–189.



- BLACKBURN, H. M. & HENDERSON, R. D. 1999 A study of two-dimensional flow past an oscillating cylinder. *J. Fluid Mech.* **385**, 255–286.
- BLACKBURN, H. M. & KARNIADAKIS, G. E. 1993 Two- and three-dimensional simulations of vortex-induced vibration of a circular cylinder. In *Proceedings of the Third International offshore and polar engineering conference, Singapore*.
- BLACKBURN, H. M. & LOPEZ, J. M. 2003 On three-dimensional quasi-periodic Floquet instabilities of two-dimensional bluff body wakes. *Phys. Fluids* **15** (8), L57–L60.
- BLACKBURN, H. M., MARQUES, F. & LOPEZ, J. M. 2005 Symmetry breaking of two-dimensional time-periodic wakes. *J. Fluid Mech.* **522**, 395–411.
- BLEVINS, R. D. 1977 *Flow-induced vibration*. Van Nostrand Reinhold Company, New York.
- BREDE, M., ECKELMANN, H. & ROCKWELL, D. 1996 On secondary vortices in the cylinder wake. *Phys. Fluids* **8** (8), 2117–2124.
- BURCHER, R. K. 1972 Developments in ship maneuverability. *Transactions of the Royal Institution of Naval Architects* **114**, 1–32.
- CANUTO, C., HUSSAINI, M., QUARTERONI, A. & ZANG, T. 1990 *Spectral Methods in Fluid Dynamics*, 2nd edn. Springer Verlag (Berlin and New York).
- CARBERRY, J. 2002 Wake states of a submerged oscillating cylinder and of a cylinder beneath a free-surface. PhD thesis, Monash University.
- CARBERRY, J., SHERIDAN, J. & ROCKWELL, D. 2001 Force and wake modes of an oscillating cylinder. *J. Fluid. Struct.* **15**, 523–532.
- CARBERRY, J., SHERIDAN, J. & ROCKWELL, D. 2005 Controlled oscillations of a cylinder: forces and wake modes. *J. Fluid Mech.* **538**, 31–69.
- CHENG, M., CHEW, Y. T. & LUO, S. C. 2001a Numerical investigation of a rotationally oscillating cylinder in mean flow. *J. Fluid. Struct.* **15**, 981–1007.
- CHENG, M., CHEW, Y. T. & LUO, S. C. 2001b Numerical simulation of flow past a rotationally oscillating cylinder. *Comput. Fluids* **30**, 365–392.
- CHENG, M. & MORETTI, P. M. 1991 *Lock-in phenomena on a single cylinder with forced transverse oscillation, Flow-Induced Vibration and Wear*, vol. 206, pp. 129–133. ASME.
- CHOI, S. & CHOI, H. 2002 Characteristics of flow over a rotationally oscillating cylinder at low Reynolds number. *Phys. Fluids* **14**, 2767–2777.

- CHOU, M.-H. 1997 Synchronization of vortex shedding from a cylinder under rotary oscillation. *Comput. Fluids* **26** (8), 755–774.
- CIMBALA, J. M., NAGIB, H. M. & ROSHKO, A. 1988 Large structure in the far wakes of two-dimensional bluff bodies. *J. Fluid Mech.* **190**, 265–298.
- COUTANCEAU, M. & BOUARD, R. 1977 Experimental determination of the main features of the viscous flow in the wake of a circular cylinder in uniform translation. Part 1. steady flow. *J. Fluid Mech.* **79**, 231–256.
- DENNIS, C. R., NGUYEN, P. & KOCABIYIK, S. 2000 The flow induced by a rotationally oscillating and translating circular cylinder. *J. Fluid Mech.* **407**, 123–144.
- DENNIS, S. C. R. & CHANG, G.-Z. 1970 Numerical solutions for steady flow past a circular cylinder at Reynolds numbers up to 100. *J. Fluid Mech.* **42** (3), 471–489.
- DU, X., BIRCH, D., PANAGAKOS, A. & LEE, T. 2003 PIV study of the vortex wake behind a rotationally oscillating cylinder. In *50<sup>th</sup> Annual conference of the Canadian aeronautics and space institute, Montreal, Québec, Canada*.
- DUNCAN, W. J. 1959 *The principles of the control and stability of aircraft*. Cambridge University Press, Cambridge.
- DUSTING, J. C. 2006 An analysis of flows within cell culture bioreactors with vortex breakdown. PhD thesis, Monash University.
- DÜTSCH, H., DURST, F., BECKER, S. & LIENHART, H. 1998 Low-Reynolds-number flow around an oscillating circular cylinder at low Keulegan–Carpenter numbers. *J. Fluid Mech.* **360**, 249–271.
- DUŠEK, J., LE GAL, P. & FRAUNIÉ, P. 1994 A numerical and theoretical study of the first Hopf bifurcation in a cylinder wake. *J. Fluid Mech.* **264**, 59–80.
- ELSTON, J. R. 1997 Wake formation of a vibrating and rotating cylinder. *Tech. Rep.*. Final year project report, Department of Mechanical Engineering, Monash University, Australia.
- ELSTON, J. R. 2005 The structures and instabilities of flow generated by an oscillating circular cylinder. PhD thesis, Monash University.
- ELSTON, J. R., BLACKBURN, H. M. & SHERIDAN, J. 2006 The primary and secondary instabilities of flow generated by an oscillating circular cylinder. *J. Fluid Mech.* **550**, 359–389.
- ELSTON, J. R., SHERIDAN, J. & BLACKBURN, H. M. 2004 Two-dimensional Floquet stability analysis of the flow produced by an oscillating circular cylinder in quiescent fluid. *Eur. J. Mech. B-Fluid* **23** (1), 99–106.

- ETKIN, B. 1972 *Dynamics of Atmospheric Flight*. Wiley, New York.
- FALTINSEN, M. O. 1990 *Sea Loads on Ships and Offshore Structures*. Cambridge University Press, Cambridge.
- FILLER, J. R., MARSTON, P. L. & MIH, W. C. 1991 Response of the shear layers separating from a circular cylinder to small amplitude rotational oscillations. *J. Fluid Mech.* **231**, 481–499.
- FOURAS, A. 1997 Development of a cross-correlation PIV image recording technique and analysis of velocity and vorticity measurement error applied to an unsteady separated flow. Master's thesis, Monash University.
- FOURAS, A., LO JACONO, D. & HOURIGAN, K. 2008 Target-free stereo PIV: A novel technique with inherent error estimation and improved accuracy. *Exp. Fluids* **44** (2), 317–329.
- FOURAS, A. & SORIA, J. 1998 Accuracy of out-of-plane vorticity measurements derived from in-plane velocity field data. *Exp. Fluids* **25** (5–6), 409–430.
- FOX, T. A. & WEST, G. S. 1990 On the use of end plates with circular cylinders. *Exp. Fluids* **9** (4), 237–239.
- FUJISAWA, N., IKEMOTO, K. & NAGAYA, K. 1998 Vortex shedding resonance from a rotationally oscillating cylinder. *J. Fluid. Struct.* **12**, 1041–1053.
- FUJISAWA, N., TANAHASHI, S. & SRINIVAS, K. 2005 Evaluation of pressure field and fluid forces on a circular cylinder with and without rotational oscillation using velocity data from PIV measurement. *Meas. Sci. Technol.* **16**, 989–996.
- GERICH, D. & ECKELMANN, H. 1982 Influence of end plates and free ends on the shedding frequency of circular cylinders. *J. Fluid Mech.* **122**, 109–121.
- GERRARD, J. H. 1978 The wakes of cylindrical bluff bodies at low Reynolds number. *Philos. T. Roy. Soc. A* **288**, 351.
- GOVARDHAN, R. & WILLIAMSON, C. H. K. 2001 Mean and fluctuating velocity fields in the wake of a freely-vibrating cylinder. *J. Fluid. Struct.* **15**, 489–501.
- GRIFFIN, O. M. 1971 The unsteady wake of an oscillating cylinder at low Reynolds number. *J. Appl. Mech.-T. ASME* **38** (4), 729–737.
- GRIFFIN, O. M. & HALL, M. S. 1991 Review of vortex shedding lock-on and flow control in bluff body wakes. *J. Fluid Eng.-T. ASME* **113**, 526–537.
- GRIFFIN, O. M. & RAMBERG, S. E. 1974 The vortex-street wakes of vibrating cylinders. *J. Fluid Mech.* **66** (3), 553–576.

- GRIFFIN, O. M. & RAMBERG, S. E. 1976 Vortex shedding from a cylinder vibrating inline with an incident uniform flow. *J. Fluid Mech.* **75**, 257–271.
- GRIFFITH, M. D. 2007 The stability and behaviour of flows in stenotic geometries. PhD thesis, Monash University.
- GU, W., CHYU, C. & ROCKWELL, D. 1994 Timing of vortex formation from an oscillating cylinder. *Phys. Fluids* **6** (11), 3677–3682.
- GUILMINEAU, E. & QUEUTEY, P. 2002 A numerical simulation of vortex shedding from an oscillating circular cylinder. *J. Fluid. Struct.* **16** (6), 773–794.
- HALL, M. S. & GRIFFIN, O. M. 1993 Vortex shedding and lock-on in a perturbed flow. *J. Fluid Eng.-T. ASME* **115**, 283–291.
- HAMMACHE, M. & GHARIB, M. 1991 An experimental study of the parallel and oblique vortex shedding from circular cylinders. *J. Fluid Mech.* **232**, 567–590.
- HAMMAN, F. H. & DALTON, C. 1971 The forces on a cylinder oscillating sinusoidally in water. *J. Eng. Ind.-T. ASME* **93** (4), 1197–1202.
- HAPPEL, J. & BRENNER, H. 1983 *Low Reynolds number hydrodynamics*. Martinus Nijhoff Publishers.
- HART, D. P. 2000 PIV error correction. *Exp. Fluids* **29** (1), 13–22.
- HARTOG, J. D. 1956 *Mechanical Vibrations*. McGraw-Hill Book Company.
- HENDERSON, R. D. 1997 Non-linear dynamics and pattern formation in turbulent wake transition. *J. Fluid Mech.* **352**, 65–112.
- HINDS, W. C. 1999 *Aerosol technology: properties, behavior, and measurement of airborne particles*, 2nd edn. Wiley.
- HONJI, H. 1981 Streaked flow around an oscillating cylinder. *J. Fluid Mech.* **107**, 509–520.
- HOPF, E. 1942 Abzweigung einer periodischen Lösung von einer stationären Lösung eines differentialsystems. *bericht der Math.-Phys. Klasse der Sächsischen Akademie der Wisasenschaften zu Leipzig* .
- HOVER, F. S., TECHET, A. H. & TRIANTAFYLLOU, M. S. 1998 Forces on oscillating uniform and tapered cylinders in crossflow. *J. Fluid Mech.* **363**, 97–114.
- HURLBUT, S. E., SPAULDING, M. L. & WHITE, F. M. 1982 Numerical solution for laminar two dimensional flow about a cylinder oscillating in a uniform stream. *J. Fluid Eng.-T. ASME* **104**, 214–220.

- ILIADIS, G. & ANAGNOSTOPOULOS, G. 1998 Viscous oscillatory flow around a circular cylinder at low Keulegan–Carpenter numbers and frequency parameters. *Int. J. Numer. Meth. Fl.* **26**, 403–442.
- JAUVTIS, N. & WILLIAMSON, C. H. K. 2003 A high-amplitude  $2t$  mode of vortex formation, and the effects of non-harmonic forcing in vortex-induced vibration. *Eur. J. Mech. B-Fluid* **23** (1), 107–114.
- JAUVTIS, N. & WILLIAMSON, C. H. K. 2004 The effects of two degrees of freedom on vortex-induced vibration. *J. Fluid Mech.* **509**, 23–62.
- JOHNSON, S. A., THOMPSON, M. C. & HOURIGAN, K. 2004 Predicted low frequency structures in the wake of elliptical cylinders. *Eur. J. Mech. B-Fluid* **23**, 229–239.
- JUSTESEN, P. 1991 A numerical study of oscillating flow around a circular cylinder. *J. Fluid Mech.* **222**, 157–196.
- VON KÁRMÁN, T. 1911 Über den mechanismus des widerstands, den ein bewegter bewegter körper in einer flüssigkeit erfährt. *Göttingen Nach. Math. Phys. Kl.* pp. 509–519.
- KARNIADAKIS, G. E., ISRAELI, M. & ORSZAG, S. A. 1991 High-order splitting methods of the incompressible Navier–Stokes equations. *J. Comp. Phys.* **97**, 414–443.
- KARNIADAKIS, G. E. & SHERWIN, S. J. 2005 *Spectral/hp methods for computational fluid dynamics*. Oxford University Press, Oxford.
- KARNIADAKIS, G. E. & TRIANTAFYLLOU, G. S. 1989 Frequency selection and asymptotic states in laminar wakes. *J. Fluid Mech.* **199**, 441–469.
- KARNIADAKIS, G. E. & TRIANTAFYLLOU, G. S. 1992 Three-dimensional dynamics and transition to turbulence in the wake of bluff objects. *J. Fluid Mech.* **238**, 1–30.
- KEULEGAN, G. H. & CARPENTER, L. H. 1958 Forces on cylinders and plates in an oscillating fluid. *J. Res. Nat. Bur. Stand.* **60** (5), 423–440.
- KING, R. 1977 A review of vortex shedding research and its application. *Ocean Eng.* **4**, 141–172.
- KISHNAMOORTHY, S., PRICE, S. J. & PAÏGDOUSSIS, P. 2001 Cross-flow past an oscillating circular cylinder: Synchronization phenomena in the near wake. *J. Fluid. Struct.* **15** (7), 955–980.
- KOCABIYIK, S. & AL-MDALLAL, Q. M. 2005 *Bluff-body flow created by combined rotary and translational oscillation, Fluid Structure Interaction and Moving Boundary Problems*, vol. 84, pp. 195–203. WIT Press, Southampton, UK.

- KÖNIG, M., EISENLOHR, H. & ECKELMANN, H. 1990 The fine structure in the Strouhal-Reynolds number relationship of the laminar wake of a circular cylinder. *Phys. Fluids A* **2** (9), 1607–1614.
- KONSTANTINIDIS, E. & BALABANI, S. 2008 Flow structure in the locked-on wake of a circular cylinder in pulsating flow: Effect of forcing amplitude. *Int. J. Heat Fluid Fl.* **29** (6), 1567 – 1576.
- KONSTANTINIDIS, E., BALABANI, S. & YIANNESKIS, M. 2002 Effect of pulsations on the wake structure of a circular cylinder. In *Proc. ASME 5th International Symposium on Fluid-Structure Interaction, New Orleans*.
- KONSTANTINIDIS, E., CASTIGLIA, D., BALABANI, S., PAPADAKIS, G. & BERGELLES, G. 2000 Vortex lock-on phenomena due to pulsating flow in tube arrays. In *Proc. Tenth International Symposium on Applications of Laser Techniques to Fluid Mechanics, Lisbon, Portugal*.
- KONSTANTINIDIS, E., YIANNESKIS, M. & BALABANI, S. 2007 Bimodal vortex shedding in a perturbed cylinder wake. *Phys. Fluids* **19** (1), 011701.
- KOOPMANN, G. H. 1967 The vortex wakes of vibrating cylinders at low Reynolds numbers. *J. Fluid Mech.* **28**, 501–512.
- LAM, K. M. & DAI, G. Q. 2002 Formation of vortex street and vortex pair from a circular cylinder oscillating in water. *Exp. Therm. Fluid Sci.* **26**, 901–915.
- LAM, K. M., HU, J. C. & LIU, P. 2010 Vortex formation processes from an oscillating circular cylinder at high Keulegan–Carpenter numbers. *Phys. Fluids* **22** (1), 015105.
- LAMB, H. 1932 *Hydrodynamics*. Dover, NY: Cambridge University Press.
- LE GAL, P., NADIM, A. & THOMPSON, M. C. 2001 Hysteresis in the forced Stuart–Landau equation: Application to vortex shedding from an oscillating cylinder. *J. Fluid. Struct.* **15**, 445–457.
- LECOINTE, Y. & PIQUET, J. 1989 Flow structure in the wake of an oscillating cylinder. *J. Fluid Eng.-T. ASME* **11** (2), 139–148.
- LEE, T. & BUDWIG, R. 1991 A study of the effect of aspect ratio on vortex shedding behind circular cylinders. *Phys. Fluids A* **3** (2), 309–315.
- LEONTINI, J. S. 2007 A numerical investigation of transversely-oscillating cylinders in two-dimensional flow. PhD thesis, Monash University.
- LEONTINI, J. S., STEWART, B. E., THOMPSON, M. C. & HOURIGAN, K. 2006a Predicting vortex-induced vibration from driven oscillation results. *Appl. Math. Model.* **30**, 1096–1102.

- LEONTINI, J. S., STEWART, B. E., THOMPSON, M. C. & HOURIGAN, K. 2006b Wake state and energy transitions of an oscillating cylinder at low Reynolds number. *Phys. Fluids* **18** (3), 067101.
- LEONTINI, J. S., THOMPSON, M. C. & HOURIGAN, K. 2007 Three-dimensional transition in the wake of a transversely oscillating cylinder. *J. Fluid Mech.* **577**, 79–104.
- LEWEKE, T. 2002 FLAIR water channel - characterisation of flow quality. *Tech. Rep.*. Monash University, Melbourne, Australia.
- LEWEKE, T. & WILLIAMSON, C. H. K. 1998 Three-dimensional instabilities in wake transition. *Eur. J. Mech. B-Fluid* **17** (4), 571–586.
- LIGHTHILL, J. 1986 Fundamentals concerning wave loading on offshore structures. *J. Fluid Mech.* **173**, 667–681.
- LIGHTHILL, J. 1989 *An informal introduction to theoretical fluid mechanics*. Clarendon Press, Oxford.
- LIN, J.-C. & ROCKWELL, D. 1996 Force identification by vorticity fields: Techniques based on flow imaging. *J. Fluid. Struct.* **10**, 663–668.
- LIN, J.-C. & ROCKWELL, D. 1997 Quantitative interpretation of vortices from a cylinder oscillating in quiescent fluid. *Exp. Fluids* **23**, 99–104.
- LIN, J.-C. & ROCKWELL, D. 1999 Horizontal oscillations of a cylinder beneath a free surface: vortex formation and loading. *J. Fluid Mech.* **389**, 1–26.
- LO JACONO, D., LEONTINI, J. S., THOMPSON, M. C. & SHERIDAN, J. 2010 Modification of three-dimensional transition in the wake of a rotationally oscillating cylinder. *J. Fluid Mech.* **643**, 349–362.
- LO JACONO, D., SØRENSEN, J. N., THOMPSON, M. C. & HOURIGAN, K. 2008 Control of vortex breakdown in a closed cylinder with a small rotating rod. *J. Fluid. Struct.* **24** (8), 1278–1283.
- LU, X.-Y. & SATO, J. 1996 A numerical study of flow past a rotationally oscillating circular cylinder. *J. Fluid. Struct.* **10** (8), 829–849.
- MAHFOUZ, F. M. & BADR, H. M. 2000 Flow structure in the wake of a rotationally oscillating cylinder. *J. Fluid Eng.-T. ASME* **122**, 290–301.
- MAIR, W. A. & STANSBY, P. K. 1975 Vortex wakes of bluff cylinders in shear flow. *SIAM J. Appl. Math.* **28** (2), 519–540.
- MARQUES, F., LOPEZ, J. M. & BLACKBURN, H. M. 2004 Bifurcations in systems with  $Z_2$  spatio-temporal and  $O(2)$  spatial symmetry. *Physica D* **189**, 247–276.

- MARRIS, A. W. 1964 A review on vortex streets, periodic wakes, and induced vibration phenomena. *J. Basic Eng.* **86**, 185–196.
- MAULL, D. J. & MILLINER, M. G. 1978 Sinusoidal flow past a circular cylinder. *Coast. Eng.* **2**, 149–168.
- MCWILLIAMS, J. 1990 The vortices of two-dimensional turbulence. *J. Fluid Mech.* **219**, 361–385.
- MEINHART, C. D., WERELEY, S. T. & SANTIAGO, J. G. 2000 A PIV algorithm for estimation time-averaged velocity fields. *J. Fluid Eng.-T. ASME* **122**, 285–289.
- MENEGHINI, J. R. & BEARMAN, P. W. 1995 Numerical simulation of high amplitude oscillatory flow about a circular cylinder. *J. Fluid. Struct.* **9**, 435–455.
- MORTON, B. R. 1984 The generation and decay of vorticity. *Geophys. Astro. Fluid* **28**, 277–308.
- MUNSON, B. R., YOUNG, D. F. & OKIISHI, T. H. 2006 *Fundamentals of Fluid Mechanics*, 5th edn. John Wiley & Sons, Inc.
- NAJJAR, F. M. & BALACHANDAR, S. 1998 Low-frequency unsteadiness in the wake of a normal flat plate. *J. Fluid Mech.* **370**, 101–147.
- NAUDASCHER, E. & ROCKWELL, D. 1994 *Flow-induced vibrations: an engineering guide*. Rotterdam, Brookfield: A.A. Balkema.
- NAZARINIA, M., LO JACONO, D., THOMPSON, M. C. & SHERIDAN, J. 2009 The three-dimensional wake of a cylinder undergoing a combination of translational and rotational oscillation in a quiescent fluid. *Phys. Fluids* **21** (6), 064101.
- NEHARI, D., ARMENIO, V. & BALLIO, F. 2004 Three-dimensional analysis of the unidirectional oscillatory flow around a circular cylinder at low Keulegan-Carpenter and  $\beta$  numbers. *J. Fluid Mech.* **520**, 157–186.
- NISHIOKA, M. & SATO, H. 1974 Measurements of velocity distributions in the wake of a circular cylinder at low Reynolds numbers. *J. Fluid Mech.* **65**, 97–112.
- NORBERG, C. 1994 An experimental investigation of the flow around a circular cylinder: influence of aspect ratio. *J. Fluid Mech.* **258**, 287 – 316.
- NORBERG, C. 2003 Fluctuating lift on a circular cylinder: review and new measurements. *J. Fluid. Struct.* **17** (1), 57 – 96.
- OBASAJU, E. D., BEARMAN, P. W. & GRAHAM, J. M. R. 1988 A study of forces, circulation and vortex patterns around a circular cylinder in oscillating flow. *J. Fluid Mech.* **196**, 467–494.



- ONGOREN, A. & ROCKWELL, D. 1988a Flow structure from an oscillating cylinder. Part 1. mechanisms of phase shift and recovery in the near wake. *J. Fluid Mech.* **191**, 197–223.
- ONGOREN, A. & ROCKWELL, D. 1988b Flow structure from an oscillating cylinder. Part 2. mode competition in the near wake. *J. Fluid Mech.* **191**, 225–245.
- PAIDOUSSIS, M. P. 1998 *Fluid Structure Interactions: Slender Structures and Axial Flow*. Academic Press, San Diego, CA.
- PARKINSON, G. V. 1974 *Mathematical models of flow-induced vibrations of bluff bodies*, chap. Flow-induced structural vibrations. (A75-15253 04-39), pp. 81–127. Springer-Verlag, Berlin.
- PARNAUDEAU, P., CARLIER, J., HEITZ, D. & LAMALLAIS, E. 2008 Experimental and numerical studies of the flow over a circular cylinder at Reynolds number 3900. *Phys. Fluids* **20** (8), 085101.
- PONCET, P. 2002 Vanishing of mode B in the wake behind a rotationally oscillating circular cylinder. *Phys. Fluids* **14**, 2021–2023.
- PRANDTL, L. 1926 Application of the “Magnus Effect” to the wind propulsion of ships. *Tech. Rep.*. NACA 387.
- PROVANSAL, M., MATHIS, C. & BOYER, L. 1987 Bénard-von Kármán instability: Transient and forced regimes. *J. Fluid Mech.* **182**, 1–22.
- RAFFEL, M., WILLERT, C., WERELEY, S. & KOMPENHANS, J. 2007 *Particle Image Velocimetry: A practical guide*, 2nd edn. Springer.
- RAYLEIGH, L. 1879 Acoustical observations ii. *Philosophical Magazine* **VII**, 149–162.
- REYNOLDS, O. 1883 An experimental investigation of the circumstances which determine whether the motion of water shall be direct or sinuous, and of the law of resistance in parallel channels. *Phil. Trans. R. Soc.* **174**, 935–982.
- REYNOLDS, W. C. & CARR, L. W. 1985 Review of unsteady, driven, separated flows. In *AIAA*, pp. 1–46. AIAA-85-0527.
- RHODES, M. 2008 *Introduction to particle technology*, 2nd edn. Hoboken, NJ : Wiley.
- ROCKWELL, D. & LIN, J.-C. 1993 Quantitative interpretation of complex, unsteady flows via high-image-density particle image velocimetry. In *In Optical Diagnostics in Fluid and Thermal Flow, Proc. SPIE (Intl Soc. Optical Engng)*, , vol. 2005, pp. 490–503.

- ROCKWELL, D., MAGNESS, C., TOWFIGHI, J., AKIN, O. & CORCORAN, T. 1993 High image-density particle image velocimetry using laser scanning techniques. *Exp. Fluids* **14**, 181–192.
- ROSEN, J. 1995 *Symmetry in science: An introduction to the general theory*. Springer-Verlag, New York.
- ROSHKO, A. 1954 On the development of turbulent wakes from vortex streets. *NACA Report 1191* pp. 1–25.
- ROSHKO, A. 1993 Perspectives on bluff body aerodynamics. *J. Wind Eng. Ind. Aerod.* **49**, 79–100.
- RYAN, K., THOMPSON, M. C. & HOURIGAN, K. 2005 Three-dimensional transition in the wake of bluff elongated cylinders. *J. Fluid Mech.* **538**, 1–29.
- SARPKAYA, T. 1976a Forces on cylinders near a plane boundary in a sinusoidally oscillating fluid. *J. Fluid Eng.-T. ASME* **98**, 499–505.
- SARPKAYA, T. 1976b Vortex shedding and resistance in harmonic flow about smooth and rough circular cylinders at high Reynolds numbers. *Tech. Rep. NPS-59SL76021*. Naval postgraduate school.
- SARPKAYA, T. 1979 Vortex induced oscillations, a selective review. *J. Appl. Mech.-T. ASME* **46**, 241–258.
- SARPKAYA, T. 1986 Force on a circular cylinder in viscous oscillatory flow at low Keulegan-Carpenter numbers. *J. Fluid Mech.* **165**, 61–71.
- SARPKAYA, T. 2002 Experiments on the stability of sinusoidal flow over a circular cylinder. *J. Fluid Mech.* **457**, 157–180.
- SARPKAYA, T. 2004 A critical review of the intrinsic nature of vortex-induced vibrations. *J. Fluid. Struct.* **19**, 389–447.
- SARPKAYA, T. 2005 On the parameter  $\beta = Re/KC = D^2/\nu T$ . *J. Fluid. Struct.* **21** (4), 435–440.
- SARPKAYA, T. & ISAACSON, M. 1981 *Mechanics of Wave Forces on Offshore Structures*. Van Nostrand Reinhold Company.
- SAVKAR, S. 1977 A survey of flow-induced vibrations of cylindrical arrays in cross flow. *J. Fluid Eng.-T. ASME* **99**, 517–519.
- SCHLICHTING, H. 1932 Berechnung ebner periodischer grenzschicht strömungen. *Physikalische Zed.* **33**, 327–335.

- SCHMIDT, C. W. & SMITH, D. R. 2004 An investigation of the wake behind a circular cylinder with sinusoidal rotational forcing. In *42<sup>nd</sup> AIAA Aerospace science meeting & exhibit, Reno, NV, USA*, pp. 1–9. AIAA-2004-0924.
- SEYDEL, R. 1994 *Practical Bifurcation and Stability Analysis*. Springer.
- SHEARD, G., THOMPSON, M. C. & HOURIGAN, K. 2003 From spheres to circular cylinders: the stability and flow structures of bluff ring wakes. *J. Fluid Mech.* **492**, 147–180.
- SHIELS, D., LEONARD, A. & ROSHKO, A. 2001 Flow-induced vibration of a circular cylinder at limiting structural parameters. *J. Fluid. Struct.* **15**, 3–21.
- SINGH, S. & MITTAL, S. 2005 Vortex-induced oscillations at low Reynolds numbers: Hysteresis and vortex-shedding modes. *J. Fluid. Struct.* **20**, 1085–1104.
- STANSBY, P. K. 1974 The effect of end plates on the base pressure coefficient of a circular cylinder. *Aeronaut. J.* **78**, 36–37.
- STANSBY, P. K. 1976 The locking-on of vortex shedding due to the cross-stream vibration of circular cylinders in uniform and shear flows. *J. Fluid Mech.* **74**, 641–665.
- STEWART, B. E., THOMPSON, M. C., LEWEKE, T. & HOURIGAN, K. 2010 The wake behind a cylinder rolling on a wall at varying rotation rates. *J. Fluid Mech.* (In press).
- STOKES, G. G. 1851 On the effect of the internal friction of fluids on the motion of pendulums. *Trans. Cambridge Philos. Soc.* **9**, 8–106.
- STREITLIEN, K., TRIANTAFYLLOU, G. S. & TRIANTAFYLLOU, M. 1996 Efficient foil propulsion through vortex control. *AIAA J.* **34** (11), 2315–2319.
- STROUHAL, V. 1878 Uber eine besondere Art der Tonerregung. *Ann. Physik. Chem.* **5** (10), 216–251.
- SUMER, B. M. & FREDSE, J. 1997 *Hydrodynamics around cylindrical structures.*, 1st edn., *Advanced Series on Ocean Engineering*, vol. 12. World Scientific.
- SZEPESSY, S. 1993 On the control of circular cylinder flow by end plates. *Eur. J. Mech. B-Fluid* **12** (2), 217–244.
- SZEPESSY, S. & BEARMAN, P. W. 1992 Aspect ratio and end plate effects on vortex shedding from a circular cylinder. *J. Fluid Mech.* **234**, 191–217.
- TANEDA, S. 1956 Experimental investigation of the wakes behind cylinders and plates at low Reynolds numbers. *J. Phys. Soc. Jpn.* **11** (3), 302–307.
- TANEDA, S. 1978a Visual observations of the flow past a circular cylinder performing a rotary oscillation. *J. Phys. Soc. Jpn.* **45** (3), 1038–1043.

- TANEDA, S. 1978b Visual observations of the flow past a sphere at Reynolds numbers between  $10^4$  and  $10^6$ . *J. Fluid Mech.* **85**, 187–192.
- TATSUNO, M. 1973 Circulatory streaming around an oscillating circular cylinder at low Reynolds numbers. *J. Phys. Soc. Jpn.* **35** (3), 915–920.
- TATSUNO, M. 1981 Secondary flow induced by a circular cylinder performing unharmonic oscillations. *J. Phys. Soc. Jpn.* **50** (1), 330–337.
- TATSUNO, M. & BEARMAN, P. W. 1988 Visual study of the flow induced by a cylinder performing sinusoidal oscillations. *Bulletin 66, Research Institute for Applied Mechanics, Kyushu University*.
- TATSUNO, M. & BEARMAN, P. W. 1990 A visual study of the flow around an oscillating circular cylinder at low Keulegan-Carpenter numbers and low Stokes numbers. *J. Fluid Mech.* **211**, 157–182.
- THIRIA, B., GOUJON-DURAND, S. & WESFREID, J. E. 2006 The wake of a cylinder performing rotary oscillations. *J. Fluid Mech.* **560**, 123–147.
- THOMPSON, M. C., HOURIGAN, K., CHEUNG, A. & LEWEKE, T. 2006a Hydrodynamics of a particle impact on a wall. *Appl. Math. Model.* **30** (11), 1356–1369.
- THOMPSON, M. C., HOURIGAN, K., RYAN, K. & SHEARD, G. 2006b Wake transition of two-dimensional cylinders and axisymmetric bluff bodies. *J. Fluid. Struct.* **22** (6), 793–806.
- THOMPSON, M. C., HOURIGAN, K. & SHERIDAN, J. 1996 Three-dimensional instabilities in the wake of a circular cylinder. *Exp. Therm. Fluid Sci.* **12**, 190–196.
- THOMPSON, M. C. & LE GAL, P. 2004 The Stuart-Landau model applied to wake transition revisited. *Eur. J. Mech. B-Fluid* **23**, 219–228.
- TOKUMARU, P. T. & DIMOTAKIS, P. E. 1991 Rotary oscillation control of a cylinder wake. *J. Fluid Mech.* **224**, 77–90.
- TOKUMARU, P. T. & DIMOTAKIS, P. E. 1993 The lift of a cylinder executing rotary motions in a uniform flow. *J. Fluid Mech.* **255**, 1–10.
- TRIANAFYLLOU, M. S., TRIANAFYLLOU, G. S. & GOPALKRISHNAN, R. 1991 Wake mechanics for thrust generation in oscillating foils. *Phys. Fluids A* **3** (12), 2835–2837.
- UZUNOĞLU, B., TAN, M. & PRICE, W. G. 2001 Low-Reynolds-number flow around an oscillating cylinder using a cell viscous boundary element method. *Int. J. Numer. Meth. Engng.* **50**, 2317–2338.
- VAN DYKE, M. 1982 *An Album of Fluid Motion*. The Parabolic Press.

- VESTOSINT 2010 VESTOSINT, high performance polymers (degussa). <http://www.vestosint.com/en/products/index.shtml>.
- WANG, C.-Y. 1968 On high-frequency oscillatory viscous flows. *J. Fluid Mech.* **32**, 55–68.
- WESTERWEEL, J. 1997 Fundamentals of digital particle image velocimetry. *Meas. Sci. Technol.* **8**, 1379–1392.
- WILLIAMSON, C. H. K. 1985 Sinusoidal flow relative to circular cylinders. *J. Fluid Mech.* **155**, 141–174.
- WILLIAMSON, C. H. K. 1988 The existence of two stages in the transition to three-dimensionality of a circular cylinder wake. *Phys. Fluids* **31**, 3165–3168.
- WILLIAMSON, C. H. K. 1989 Oblique and parallel mode of vortex shedding in the wake of a circular cylinder at low Reynolds numbers. *J. Fluid Mech.* **206**, 579–627.
- WILLIAMSON, C. H. K. 1996a Three-dimensional vortex dynamics in bluff body wakes. *Exp. Therm. Fluid Sci.* **12** (2), 150–168.
- WILLIAMSON, C. H. K. 1996b Three-dimensional wake transition. *J. Fluid Mech.* **328**, 345–407.
- WILLIAMSON, C. H. K. 1996c Vortex dynamics in the cylinder wake. *Annu. Rev. Fluid Mech.* **28**, 477–539.
- WILLIAMSON, C. H. K. & GOVARDHAN, R. 2004 Vortex-induced vibration. *Annu. Rev. Fluid Mech.* **36**, 413–455.
- WILLIAMSON, C. H. K. & ROSHKO, A. 1988 Vortex formation in the wake of an oscillating cylinder. *J. Fluid. Struct.* **2** (4), 355–381.
- WILLIAMSON, C. H. K. & ROSHKO, A. 1990 Measurements of base pressure in the wake of a cylinder at low Reynolds number. *Z. Flugwiss. Weltraumforsch.* **14**, 38–46.
- WU, J., SHERIDAN, J., WELSH, M. C. & HOURIGAN, K. 1996 Three-dimensional vortex structures in a cylinder wake. *J. Fluid Mech.* **312**, 201–222.
- WU, J. M., MO, J. D. & VAKILI, A. D. 1989 On the wake of a cylinder with rotational oscillations. In *AIAA 2<sup>nd</sup> Shear Flow Conference*, pp. 1–10. AIAA-89-1024.
- YANG, Y. & ROCKWELL, D. 2002 Wave interaction with a vertical cylinder: spanwise flow patterns and loading. *J. Fluid Mech.* **460**, 93–129.
- ZDRAVKOVICH, M. M. 1997 *Flow around circular cylinders, Vol 1: Fundamentals*. Oxford University Press, Oxford.

- ZHANG, H.-L. & ZHANG, X. 1997 Flow structure analysis around an oscillating circular cylinder at low KC number: A numerical study. *Comput. Fluids* **26** (1), 83–106.
- ZHANG, H.-Q., FEY, U., NOACK, B. R., KÖNIG, M. & ECKELMANN, H. 1995 On the transition of the cylinder wake. *Phys. Fluids* **7** (4), 779–793.
- ZHANG, J. & DALTON, C. 1999 The onset of three-dimensionality in an oscillating flow past a fixed circular cylinder. *Int. J. Numer. Meth. Fl.* **30** (1), 19–42.
- ZHOU, T., WANG, H., MOHD. RAZALI, S. F., ZHOU, Y. & CHENG, L. 2010 Three-dimensional vorticity measurements in the wake of a yawed circular cylinder. *Phys. Fluids* **22** (1), 015108.